AN EXACT ANALYSIS AND DESIGN OF AUTO-SEQUENTIALLY COMMUTATED CURRENT SOURCE INVERTERS (ASCI)

BY

MORTEZA SHOWLEH

A THESIS
IN
THE DEPARTMENT
OF
ELECTRICAL ENGINEERING

PRESENTED IN PARTIAL FULFILLMENT OF THE REQUIREMENTS FOR
THE DEGREE OF MASTER OF ENGINERING AT
CONCORDIA UNIVERSITY
MONTREAL, QUEBEC, CANADA

JULY 1979

SOMMAIRE

CONCEPTION ET ANALYSE D'UN COMMUTATEUR DE COURANT À COMMUTATION AUTO-SÉQUENTIELLE

MORTEZA SHOWLEH

Ce mémoire décrit un commutateur de courant à commutation auto-séquentielle et en donne une analyse détaillée qui tient compte des effets de la bobine de lissage, du chevauchement partiel et de l'opération des circuits limiteurs de tension. Dans ce but, une nouvelle méthode a été développée pour calculer les divers paramètres du commutateur à partir du modèle classique et approximatif qui considère constant le courant continu. Des graphiques obtenus à partir du modèle approximatif et d'un modèle exact, montrent la variation des paramètres clefs du commutateur en fonction des conditions d'opération. De plus, ils indiquent clairement que l'hypothèse de considérer le courant continu comme constant est justifiée la plupart du temps. Cette conclusion a été vérifiée en comparant les tensions et les courants obtenus à partir des deux modèles.

De nombreux essais en laboratoire ont permis de certifier le validité du modèle exact. La comparaison des résultats expérimentaux et des valeurs calculées démontrent que le modèle exact prédit non seulement l'allure générale des courants et des tensions mais aussi leurs variations mineures (ondulation, etc.)

Finalement, ce mémoire donne tous les renseignement utiles pour concevoir un commutateur de courant à partir de l'un ou l'autre des deux modèles.

ABSTRACT

AN EXACT ANALYSIS AND DESIGN OF AUTO-SEQUENTIALLY COMMUTATED CURRENT SOURCE INVERTERS (ASCI)

MORTEZA SHOWLEH

An exact analysis and a design of an autosequentially commutated (current source) inverter, which includes the effects of a dc link filter, partial commutation overlap and the operation of a voltage clamping circuit is presented. At the same time, a new method for calculating the inverter variables by using a standard, approximate model, which assumes a constant dc link current, is developed. The curves showing the variation of key inverter variables with a change in operating conditions are obtained by using both exact and approximate models. The comparison of these curves shows that the assumption of a constant dc link current is justified in most cases. This conclusion is corroborated by comparing the voltage and current waveforms obtained by using these two models.

Extensive laboratory tests were conducted in order to verify the correctness of the exact model. The comparison of the experimental and the computed results show that the exact model predicts not only the general shape of the voltage and current waveforms, but also the minor variations, ripples, etc.

Finally, all information necessary for a design of a current source inverter by using either the approximate or the exact model is presented.

ACKNOWLEDGEMENTS

I wish to express my thanks to Dr. V.R. Stefanovic, my research advisor, for his guidance, support and encouragement during all the stages of this project.

My gratitude to the Power Control Division; Cutler-Hammer, Milwaukee, for their financial assistance for this study and for providing the author with the experimental results is also acknowledged. The few oscillograms used in this thesis were selected from among over 200 photographs which have been produced in the C-H laboratories.

My indebtedness to Mr. J.R. Hwang, with whom I had useful discussions in the early stages of this research is acknowledged, and my deepest appreciation is reserved for my parents for their unsparing support, and for my wife, Mehrnaz, without whose patience this task could not have been accomplished. My thanks also to my daughter, Anousheh, who was not receiving the full services of a father.

The excellent typing of this manuscript was done by Ms. Evelyn Sadubin and Ms. June Anderson, whom I also wish to acknowledge.

TABLE OF CONTENTS

Page

Page

Page

Page

LIST OF FIGURES AND TABLES

Page

CHAPTER IV

CHAPTER V

CHAPTER VI

CHAPTER VII

CHAPTER VIII

LIST OF SYMBOLS

As far as possible, lower case letters indicate instantaneous values of the quantities concerned, while upper case letters signify constant, RMS, average, direct or peak values. The symbols are employed with subscripts to refer to particular circuit quantities.

$d_1 - d_6$	Clamping circuit diodes
e	Base of natural logarithms
e_1	Motor phase CEMF
f	Inverter output or motor input frequency
f_b	Base frequency
f_{max}	Inverter maximum output frequency
f_r	Rotor rotational frequency
f_s	Motor fundamental synchronous frequency
i	current
i_{1A}	Motor terminal A fundamental harmonic of input current
i_d	dc link current
i_{d1}, i_{d2}, i_{d3}, i_{d4}	dc link current at $t=t_1$, t_2, t_3 or t_4, respectively

$i_{o_{d1}}$	Initial value of i_{d1} at the start of each iteration
i_{os}	Oscillating current during thyristor commutation
i_s	Stator input current
i_z	Clamping circuit current
$j = \sqrt{-1}$	Complex number operator
$\ell_1 - \ell_6$	Thyristor T_1 - T_6 di/dt inductances
m	A damping factor appearing in the derivations of a transfer mode in case (g)
n	Stator harmonic number
n	Subscript for a newly calculated variable in the flowcharts
n	An angular frequency appearing in the derivations of a transfer mode in case (g)
o	Subscript for a previously calculated variable in the flowcharts
p	$\frac{d}{dt}$ operator
s	Laplace transform operator
t	Time scale with the positive crossover of i_{1A} as the time origin

t_1, t_4, t_7, t_{10}, t_{13}, t_{16}

The instant T_1, T_2, T_3, T_4, T_5 or T_6 is triggered, respectively, in all cases

t_2, t_5, t_8, t_{11}, t_{14}, t_{17}

The instant D_1, D_2, D_3, D_4, D_5 or D_6 is turned on, respectively, in all cases

t_3, t_6, t_9, t_{12}, t_{15}, t_{18}

The instant D_5, D_6, D_1, D_2, D_3 or D_4 is turned off, respectively, in the non-clamped cases

t_3, t_6, t_9, t_{12}, t_{15}, t_{18}

The instants D_z is turned off in a clamped case

t_{21}, t_{51}, t_{81}, t_{111}, t_{141}, t_{171}

The instant D_5, D_6, D_1, D_2, D_3 or D_4 is turned off, respectively, in a clamped case, while D_z is turned on

t_a Time scale with t_1 as the time origin, case (g)

t_{a1} Charging interval in case (g)

t_{ch} Charging interval

t_{co} Commutation interval

t_{no} Normal interval

t_{o1} Initial value for t_1 at the start of each iteration

t_{ov}	Overlap interval
t_{tr}	Transfer interval
t'	Time scale with t_2 as the time origin
t'_1	Same as t_{tr}, in a non-clamped case
t'_1	The first part of t_{tr} in a clamped case
t''	Time scale with t_3 as the time origin, case (g)
t''	Time scale with t_{21} as the time origin in a clamped case
t''_1	Same as t_{no}, case (g)
t''_1	Clamping interval or the second part of t_{tr} in a clamped case
v	Voltage
v_I	Inverter input voltage
v_s	Stator terminal voltage
A, B, C, N	Motor terminals and neutral point
ASCI	Auto-sequentially commutated current source inverter
C	Capacitance of commutating capacitors

$C_1 - C_6$	Commutating capacitors
CI	Constant dc link current assumption
CL	ASCI operation with a clamping circuit
CV	dc link constant input voltage assumption
$D_1 - D_6$	Series diodes
D_z	String of zener diodes in the clamping circuit
E_1	Peak fundamental harmonic of motor phase CEMF
I	Current
I_1	Peak fundamental harmonic of motor phase input current
I_{1A}	Peak fundamental harmonic of motor phase A input current
I_{av1}	dc link average current in a charging mode
I_{av2}	dc link average current in a transfer mode
I_{av3}	dc link average current in a normal mode
I_{CRMS}	Commutating capacitor RMS current
I_d	dc link average current
$I_m(Z)$	Imaginary part of Z

I_{ns}	Motor peak input current for n-th harmonic
I_{Zmax}	Clamping circuit maximum current
I_{ZRMS}	Clamping circuit RMS current
L	Inductance
L	Sum of stator leakage and rotor referred leakage inductances
L^{-1}	Inverse Laplace transform operator
L_1	Stator leakage inductance
L_2	Rotor referred leakage inductance
$L_a = L_f + L$	
$L_{eq} = L_f + 2L$	
L_f	dc link inductance
L_m	Magnetizing inductance
NC	ASCI operation without a clamping circuit
N_p	Motor pole numbers
P	Power
P_1	Per phase motor total input power
P_{tm}	Motor total input power

P_z	Clamping circuit power loss
R	Resistance
R_1	Stator resistance
R_2	Rotor referred resistance
$R_a = R_f + R_1$	
$R_{eq} = R_f + 2R_1$	
$R_e(Z)$	Real part of Z
R_f	dc link resistance
R_m	Magnetizing referred resistance
S_n	Motor slip for n-th harmonic
T	Periodic time
T	Torque
$T_1 - T_6$	Inverter thyristors
T_{max}	Motor pull-over torque
T_{PU}	Per unit output torque
T_{os}	Thyristor commutation interval
V	Voltage
V_o	Commutating capacitor maximum voltage at each operating point

V_{oo}	Initial value for V_o at the start of each iteration
V_d	dc link average input voltage
V_{od}	Initial value for V_d at the start of each iteration
V_{DRmin}	Series diode minimum reverse voltage
V_{DRmax}	Series diode maximum reverse voltage
V_I	Inverter average input voltage
V_L	Motor rated line-to-line RMS voltage
V_L	Bridge input line-to-line RMS voltage
V_{ns}	Peak motor phase voltage for n-th harmonic
$V_{ph} = V_{RMS}$	Motor phase RMS voltage
V_z	Clamping circuit breakdown voltage
W_{z1}	Clamping circuit energy loss in each clamping period
W_{z6}	Clamping circuit energy loss in each inverter period
X_1	Stator reactance at fundamental frequency
X_2	Rotor referred reactance at fundamental frequency

X_m	Magnetizing reactance at fundamental frequency
Z_{1n}	Stator impedance for n-th harmonic
Z_{2n}	Rotor referred impedance for n-th harmonic
Z_{en}	Referred impedance across magnetizing branch in the exact equivalent circuit for n-th harmonic
Z_{eqn}	Referred impedance across magnetizing branch in the series equivalent circuit for n-th harmonic
Z_{mn}	Magnetizing referred impedance for n-th harmonic
Z_{tn}	Motor input impedance for n-th harmonic
$\alpha = R_1/2L$	Damping factor during a transfer mode in case (a)
$\alpha = R_1/2L$	Damping factor during the first part of a transfer mode in case (d)
$\alpha_1 = R_1/L$	Damping factor during a clamping mode in case (d)
$\alpha_1 = R_{eq}/2L_{eq}$	Damping factor during a charging mode in case (g)
$\alpha = R_{eq}/L_{eq}$	Damping factor during a normal mode in case (g)
α_{ch}	Charging mode angle in degrees
α_{co}	Commutation angle in degrees
α_{tr}	Transfer angle in degrees

ε, ε_1, ε_2	Relative errors
η	System efficiency without thyristor and diode switching losses
ν	Shift angle of i_{1A} with respect to the previous origin of time in each iteration
τ	Time scale with $t' = 0$ as the time origin
ω	Motor fundamental input angular frequency
ω_{max}	Inverter maximum output angular frequency
$\omega_o = (1/3LC)^{1/2}$	Resonant frequency in a transfer mode in case (a)
$\omega_o = (1/3LC)^{1/2}$	Resonant frequency in the first part of a transfer mode in case (d)
$\omega_o = (2/3L_{eq}C)^{1/2}$	Resonant frequency in a charging mode in case (g)
$\omega_1 = (\frac{1}{3LC} - \frac{R1}{2L})^{1/2}$	Ringing frequency in a transfer mode in case (a)
$\omega_1 = (\frac{1}{3LC} - \frac{R1}{2L})^{1/2}$	Ringing frequency in the first part of a transfer mode in case (d)
$\omega_1 = (\frac{2}{3L_{eq}C} - \frac{R_{eq}}{2L_{eq}})^{1/2}$	Ringing frequency in a charging mode in case (g)
ϕ_1	Phase angle between I_1 and E_1

CHAPTER I

INTRODUCTION

The present trend towards increased application of variable speed AC motor drives is reflected in continuing development of static power converters. Specifically, the inverter design procedures which were until recently based mostly on experience and state of the art, are now being rationalized and standardized. Among many different inverter types used in adjustable speed AC motor drives, the auto-sequentially commutated current source inverter has received special attention in recent years. This is mainly due to its simple circuit, the capability to ride through misfirings and temporary commutation failures, immunity against short circuits and the ability to regenerate. An induction motor has excellent inherent characteristics such as ruggedness, simplicity, low inertia rotor, low maintenance cost, the ability to operate in hazardous environments, the possiblity of high speed operation without gears and the availability of very large horsepowers. When such a motor is connected to an ASCI, one obtains a drive with outstanding qualities. Such a drive has a fast response to load changes, a wide range of speeds and a capability of four quadrant operation [1-9].

The basic scheme of an ASCI-induction motor drive is shown in fig. 1.1. While other inverter configurations may also be used, in this thesis only an ASCI is considered. The thyristor bridge along with

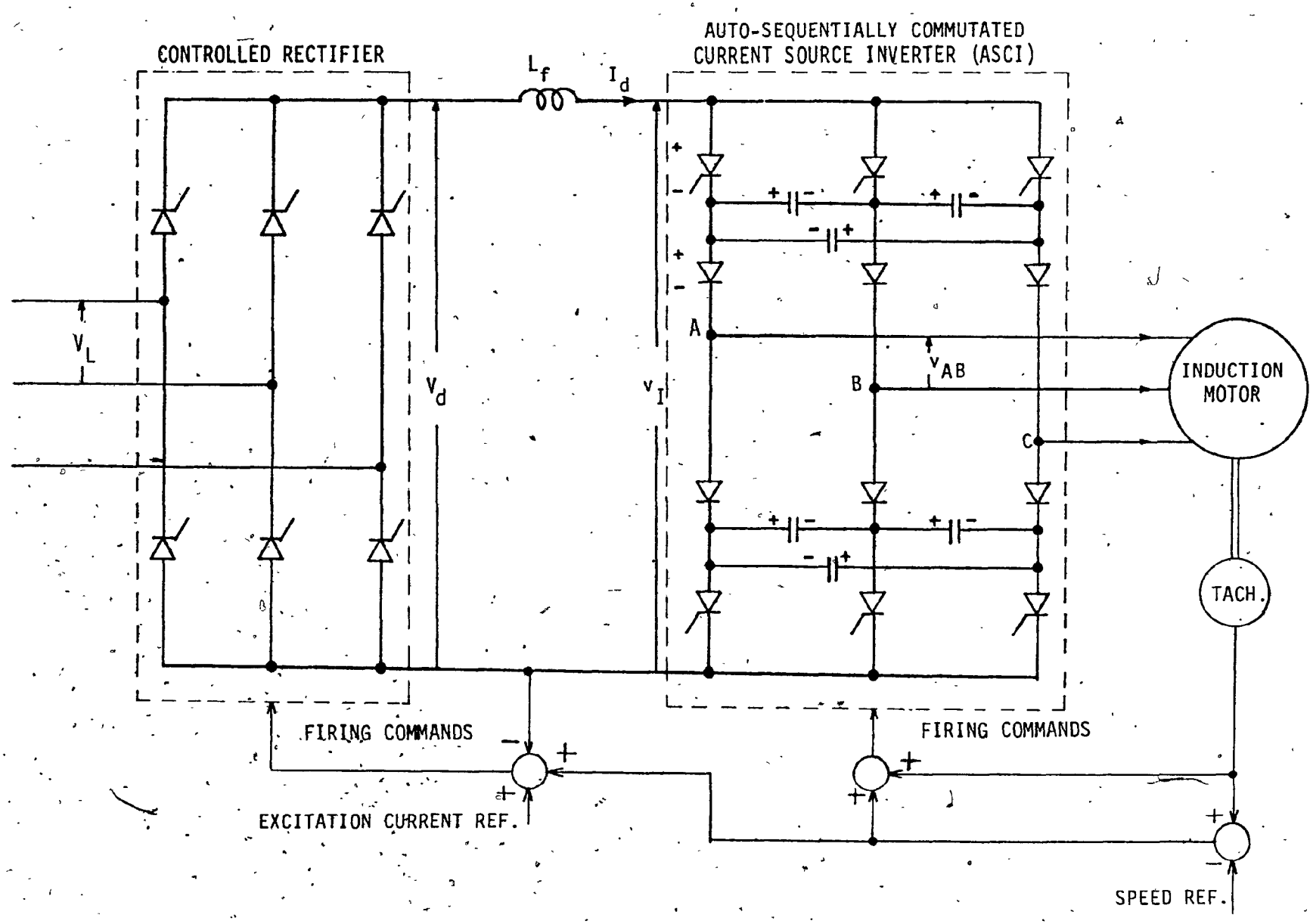

FIG. 1.1. Basic circuit of an auto-sequentially commutated current-source inverter (ASCI) - induction motor drive.

the dc link choke represent a dc current source which provides the inverter with a regulated, almost constant dc current.

This thesis presents a detailed study of a computer aided design procedure for an auto-sequentially commutated current source inverter supplying an induction motor load, fig. 1.1. The procedure specifies the voltage and the current ratings of all ASCI components for a given set of input data, which normally includes:

- All electrical parameters of the connected induction motor,
- Motor rated current, voltage, frequency and horsepower,
- Motor speed range, and
- Motor permissible overloading.

In order to calculate the ratings of the inverter components, it is necessary to have an accurate model of the inverter-motor drive operation, especially with respect to the inverter commutation process. Although the ASCI commutation circuit is very simple, its analysis is complex due to the interaction of the commutating phase with the other two phases and the motor load. Thus, unlike the voltage source, impulse commutated inverters, where the analysis of the commutation circuit can be decoupled from the rest of the system, the

exact modelling of an ASCI has to include not only all three phases at the same time, but also the motor parameters and the effect of the operating point.

The concept of a current source inverter has been known for decades [10]. With the invention of the thyristor, many converter circuits, developed in the age of thyratrons and mercury arc rectifiers were revived. Ward [11] was first to use thyristors in the original Mittag bridge [10] while studying the performance of single and three phase current source inverters with resistive loads. Since the main characteristic of such inverters is the generation of voltage spikes several times the supply voltage, application of such inverters to induction motor drives had to wait for the development of high voltage thyristors. The first general description of an ASCI-induction motor drive was given by Phillips [1] while a more detailed analysis of a commutation process and a derivation of a series equivalent circuit for the induction motor was presented by Farrer et.al. [3]. (The series equivalent circuit takes into account the higher harmonics of the input current. With a minor modification this circuit is used in this study.) A very complete study and a comparison of an ASCI with an auxiliary commutated current source inverter was done by Brennen [4]. Due to the modelling complexity, most of the studies of an ASCI-squirrel cage motor drive have assumed a constant dc link current and an instantaneous commutation [1, 2, 5, 12, 13]. More detailed studies have been performed by either digital or analog simulation [4, 7, 14, 15]. Also, some investigations have been accomplished by other approaches; Park's vector [16], symmetrical

components [17] and signal flow graphs [18]. For a stable operation, an ASCI-motor drive has to work in a closed-loop configuration. The control, stability and transient behaviour of such drives has been a topic of several papers [6, 8, 12, 13, 19 - 22].

The performance of a current source inverter at high frequencies, especially with light loads, is different from its behaviour at low frequencies. Under these conditions, due to the interaction between phases, the analysis of the inverter operation becomes rather difficult. For a single phase inverter, [23] gives an analytical approach to the study of the inverter different operational modes, while [24] provides more details and employs digital simulation for this purpose. For an ASCI-induction motor, the study of the operational modes has been mostly performed by digital simulation [14 - 16], owing to the number of switching components. These references give the details of the performance of the drive under partial and full commutation overlap. The transient forward biasing of a series diode has also been studied. This case may occur even with commutation angles less than 60° where an isolating diode may become forward biased in the group of thyristors in which the commutating capacitors are under linear charging. This phenomenon causes the conduction of three diodes at the same time such that some part of the dc link current bypasses the motor and causes the motor output power to be reduced [14, 16, 25].

In addition to the approximation introduced by considering a constant dc link current, the stator resistance and the variation

of the motor counter electromotive force during commutation period were also often neglected. Although such modelling is generally justified, it is not always accurate in the inverter design which then has to rely very much on the previous experience. A better model is obtained by including the effects of the dc link filter, stator resistance, counter electromotive force (CEMF) and possibly magnetic saturation on the commutation process. In order to include the dc link filter, one should replace the assumption of a constant dc link current by an assumption of a constant rectifier voltage, V_d, fig. 1.1.

The assumption of a constant voltage at the input terminals of the dc link has already been studied but in different ways. In [12], the same value of the dc link average input voltage has been applied to all operating points. This implies the same firing angle for the bridge thyristors while the load at the motor shaft is changed, which is rarely the way the system operates. In [13] and [26], the assumption of a constant voltage is employed for obtaining an equivalent circuit for the system. In all of the above cases, a square waveform has been considered for the motor input currents. In this thesis, the concept of a constant voltage at the input terminals of the dc link has been employed for setting up the system equations without neglecting the stator resistance, the commutation process and the variation of the motor CEMF during each commutation period. In addition, the constant voltage assumption can be extended to the study of the effects of different dc link parameters on the system operation and consequently, the design of the dc link filter.

The content of each chapter is now briefly summarized. In Chapter II, a description of the system operation and a derivation of a series equivalent circuit for an induction motor fed by an ASCI is presented. The method to estimate the average dc link current and the summary of the assumptions used in this thesis are also given in this chapter. In Chapter III, the equations of the system are obtained for three basic operating modes for a no-overlap, constant dc link current case. The equations obtained in this stage of the study do not have a closed form so that two methods for solving these equations, one approximate and one exact, are presented. In the approximate method, a new equation is developed while in the second method, an iterative procedure is followed. Each method is then summarized in a flowchart. Besides, the results obtained in this stage are used as initial values in solving the equations determined for the system with a constant voltage approach, which again are not in a closed form.

In order to exploit the system to its full capabilities, the operation with a commutation overlap, while the dc link current is constant, has been examined in Chapter IV. This study shows that the system can operate without any problems under partial commutation overlap, where the commutation process may occupy one third of the output period. The only constraint is that there should be no current bypassing the induction motor [14 - 16, 25]. Under these conditions, the same procedure used in a no-overlap case can also be applied to a partial overlap mode for calculating the values of the variables. In this way, the capacitance of the commutating capacitor is determined,

using the maximum limit frequency of the system for a partial commutation overlap. In Chapter V, the results of the study done in Chapter III are presented in two sets of graphs. The first set shows the different voltage and current waveforms of the system, while the second one displays the variation of each variable for different load conditions.

An ASCI is characterized by the voltage spikes across its output. These spikes can reach levels several times the motor rated voltage. Although the high values of these spikes might not cause any problems to the performance of the motor due to their short intervals, the voltage ratings of the inverter components are directly dependent on them. In some applications, owing to economical or technical reasons, these high levels of voltage are not desirable and are limited by some type of clamping circuit. The study of the system performance with a zener clamping circuit and a constant dc link current is presented in Chapter VI. This clamping circuit consists of a three phase diode bridge, with a string of zener diodes connected across its dc terminals. The zener clamping circuit has been used in industry for several years and is not new, but a detailed study of an ASCI-induction motor with a zener clamping circuit is lacking in the literature. The derived equations are solved by iterative methods in two ways. Each method is illustrated in a flowchart. The second flowchart is employed in plotting two sets of graphs. The first set exhibits the different voltage and current waveforms of the system at an operating point in which the clamping circuit enters into the system. The second set of graphs is used for comparison of the variations of variables in a

clamped operation with those of a non-clamped condition. This comparison reveals that the operation of the system under heavy loads and with high frequencies is not possible. The reason is the exorbitant power loss in the zener diodes. In addition, under these conditions, the bridge output average voltage reaches its limit so that for the required current, the voltage would not be sufficient.

The partial commutation overlap study for the case with a clamping circuit shows that the system can obtain frequencies higher than the limit required for a 60° commutation angle. Here again, the same procedure as in a no-overlap case mentioned above can be applied for calculating the results. For a proper operation of the drive the constraint on the transient forward biasing of the series diodes should be satisfied in this case too.

The last step in analysing the system is introduced in Chapter VII, where by assuming a constant voltage across the input terminals of the dc link, the equations of the system are derived for a no-overlap operation. The discussion for solving the equations and a flowchart follows next. This chapter ends by showing two sets of graphs in which the results of constant voltage approach are compared with those already obtained in Chapter V. This comparison shows two major differences. First, the commutating capacitor maximum voltage obtains higher values with a constant voltage assumption than with a constant current assumption, which, at the same time, are closer to the values measured experimentally. Second, the voltage and current waveforms are very similar to those of the actual system. The dif-

ference in the commutating capacitor maximum voltage obtained in the two approaches is not too high (about 5%) so that the design of the inverter components can be performed by the constant dc link current assumption as long as the iterative method is applied to it.

The comparison between the theoretical and the experimental results is considered in Chapter VIII, where the voltage and current waveforms at two operating points are shown and compared with those obtained by digital simulation. The last chapter gives the conclusions of this study and the contributions made in analysis and design of an ASCI.

The Appendices include the motor parameters used for obtaining the experimental results, the specifications of two operating points, the magnetizing, leakage inductance and core-loss resistance curves, the Fourier analysis for calculating the fundamental harmonic of the motor input current for different steps of the study.

CHAPTER II

CURRENT SOURCE INDUCTION MOTOR DRIVE

2.1 INTRODUCTION

The circuit of an auto-sequential current source inverter (ASCI) has been fully described in literature [1-5,9]. This description will be briefly repeated here. In addition, a modified equivalent circuit of an induction motor (fig. 2.9) which includes the effects of all current harmonics will be shown [3]. The exact equivalent circuit of an induction motor (fig. 2.7 for n=1) will be used to calculate the fundamental components of current and torque.

The assumption of an ideal square waveform for the inverter output current will provide an approximate relationship between the inverter input dc current and the fundamental component of the load current. The assumptions used in deriving the mathematical model of such a drive will also be given.

2.2 AUTO-SEQUENTIAL CURRENT-SOURCE INVERTER (ASCI)

In its simplest form an auto-sequential commutated current source inverter consists of 6 thyristors, 6 blocking diodes and 6 commutating capacitors, fig. 2.1. We will also use this figure to describe the way in which such an inverter operates. The controlled rectifier, along with the dc link inductor, create a dc current which is fed into the inverter. For the time being, we assume this current to be constant and without any ripples, which implies that the dc link inductor has a very large value. As well, to simplify the description,

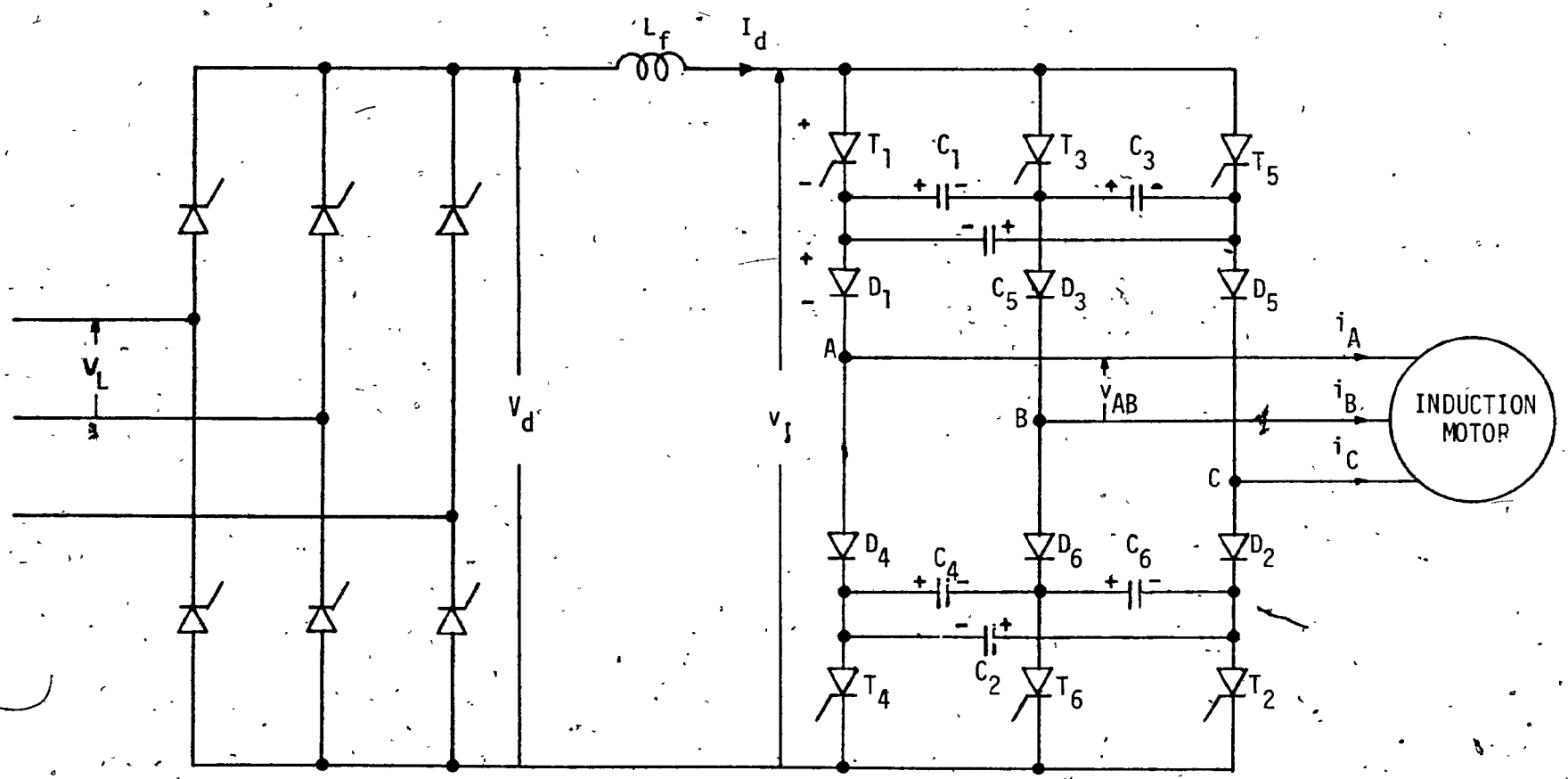

FIG. 2.1. Simplified circuit of a variable speed drive using an auto-sequential current source inverter (ASCI)

it will be supposed that the switching components, i.e., thyristors and diodes are ideal. These assumptions give zero voltage drops across conducting devices as well as their instantaneous turn-on and turn-off.

The T_1-T_6 thyristors are fired by an appropriate firing circuit which is not shown in figure 2.1. Only one thyristor is fired at a time. The firing sequence for the SCR's of figure 2.1 is shown in figure 2.2 In this figure t_1, t_4, ... denote the instants at which thyristors T_1, T_2, ... are fired. The sinusoidal waveform shows the fundamental component of the motor current in phase A. The instant at which this current passes through zero is selected as the starting point, $\omega t=0$. This SCR gating sequence would be the same for all steps in this report.

The rate at which SCR's are triggered determines the inverter output frequency. Commutating capacitors C_1-C_6 provide the necessary energy for turning off the thyristors, while diodes D_1-D_6 prevent the discharge of capacitors into the load. Each thyristor conducts for 120° with only two thyristors conducting at the same time. This report presents the system description and the inverter-motor mathematical model for a steady-state operation.

First we will explain the operation of the system for a no-overlap mode. A no-overlap mode is defined as an operation whereas one SCR is fired, no capacitor is in the process of charging or discharging.

In figure 2.1 thyristors T_1,T_3,T_5, capacitors C_1,C_3,C_5 and diodes D_1,D_3,D_5 show the upper group components while the others constitute the lower group. Figure 2.3 shows the circuit just before firing T_1 . In this case the dc link current flows through T_5, D_5 ,

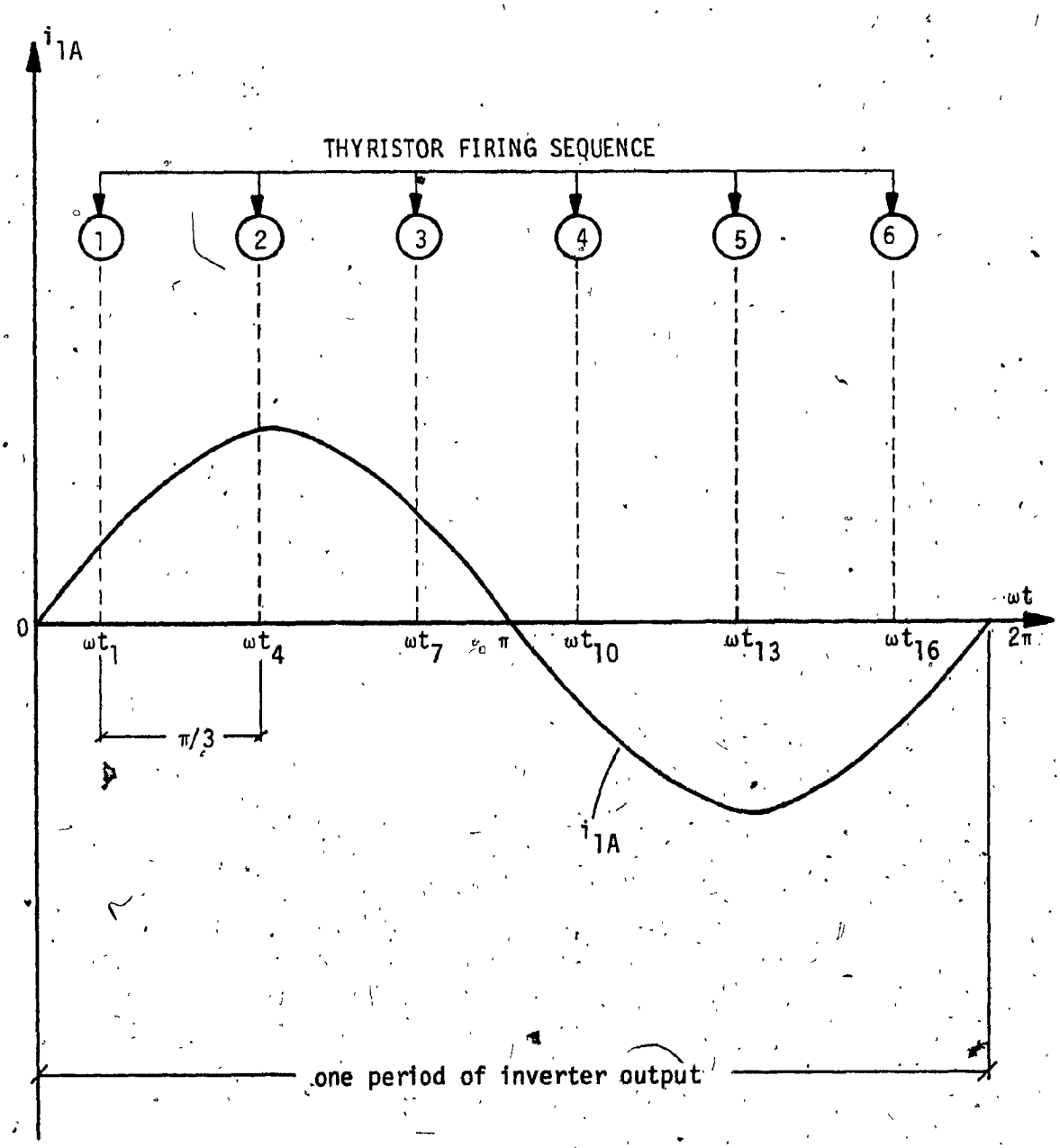

FIG. 2.2. The sequence of triggering SCR's in an ASCI

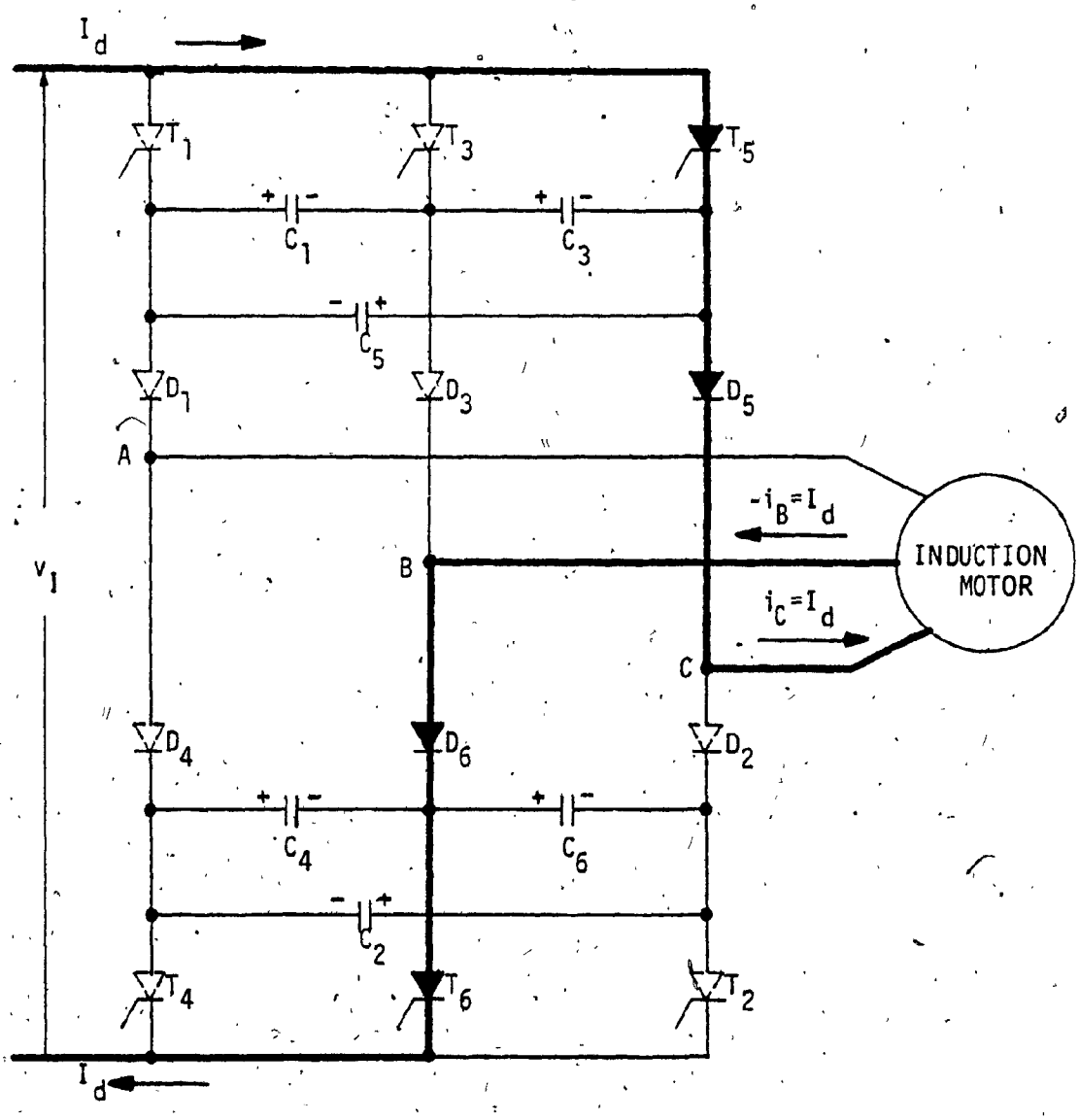

FIG. 2.3 ASCI-induction motor operation without commutation overlap during mode 18 (normal mode) when all capacitor voltages are constant. This mode ends when T_1 is fired.

motor phase C, motor phase B, D_6, T_6 and back to the supply. Note that C_5 has already been charged with polarities shown in fig. 2.3. At time $t=t_1$ thyristor T_1 is fired which commutates T_5. The clockwise convention is adopted to denote a positive capacitor voltage. Figure 2.4 shows the circuit just after firing T_1. Capacitor C_5 will be discharged linearly until $t=t_2$, when diode D_1 becomes forward biased. Figure 2.5 shows the circuit just after $t=t_2$. In this circuit current transfers from D_5 to D_1 and from motor phase C to motor phase A. This transfer continues till $t=t_3$ at which time the current in motor phase C becomes zero and all the dc link current flows through T_1, D_1, motor phase A, motor phase B, D_6 and T_6, fig. 2.6. This completes the commutation period of diode D_5.

The above explanation was based on the assumption that the inverter operates without a commutation overlap, i.e., all the capacitor currents are zero prior to the instant a thyristor is fired. Later, this assumption will be revised to include the case of commutation overlap.

A full cycle of inverter operation is obtained by completing the firing sequence for all thyristors, fig. 2.2. Each thyristor firing defines three different modes, giving a total of 18 modes for one complete cycle of the inverter output.

Tables 1.1-1.3 summarize these modes and give complete information about the status of each device during each of the modes.

2.3 THE EQUIVALENT CIRCUIT OF AN INDUCTION MOTOR

The system analyzed in this study consists of an inverter and an induction motor. In order to complete the mathematical model for

MODE			AT THE BEGINNING OF EACH MODE				DURING EACH MODE				
NO.	TYPE	INSTANT STARTS	TRIGGERED SCR	TURNED-OFF SCR	TURNED-ON DIODE	TURNED-OFF DIODE	CONDUCTING SCR's	CONDUCTING DIODES	MOTOR INPUT CURRENTS	COM.CAP.VOLTAGES CONSTANT	COM.CAP.VOLTAGES VARYING
1	charging	t_1	T1	T5	-	-	T1, T6	D5, D6	$i_A = 0$ $i_B = -I_d$ $i_C = I_d$	VC2 = 0 VC4 = $+V_o$ VC6 = $-V_o$	VC1 VC3 VC5
2	transfer	t_2	-	-	D1	-	T1, T6	D5, D6, D1	i_A ↗ $i_B = -I_d$ i_C ↘	VC2 = 0 VC4 = $+V_o$ VC6 = $-V_o$	VC1 VC3 VC5
3	normal	t_3	-	-	-	D5	T1, T6	D6, D1	$i_A = I_d$ $i_B = -I_d$ $i_C = 0$	VC2=VC3=0 VC4=VC1=$+V_o$ VC6=VC5=$-V_o$	-
4	charging	$t_4 = t_1 + \pi/3\omega$	T2	T6	-	-	T1, T2	D6, D1	$i_A = I_d$ $i_B = -I_d$ $i_C = 0$	VC1 = $+V_o$ VC3 = 0 VC5 = $-V_o$	VC2 VC4 VC6
5	transfer	$t_5 = t_2 + \pi/3\omega$	-	-	D2	-	T1, T2	D6, D1, D2	$i_A = I_d$ $-i_B$ ↘ $-i_C$ ↗	VC1 = $+V_o$ VC3 = 0 VC5 = $-V_o$	VC2 VC4 VC6
6	normal	$T_6 = t_3 + \pi/3\omega$	-	-	-	D6	T1, T2	D1, D2	$i_A = I_d$ $i_B = 0$ $i_C = -I_d$	VC1=VC6=$+V_o$ VC3=VC4=0 VC5=VC2=$-V_o$	-

↗ increasing
↘ decreasing

TABLE 1.1 Summary of ASCI modes 1-6, operation without commutation overlap.

MODE			AT THE BEGINNING OF EACH MODE				DURING EACH MODE				
NO.	TYPE	INSTANT STARTS	TRIGGERED SCR	TURNED-OFF SCR	TURNED-ON DIODE	TURNED-OFF DIODE	CONDUCTING SCR's	CONDUCTING DIODES	MOTOR INPUT CURRENTS	COM.CAP.VOLTAGES CONSTANT	COM.CAP.VOLTAGES VARYING
7	charging	$t_7 = t_1 + 2\pi/3\omega$	T3	T1	-	-	T3, T2	D1, D2	$i_A = I_d$ $i_B = 0$ $i_C = -I_d$	$VC2 = -V_o$ $VC4 = 0$ $VC6 = +V_o$	VC1 VC3 VC5
8	transfer	$t_8 = t_2 + 2\pi/3\omega$	-	-	D3	-	T3, T2	D1, D2, D3	$i_A \searrow$ $i_B \nearrow$ $i_C = -I_d$	$VC2 = -V_o$ $VC4 = 0$ $VC6 = +V_o$	VC1 VC3 VC5
9	normal	$t_9 = t_3 + 2\pi/3\omega$	-	-	-	D1	T3, T2	D2, D3	$i_A = 0$ $i_B = I_d$ $i_C = -I_d$	$VC2=VC1=-V_o$ $VC4=VC5=0$ $VC6=VC3=+V_o$	-
10	charging	$t_{10} = t_1 + n/\omega$	T4	T2	-	-	T3, T4	D2, D3	$i_A = 0$ $i_B = I_d$ $i_C = -I_d$	$VC1 = -V_o$ $VC3 = +V_o$ $VC5 = 0$	VC2 VC4 VC6
11	transfer	$t_{11} = t_2 + n/\omega$	-	-	D4	-	T3, T4	D2, D3, D4	$-i_A \nearrow$ $i_B = I_d$ $-i_C \searrow$	$VC1 = -V_o$ $VC3 = +V_o$ $VC5 = 0$	VC2 VC4 VC6
12	normal	$t_{12} = t_3 + n/\omega$	-	-	-	D2	T3, T4	D3, D4	$i_A = -I_d$ $i_B = I_d$ $i_C = 0$	$VC1=VC4=-V_o$ $VC3=VC2=+v_o$ $VC5=VC6=0$	-

$\nearrow$ increasing
$\searrow$ decreasing

TABLE 1.2 Summary of ASCI modes 7-12, operation without commutation overlap.

MODE			AT THE BEGINNING OF EACH MODE				DURING EACH MODE				
NO.	TYPE	INSTANT STARTS	TRIGGERED SCR	TURNED-OFF SCR	TURNED-ON DIODE	TURNED-OFF DIODE	CONDUCTING SCR's	CONDUCTING DIODES	MOTOR INPUT CURRENTS	COM.CAP.VOLTAGES CONSTANT	COM.CAP.VOLTAGES VARYING
13	charging	$t_{13} = t_1 + 4\pi/3\omega$	T5	T3	-	-	T5, T4	D3, D4	$i_A = -I_d$ $i_B = I_d$ $i_C = 0$	VC2 = $+V_o$ VC4 = $-V_o$ VC6 = 0	VC1 VC3 VC5
14	transfer	$t_{14} = t_2 + 4\pi/3\omega$	-	-	D5	-	T5, T4	D3, D4, D5	$i_A = -I_d$ $i_B \searrow$ $i_C \nearrow$	VC2 = $+V_o$ VC4 = $-V_o$ VC6 = 0	VC1 VC3 VC5
15	normal	$t_{15} = t_3 + 4\pi/3\omega$	-	-	-	D3	T5, T4	D4, D5	$i_A = -I_d$ $i_B = 0$ $i_C = I_d$	VC2=VC5=$+V_o$ VC4=VC3=$-V_o$ VC6=VC1= 0	-
16	charging	$t_{16} = t_1 + 5\pi/3\omega$	T6	T4	-	-	T5, T6	D4, D5	$i_A = -I_d$ $i_B = 0$ $i_C = I_d$	VC1 = 0 VC3 = $-V_o$ VC5 = $+V_o$	VC2 VC4 VC6
17	transfer	$t_{17} = t_2 + 5\pi/3\omega$	-	-	D6	-	T5, T6	D4, D5, D6	$-i_A \searrow$ $-i_B \nearrow$ $i_C = I_d$	VC1 = 0 VC3 = $-V_o$ VC5 = $+V_o$	VC2 VC4 VC6
18	normal	$t_{18} = t_3 + 5\pi/3\omega$	-	-	-	D4	T5, T6	D5, D6	$i_A = 0$ $i_B = -I_d$ $i_C = I_d$	VC1=VC2=0 VC3=VC6=$-V_o$ VC5=VC4=$+V_o$	-

TABLE 1.3 Summary of ASCI modes 13-18, operation without commutation overlap.

$\nearrow$ increasing
$\searrow$ decreasing

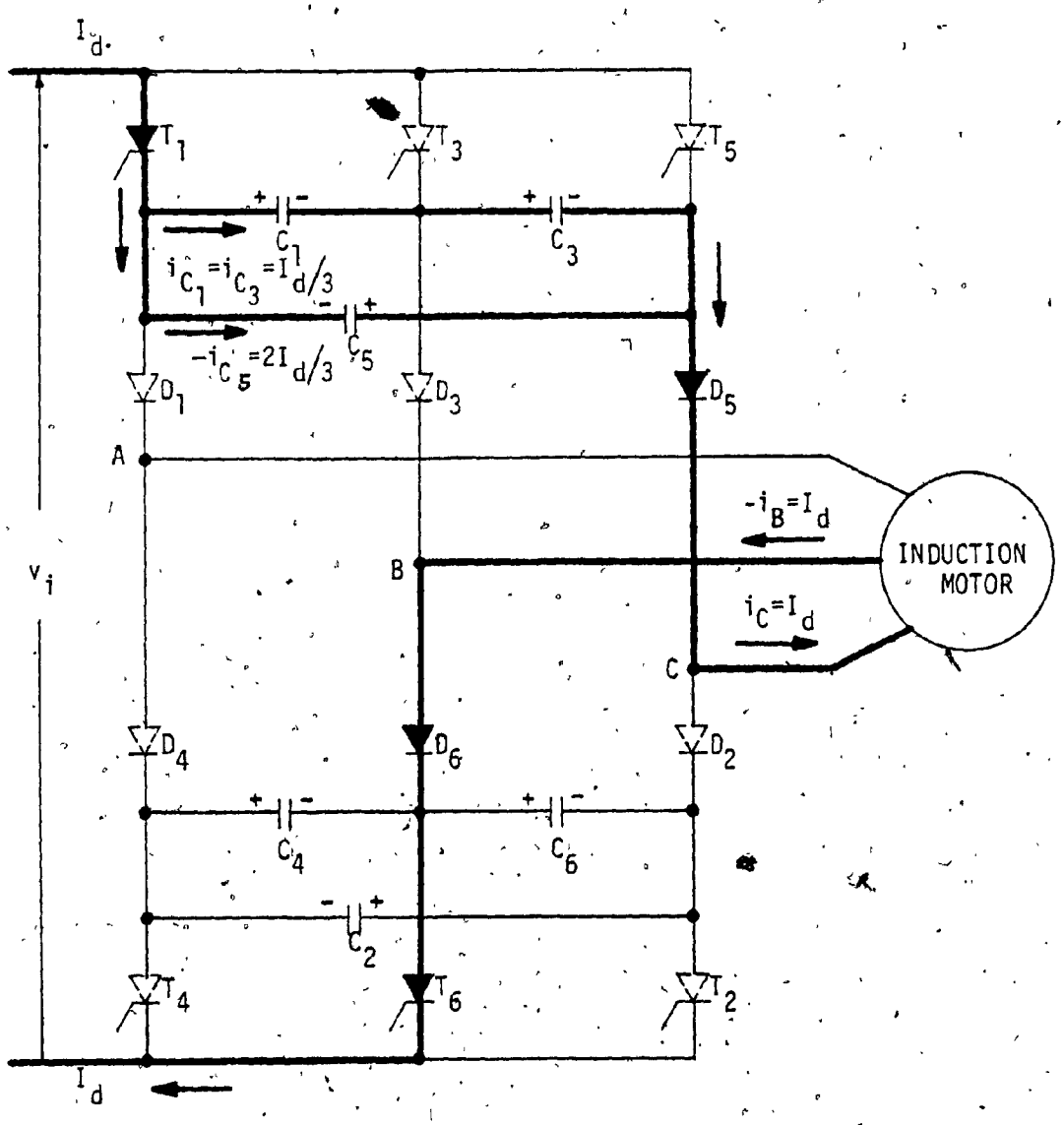

FIG. 2.4 ASCI-induction motor operation without commutation overlap during mode 1 (charging mode) when upper group capacitors are linearly charged. This mode ends when D_1 starts conducting.

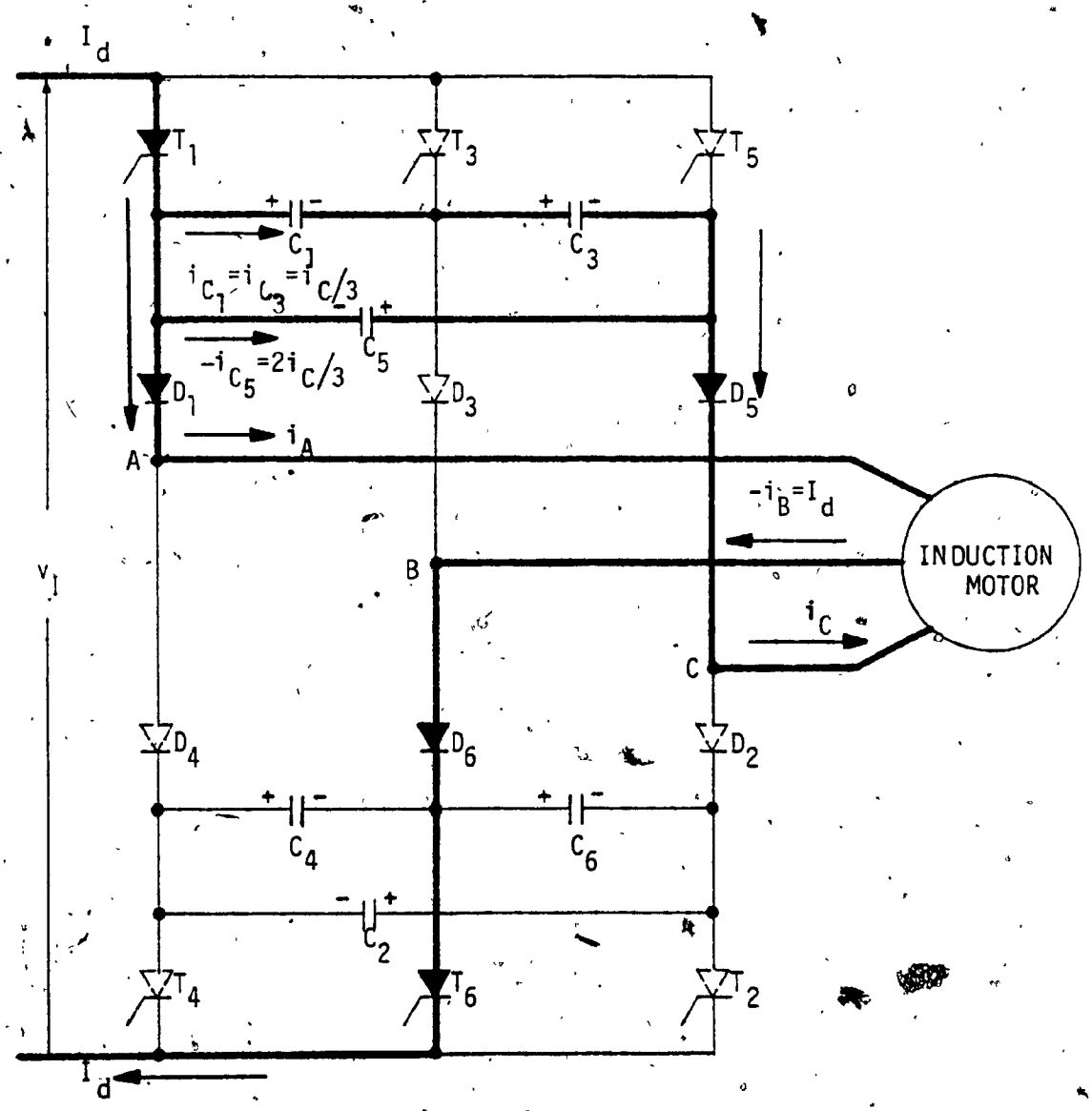

FIG. 2.5 ASCI-induction motor operation without commutation overlap during mode 2 (transfer mode) when current is being transferred from Phase C to Phase A. Switching currents generate voltage spikes at terminals A and C. This mode ends when D_5 stops conducting.

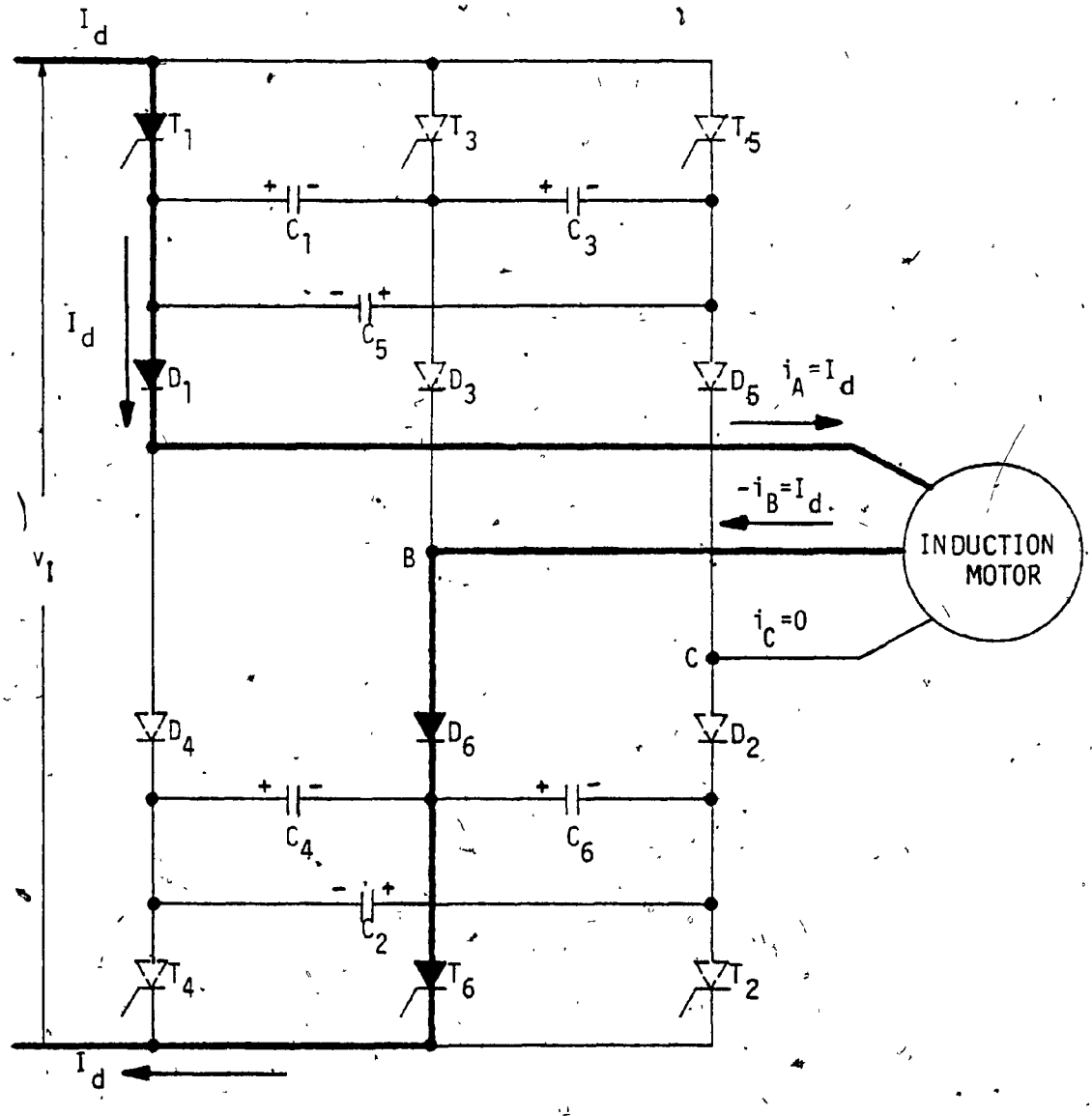

FIG. 2.6 ASCI-induction motor operation without commutation overlap during mode 3 (normal mode) when current has been commutated from Phase C to Phase A.

the system, the operation of the induction motor is described by using equations derived from a modified equivalent motor circuit, fig. 2.9. This circuit includes the effects of higher harmonics, caused by the square-wave input current [3]. Note that the alternative approach would be to use a classical equivalent circuit for each current harmonic and then to add the results so obtained in order to have the complete motor representation. Using the results given in [3], a modified equivalent circuit, which includes the core losses, is obtained. The value of the core loss resistor can be determined from the no-load test for each supply frequency. As an approximation, the core-loss resistance can be selected to give the same input current, calculated at the rated operating point by using the exact equivalent circuit, as that read from the motor nameplate for rated conditions. Obviously, by assigning a high value to R_m we will neglect the core-losses.

Figure 2.7 shows the exact equivalent circuit of an induction motor for each harmonic. All the parameters have been referred to the stator side; n shows the harmonic number while S_n is the corresponding slip. Also V_{ns} and I_{ns} show the stator peak voltage and current respectively. From fig. 2.7 the stator, rotor and magnetizing impedances are

$$Z_{1n} = R_1 + jnX_1$$

$$Z_{2n} = \frac{R_2}{S_n} + jnX_2 \qquad (2.3.1)$$

$$Z_{mn} = (R_m jnX_m)/(R_m + jnX_m)$$

while the input impedance is

$$Z_{tn} = Z_{1n} + (Z_{2n}Z_{mn})/(Z_{2n}+Z_{mn}) = Z_{1n}+Z_{en} \qquad (2.3.2)$$

where $$Z_{en} = (Z_{2n}Z_{mn})/(Z_{2n}+Z_{mn}) \qquad (2.3.3)$$

Equation (2.3.2) can also be written in the following form

$$Z_{tn} = Z_{1n}+jnX_2+Z_{en}-jnX_2 = R_1+jn(X_1+X_2)+Z_{en}-jnX_2$$

$$= R_1+jn(X_1+X_2) + Z_{eqn} \qquad (2.3.4)$$

where $$Z_{eqn} = Z_{en}-jnX_2 \qquad (2.3.5)$$

Equation (2.3.4) suggests another motor equivalent circuit for the n-th harmonic, fig. 2.8. Note that for n=1 figures 2.7 and 2.8 give identical stator current at the same operating point.

Next we want to prove that when the circuit shown in fig. 2.8 is connected to the output of an ASCI, the impedance seen by the current fundamental harmonic is equal to

$$Z_{t1} = R_1+j(X_1+X_2) + Z_{eq1} \qquad (2.3.6)$$

while that seen by the n-th harmonic is

$$Z_{tn} = R_1+jn(X_1+X_2) \qquad (2.3.7)$$

As the ASCI output current is the resultant of the fundamental and other harmonics of the current the circuit seen by the inverter output

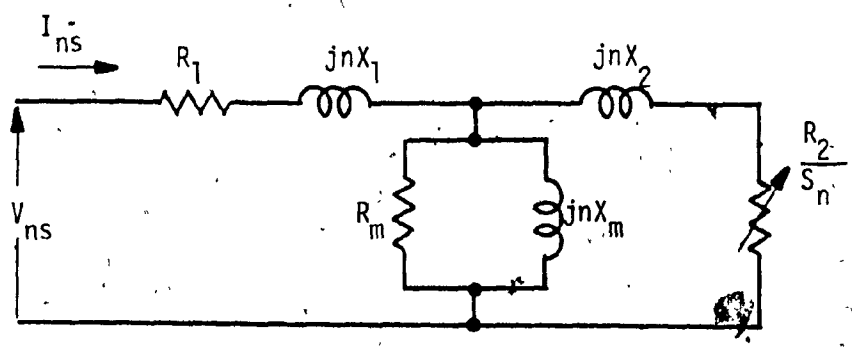

FIG. 2.7. The exact equivalent circuit of an induction motor per phase for the n-th harmonic.

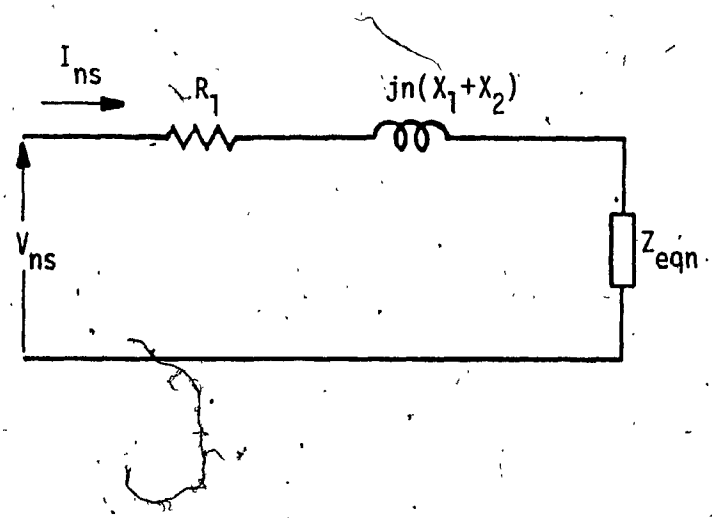

FIG. 2.8. The series equivalent circuit of an induction motor per phase for the n-th harmonic.

current will be fig. 2.9(c). The proof will be given later. For this circuit we can write

$$v_s = R_1 i_s + L \, di_s/dt + E_1 \sin(\omega t+\phi_1) \qquad (2.3.8)$$

where v_s and i_s are the stator instantaneous voltage and current respectively. E_1 is the peak voltage across Z_{eq1} due to the peak value of the fundamental harmonic of the stator current, I_{1s} ; ϕ_1 is the displacement angle between the fundamental harmonic of current, I_{1s} , and E_1 , and L is the sum of the stator leakage inductance and the referred rotor leakage inductance. Thus

$$E_1 = I_{1s} Z_{eq1}$$

$$L = L_1+L_2$$

$$\phi_1 = \arctan \frac{I_m(Z_{eq1})}{Re\,(Z_{eq1})} \qquad (2.3.9)$$

in which $I_m(Z_{eq1})$ is the imaginary part of Z_{eq1} and $Re(Z_{eq1})$ is the real part of Z_{eq1} . Note that E_1 is almost the same as the air-gap voltage and henceforth will be referred to as the CEMF of the induction motor.

Now, we wish to prove that the circuits given in fig. 2.9 indeed represent motor input impedances, for the corresponding currents, as seen from the inverter output terminals. Assuming a perfect square current waveform at the ASCI output we have only the odd current harmonics which are not a multiple of 3, [3,13]. Then

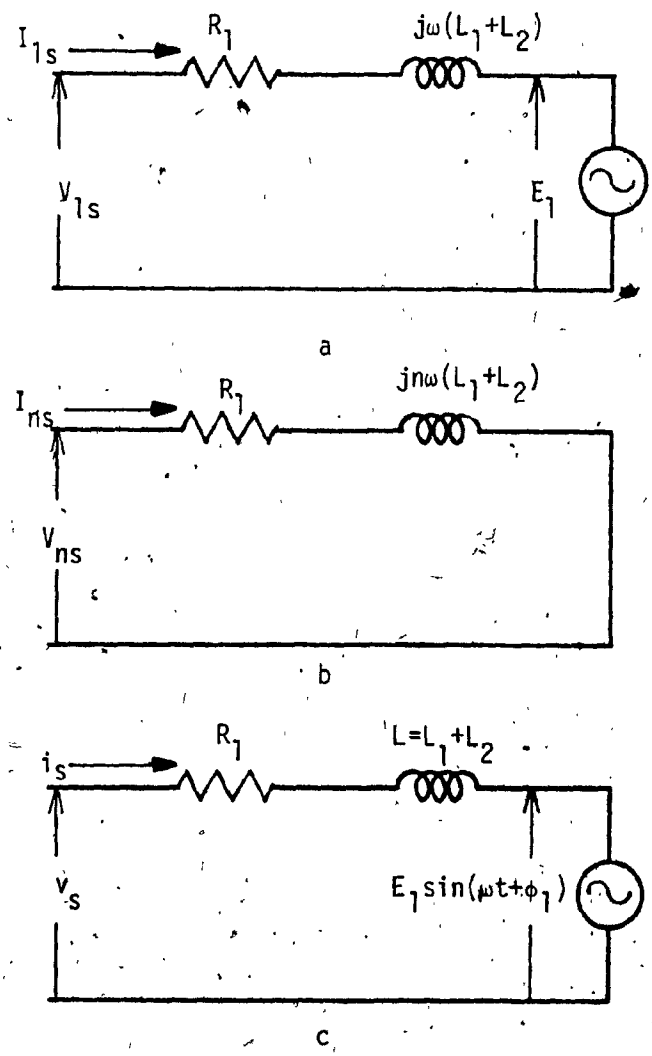

FIG. 2.9 Induction motor series equivalent circuits per phase

(a) For a fundamental harmonic

(b) For an n-th harmonic, $n \neq 1$

(c) For a total impedance as seen from the inverter output terminals.

$$n = 1,5,7,11, \tag{2.3.10}$$

Besides, the slip for the n-th harmonic is,

$$S_n = \frac{\pm nf_s - f_r}{\pm nf_s} \tag{2.3.11}$$

where f_s is the synchronous frequency due to the fundamental harmonic of MMF and f_r is the rotor rotational frequency. The positive and negative signs show the direction of rotation of the n-th MMF relative to the rotor direction of rotation. For the first harmonic of MMF the sign is positive and for the other harmonics it changes alternately, starting with the 5-th harmonic where the sign is negative.

Tables A-2.1 and A-2.2 in Appendix A-2 show some of the results obtained by running a computer program for evaluating the different impedances and the other variables in fig. 2.9. The parameters of the motor used in this program are given in Appendix A-1. It is seen from these results that Z_{eq5} and Z_{eq7} representing Z_{eqn} in fig. 2.8 for n=5 and 7 are much lower than Z_{h5} and Z_{h7} representing $n(X_1+X_2)$ respectively for n=5 and 7 in the same figure. Also Z_{eq1} is much larger than Z_{eq5} and Z_{eq7}. Thus the validity of the circuits in fig. 2.9 is proven and (2.3.8) is employed for expressing the stator terminal voltage per phase when the motor is supplied from an ASCI. In this case, as long as the current in one motor phase is zero or constant the voltage of this phase would be varying almost sinusoidally. When the current changes, which happens during the transfer of current from one to another phase, we have voltage spikes which are added to or

subtracted from the sinusoidal term. These spikes are obviously produced by current switching in the total leakage inductance L, fig. 2.9.

For a 3-phase star connected induction motor the equivalent circuit would be the circuit shown in fig. 2.10.

2.4 MOTOR FUNDAMENTAL TORQUE AND CURRENT

According to (2.3.9), one should know the magnitude of the fundamental component of the motor current, I_{1s}, in order to calculate the CEMF, E_1. The magnitude of the voltage across the stator terminals is determined by the control strategy applied to the inverter-induction motor drive (the relationship between the motor airgap flux, that is, the input current, and the operating load and frequency). In this study, a constant volts per hertz (V/Hz) control is used for frequencies below the base frequency (60 Hz), while for frequencies above 60 Hz, the terminal voltage is maintained constant and equal to the motor rated voltage, thus giving a constant power operation.

The terminal voltage calculated on the basis of the constant V/Hz control represents the fundamental component of the motor input voltage. This voltage is then used to calculate, from the exact equivalent circuit, the fundamental component of the motor input current. As mentioned before, in order to make this component equal to the rated nameplate current, at the rated input voltage and frequency, an appropriate value of the core-loss resistance, R_m, is selected in fig. 2.7 with n being equal to one. In addition, the average output torque is calculated for the fundamental component of the motor input current using

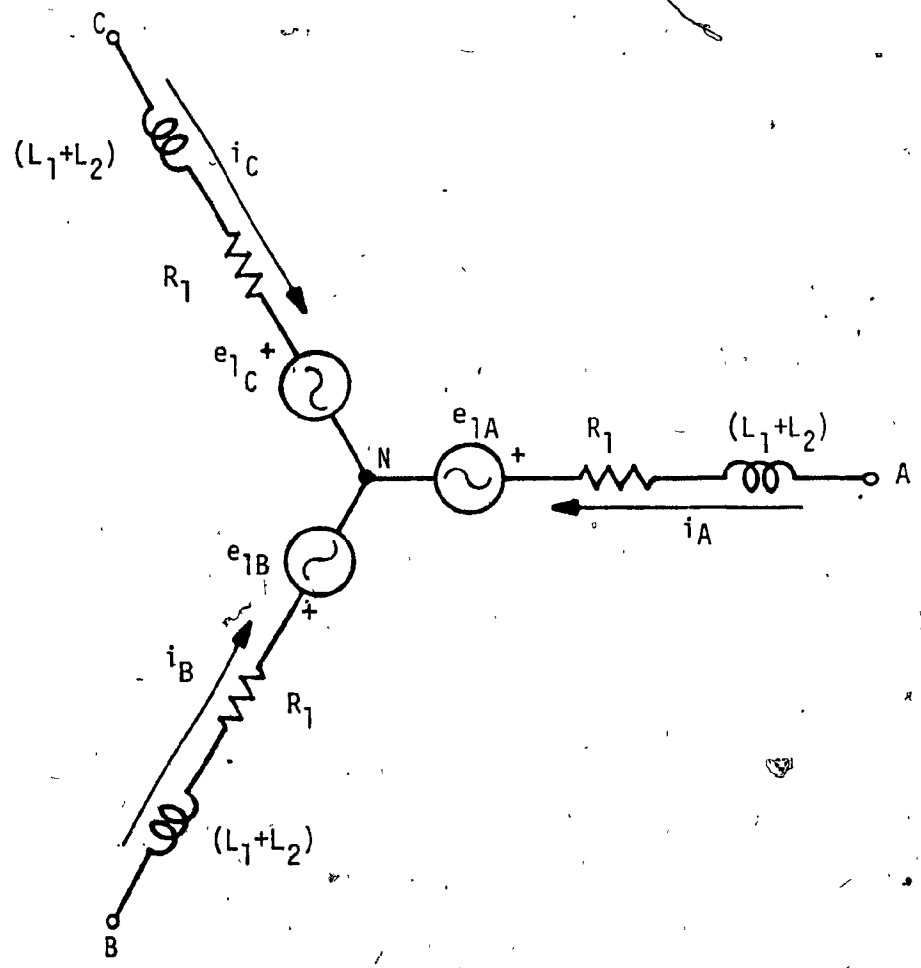

FIG. 2.10 The equivalent circuit of a 3-phase star connected induction motor as seen from an ASCI terminals

the exact equivalent circuit.

2.5 ESTIMATION OF DC LINK CURRENT

By neglecting the commutation invterval (the time needed for a transfer of the current from one to another phase, fig. 2.4 and 2.5) one obtains rectangular waveforms for the motor input currents [5, 12 - 13]. Figure 2.11 shows these waveforms for all three phases.

In fig. 2.11 the fundamental component of i_A, i.e., i_{1A} is also shown. The i_{1A} waveform defines then the time origin, $t=0$. The Fourier series of i_A is

$$i_A = \frac{2\sqrt{3}}{\pi} I_d \left[\sin \omega t - \frac{1}{5} \sin 5\,\omega t + \frac{1}{7} \sin 7\,\omega t - \frac{1}{11} \sin 11\,\omega t \ldots\right] \tag{2.5.1}$$

where I_d is the dc link current while ω is the inverter output frequency in rad/sec.

From (2.5.1) the peak value of the fundamental component of the phase A current is

$$I_{1A} = I_{1S} = \frac{2\sqrt{3}}{\pi} I_d \tag{2.5.2}$$

from which I_d is obtained

$$I_d = \frac{\pi}{2\sqrt{3}} I_{1A} \tag{2.5.3}$$

It was assumed before that only the fundamental component of the motor current, I_{1A}, produces the output torque. Therefore, the

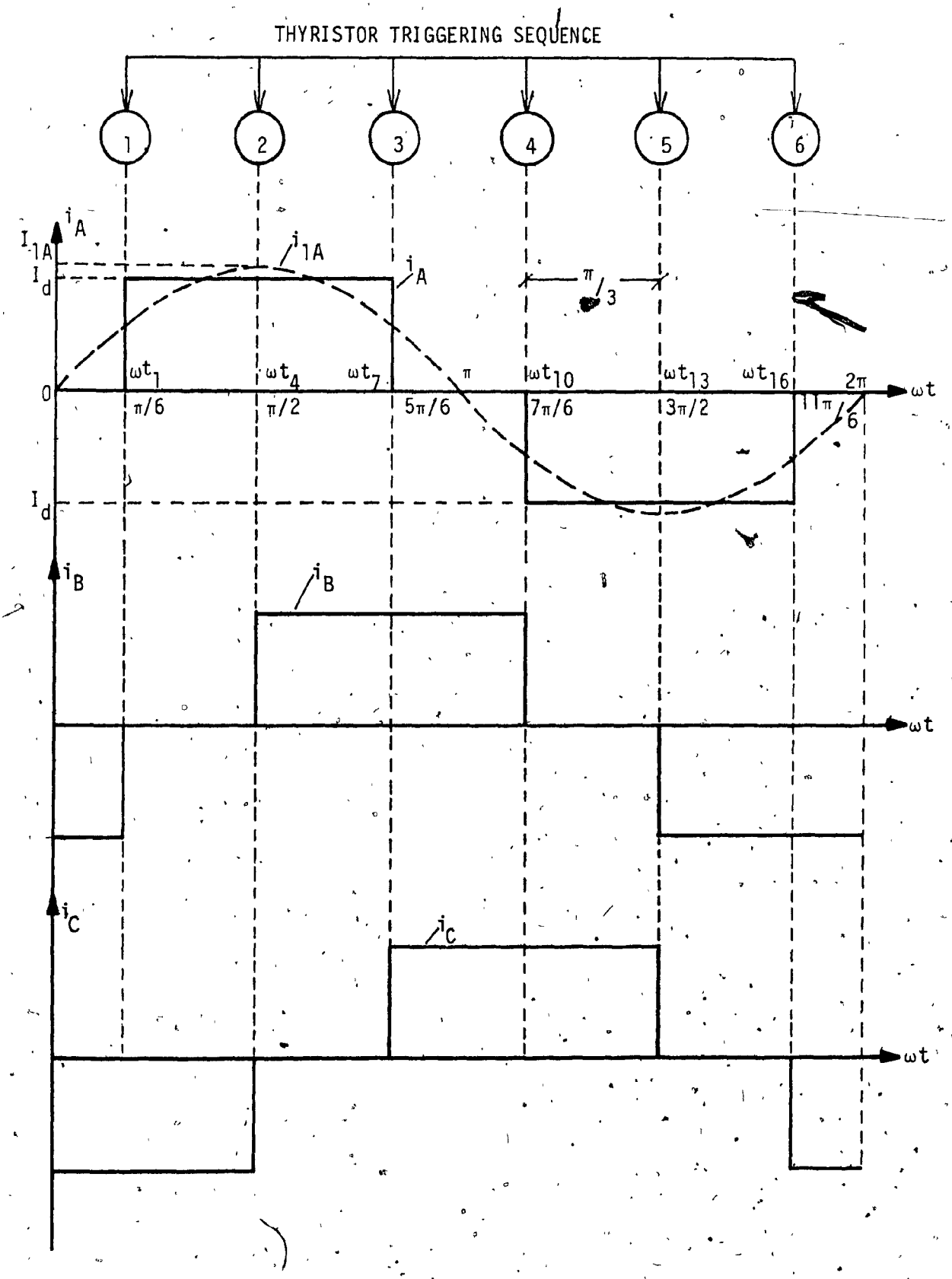

FIG. 2.11 Three phase and phase A fundamental harmonic current waveforms of an induction motor connected to an ideal ASCI.

dc link current given by (2.5.3) is calculated by using I_{1A} which was computed from the exact equivalent circuit, fig. 2.7 for n=1 .

The assumption of a square waveform for the motor input current yields a very good approximate value for the dc link current through (2.5.3).

2.6 SUMMARY OF ASSUMPTIONS

The various assumptions made at different stages of this chapter are now summarized here. Most of these assumptions which are listed below will be used throughout this report (assumptions 1,2,3,5, 7,8,9,11,12,13,14 and 15).

1 - Steady-state conditions.

2 - No saturation.

3 - No skin effect.

4 - Constant dc link current.

5 - Constant V/Hz for frequencies lower than the base frequency and constant voltage for frequencies higher than the base frequency.

6 - No commutation overlap.

7 - No transient forward-biasing of the series diodes.

8 - Instantaneous turn-on and turn-off times for the diodes and SCR's.

9 - No voltage drops in the SCR's and in the diodes.

10 - No clamping cirucit.

11 - Use of the exact equivalent circuit of the induction motor for calculating the motor power factor and the fundamental components of the current and torque.

12 - Use of the series equivalent circuit for computing the motor CEMF, E_1, and its displacement angle, ϕ_1, relative to the fundamental component of the motor current, I_{1s}.

13 - The inverter output frequency f, the fundamental slip S_1 (or the output torque) and the commutating capacitor C are known.

14 - The origin of time is the instant at which the fundamental component of the phase A current crosses the time axis with a positive slope.

15 - Estimation of the dc link current from the fundamental component of the motor input current with the assumption of a square waveform motor input current.

2.7 CONCLUSION

A brief discussion of the operation of an auto-sequentially commutated current source inverter was presented and 18 distinct modes (three for each 60° of conduction) of inverter operation were defined. Three tables were given which yielded the required information about the different variables of the inverter and its load at each of the operating modes. These tables were based on a selected SCR firing sequence. To avoid using the exact equivalent circuit of an induction motor for each harmonic in the motor input current, a modified equivalent circuit which takes into account the effect of all harmonics (including the fundamental) was described. However, the exact equivalent circuit was used to calculate the motor fundamental current and torque. The procedure of calculating the dc link current from the motor fundamental current was also outlined. The chapter ended by giving a summary of the assumptions used in this thesis.

CHAPTER III

MATHEMATICAL MODELING OF THE SYSTEM WITH A CONSTANT DC LINK CURRENT AND NO CLAMPING CIRCUIT - CASE(a)

3.1. INTRODUCTION

The equations describing a system consisted of an auto-sequential current source inverter and an induction motor have already been reported in the literature [3,9]. These references have used different methods in the system modeling, the common assumption being that the dc link current is constant during the steady-state motor operation. Such an assumption obviously implies a very large dc link inductance. As the purpose of this report is to find the exact solution of the system by assuming a constant converter output voltage, it is necessary to start the study by assuming a constant dc link current. The approximate solution thus obtained is then used in finding the exact solution on which the designing and selecting of the different inverter components are based.

The equations will be derived for a no-overlap case in which the commutation angle is less than 60° and also on the condition that the diodes do not become transiently forward biased. Furthermore, it will be shown that as long as we have only a partial overlap for which the commutation angle is between 60° and 120°, the transfer angle is less than 60° and also that the diodes do not conduct transiently the same main equations derived for a no-overlap case are still valid.

The solution of these equations will be simplified by assuming a constant CEMF and a linear transfer of currents during the transfer time. Further, by neglecting the stator resistance even simpler expressions can be obtained.

3.2 MECHANISM OF THE CURRENT TRANSFER FROM ONE TO THE OTHER SCR

The equivalent circuit of an induction motor fed by an ASCI was given in fig. 2.10. For the chosen SCR firing sequence, and with the use of fig. 2.10, the circuit of the system just before the firing of thyristor T_1 is shown in fig. 3.1. Since we are explaining the steady-state operation of the system, the commutating capacitors are assumed to have voltages according to Table 1.1 at the beginning of mode 1. Obviously, before starting the system, in order to reach to the steady-state operation, the commutating capacitors should have been precharged to such levels enough for commutating the thyristors. This is done by a precharging circuit. The precharging circuit as well as the firing circuit are not shown in the figures but we assume that we have the necessary conditions for a proper system operation. The value of V_o shown in Tables 1.1-1.3 is the maximum voltage across the commutating capacitors during the steady-state operation. This quantity is one of the unknowns to be found later.

When explaining fig. 2.4 it was assumed that the thyristor T_5 is turned off as soon as T_1 is fired. Although this hypothesis is not quite correct, it still provides a good approximation. The true mechanism of a current transfer from one thyristor to the other is now explained.

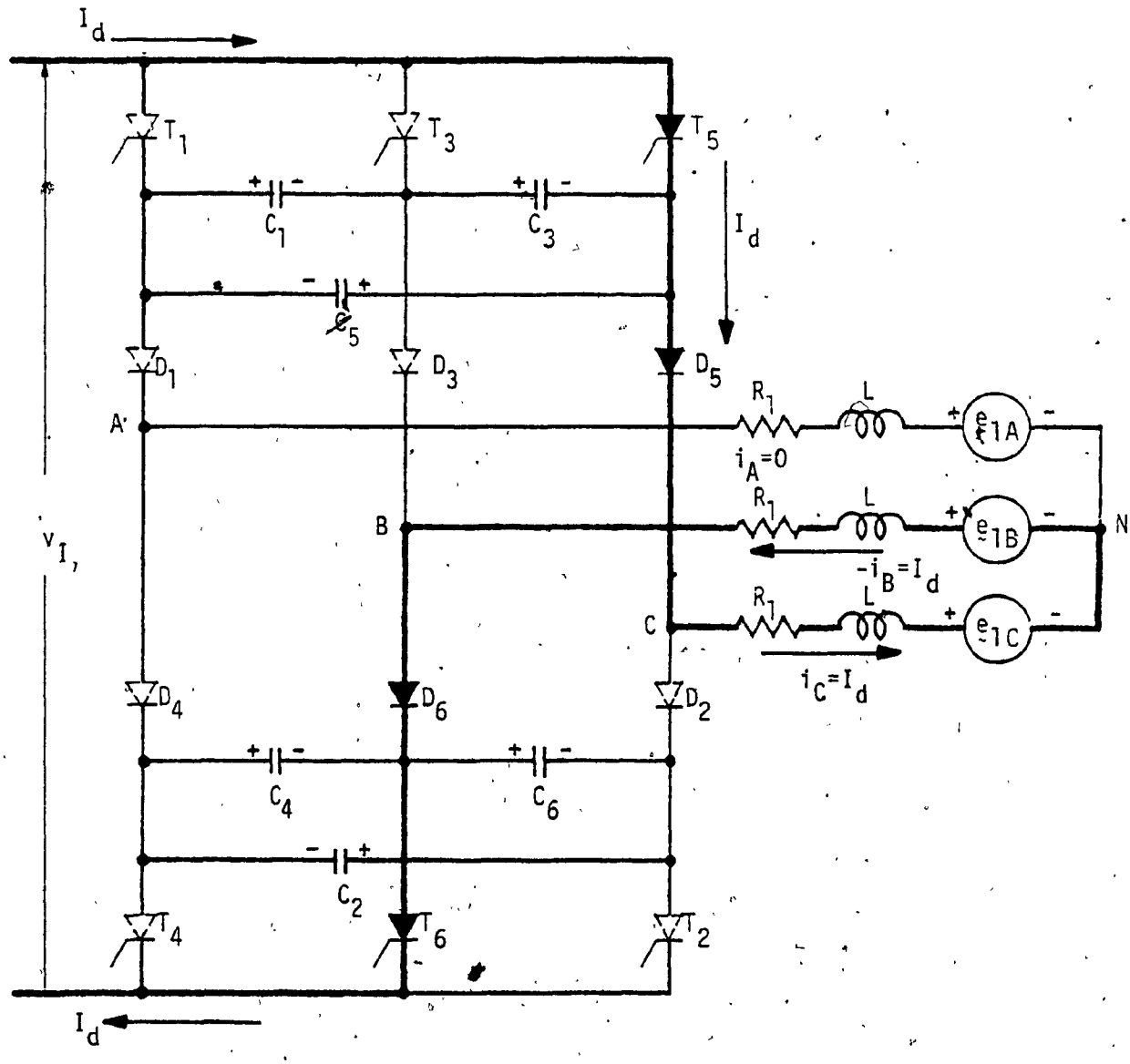

FIG. 3.1 ASCI-induction motor current routes during mode 18 in case (a) just before firing T_1.

It is well-known that SCR's are sensitive to di/dt . To protect them against an excessive rate of current change, a small inductance is placed in series with each SCR. This inductance is much less than the motor leakage inductance L and is therefore usually neglected. However, it has to be taken into account during a thyristor commutation and the upper part of fig. 3.1 will change into fig. 3.2 when di/dt inductances are included in the circuit. As we trigger T_1 at $t=t_1$, fig. 3.2 changes into fig. 3.3 which now shows an oscillatory circuit consisting of ℓ_1, ℓ_5 and the combination of C_1, C_3 and C_5 . Neglecting the resistances, the commutating resonant frequency is equal to.

$$\omega_{os} = \frac{1}{\sqrt{2\ell . 1.5c}} = \frac{1}{\sqrt{3\ell c}} \qquad (3.2.1)$$

where $\ell = \ell_1 = \ell_5$, and $C = C_1 = C_3 = C_5$

The charging oscillating current, i_{os} , is equal to

$$i_{os} = \frac{V_o}{2\omega_{os} \cdot \ell} \sin \omega_{os} t \qquad (3.2.2)$$

which is also the current through T_1 . The current through T_5 is

$$i_{T5} = I_d - i_{os} = I_d - \frac{V_o}{2\ell\omega_{os}} \sin \omega_{os} t \qquad (3.2.3)$$

When the current through T_5 becomes zero this SCR assumes a blocking state and all the dc link current flows through T_1 . The time required to reach this state after T_1 is fired is

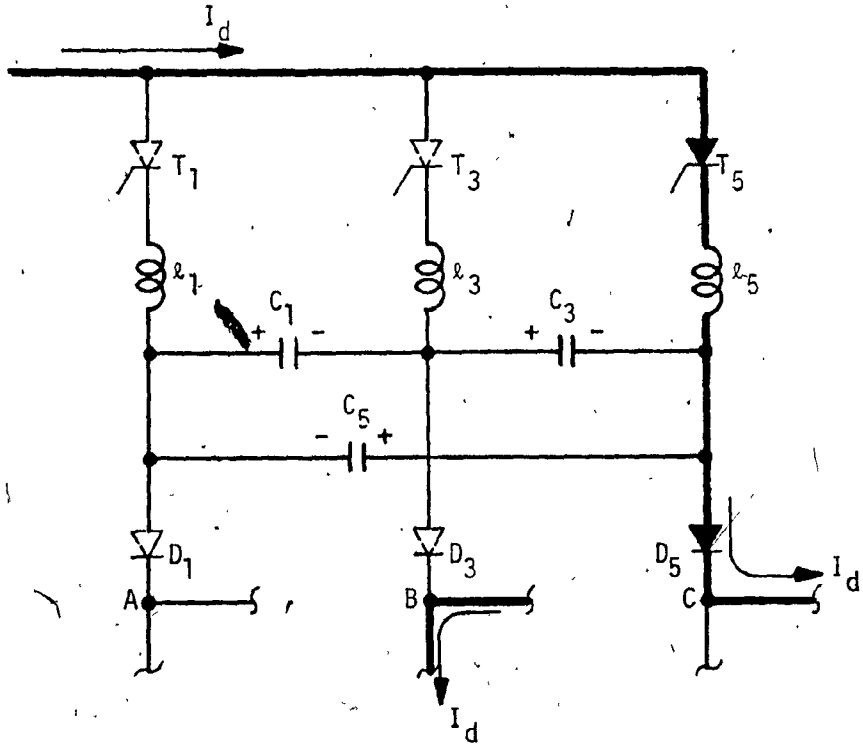

FIG. 3.2 Upper part of an ASCI with protecting inductances when T_5 and D_5 are conducting during mode 18.

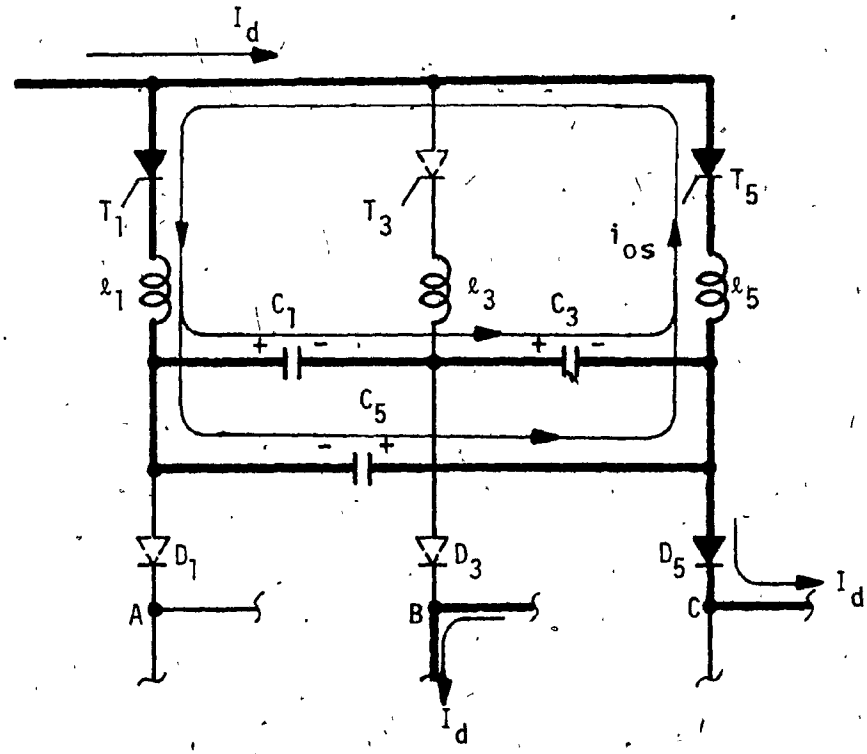

FIG. 3.3 Upper part of an ASCI with protecting inductances just after triggering T_1.

$$T_{os} = \frac{1}{\omega_{os}} \sin^{-1} \frac{I_d \cdot 2\ell\omega_{os}}{V_o} \qquad (3.2.4)$$

Also, the maximum di/dt for T_1 is

$$\left.\frac{di_{os}}{dt}\right|_{t=o} = \frac{V_o}{2\ell} \qquad (3.2.5)$$

As an example, in order to have an idea as to the time needed for i_{os} to reach I_d and the maximum di/dt, we assume the following typical values for the different components and variables for a circuit similar to that given in fig. 3.3.

$$I_d = 100 \text{ A} \quad , \quad V_o = 1000\text{V}, \ \ell = 10 \ \mu\text{H} \ , \ C = 10 \ \mu\text{F}$$

Then the following results

$$\omega_{os} = 57.735 \times 10^3 \text{ rad/s}$$

$$T_{os} = 2 \ \mu\text{s}$$

$$di/dt|_{max} = 50 \text{ A}/\mu\text{s}$$

It is thus a good approximation to suppose that this interval (i.e. T_{os}) is negligible, resulting in instantaneous current transfer from one SCR to the other. This conclusion defines then the SCR's conduction periods. Each SCR conducts current only for 120° or 1/3 of the inverter output period. Figure 3.4 shows the current waveforms for thyristors T_1-T_6.

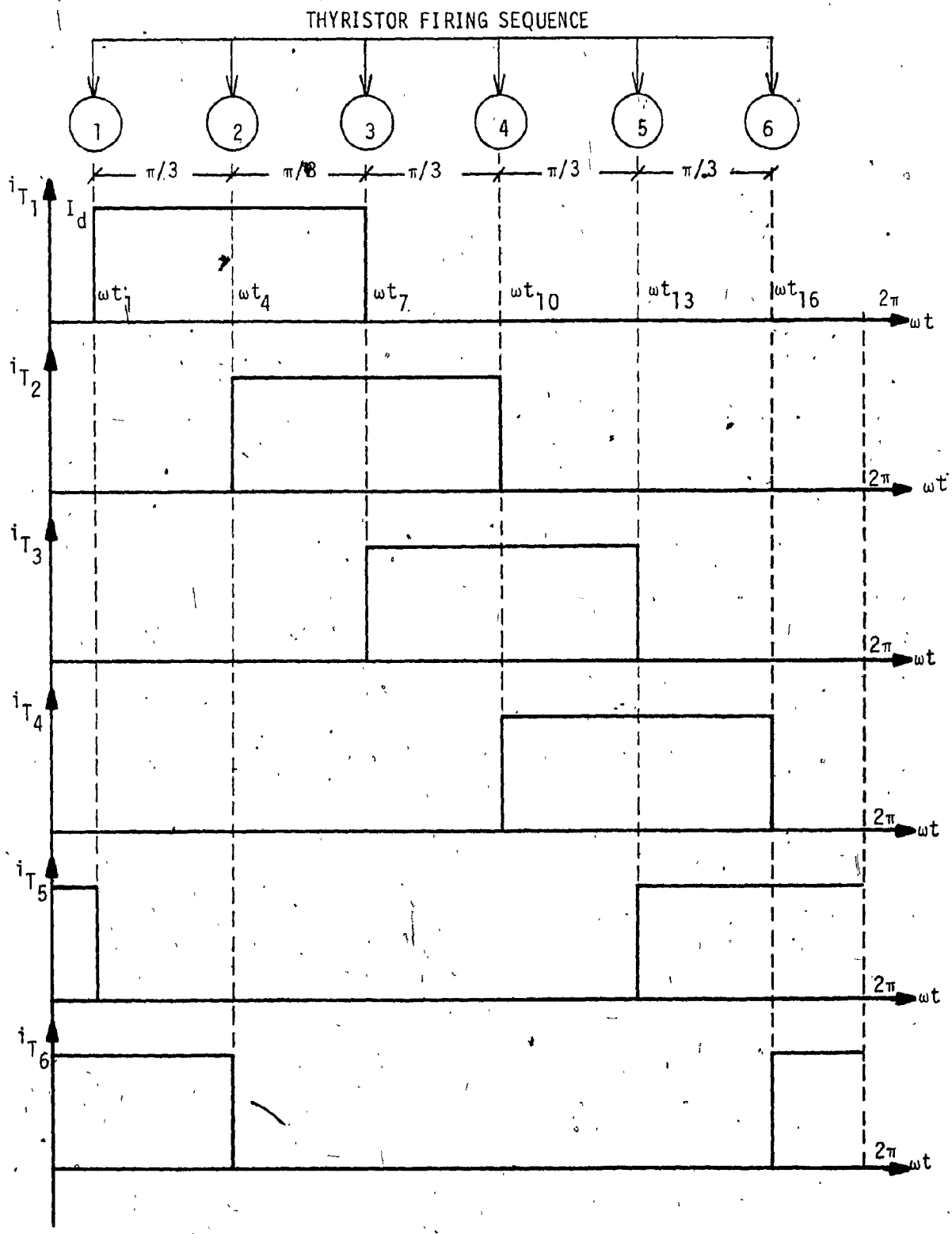

FIG. 3.4 Thyristor T_1-T_6 current waveforms of an ASCI with corresponding firing instants for a general case.

In fig. 2.11 we neglected the commutation interval and assumed it to be zero. This resulted in $\omega t_1=\pi/6$ rad. However, in reality this assumption is not usually true. For this reason we have not specified ωt_1 in fig. 3.4. As will be seen later, ωt_1 can even obtain negative values.

3.3 MODE 1 OR CHARGING MODE

This mode exists for $t_1<t<t_2$, where t_1 is the time of firing the thyristor T_1 and t_2 is the moment when the diode D_1 becomes forward biased. The thyristor T_5 is turned off as soon as T_1 is fired at $t=t_1$ and from fig. 3.5 we find that $i_A=0$ and $i_C = -i_B = I_d$. Also, the commutating capacitors have been charged according to Table 1.1. Just before T_1 is triggered, the voltages across the diodes D_1 and D_3 are equal to

$$v_{D1}(t_1^-) = -v_{C5}(t_1^-) + v_{CA}(t_1^-)$$
$$v_{D3}(t_1^-) = +v_{C3}(t_1^-) + v_{CB}(t_1^-) \qquad (3.3.1)$$

In (3.3.1) t_1^- refers to the time just before t_1. But from Table 1.1 we know that

$$v_{C5}(t_1^-) = +V_o$$
$$v_{C3}(t_1^-) = -V_o \qquad (3.3.2)$$

Then equation (3.3.1) becomes

$$v_{D1}(t_1^-) = -V_o + v_{CA}(t_1^-)$$
$$v_{D3}(t_1^-) = -V_o + v_{CB}(t_1^-) \qquad (3.3.3)$$

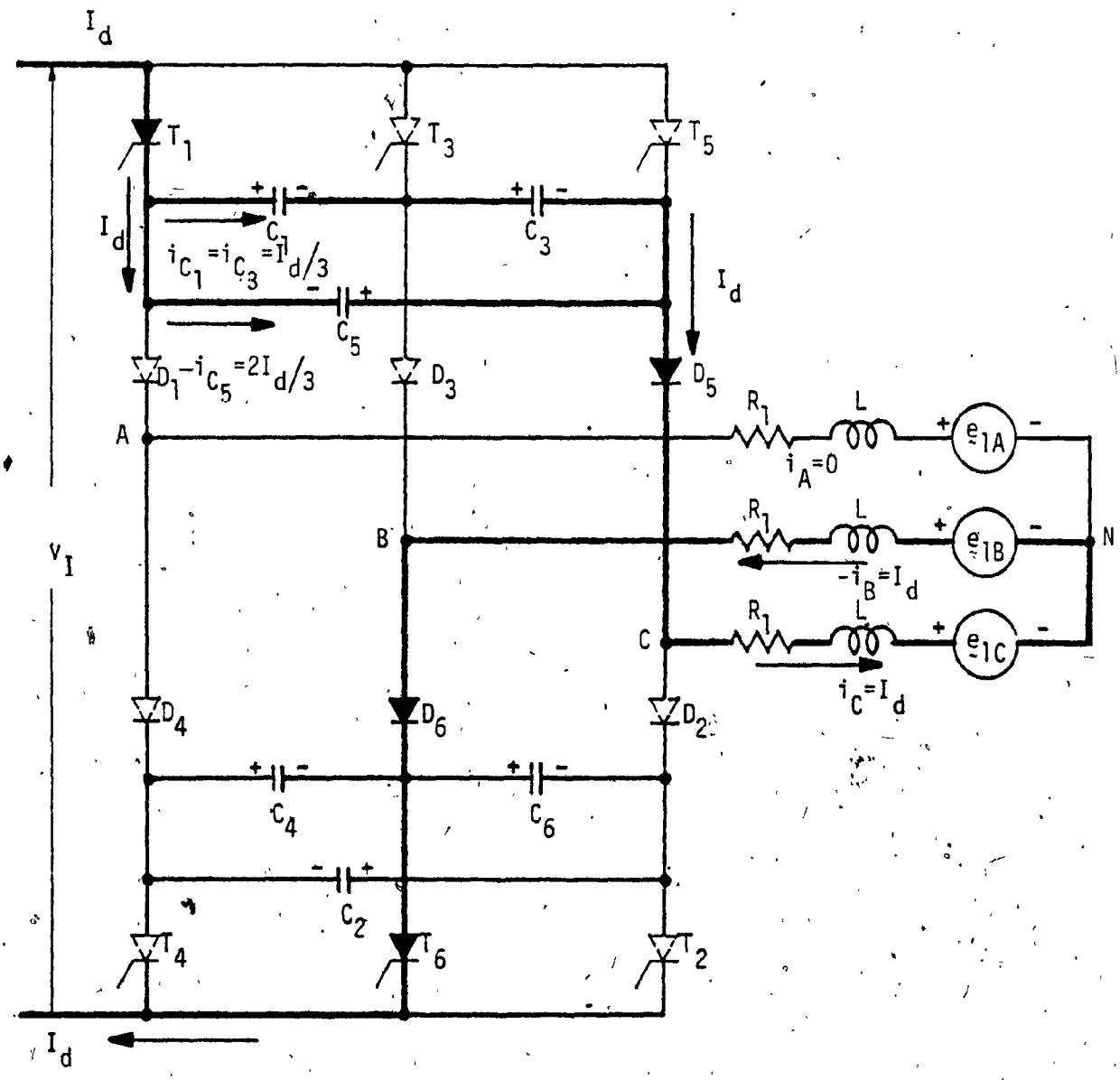

FIG. 3.5 ASCI-induction motor current routes during mode 1 (charging mode) in case (a) after firing T_1 at $t=t_1$. Upper group capacitor currents are constant during this mode.

As will be seen later, the magnitude of V_o is always greater than the peak value of motor line-to-line voltage. This results in D_1 and D_3 being reversed biased, as was assumed when describing the system in section (2.2),

$$v_{D1}(t_1^-) < 0$$
$$v_{D3}(t_1^-) < 0 \qquad (3.3.4)$$

Equation (3.3.4) also holds true at $t=t_1^+$ which is the time just after firing T_1. Therefore, all the dc link current I_d will pass through all three upper group capacitors. As all the commutating capacitors have the same capacitance, C, the following results

$$i_{C1}(t) = i_{C3}(t) = \frac{1}{3} I_d$$
$$-i_{C5}(t) = \frac{2}{3} I_d \qquad (3.3.5)$$

where $i_{Cn}(t)$ with n=1,3,5 are the instantaneous capacitor currents during mode 1. Due to the constant capacitor currents, the upper group capacitors are charged and discharged linearly. This phenomenon suggests that this mode be called a <u>'charging mode'</u> and its duration named <u>'charging time'</u>, t_{ch}. With the origin of time as defined by assumption #14 in section (2.6) and the peak value of the fundamental component of motor current I_1, obtained from the exact equivalent circuit we can write

$$i_{1A}(t) = I_1 \sin \omega t$$
$$i_{1B}(t) = I_1 \sin (\omega t - \frac{2\pi}{3}) \qquad (3.3.6)$$
$$i_{1C}(t) = I_1 \sin (\omega t - \frac{4\pi}{3})$$

where i_{1A}, i_{1B}, i_{1C} are the instantaneous fundamental components of motor line currents, ω is the angular frequency of inverter output and I_1 has been used interchangeably for I_{1S} given by (2.5.2).

Also, from (2.3.9) the instantaneous CEMF for each of the motor phases would be

$$e_{1A}(t) = E_1 \sin (\omega t + \phi_1)$$
$$e_{1B}(t) = E_1 \sin (\omega t - \frac{2\pi}{3} + \phi_1) \qquad (3.3.7)$$
$$e_{1C}(t) = E_1 \sin (\omega t - \frac{4\pi}{3} + \phi_1)$$

Referring to fig. 3.5, the actual instantaneous motor terminal voltages during the charging mode result as

$$v_A(t) = e_{1A}(t) = E_1 \sin (\omega t + \phi_1)$$
$$v_B(t) = R_1 I_d + e_{1B}(t) = -R_1 I_d + E_1 \sin (\omega t - \frac{2\pi}{3} + \phi_1) \qquad (3.3.8)$$
$$v_C(t) = R_1 I_d + e_{1C}(t) = R_1 I_d + E_1 \sin (\omega t - \frac{4\pi}{3} + \phi_1)$$

The line-to-line voltages during the charging mode are

$$v_{AB}(t) = v_A(t) - v_B(t) = R_1 I_d + E_1 \sqrt{3} \cos(\omega t + \phi_1 - \frac{\pi}{3})$$

$$v_{BC}(t) = v_B(t) - v_C(t) = -2R_1 I_d + E_1 \sqrt{3} \cos(\omega t + \phi_1 - \pi)$$

$$v_{CA}(t) = v_C(t) - v_A(t) = R_1 I_d - E_1 \sqrt{3} \cos(\omega t + \phi_1 - \frac{2\pi}{3})$$

(3.3.9)

The diode currents are

$$i_{D1}(t) = i_{D3}(t) = i_{D2}(t) = i_{D4}(t) = 0$$

$$i_{D5}(t) = i_{D6}(t) = I_d \qquad (3.3.10)$$

The voltages of the upper group commutating capacitors are equal to

$$v_{C1}(t) = \frac{1}{c}\int_{t_1}^{t} i_{C1}(t)dt+0 = \frac{1}{3C} I_d(t-t_1)$$

$$v_{C3}(t) = \frac{1}{c}\int_{t_1}^{t} i_{C3}(t)dt-V_o = \frac{1}{3C} I_d(t-t_1)-V_o \qquad (3.3.11)$$

$$v_{C5}(t) = -\frac{1}{c}\int_{t_1}^{t} i_{C5}(t)dt+V_o = -\frac{2}{3C} I_d(t-t_1)+V_o$$

The thyristor T_1 is conducting during this mode so that the voltage drop across it is supposed to be zero. Therefore

$$v_{T1}(t) = 0$$

$$v_{T3}(t) = v_{C1}(t) = \frac{1}{3C} I_d(t-t_1) \qquad (3.3.12)$$

$$v_{T5}(t) = -v_{C5}(t) = \frac{2}{3C} I_d(t-t_1)-V_o$$

The lower group commutating capacitor voltages are constant during this mode. Thus from Table 1.1 we can write

$$v_{C2}(t) = 0$$

$$v_{C4}(t) = +V_o \qquad (3.3.13)$$

$$v_{C6}(t) = -V_o$$

Again, as T_6 is conducting and its voltage drop is equal to zero we obtain

$$v_{T2}(t) = v_{C6}(t) = +V_o$$

$$v_{T4}(t) = v_{C4}(t) = +V_o \qquad (3.3.14)$$

$$v_{T6}(t) = 0$$

The voltages across upper and lower group diodes can be found in the same way to be

$$v_{D1}(t) = -v_{C5}(t) + v_{CA}(t)$$

$$v_{D1}(t) = \frac{2}{3C} I_d(t-t_1) - V_o+R_1 I_d-E_1 \sqrt{3} \cos(\omega t+\phi_1 - \frac{2\pi}{3})$$

$$v_{D3}(t) = v_{C3}(t) + v_{CB}(t) \qquad (3.3.15)$$

$$v_{D3}(t) = \frac{1}{3C} I_d(t-t_1) - V_o+2R_1 I_d-E_1 \sqrt{3} \cos(\omega t+\phi_1-\pi)$$

$$v_{D5}(t) = 0$$

$$
\begin{aligned}
v_{D2}(t) &= v_{CB}(t) + v_{C5}(t) \\
v_{D2}(t) &= 2R_1 I_d - E_1 \sqrt{3} \cos(\omega t+\phi_1-\pi)-V_o \\
v_{D4}(t) &= v_{AB}(t) - v_{C4}(t) \\
v_{D4}(t) &= R_1 I_d + E_1 \sqrt{3} \cos(\omega t+\phi_1-\tfrac{\pi}{3})-V_o \\
v_{D6}(t) &= 0
\end{aligned}
\qquad (3.3.16)
$$

At this point we should mention one important point regarding the voltage across D_3. In section (3.1) we mentioned that this study is based on the condition that the diodes do not get transiently forward biased. This point will be explained later by the voltage waveform across one of the series diodes, but for the time being we will discuss the main idea. According to (3.3.3), just before firing T_1, the voltage across D_3 is negative. But from (3.3.15) it is clear that this voltage, v_{D3}, starts increasing during the charging mode. Under some conditions, which depend on the motor parameters, commutating capacitor value, C, and the motor operating point, the diode D_3 might become forward biased before D_1 which is undesirable. This results in the bypass of some part of the dc link current, I_d, through D_3, D_6 and T_6, fig. 3.6. In this case the motor input current will decrease and we will have a reduction in the output torque. According to [16], this phenomena lasts for a while and the system reverts again to its previous operation. If D_3 conducts before D_1 we say that the diodes have become "transiently forward biased", [25]. However, we do not consider this case of the inverter operation and this study is valid as long as the diodes do not become transiently

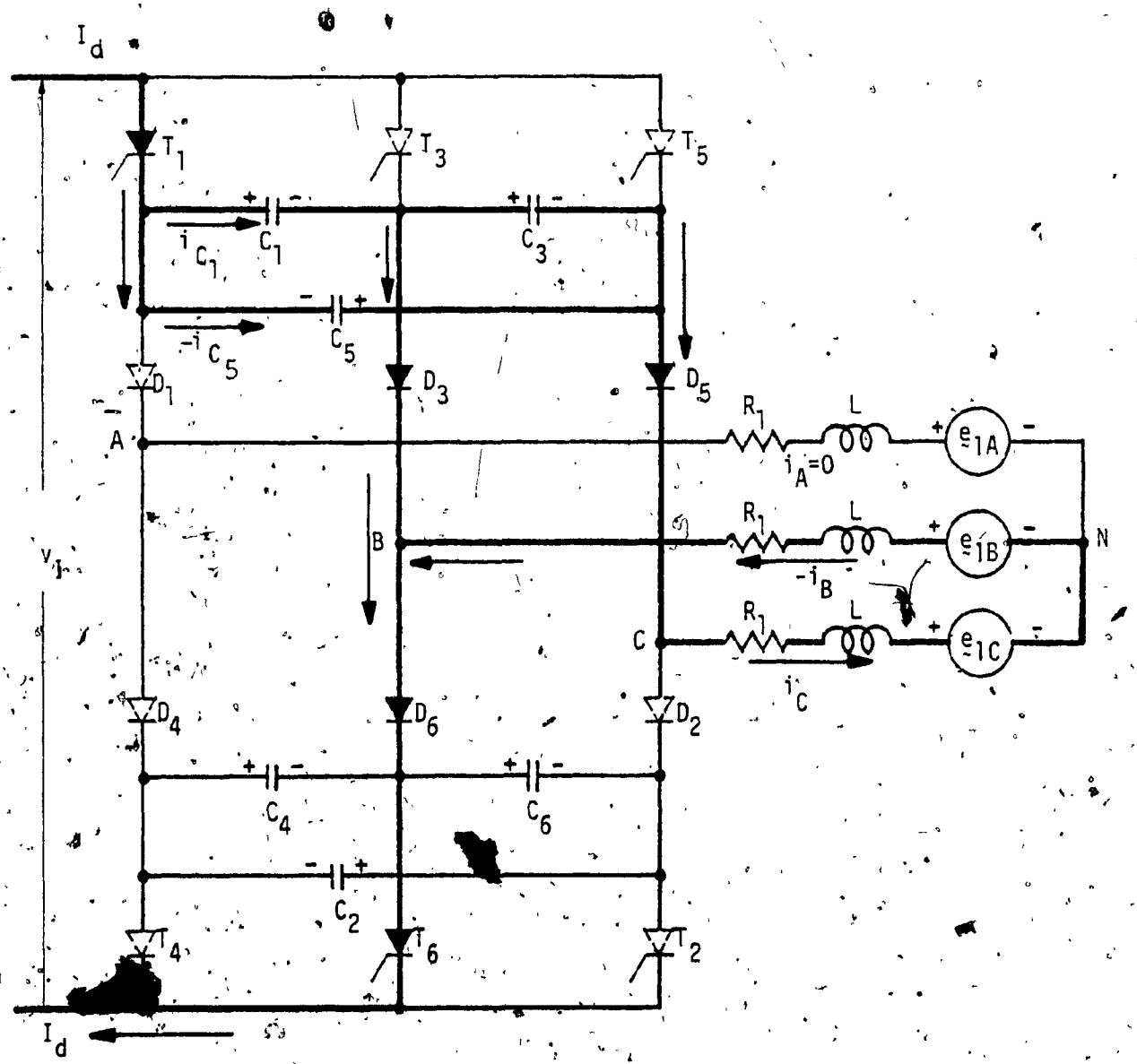

FIG. 3.6 The transient forward biasing of diode D_3 during mode 1 (charging mode) when D_3 starts conducting before D_1. Due to dc link current bypass motor output power is decreased.

forward biased.

At last, the inverter input voltage is equal to

$$v_I = -v_{C5}(t) + v_{CB}(t)$$

$$= \frac{2}{3C} I_d(t-t_1) - V_o + 2R_1 I_d - E_1 \sqrt{3} \cos(\omega t + \phi_1 - \pi) \qquad (3.3.17)$$

The charging mode ends at $t=t_2$ when the diode D_1 becomes forward biased. When explaining mode 2 it will be shown how D_1 is forward biased. The duration of the charging mode is then obtained to be

$$t_{ch} = t_2 - t_1 \qquad (3.3.18)$$

t_{ch} is called "charging time" and its value is one of the unknowns to be found.

3.4 MODE 2 OR TRANSFER MODE

This mode is defined for $t_2<t<t_3$ where t_2 is the instant at which D_1 starts conducting while t_3 is the moment when D_5 becomes reverse biased. Referring back to (3.3.5) it is seen that the current charging the capacitor C_5 during mode 1 is double that flowing through C_3. Then, if the motor parameters, the commutating capacitors and the operating point are such that D_1 becomes forward biased before D_3, the system enters mode 2 of its operation, fig. 3.7. As was mentioned before, if D_3 gets forward biased before D_1, we will have the transient conduction of diodes which is not desirable and is not considered in this thesis. As soon as D_1 is forward biased we will

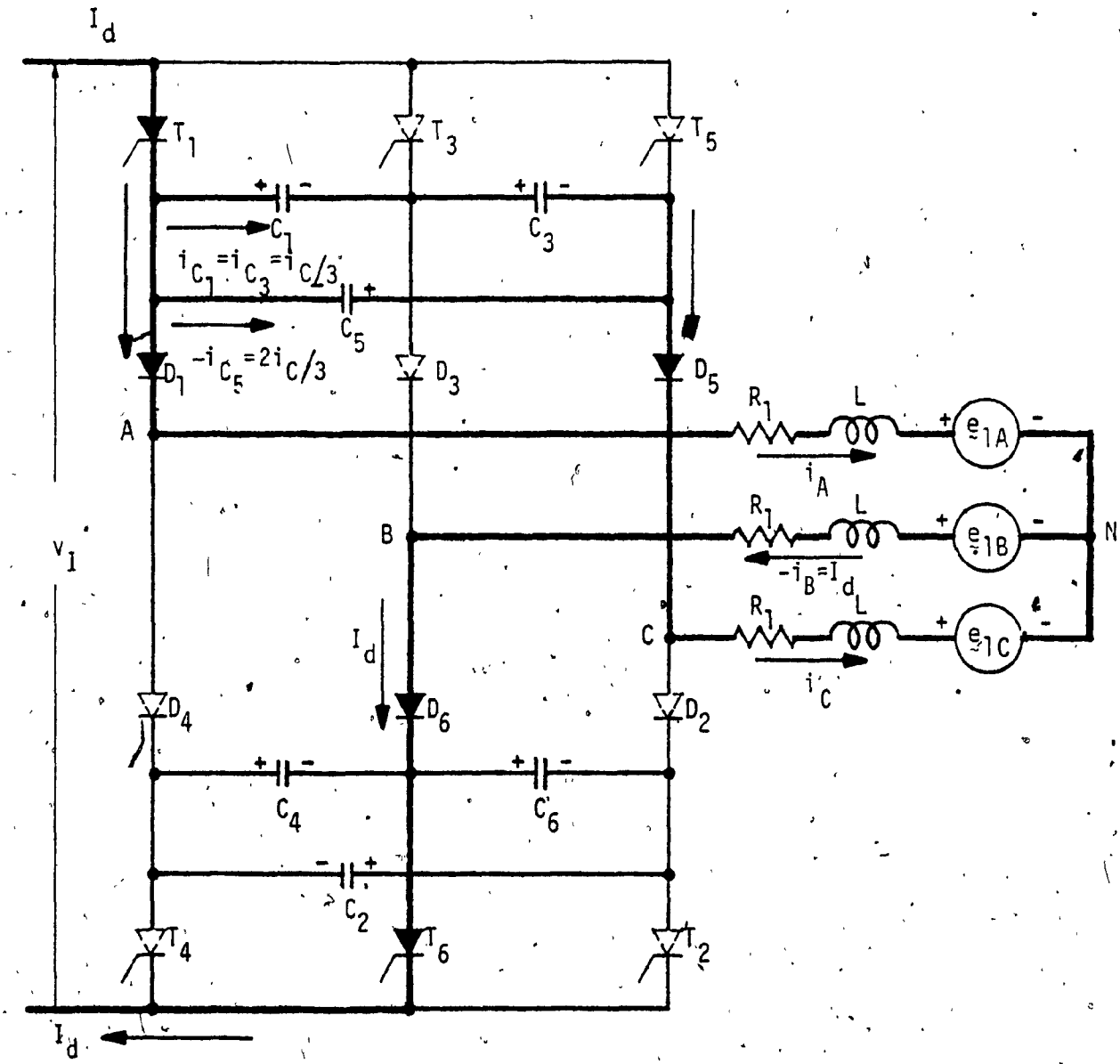

FIG. 3.7 ASCI-Induction motor current routes during mode 2 (transfer mode) in case (a) when current in phase C is being transferred to phase A. Voltage spikes are generated during this mode.

have an RLC circuit with a sinusoidal voltage source and an externally injected dc link current I_d. Figure 3.8 shows this circuit. Just before the diode D_1 starts to conduct, this circuit contains a magnetic energy stored in the leakage inductance of the phase C and equal to $\frac{1}{2} LI_d^2$. For a typical induction motor connected to an ASCI we have always $\frac{4(2L)}{1.5(C)} > (2XR_1)^2$ which implies an oscillatory circuit. Thus as soon as D_1 conducts, we will have an oscillating current in addition to a current due to the sinusoidal driving force. The resultant current is opposed to the current I_d in phase C and when its magnitude reaches I_d the diode D_5 becomes blocked. At this moment all the dc link current has been transferred to phase A and mode 2 ends.

The above was the interpretation of the current transferring process in mode 2. In the following we will derive the equations which govern this mode.

Going back to fig. 3.7 we notice that when D_1 is forward biased the diode D_5 is still conducting. Then, neglecting the voltage drops across these two semiconductors, we can write

$$v_{C5}(t) = v_{CA}(t) \tag{3.4.1}$$

The above is also true at $t=t_2$ when D_1 has just begun conducting

$$v_{C5}(t_2) = v_{CA}(t_2) \tag{3.4.2}$$

Using (3.3.11) for $v_{C5}(t)$ and (3.3.9) for $v_{CA}(t)$ in (3.4.2) one obtains

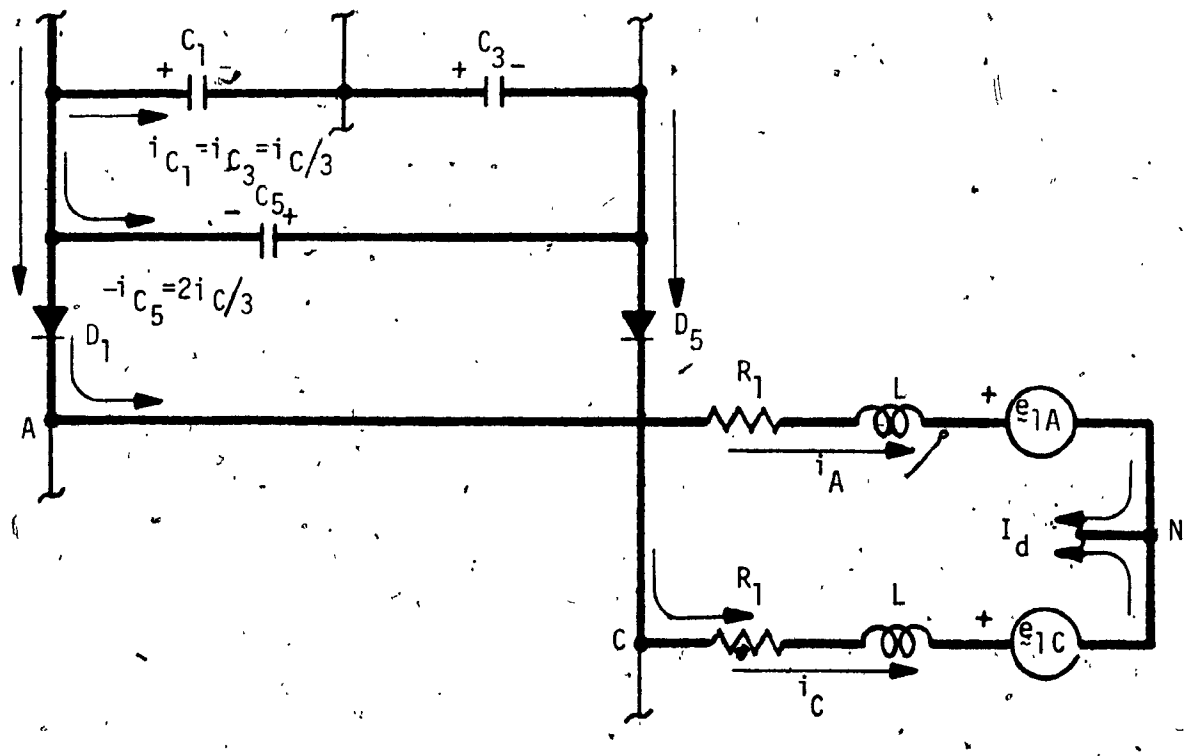

FIG. 3.8 The mechanism of a current transfer from phase C to phase A.

$$-\frac{2}{3C} I_d(t_2-t_1)+V_o = R_1 I_d - E_1\sqrt{3}\cos(\omega t_2+\phi_1-\frac{2\pi}{3}) \qquad (3.4.3)$$

but by employing (3.3.18) it resolves

$$-\frac{2}{3C} I_d\ t_{ch}+V_o = R_1 I_d - E_1\sqrt{3}\,\mathrm{Cos}(\omega t_2+\phi_1-\frac{2\pi}{3}) \qquad (3.4.4)$$

The above is one of the relations which exists between the different variables of the system during mode 2.

For currents we have the following

$$i_A(t) + i_C(t) = I_d \quad , \quad i_B(t) = -I_d$$

$$i_{C1}(t) = i_{C3}(t) = \frac{1}{3} i_C(t) \qquad (3.4.5)$$

$$-i_{C5}(t) = \frac{2}{3} i_C(t)$$

$$i_{D3}(t) = i_{D2}(t) = i_{D4}(t) = 0$$

$$i_{D1}(t) = i_A(t) \qquad (3.4.6)$$

$$i_{D5}(t) = i_C(t)$$

$$i_{D6}(t) = I_d .$$

The equations for different voltages are

$$v_A(t) = R_1 i_A(t) + L\frac{di_A(t)}{dt} + e_{1A}(t)$$

$$= R_1 i_A(t) + L\frac{di_A(t)}{dt} + E_1 \sin(\omega t+\phi_1)$$

$$v_B(t) = -R_1 I_d + e_{1B}(t) = -R_1 I_d + E_1 \sin(\omega t+\phi_1-\frac{2\pi}{3})$$

$$v_C(t) = R_1 i_C(t) + L\frac{di_C(t)}{dt} + e_{1C}(t)$$

$$= R_1 i_C(t) + L\frac{di_C(t)}{dt} + E_1 \sin\left(\omega t+\phi_1 - \frac{4\pi}{3}\right) \qquad (3.4.7)$$

$$v_{AB}(t) = R_1 i_A(t) + L\frac{di_A(t)}{dt} + R_1 I_d + E_1\sqrt{3}\cos\left(\omega t+\phi_1 - \frac{\pi}{3}\right)$$

$$v_{BC}(t) = -\left[R_1 I_d + R_1 i_C(t) + L\frac{di_C(t)}{dt}\right] + E_1\sqrt{3}\cos(\omega t+\phi_1-\pi)$$

$$= -2R_1 I_d + R_1 i_A(t) + L\frac{di_A(t)}{dt} + E_1\sqrt{3}\cos(\omega t+\phi_1-\pi)$$

$$v_{CA}(t) = R_1 I_d - 2R_1 i_A(t) - 2L\frac{di_A(t)}{dt} - E_1\sqrt{3}\cos\left(\omega t+\phi_1 - \frac{2\pi}{3}\right)$$

$$(3.4.8)$$

$$v_{C1}(t) = \frac{1}{C}\int_{t_2}^{t} i_{C1}(t)dt + v_{C1}(t_2)$$

$$= \frac{1}{C}\int_{t_2}^{t} i_{C1}(t)dt + \frac{1}{3C} I_d(t_2-t_1)$$

$$= \frac{1}{3C}\int_{t_2}^{t} i_C(t)dt + \frac{1}{3C} I_d t_{ch}$$

$$v_{C3}(t) = \frac{1}{C}\int_{t_2}^{t} i_{C3}(t)dt + v_{C3}(t_2) \qquad (3.4.9)$$

$$= \frac{1}{3C}\int_{t_2}^{t} i_C(t)dt + \frac{1}{3C} I_d t_{ch} - V_o$$

$$v_{C5}(t) = -\frac{1}{C}\int_{t_2}^{t} i_{C5}(t)dt + v_{C5}(t_2)$$

$$v_{C5}(t) = -\frac{2}{3C}\int_{t_2}^{t} i_C(t)dt - \frac{2}{3C} I_d t_{ch} + V_o$$

$$v_{T1}(t) = 0$$

$$v_{T3}(t) = v_{C1}(t) \qquad (3.5.10)$$

$$v_{T5}(t) = -v_{C5}(t)$$

Since the voltages $v_{C2}(t)$, $v_{C4}(t)$, $v_{C6}(t)$ remain unchanged during this mode there would be no change in $v_{T2}(t)$ and $v_{T4}(t)$. Thus, the equations in (3.3.14) hold true also for the transfer mode.

The voltages across the blocking diodes during this mode are expressed by

$$v_{D1}(t) = v_{D5}(t) = v_{D6}(t) = 0$$

$$v_{D3}(t) = v_{C3}(t) + v_{CB}(t) = -v_{C1}(t) + v_{AB}(t) \qquad (3.4.11)$$

$$v_{D2}(t) = v_{CB}(t) + v_{C6}(t) = v_{CB}(t) - V_o$$

$$v_{D4}(t) = v_{AB}(t) - v_{C4}(t) = v_{AB}(t) - V_o$$

in which $v_{C3}(t)$, $v_{C6}(t)$, $v_{C4}(t)$ are given by (3.4.9) and (3.3.13) and $v_{CB}(t)$, $v_{AB}(t)$ are found using (3.4.8). And, at last, the inverter input voltage would be

$$v_I(t) = v_{AB}(t) \qquad (3.4.11a)$$

where $v_{AB}(t)$ is given by (3.4.8).

It should be noted that the equations for the fundamental components of currents and CEMF's for the induction motor remain the same as (3.3.6) and (3.3.7) but for $t_2<t<t_3$.

The transfer mode ends at $t=t_3$ for which

$$i_A(t_3) = I_d \qquad i_C(t_3) = 0 \tag{3.4.12}$$

Therefore, the duration of this mode which is called <u>'transfer time'</u> would be

$$t_{tr} = t_3-t_2 \tag{3.4.13}$$

The sum of the 'charging time' and the 'transfer time' is called <u>'commutation time'</u>. Using (3.3.18) and (3.4.13) the commutation time is given by

$$t_{co} = t_{ch}+t_{tr} = t_2-t_1+t_3-t_2 = t_3-t_1 \tag{3.4.14}$$

The <u>'commutation time'</u> is the time needed for the transfer of the current from one phase to the other after firing one of the SCR's.

In (3.4.5-9), $i_A(t)$ and $i_C(t)$ have been used without specifying the equations representing them. In the following, first we will obtain the expression of the current $i_A(t)$ in phase A. Then the current $i_C(t)$ in phase C is easily found by knowing $i_A(t)+i_C(t) = I_d$. In order to obtain the equation of the current $i_A(t)$ in phase A it is

necessary to define a new time scale for this mode

$$t' = t - t_2 \Rightarrow t = t' + t_2 \tag{3.4.15}$$

which implies that the origin of time is now shifted to the beginning of the transfer time. Since $v_{C5}(t_2) = v_{CA}(t_2)$ equation (3.4.1) yields

$$v_{C5}(t') = v_{CA}(t') \tag{3.4.16}$$

From (3.4.8 and 9) one obtains

$$v_{CA}(t') = R_1 I_d - 2R_1 i_A(t') - 2L \frac{di_A(t')}{dt'} - E_1\sqrt{3}\cos\left[\omega(t'+t_2)+\phi_1 - \frac{2\pi}{3}\right] \tag{3.4.17}$$

$$v_{C5}(t') = -\frac{2}{3C} I_d t' + \frac{2}{3C}\int_0^{t'} i_A(t')dt' - \frac{2}{3C} I_d t_{ch} + V_o \tag{3.4.18}$$

In (3.4.18) $i_C(t')$ has been replaced by $I_d - i_A(t')$ which is obtained from (3.4.5). Inserting (3.4.17-18) back into (3.4.16) gives

$$-\frac{2}{3C} I_d t' + \frac{2}{3C}\int_0^{t'} i_A(t')dt' - \frac{2}{3C} I_d t_{ch} + V_o = R_1 I_d - 2R_1 i_A(t') - 2L\frac{di_A(t')}{dt'} - E_1\sqrt{3}\cos\left[\omega(t'+t_2)+\phi_1 - \frac{2\pi}{3}\right] \tag{3.4.19}$$

The Laplace transform of (3.4.19) gives

$$\frac{1}{s}\left[R_1 I_d + \frac{2}{3C} I_d t_{ch} - V_o\right] + \frac{1}{s^2}\frac{2I_d}{3C}$$

$$+E_1\sqrt{3}\,\frac{-s\cos(\omega t_2+\phi_1-\frac{2\pi}{3})+\omega\sin(\omega t_2+\phi_1-\frac{2\pi}{3})}{s^2+\omega^2} =$$

$$\frac{2}{3Cs} I_A(s) + 2R_1 I_A(s) + 2L\left[sI_A(s)-i_A(0^+)\right] \qquad (3.4.20)$$

where s is the Laplace operator and $I_A(s)$ is the Laplace transform of $i_A(t')$. Defining the two new constants

$$V_1 = R_1 I_d + \frac{2}{3C} I_d t_{ch} - V_o \qquad (3.4.21)$$

$$\theta = \omega t_2 + \phi_1 - \frac{2\pi}{3} \qquad (3.4.22)$$

and noticing that at $t=t_2^+$ i.e. at $t'=0^+$ the current $i_A(t')$ in phase A is zero, (3.4.20) yields

$$I_A(s) = \frac{V_1}{2L(s^2+\frac{R_1}{L}s+\frac{1}{3LC})} + \frac{I_d}{3LCs(s^2+\frac{R_1}{L}s+\frac{1}{3LC})}$$

$$-\frac{E_1\sqrt{3}\,(s^2\cos\theta-\omega s\sin\theta)}{2L(s^2+\frac{R_1}{L}s+\frac{1}{3LC})(s^2+\omega^2)} \qquad (3.4.23)$$

The term $(s^2+\frac{R_1}{L}s+\frac{1}{3LC})$ can be written in the following way

$$s^2+\frac{R_1}{L}s+\frac{1}{3LC} = s^2+2\alpha s+\omega_o^2 = (s+\alpha)^2+\omega_o^2-\alpha^2$$

$$= (s+\alpha)^2+\omega_1^2$$

where $\alpha = \frac{R_1}{2L}$

$$\omega_o = \frac{1}{\sqrt{3LC}}$$

$$\omega_1 = \sqrt{\omega_o^2 - \alpha^2} \qquad (3.4.24)$$

In the above α presents the damping factor, ω_o gives the resonant frequency and ω_1 is the ringing frequency. Using (3.4.24), the new form of (3.4.23) becomes

$$I_A(s) = \frac{V_1}{2L} \cdot \frac{1}{(s+\alpha)^2+\omega_1^2} + I_d\omega_o^2 \frac{1}{s[(s+\alpha)^2+\omega_1^2]}$$

$$- \frac{E_1\sqrt{3}\cos\theta}{2L} \cdot \frac{s^2-\omega s\tan\theta}{(s^2+\omega^2)[(s+\alpha)^2+\omega_1^2]} \qquad (3.4.25)$$

The inverse Laplace transform of the above equation gives the expression for the current i_A in phase A during the transfer time

$$i_A(t') = \frac{V_1}{2L} L^{-1}\left\{\frac{1}{(s+\alpha)^2+\omega_1^2}\right\} + I_d\omega_o^2 L^{-1}\left\{\frac{1}{s[(s+\alpha)^2+\omega_1^2]}\right\}$$

$$- \frac{E_1\sqrt{3}\cos\theta}{2L} L^{-1}\left\{\frac{s^2-\omega s\tan\theta}{(s^2+\omega^2)[(s+\alpha)^2+\omega_1^2]}\right\} \qquad (3.4.26)$$

In the above equation, the $E_1\sqrt{3}\cos\theta$ term is equal to V_1 given by (3.4.21). This can be found by substituting (3.4.22) into (3.4.4) which yields

$$E_1\sqrt{3}\cos\theta = R_1 I_d + \frac{2}{3C} I_d t_{ch} - V_o \qquad (3.4.27)$$

However, the right hand side term in (3.4.27) is the same as the corresponding term in (3.4.21) so that we can write

$$V_1 = E_1 \sqrt{3} \cos \theta \tag{3.4.28}$$

Inserting (3.4.28) back into (3.4.26) and finding the inverse Laplace transforms of the three terms we have

$$i_A(t') = \frac{E_1\sqrt{3}\cos\theta}{2L\omega_1} e^{-\alpha t'} \sin \omega_1 t' + I_d \left[\frac{\omega_0}{\omega_1} e^{-\alpha t'} \sin(\omega_1 t' + \beta) + 1\right]$$

$$- \frac{E_1\sqrt{3}\cos\theta}{2L} \left[A_2 e^{-\alpha t'} \sin(\omega_1 t' + \gamma) + B_2 \sin(\omega t' + \delta)\right] \tag{3.4.29}$$

where $\beta = -\text{arc tan} \dfrac{\omega_1}{-\alpha}$

$$A_2 = \frac{1}{\omega_1} \left[\frac{(\alpha^2 - \omega_1^2 + \alpha\omega \tan\theta)^2 + \omega_1^2 (2\alpha + \omega \tan\theta)^2}{(\omega_0^2 - \omega^2)^2 + 4\alpha^2\omega^2}\right]^{1/2}$$

$$B_2 = \omega \left[\frac{1 + \tan^2\theta}{(\omega_0^2 - \omega^2)^2 + 4\alpha^2\omega^2}\right]^{1/2} \tag{3.4.30}$$

$$\gamma = \text{arc tan} \frac{\omega_1(-2\alpha - \omega \tan\theta)}{\alpha^2 - \omega_1^2 + \alpha\omega \tan\theta} - \text{arc tan} \frac{-2\alpha\omega_1}{\alpha^2 - \omega_1^2 + \omega^2}$$

$$\delta = \text{arc tan} \frac{-\tan\theta}{-1} + \text{arc tan} \frac{-2\alpha\omega}{\omega_0^2 - \omega^2}$$

Notice that in obtaining β, γ, and δ angles, we have kept the signs in arc tan terms. This is necessary in order to find the

correct quadrants in which these angles are located. This approach will always be used in this study.

From (3.4.5) we know that

$$i_A(t) + i_C(t) = I_d$$

or

$$i_A(t') + i_C(t') = I_d \tag{3.4.31}$$

By using (3.4.29) the last equation yields

$$i_C(t') = I_d - i_A(t') = \frac{E_1\sqrt{3}\cos\theta}{2L}[A_2 e^{-\alpha t'}\sin(\omega_1 t'+\gamma)$$

$$+ B_2 \sin(\omega t'+\delta)] - \frac{E_1\sqrt{3}\cos\theta}{2L\omega_1} e^{-\alpha t'}\sin\omega_1 t'$$

$$- \frac{\omega_0}{\omega_1} I_d e^{-\alpha t'} \sin(\omega_1 t'+\beta) \tag{3.4.32}$$

By examining (3.4.29) we see that the current $i_A(t')$ in the phase A consists of three distinct components:

1 - I_d, which is a dc component imposed by the injection of the dc current into the inverter.

2 - A sinusoidal component with an angular frequency ω. This component is due to the motor CEMF.

3 - A damped oscillating component with an angular frequency ω_1 and a damping factor α. This component is due to the initial conditions existing at the beginning of this mode $(t=t_2)$. The circuit of fig. 3.8 corroborates the above explanation.

As mentioned before, the transfer mode ends when the current $i_C(t')$ through phase C becomes zero. Thus, to find the duration of the transfer mode we have

$$i_C(t_1') = 0 \tag{3.4.33}$$

where $$t_1' = t_{tr} = t_3 - t_2 \tag{3.4.34}$$

To find t_1' use (3.4.32)

$$i_C(t_1') = \frac{E_1\sqrt{3}\cos\theta}{2L}\left[A_2\, e^{-\alpha t_1'}\sin(\omega_1 t_1'+\gamma)+B_2\sin(\omega t_1'+\delta)\right]$$

$$-\frac{E_1\sqrt{3}\cos\theta}{2L\omega_1}\, e^{-\alpha t_1'}\sin\omega_1 t_1' - \frac{\omega_0}{\omega_1} I_d\, e^{-\alpha t_1'}\sin(\omega_1 t_1'+\beta) = 0 \tag{3.4.35}$$

To solve the above equation, we must know the values of the motor parameters, commutating capacitors, as well as the values of θ, A_2, B_2, β, γ and δ. From (3.4.22) it is seen that θ is a function of t_2 while A_2, B_2, γ and δ are functions of θ. Under these conditions, and with the information we have, it is difficult to find t_1' from (3.4.35). Later on, the solution of this equation, using the approximate and the exact methods, will be given.

As was mentioned in section (3.2), the maximum voltage across the capacitors, V_o, is one of the <u>unknowns</u> whose value should be found. This can be done in the following way.

Referring to fig. 3.8 we notice that at the end of this mode the currents through C_1, C_3 and C_5 are zero. This condition remains

unchanged until the instant at which T_3 is fired. Now, as was noticed earlier, for a successful triggering of T_3, C_1 should have a positive voltage equal to V_o. That is

$$v_{C1}(t_3) = V_o \tag{3.4.36}$$

From (3.4.9) one obtains

$$v_{C1}(t_3) = \frac{1}{3C}\int_{t_2}^{t_3} i_C(t)dt + \frac{1}{3C} I_d t_{ch} \tag{3.4.37}$$

or

$$v_{C1}(t_3) = \frac{1}{3C}\int_{0}^{t_1'} i_C(t')dt' + \frac{1}{3C} I_d t_{ch} \tag{3.4.38}$$

in which $t_1' = t_{tr}$ (3.4.38a)

Inserting (3.4.38) into (3.4.36) provides

$$V_o = \frac{1}{3C}\int_{0}^{t_1'} i_C(t')dt' + \frac{1}{3C} I_d t_{ch} \tag{3.4.39}$$

The above equation yields another relationship between different variables of the system during the transfer mode. From (3.4.4) we obtain

$$\frac{1}{3C} I_d t_{ch} = V_o/2 - R_1 I_d/2 + (E_1\sqrt{3}/2)\cos(\omega t_2 + \phi_1 - \frac{2\pi}{3}) \tag{3.4.40}$$

Using (3.4.22) the last expression becomes

$$\frac{1}{3C} I_d t_{ch} = \frac{V_o}{2} - \frac{R_1 I_d}{2} + \frac{E_1\sqrt{3}}{2} \cos\theta \qquad (3.4.41)$$

Inserting the above equation into (3.4.39) one obtains

$$V_o = \frac{2}{3C}\int_0^{t_1'} i_C(t')dt' - R_1 I_d + E_1\sqrt{3}\cos\theta$$

or

$$V_o = \frac{2}{3C}\int_0^{t_1'} [I_d - i_A(t')]dt' - R_1 I_d + E_1\sqrt{3}\cos\theta$$

$$= \frac{2}{3C} I_d t_1' - \frac{2}{3C}\int_0^{t_1'} i_A(t')dt' - R_1 I_d + E_1\sqrt{3}\cos\theta \qquad (3.4.42)$$

After finding θ and t_1' we can calculate V_o from the above equation. For $t=t_3$ equations (3.4.9) give

$$v_{C3}(t_3) = \frac{1}{3C}\int_{t_2}^{t_3} i_C(t)dt + \frac{1}{3C} I_d t_{ch} - V_o$$

$$v_{C5}(t_3) = -\frac{2}{3C}\int_{t_2}^{t_3} i_C(t)dt - \frac{2}{3C} I_d t_{ch} + V_o$$

or

$$v_{C3}(t_3) = \frac{1}{3C}\int_0^{t_1'} i_C(t')dt' + \frac{1}{3C} I_d t_{ch} - V_o$$

$$v_{C5}(t_3) = -\frac{2}{3C}\int_0^{t_1'} i_C(t')dt' - \frac{2}{3C} I_d t_{ch} + V_o \qquad (3.4.43)$$

Inserting (3.4.41-42) into (3.4.43) provides

$$v_{C3}(t_3) = 0$$
$$v_{C5}(t_3) = -V_o \tag{3.4.44}$$

The results obtained in (3.4.44) along with (3.4.36) are the same as those predicted in Table 1.1. This verifies then the pattern of the capacitor voltages which we assumed when describing the operation of the system.

Equation (3.4.1) is valid during the transfer mode including at $t=t_3$. From this equation and (3.4.44) we can write

$$v_{C5}(t_3) = v_{CA}(t_3)$$
$$v_{CA}(t_3) = -V_o \tag{3.4.44a}$$

Some of the equations derived in this chapter have terms showing derivatives or integrals of $i_C(t')$ and $i_A(t')$. For these cases, the following expressions can be used. From (3.4.29) it follows

$$\frac{d_{iA}(t')}{dt'} = \frac{E_1\sqrt{3}\cos\theta}{2L\omega_1}[-\alpha e^{-\alpha t'}\sin\omega_1 t' + \omega_1 e^{-\alpha t'}\cos\omega_1 t')$$
$$+ I_d\frac{\omega_o}{\omega_1}[-\alpha e^{-\alpha t'}\sin(\omega_1 t'+\beta) + \omega_1 e^{-\alpha t'}\cos(\omega_1 t'+\beta)]$$
$$- \frac{E_1\sqrt{3}\cos\theta}{2L}[-\alpha A_2 e^{-\alpha t'}\sin(\omega_1 t'+\gamma) + \omega_1 A_2 e^{-\alpha t'}\cos(\omega_1 t'+\gamma)]$$
$$- \frac{E_1\sqrt{3}\cos\theta}{2L}[\omega B_2\cos(\omega t'+\delta)] \tag{3.4.45}$$

$$\int_0^{t'} i_A(t')dt' = \frac{E_1\sqrt{3}\cos\theta}{2L\omega_1}\cdot\frac{1}{\omega_o^2}\left[e^{-\alpha t'}(-\alpha\sin\omega_1 t'-\omega_1\cos\omega_1 t')+\omega_1\right]$$

$$+\frac{I_d}{\omega_1\cdot\omega_o}\left[-\alpha e^{-\alpha t'}\sin(\omega_1 t'+\beta)-\omega_1 e^{-\alpha t'}\cos(\omega_1 t'+\beta)+\alpha\sin\beta\right.$$

$$\left.+\omega_1\cos\beta\right]+I_d t' - \frac{A_2E_1\sqrt{3}\cos\theta}{2L\omega_o^2}\left[-\alpha e^{-\alpha t'}\sin(\omega_1 t'+\gamma)\right.$$

$$\left.-\omega_1 e^{-\alpha t'}\cos(\omega_1 t'+\gamma)+\alpha\sin\gamma+\omega_1\cos\gamma\right]$$

$$-\frac{B_2E_1\sqrt{3}\cos\theta}{2L\omega}\left[\cos\delta-\cos(\omega t'+\delta)\right] \qquad (3.4.46)$$

and

$$\frac{di_C(t')}{dt'} = -\frac{di_A(t')}{dt'}$$

$$\int_0^{t'} i_C(t')dt' = I_d\cdot t' - \int_0^{t'} i_A(t')dt' \qquad (3.4.47)$$

3.5 MODE 3 OR NORMAL MODE

This mode is defined for $t_3<t<t_4$ where t_3 is the instant when the diode D_5 stops conducting and t_4 is the moment when the thyristor T_2 is fired. At the end of the transfer mode $(t=t_3)$ all current in phase C has been transferred to phase A and the normal mode begins. Figure 3.9 shows the circuit during this mode. It is seen that in mode 3 only T_1, D_1, D_6 and T_6 are conducting. As well, no current flows through the commutating capacitors, thus keeping their voltages

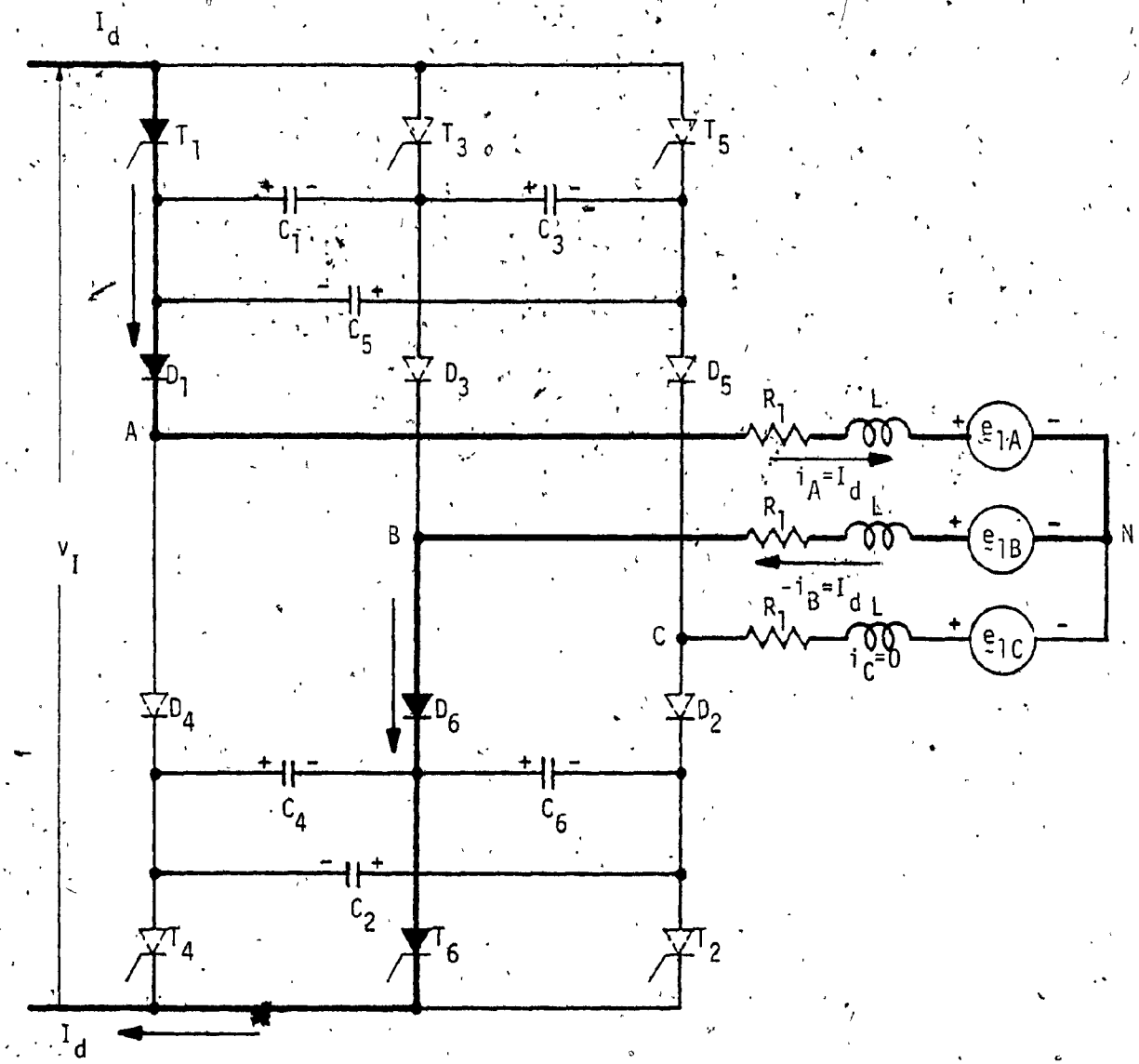

FIG. 3.9 ASCI-Induction motor current routes during mode 3 (normal mode) in case (a) when only phase A and phase B carry the dc link current, I_d .

constant. According to the sequence chosen for firing the SCR's (fig. 2.2) we can write

$$\omega t_4 - \omega t_1 = \omega(t_4 - t_1) = \pi/3 \text{ rad} \tag{3.5.1}$$

The inverter operates without a commutation overlap if the commutation interval is shorter or equal to $\pi/3$ rad.

$$\omega t_{co} = \omega(t_{ch} + t_{tr}) = \omega(t_3 - t_1) \leq \pi/3 \text{ rad} \tag{3.5.2}$$

Later on, we will see that when the commutation interval becomes more than $\pi/3$ rad we obtain partial or full overlap, [14-16]. If this happens, we would not have a normal mode. Thus, the normal interval can be defined as a period between firing two consecutive thyristors, and during which only two motor phases carry the current I_d while no currents flow through the commutating capacitors.

$$t_{no} = t_4 - t_3 \tag{3.5.2a}$$

The fundamental components of the motor phase currents and their CEMF's during this mode are the same as given by (3.3.6) and (3.3.7) but for $t_3 < t < t_4$. The other equations describing the system during this mode are

$$\begin{aligned} v_A(t) &= R_1 I_d + e_{1A}(t) = R_1 I_d + E_1 \sin(\omega t + \phi_1) \\ v_B(t) &= -R_1 I_d + e_{1B}(t) = -R_1 I_d + E_1 \sin(\omega t - \tfrac{2\pi}{3} + \phi_1) \\ v_C(t) &= e_{1C}(t) = E_1 \sin(\omega t - \tfrac{4\pi}{3} + \phi_1) \end{aligned} \tag{3.5.3}$$

$$v_{AB}(t) = 2R_1 I_d + E_1\sqrt{3}\cos(\omega t+\phi_1-\frac{\pi}{3})$$

$$v_{BC}(t) = -R_1 I_d + E_1\sqrt{3}\cos(\omega t+\phi_1-\pi) \qquad (3.5.4)$$

$$v_{CA}(t) = -R_1 I_d - E_1\sqrt{3}\cos(\omega t+\phi_1-\frac{2\pi}{3})$$

$$v_{C1}(t) = v_{C1}(t_3) = +V_o$$

$$v_{C3}(t) = v_{C3}(t_3) = 0 \qquad (3.5.5)$$

$$v_{C5}(t) = v_{C5}(t_3) = V_o$$

$$v_{T1}(t) = 0$$

$$v_{T3}(t) = v_{C1}(t) = v_{C1}(t_3) = +V_o \qquad (3.4.6)$$

$$v_{T5}(t) = -v_{C5}(t) = -v_{C5}(t_3) = +V_o$$

The equations given in (3.3.14) hold for this mode as well. Besides

$$v_{D1}(t) = v_{D6}(t) = 0$$

$$v_{D2}(t) = v_{CB}(t) + v_{C6}(t) = v_{CB}(t) - V_o$$

$$v_{D3}(t) = -v_{C1}(t) + v_{AB}(t) = -V_o + v_{AB}(t) \qquad (3.5.7)$$

$$v_{D4}(t) = v_{AB}(t) - v_{C4}(t) = v_{AB}(t) - V_o$$

$$v_{D5}(t) = v_{C5}(t) + v_{AC}(t) = -V_o + v_{AC}(t)$$

$$i_{C1}(t) = i_{C3}(t) = i_{C5}(t) = i_{C2}(t) = i_{C4}(t) = i_{C6}(t) = 0 \qquad (3.5.8)$$

$$i_{D1}(t) = i_{D6}(t) = I_d \qquad (3.5.9)$$

$$i_{D3}(t) = i_{D5}(t) = i_{D4}(t) = i_{D2}(t) = 0$$

$$i_A(t) = I_d; \quad i_B(t) = -I_d; \quad i_C(t) = 0 \qquad (3.5.10)$$

and at last $$v_I(t) = v_{AB}(t) \tag{3.5.11}$$

Also the inverter average input voltage during each cycle, V_I, is calculated from fig. 2.9c where the higher current harmonics are neglected. In the following expression P_{tm} shows the motor approximate input power while I, and E, denote peak values.

$$V_I = (3/2I_d)(R_1 I_1^2 + E_1 I_1 \cos \phi_1) \tag{3.5.12}$$

In the next section we will solve the main equations from which we can find the unknown variables. This is done by using both exact and approximate methods.

3.6 SOLUTION OF THE EQUATIONS

In the previous three sections we have derived the key equations which we will use to find the unknowns. One is reminded that we are still dealing with a case in which the commutation interval is less than one sixth of the period of the inverter output, and the diodes do not become transiently forward biased. The unknowns are

$$t_1, t_2, t_3, t_4, t_{ch}, t_{tr}, t_{co} \text{ and } V_o . \tag{3.6.1}$$

Knowing the motor input frequency for constant V/Hz or constant hp control strategy will provide us with the motor input voltage. Then, using the exact equivalent circuit of the induction motor one can calculate a stator current for each desired slip. This current would be equal to I_{1s} as defined in (2.3.9). In conclusion, we can easily find all variables given in (2.3.9), i.e., ϕ_1, E_1 and I_{1s}. Also, the

appropriate value of I_d can be found using (2.5.3).

The list of key equations obtained before would be

$$t_{ch} = t_2 - t_1 \tag{3.3.18}$$

$$-\frac{2}{3C} I_d t_{ch} + V_o = R_1 I_d - E_1\sqrt{3}\cos(\omega t_2 + \phi_1 - \frac{2\pi}{3}) \tag{3.4.4}$$

$$t_{tr} = t_3 - t_2 = t_1' \tag{3.4.34}$$

$$t_{co} = t_{ch} + t_{tr} = t_3 - t_1 \tag{3.4.14}$$

$$i_C(t_1') = \frac{E_1\sqrt{3}\cos\theta}{2L}[A_2 e^{-\alpha t_1'}\sin(\omega_1 t_1' + \gamma) + B_2\sin(\omega t_1' + \delta)]$$
$$- \frac{E_1\sqrt{3}\cos\theta}{2L\omega_1} e^{-\alpha t_1'}\sin\omega_1 t_1' - \frac{\omega_o}{\omega_1} I_d e^{-\alpha t_1'}\sin(\omega_1 t_1' + \beta) = 0 \tag{3.4.35}$$

where θ is calculated from (3.4.22) and β, A_2, B_2, γ and δ are given in (3.4.30).

$$V_o = \frac{2}{3C} I_d t_1' - \frac{2}{3C}\int_0^{t_1'} i_A(t')dt' - R_1 I_d + E_1\sqrt{3}\cos\theta \tag{3.4.42}$$

$$t_4 - t_1 = \frac{\pi}{3\omega} \tag{3.5.1}$$

As can be seen there are seven key equations, whereas we have eight unknowns in (3.6.1). In order to make the number of the unknowns equal to the number of equations, we formulate one constraint on the motor current. This constraint is based on the fact that whatever the current waveform is in phase A of the motor, its fundamental

component should pass through $t=0$ point with a positive slope. It will be shown later that this constraint yields the value of t_2, thus causing the number of the unknowns to decrease by one.

Also, the exactly calculated fundamental component of the motor line current should have an rms value equal to the rms value obtained from the exact equivalent circuit for a specific input frequency and slip. This constraint determines the corresponding value of the dc link current, I_d.

In the next two parts we will derive first the equations needed for an approximate solution and give a flowchart which can be used in writing the corresponding computer program. Second, we will present another flowchart which is useful since it can be adopted to yield the exact solution, the equations of which were obtained in sections (3.3-5).

3.6.1 Approximate Approach

The approximate solution of the key equations is based on two new assumptions:

a) The CEMF during transfer mode is constant.

b) The current transfer from one phase to the other is linear.

The first assumption will result in a simple form for (3.4.35) while the second provides us with the value of t_2. In addition, I_d is calculated from (2.5.3).

The results obtained from this method can be used either to design the system or as an initial guess in solving the equations

by the exact approach.

Applied to (3.4.19) the assumption (a) gives

$$E_1\sqrt{3}\cos\left[\omega(t'+t_2)+\phi_1-\frac{2\pi}{3}\right] \simeq E_1\sqrt{3}\cos\left(\omega t_2+\phi_1-\frac{2\pi}{3}\right) \qquad (3.6.1.1)$$

The right hand side term in (3.6.1.1) is a constant. Substituting it into (3.4.19) we find

$$-\frac{2}{3C}I_d t' + \frac{2}{3C}\int_0^{t'} i_A(t')dt' - \frac{2}{3C}I_d t_{ch} + V_o$$
$$= R_1 I_d - 2R_1 i_A(t') - 2L\frac{di_A(t')}{dt'} - E_1\sqrt{3}\cos\left(\omega t_2+\phi_1-\frac{2\pi}{3}\right) \qquad (3.6.1.2)$$

Inserting (3.4.4) back into (3.6.1.2) one obtains

$$-\frac{2}{3C}I_d t' + \frac{2}{3C}\int_0^{t'} i_A(t')dt' = -2R_1 i_A(t') - 2L\frac{di_A(t')}{dt'} \qquad (3.6.1.3)$$

The Laplace transform of the above expression is

$$-\frac{1}{s^2}\frac{2I_d}{3C} + \frac{2}{3Cs}I_A(s) = -2R_1 I_A(s) - 2LsI_A(s) \qquad (3.6.1.4)$$

from which one obtains

$$I_A(s) = \frac{I_d}{3LCs\left(\frac{1}{3LC}+\frac{R_1}{L}s+s^2\right)} \qquad (3.6.1.5)$$

Using the notations given by (3.4.24) yields

$$I_A(s) = \frac{\omega_0^2 I_d}{s[(s+\alpha)^2+\omega_1^2]} \qquad (3.6.1.6)$$

The inverse Laplace transform of (3.6.1.6) is

$$i_A(t') = \frac{\omega_o}{\omega_1} I_d e^{-\alpha t'} \sin(\omega_1 t' + \beta) + I_d \qquad \text{APX}$$

where $\beta = -\text{arc tan} \frac{\omega_1}{-\alpha}$ (3.6.1.7)

APX, appearing above, means that the solution or the result has been obtained by an approximation. The current in phase C for this mode is

$$i_C(t') = I_d - i_A(t') = -\frac{\omega_o}{\omega_1} I_d e^{-\alpha t'} \sin(\omega_1 t' + \beta)$$

where $\beta = -\text{arc tan} \frac{\omega_1}{-\alpha}$ (3.6.1.8) APX

As mentioned before, the transfer period can be calculated by solving the following equation

$$i_C(t_1') = 0 \qquad (3.4.33)$$

or $$-\frac{\omega_o}{\omega_1} I_d e^{-\alpha t_1'} \sin(\omega_1 t_1' + \beta) = 0 \qquad (3.6.1.9)\text{APX}$$

where $t_1' = t_{tr} = t_3 - t_2$ (3.4.34)

From (3.6.1.9) we obtain the result

$$\sin(\omega_1 t_1' + \beta) = 0 = \sin K\pi \quad K = 0,1,2, \qquad (3.6.1.10)$$

which yields

$$\omega_1 t_1' + \beta = K\pi$$

$$t_1' = \frac{K\pi - \beta}{\omega_1} \qquad (3.6.1.11)\text{ APX}$$

According to (3.6.1.8) β is negative so that the first solution of (3.6.1.11) is obtained for $K=0$;

$$t_1' = \frac{-\beta}{\omega_1} \qquad (3.6.1.12)\ \text{APX}$$

One significant conclusion can be derived from (3.6.1.12). Since β and ω_1 depend only on the motor parameters and the commutating capacitor, one can state that the approximate value of the transfer time is the same for all operating points. Indeed, the value obtained in (3.6.1.12) does not depend on the inverter output frequency, neither does it depend on the motor slip load. We can even find another approximate expression for t_1' . If we neglect the stator resistance, R_1 , we obtain

$$R_1 = 0 \quad ; \quad \alpha = \frac{R_1}{2L} = 0 \quad ; \quad \omega_1 = [\omega_0^2 - \alpha^2]^{1/2} = \omega_0$$

$$\beta = -\text{arc tan}\,\frac{\omega_1}{-\alpha} = -\text{arc tan}\,\frac{\omega_0}{-0} = -\frac{\pi}{2}$$

$$t_1' = -\frac{\beta}{\omega_1} = \frac{\pi}{2\omega_0} \qquad (3.6.1.13)\ \text{APX}$$

which means that in this case t_1' is 1/4 of the resonant period.

$$t_1' = \frac{\pi}{2\omega_0} = \frac{\pi}{2(2\pi f_0)} = \frac{T_0}{4} \qquad (3.6.1.14)\ \text{APX}$$

When $\alpha \neq 0$, we know that $\omega_1 < \omega$ and that $\beta < -\pi/2$, fig. 3.10. By comparing (3.6.1.12) with (3.6.1.13) one can see that the stator resistance makes the transfer time longer.

The maximum voltage of commutating capacitors is calculated using (3.4.42) and the expression for $i_C(t')$ given in (3.6.1.8),

$$V_o = \frac{2}{3C}\int_0^{t_1'}[-\frac{\omega_o}{\omega_1} I_d e^{-\alpha t'}\sin(\omega_1 t'+\beta)]dt' - R_1 I_d + E_1\sqrt{3}\cos\theta \qquad (3.6.1.15)\ \text{APX}$$

The integral term in (3.6.1.15) can be solved as

$$\int_0^{t_1'} e^{-\alpha t'}\sin(\omega_1 t'+\beta)dt' = \frac{1}{\alpha^2+\omega_1^2}[-\alpha\cdot e^{-\alpha t_1'}\sin(\omega_1 t_1'+\beta)$$

$$-\omega_1\cdot e^{-\alpha t_1'}\cos(\omega_1 t_1'+\beta)+\alpha\sin\beta+\omega\cos\beta] \qquad (3.6.1.16)$$

We know that in (3.6.1.7) ω_1 and α are positive quantities. This implies that arc tan $\frac{\omega_1}{-\alpha}$ is in the second quadrant. Consequently, β is in the third quadrant as shown in fig. 3.10. From (3.6.1.7) and fig. 3.10 we obtain

$$\sin\beta = -\frac{\omega_1}{\omega_o}$$

$$\cos\beta = -\frac{\alpha}{\omega_o} \qquad (3.6.1.17)$$

Using (3.6.1.17), (3.6.1.12) and knowing $\omega_o^2 = \omega_1^2+\alpha^2$ we obtain from (3.6.1.16)

$$\int_0^{t_1'} e^{-\alpha t'}\sin(\omega_1 t'+\beta)dt' = -\frac{\omega_1 e^{-\alpha t_1'}}{\omega_o^2} - \frac{2\alpha\omega_1}{\omega_o^3} \qquad (3.6.1.18)$$

The above equation is placed into (3.6.1.15) so as to obtain

$$V_o = \frac{2}{3C} I_d\,[\frac{e^{-\alpha t_1'}}{\omega_o} + \frac{2\alpha}{\omega_o^2}] - R_1 I_d + E_1\sqrt{3}\cos\theta$$

but $\frac{2\alpha}{\omega_o^2} = 2 \cdot \frac{R_1}{2L} \cdot 3LC = 3R_1C$

Then

$$V_o = \frac{2I_d}{3C} \frac{e^{-\alpha t_1'}}{\omega_o} + R_1 I_d + E_1\sqrt{3}\cos\theta \qquad (3.6.1.19)$$

Again, if we neglect R_1 we will obtain another approximate expression for V_o

$$R_1 = 0 \quad ; \quad \alpha = \frac{R_1}{2L} = 0 \quad ; \quad \omega_1 = \omega_o$$

$$V_o = \frac{2}{3C\omega_o} I_d + E_1\sqrt{3}\cos\theta \qquad (3.6.1.20)\ \text{APX}$$

which indicates that, for the same operating point a decrease in C produces an increase in V_o.

The charging period t_{ch} is obtained by using the expression for V_o in (3.4.4)

$$t_{ch} = \frac{3C}{I_d} E_1\sqrt{3}\cos\theta + \frac{e^{-\alpha t_1'}}{\omega_o} + \frac{2\alpha}{\omega_o^2} 3R_1C$$

but $\frac{2\alpha}{\omega_o^2} = 3R_1C$

then

$$t_{ch} = \frac{e^{-\alpha t_1'}}{\omega_o} + \frac{3C}{I_d} E_1\sqrt{3}\cos\theta \qquad (3.6.1.21)\ \text{APX}$$

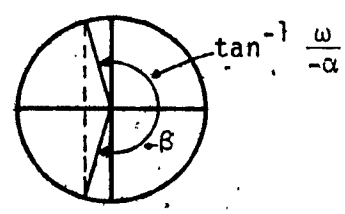

FIG. 3.10 Determination of β and $\tan^{-1}\frac{\omega}{-\alpha}$ angles.

Again, for $R_1=0$ we will obtain

$$t_{ch} = \frac{1}{\omega_o} + \frac{3C}{I_d} E_1 \sqrt{3} \cos \theta \qquad (3.6.1.22) \text{ APX}$$

We know all the variables in (3.6.1.19) and (3.6.1.22) except θ. According to (3.4.22), θ is a function of t_2. Then the only unknown in this case would be t_2. Assumption (b) mentioned at the beginning of this section solves our problem. In order to derive the required equation from assumption (b) it is necessary to plot the motor current waveforms. Remembering that we have three modes during each interval between firing the two consecutive SCR's, we will obtain 18 modes for one complete inverter output cycle. These modes have already been shown in Tables 1.1-1.3. Using (3.6.1.7 and 8) for currents in phases A and C during the transfer mode we can plot fig. 3.11. The encircled numbers show the instants at which each SCR is triggered. Assumption (b) which yields a linear current during the transfer mode results in straight broken lines instead of solid lines.

One notices that the current waveforms have the shape of trapeziods. Due to their symmetry, the fundamental component of each trapezoidal waveform intersects the harizontal axis exactly at the mid-point between the positive and negative cycle. Thus, the constraint of section (3.6) concerning the fundamental component of the motor current is fulfilled.

In fig. 3.11 $e_{1A}(t)$ and ϕ_1 have been shown for a motoring mode. Aslo $t_1, t_2, t_3, t_4, t_{ch}, t_1', t_{co}$ and t_{no} have the same definitions as given previously. Notice that each three successive modes have an angle equal to

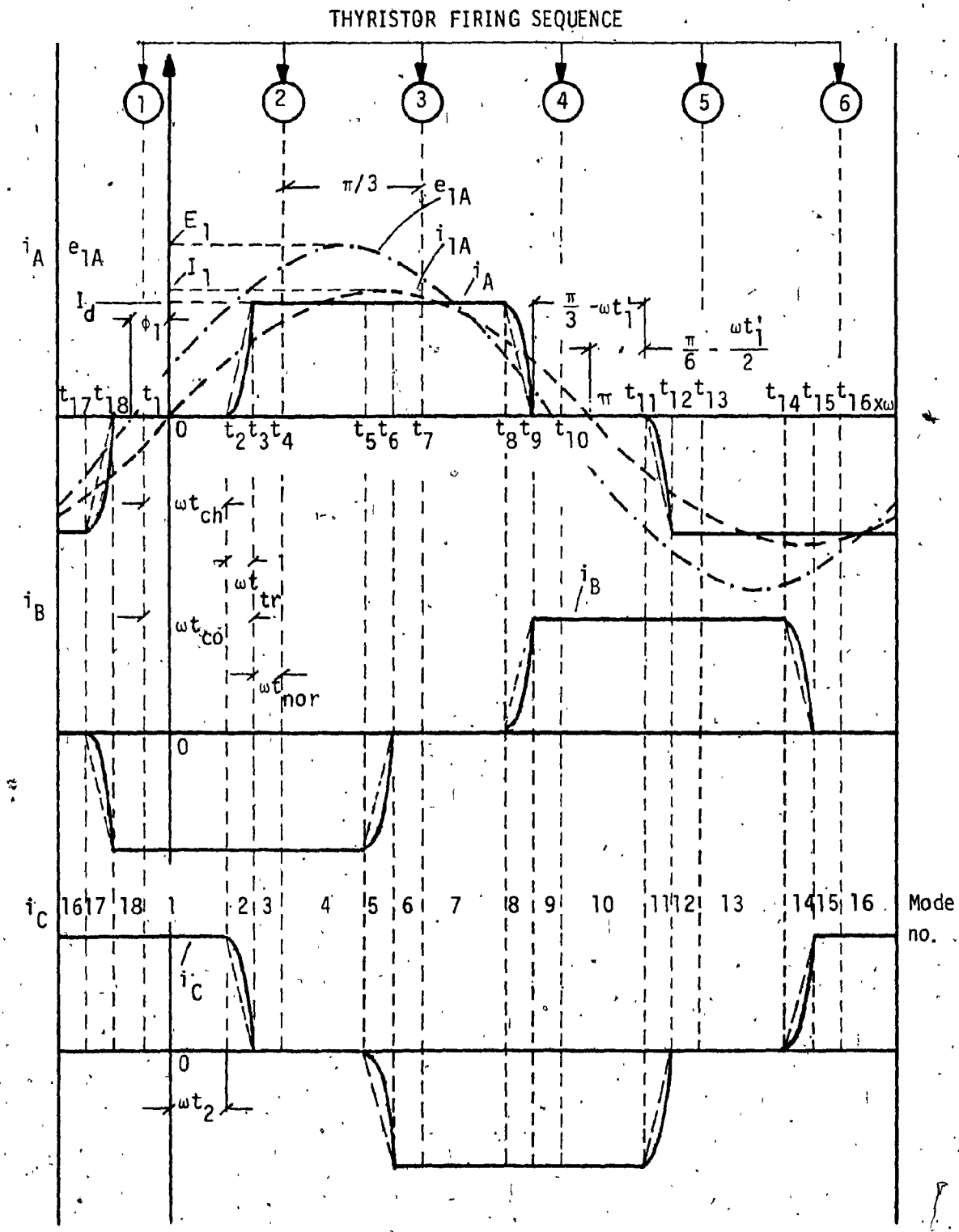

FIG. 3.11. Motor phase currents, the CEMF of phase A along with its fundamental component of current are shown for an ASCI operating with a constant dc link current and a linear transfer of current during each transfer mode

$$\omega(t_{ch}+t_1'+t_{no}) = \omega(t_{ch}+t_{tr}+t_{no}) = \frac{\pi}{3} \text{ rad} \qquad (3.6.1.23)$$

Also, a positive cycle of $i_A(t)$ ends at the end of mode 8 while its negative cycle starts at the beginning of mode 11. Thus, the angle during which $i_A(t) = 0$ would be

$$\omega(t_{11}-t_9) = \frac{\pi}{3} - \omega t_1' \qquad (3.6.1.24)$$

Half of the above angle, i.e. from the end of mode 8 to the point where $i_{1A}(t)$ passes through the horizontal axis at π would be equal to

$$\pi-\omega t_9 = \frac{\pi}{6} - \frac{\omega t_1'}{2} \qquad (3.6.1.25) \text{ APX}$$

The above is also equal to the angle between the origin and the beginning of mode 2

$$\omega t_2 = \frac{\pi}{6} - \frac{\omega t_1'}{2} \qquad (3.6.1.26) \text{ APX}$$

From (3.6.1.26) we can obtain the approximate value of t_2,

$$t_2 = \frac{\pi}{6\omega} - \frac{t_1'}{2} \qquad (3.6.1.27) \text{ APX}$$

The above relationship between t_2 and t_1' is the missing equation which we needed and should be added to the list of key equations given in section (3.6).

At this point we have the necessary information to calculate all the unknowns. From (3.4.22) and (3.6.1.27) we can write

$$\theta = \omega t_2+\phi_1-\frac{2\pi}{3} = \phi_1 - \frac{\omega t_1'}{2} - \frac{\pi}{2} \qquad (3.6.1.28) \text{ APX}$$

and, putting it into (3.6.1.19 and 21) we will have

$$V_o = e^{-\alpha t_1'} \frac{2I_d}{3C\omega_o} + R_1 I_d + E_1\sqrt{3}\sin(\phi_1 - \frac{\omega t_1'}{2}) \qquad (3.6.1.29)\ \text{APX}$$

$$t_{ch} = \frac{e^{-\alpha t_1'}}{\omega_o} + \frac{3C}{I_d} E_1\sqrt{3}\sin(\phi_1 - \frac{\omega t_1'}{2}) \qquad (3.6.1.30)\ \text{APX}$$

And t_1 can be easily calculated from (3.3.18) by using (3.6.1.27) and (3.6.1.30). Also, (3.4.13) and (3.4.34) yield t_3

$$t_3 = t_2 + t_{tr} = t_2 + t_1' = \frac{\pi}{6\omega} + \frac{t_1'}{2} \qquad (3.6.1.31)\ \text{APX}$$

in which t_2 has been substituted by (3.6.1.27). The duration of commutation mode would result from (3.4.14) in which (3.6.1.30) has been replaced for t_{ch}

$$t_{co} = t_{ch} + t_{tr} = \frac{e^{-\alpha t_1'}}{\omega_o} + \frac{3C}{I_d} E_1\sqrt{3}\sin(\phi_1 - \frac{\omega t_1'}{2}) + t_1' \qquad (3.6.1.32)\ \text{APX}$$

And, at last, t_4 is simply found by using (3.5.1). In all of the above expressions, t_1' is calculated from (3.6.1.12).

From (3.6.1.29, 30 and 32), and after some simplifications in E_1 and ϕ_1, we can derive a few significant conclusions. If we omit R_m in fig. 2.7 and assume $X_m >> X_2$ then [3] yields

$$\phi_1 = \text{arc tan}\,(1/B_1 S_1) \qquad \text{APX}$$

$$E_1 = I_1 X_m/(1+B_1^2 S_1^2)^{1/2} \qquad \text{APX}$$

where $B_1 = X_m/R_2$ (3.6.1.32a)

and I_1 is the peak value of the fundamental harmonic of the stator current. In this case, at no-load, since, $S_1=0$ it results,

$$\phi_1 = \pi/2 \text{ rad}$$
$$E_1 = I_1 X_m = 2\pi f L_m I_1 \qquad (3.6.1.33)\text{APX}$$

Also, we know I_d in terms of I_1 from (2.5.3), which along with (3.6.1.33) yield the following expressions for the given list of variables at no-load

$$V_o = e^{-\alpha t_1'} \frac{2I_1 \cdot \pi}{3C\omega_o\sqrt{3}} + R_1 \cdot \frac{I_1 \pi}{2\sqrt{3}} + 2\pi f L_m I_1 \sqrt{3} \sin(\frac{\pi}{2} - \frac{\omega t_1'}{2}) \qquad (3.6.1.34)\text{APX}$$

$$t_{ch} = \frac{e^{-\alpha t_1'}}{\omega_o} + 36C\, f\, L_m \sin(\frac{\pi}{2} - \frac{\omega t_1'}{2}) \qquad (3.6.1.35)\text{APX}$$

$$t_{co} = \frac{e^{-\alpha t_1'}}{\omega_o} + 36C\, f\, L_m \sin(\frac{\pi}{2} - \frac{\omega t_1'}{2}) + t_1' \qquad (3.6.1.36)\text{APX}$$

In the above equations, the $\omega t_1'/2$ term is negligible, even at high frequencies, when compared with $\pi/2$. Besides, we know that t_1', according to (3.6.1.12), is the same for all operating points. Then the result is that the charging time t_{ch} and the commutation time t_{co}, for a fixed C, increase with frequency, reaching their maximum value at the maximum output frequency. This conclusion was based on a no-load operation. Comparing (3.6.1.30) (load condition) with (3.6.1.35) (no-load condition), for the same output frequency, one can see that the no-load operation gives higher values of the phase angle ϕ_1, the commutation period t_{co} and the charging time t_{ch}.

Thus, the charging and commutation periods are largest for no-load operation at the maximum output frequency.

The other points to be considered are the variations of the maximum commutating capacitors voltage, V_o, as the capacitance of the commutating capacitors, C, or the output torque changes. Equation (3.6.1.29) reveals these two points. In this expression the coefficient involving C is equal to $\frac{1}{C\omega_o}$ which from (3.4.24) results

$$\frac{1}{C\omega_o} = \frac{\sqrt{3LC}}{C} = \frac{\sqrt{3L}}{\sqrt{C}}$$

Then, for a specific operating point, an increase in C results in a lower V_o and vice versa.

To find the way in which V_o changes when the output torque is varied we should notice: 1) For a specific output frequency, when the output torque is increased the dc link current, I_d, will also increase while the term containing E_1 on the right hand side of (3.6.1.29) will remain almost constant providing that a constant V/Hz or a constant voltage control is employed, and 2) In practical applications the magnitude of V_o is principally determined by the first term on the right hand side of (3.6.1.29). Then we conclude that V_o obtains its highest value at the maximum output frequency and torque.

3.6.1.1 Flowchart for the Approximate Approach

The approximate method for finding the unknown variables defined in the previous section can be summarized in the following flowchart and used in the programming. The input frequency and the motor

load (per unit output torque) are assumed to be known. The corresponding slip value can be easily obtained from the exact equivalent circuit (the flowchart is given in Appendix A-3). This slip value is then used in the calculation of the commutation variables, flowchart 3.1. The subroutines CEMF1 and CEMF2 are the two subprograms which compute the peak stator circuit, I_1, motor power factor, $\cos\phi$, motor output torque, T, peak CEMF, E_1, and ϕ_1. The subroutine CEMF1 is used for a no-load operation, $S=0$, while the subroutine CEMF2 is employed for all other cases, $S\neq 0$.

3.6.2 Exact Approach

In section (3.6.1) we found the unknown variables by using an approximate approach. This was done by formulating two new assumptions regarding the value of the CEMF, E_1, and the variations of the motor line current during the transfer mode. The first one helped us in simplifying the transcendental equation (3.4.35) while the second one gave us a new equation, (3.6.1:27). It should be noticed that (3.6.1:27) actually gives an approximate value for t_2. The value of t_2 obtained in this way, along with the expression for t_1' presented by (3.6.1.12) enabled us to find all the unknowns.

The same procedure should be followed if we want to obtain more accurate results. The reason is that the knowledge of t_2 permits the calculation of θ from (3.4.22) which in turn yields β, A_2, B_2, γ and δ from (3.4.30). Now we know all the constants in (3.4.35) and by employing iterative methods this equation can be solved for t_1'. The next step is the calculation of V_o from (3.4.42). The value of

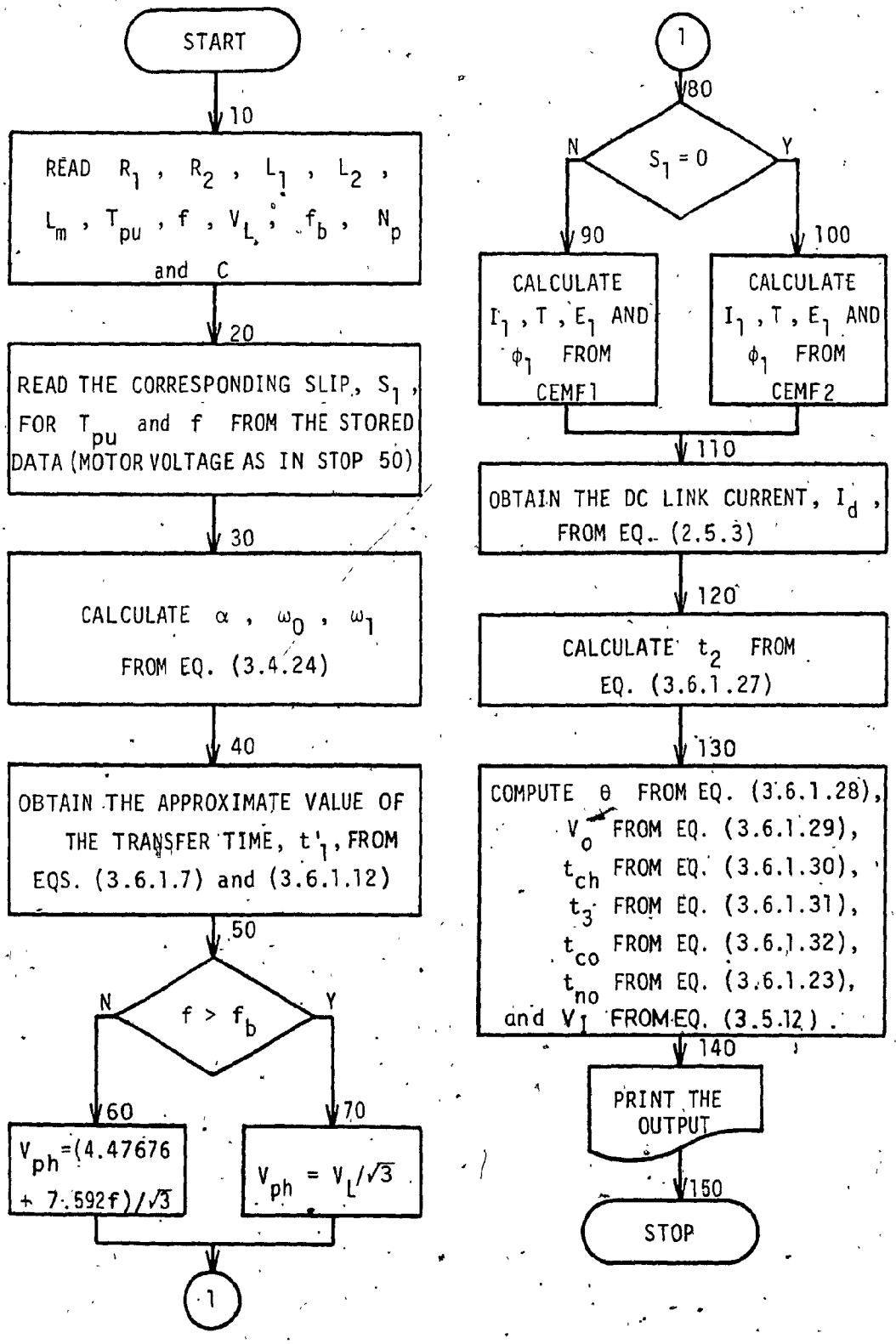

FLOWCHART 3.1 The flowchart employed for calculating the system unknowns using the approximate method.

V_o can be used to obtain t_{ch} from (3.4.4). The other unknowns can be found easily using (3.4.14) and (3.5.1).

3.6.2.1 Flowchart for the Exact Approach

Flowchart 3.2 outlines the steps needed for computing the results by employing the exact approach. Here the value of t_2 is calculated iteratively such that the exactly computed fundamental component of the motor current (Appendix B-2) passes through zero at t=0 . Furthermore, this component should have the same magnitude as that obtained from the exact equivalent circuit. The latter constraint is usually achieved when (2.5.3) is employed for calculating I_d . Otherwise I_d should also be obtained iteratively, as shown in flowchart 3.2

Flowchart 3.2 will be used in chapter V for two purposes. Firstly, to plot the voltage and current waveforms at different points of the system for a specific operating condition, and secondly, to show the variations of different variables as functions of motor output torques and motor input frequencies.

3.7 Conclusion

By using an exact analysis, it was shown that the commutation time on each SCR is so short that it can be neglected in the modelling of the inverter operation. When an inverter operates without a commutation overlap, as long as the diodes do not become transiently forward biased, the last assumption results in three different modes in the interval between two consecutive SCR firings. This analysis

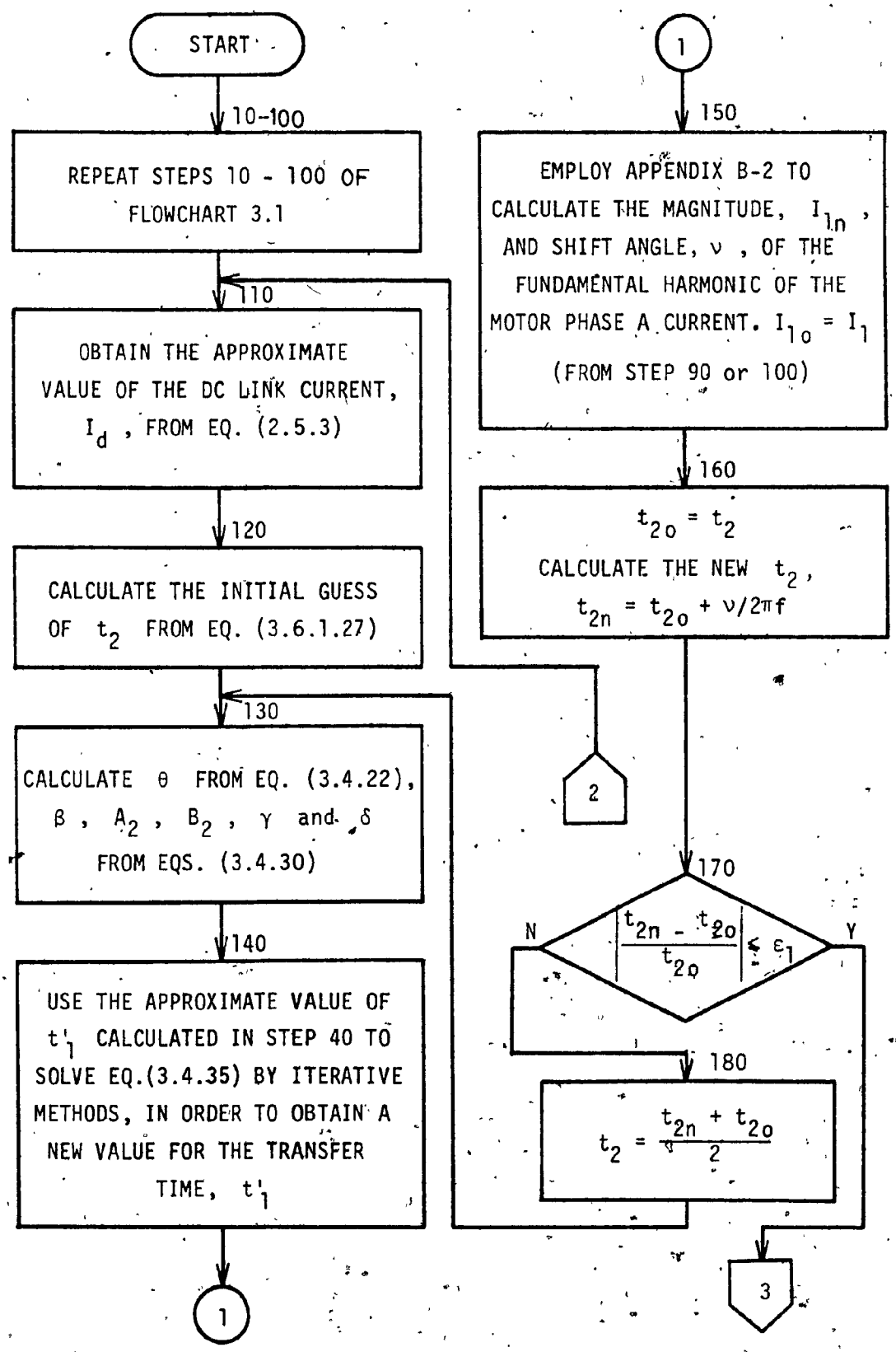
START
10-100
REPEAT STEPS 10 - 100 OF FLOWCHART 3.1
110
OBTAIN THE APPROXIMATE VALUE OF THE DC LINK CURRENT, I_d , FROM EQ. (2.5.3)
120
CALCULATE THE INITIAL GUESS OF t_2 FROM EQ. (3.6.1.27)
130
CALCULATE θ FROM EQ. (3.4.22), β , A_2 , B_2 , γ and δ FROM EQS. (3.4.30)
140
USE THE APPROXIMATE VALUE OF t'_1 CALCULATED IN STEP 40 TO SOLVE EQ.(3.4.35) BY ITERATIVE METHODS, IN ORDER TO OBTAIN A NEW VALUE FOR THE TRANSFER TIME, t'_1
1
1
150
EMPLOY APPENDIX B-2 TO CALCULATE THE MAGNITUDE, I_{1n} , AND SHIFT ANGLE, ν , OF THE FUNDAMENTAL HARMONIC OF THE MOTOR PHASE A CURRENT. $I_{1o} = I_1$ (FROM STEP 90 or 100)
160
$t_{2o} = t_2$
CALCULATE THE NEW t_2 ,
$t_{2n} = t_{2o} + \nu/2\pi f$
2
170
$\left|\frac{t_{2n} - t_{2o}}{t_{2o}}\right| \leq \varepsilon_1$
N
Y
180
$t_2 = \frac{t_{2n} + t_{2o}}{2}$
3

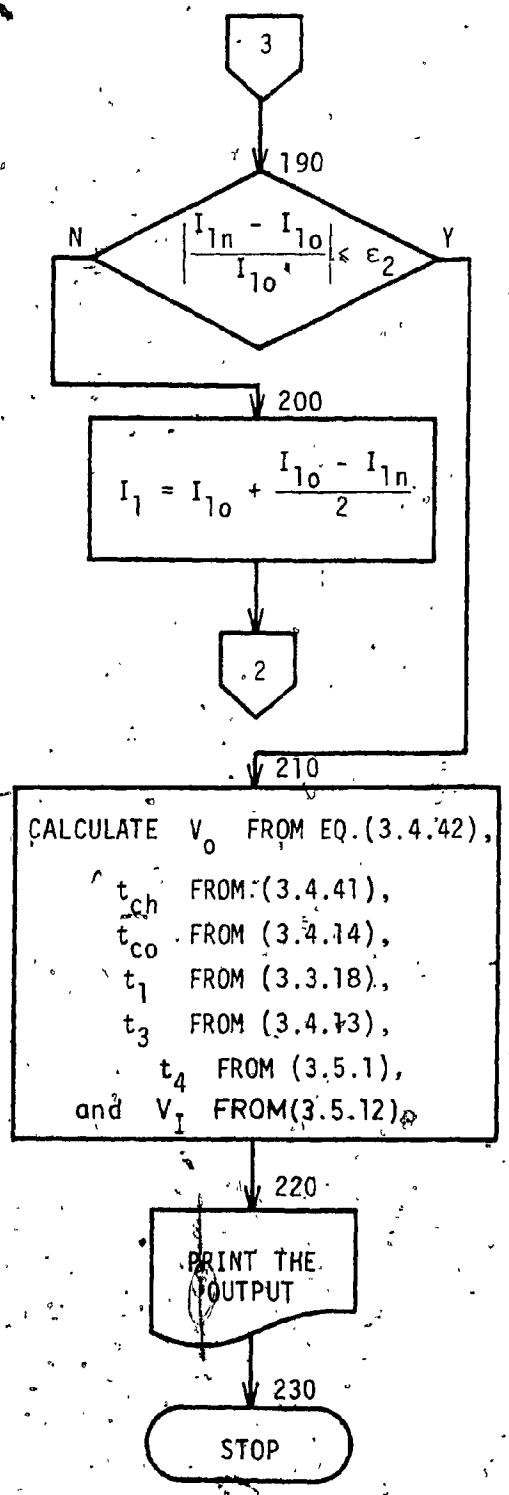

FLOWCHART 3.2 The flowchart employed for calculating the system unknowns by the exact method in case (a).

gave (n-1) equations, (n) being the number of the unknown variables. Therefore, one additional constraints was formulated. This constraint resulted from the fact that the fundamental component of the current in phase A should be zero at the origin of time $t=0$, while it has a positive slope. Two methods, one exact and one approximate, were presented for solving the resulting equations. In the approximate approach, the CEMF was assumed to remain unchanged during the transfer time and the motor input current was represented by trapezoidal waveforms. The first assumption resulted in simpler equations, while the second one provided us with the missing equation. In the exact approach, the value of t_2 was found iteratively and thus decreasing the number of the unknown variables by one. The exact value of the dc link current was also obtained through iterations.

The approximate method also showed that the largest charging and commutation times occur at the maximum inverter frequency and at a no-load operation. Furthermore, the maximum voltage across the commutating capacitors, V_0, reaches its highest value at the maximum load and at the maximum operating frequency. Figures (5.12), (5.16) and (5.18) in chapter V, which are obtained by employing the exact method, provide the same results.

CHAPTER IV

ANALYSIS OF THE COMMUTATION OVERLAP FOR THE SYSTEM WITH A CONSTANT DC LINK CURRENT AND NO CLAMPING CIRCUIT

4.1 INTRODUCTION

In the previous chapters it was assumed that the commutation angle is smaller or equal to 60° . This then resulted in only three distinct modes of operation between two successive SCR firings. However, in some situations the commutation angle can exceed 60° . It will now be shown that all the key equations presented before are valid as long as

1) The transfer angle does not exceed 60° while the commutation angle remains less than 120° and

2) The diodes do not become transiently forward biased.

The limit on the commutation angle defines, at the same time, the maximum practical operating frequency. Finally, an approximate method will be presented which gives the values of the commutating capacitors for a specified maximum frequency.

4.2 LIMITS OF THE SYSTEM OPERATION

The approximate durations of charging and commutation modes at no load were presented by (3.6.1.35 and 36). If we neglect the stator resistance and use (3.6.1.13) we have:

$$t_{ch} = \frac{1}{\omega_o} + 36\ Cf\ L_m \sin\left(\frac{\pi}{2} - \frac{\pi\omega}{4\omega_o}\right) \qquad (4.2.1)\ \text{APX}$$

$$t_{co} = \frac{1}{\omega_o} + \frac{\pi}{2\omega_o} + 36\ Cf\ L_m \sin(\frac{\pi}{2} - \frac{\pi\omega}{4\omega_o}) \qquad (4.2.2)\ APX$$

When the output frequency is very small and near zero we have:

$$t_{ch} \simeq \frac{1}{\omega_o} \qquad (4.2.3)\ APX$$

Comparing (4.2.3) with (3.6.1.13) one can see that at no load and with the output frequency near zero

$$t_1' > t_{ch} \qquad (4.2.3)$$

By increasing the output frequency, f , t_{ch} in (4.2.1) obtains higher values while t_1' remains constant. At some frequency which is well below the rated frequency for typical current source inverters t_{ch} exceeds t_1' . The same is also true for the corresponding angles.

From this discussion, three distinct cases of inverter commutation can be defined

a) $\omega t_{ch} < \frac{\pi}{3}$, $\omega t_{tr} < \frac{\pi}{3}$ and $\omega(t_{ch}+t_{tr})=\omega t_{co} < \frac{\pi}{3}$

b) $\omega t_{ch} < \frac{\pi}{3}$, $\omega t_{tr} < \frac{\pi}{3}$ and $\frac{\pi}{3} < \omega t_{co} < \frac{2\pi}{3}$

c) $\omega t_{ch} > \frac{\pi}{3}$, $\omega t_{tr} < \frac{\pi}{3}$ and $t_{co} < \frac{2\pi}{3}$

The analysis of case (a) was given in chapter III. Case (a) is called a "no-overlap case" since the transfer of current from one phase to the other phase ends before the next thyristor is fired, fig. 4.1. By increasing the output frequency the commutation angle eventually

exceeds 60° . When this happens each SCR is fired while the last transfer of current is not finished or has not yet started. In this case, we say that the inverter has gone to overlap mode. We will study only the modes with commutation angles smaller than 120° . These modes are called "partial overlap" modes and are further divided into cases (b) and (c). Note that in all three cases (a), (b) and (c), the transfer angle, ωt_{tr} , is always less than 60° and we assume not to face the transient forward biasing of the diodes. Regarding the second assumption, later on we will summarize the conditions necessary for securing a successful operation of the inverter in case (b) or case (c).

In the following we wish to show that the key equations given for case (a) are also applicable to cases (b) and (c). Figures 4.1, 4.2 and 4.3 illustrate all three cases. In these figures the charging, transfer and commutation angles are shown with respect to SCR's firing instants. In Fig. 2.12, $\omega t_1 = \pi/6$ because rectangular waveforms were assumed for the motor input currents. The actual case shows $\omega t_1 \neq \pi/6$. This is why this angle has not been specified in figures 4.1, 4.2 and 4.3.

Figure 3.11 showed the motor current waveforms for case (a) while figures 4.4 and 4.5 show the corresponding waveforms for cases (b) and (c). In figures 3.11 and 4.1 to 4.5 the same notations have been used for the different instants of time $(t_1, t_2, \ldots, t_{18})$. For example, in all these figures, t_6 specifies the instant at which the diode D_6 is turned off. Also, the number between each two consecutive times indicates the corresponding mode number for that case.

The necessary equations for cases (b) and (c) are derived in the next two sections.

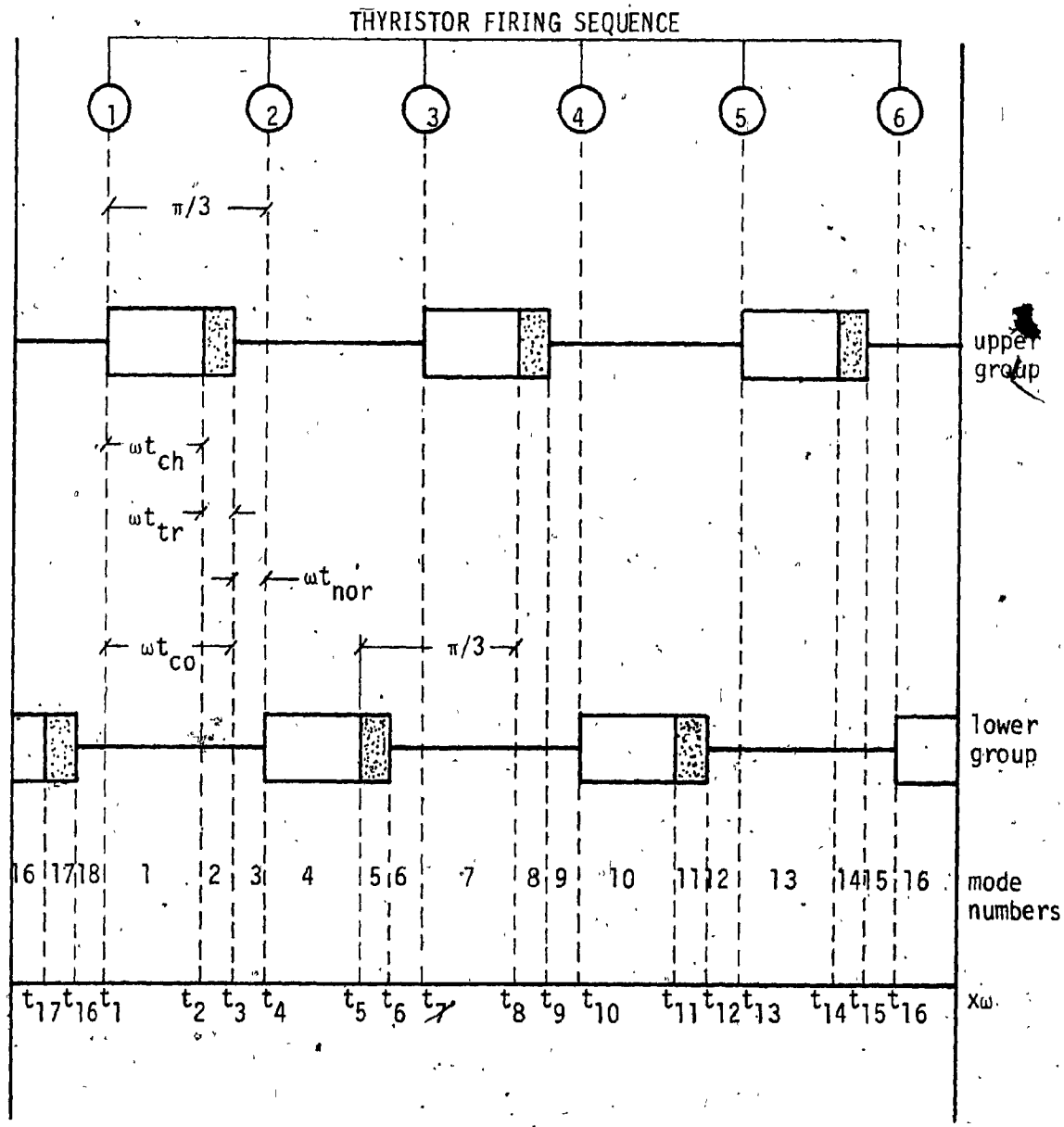

FIG. 4.1. Different angles for an ASCI operating with a no-overlap commutation where angles ωt_{ch}, ωt_{tr} and ωt_{co} are all less than $\pi/3$ rad, Case (a).

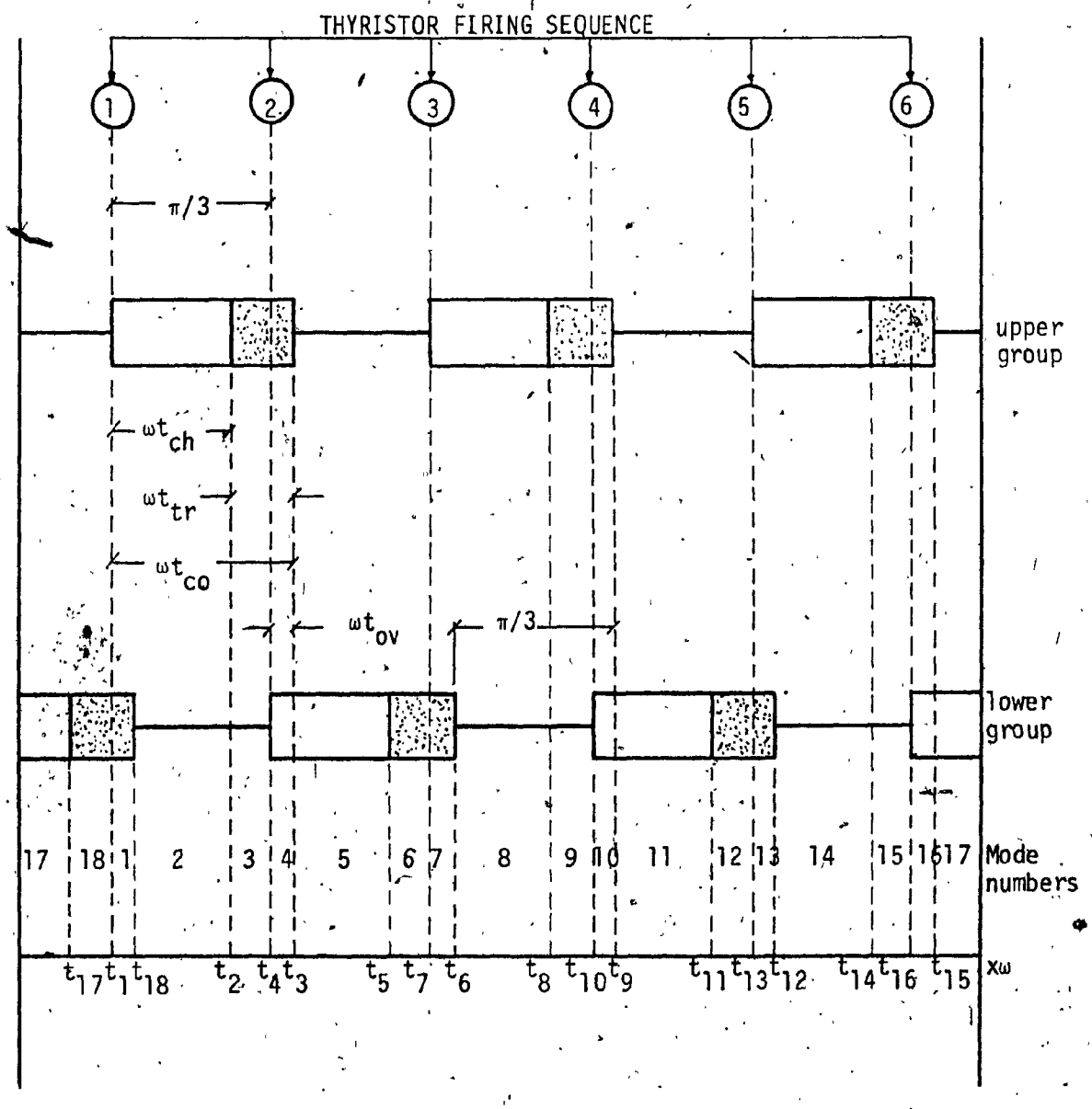

FIG. 4.2. Different angles for an ASCI operating under a partial overlap commutation where $\omega t_{ch} < \pi/3$, $\omega t_{tr} < \pi/3$ and $\pi/3 < \omega t_{co} < 2\pi/3$ Case (b).

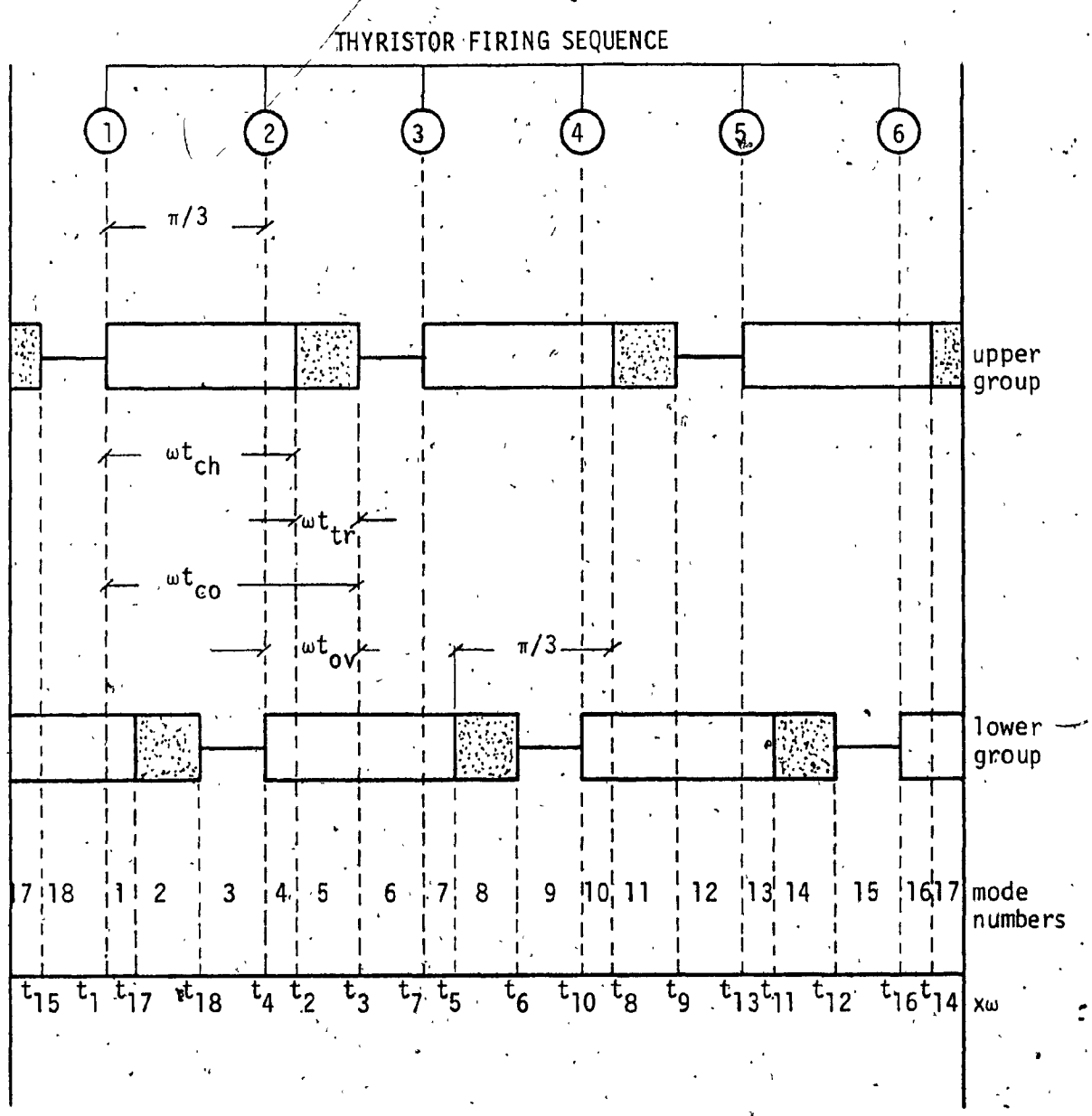

FIG. 4.3. Different angles for an ASCI operating under a partial overlap commutation where $\omega t_{ch} > \pi/3$, $\omega t_{tr} < \pi/3$ and $\omega t_{co} < 2\pi/3$, Case (c).

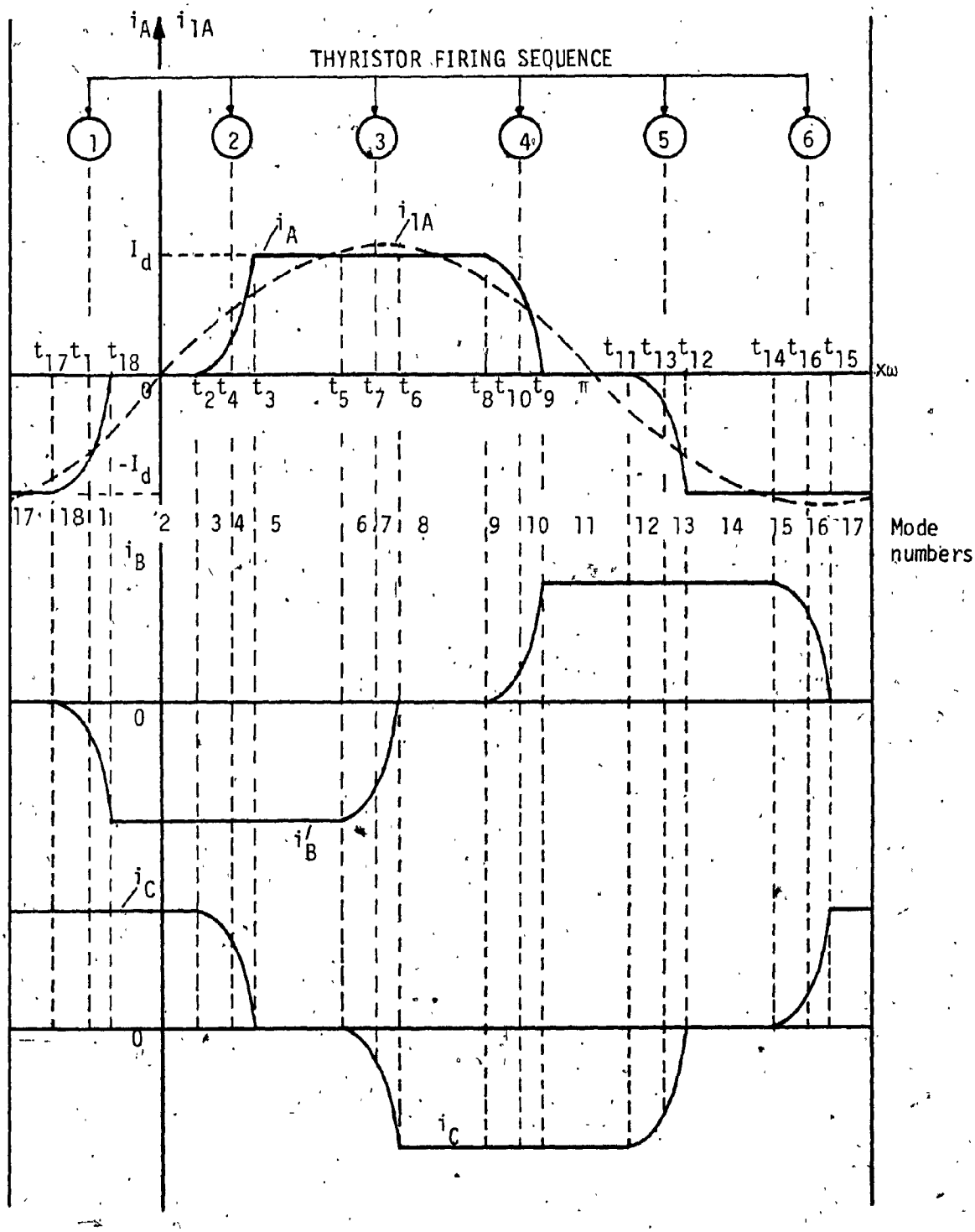

FIG. 4.4 Three phase and fundamental harmonic of phase A current waveforms of an ASCI operating under a partial overlap in case (b).

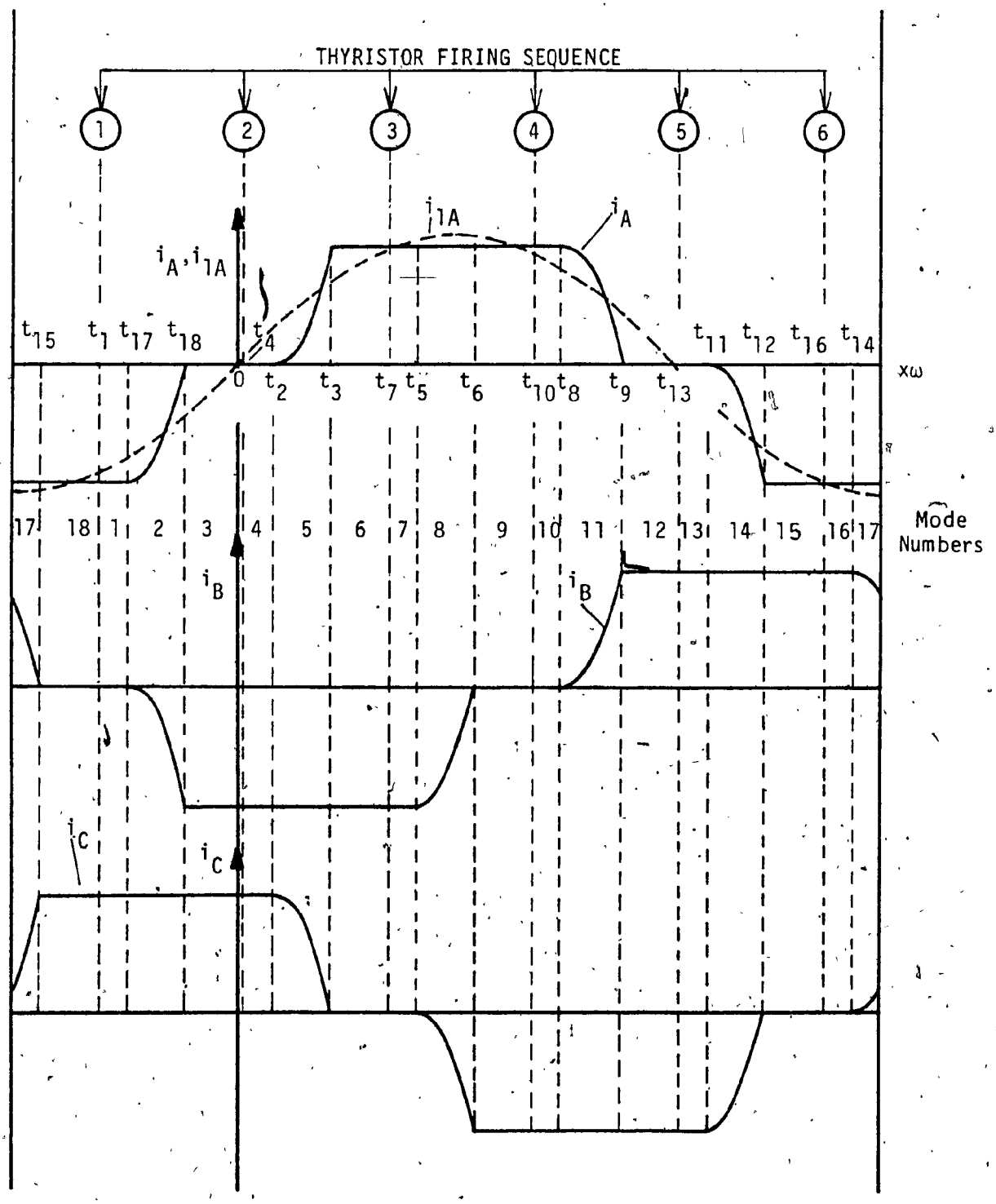

FIG 4.5 Waveforms of the fundamental harmonic of phase A and the motor input currents for the partial commutation overlap in case (c).

4.3 PARTIAL OVERLAP CASE (b)

This case is characterized by the charging, transfer and commutation times for which $\omega t_{ch}<\pi/3$, $\omega t_{tr}<\pi/3$ and $\pi/3<\omega t_{co}<2\pi/3$ rad. Fig. 4.2 displays the relationships between the different angles for this case. It is seen that when the thyristor T_1 is fired at $t=t_1$ in the upper group, the transfer mode still exists in the lower group. Consequently, the commutation angle is larger than $\pi/3$ rad. Also, we do not have a 'normal mode' as defined in Tables 1.1-1.3 and in section (3.5). Instead, we can specify the overlap mode, the angle of which is defined as

$$\omega t_{ov} = \omega t_{co}-\pi/3 \qquad (4.3.1)$$

Figure 4.6 shows the circuit of the system during mode 18 before firing T_1 at $t=t_1$. To obtain the required equations we will divide the time periods in the following way.

4.3.1 MODE 1 OR THE FIRST PART OF THE CHARGING MODE

This mode is defined for $t_1<t<t_{18}$ where t_1 is the instant when the thyristor T_1 is triggered and t_{18} is the moment when the diode D_4 stops conducting. The firing of the thyristor T_1 at $t=t_1$ results also in the turn-off of the thyristor T_5 . In this way, the upper group components go into charging mode while we still have a transfer mode going on in the lower group, fig. 4.7. It is seen that the firing of T_1 at $t=t_1$ does not affect the lower group operation. We have as in the case with no overlap

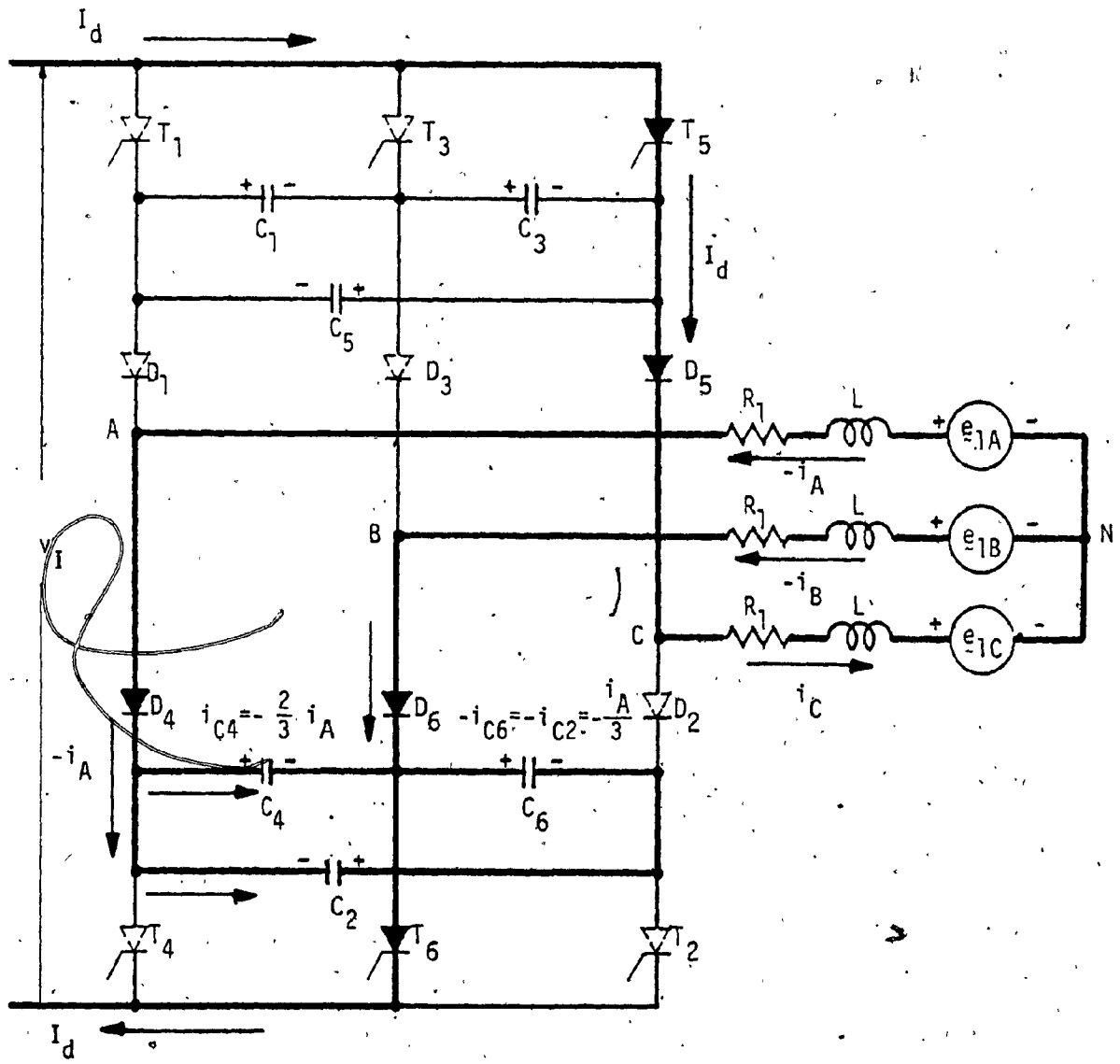

FIG. 4.6 ASCI-induction motor operation in mode 18 of case (b). This mode ends at $t=t_1$ when the thyristor T_1 is triggered.

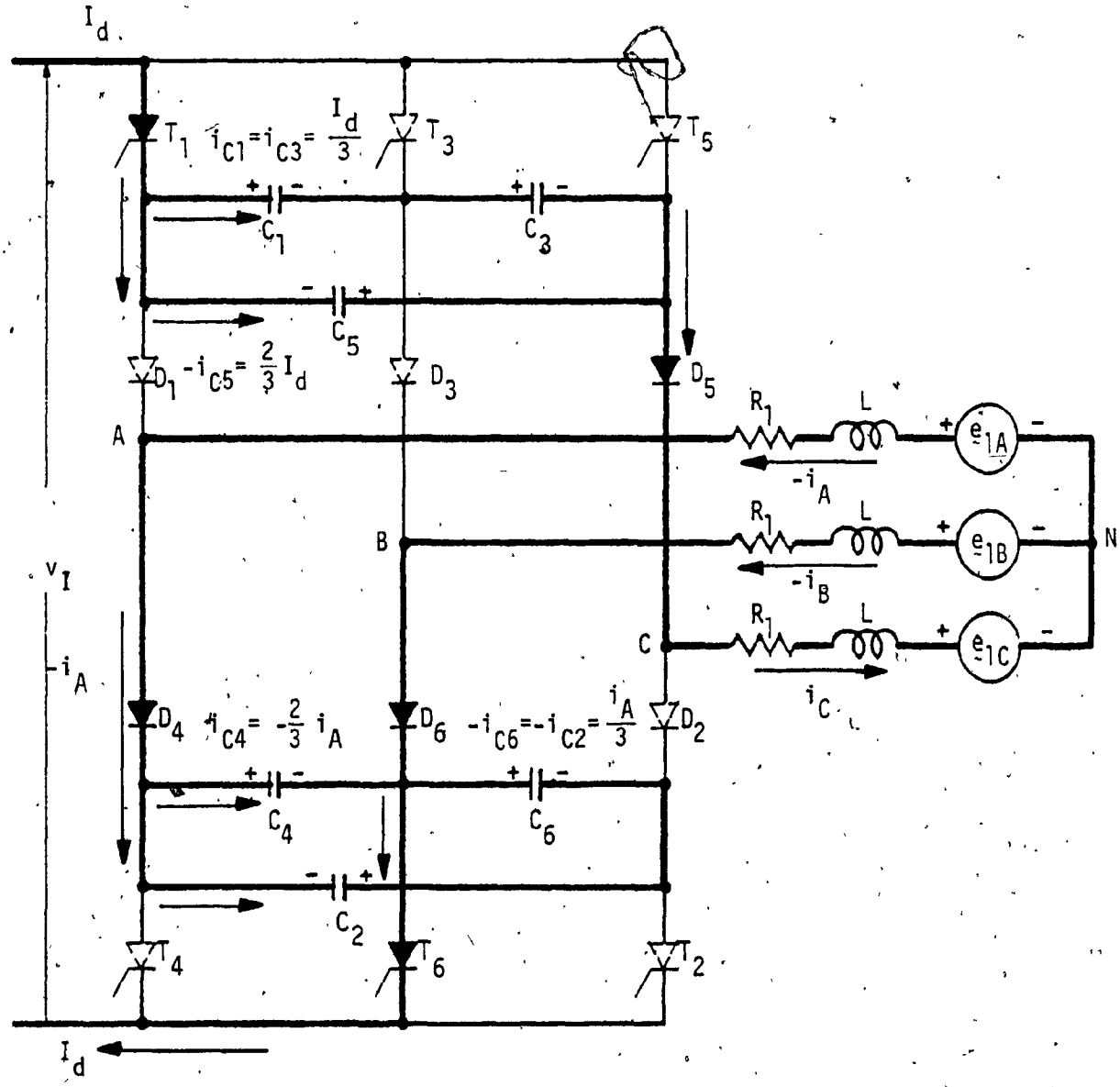

FIG. 4.7 ASCI-induction motor operation in mode 1 of case (b). By firing T_1 at $t=t_1$ the first part of a charging mode starts in the upper group while the lower group is still under diode commutation. This mode ends at $t=t_{18}$ when D_4 stops conducting.

$$v_{C5}(t_1^-) = +V_o$$

$$v_{C3}(t_1^-) = -V_o$$

$$v_{C1}(t_1^-) = 0 \qquad (4.3.1.1)$$

Equations (3.3.5-7) and (3.3.11-12) are also valid for this mode but with $t_1<t<t_{18}$. The other equations become

$$v_A(t) = +R_1 i_A(t) + L\frac{di_A(t)}{dt} + E_1 \sin(\omega t+\phi_1)$$

$$v_B(t) = +R_1 i_B(t) + L\frac{di_B(t)}{dt} + E_1 \sin(\omega t+\phi_1 - \frac{2\pi}{3})$$

$$v_C(t) = R_1 I_d + E_1 \sin(\omega t+\phi_1 - \frac{4\pi}{3}) \qquad (4.3.1.2)$$

where $$i_C(t) = I_d = -i_A(t)-i_B(t) \qquad (4.3.1.3)$$

Then $$v_{AB}(t) = 2R_1 i_A(t) + 2L\frac{di_A(t)}{dt} + R_1 I_d + E_1\sqrt{3}\cos(\omega t+\phi_1-\pi/3)$$

$$v_{BC}(t) = -R_1 i_A(t) - L\frac{di_A(t)}{dt} - 2R_1 I_d + E_1\sqrt{3}\cos(\omega t+\phi_1-\pi)$$

$$v_{CA}(t) = -R_1 i_A(t) - L\frac{di_A(t)}{dt} + R_1 I_d - E_1\sqrt{3}\cos(\omega t+\phi_1-\frac{2\pi}{3})$$

$$(4.3.1.4)$$

$$i_{D1}(t) = i_{D2}(t) = i_{D3}(t) = 0$$

$$i_{D4}(t) = -i_A(t)$$

$$i_{D5}(t) = I_d \;, \quad i_{D6}(t) = -i_B(t) \qquad (4.3.1.5)$$

$$v_{T2}(t) = -v_{C6}(t)$$

$$v_{T4}(t) = v_{C4}(t) \;, \quad v_{T6}(t) = 0 \qquad (4.3.1.6)$$

$$v_{D1}(t) = -v_{C5}(t) + v_{CA}(t)$$
$$v_{D3}(t) = v_3(t) + v_{CB}(t)$$
$$v_{D5}(t) = 0 \qquad (4.3.1.7)$$

$$v_{D2}(t) = v_{CB}(t) + v_{C6}(t)$$
$$v_{D4}(t) = v_{D6}(t) = 0 \qquad (4.3.1.8)$$

$$v_1(t) = -v_{C5}(t) = v_{CB}(t) \qquad (4.3.1.9)$$

At $t=t_{18}$ the transfer mode in the lower group is completed — thus ending mode 1. At the end of this mode, the capacitor voltages in the lower group have reached their constant values.

$$v_{C2}(t_{18}) = 0$$
$$v_{C4}(t_{18}) = +V_o$$
$$v_{C6}(t_{18}) = -V_o \qquad (4.3.1.10)$$

Also $\quad i_A(t_{18}) = 0$

$$i_B(t_{18}) = -I_d \qquad (4.3.1.11)$$

4.3.2 MODE 2 OR THE SECOND PART OF THE CHARGING MODE

This mode is defined for $t_{18}<t<t_2$ where t_{18} is the moment at which the diode D_4 is blocked and t_2 is the instant at which the diode D_1 starts conducting. Figure 4.8 shows the circuit of the system during this mode. Except for the initial voltages across the capacitors C_1, C_3 and C_5, everything else is the same as in mode 1, section (3.3).

4.3.3 MODE 3 OR THE FIRST PART OF THE TRANSFER MODE

This mode exists for $t_2<t<t_4$ where t_2 is the time when D_1 becomes forward biased and t_4 denotes the moment when T_4 is fired.

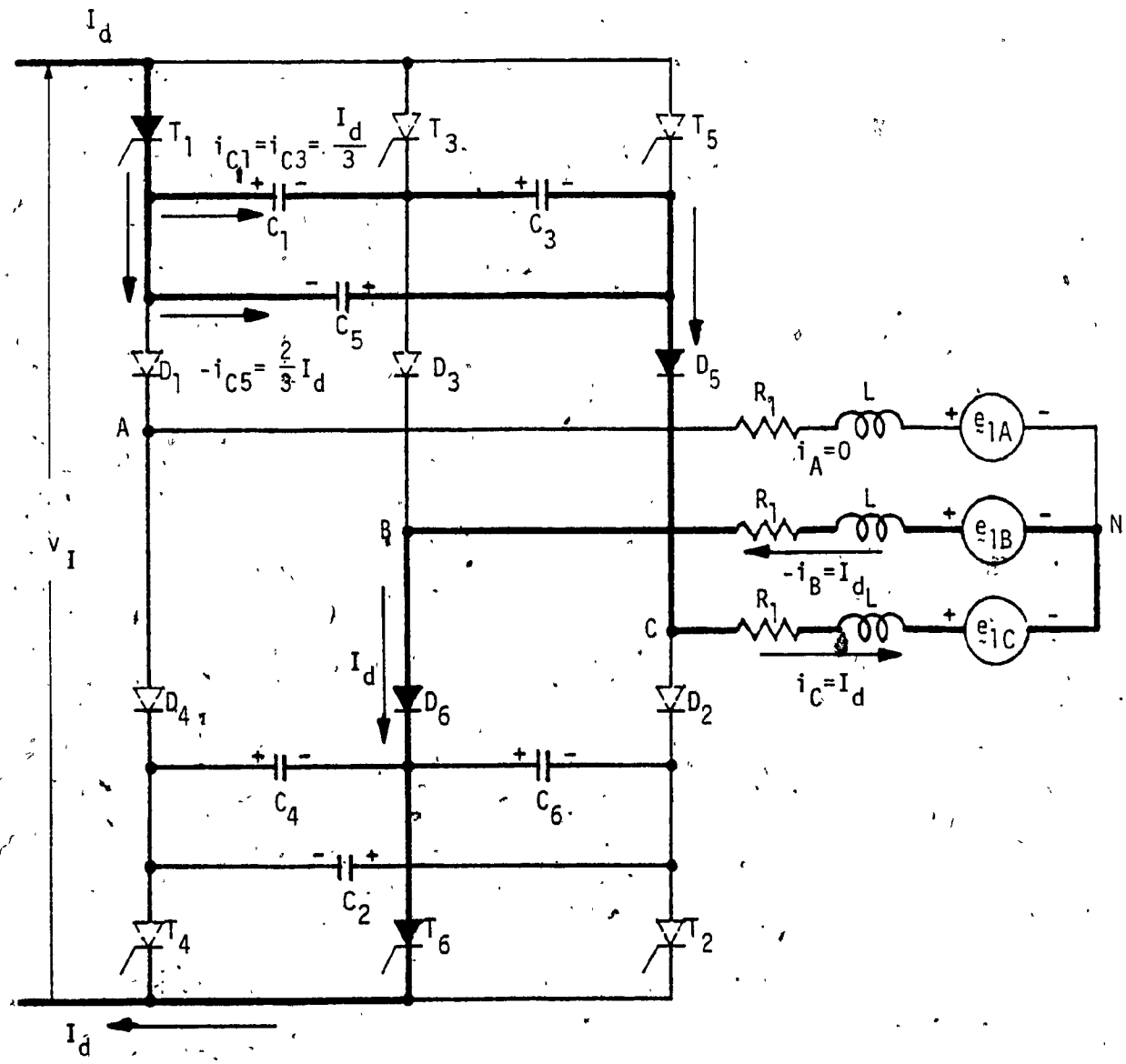

FIG. 4.8 ASCI-induction motor operation in mode 2 of case (b). At $t=t_{18}$ the diode D_4 ceases conducting while the second part of a charging mode starts in the upper group. This mode ends at $t=t_2$ when D_1 starts conducting.

The first part of the transfer mode for the upper group starts at $t=t_2$, fig. 4.9. This mode is similar to mode 2 which was explained in section (3.4). All the equations from (3.4.1) to (3.4.12) and from (3.4.15) to (3.4.33) are applicable to this mode. Only the time limits should be changed in the above equations to $t_2 < t < t_4$ and $0 < t' < t_4-t_2$.

4.3.4 MODE 4 OR THE SECOND PART OF THE TRANSFER MODE

This mode lasts from $t=t_4$ the moment when T_2 is fired till $t=t_3$ the time when D_5 is blocked. At $t=t_4$ the charging mode starts in the lower group while the transfer mode goes on in the upper group, fig. 4.10. This mode is similar to mode 1 explained in section (4.3.1). It is seen that the firing of T_2 does not change the operation of the upper group. Therefore, the equations given by (3.4.29) and (3.4.32) are also valid for this mode but with the time limits changed to $(t_4-t_2) < t' < (t_3-t_4)$. Furthermore, (3.4.33) and (3.4.34) are used at the end of this mode and the transfer time can be calculated by employing (3.4.35). The general forms of the voltage and current equations for the upper inverter group and motor phases would be the same as in mode 3, case (b), but for $t_4 < t < t_3$. The corresponding equations for the lower SCR group would be different from those in the previous mode. However, these equations can be found easily from fig. 4.10.

It is noticed that case (b), which was described by the previous four modes, does not include a normal mode as defined in section (3.5). Instead, we have an 'overlap time', as given by (4.3.1), the maximum value of which can be equal to $\pi/3$ rad.

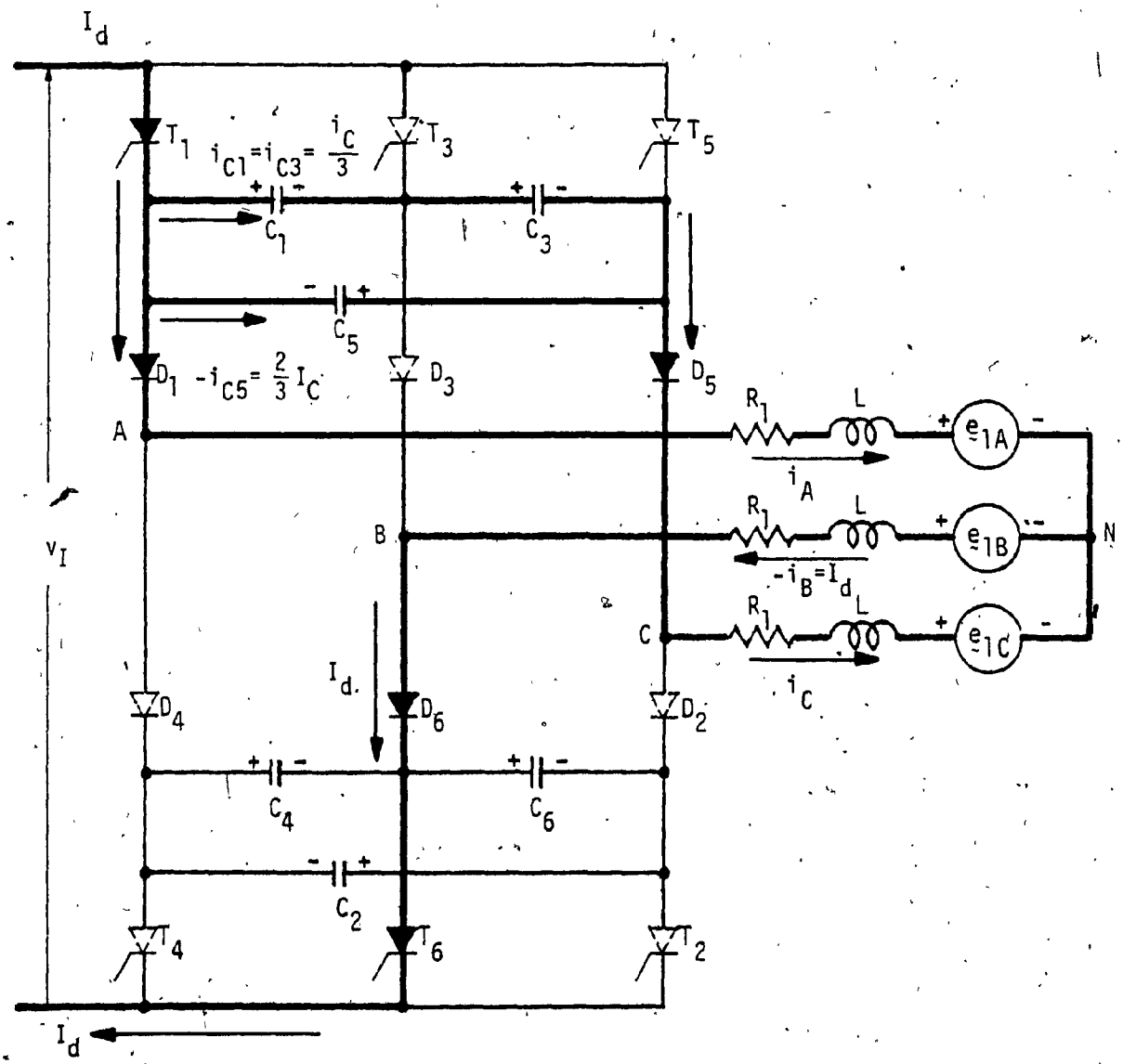

FIG. 4.9 ASCI-induction motor operation in mode 3 of case (b). Conduction of D_1 at $t=t_2$ starts the first part of a transfer mode in the upper group. This mode ends at $t=t_4$ when T_2 is fired.

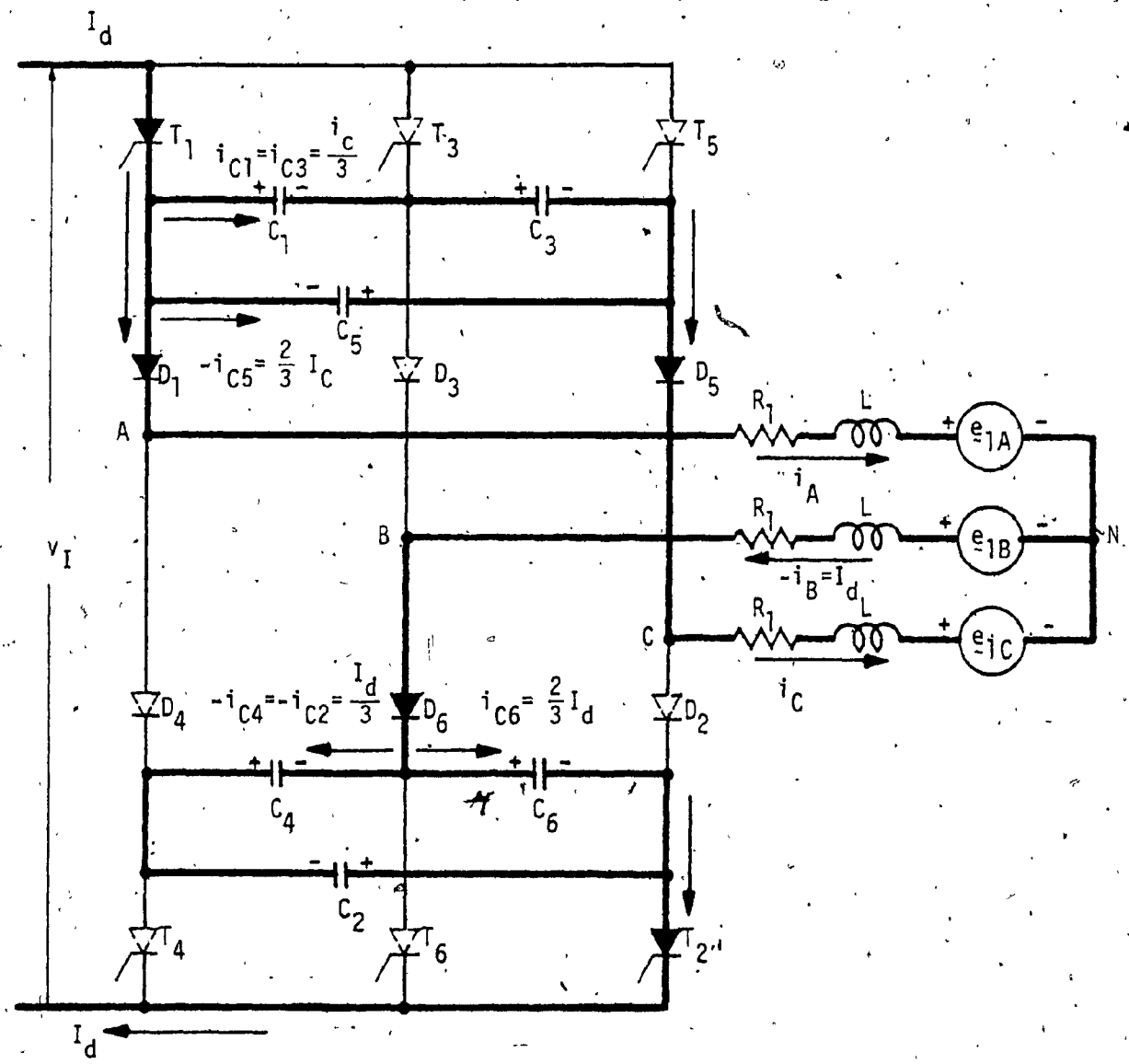

FIG. 4.10 ASCI-induction motor operation in mode (4) of case (b). Firing T_2 at $t=t_4$ initiates the first part of a charging mode in the lower group while the upper group undergoes the second part of a transfer mode. This mode ends at $t=t_3$ when D_1 stops conducting.

In conclusion, the same principal equations which were used to find the unknowns in case (a) are also valid for case (b). Furthermore, the same procedure for solving these equations by either approximate or exact method can be applied in case (b).

4.4 PARTIAL OVERLAP CASE (c)

In case (c), charging, transfer and commutation times are such that $\omega t_{ch} > \pi/3$, $\omega t_{tr} < \pi/3$ and $\omega t_{co} < \frac{2\pi}{3}$ rad. Figure 4.3 shows the relationships between different angles for this mode. It is seen that when the thyristor T_1 is fired in the upper group at $t=t_1$ the charging mode is not yet completed in the lower group. Again, $\omega t_{co} > \pi/3$ rad and we have an overlap angle as defined by (4.3.1). Figure 4.11 displays the circuit for mode 18 just before the thyristor T_1 is fired.

4.4.1 MODE 1 OR THE FIRST PART OF THE CHARGING MODE

This mode exists for $t_1 < t < t_{17}$ where t_1 denotes the time when the thyristor T_1 is triggered and the charging mode starts in the upper group while t_{17} is the moment when D_6 starts conducting, fig. 4.12. For this mode we have

$$i_A(t) = -I_d$$

$$i_B(t) = 0$$

$$i_C(t) = I_d \qquad (4.4.1.1)$$

The expressions given in section 3.3, from (3.3.1) to (3.3.8), as well as (3.3.11-12) are also valid for this case. The remaining equations necessary to describe the system in this mode are:

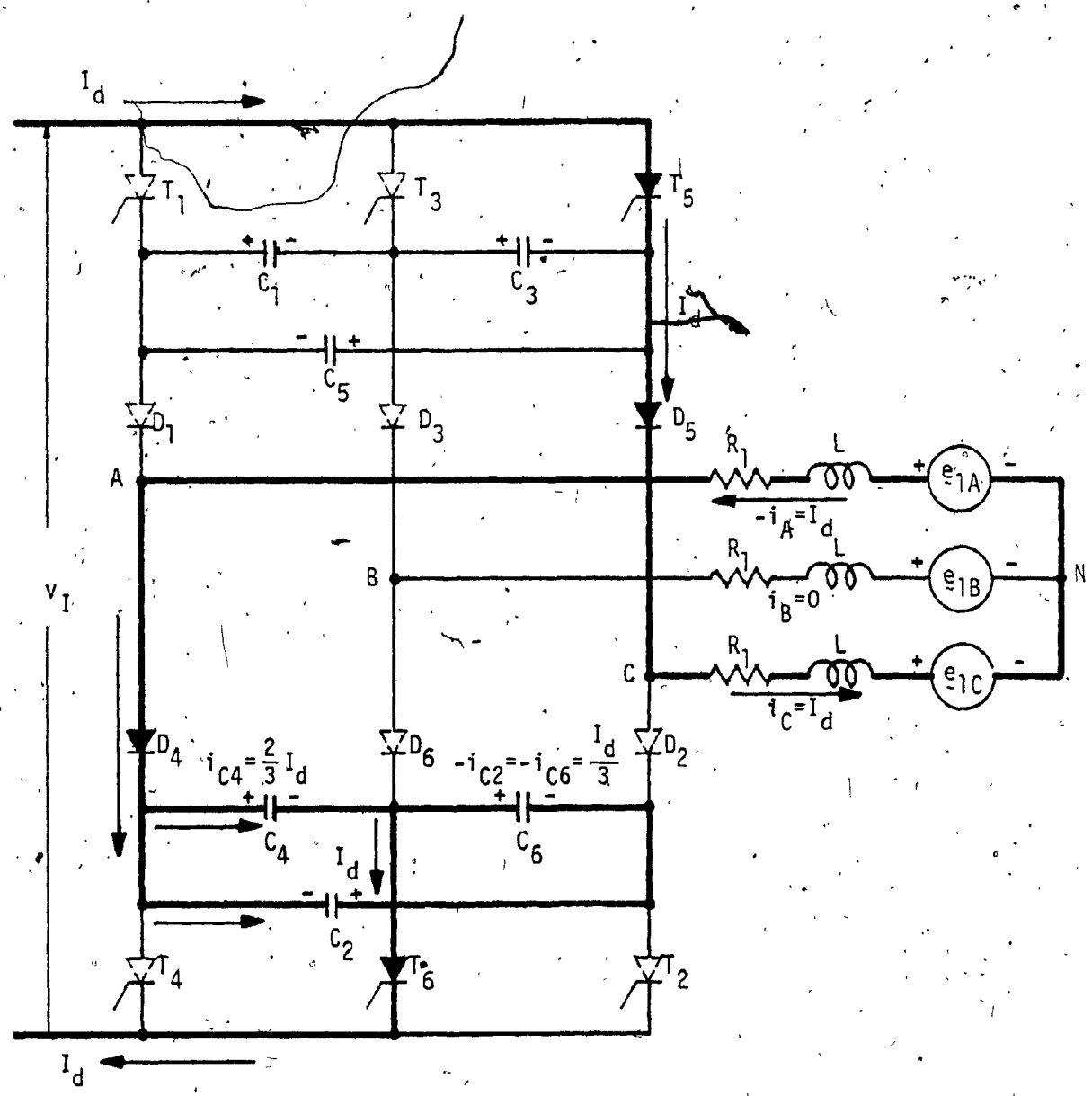

FIG. 4.11 ASCI-induction motor operation in mode 18 of case (c). This mode ends at $t=t_1$ when the thyristor T_1 is fired.

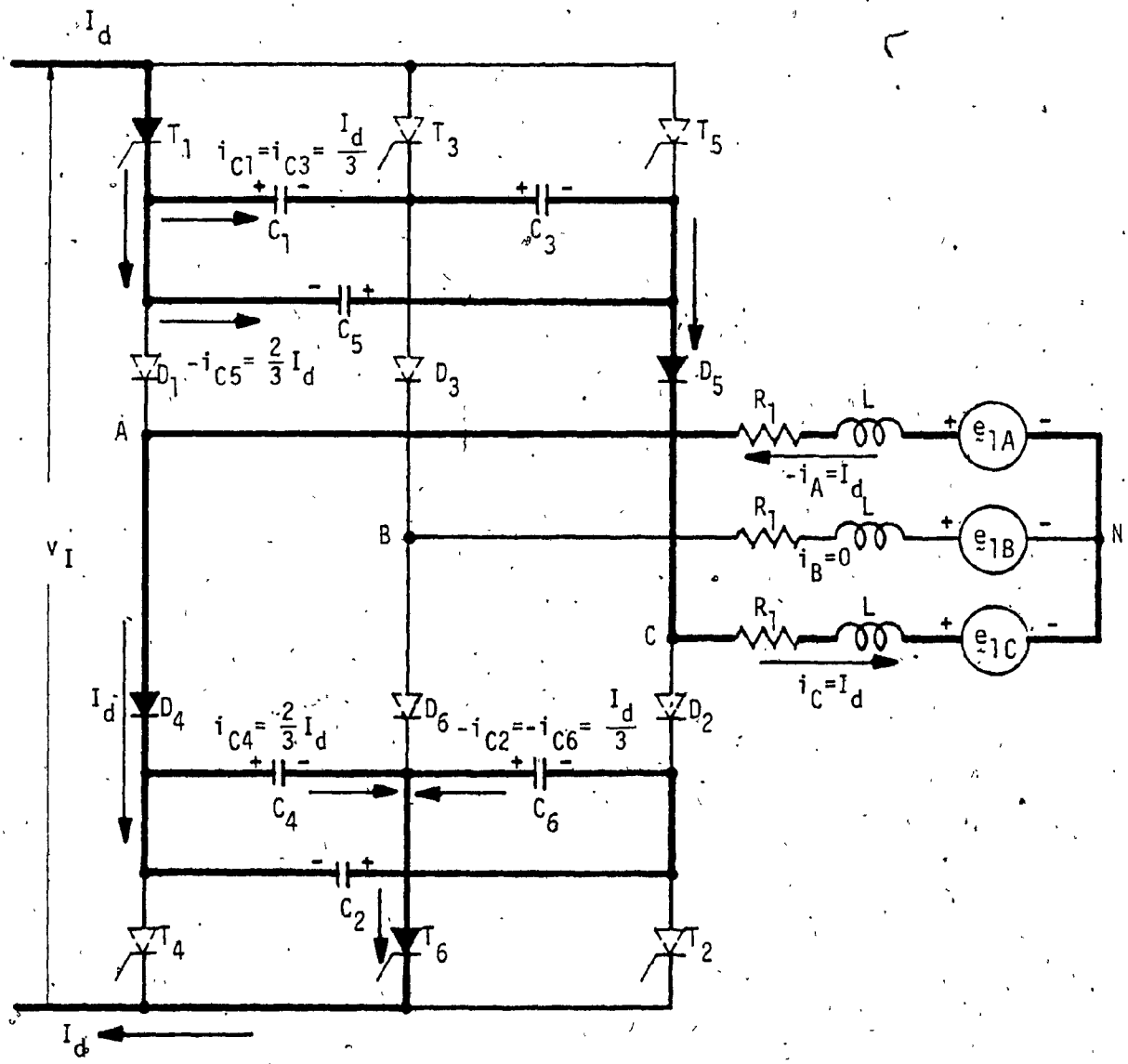

FIG. 4.12 ASCI-induction motor operation in mode 1 of case (c). Firing T_1 at $t=t_1$ commences the first part of a charging mode in the upper group while the lower group is still under its charging mode. This mode ends at $t=t_{17}$ when D_6 starts conducting.

$$v_A(t) = -R_1 I_d + E_1 \sin(\omega t+\phi_1)$$

$$v_B(t) = E_1 \sin(\omega t+\phi_1 - \frac{2\pi}{3})$$

$$v_C(t) = R_1 I_d + E_1 \sin(\omega t+\phi_1 - \frac{4\pi}{3}) \qquad (4.4.1.2)$$

$$v_{AB}(t) = -R_1 I_d + E_1\sqrt{3} \cos(\omega t+\phi_1-\pi/3)$$

$$v_{BC}(t) = -R_1 I_d + E_1\sqrt{3} \cos(\omega t+\phi_1-\pi)$$

$$v_{CA}(t) = 2R_1 I_d - E_1\sqrt{3} \cos(\omega t+\phi_1 - \frac{2\pi}{3}) \qquad (4.4.1.3)$$

$$i_{D1}(t) = i_{D3}(t) = i_{D6}(t) = i_{D2}(t) = 0$$

$$i_{D5}(t) = i_{D4}(t) = I_d \qquad (4.4.1.4)$$

Equations (4.3.1.6) and (4.3.1.7) are also applicable to this mode.

$$v_{D2}(t) = v_{CA}(t) - v_{C2}(t)$$

$$v_{D6}(t) = v_{BA}(t) + v_{C4}(t)$$

$$v_{D4}(t) = 0 \qquad (4.4.1.5)$$

$$v_1(t) = -v_{C5}(t) + v_{CA}(t) + v_{C4}(t) \qquad (4.4.1.6)$$

This mode ends at $t=t_{17}$, the instant at which D_6 becomes forward biased.

4.4.2 MODE 2 OR THE SECOND PART OF THE CHARGING MODE

This mode lasts from $t=t_{17}$ when D_6 starts conducting to $t=t_{18}$ when D_4 is blocked and i_A becomes zero. The transfer mode in the lower group begins at $t=t_{17}$ while the charging mode continues in the upper group so that each group operates independently.

Figure 4.13 illustrates this mode. One can see that this mode is similar to mode 1, case (b). Consequently, all equations given there are applicable to this mode but with the time limits modified, $t_{17} < t < t_{18}$.

4.4.3 MODE 3 OR THE THIRD PART OF THE CHARGING MODE

This mode is defined for $t_{18} < t < t_4$ where t_{18} is the time when D_4 is reversed biased and t_4 is the moment when T_2 is fired. Figure 4.14 shows the inverter circuit during this mode. By comparing fig. 3.5 and 4.14 one can see that this mode is similar to mode 1, case (a), so that the same equations apply, but with different time limits, $t_{18} < t < t_4$. An additional consideration is the difference in the limit conditions for these two modes. For mode 1, case (a), the charging time finishes at $t=t_2$, while for this mode, at $t=t_4$ the charging mode still exists in the upper group.

4.4.4 MODE 4 OR THE FOURTH PART OF THE CHARGING MODE

This mode lasts from $t=t_4$ the time when T_2 is fired to $t=t_2$ the moment at which D_1 starts conducting, fig. 4.15. The equations for the upper SCR group and the motor are the same as in the previous mode but with different initial conditions. The equations for the lower SCR group are different however and can be derived from fig. 4.15.

Therefore, one can conclude that during modes 7-4, case (c), the inverter upper group operates with linear charging which is not affected by the lower group operation.

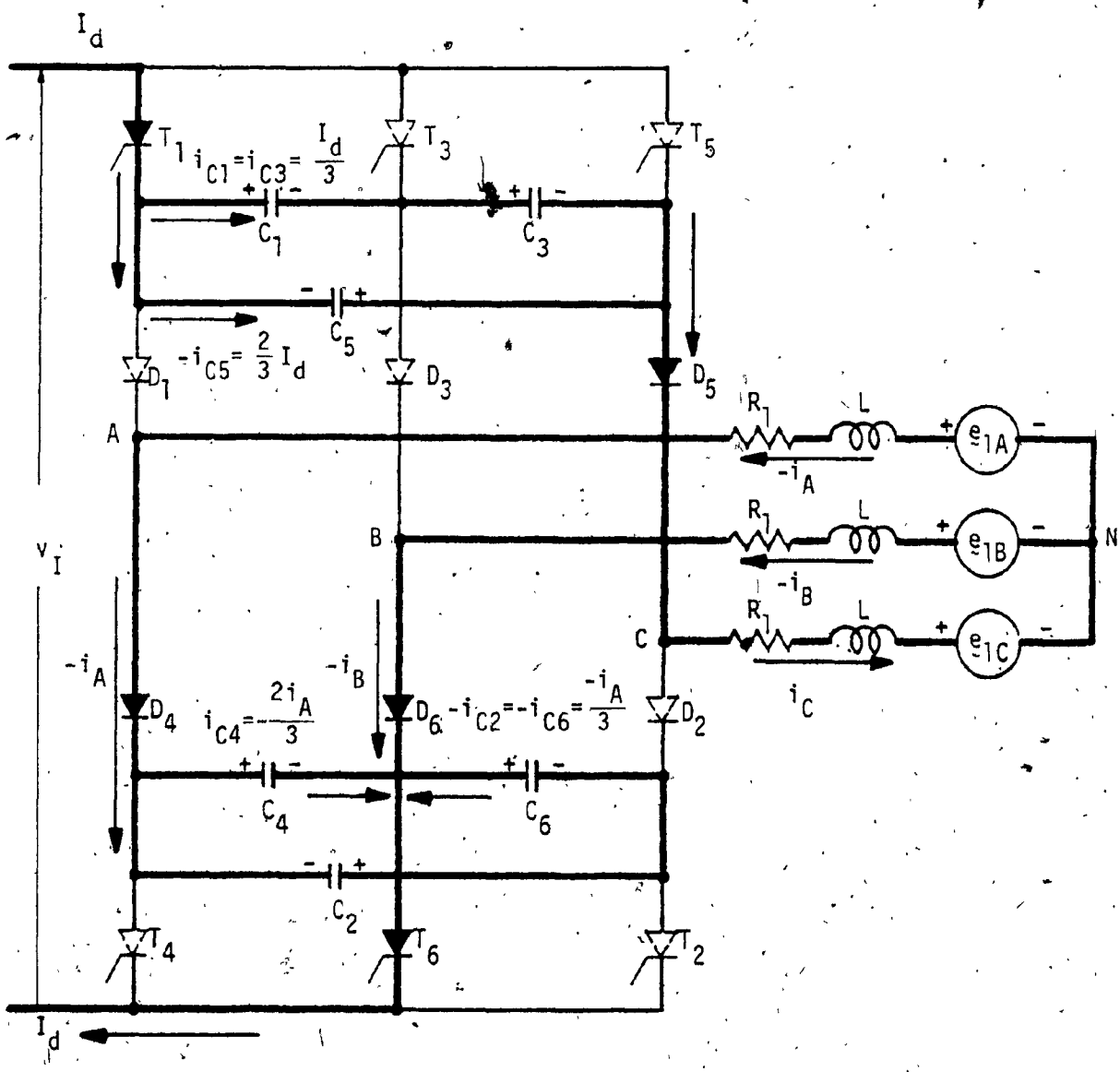

FIG. 4.13 ASCI-induction motor operation in mode 2 of case (c). Conduction of D_6 starts the first part of a transfer mode in the lower group while the second part of a charging mode continues in the upper group. This mode ends at $t=t_{18}$ when D_4 stops conducting.

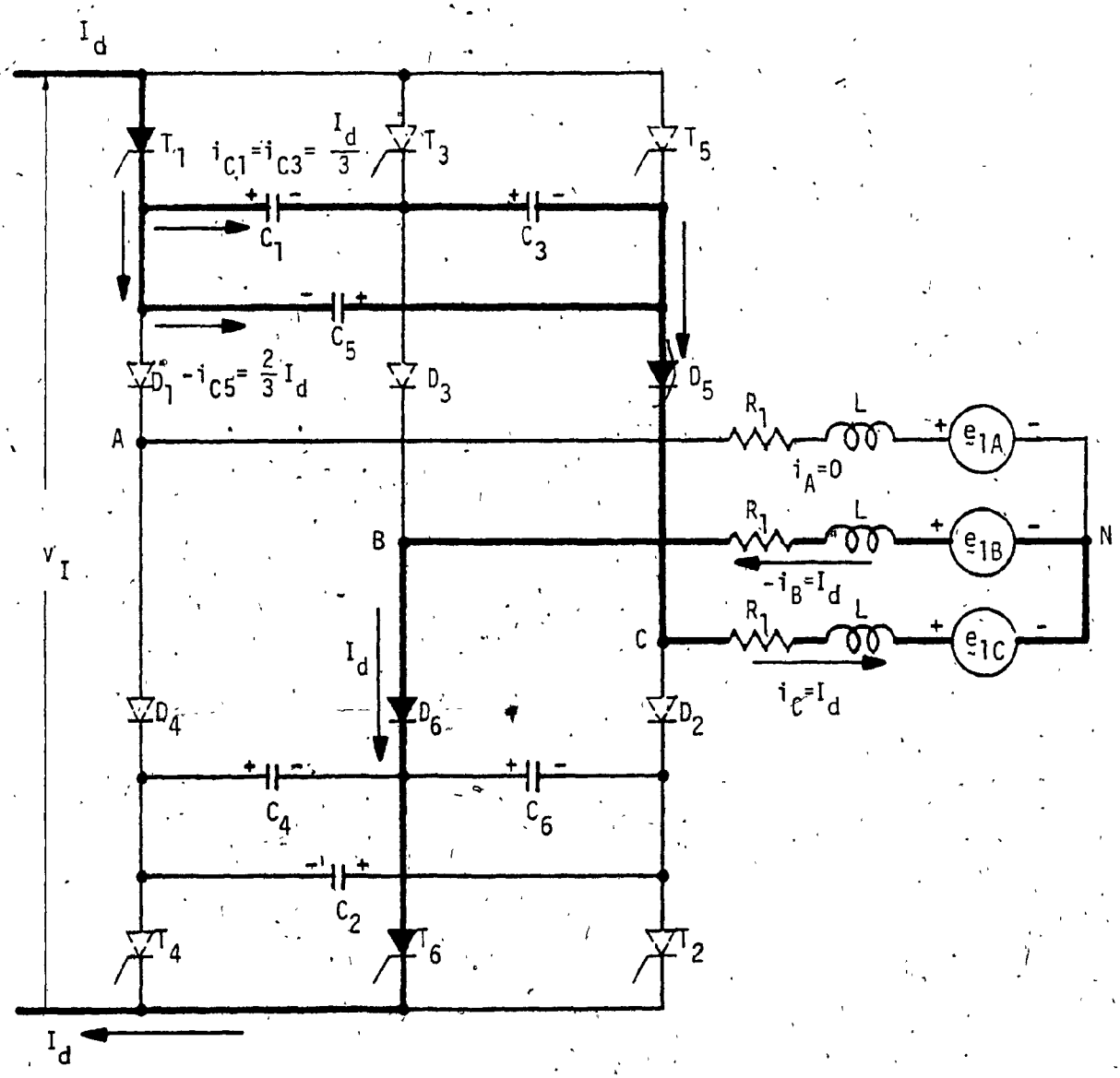

FIG. 4.14 ASCI-induction motor operation in mode 3 of case (c). Blocking of D_4 at $t=t_{18}$ terminates a commutation cycle in the lower group while the upper group enters its third part of a charging mode. This mode ends at $t=t_4$ when T_2 is triggered.

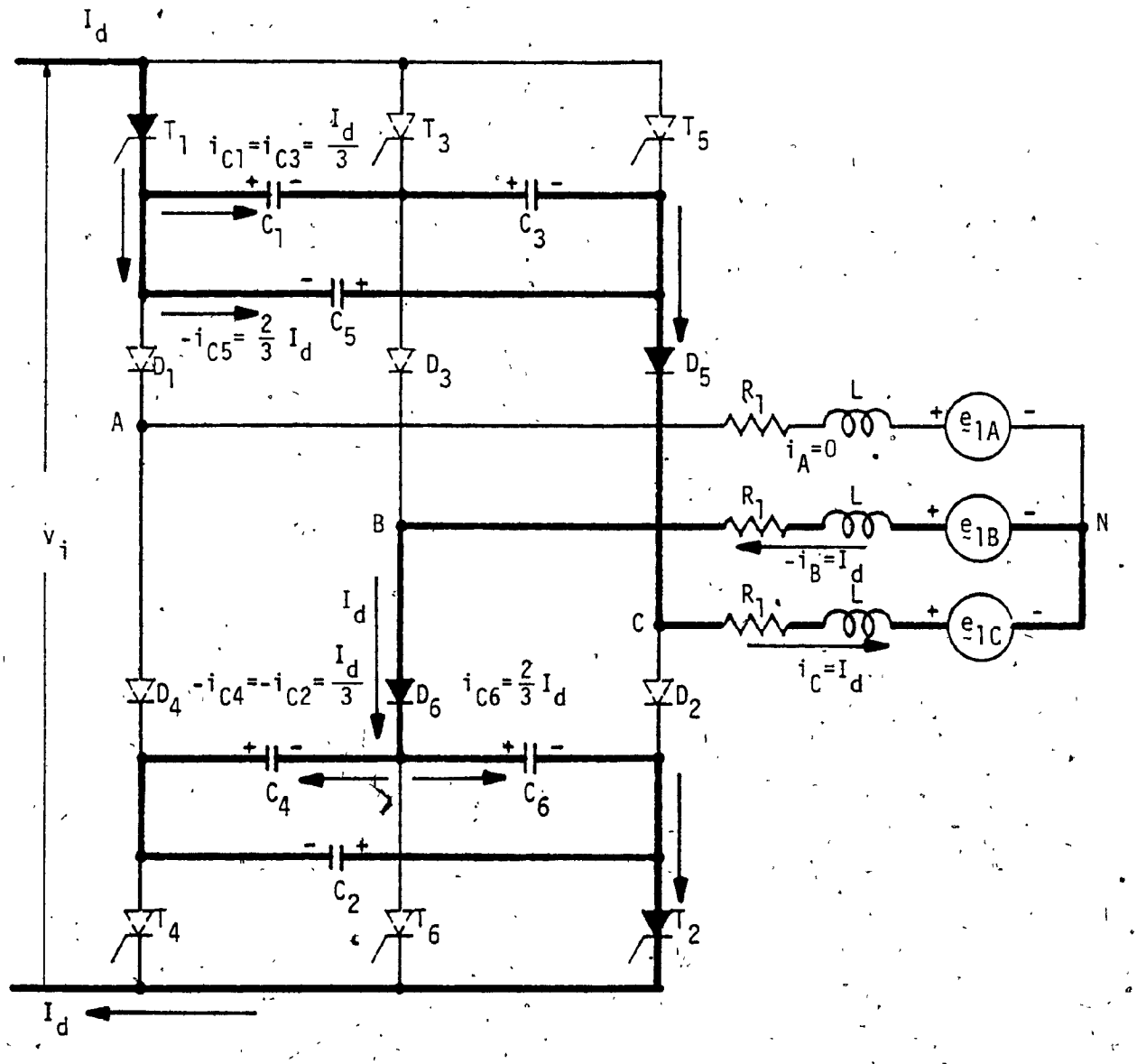

FIG. 4.15 ASCI-induction motor operation in mode 4 of case (c). Firing of T_2 at $t=t_4$ initiates the first part of a charging mode in the lower group while the fourth part of a charging mode continues in the upper group. This mode ends at $t=t_2$ when D_1 commences conducting.

4.4.5 MODE 5 OR TRANSFER MODE

This mode begins at $t=t_2$ when D_1 starts conducting. The lower group is in the charging mode so that it does not affect the operation of the upper group, fig. 4.16. This mode is similar to mode 4, case (b). The only difference being in the initial conditions. This mode and therefore the complete commutation period for the upper group ends at $t=t_3$ when D_5 becomes blocked. Again, the same performance described for the transfer mode case (b) applies here. Therefore, the same equations used for the transfer mode in cases (a) and (b) are also valid for the transfer mode in case (c).

The above discussion for different modes in case (c) results in the same conclusion as in case (b). In other words, as long as the commutation angle is smaller than 120° while the transfer angle does not exceed 60° and the diodes are under the constraint mentioned before, we can calculate the unknown variables by using the steps as in the no-overlap case.

4.5 CONDITIONS NECESSARY FOR EXISTENCE OF CASE (b) AND CASE (c)

In section (3.3) it was pointed out that the condition necessary for existence of case (a) where charging, transfer and commutation angles are all less than 60° is that D_3 should not become transiently forward biased (D_3 is not allowed to become forward biased before D_1 does in mode 1), fig. 3.5. In a similar way, there are two conditions necessary for existence of case (b) and case (c). These two requirements were mentioned in section (4.1). The first condition regarding the transfer angle can easily be verified by calculating this

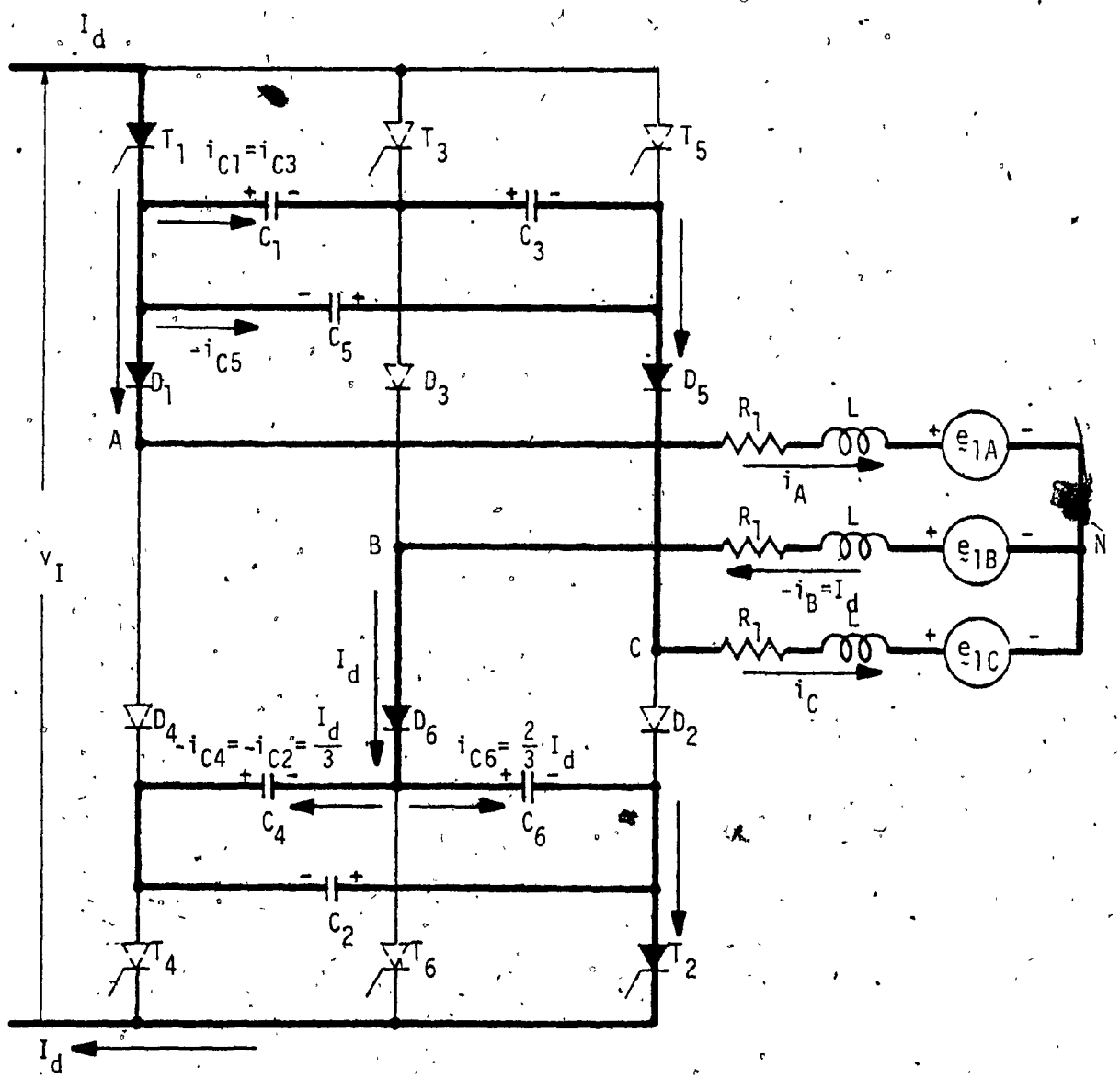

FIG. 4.16 ASCI-induction motor operation in mode 5 of case (c). Conduction of D_1 starts the transfer mode in the upper group while the second part of a charging mode goes on in the lower group. This mode and a cycle of commutation in the upper group end at $t=t_3$ when D_5 stops conducting.

angle for each operating point. For the second condition regarding the transient forward biasing of the diodes we can specify the diodes which should remain blocked during all the modes in cases (b) and (c). After indicating these diodes it would be enough to obtain the voltages across them at the beginning and at the end of three consecutive modes and to check whether they are negative. In order to obtain similar expressions for both cases it would be better to choose modes 2, 3 and 4 for case (b) while modes 3, 4 and 5 are selected for case (c).

For case (b), the diodes which should remain blocked during modes 2, 3 and 4 can be determined from figures 4.2, 4.8, 4.9 and 4.10. It then results

1) D_1, D_2, D_3 and D_4 should remain blocked during mode 2.
2) D_2, D_3 and D_4 " " " " " 3.
3) D_2, D_3 and D_4 " " " " " 4.

Note that only D_1 becomes forward biased at the end of mode 2.

In the same way, the diodes which should remain blocked during modes 3, 4 and 5 in case(c) can be specified from figures 4.3, 4.14, 4.15 and 4.16 which yields

1) D_1, D_2, D_3 and D_4 should remain blocked during mode 3.
2) D_1, D_2, D_3 and D_4 " " " " " 4.
3) D_2, D_3 and D_4 " " " " " 5.

Again, only D_1 becomes forward biased at the end of mode 4.

4.6 FULL OVERLAP

By increasing the output frequency we increase also the commutation angle as shown in fig. 4.1-4.3. In doing so, we will

eventually reach a condition when a transfer mode in either upper or lower group is not yet completed when the next thyristor in the same group is fired. Thus, the inverter goes into a full overlap mode. Note that this happens when the commutation angle becomes $2\pi/3$ rad. This situation has been studied by simulation and by Park's vector techniques [14 - 16] and is out of the scope of this thesis. However, a brief discussion of a full overlap mode is now presented.

We know that during the commutation period in each group all the capacitors of that group are in the circuit (i.e. during charging and transfer modes). After the current from one phase of the motor has been transferred to the other phase the capacitors of the group under diode commutation become disconnected from the rest of the circuit. This is true only for the case when the next thyristor in the same group has not yet been triggered. If the next thyristor is triggered before the transfer mode in the same group is terminated, the capacitors would be constantly charging or discharging. By increasing the output frequency and thus reaching the $2\pi/3$ rad limit for the commutation angle, one creates this situation. When the system goes into a full overlap the transfer angle is either less than or more than $\pi/3$ rad. If the transfer angle is less than $\pi/3$ rad the system can continue its operation but the capacitor voltages would be changing all the time with the capacitors either charging or discharging.

If we increase the output frequency further, there are two possibilities:

1) The capacitor voltages would not obtain proper values necessary to commutate the thyristors in the desired sequence while the

transfer angle remains less than $\pi/3$ rad.

2) The transfer angle exceeds $\pi/3$ rad which results in the conduction of four diodes at the same time. Figure 4.17 shows a case of a full overlap mode where the transfer mode in the upper group is still not completed when the transfer mode starts in the lower group. This means that we have a transfer angle of more than $\pi/3$ rad. In this figure, just before the beginning of the transfer mode in the lower group only D_6 and T_2 were conducting in the same group. The transfer mode in the lower group starts when D_2 is forward biased. As is seen, D_5, D_2 and T_2 will all be conducting at the same time which causes some part of the dc link current to bypass the motor thus resulting in a reduction of the output power.

The equations derived previously are valid only for the case in which the transfer and commutation angles are less than $\pi/3$ and $2\pi/3$ rad, respectively, and the diodes do not become transiently forward biased. However, in practical applications, due to the turn-off time needed for the thyristors, the maximum commutation angle should be a little less than $2\pi/3$ rad in order to avoid current bypass (full overlap mode).

4.7 COMMUTATING CAPACITOR RATING

In section 4.2 the approximate values of charging and commutation times at no-load were calculated by neglecting the stator resistance and given respectively by (4.2.1) and (4.2.2). It was also noticed from these equations that for any given output frequency, the charging and commutation times have their highest values at a no-load operation.

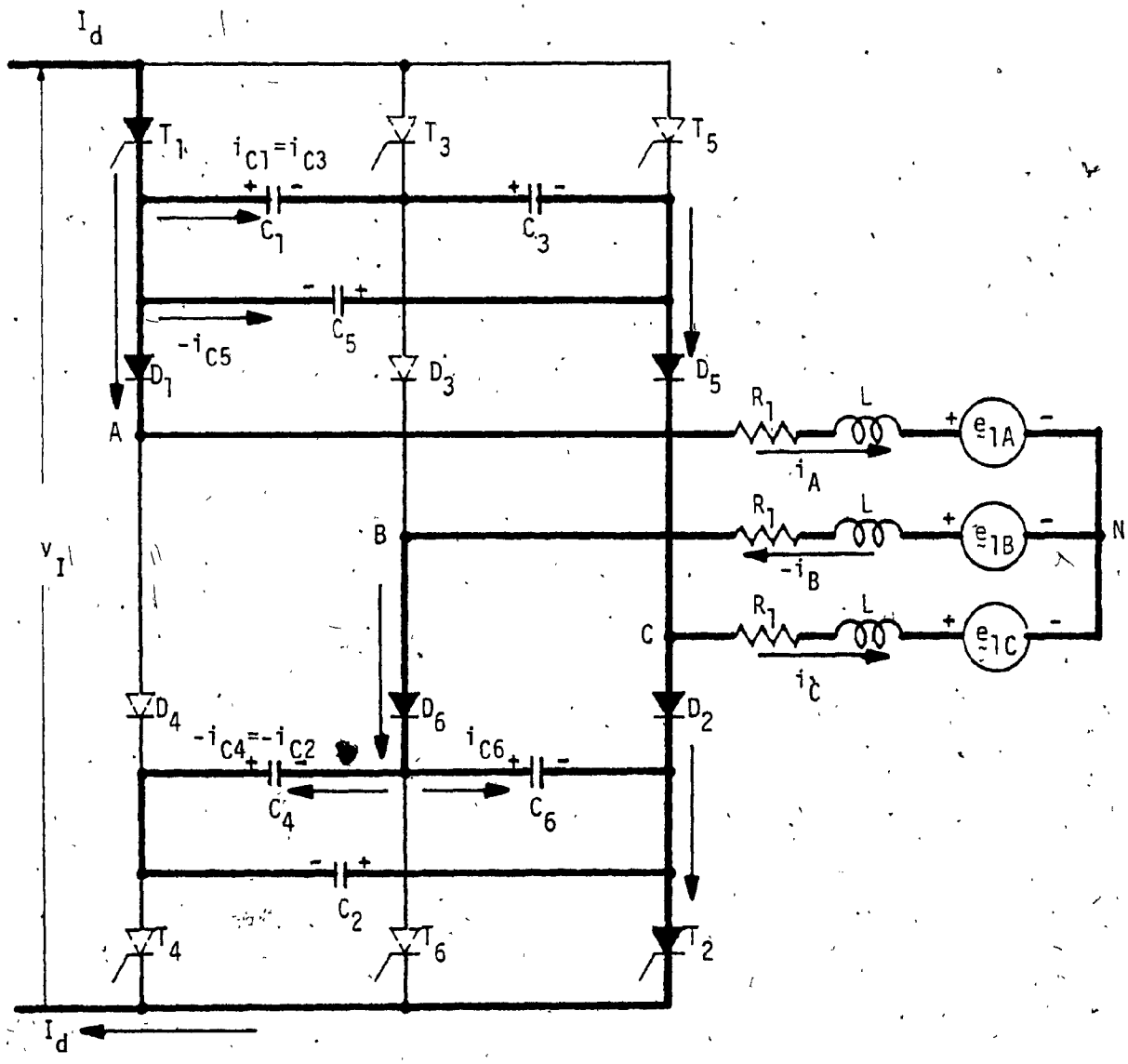

FIG. 4.17 ASCI-induction motor operation with a full commutation overlap where $\omega t_{tr} > \frac{\pi}{3}$. The upper group is under a diode commutation while conduction of D_2 starts a diode commutation in the lower group. Due to the simultaneous conduction of D_5, D_2 and T_2 some part of the dc link current bypasses the motor.

In cases (b) and (c) the maximum commutation angle is limited to $2\pi/3$ rad while the maximum transfer time is $T/6$, where T is a period of the output current. The maximum permissible operating frequency for cases (b) and (c) is defined by these limitations and the conditions specified for diode voltages in section (4.5) and occurs at no-load when the commutation angle can reach $2\pi/3$ rad. Denoting this maximum frequency by f_{max} we have:

$$\omega_{max} = 2\pi f_{max}$$

$$\omega_{max} \cdot t_{co(max)} = 2\pi/3 \qquad (4.7.1)$$

At maximum output frequency and with the above notation (4.2.2) becomes

$$\frac{1}{\omega_o}\left(1+\frac{\pi}{2}\right) + 36Cf_{max}\, L_m \sin\left[\frac{\pi}{2}\left(1-\frac{\omega_{max}}{2\omega_o}\right)\right] = \frac{2\pi}{3\omega_{max}} \qquad (4.7.2)\ \text{APX}$$

Knowing the maximum frequency f_{max}, we can obtain a value of the commutating capacitor, C, for a particular drive by solving numerically the transcendental equation (4.7.2). Although this method is feasible, there is an analytical approach which yields almost the same result. Consider the sine expression in (4.7.2). The term $\omega_{max}/2\omega_o$ can be written as

$$\frac{\omega_{max}}{2\omega_o} = \frac{\omega_{max}\sqrt{3LC}}{2} \qquad (4.7.3)$$

The magnitude of L is normally in the order of a few milihenries while C is usually in the order of a few micro-farads. Using the data given in Appendix A-1 for the parameters of the drive

under this study we obtain

$$L = L_1 + L_2 = .436 + .748 = 1.184 \text{ mH}$$

Specifying a maximum output frequency of 200 Hz and using the standardized values of C we can calculate the magnitudes of ω_{max}/ω_o in (4.7.3), Table 4.1.

Table 4.1 suggests that the term $\omega_{max}/2\omega_0$ is negligible with respect to 1 in the sine expression, (4.7.3). This assumption becomes even more justified, when higher maximum output frequencies are desired since then one has to select smaller commutation capacitors, Table 4.1. With this assumption (4.7.3) becomes

$$\sqrt{3LC}\,(1+\tfrac{\pi}{2}) + 36C\, f_{max}\, L_m = \frac{2\pi}{3\omega_{max}} \qquad (4.7.4)\ \text{APX}$$

but $\omega_{max} = 2\pi\, f_{max}$ which yields

$$36\, L_m\, f_{max}\, C + \sqrt{3L}\,(1+\tfrac{\pi}{2})\sqrt{C} - \frac{1}{3f_{max}} = 0 \qquad (4.7.5)\ \text{APX}$$

The above is a quadratic equation from which we can find C. Taking only the positive root of (4.7.5)

$$\sqrt{C} = \frac{-\sqrt{3L}\,(1+\frac{\pi}{2}) + \sqrt{[3L(1+\frac{\pi}{2})^2] + 48\, L_m}}{72\, L_m\, f_{max}} \qquad (4.7.6)\ \text{APX}$$

After calculating $\sqrt{C}$ and then C from (4.7.6), we should compare the result with the capacitor values given in Table 4.1 and determine the next higher and lower standard ratings. If the calculated

C μF	2	3	5	10	15	20	30
$\frac{\omega_{max}\sqrt{3LC}}{2}$	.052	.064	.082	.118	.142	.166	.204

TABLE 4.1 Values of $\omega_{max}/2\omega_o$ at f_{max} = 200 Hz and with standard commutating capacitors.

value of C is less than 80% of the next bigger standard capacitor we should choose the smaller capacitor. Otherwise, the bigger one would be selected. Having determined C , we can check whether the inverter can attain the specified maximum frequency. Later on, we will discuss this point.

For the drive under study, we want a maximum output frequency of 200 Hz . Then, (4.7.6) yields

$$C = 10.6\times10^{-6}\ F = 10.6\ \mu F$$

Comparing the above value with the standardized capacitor values in Table 4.1 one can see that the calculated capacitor rating lies between 10 and 15 μF . Since 80% of 15 is equal to 12 which is larger than 10.6 , the final value of C becomes 10 μF . In the rest of this study this is the value of C which will be used.

The dependence of f_{max} on C is also noticed in (4.7.6). For the same drive an increase in C yields a smaller f_{max} and vice versa.

Using (4.7.6) we can plot the variations of C versus f_{max} . For the drive under study (4.7.6) gives

$$C = \frac{.4244978}{f_{max}^2} \qquad (4.7.7)\ APX$$

Figure 4.18 shows the resulting plot of (4.7.7). By knowing the maximum output frequency, we can easily determine the value of the commutating capacitors for each particular drive by constructing a plot similar to that in Fig. 4.18.

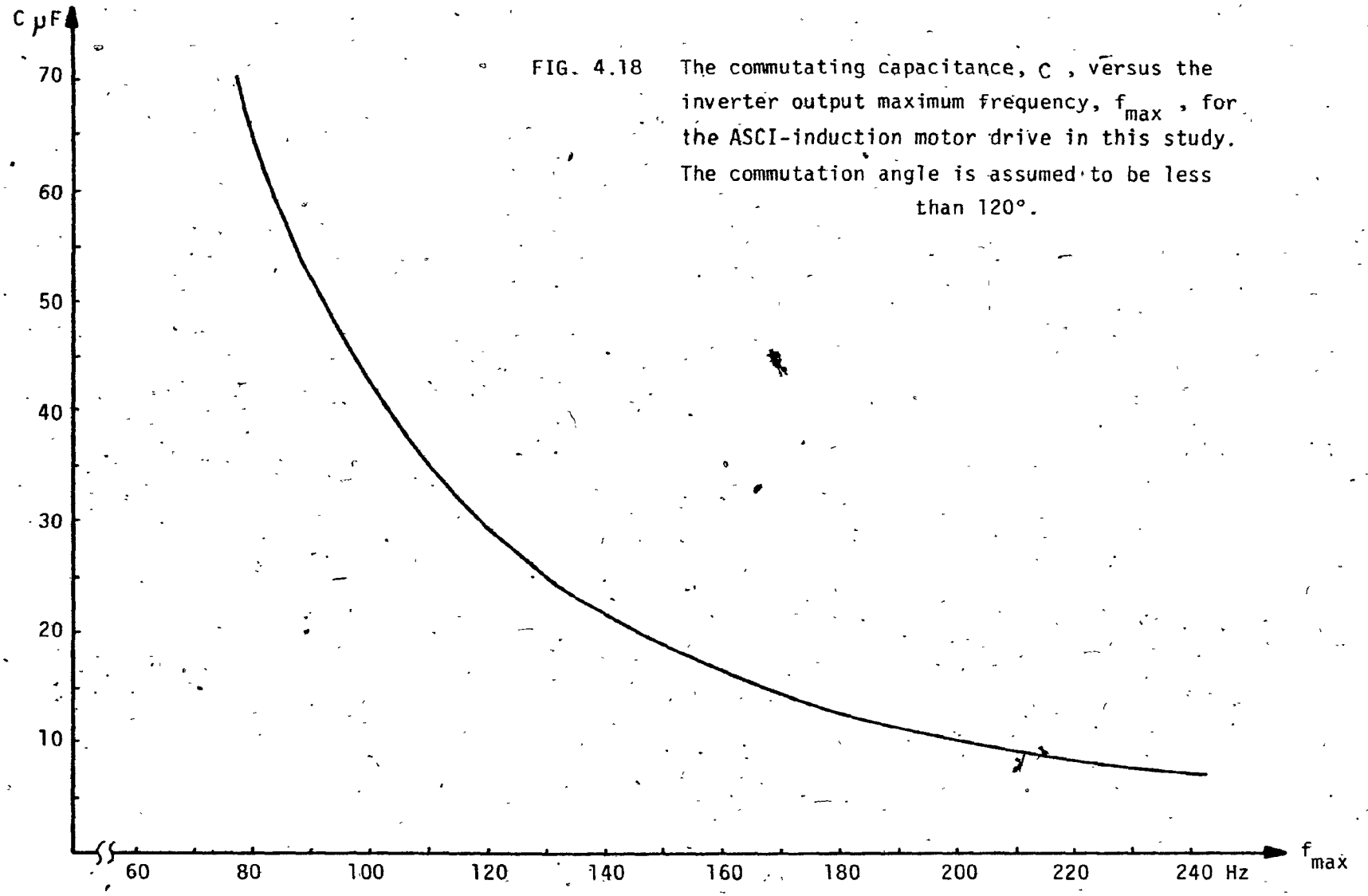

FIG. 4.18 The commutating capacitance, C , versus the inverter output maximum frequency, f_{max} , for the ASCI-induction motor drive in this study. The commutation angle is assumed to be less than 120°.

We can now find the commutation angle to check whether it is less than 120° at 200 Hz. Again, an approximate method is used. For an exact solution we should use the exact approach as described in section (3.6.2). The approximate result is obtained by finding the values of equations (3.4.24), (3.6.1.7) and (3.6.1.12) for the parameters of this drive (Appendix A-1).

$$\alpha = \frac{R_1}{2L} = \frac{R_1}{2(L_1+L_2)} = \frac{.0656}{2\cdot 1.184\cdot 10^{-3}} = 27.703 \text{ rad/s}$$

$$C = 10 \ \mu F$$

$$\omega_o = \frac{1}{\sqrt{3LC}} = \frac{1}{\sqrt{3\cdot 1.184\cdot 10^{-3}\cdot 10\cdot 10^{-6}}} = 5305.954 \text{ rad/s}$$

$$\omega_1 = \sqrt{\omega_o^2 - \alpha^2} = 5305.882 \text{ rad/s}$$

$$\beta = -\text{arc tan}\,\frac{\omega_1}{-\alpha} = -1.576 \text{ rad.}$$

$$t_1' = t_{tr} = \frac{-\beta}{\omega_1} = 297.03\cdot 10^{-6} \text{ s}$$

$$f_{max} = 200 \text{ Hz}$$

Putting the above results into (3.6.1.36) provides the commutation time

$$t_{co} = 1564.93\cdot 10^{-6} \text{ s}$$

and the commutation angle would be

$$\omega t_{co} = 1.966 \text{ rad} = 112.67°$$

$$\omega t_1' = \omega t_{tr} = .373 \text{ rad} = 21.38°$$

One can see that the conditions regarding the commutation and transfer limit angles are satisfied. For conditions imposed by diode voltages mentioned in section (4.5) a computer program was run up to 200 Hz at no-load conditions. It was found that we have no transient forward biasing for any diodes specified in section (4.5) up to 200 Hz for the drive in this study.

4.8 CONCLUSION

The operation of an auto-sequential current source inverter for a case of partial overlap when the commutation angle exceeds 60° but remains less than 120° while the transfer angle is less than 60° and no diodes become transiently forward biased was studied in detail. It was shown that the same key equations derived for the no-overlap case are also valid for a partial overlap case. Thus, the analysis of a partial overlap operation can be performed in the same way as for a no-overlap mode. In this study, the maximum output frequency is defined as the frequency for which the commutation angle becomes 120° at no-load. If the frequency is further increased, the inverter would go into a full overlap operation. For constant V/Hz and constant voltage control strategy, the peak value of the capacitor maximum voltage, V_{omax}, occurs at the maximum load and the maximum operating frequency. Thus, the no-load and full load operations at the maximum frequency define the two critical operating points which should be investigated thoroughly when designing the system.

CHAPTER V

WAVEFORMS AND RESULTS FOR CASE (a)

5.1 INTRODUCTION

In chapter III we described the system for case (a) and suggested an exact and an approximate method for calculating the unknown variables. Since the exact approach gives more accurate results than the other one, it is employed here for obtaining two different sets of graphs. The first set shows the voltage and current waveforms at different points of the system for one specific operating condition. Later on, these graphs will be compared with those obtained experimentally and the differences will be discussed. The second set of graphs shows the variations of system variables when the operating point changes. Each graph is briefly explained and discussed.

In order to attain results compatible with those obtained experimentally, it is necessary to include the effects of saturation on the magentizing and leakage inductance magnitudes. In addition, for each frequency, a specific core-loss resistance, obtained from the manufacturer's data, is considered.

5.2 MOTOR SATURATION AND CORE-LOSS RESISTANCE

It is well known that the induction motor operation at a saturated condition delivers an output torque less than that of an unsaturated case [5], [8]. This is mainly due to the magnetizing inductance saturation which weakens the air-gap flux. There is also some

saturation in the stator and rotor leakage inductances. For an induction motor fed by an ASCI, both kinds of saturation should be examined if an accurate outcome is expected from the derivations of this study. The magnetizing inductance saturation affects principally the motor operation, while the stator and rotor leakage inductance saturation acts basically on the inverter performance. According to (3.4.24), the commutation resonant frequency ω_0, besides the commutation capacitor capacitance, C, depends on the sum of the stator and rotor leakage inductances, L. Therefore, a decrease in L, due to saturation, leads to an increase in ω_0 and consequently a decrease in the transfer time, Eq.(3.6.1.13), and in the commutation time, Eq. (3.6.1.32).

For the induction motor used as an example in this study, the magnitudes of the inductances were measured and are shown by Figures A-1.1 and A-1.2 in Appendix A-1, along with the motor parameters at the rated operating point. From the magnetizing inductance curve, Figure A-1.1, it is clear that the rated operating point corresponds to a saturated condition. For frequencies below 60 Hz, the constant V/Hz control yields an almost constant air-gap flux, Figure 5.11. Under such conditions, the magnitude of the magnetizing inductance is the same for all operating points below 60 Hz and equal to that of the rated operating point. Thus, by using the same value of the magnetizing inductance for all operating points below 60 Hz, the saturation effect regarding the magnetizing inductance is considered. For frequencies above 60 Hz, the motor terminal voltage is kept con-

stant so that increasing frequency results in the weakening of the air-gap flux, Figure 5.11. In order to include the saturation of the magnetizing inductance for frequencies above 60 Hz, iterative methods should be applied. The method consists of selecting some value for the magnetizing inductance, L_m, for each operating condition and calculating the magnetizing current by using the motor exact equivalent circuit. The magnetizing current obtained in this way is then employed to find a new value for L_m from Figure A-1.1 in Appendix A-1. The iterations are repeated for such a number of times so that the magnitudes of L_m used in two consecutive iterations are equal to each other.

The above procedure was applied for frequencies above 60 Hz and it was found that the motor input current is almost the same as the case in which the rated L_m is used for such frequencies. Since the motor input current is the main factor in determining the peak capacitor voltage, V_o, and the rating of the inverter components, L_m is not obtained through iterations as described above for frequencies above 60 Hz. In all of the second set of graphs, the same value of L_m as that of the rated operating conditions is utilized for all operating points.

Regarding the leakage inductances, Figure A-1.2, given in Appendix A-1, is only used for the first set of the graphs where the simulated waveforms are to be compared with those obtained experimentally. For the second set of graphs, the unsaturated values of the leakage inductances are used for all operating conditions. The reason is that

the primary purpose of generating the second set of the graphs is to show the way in which, under different operating conditions, the system variables change. The leakage inductance saturation would not affect the trend of these changes.

Figure A-1.3 in Appendix A-1 yields the approximate values of the core-loss resistance, R_m , for frequencies from 5Hz to 125 Hz. This figure is employed by both sets of graphs.

Although the following graphs have been provided for case (a) only, the same procedure applies for cases (b) and (c), and similar graphs can be produced for the latter cases.

5.3 VOLTAGE AND CURRENT WAVEFORMS

In this section, the voltage and current waveforms at different points of the system for one specific operating condition are exhibited and discussed. The comparison with the experimental results will be done later. In order to avoid the clamping of the voltage spikes by the zener diode circuit connected to the actual system, it was necessary to reduce the applied motor terminal voltage. Consequently, the motor fundamental terminal voltage does not follow the control strategy explained earlier and used for the second set of graphs. The operating point chosen for this section is called point "A". The data specifying point (A) are given in Appendix A-1.

Figures 5.1 to 5.6 show the results of digital simulation

for point (A). Each waveform has been plotted for one cycle and starts from the instant at which the fundamental harmonic of phase A current crosses the x axis, Figure 5.1. The waveforms are:

1. Waveforms of phase B terminal voltage, v_B, fundamental harmonic, i_{1B}, and instantaneous, i_B, currents:

Figure 5.1 shows these three waveforms. Note the $\frac{2\pi}{3}$ rad delay angle of i_{1B}. From waveform i_B it is seen that there are four switchings for each motor line current during one cycle. The duration of each switching is the same as the duration of a transfer mode. Also note the generation of the voltage spikes during each transfer mode.

Each voltage spike reaches its peak at the end of the corresponding transfer mode. Neglecting the voltage drop in the stator resistance, waveform v_B is essentially a sinusoid for intervals other than the transfer times. This sinusoid represents the motor CEMF in each phase. The shift angle between the fundamental harmonic of phase B current and the voltage waveform (neglecting the spikes) displays ϕ_1 as defined by (2.3.9).

2. Waveforms of line voltage, v_{AB}, and phase B current, i_B:

Figure 5.2 shows v_{AB} along with i_B waveforms. The first voltage spike at the left starts at ωt_2 and ends at ωt_3. There are six spikes during one cycle of each motor line voltage. In Figure 5.2

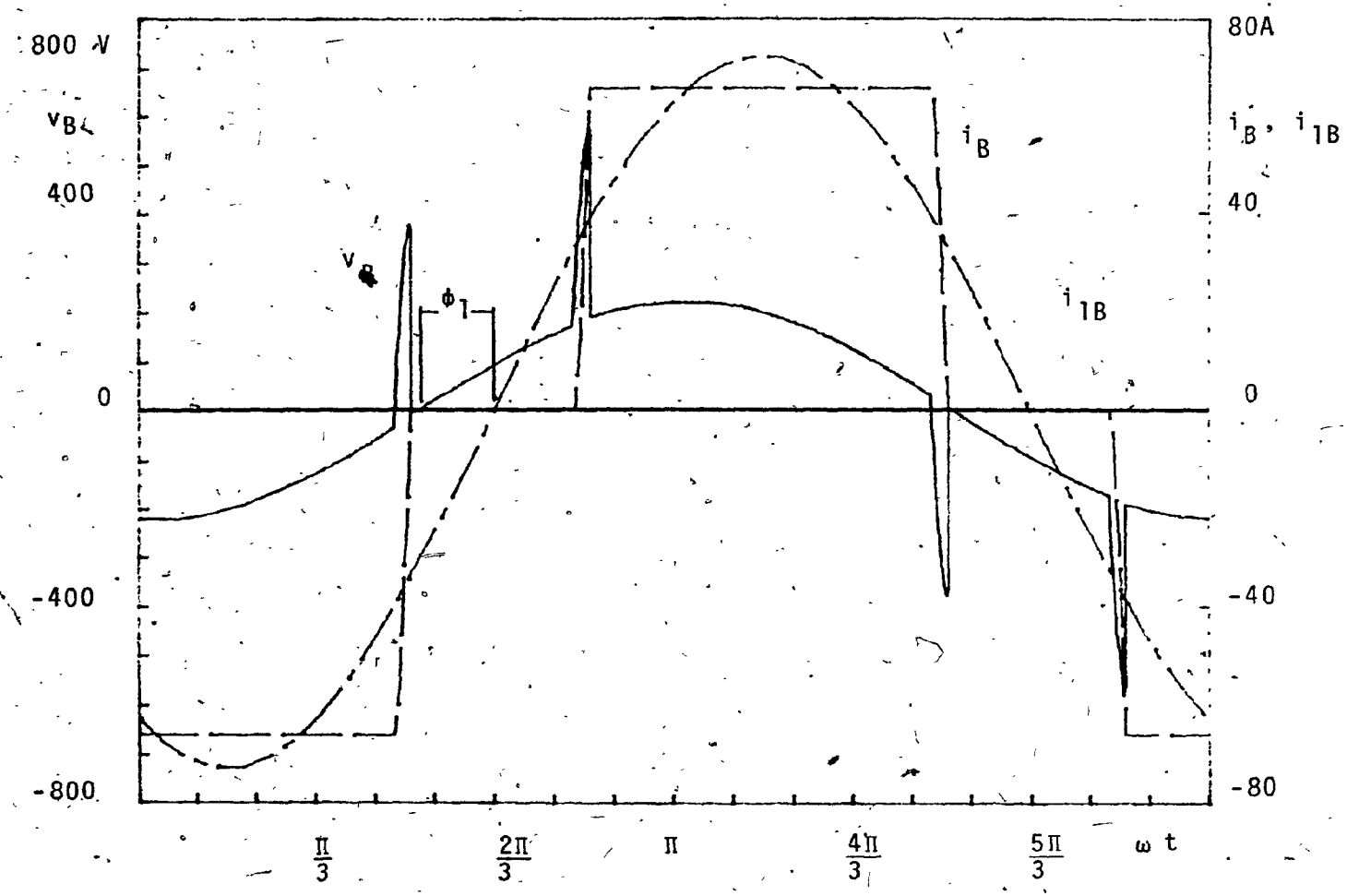

FIGURE 5.1 Waveforms of v_B, i_B and i_{1B} for operating point (A). Each division of the x axis is equivalent to 1.0028 ms.

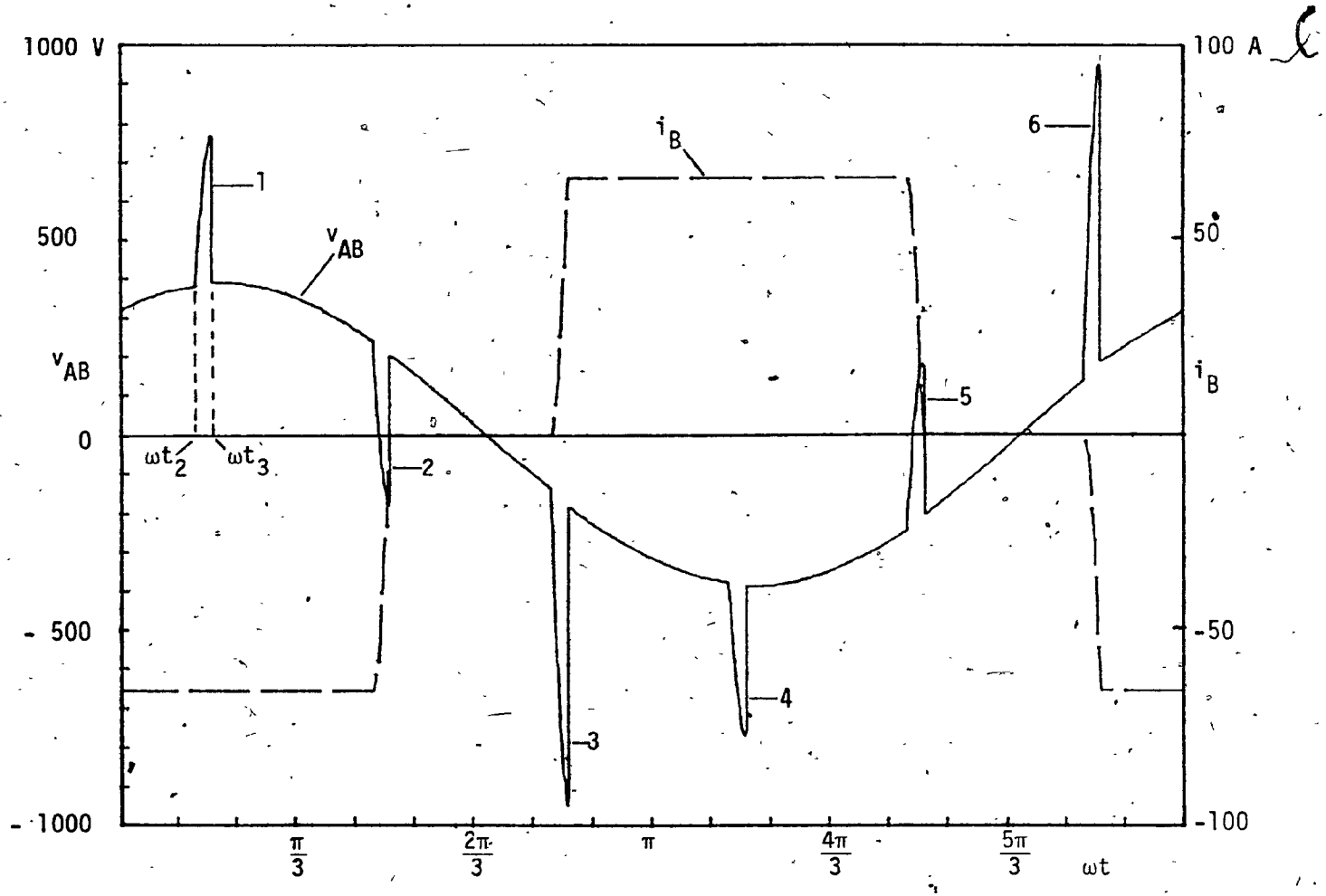

FIG. 5.2 Waveforms of v_{AB} and i_B for operating point (A). $\omega(t_3-t_2)$ shows the transfer angle. Each division of the x axis is equivalent to 1.0028 ms.

the spikes are numbered from 1 to 6. There are two big and four small spikes. The big spikes (3 and 6) occur when the current is being transferred from phase A to phase B, while the small spikes are due to the transfer of a current from phase C to phase A (1 and 4) and from phase B to phase C (2 and 5). Note that the magnitude of a big spike is double that of a small one. Also, the peak value of the big spikes represents the maximum voltage across the commutating capacitors (compare Fig. 5.2 with Fig. 5.3).

3. Waveforms of capacitor C_1 voltage, v_{C1}, and current, i_{C1} :

Figure 5.3 exhibits $-v_{C1}$ and $-i_{C1}$ waveforms. The current waveform consists of three parts. Each part starts at the beginning of a charging mode and ends at the end of a transfer mode, so that each pulse of current lasts for a commutation period. The maximum capacitor current is $\frac{2}{3} I_d$, which is clear from Figure 5.3. For the voltage waveform, it is seen that the capacitor voltage remains constant during the normal modes with values at either V_o or $-V_o$. Only during the charging and transfer modes the voltage changes.

4. Waveforms of thyristor T_1 voltage, v_{T1}, and phase B current i_B:

Figure 5.4 shows v_{T1} and i_B waveforms. At ωt_1 the thyristor T_1 is fired so that its voltage drops to zero. At ωt_7 the thyristor T_3 is fired, which commutates T_1 and the reverse voltage across C_1 is applied to T_1 (compare Fig. 5.4 with Fig. 5.3). In Figure 5.4, the available angle for T_1 turn off has also been

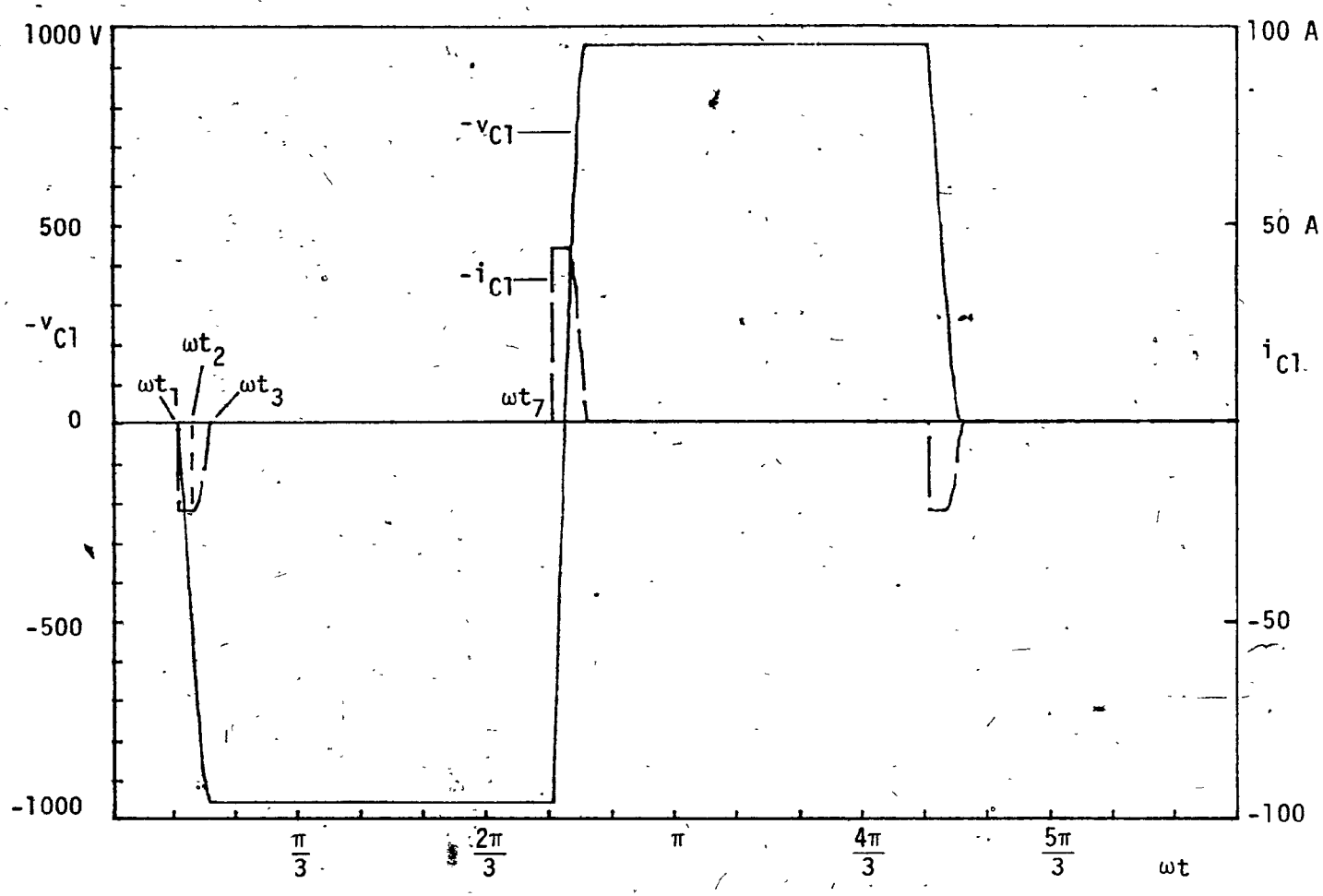

FIG. 5.3 Waveforms of $-v_{C1}$ and $-i_{C1}$ for operating point (A). $\omega(t_2-t_1)$ and $\omega(t_3-t_1)$ show the charging and commutation angles, respectively. Each division of the x axis is equivalent to 1.0028 ms.

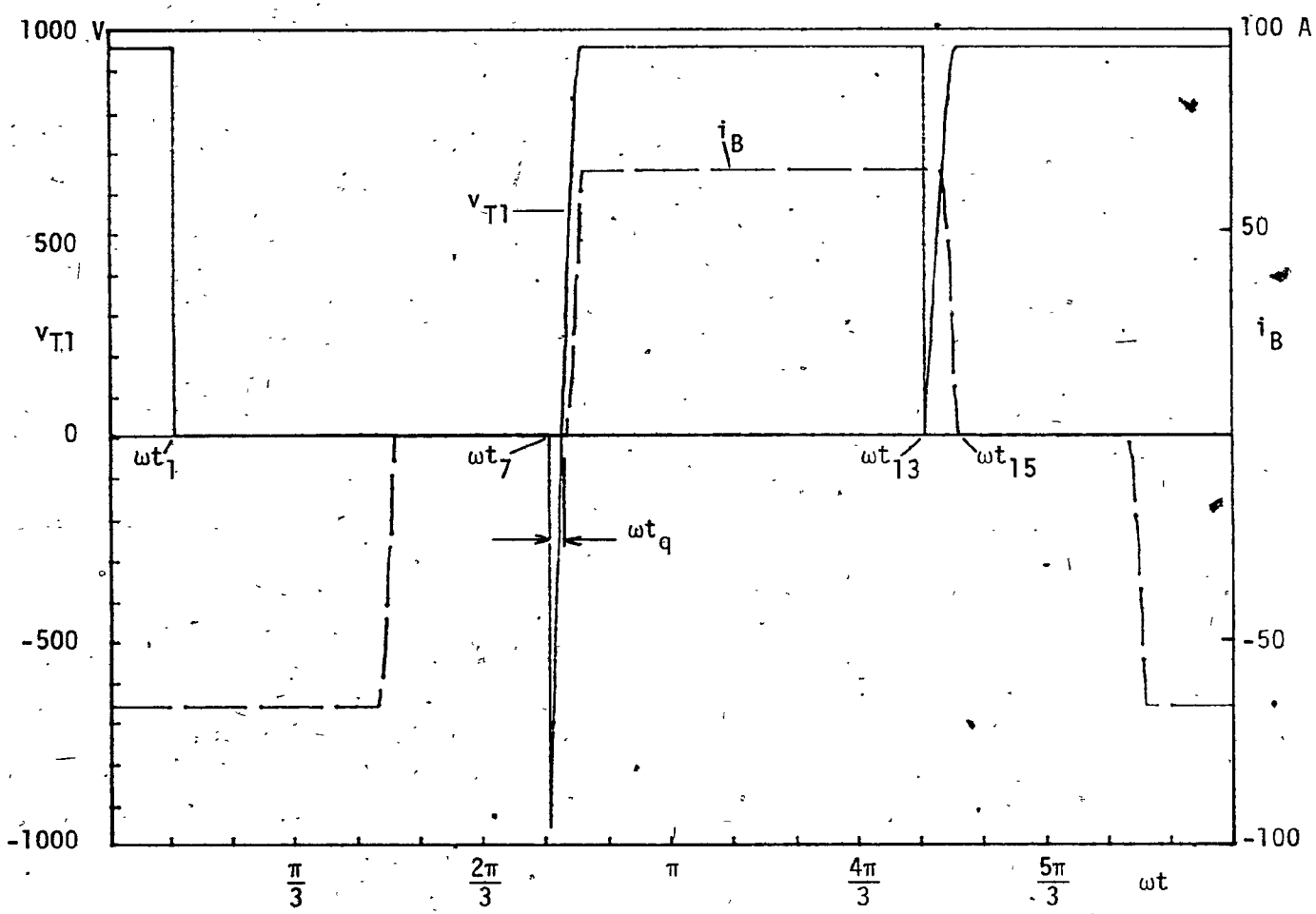

FIG. 5.4 Waveforms of v_{T1} and i_B for operating point (A). Note the available angle for T_1 turn off. Each division of the x axis corresponds to 1.0028 ms.

indicated. At ωt_{13} the thyristor T_5 is fired so that the voltage across C_5 is connected to T_1, causing v_{T1} to drop to zero. During $\omega(t_{15}-t_{13})$ the capacitor C_5 is charged and thus v_{T1} starts increasing. At ωt_{15} this voltage is stabilized and the maximum voltage of commutating capacitors is maintained across T_1.

5. Waveforms of diode D_3 voltage, v_{D3}, and phase B current i_B :

Figure 5.5 exhibits v_{D3} and i_B waveforms. As mentioned in section (3.3), in order to have 18 modes as defined by Tables 1.1 - 1.3, the diode D_3 should remain reverse biased at the end of mode 2. The diode minimum reverse voltage appears at ωt_2 Figure 5.5. Also, the diode maximum reverse voltage occurs at ωt_6 when the reverse current of phase B is commutated. The value of this voltage at the maximum frequency and output torque determines the voltage rating of the diodes. This quantity is less than two times the maximum capacitor voltage V_o. In practical applications, the diode maximum reverse voltage is assumed to be $2V_o$. The diode D_3 current is seen to be equal to the positive pulse of phase B current so that the rms value of each diode current is $1/\sqrt{2}$ of the line rms current.

6. Waveforms of inverter intput voltage, v_I, and dc link current, I_d:

Figure 5.6 shows these two waveforms. The inverter input voltage waveform, v_I, is repeated six times during each cycle so that its

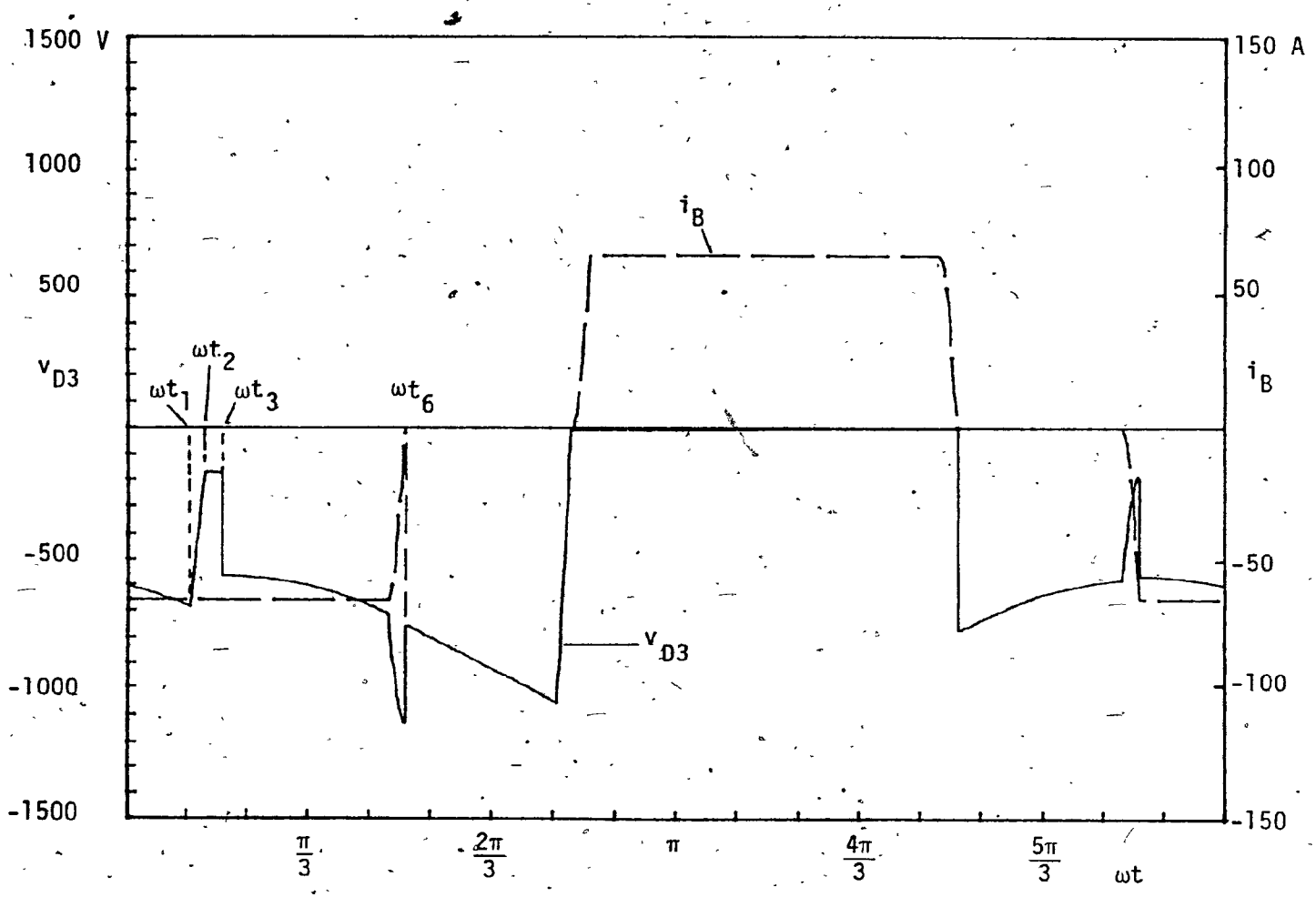

FIG. 5.5 Waveforms of v_{D3} and i_B. The positive cycle of i_B shows also the current through D_3. The diode minimum and maximum reverse voltages occur at ωt_2 and ωt_6, respectively. Each division of the x axis corresponds to 1.0028 ms.

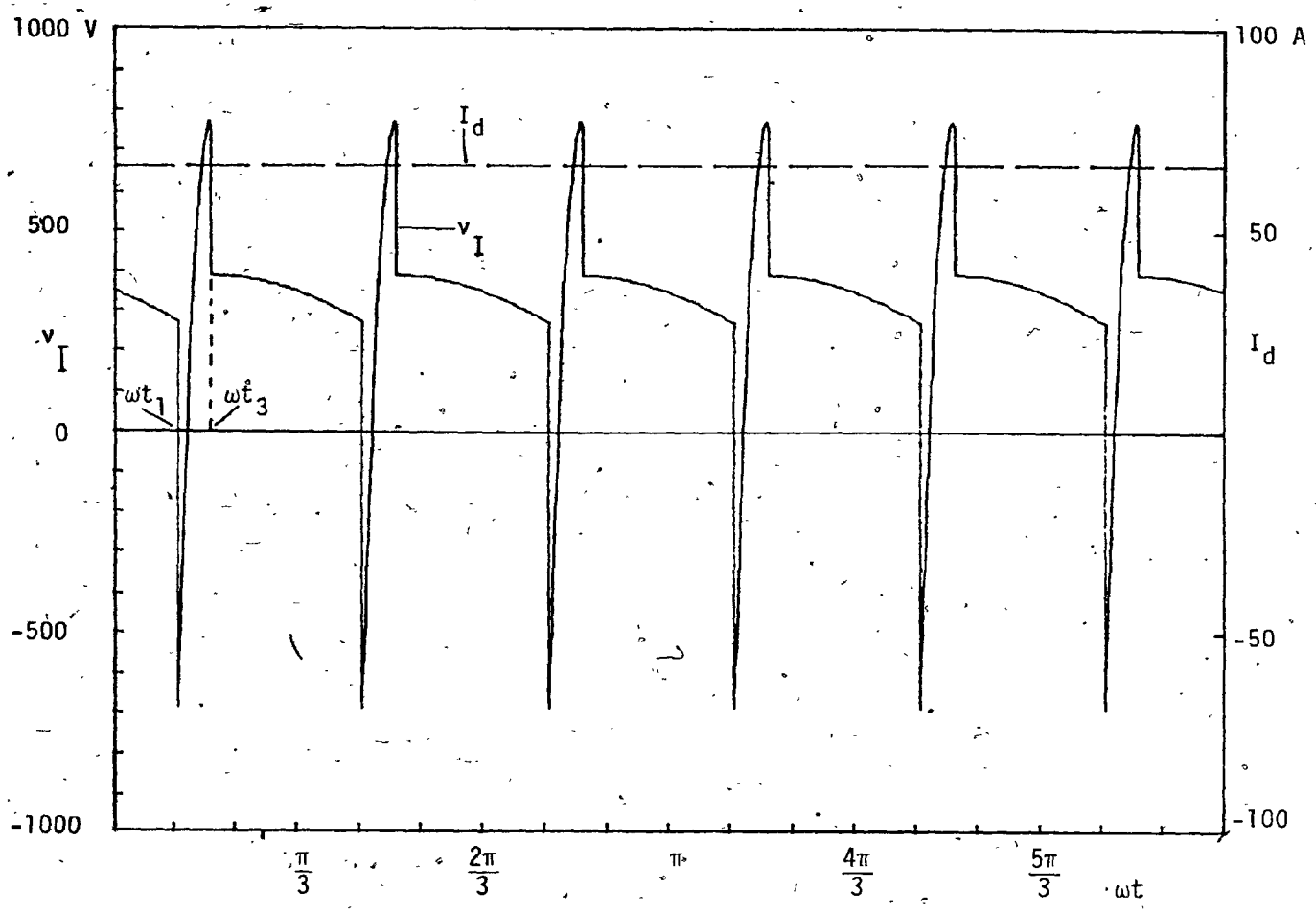

FIG. 5.6 Waveforms of inverter input voltage v_I, and dc link current, I_d, for operating point (A). For a motoring operation, the average value of v_I is positive. Each division of the x axis corresponds to 1.0028 ms.

frequency is six times that of the inverter input frequency. During $\omega(t_3-t_1)$ the inverter input voltage is equal to $-V_{C5}+V_{CB}$ so that for this internal the variation of the inverter input voltage resembles that of $-V_{C5}$. During each normal mode, the inverter input voltage is essentially the same as one of the motor line-to-line voltages. The dc link current has a constant value for the whole period so that the motor average input power can be calculated by multiplying this current by the average value of the inverter input voltage, V_I.

5.4 VARIATIONS OF VARIABLES IN CASE (a)

The variations of different variables of an ASCI-induction motor drive as functions of operating conditions are presented and discussed in this section. Flowchart 3.2 obtained in section (6.2.2.1) is employed for calculating the magnitudes of variables. The results of these computations are then used for plotting a set of graphs, figures 5.7-5.24. Each graph shows the variations of the corresponding variable at different constant per unit output torques when the frequency is varied from 5 to 125 Hz. The variations of currents and voltages are in per unit. The per unit quantities are given in Appendix A-1. The magnitude of the fundamental harmonic of the motor terminal voltage is determined by the control strategy and is shown in figure 5.7. Based on the applied voltage according to figure 5.7, the maximum available output torque can be calculated for each operating frequency, figure 5.8. Note that no restriction is assumed for the current source supply feeding the inverter with respect to the

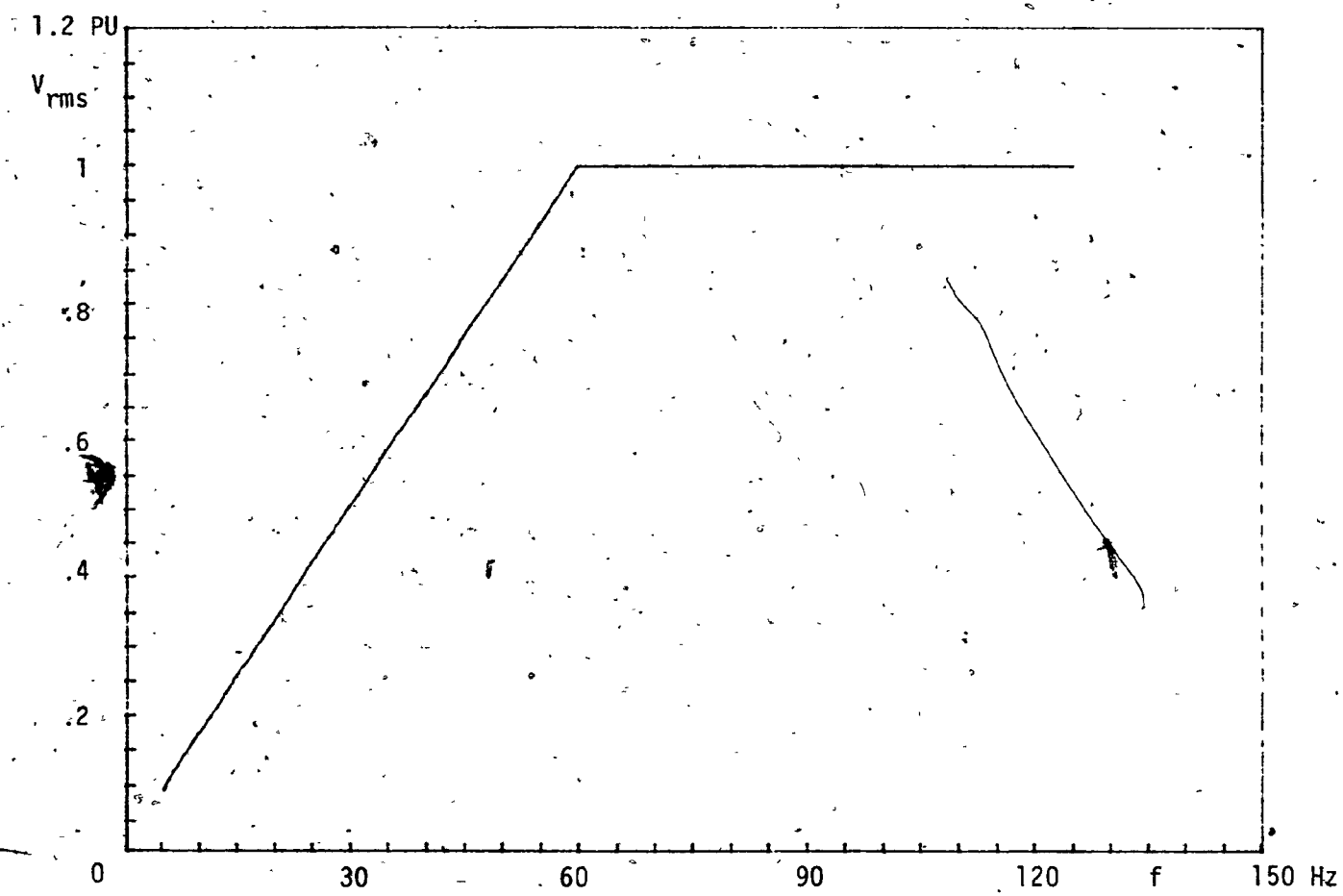

FIG. 5.7 The motor fundamental harmonic of phase voltage in which $V_{rms}=(4.47676+7.592f)/\sqrt{3}$ V for $f < 60$ Hz and $V_{rms} = 460/\sqrt{3}$ V for $f \geq 60$ Hz. This control strategy is applicable to all cases.

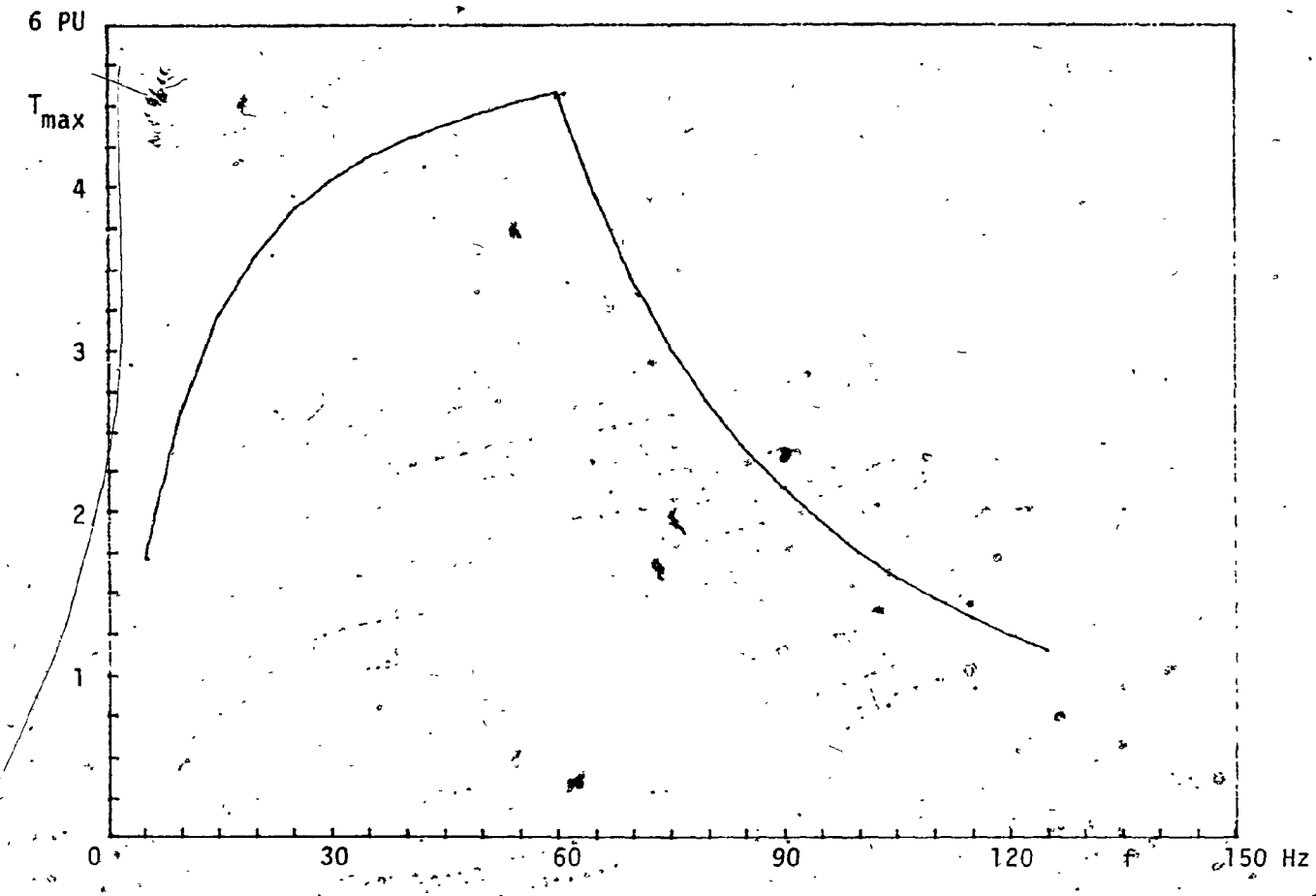

FIG. 5.8 Pull-over torques for the induction motor with the specifications as given in Appendix A-1. The motor terminal voltage changes according to Figure 5.7.

dc link current. The operation of the system is only limited by three constraints imposed by the inverter operation and one imposed by the induction motor operation. The limiting factors from the inverter side are the values of the commutation and transfer angles and the voltages across the series diodes. In other words, the transfer and commutation angles should not exceed $\pi/3$ and $2\pi/3$ rad, respectively, and no diodes should become transiently forward biased. The limiting factor from the motor side is the fact that the motor cannot remain stable beyond its pull-over torque of each frequency. In the following figures, the maximum allowable output torque is 95% of the pull-over torque at each frequency, so that for 1.5 per unit torque the maximum frequency is 115 Hz, and for 2.0 per unit torque, frequencies are changed from 10 to 95 Hz. Besides, all the figures showing the variations of variables are plotted for a no-overlap operation.

1. Fundamental slip, S_1, versus frequency, f, Figure 5.9:

This figure shows the variations of the fundamental slip as a function of the stator frequency for T=0.-2.PU torques. These slips are calculated iteratively for each specific torque. Note that with constant V/Hz and constant voltage control, the minimum slip occurs at the base frequency (60 Hz) for each constant output torque. At low frequencies, due to the decreased voltages (fig. 5.7), high values of slips are required in order to produce the same magnitude of output torques.

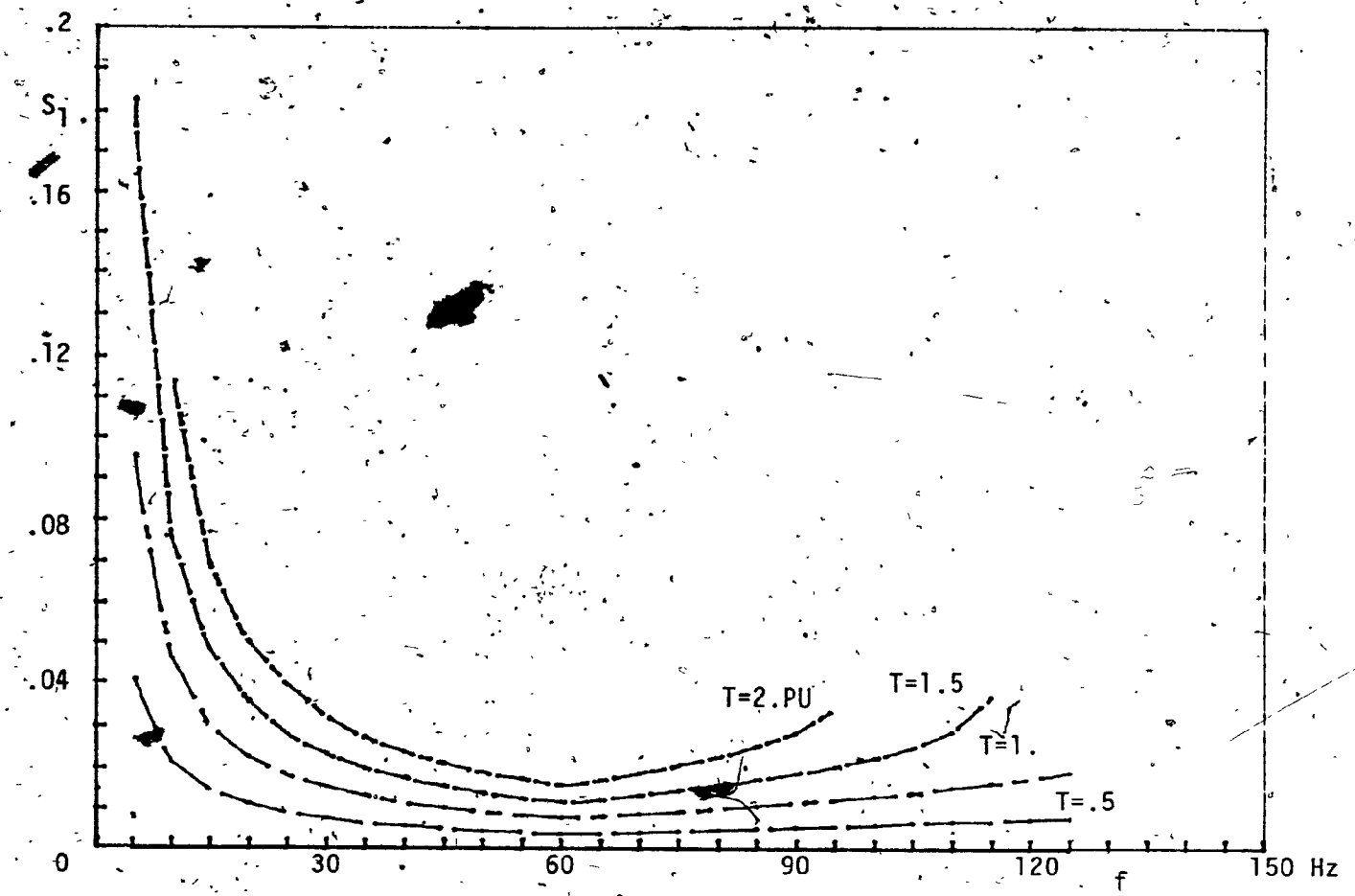

FIG: 5.9 Variations of the motor fundamental slip with terminal voltages as given in Figure 5.7. Note that, for each constant torque, the least slip occurs at 60 Hz.

2. Motor CEMF, E_1 ; versus frequency, f , Figure 5.10:

This figure shows the per phase peak value of the CEMF, E_1 , versus f for different torques. It is evident from this figure that the operation of an induction motor with constant V/Hz is almost the same as the operation with a constant air-gap flux. It is then reasonable to use the same value of the magentizing inductance, as that of the rated operating point, for all frequencies below 60 Hz. For frequencies above 60 Hz, the magnetizing inductance recovers gradually from saturation and a weakening air-gap flux happens. The value of the magnetizing inductance, however, differs from the rated one. As mentioned earlier, by using iterations the correct values of L_m can be obtained for frequencies above 60 Hz by employing figure A-1.1 in Appendix A-1. For the reason declared in section (5.1), this procedure is not followed in this section and the rated L_m is used for all operating points.

3. dc link current, I_d , versus frequency, f , Figure 5.11:

The dc link current is calculated by knowning the peak value of the fundamental component of the motor line current, I_1 , and by using (2.5.3). Figure 5.11 exhibits the variations of I_d in per unit which are essentially the same as I_1 variations, but with a factor of $\frac{\Pi}{2\sqrt{3}}$. From figure 5.11, it is clear that I_d remains almost constant for each constant torque up to 60 Hz. For frequencies above 60 Hz, I_d does not follow a specific pattern so

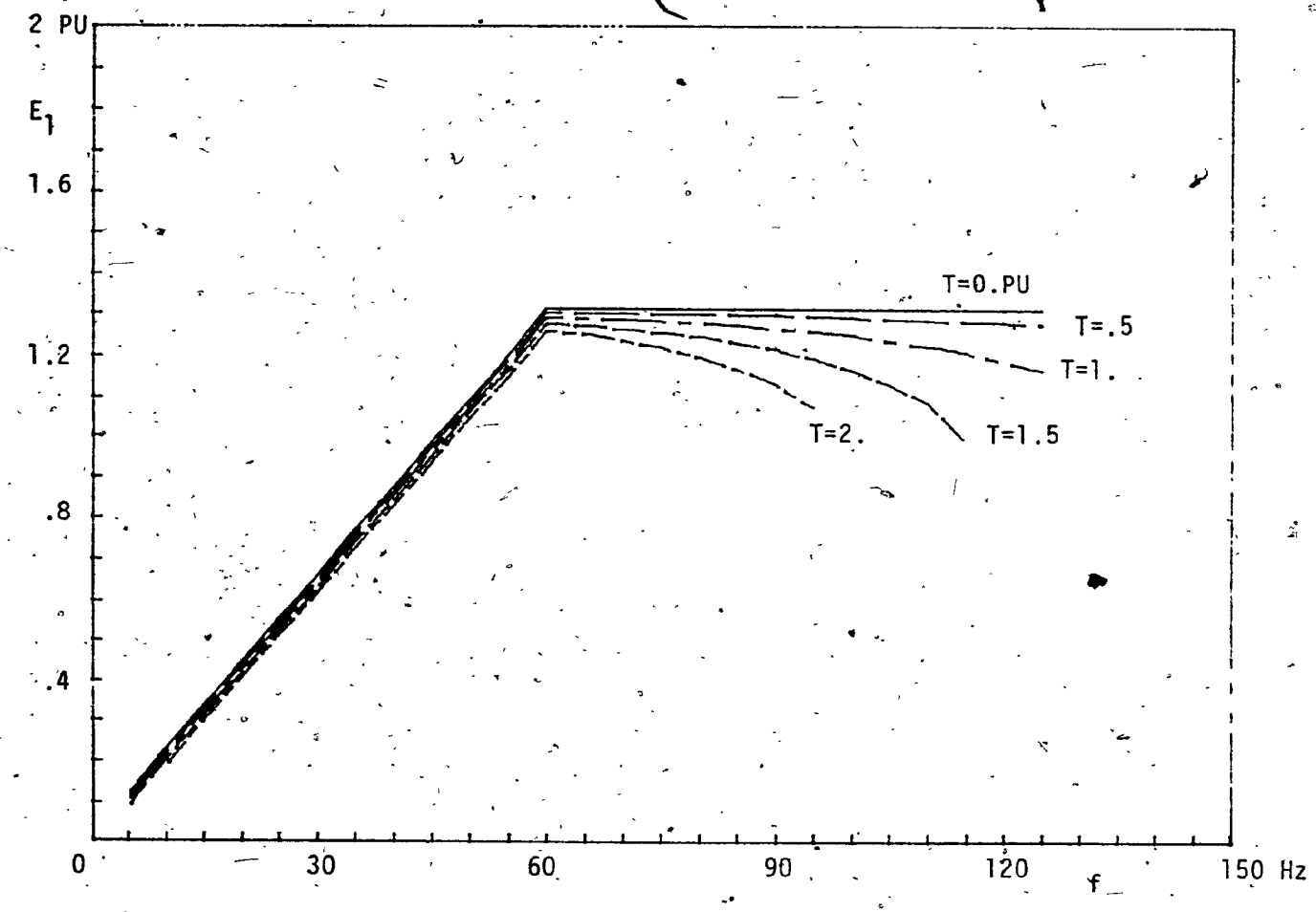

FIG. 5.10 The motor per phase peak value of the fundamental harmonic of CEMF with terminal voltages as given in Figure 5.7. Note the almost constant air-gap flux motor operation at frequencies less than 60 Hz.

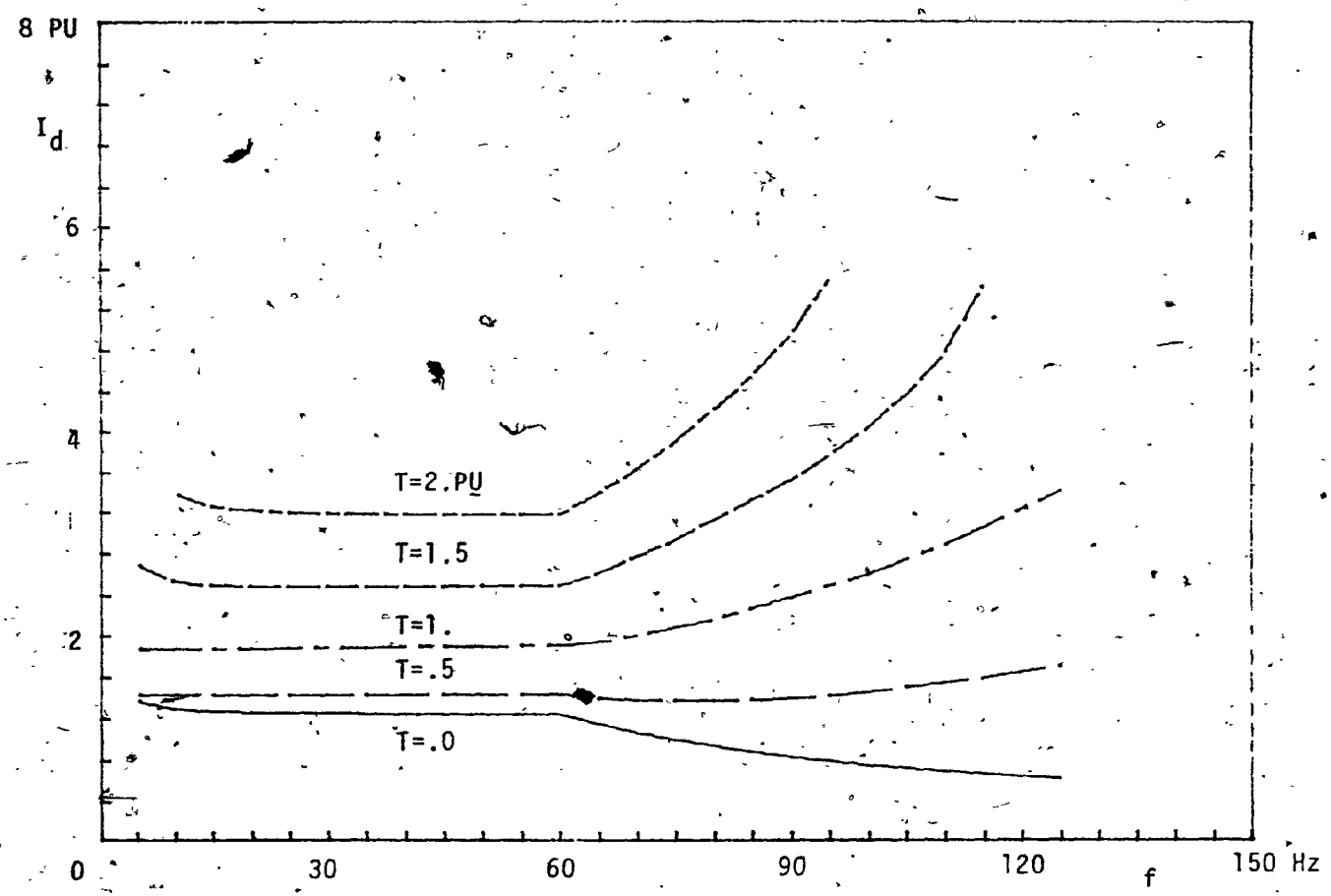

FIG. 5.11 The dc link current variations for different operating conditions. The motor fundamental harmonic of current varies in the same way. Note the constant currents at frequencies less than 60 Hz.

that for T=0 and .5 PU torques, I_d decreases with increasing the frequency, while for T=1 PU and above, I_d tends to increase almost rapidly.

4. Charging time, t_{ch}, and angle, α_{ch}, versus frequency, f, Figures 5.12-13:

These figures show the variations of the charging time and angle versus frequency for constant torques. From these figures, it is seen that the charging time and angle obtain their highest values at no-load conditions and with maximum frequency as predicted in section (3.6.1). For the charging time, figure 5.12 presents a linear increase in this variable, with frequencies up to 60 Hz at each constant torque. For frequencies above 60 Hz and under loaded conditions, a decrease in the charging time is noticed when the frequency goes up.

5. Transfer time, t_{tr}, and angle, α_{tr}, versus frequency, f, Figures 5.14-15:

The first figure presents the transfer time as a function of frequency. From this figure, it is easily concluded that the transfer time is almost the same for all operating points. This conclusion was also obtained previously in section (3.6) and given by (3.6.1.12). Figure 5.15 displays the transfer angle versus frequency. This angle is linearly dependent on the frequency so that its maximum value, for

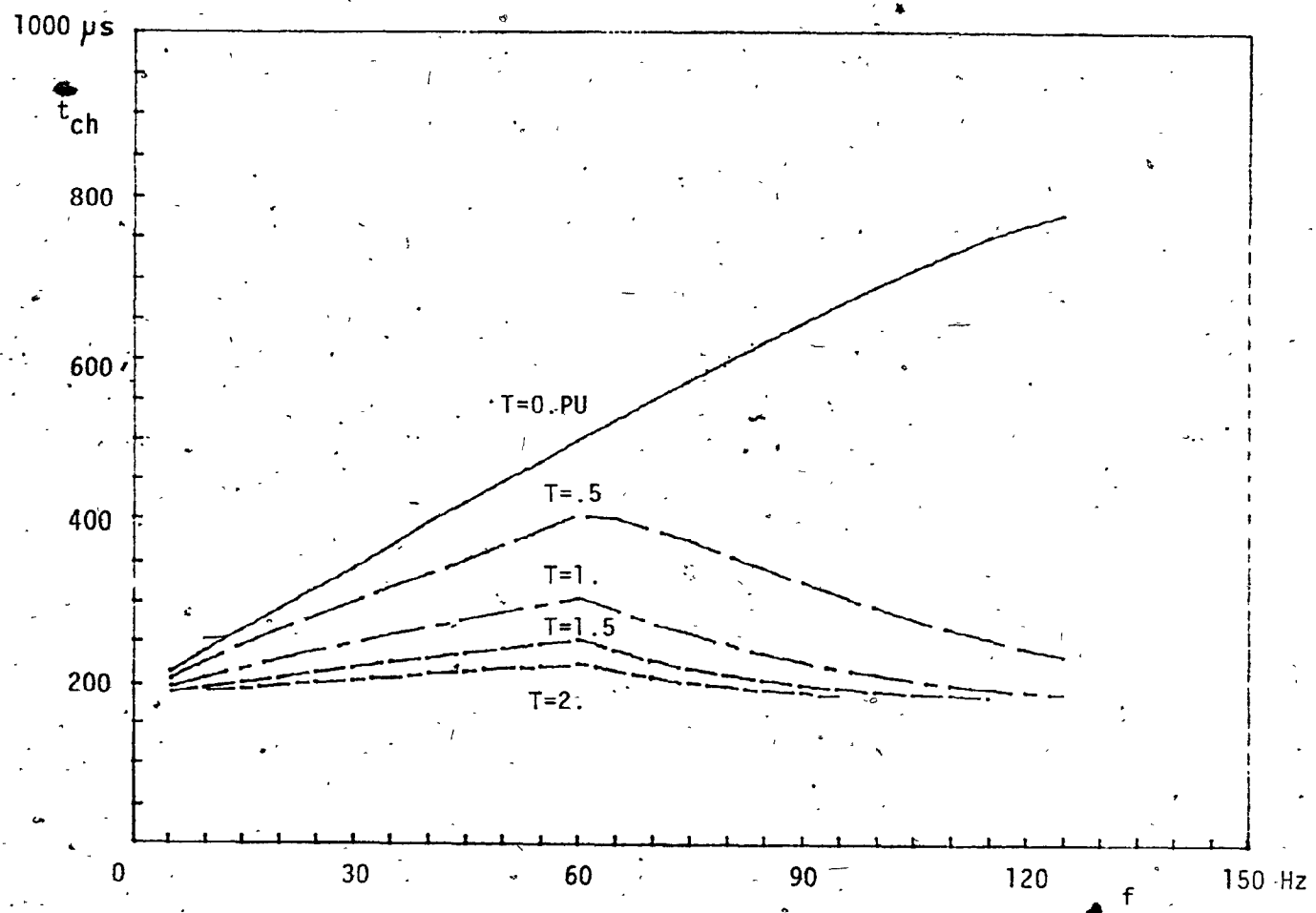

FIG. 5.12 The charging time variations. Note that the maximum value of this variable occurs at no-load conditions while the frequency is maximum.

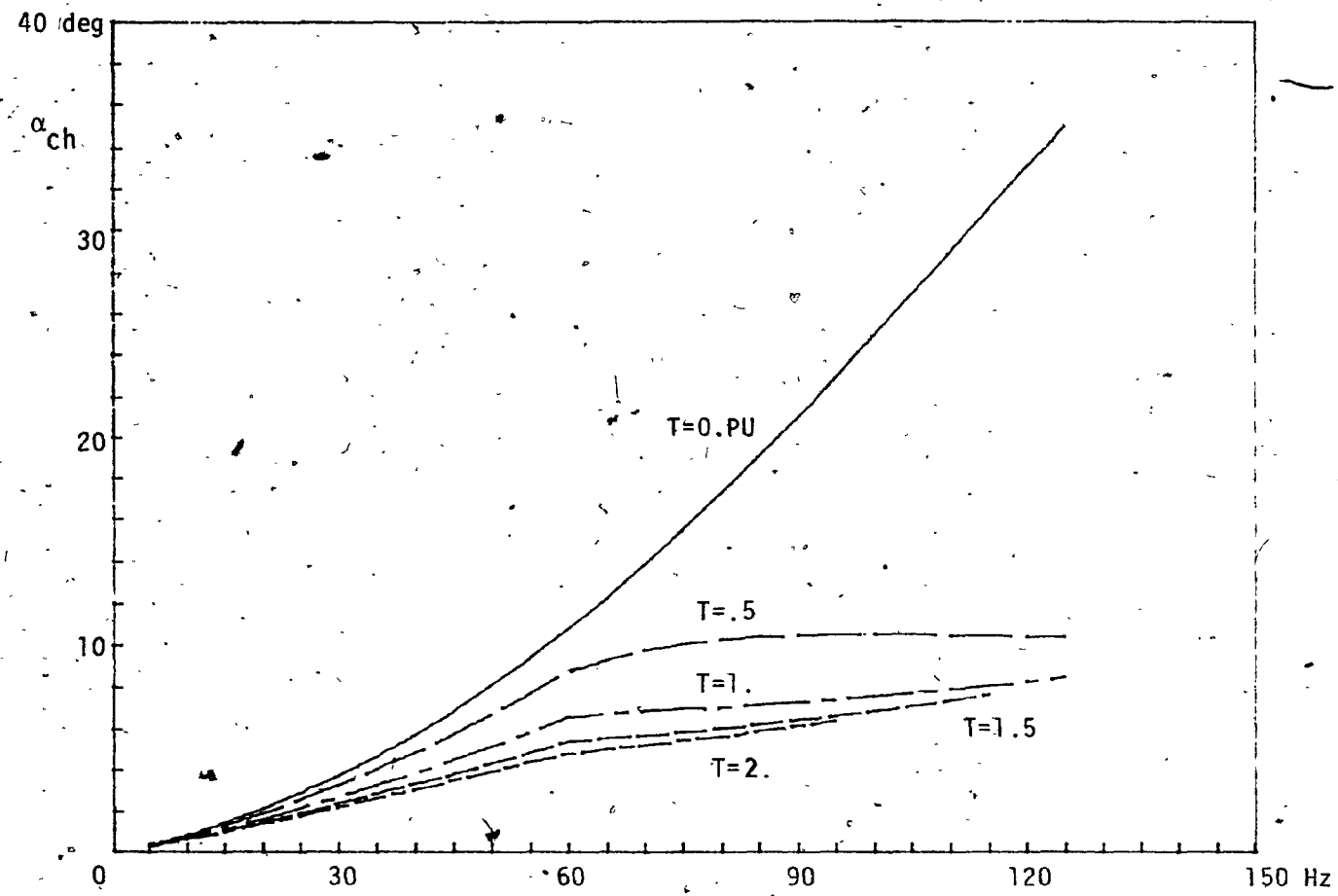

FIG. 5.13 The charging angle variations. Note the no-load, maximum frequency value of this variable.

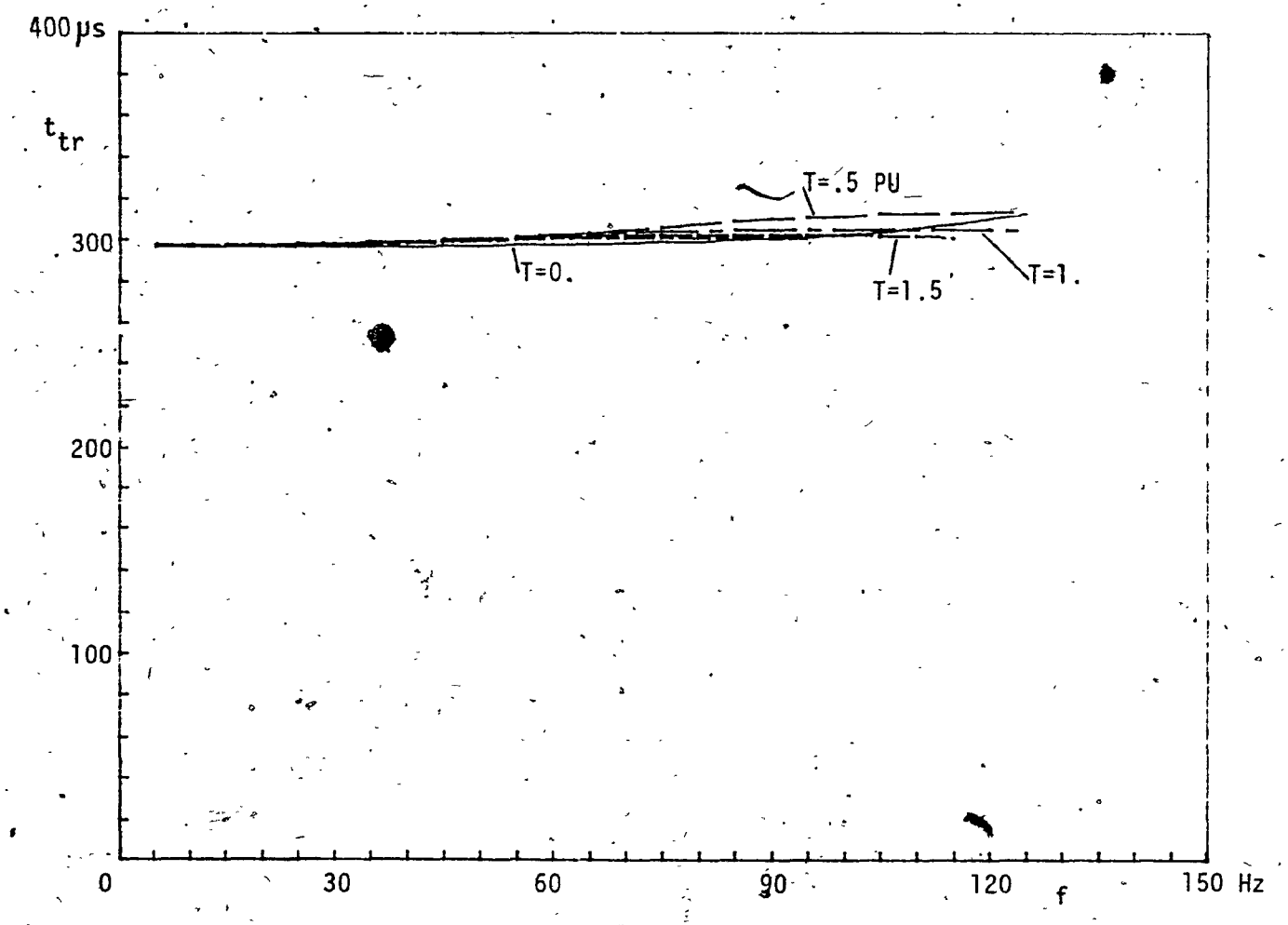

FIG. 5.14 The transfer time variations. Note the almost constant value of this variable at all operating conditions.

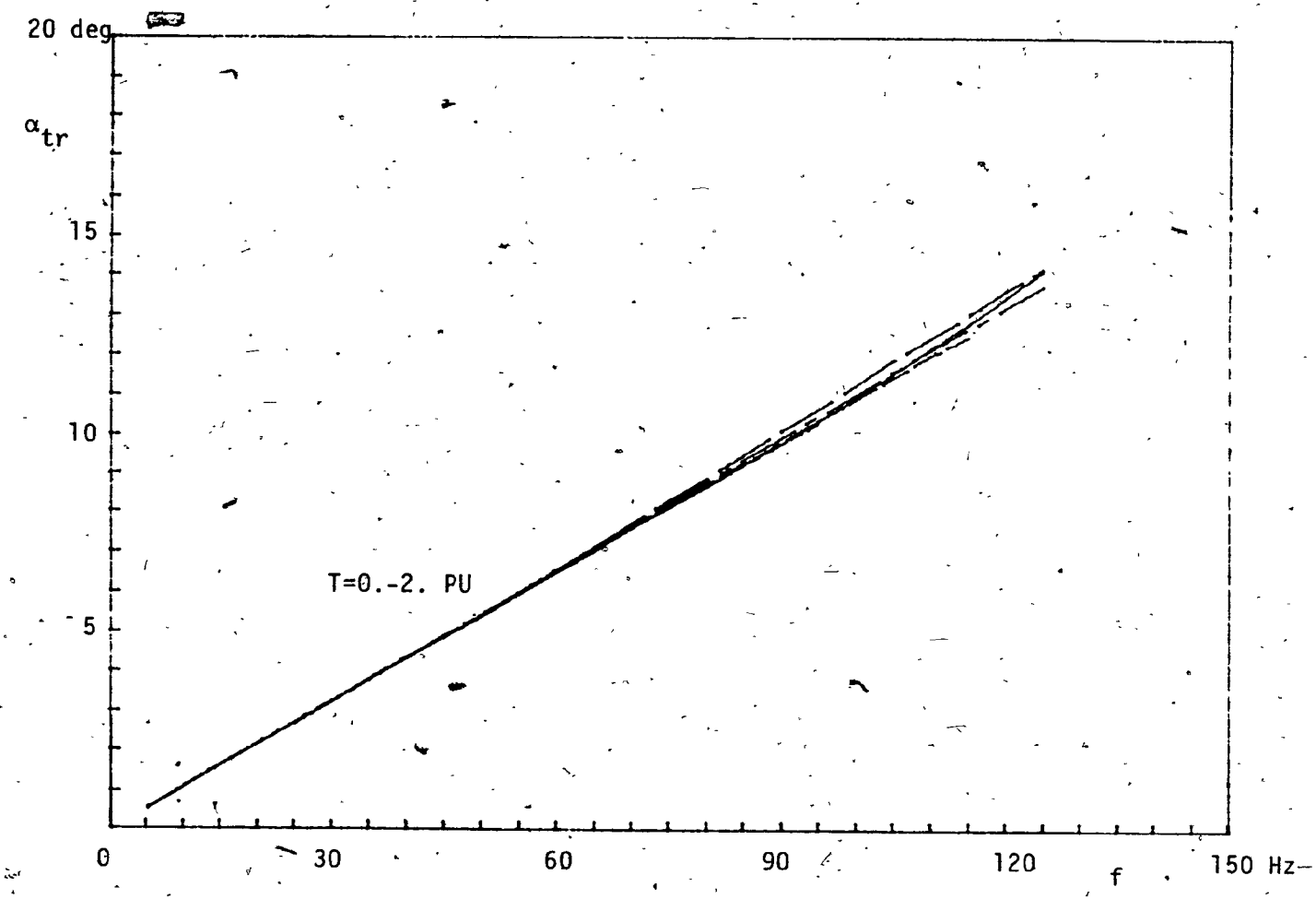

FIG. 5.15 The transfer angle variations. Note the linear change in this variable with the frequency.

all the output torques, occurs at maximum frequency.

6. Commutation time, t_{co}, and angle, α_{co}, versus frequency, f, Figures 5.16-17:

The first figure gives the variation of the commutation time versus frequency. Due to the constant values of the transfer time, figure 5.14, the commutation time changes in the same way as the charging time does in figure 5.12. Figure 5.17 shows the corresponding angles at different frequencies. This figure reveals that the commutation angle attains its maximum value at T=0 PU and with the maximum frequency, so that the operation of the system in case (b) and case (c) occurs basically at no-load conditions when the stator frequency is quite high.

7. Maximum commutating capacitor voltage, V_o, versus frequency, f:

Figure 5.18 yields the variations of the maximum capacitor voltage, V_o, as a function of f for different torques. It is noticed that there is a linear increase in V_o versus f for different torques up to the base frequency. For T=0 and .5 PU torques when the frequency goes above 60 Hz, there appears a decrease in V_o while for T=1.-2 PU there is a rapid increase in V_o with frequency. Comparing this figure with figure 5.11, a close similarity is found between the variations of I_d and V_o. Figure 5.18 suggests that the maximum capacitor voltage, V_o, and, as a result, the voltage ratings of all the components, should be

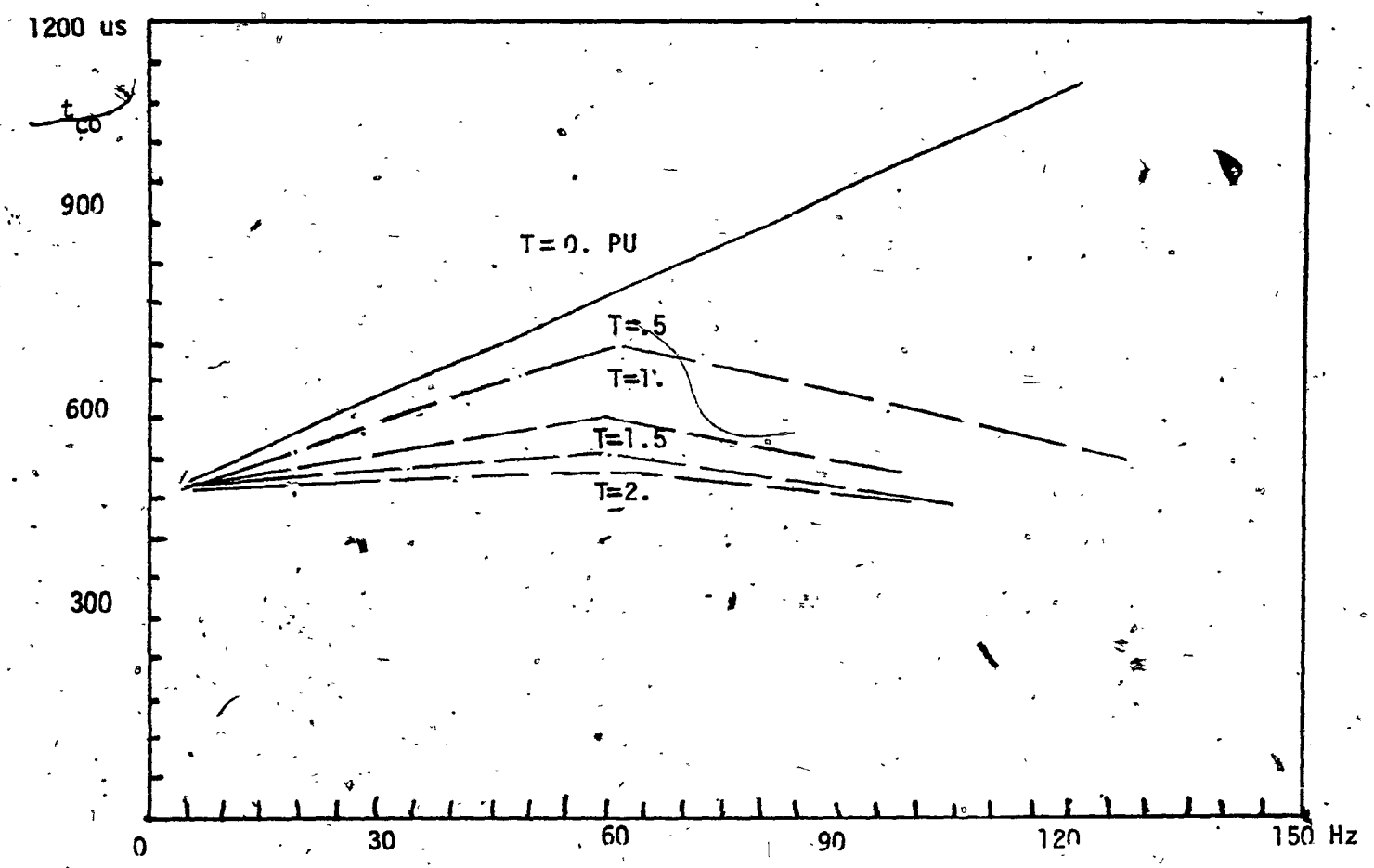

FIG. 5.16 The commutation time variations. Note the no-load, maximum frequency value of this variable.

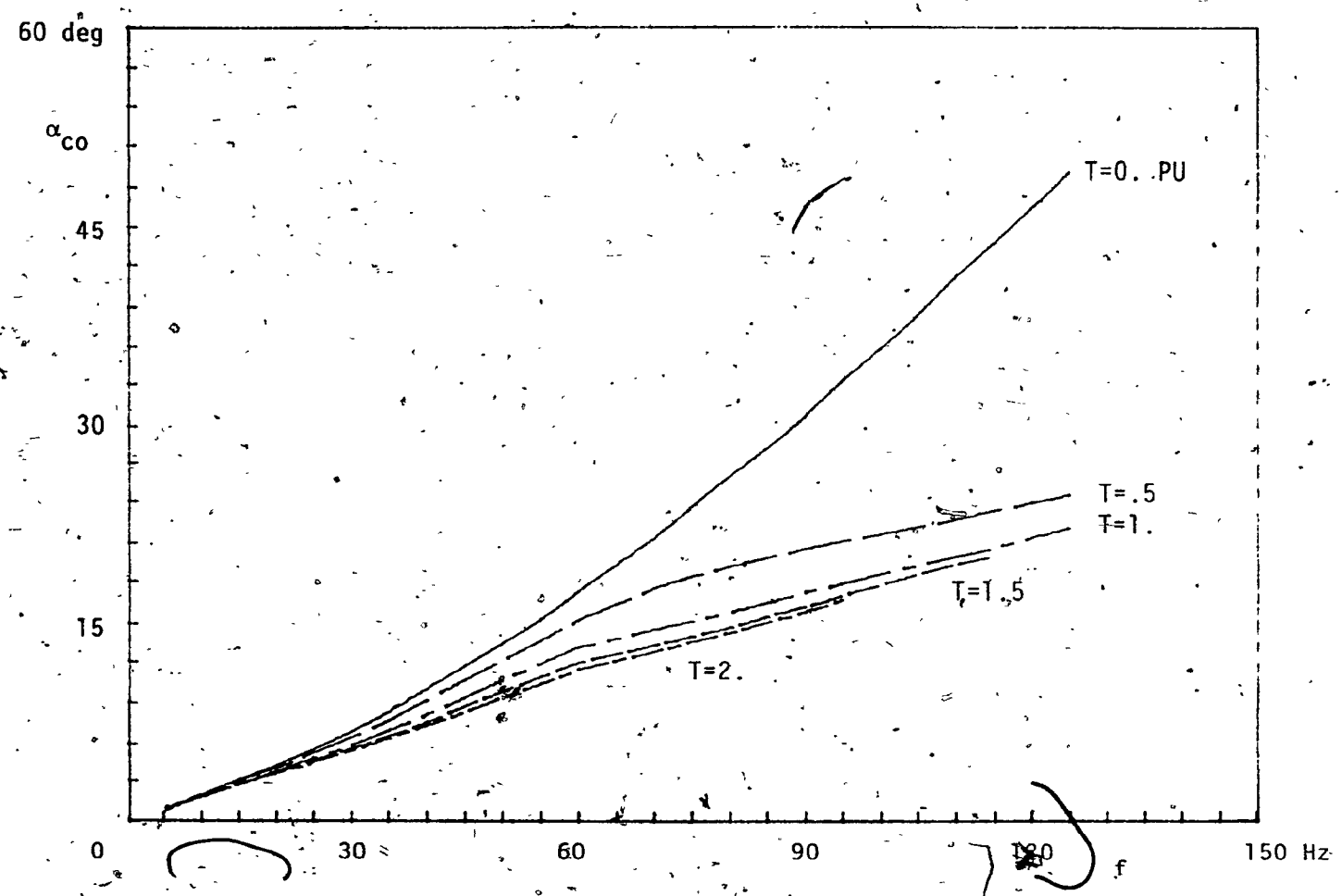

FIG. 5.17 The commutation angle variations. By increasing the frequency the system enters into case (b) operation where $\alpha_{co} > 60°$.

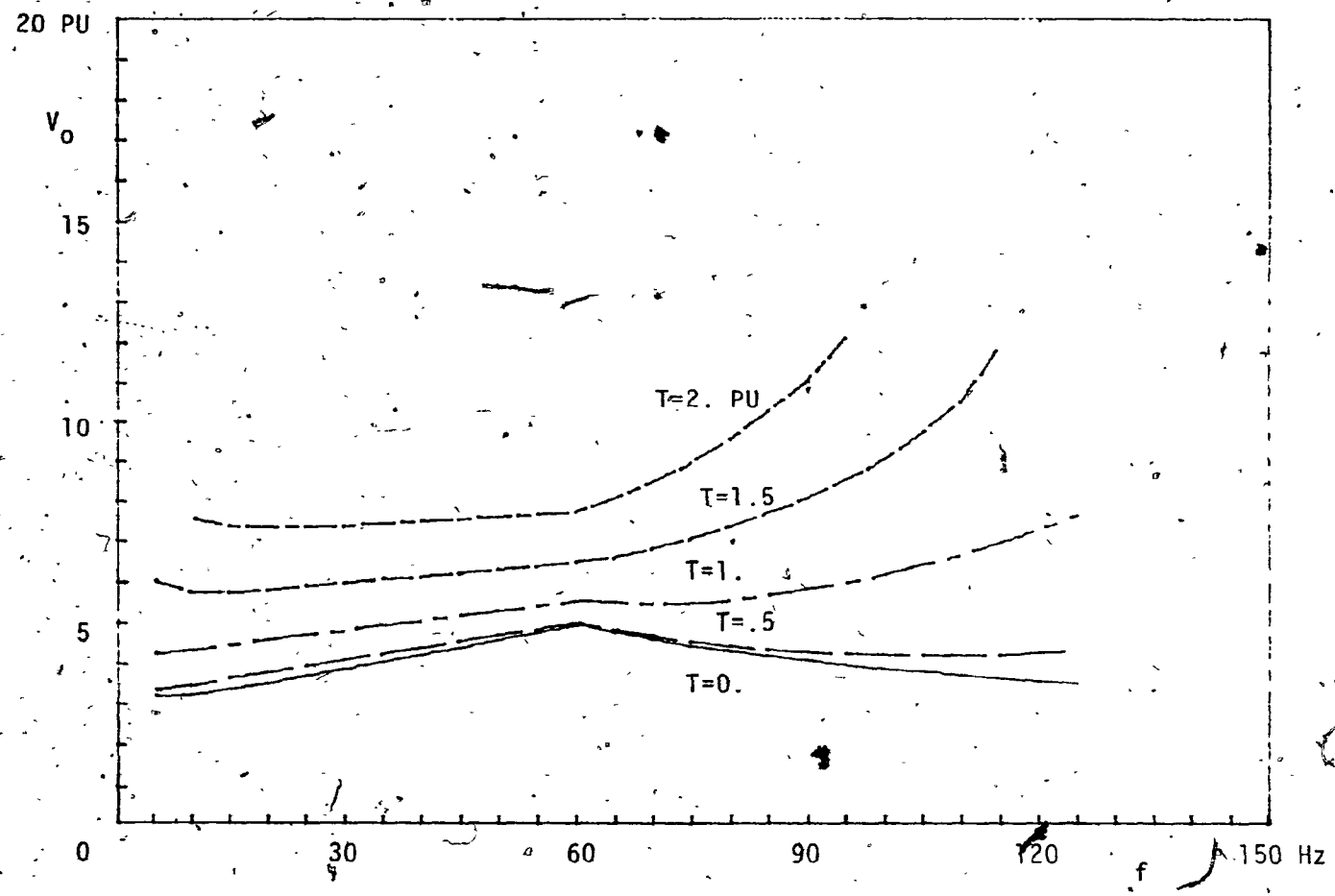

FIG. 5.18 The maximum capacitor voltage variations. Note the maximum load system operation at the maximum frequency.

determined at the highest torque and with the highest frequency under which the system is allowed to operate.

8. Average inverter input voltage, V_I , versus frequency, f :

For T=0 PU , figure 5.19 shows small values of V_I due to the small power absorbed by the motor only to compensate its losses. For T=.5 PU and higher torques a rapid linear increase in V_I is noticed up to 60 Hz. To explain this, it is known that for each constant torque, the motor input power is proportional to the stator frequency ($P = T_{em}\omega$) where T_{em} is the electromagnetic torque. Due to an almost constant dc link current for f = 5-60 Hz at each constant torque (fig. 5.11) and since $P = V_I I_d$, the result is that V_I is a linear function of f for each torque up to 60 Hz. For frequencies above 60 Hz where T≠0 , a limit is noticed for V_I at each constant torque. This limit is the same for all output torques and shows the maximum average voltage which might appear at the inverter input terminals.

9. Commutating capacitor rms current, I_{CRMS} , versus frequency, f , Figure 5.20:

The waveforms of capacitor C_1 current was shown in figure 5.3. From this figure, the rms current of each commutating capacitor results

$$I_{CRMS} = [\frac{1}{T}\int_0^T i_{C1}^2(t)dt]^{\frac{1}{2}}$$

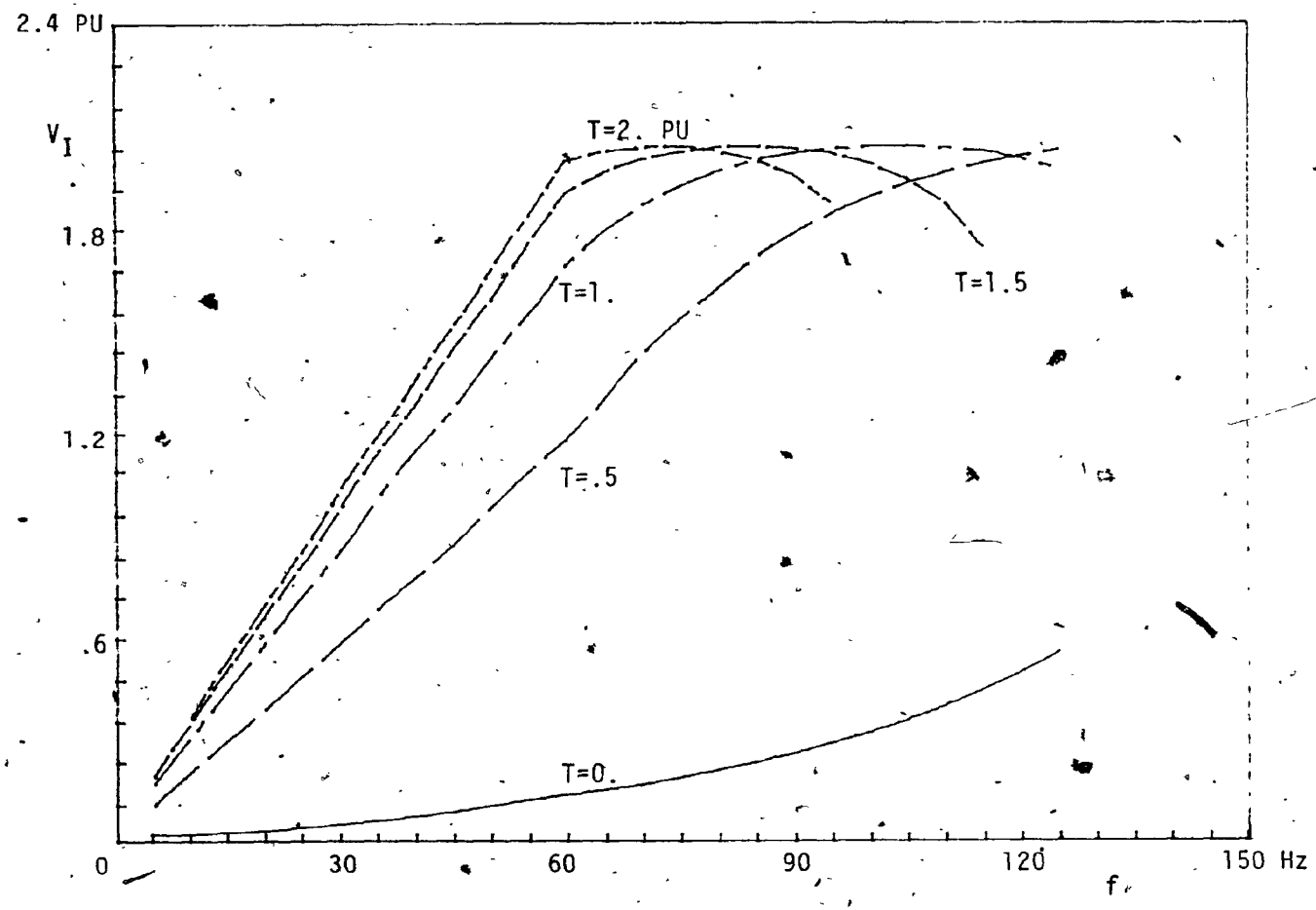

FIG. 5.19 The inverter input average voltage. Note the limit value of this variable for the loaded conditions.

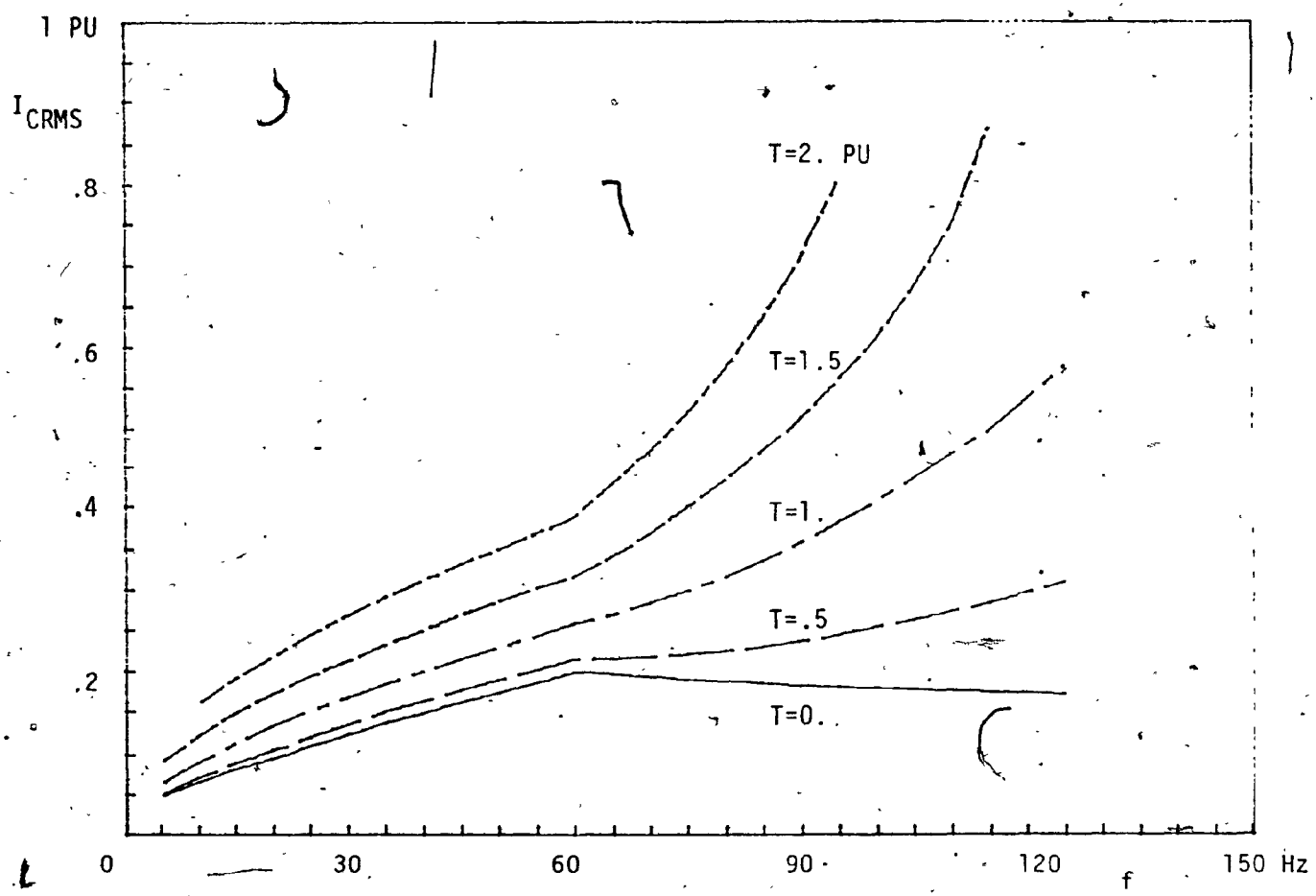

FIG. 5.20 The commutating capacitor rms current variations. The commutating capacitor should be rated for the maximum load at the maximum operating frequency.

$$I_{CRMS} = \{\frac{1}{T}[2\int_0^{t_{ch}}(-\frac{I_d}{3})^2 dt + 2\int_0^{t'_1}(-\frac{i_C(t')}{3})^2 dt'$$

$$+ \int_0^{t_{ch}}(\frac{2I_d}{3})^2 dt + \int_0^{t'_1}(\frac{2i_C(t')}{3})^2 dt']\}^{\frac{1}{2}}$$

$$= [\frac{2}{3} f(I_d^2 t_{ch} + \int_0^{t'_1} i_C^2(t')\,dt')]^{\frac{1}{2}} \qquad (5.4.1)$$

where $i_C(t')$ was given by (3.4.32) and the integral term is computed numerically.

Figure 5.20 shows the results obtained by using (5.4.1). Again, an almost linear increase in this quantity is observed for frequencies up to 60 Hz. For frequencies higher than 60 Hz, there is no definite pattern for variations of I_{CRMS} which can be applied to all constant torques. Like the commutating capacitor voltage rating, the rms current rating of the capacitor should be determined by the value of this current at maximum output torque and maximum input frequency.

10. Thyristor available turn-off time, t_q, versus frequency, f, Figure 5.21:

The available turn-off time for thyristors was shown in figure 5.4. This interval can be easily calculated from figure 5.4 where after firing T_3 at ωt_7 the capacitor C_1 is charged linearly with an initial voltage of $+V_o$. Since the negative voltage of

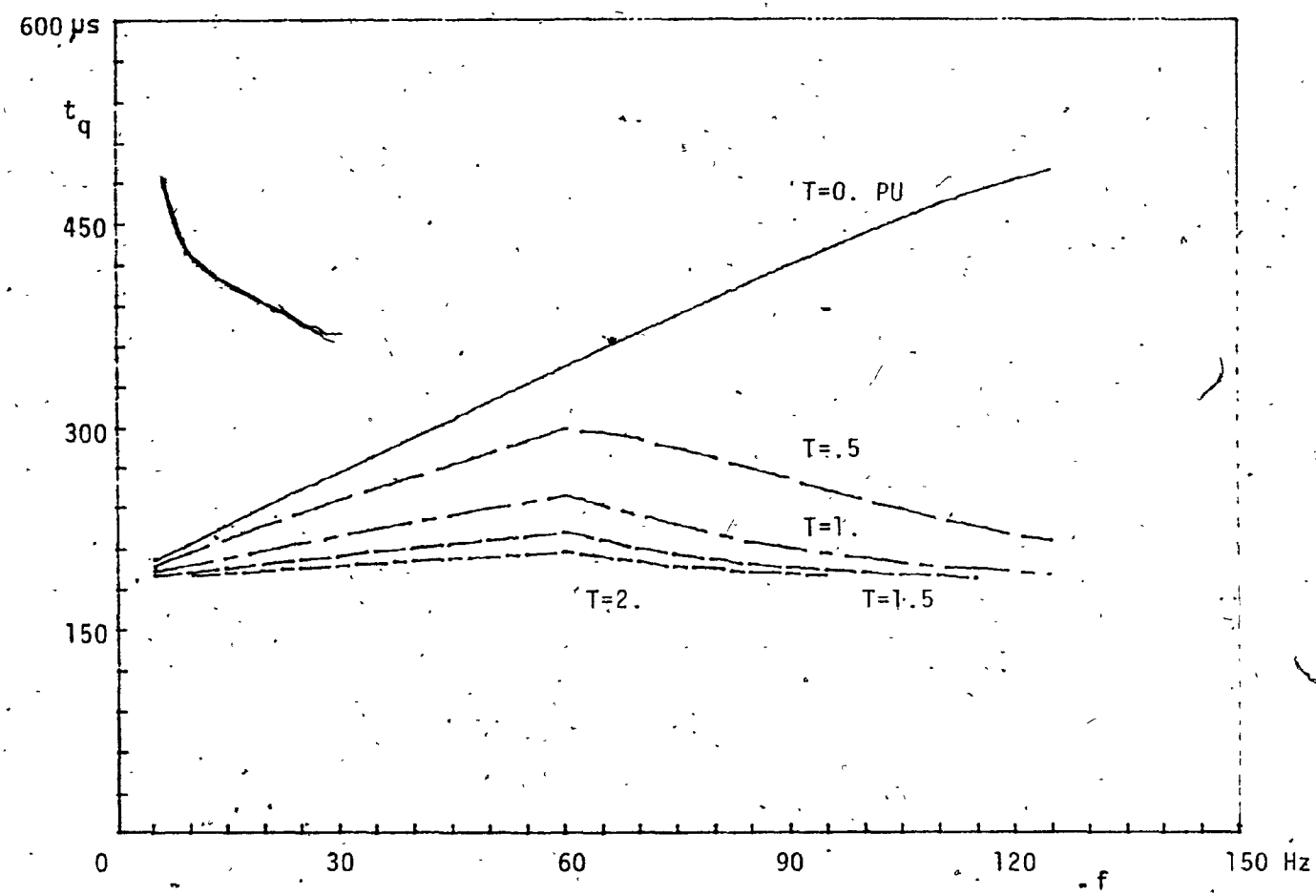

FIG. 5.21 The available thyristor turn-off time. The least value of this variable occurs at maximum load and frequency.

C_1 is applied across T_1, this thyristor becomes forward biased when v_{C1} starts gaining a negative voltage across its terminals. Then T_1 should have been turned-off by the time v_{C1} becomes zero. The available turn-off time for each thyristor can be calculated by:

$$t_q = 1.5 \frac{V_o}{I_d} 10^6 \quad \mu s \qquad (5.4.2)$$

Figure 5.21 shows the variations of t_q obtained from (5.4.2). It is noticed that again, the maximum load at maximum frequency is the worst case where t_q has the least value. In practical applications, the least available turn-off time is usually much longer than the turn-off time of inverter type thyristors. It is then possible to use the common types of thyristors in the ASCI applications.

11. Efficiency, η, versus frequency, f, Figure 5.22:

For an exact calculation of the system efficiency, the thyristor and diode losses should also be considered. However, figure 5.22 does not include these losses and is simply obtained by dividing the motor output power by the inverter input power, $V_I I_d$. It is seen that for $f = 25 - 125$ Hz the efficiency is almost constant for all operating points. The lowest efficiency occurs at maximum load and minimum frequency so that the ASCI operation is not recommended in this region.

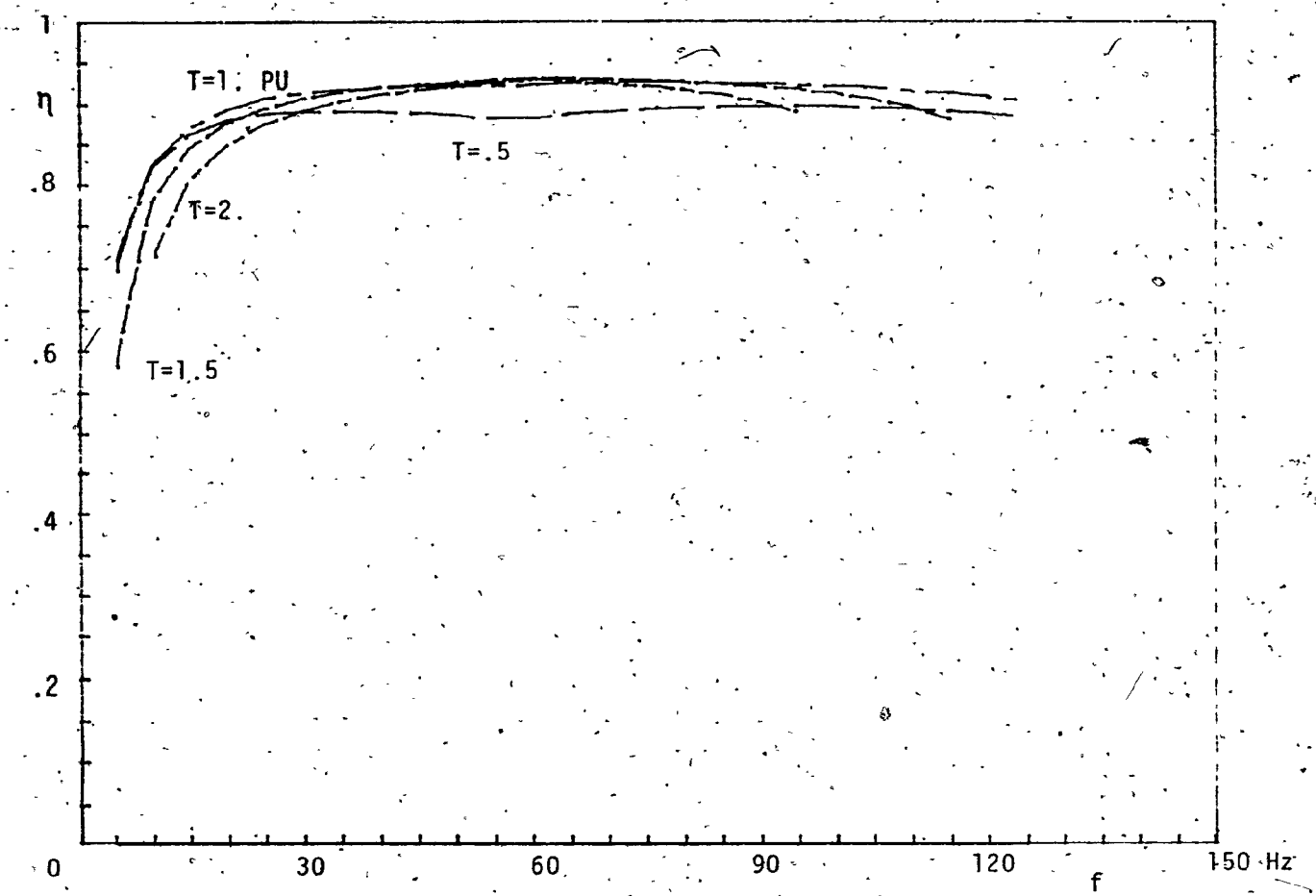

FIG. 5.22 The system efficiency variations without considering the diode and thyristor losses.

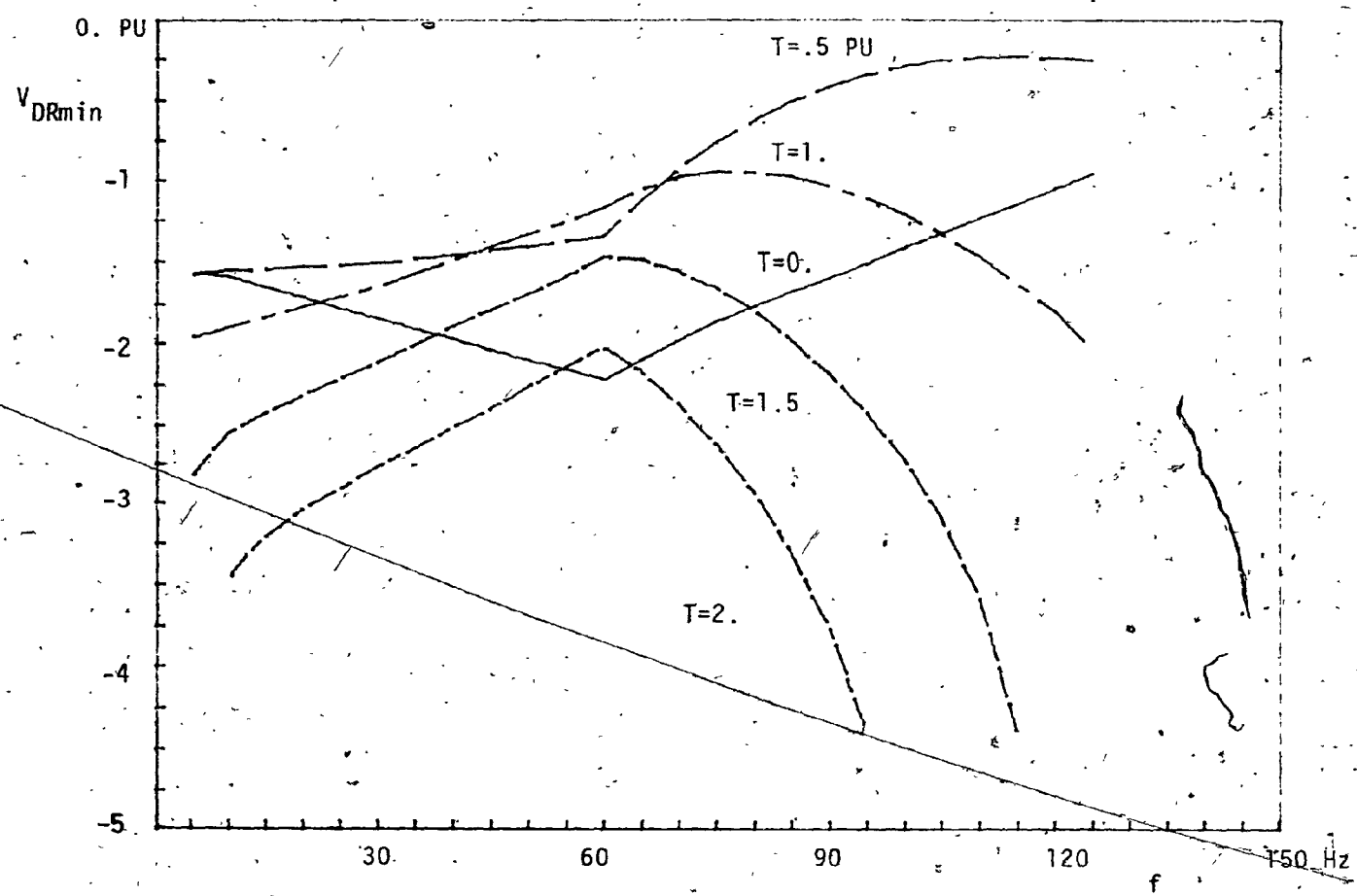

FIG. 5.23 The diode minimum reverse voltage variations. At a torque between T=0. and .5 Pu the diodes become transiently forward biased.

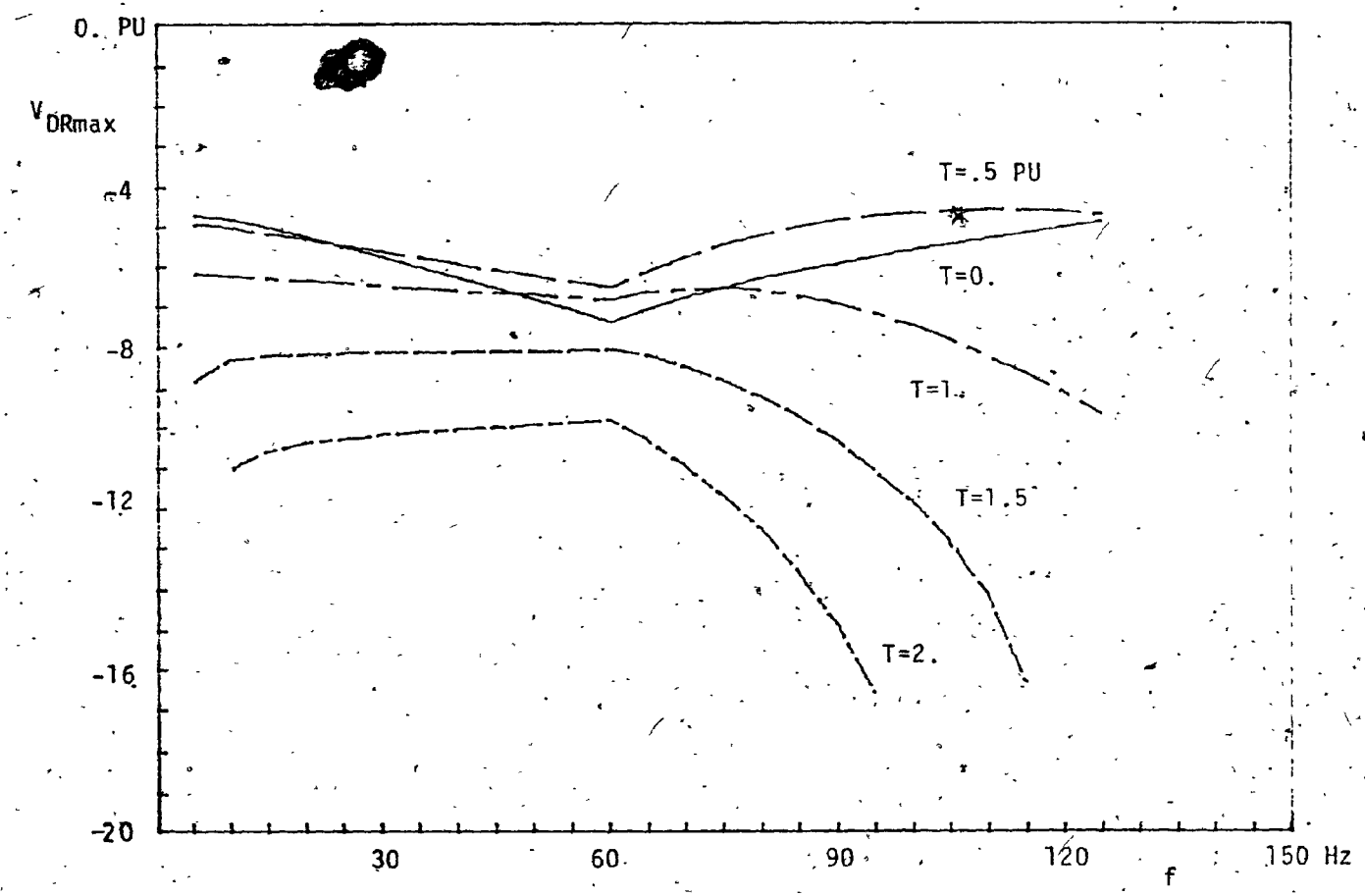

FIG. 5.24 The diode maximum reverse voltage. The diodes are usually rated at two times the maximum capacitor voltage.

12. Diode minimum and maximum reverse voltages, V_{DRmin}, V_{DRmax}, versus frequency, f, Figures 5.23 and 5.24:

Figure 5.23 shows the diode minimum reverse voltage variations as defined in figure 5.5. It is seen that there is no definite pattern for the variations of this quantity. Through this figure, the constraint on the diodes can also be checked, section (3.3). It was found that for T=.2 PU and for frequencies above 120 Hz, a transient diode forward biasing occurs, which by increasing or decreasing the torque at the same frequency, the inverter recovers to the normal operation. Figure 5.24 resembles figure 5.23 to some extent, but it shows the diode maximum reverse voltage. It is noticed that for the same frequency the value of V_{DRmax} has its peak at the maximum output torque.

5.5 CONCLUSION

The results of the study done in chapters I-IV were presented in this chapter by generating two sets of graphs. The first set showed the voltage and current waveforms at the different points of the system, under one specific operating condition, for which the experimental results were already obtained. The second set displayed the variations of the different system variables under constant torque-variable frequency operating points. In order to find a good correlation between the simulated and the experimental results, both the magnetizing and the leakage inductance saturations were considered in the first set of graphs. This was done by finding the actual values of these inductances

from their corresponding curves. For the second set of graphs, the constant V/Hz and constant voltage was chosen as the control strategy. This resulted in an almost constant flux operation below 60 Hz so that the same value of the magnetizing inductance was used for all operating points below 60 Hz. Besides, it was found that applying the rated value of the magnetizing inductance to all frequencies above the base frequency yields a good approximation for such frequencies. The saturation of the leakage inductances was neglected in the second set of graphs. An exact method was used in obtaining all the graphs while an appropriate value of the core-less resistance was examined for each operating frequency. Every graph was interpreted and discussed. It was concluded that the no-load and maximum load operations with the maximum stator frequency were two critical operating conditions which should be investigated thoroughly. Also, the possibility of transient forward biasing of the series diodes was pointed out and a way was shown to predict the limit frequency under this constraint.

CHAPTER VI

MATHEMATICAL MODELING OF THE SYSTEM WITH DC LINK CURRENT AND A CLAMPING CIRCUIT CASE (d)

6.1 INTRODUCTION

One of the salient characteristics of current source inverter supplied drives is the presence of voltage spikes in the motor input voltage, fig. 5.1. As already explained, these spikes are caused by the switching of the input current through the motor leakage inductances. The power content associated with the spikes is small since their width is narrow so that the motor operation is very little affected. However, voltage spikes appear across the inverter components requiring their higher ratings. In fact, the application of ASCI to motor drives became practical only after thyristors with sufficiently high blocking voltages became availabe. Even now, when high voltage thyristors are available, the trend is to suppress the voltage spikes for economical reasons. One of the possible circuits which limits the spikes is given in fig. 6.1. The circuit consists of a simple diode bridge (d_1 - d_6) connected to a string of zener diodes (D_z). The number of diodes in the string determines the clamping voltage to which the spikes are limited. By using this clamping circuit, one can either increase the motor rated voltage or decrease the voltage ratings of the inverter components. While there are several other circuits which can be applied to clamping of voltage spikes, the one given in figure 6.1 gives the most precise clamping voltage with the smallest power loss.

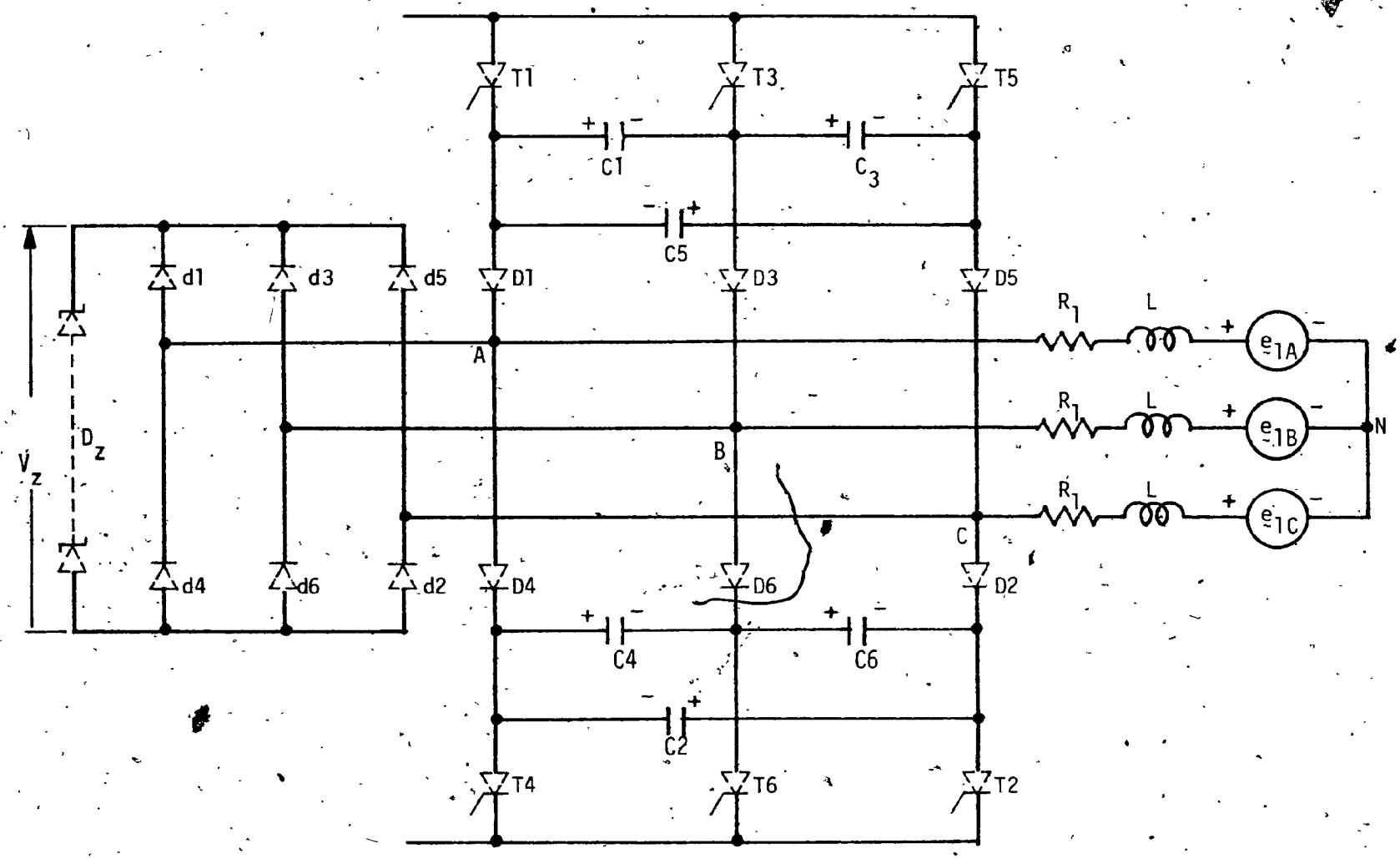

FIG. 6.1 ASCI with Zener Clamping Circuit

For the case when the peak value of the voltage spikes is smaller than the total breakdown voltage of the zener diodes, the system operates as described in the previous chapters. When the motor terminal voltage instantaneously exceeds this breakdown value, the zener diodes conduct in the reverse direction taking a part of the dc link current. In this way the energy due to the voltage spikes is transferred away from the main components and is dissipated in the zener diodes. The zener diode and the associated heat sink ratings are determined on the basis of the highest voltage spikes which would exist if the clamping circuit were not used.

In the following section we are going to derive the necessary equations which describe an ASCI with a zener diode clamping circuit. It will be shown that the maximum permitted output frequency may be different from the case without the clamping circuit and that its value, in addition to the other parameters, depends on the selected breakdown voltage of the clamping circuit.

The study is based on the same assumptions made in section (2.6) except the assumption 9. Instead, we assign the following two constraints for the breakdown voltage.

1) The zener diodes may conduct only during the transfer period, if the voltage across two of the motor phases exceeds the breakdown level.

2) During the period when the zener diodes are in the circuit, the other two motor line-to-line voltages do not reach the breakdown voltage.

The following modes are distinguished during case(d).

6.2 MODE 1 OR CHARGING MODE

As in mode 1 of case (a), we assume T_5, D_5, D_6 and T_6 to be conducting just before firing T_1. This mode is defined from $t=t_1$ to $t=t_2$. At $t=t_1$, the thyristor T_1 is triggered and the circuit of the system becomes as shown in fig. 6.2. The current paths are identical to those in fig. 3.7 and the equations derived in section (3.3) are all still valid. This mode ends at $t=t_2$, the time at which D_1 becomes forward biased. As before the duration of the charging mode is

$$t_{ch} = t_2 - t_1 \tag{3.3.18}$$

6.3 MODE 2 OR THE FIRST PART OF THE TRANSFER MODE

This mode lasts from $t=t_2$, the instant at which D_1 is forward biased to $t=t_{21}$, the time the zener diodes start to conduct. This mode is similar to mode 2 in case (a). Figure 6.3 which resembles fig. 3.8 describes this mode. Equations (3.4.1) to (3.4.12) and (3.4.15) to (3.4.32) obtained in section (3.4) are still applicable. This mode ends at $t=t_{21}$ when the clamping circuit starts conducting due to the voltage spike across the A and C motor terminals. The magnitude of the breakdown voltage is shown by V_z. Later on, it will be noticed that this voltage is also equal to the maximum voltage across the commutating capacitors, V_0. The duration of this mode is

$$t_1' = t_{21} - t_2 \tag{6.3.1}$$

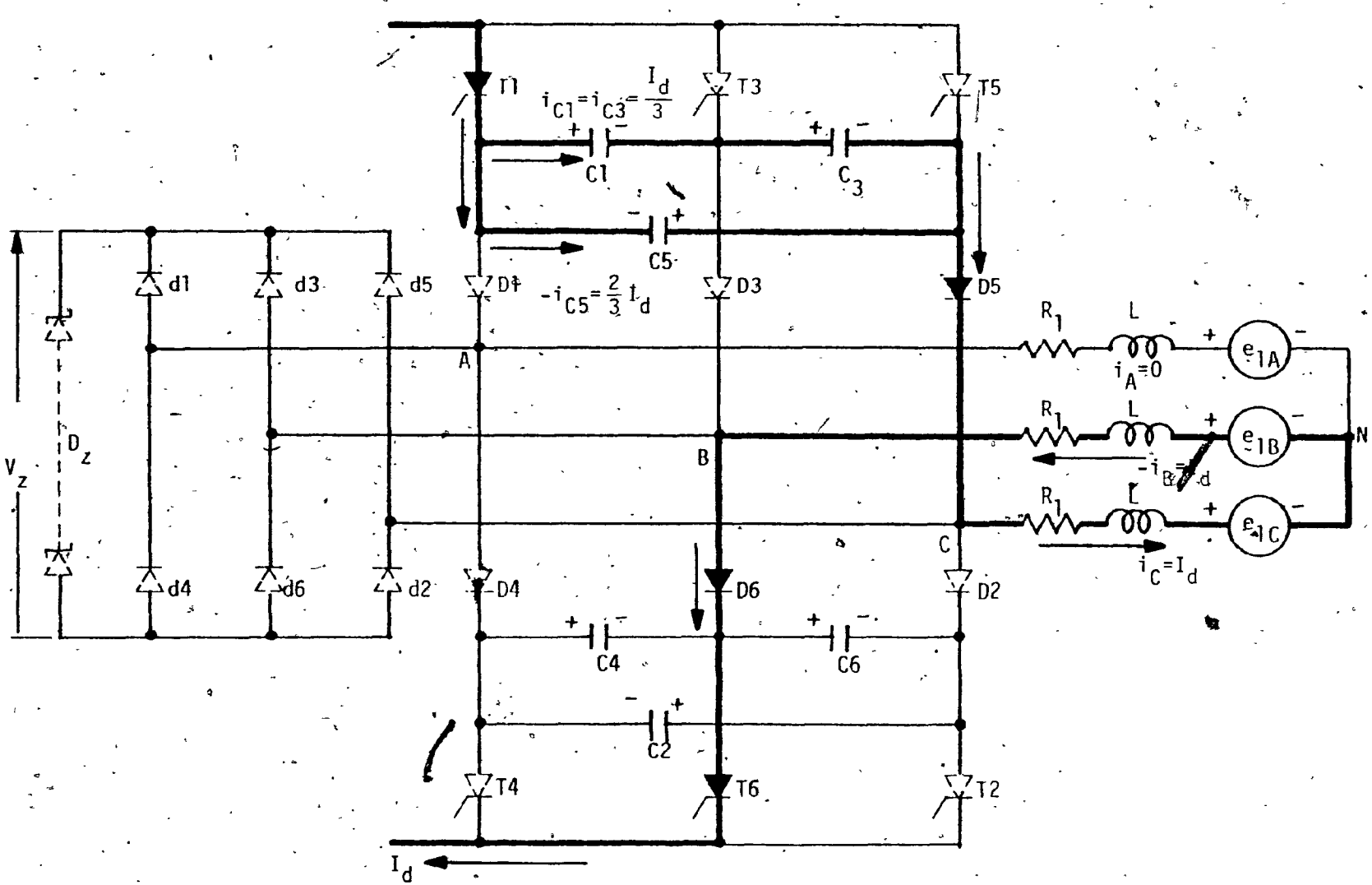

FIG. 6.2 ASCI-induction motor operation in mode 1 of case (d). Firing T_1 at $t=t_1$ starts a charging mode in the upper group. This mode ends at $t=t_2$ when D_1 commences to conduct.

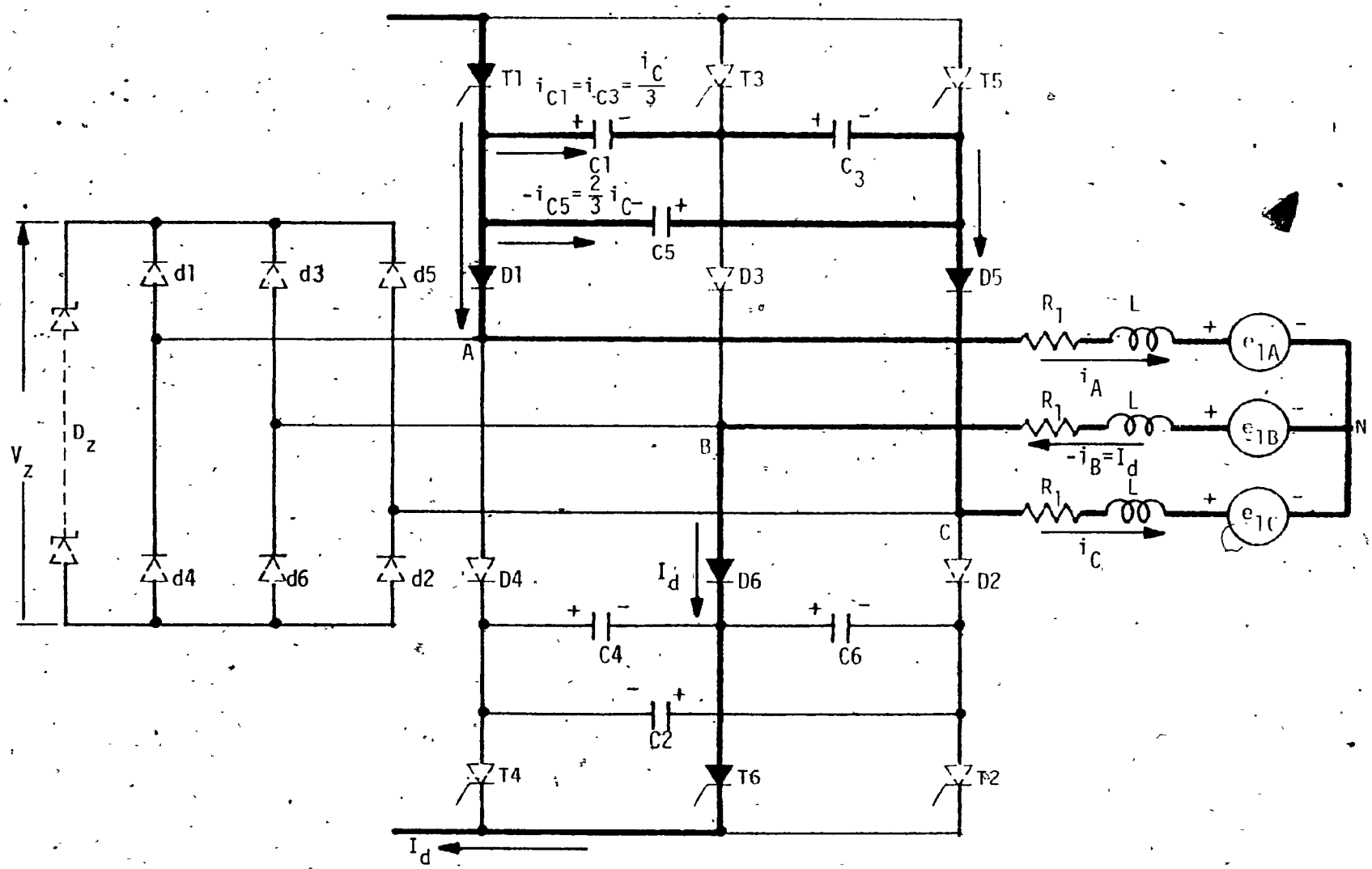

FIG. 6.3 ASCI-induction motor operation in mode 2 of case (d). Conduction of D_1 at $t=t_2$ starts a transfer mode in the upper group. This mode ends at $t=t_{21}$ when the zener diode clamping circuit starts conducting.

which can be found by solving the following equation

$$v_{AC}(t_1') = V_z = V_o \tag{6.3.2}$$

The left hand side term in (6.3.2) was given by (3.4.17) which yields

$$E_1\sqrt{3}\cos\left[\omega(t_2+t_1') + \phi_1 - \frac{2\pi}{3}\right] + 2L\left.\frac{di_A(t')}{dt'}\right|_{t'=t_1'} + 2R_1 i_A(t_1') - R_1 I_d = V_o \tag{6.3.3}$$

where $i_A(t')$ and $di_A(t')/dt'$ are given by (3.4.29) and (3.4.45), respectively. Again, the only unknown is t_2 which, as will be explained later, is calculated by an iterative procedure.

Owing to the first constraint upon V_o given in section (6.1), $v_{AB}(t_1')$ and $v_{BC}(t_1')$ should be calculated by using (3.4.8) in which the new time scale, $t' = t-t_2$, is employed. If any of these voltages have absolute values more than V_o the second constraint specified in section (6.1) is violated and the analysis presented here becomes invalid. In this case the value of V_z may be increased in order to satisfy the above constraint.

6.4 MODE 3 OR THE SECOND PART OF THE TRANSFER MODE

This mode starts at $t=t_{21}$ and ends at $t=t_3$. At $t=t_{21}$ v_{AC} reaches V_z causing the zener diodes to conduct. As long as the zener diodes are in the circuit, the voltage across the two motor phases, v_{AC}, remains constant. Referring to fig. 6.4 one can see that no currents can flow through the upper group commutating capacitors under this condition. As the voltage v_{AC} becomes clamped to V_z and

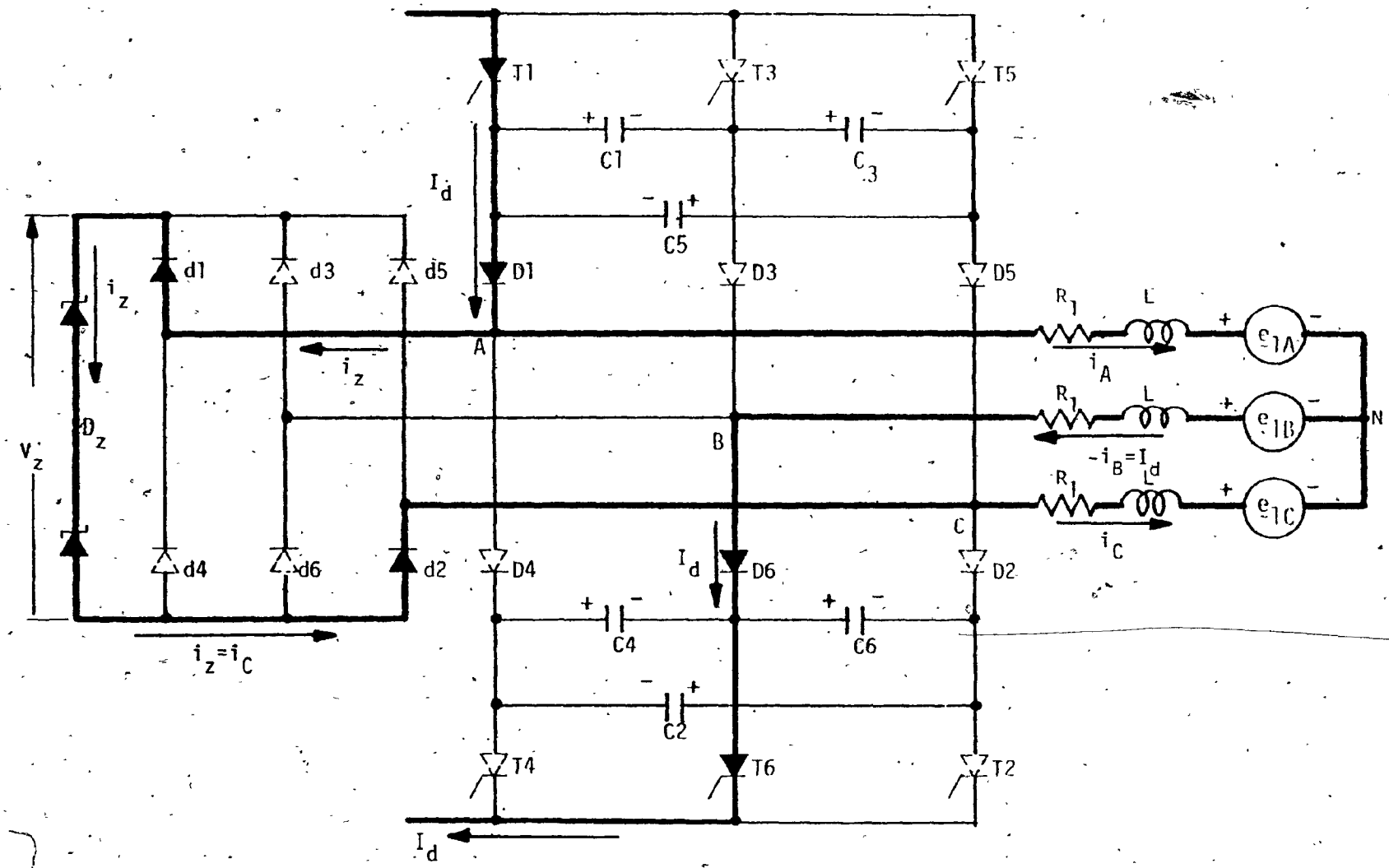

FIG. 6.4 ASCI-induction motor operation in mode 3 of case (d). Breakdown of the zener diodes blocks D_5 and phase C current is directed through the clamping circuit. This mode ends at $t=t_3$ when the clamping circuit stops conducting.

the capacitor currents go to zero, D_5 stops conducting. Thus the current to the phase C flows not through the upper group commutating capacitors but through the zener diodes. It is seen that although D_5 has stopped conducting the transfer mode is not finished yet and there are still currents in all motor phases.

To obtain the expressions describing the system, we should select a new time scale, t'', the origin of which is the beginning of mode 3

$$t'' = t - t_{21} \tag{6.4.1}$$

where its limits are

$$0 \leq t'' \leq (t_3 - t_{21}) \tag{6.4.2}$$

The circuit of fig. 6.4 gives us a new loop. This loop consists of R_1, L, e_{1A}, e_{1C}, L, R_1, d_2, D_z and d_1. Figure 6.5 displays this new loop in which the zener diodes have been replaced by a voltage source and a switch. The switch SW shows the switching operation of the zener diodes while the voltage source substitutes for the constant voltage across these diodes. After closing SW at $t''=0$ we can expect the total current in the phase A to consist of three components

1) A transient current due to the initial conditions.
2) A dc steady-state current due to V_z.
3) An ac steady-state current due to e_{1AC}.

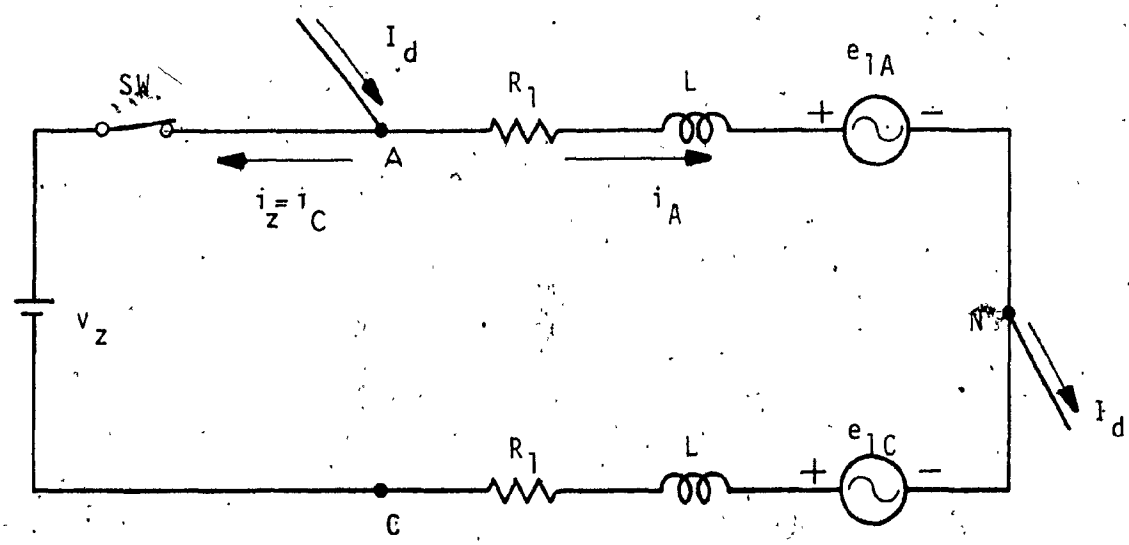

FIGURE 6.5 The new loop in mode 3. v_z shows the voltage across the zener diodes as soon as these diodes start conducting.

This mode and consequently the entire transfer mode, ends at $t=t_3$ when i_C becomes zero and the clamping circuit is disconnected.

In the following we are going to derive the currents $i_A(t'')$ and $i_C(t'')$ during the clamping mode. Going back to fig. 6.4 we can write

$$i_C(t'') = i_z(t'') \tag{6.4.3}$$

$$i_A(t'') + i_C(t'') = I_d \tag{6.4.4}$$

$$v_{AC}(t'') = V_z = V_o \tag{6.4.5}$$

where $v_{AC}(t'')$ is similar to (3.4.17) with t' and t_2 replaced by t'' and t_{21} respectively. Then we will have

$$E_1\sqrt{3}\cos[\omega(t_{21}+t'') + \phi_1 - \frac{2\pi}{3}] + 2L\frac{di_A(t'')}{dt''} + 2R_1 i_A(t'') - R_1 I_d = V_o \tag{6.4.6}$$

The Laplace transform of the above equation is

$$\frac{1}{s}(V_o+R_1 I_d) = 2R_1 \cdot I_A(s) + 2L[sI_A(s) - i_A(0^+)] + E_1\sqrt{3}\frac{s\cos(\omega t_{21}+\phi_1-\frac{2\pi}{3})}{s^2+\omega^2} - E_1\sqrt{3}\frac{\omega\sin(\omega t_{21}+\phi_1-\frac{2\pi}{3})}{s^2+\omega^2} \tag{6.4.7}$$

where $i_A(0^+)$ is the same as $i_A(t_1')$ and can be calculated from (3.4.29) for $t'=t_1'$:

$$i_A(0^+) = i_A(t_1') = i_A(t_{21}) \tag{6.4.8}$$

Here, we define two new constants

$$V_2 = V_o + R_1 I_d \tag{6.4.9}$$

$$\theta_2 = \omega t_{21} + \phi_1 - \frac{2\pi}{3} \tag{6.4.10}$$

and

$$\frac{R_1}{L} = 2\alpha = \alpha_1 \tag{6.4.11}$$

we can extract $I_A(s)$ from (6.4.7) using (6.4.9-11):

$$I_A(s) = \frac{V_2}{2L} \cdot \frac{1}{s(s+\alpha_1)} - \frac{E_1\sqrt{3}\cos\theta_2}{2L} \cdot \frac{s}{(s+\alpha_1)(s^2+\omega^2)}$$

$$+ \frac{\omega E_1\sqrt{3}\sin\theta_2}{2L} \cdot \frac{1}{(s+\alpha_1)(s^2+\omega^2)} + i_A(t_1') \cdot \frac{1}{s+\alpha_1} \tag{6.4.12}$$

The inverse Laplace transform of the above is

$$i_A(t'') = \frac{V_2}{2L\alpha_1}(1-e^{-\alpha_1 t''}) - \frac{E_1\sqrt{3}\cos\theta_2}{2L}[A_3\sin(\omega t''+\beta_3)+B_3 e^{-\alpha_1 t''}]$$

$$+ \frac{\omega E_1\sqrt{3}\sin\theta_2}{2L}[A_4\sin(\omega t''+\beta_4)+B_4 e^{-\alpha_1 t''}]+i_A(t_1')e^{-\alpha_1 t''} \tag{6.4.13}$$

in which the new constants are

$$A_3 = \frac{1}{(\alpha_1^2+\omega^2)^{1/2}}$$

$$B_3 = -\frac{\alpha_1}{\alpha_1^2+\omega^2}$$

$$\beta_3 = \frac{\pi}{2} - \text{arc tan}\,\frac{\omega}{\alpha_1} = \text{arc tan}\,\frac{\alpha_1}{\omega}$$

$$A_4 = \frac{1}{\omega}\left(\frac{1}{\alpha_1^2+\omega^2}\right)^{1/2}$$

$$B_4 = \frac{1}{\alpha_1^2+\omega^2}$$

$$\beta_4 = -\arctan\frac{\omega}{\alpha_1} \qquad (6.4.13a)$$

From (6.4.11) results

$$R_1 = L\alpha_1$$

which, by putting it in (6.4.13) and rearranging, we obtain

$$i_A(t'') = \frac{V_2}{2R_1} + e^{-\alpha_1 t''}\left[-\frac{V_2}{2R_1} - \frac{B_3E_1\sqrt{3}\cos\theta_2}{2L} + \frac{B_4\omega E_1\sqrt{3}\sin\theta_2}{2L}\right.$$

$$\left. + i_A(t_1')\right] + \frac{E_1\sqrt{3}}{2L}\left[\omega A_4\sin\theta_2\sin(\omega t''+\beta_4) - A_3\cos\theta_2\sin(\omega t''+\beta_3)\right]$$

$$(6.4.14)$$

Considering (6.4.9), it is noticed that (6.4.14) includes all the current components discussed earlier. A more compact form of (6.4.14) is found by introducing a few more constants

$$C_{20} = \frac{V_2}{2R_1}$$

$$C_{21} = i_A(t_1') + \frac{B_4\omega E_1\sqrt{3}\sin\theta_2}{2L} - \frac{B_3E_1\sqrt{3}\cos\theta_2}{2L} - C_{20}$$

$$C_{22} = \frac{E_1\sqrt{3}}{2L}$$

$$C_{23} = \omega A_4 \sin\theta_2$$

$$C_{24} = A_3 \cos\theta_2 \tag{6.4.15}$$

$$i_A(t'') = C_{20}+C_{21}\cdot e^{-\alpha_1 t''}+C_{22}[C_{23}\sin(\omega t''+\beta_4) - C_{24}\sin(\omega t''+\beta_3)] \tag{6.4.16}$$

and from (6.4.3-4) the result is

$$i_C(t'') = i_z(t'') = I_d-C_{20}-C_{21}e^{-\alpha_1 t''}-C_{22}[C_{23}\sin(\omega t''+\beta_4) - C_{24}\sin(\omega t''+\beta_3)] \tag{6.4.17}$$

As was mentioned before, this mode and, as a result, the transfer mode ends at $t''=t''_1$ when the total current is transferred to phase A

$$i_A(t''_1) = I_d \quad \text{or} \quad i_C(t''_1) = 0 \tag{6.4.18}$$

Using either (6.4.17) or (6.4.18) yields

$$I_d-C_{20}-C_{21}e^{-\alpha_1 t''_1} - C_{22}[C_{23}\sin(\omega t''_1+\beta_4) - C_{24}\sin(\omega t''_1+\beta_3)] = 0 \tag{6.4.19}$$

Then the transfer mode duration is

$$t_{tr} = t'_1+t''_1 = t_{21}-t_2+t_3-t_{21} = t_3-t_2 \tag{6.4.20}$$

In order to solve (6.4.19) for t_1'' we should have calculated t_1' which in turn, according to (6.3.3), needs the knowledge of t_2. In sections (3.6.1) and (3.6.2) we noticed the dependence of t_2 on the transfer period. In this case, the transfer period consists of t_1' and t_1''. Thus, t_2 depends on both t_1' and t_1''. Later on, we will explain the procedure for finding t_2.

Referring to fig. 6.4 one can see that all the capacitors have constant voltages during the clamping mode. Also from fig. 6.3 it is clear that only the upper group capacitors are under charging or discharging during mode 2. Then it results that the upper group capacitor voltages during the clamping period are the same as their corresponding values at the end of mode 2. In addition, for a successful operation of the inverter, under clamping conditions, the capacitor voltages should follow the same pattern which was predicted in Tables 1.1 - 1.3 for case (a). For the upper group capacitors we should have

$$v_{C1}(t_1') = +V_o = V_z$$

$$v_{C3}(t_1') = 0$$

$$v_{C5}(t_1') = -V_o = -V_z \qquad (6.4.21)$$

By using one or more of the above equations we can check the validity of the derivations done up to this point.

The motor terminal voltages during mode 3 (clamping mode) are

$$v_A(t'') = R_1 i_A(t'')+L\frac{di_A(t'')}{dt''} + E_1\sin(\omega t''+\omega t_{21}+\phi_1)$$

$$v_B(t'') = -R_1 I_d+E_1\sin(\omega t''+\omega t_{21}+\phi_1-\frac{2\pi}{3})$$

$$v_C(t'') = R_1 i_C(t'')+L\frac{di_C(t'')}{dt''} + E_1\sin(\omega t''+\omega t_{21}+\phi_1-\frac{4\pi}{3})$$

(6.4.22)

and the line voltages become

$$v_{AB}(t'') = R_1 i_A(t'')+L\frac{di_A(t'')}{dt''} + R_1 I_d+E_1\sqrt{3}\cos(\omega t''+\omega t_{21}+\phi_1-\frac{\pi}{3})$$

$$v_{BC}(t'') = -2R_1 I_d+R_1 i_A(t'')+L\frac{di_A(t'')}{dt''} + E_1\sqrt{3}\cos(\omega t''+\omega t_{21}+\phi_1-\pi)$$

$$v_{CA}(t'') = -V_o \qquad (6.4.23)$$

Note that for obtaining $v_{BC}(t'')$ in (6.4.23) we have used (6.4.4). Also, the first derivative of $i_A(t'')$ in the above equation is

$$\frac{di_A(t'')}{dt''} = -\alpha_1 C_{21} e^{-\alpha_1 t''} +\omega C_{22}[C_{23}\cos(\omega t''+\beta_4)-C_{24}\cos(\omega t''+\beta_3)]$$

(6.4.24)

At this point, in order to check the validity of assumption number 2 in section (6.1), $v_{AB}(t'')$ and $v_{BC}(t'')$ should be calculated for $t''=t''_1$. The absolute values of these voltages should be less than V_z. Otherwise, the results presented here become inaccurate. In order to use the commutation model developed in this study, the value of the breakdown voltage, V_z, may be increased to such a value that the above assumption is true.

The thyristors voltages during this mode are

$$v_{T1}(t'') = v_{T6}(t'') = 0$$

$$v_{T3}(t'') = v_{C1}(t'') = V_o$$

$$v_{T5}(t'') = -v_{C5}(t'') = V_o$$

$$v_{T4}(t'') = v_{C4}(t'') = V_o$$

$$v_{T2}(t'') = -v_{C6}(t'') = V_o \qquad (6.4.25)$$

and for the diodes we can write

$$v_{D1}(t'') = v_{D6}(t'') = 0$$

$$v_{D3}(t'') = -v_{C1}(t'') + v_{AB}(t'') = -V_o + v_{AB}(t'')$$

$$v_{D5}(t'') = v_{C5}(t'') + v_{AC}(t'') = -V_o + V_o = 0$$

$$v_{D2}(t'') = v_{CB}(t'') + v_{C6}(t'') = v_{CB}(t'') - V_o$$

$$v_{D4}(t'') = v_{AB}(t'') - v_{C4}(t'') = v_{AB}(t'') - V_o \qquad (6.4.26)$$

and, at last, the inverter input voltage during this mode is

$$v_I(t'') = v_{AB}(t'') \qquad (6.4.27)$$

6.4.1 Power Loss in Zener Diodes

As mentioned earlier, by connecting the clamping circuit to the system, some energy loss occurs in the zener diodes which otherwise would be dissipated in the other parts of the inverter. During each cycle of the inverter output, there are six equal clamping periods. The amount of energy dissipated in the clamping circuit during each of

these periods is

$$W_{z1} = \int_0^{t_1''} V_z i_z(t'')dt'' = \int_0^{t_1''} V_z i_C(t'')dt'' \qquad (6.4.1.1)$$

but $V_z = V_o$ is constant during mode 3 (clamping period) and $i_C(t'')$ is given by (6.4.17). The result is then

$$W_{z1} = V_o \int_0^{t_1''} \left\{ I_d - C_{20} - C_{21} e^{-\alpha_1 t''} - C_{22}[C_{23}\sin(\omega t''+\beta_4) - C_{24}\sin(\omega t''+\beta_3)] \right\} dt''$$

or

$$W_{z1} = V_o(I_d - C_{20})t_1'' + \frac{V_o C_{21}}{\alpha_1}(e^{-\alpha_1 t_1''} - 1) + \frac{V_o C_{22} C_{23}}{\omega}[\cos(\omega t_1''+\beta_4) - \cos\beta_4] + \frac{V_o C_{22} C_{24}}{\omega}[\cos\beta_3 - \cos(\omega t_1''+\beta_3)] \qquad (6.4.1.2)$$

And by introducing the new constants

$$C_{24a} = e^{-\alpha_1 t_1''}$$

$$C_{30} = V_o(I_d - C_{20})t_1''$$

$$C_{31} = \frac{V_o C_{21}}{\alpha_1}(C_{24a} - 1)$$

$$C_{32} = \frac{V_o C_{22} C_{23}}{\omega}[\cos(\omega t_1''+\beta_4) - \cos\beta_4]$$

$$C_{33} = \frac{V_o C_{22} C_{24}}{\omega}[\cos\beta_3 - \cos(\omega t_1''+\beta_3)] \qquad (6.4.1.2a)$$

the above expression can be written in a new form

$$W_{z1} = C_{30} + C_{31} + C_{32} + C_{33} \qquad (6.4.1.2b)$$

For one inverter output cycle the energy loss is

$$W_{z6} = 6W_{z1} \qquad \text{joule/cycle} \qquad (6.4.1.3)$$

and its corresponding power loss becomes

$$P_z = \frac{W_{z6}}{T} = fW_{z6} \quad W \qquad (6.4.1.4)$$

where T and f are the inverter output period and frequency respectively. The maximum value of the power loss, P_z, in the zener diodes, is the main criterion in designing the clamping circuit.

6.5 MODE 4 OR THE NORMAL MODE

This mode lasts from $t=t_3$ to $t=t_4$. At $t=t_3$ the current in phase C becomes zero, thus terminating the transfer mode. At the same time, the clamping circuit becomes disconnected from the system, fig. 6.6. This mode is exactly the same as mode 3 in case (a). All the equations given there are also applicable to this mode.

Operation of an ASCI with the zener clamping circuit is presented in fig. 6.7 which is analogous to fig. 4.1. The same notation as in fig. 4.1 is used in fig. 6.7. Comparing these two figures one can see that the only difference is the splitting of the transfer mode into two sub-modes in fig. 6.7. This results in the total number of the modes increasing from 18 to 24 for case (d). The motor current waveforms are also similar to fig. 3.11 but are expressed by (3.4.45) and (6.4.16), respectively, during the new transfer mode.

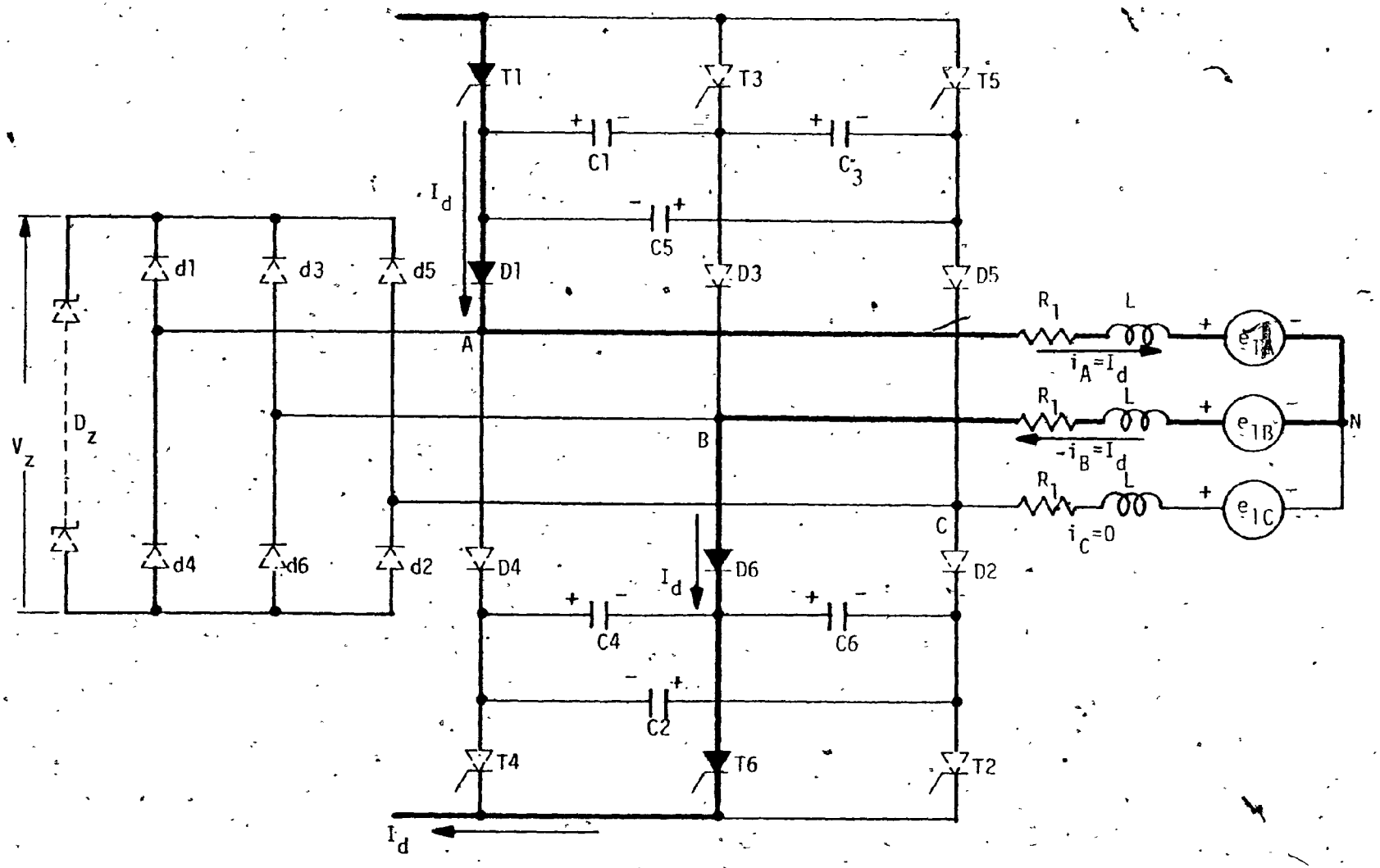

FIG. 6.6 ASCI-induction motor operation in mode 4 of case (d). At $t=t_3$ the clamping circuit stops conducting and the phase C current reaches zero while the inverter enters into a normal mode. This mode ends at $t=t_4$ when T_2 is fired.

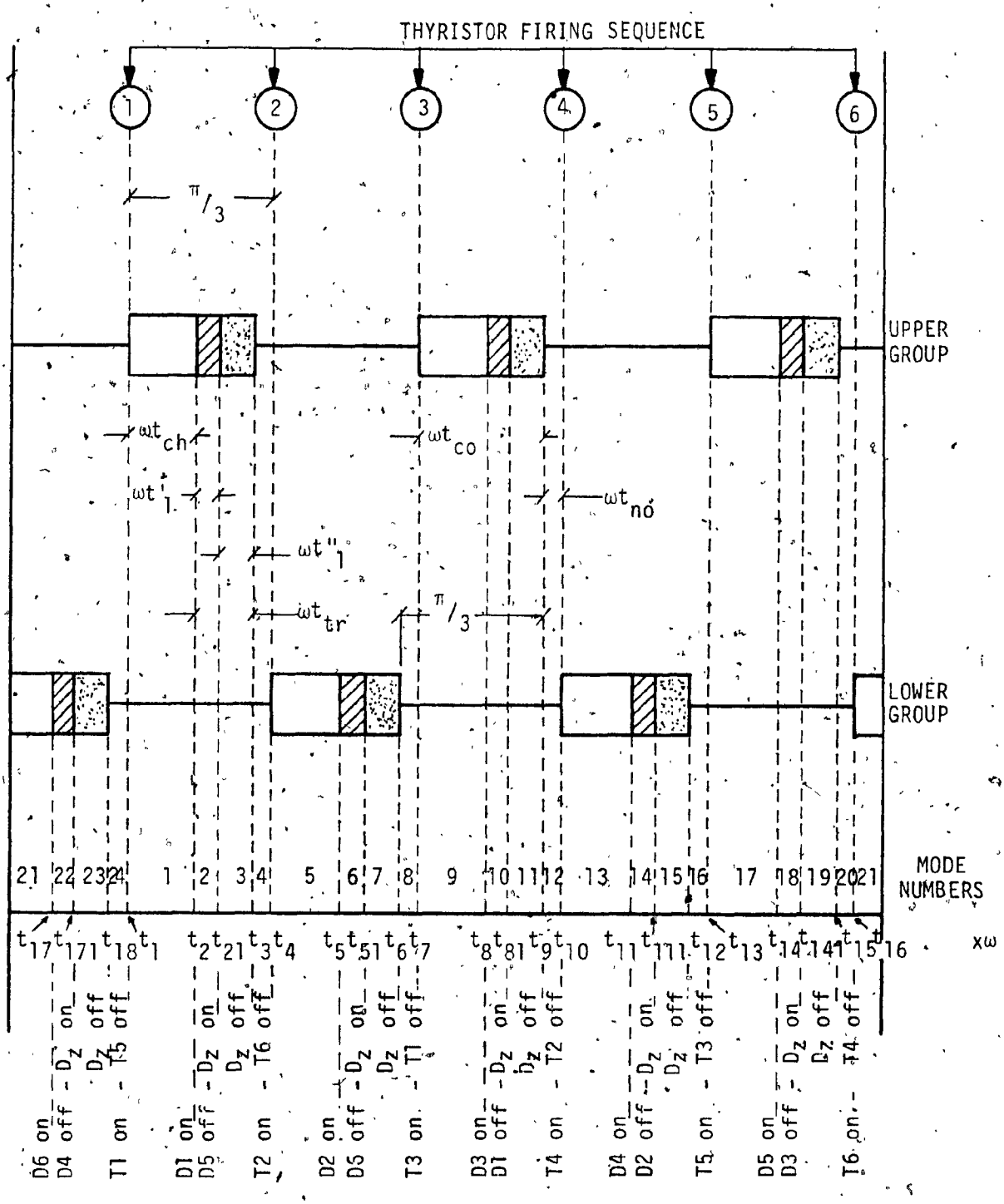

FIG. 6.7 The inverter operation with a clamping circuit in case (d) where $\omega t_{ch} < \frac{\pi}{3}$, $\omega t_{tr} < \frac{\pi}{3}$ and $\omega t_{co} < \frac{\pi}{3}$.

6.6 COMMUTATION OVERLAP WITH A CLAMPING CIRCUIT

In section (4.2) it was found that the maximum commutation angle occurs at a no-load condition when the inverter output frequency has the maximum value. The partial overlap condition was defined as an operation where the commutation angle is large than 60° but less than 120° while the transfer angle is smaller than 60°. The partial overlap operation was then analyzed in sections (4.3) and (4.4). However, this analysis does not include the clamping circuit operation. Although, in practice, the clamping circuit does not operate at a no-load condition, which is critical in the overlap considerations, we will explain the general situation when the commutation overlap may occur while the clamping circuit is conducting.

In this case, the limiting frequency at which the commutation angle equals 120° cannot be predicted through a simplified equation as was done for a no-clamping case, section (4.7). Here, for each frequency at no-load operation, t'_1 and t''_1 should be calculated through the two transcendental equations, (6.3.3) and (6.4.19). The charging time, t_{ch}, is found, as before, by employing (3.4.41). Then, using (6.4.20) and (3.4.14) the commutation time, t_{co}, and its angle, ωt_{co}, are found and checked to see whether ωt_{co} is less than $\frac{2\pi}{3}$

The cases similar to cases (b) and (c) but with a clamping circuit are called cases (e) and (f), respectively. Case (e) is defined as a case in which the charging and the transfer angles are both less than 60° while the commutation angle is limited between 60° and 120°.

In case (f), the transfer angle is still less than 60° while the charging angle exceeds 60° and the commutation angle does not go beyond 120°. Also note that no diodes should become transiently forward biased in case (e) and case (f).

6.6.1 Partial overlap, case (e) and case (f)

Case (e) is similar to case (b) so that the same limits for the commutation, charging and transfer angles apply:

$$\omega t_{ch} < \frac{\pi}{3} \quad , \quad \omega t_{tr} < \frac{\pi}{3} \quad \text{and} \quad \frac{\pi}{3} < \omega t_{co} < \frac{2\pi}{3} \qquad (6.6.1.1)$$

This case can be further subdivided into two other cases; one in which the first part of the transfer mode ends before triggering the next thyristor, fig. 6.8, and the other in which the first part of the transfer mode ends after firing the next thyristor, fig. 6.9.

In analysing the system operation for case (e), the same approach as in section (4.3) is followed. For the sake of briefness, we will not derive any expressions as before. Starting from the mode just before triggering the thyristor T_1, figures 6.10 to 6.16 show the system during seven consecutive modes for case (e) in which the zener diodes start conducting before the next thryistor is triggered, fig. 6.8. As in case (d), these figures have been drawn using the two assumption specified in section 6.1. It is noticed that modes 1 and 2 constitute a period of the charging mode during which the total current in the upper group capacitors remains constant and equal to

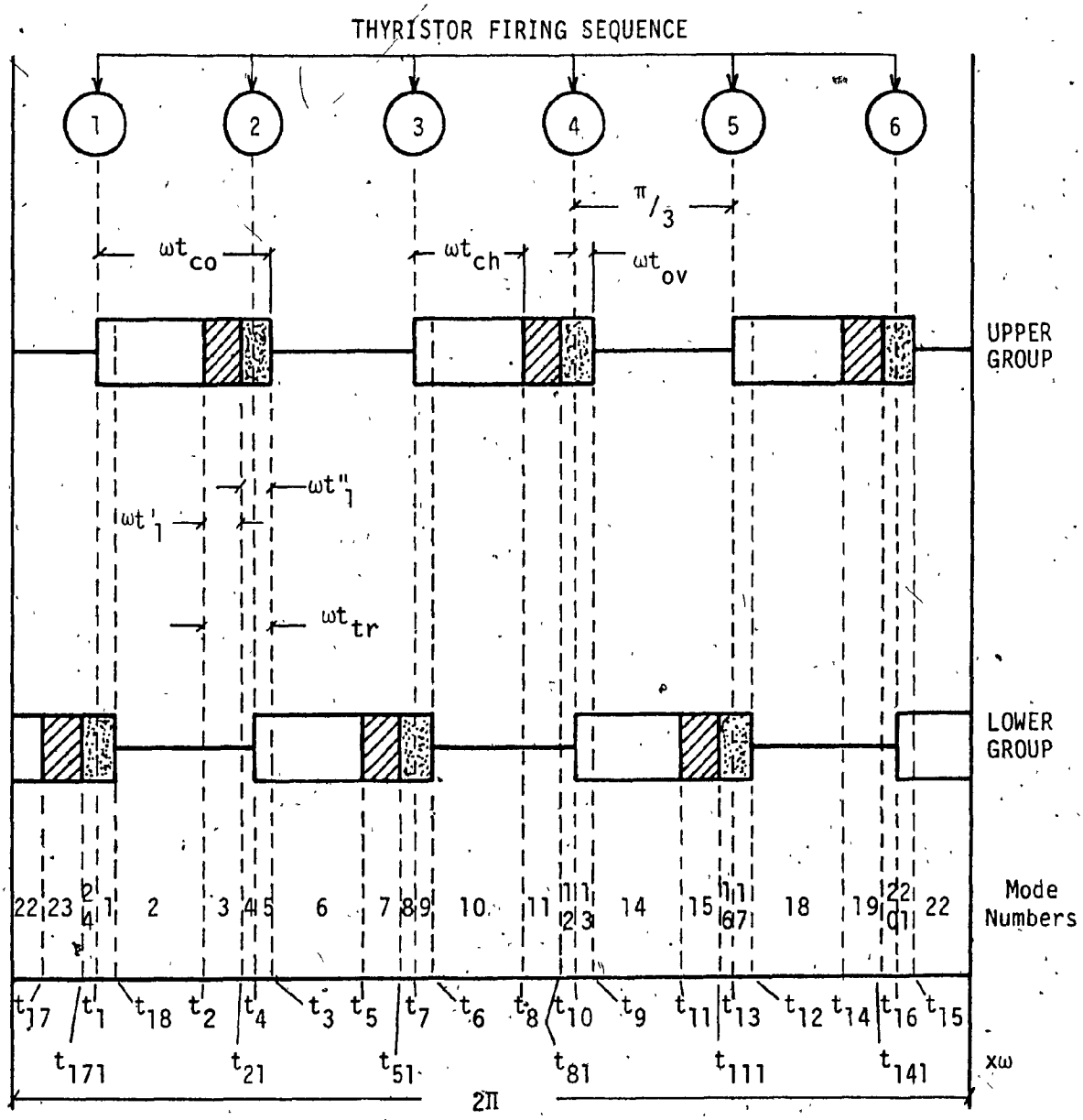

FIG. 6.8 Operation of an ASCI with a partial commutation overlap under clamped conditions in case (e) where $\omega t_{ch} < \frac{\pi}{3}$, $\omega(t_{ch}+t'_1) < \frac{\pi}{3}$ and $\frac{\pi}{3} < \omega t_{co} < \frac{2\pi}{3}$.

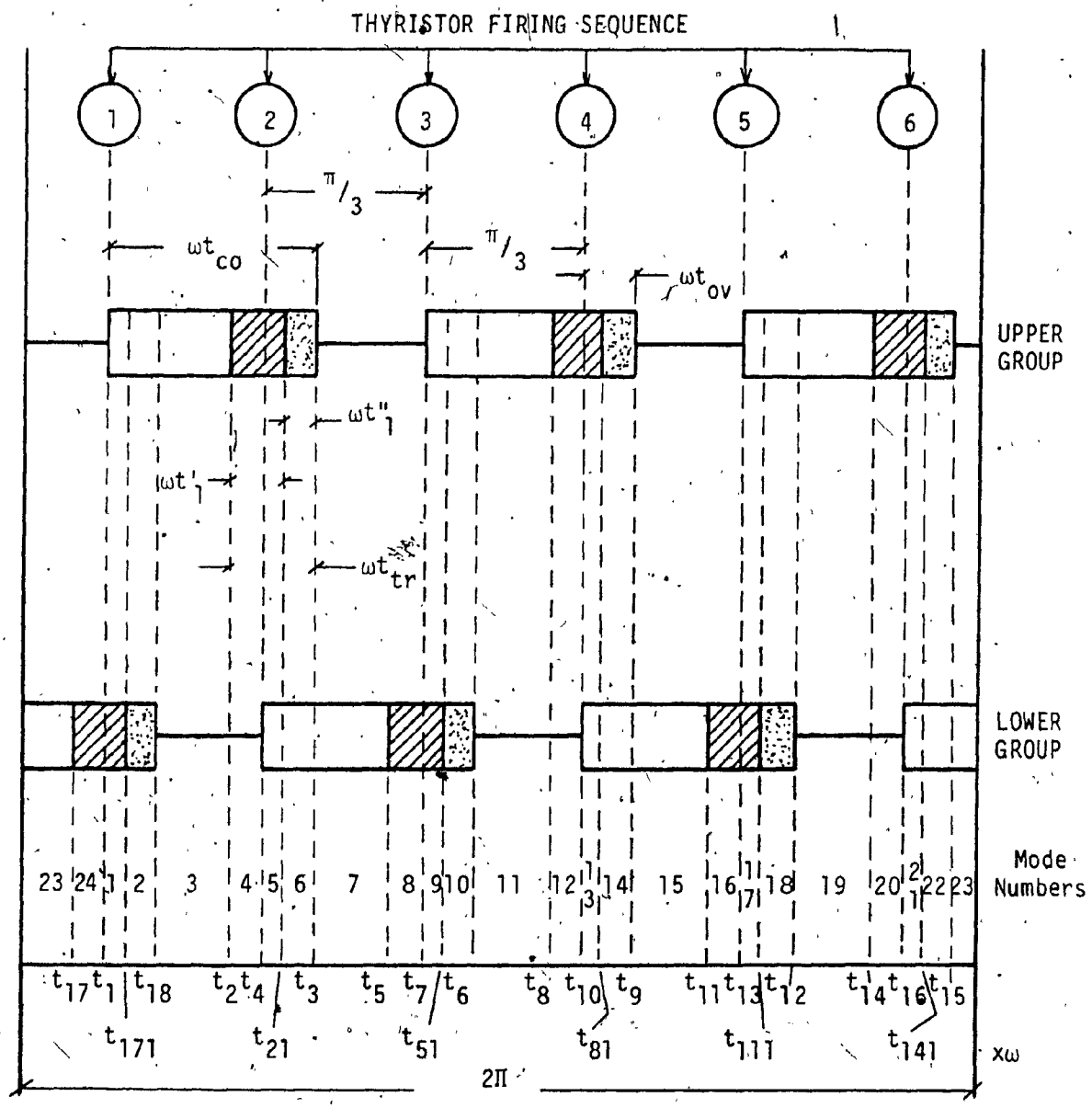

FIG. 6.9 Operation of an ASCI with a partial commutation overlap under clamped voltage conditions in case (e) where $\omega t_{ch} < \frac{\pi}{3}$, $\omega t_{tr} < \frac{\pi}{3}$, $\omega(t_{ch}+t'_1) > \frac{\pi}{3}$ and $\frac{\pi}{3} < \omega t_{co} < \frac{2\pi}{3}$.

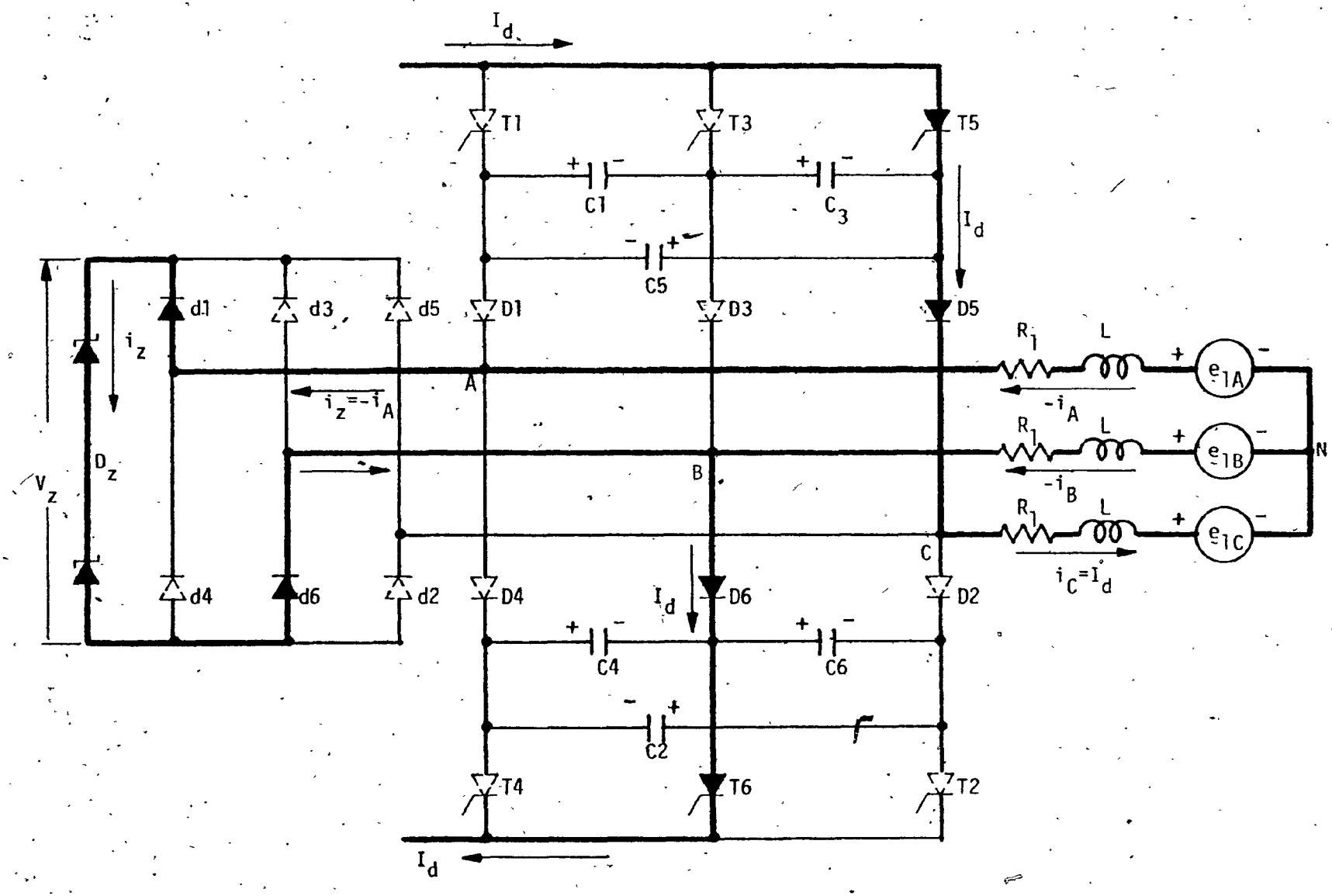

FIG. 6.10 ASCI-induction motor operation in mode 24 of case (e) as defined in Fig. 6.8. The current is being transferred from phase A to phase B through the clamping circuit. This mode ends at $t=t_1$ when T_1 is triggered.

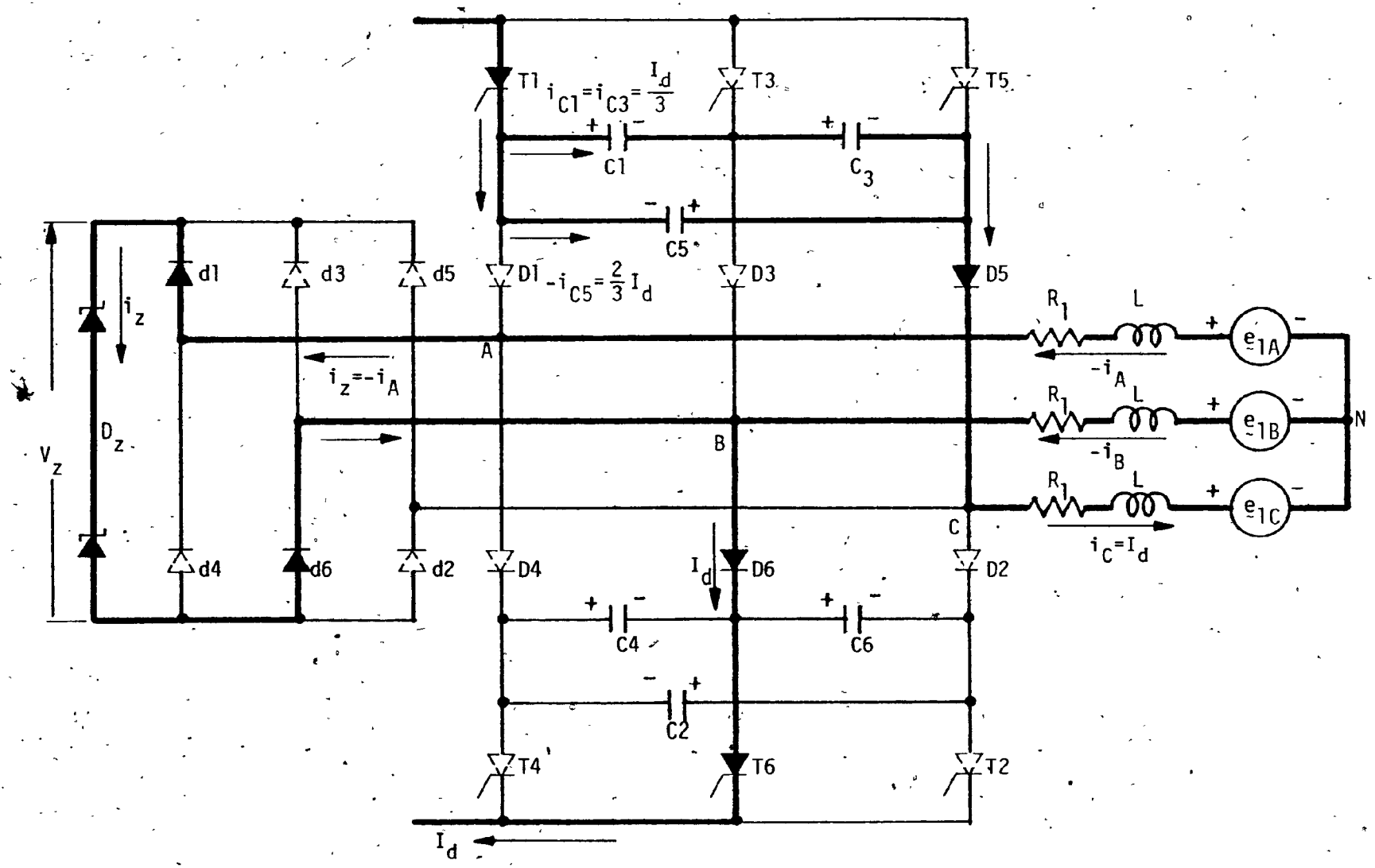

FIG. 6.11 ASCI-induction motor operation in mode 1 of case (e) as defined in Fig. 6.8. Firing T_1 at $t=t_1$ initiates the first part of a charging mode in the upper group while the current is still being transferred from phase A to phase B through the clamping circuit. This mode ends at $t=t_{18}$ when the clamping circuit stops conducting.

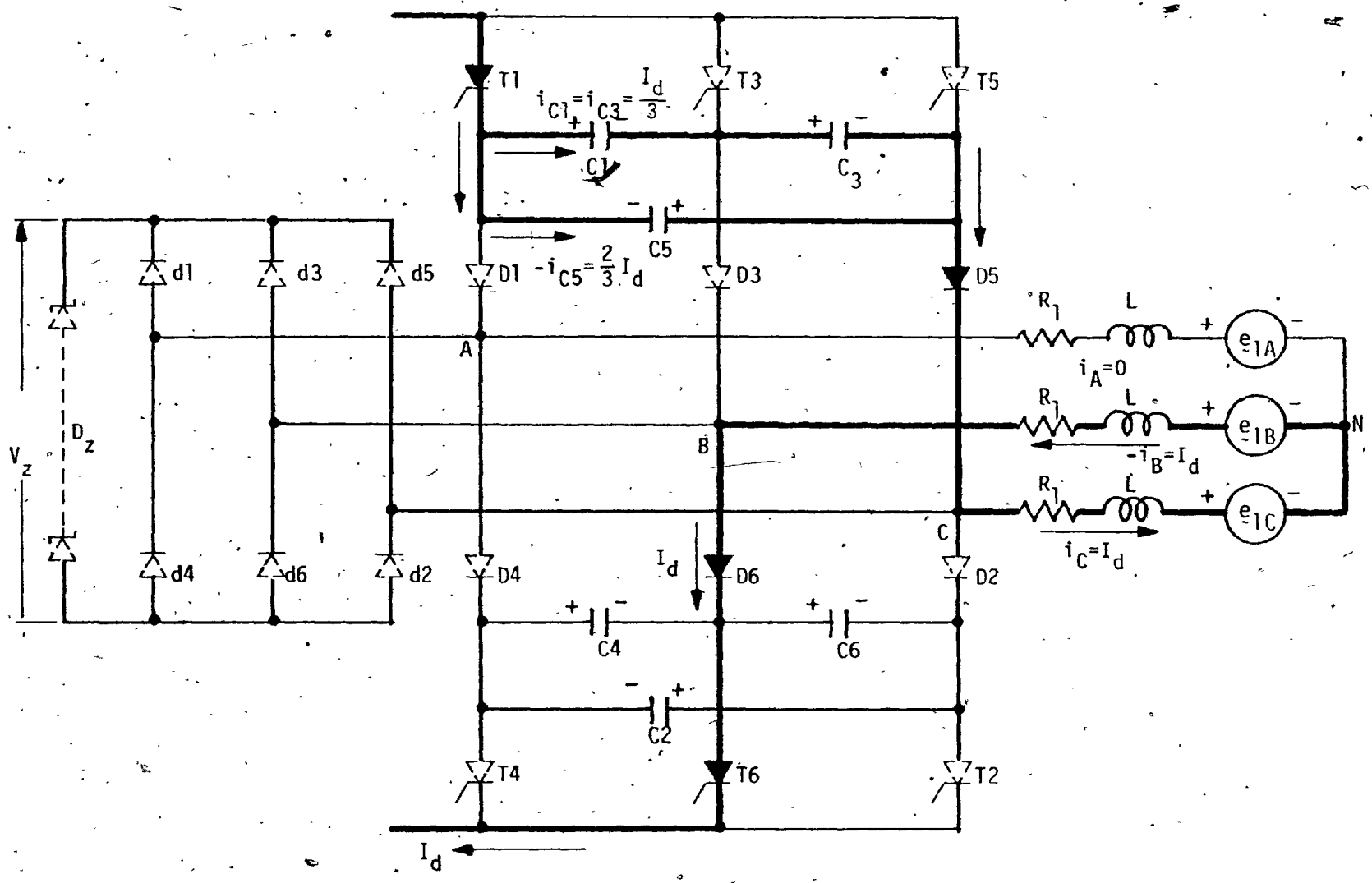

FIG. 6.12 ASCI-induction motor operation in mode 2 of case (e) as defined in Fig. 6.8. At $t=t_{18}$ the clamping circuit stops conducting while the second part of a charging mode continues in the upper group. This mode ends at $t=t_2$ when D_1 becomes forward biased.

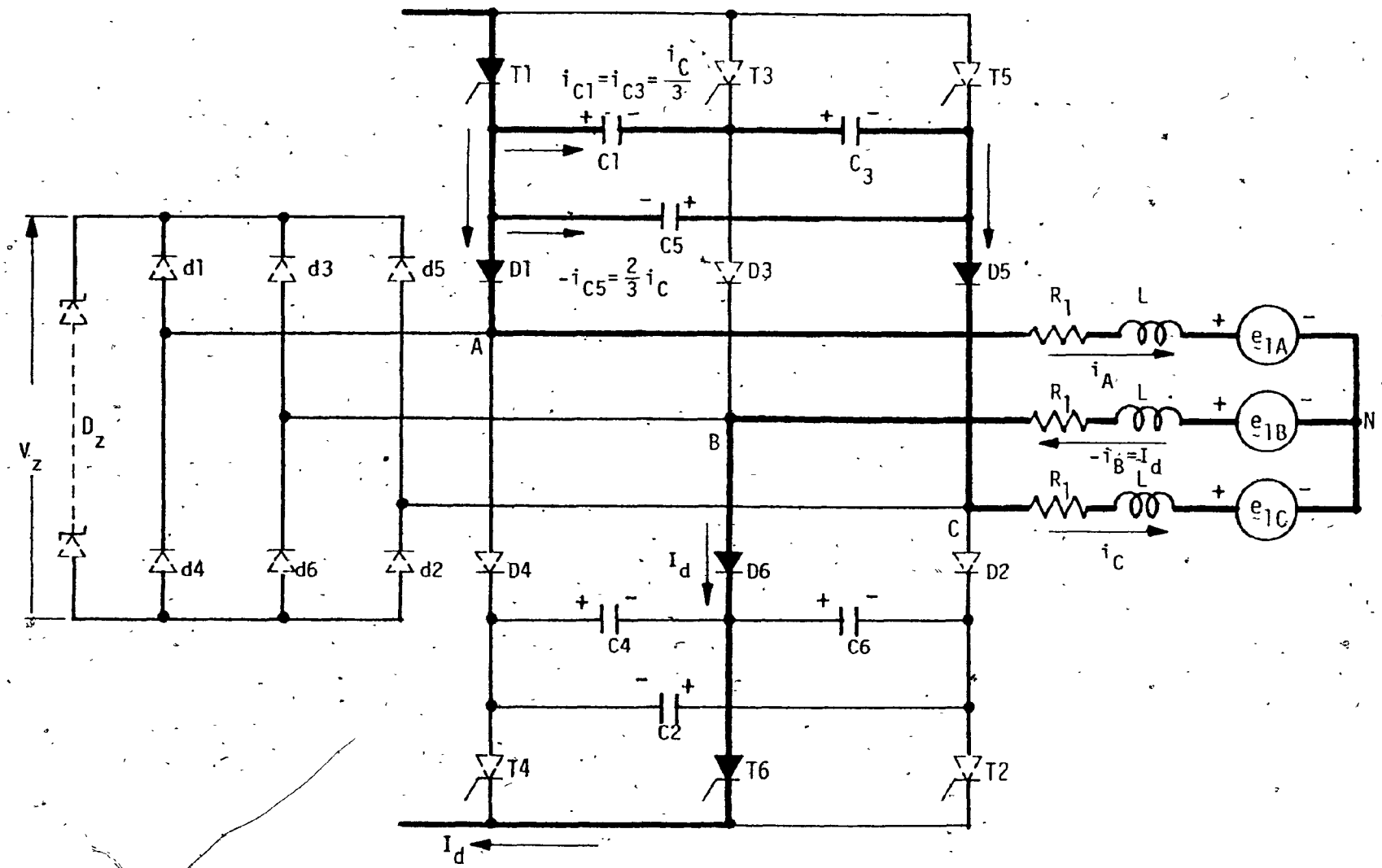

FIG. 6.13 ASCI-induction motor operation in mode 3 of case (e) as defined in Fig. 6.8. At $t=t_2$ D_1 starts conducting and the first part of a transfer mode commences in the upper group. This mode ends at $t=t_{21}$ when the zener circuit clamps the voltage across A and C.

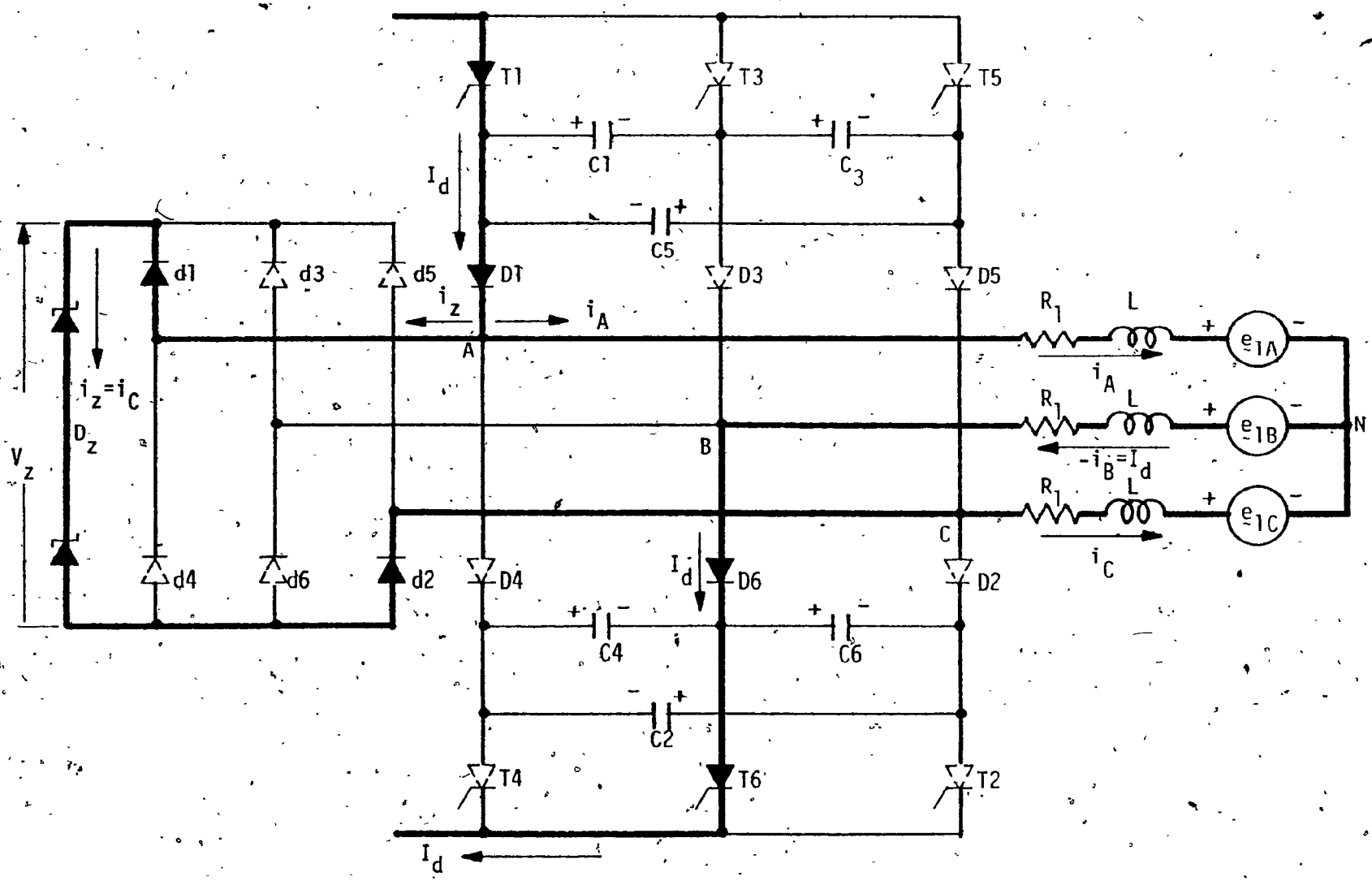

FIG. 6.14 ASCI-induction motor operation in mode 4 of case (e) as defined in Fig. 6.8. At $t=t_{21}$ the clamping circuit conduction starts the second part of a transfer mode in the upper group while D_1 is blocked. This mode ends at $t=t_4$ when T_2 is triggered.

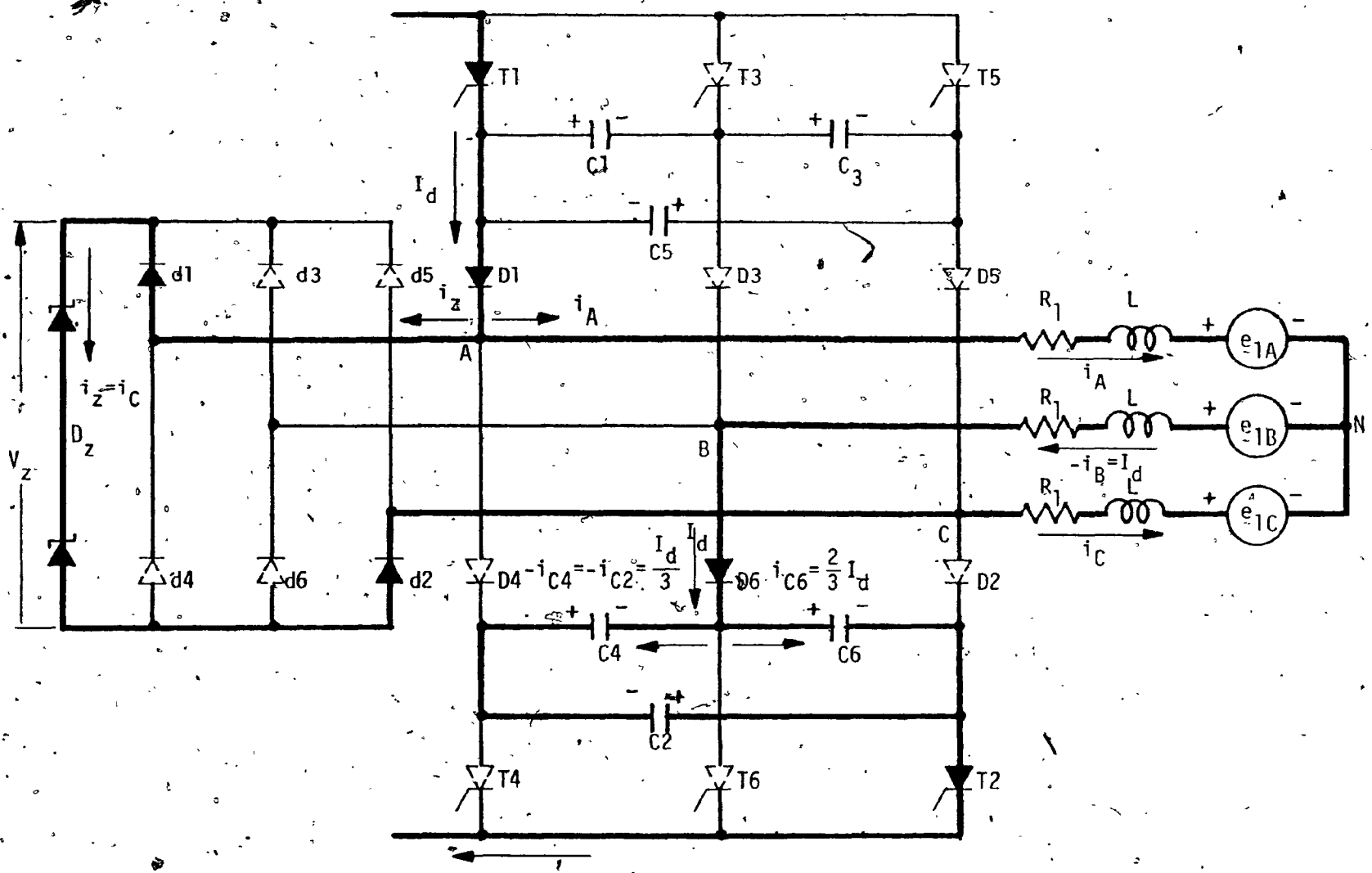

FIG. 6.15 ASCI-induction motor operation in mode 5 of case (e) as defined in Fig. 6.8. Firing T_2 at $t=t_4$ starts the first part of a charging mode in the lower group which overlaps the third part of a transfer mode in the upper group. This mode ends at $t=t_3$ when the clamping circuit stops conducting.

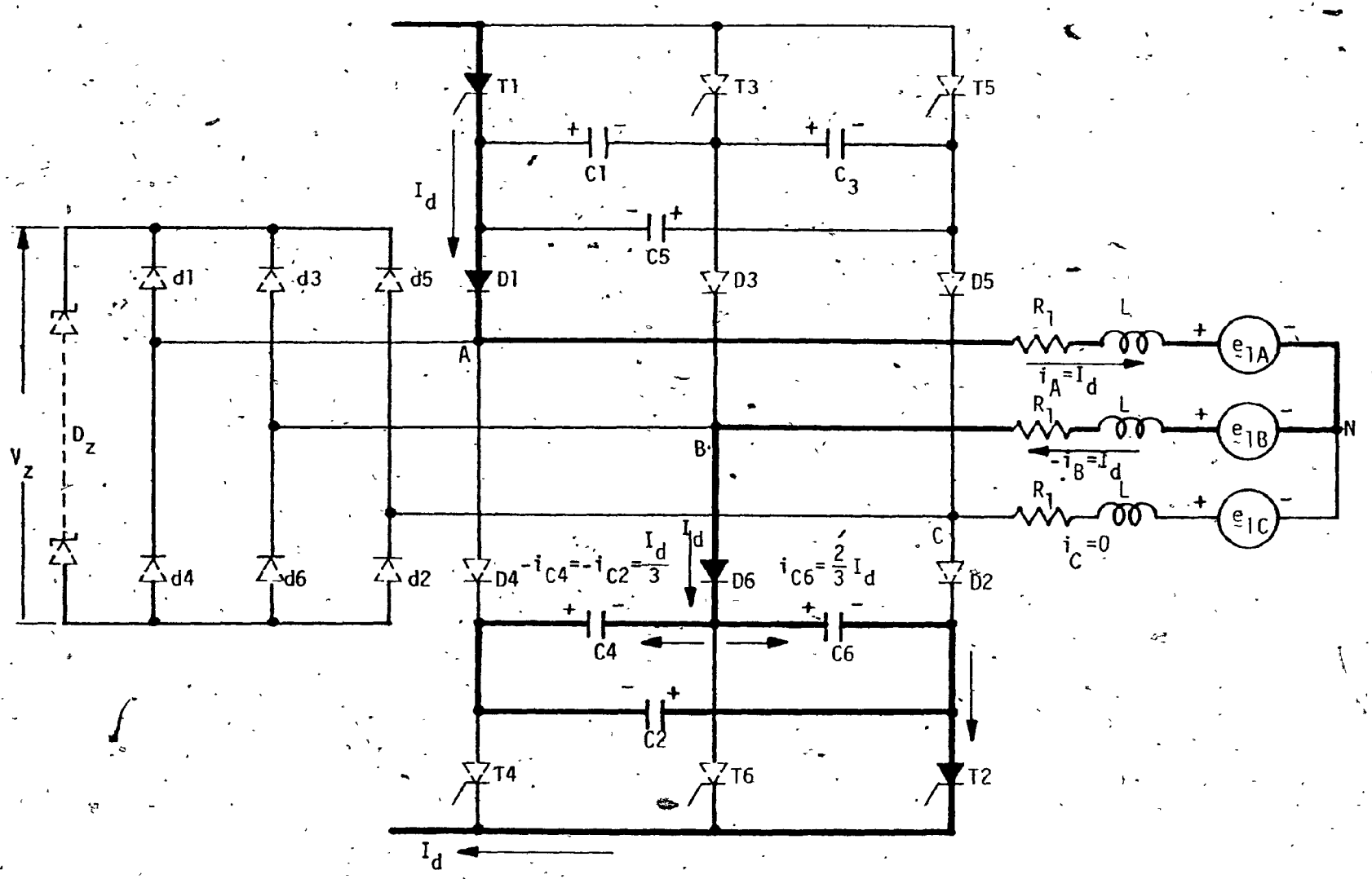

FIG. 6.16 ASCI-induction motor operation in mode 6 of case (e) as defined in Fig. 6.8. At $t=t_3$ the current in phase C is completely transferred to Phase A while the second part of a charging mode starts in the lower group. This mode ends at $t=t_5$ when D_2 starts conducting.

I_d. Thus the same key equation given by (3.3.5) and (3.3.11) are also valid for the charging mode in this case.

Mode 3, shown by fig. 6.13, is the same as mode 2 in case (d) and the same equations derived in section 6.3 hold here. Figures 6.14 and 6.15 constitute the second part of the transfer mode during which the zener diodes are in the circuit. It is seen that when at the beginning of mode 5, the thyristor T_2 is triggered, the mechanism of current transfer from phase C to phase A (through zener diodes) will not be affected by the charging in the lower inverter group. This implies that the key equations (6.4.3) to (6.4.6) can also be used for modes 4 and 5, figs. 6.14 and 6.15. As a result, (6.4.16) to (6.4.25) would also be applicable for this case. Figure 6.16 shows mode 6 in which only the lower group capacitors are under charging or discharging.

For case (e), but with zener diodes conducting only after the next thyristor is fired (fig. 6.9), we can plot a series of figures similar to figs. 6.10 to 6.16 but for eight consecutive modes. These figures can then be used to prove that the same key equations given for case (d) are also applicable to case (e).

Case (f) is similar to case (c), for which we have the following relationships:

$$\omega t_{ch} > \frac{\pi}{3}, \quad \omega t_{tr} < \frac{\pi}{3} \quad \text{and} \quad \frac{\pi}{3} < \omega t_{co} < \frac{2\pi}{3}$$

Figure 6.17 defines the different modes for the case. The discussion

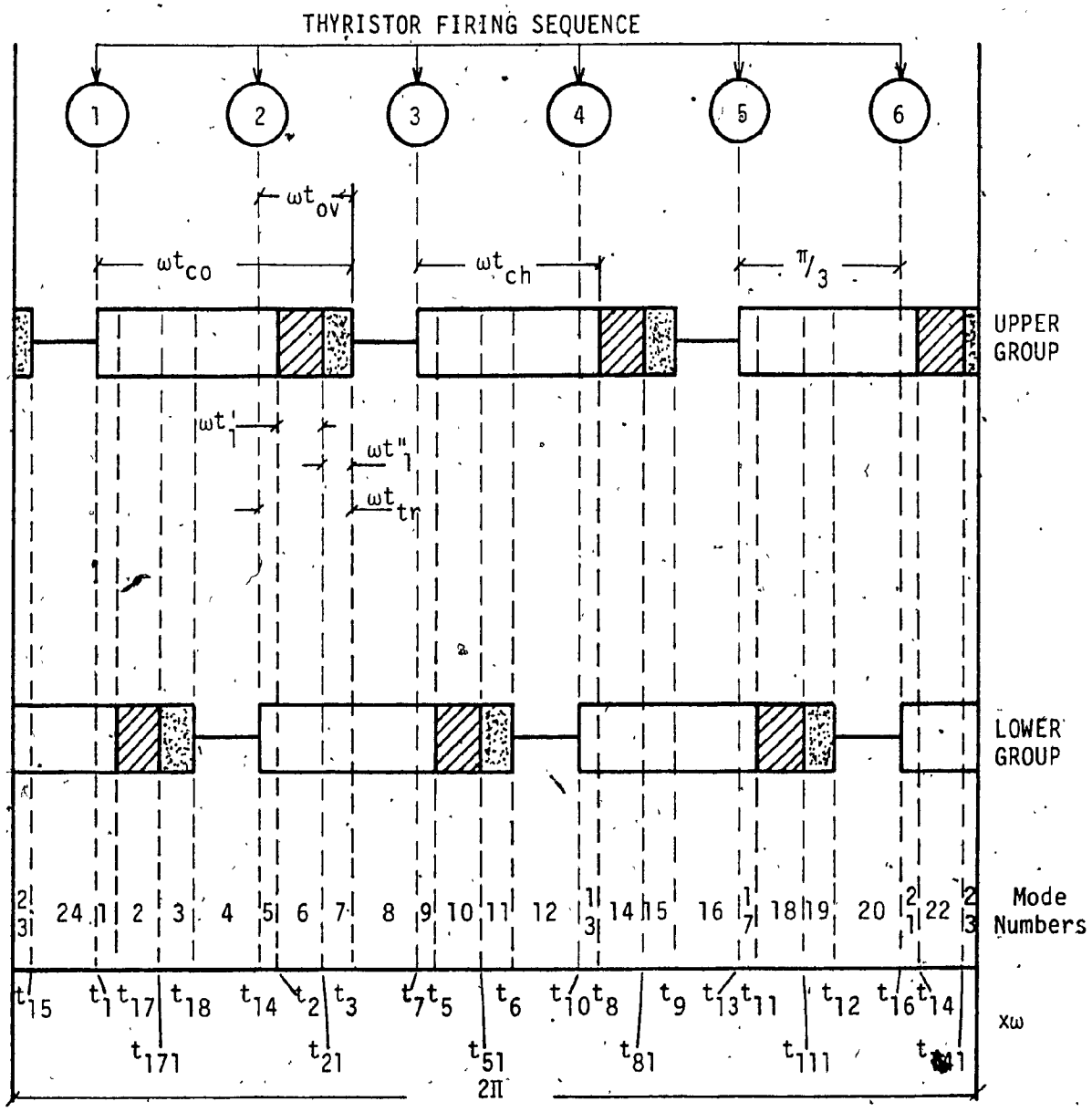

FIG. 6.17 ASCI operation with a partial commutation overlap under clamped conditions in case (f) where $\omega t_{ch} > \frac{\pi}{3}$, $\omega t_{tr} < \frac{\pi}{3}$ and $\omega t_{co} < \frac{2\pi}{3}$.

presented for case (e) is also applicable here and can be verified by a set of figures similar to those given by figs. 6.10 to 6.16.

In conclusion, for the system with the clamping circuit and a constant dc link current, we are allowed to use the same key equations as provided in section (6.4) as long as $\omega t_{tr} < \frac{\pi}{3}$ and $\omega t_{co} < \frac{2\pi}{3}$ where t_{tr} is the transfer mode period and t_{co} is the duration of the commuation mode. Note that in all the cases analysed in this chapter, it was assumed that the diodes do not become transiently forward biased.

6.7 SOLUTION OF THE EQUATIONS

As in section 3.6, the unknowns are calculated from the corresponding equations. For the system with a constant dc link current and a clamping circuit, the unknowns are:

$$t_1, t_2, t_{21}, t_3, t_4, t'_1, t''_1, t_{ch}, t_{tr} \text{ and } t_{co} \qquad (6.7.1)$$

The equations from which the above variables should be computed are:

$$t_{ch} = t_2 - t_1 \qquad (3.3.18)$$

$$-\frac{2}{3C} I_d \cdot t_{ch} + V_o = R_1 I_d - E_1\sqrt{3}\cos(\omega t_2 + \phi_1 - \frac{2\Pi}{3}) \qquad (3.4.4)$$

$$t'_1 = t_{21} - t_2 \qquad (6.3.1)$$

$$E_1\sqrt{3}\cos[\omega(t_2+t'_1)+\phi_1-\frac{2\Pi}{3}]+2L\left.\frac{di_A(t')}{dt'}\right|_{t'=t'_1}$$

$$+2R_1 i_A(t'_1)-R_1 I_d = V_o \qquad (6.3.3)$$

$$t''_1 = t_3 - t_{21}$$

$$I_d - C_{20} - C_{21}e^{-\alpha_1 t''_1} - C_{22}[C_{23}\sin(\omega t''_1+\beta_4)$$

$$- C_{24}\sin(\omega t''_1+\beta_3)] = 0 \qquad (6.4.19)$$

$$t_{tr} = t'_1 + t''_1 \qquad (6.4.20)$$

$$t_{co} = t_{ch} + t_{tr} \qquad (3.4.14)$$

$$t_4 - t_1 = \Pi/3\omega$$

One can see that here again, as in the case without a clamping circuit, there are ten unknowns with nine equations. In the same manner as in section 3.6, by finding the value of t_2 this ambiguity can be overcome and the same number of unknowns and equations would result.

Two methods, one approximate and one exact, are used for calculating t_2 and the other unknowns. Flowchart (6.1) presents

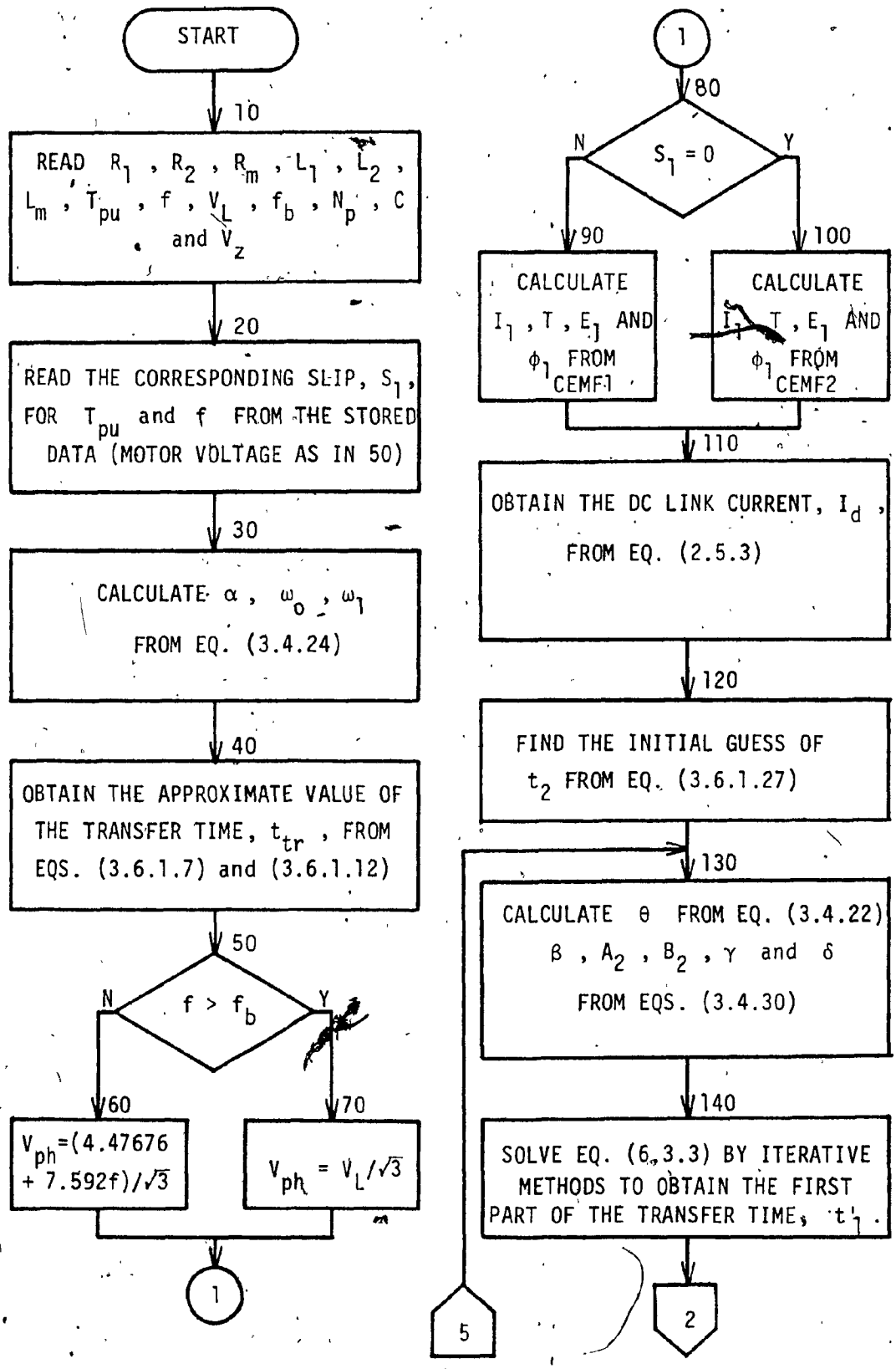
START
10
READ R_1, R_2, R_m, L_1, L_2, L_m, T_{pu}, f, V_L, f_b, N_p, C and V_z
20
READ THE CORRESPONDING SLIP, S_1, FOR T_{pu} and f FROM THE STORED DATA (MOTOR VOLTAGE AS IN 50)
30
CALCULATE α, ω_o, ω_1 FROM EQ. (3.4.24)
40
OBTAIN THE APPROXIMATE VALUE OF THE TRANSFER TIME, t_{tr}, FROM EQS. (3.6.1.7) and (3.6.1.12)
50
$f > f_b$
N
Y
60
$V_{ph}=(4.47676 + 7.592f)/\sqrt{3}$
70
$V_{ph} = V_L/\sqrt{3}$
1
1
80
$S_1 = 0$
N
Y
90
CALCULATE I_1, T, E_1 AND ϕ_1 FROM CEMF1
100
CALCULATE I_1, T, E_1 AND ϕ_1 FROM CEMF2
110
OBTAIN THE DC LINK CURRENT, I_d, FROM EQ. (2.5.3)
120
FIND THE INITIAL GUESS OF t_2 FROM EQ. (3.6.1.27)
130
CALCULATE θ FROM EQ. (3.4.22) β, A_2, B_2, γ and δ FROM EQS. (3.4.30)
140
SOLVE EQ. (6.3.3) BY ITERATIVE METHODS TO OBTAIN THE FIRST PART OF THE TRANSFER TIME, t_1.
5
2

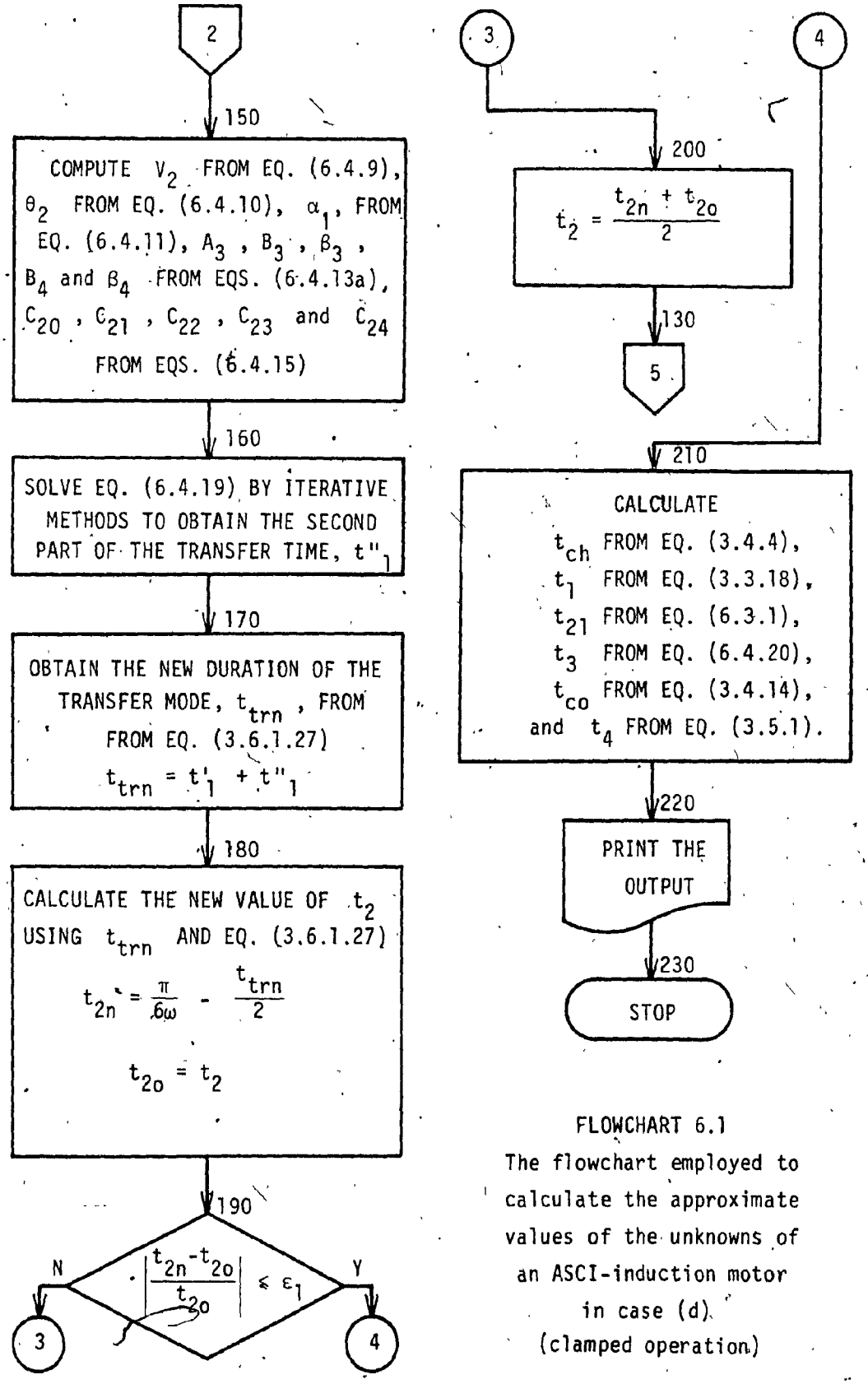

FLOWCHART 6.1
The flowchart employed to calculate the approximate values of the unknowns of an ASCI-induction motor in case (d) (clamped operation)

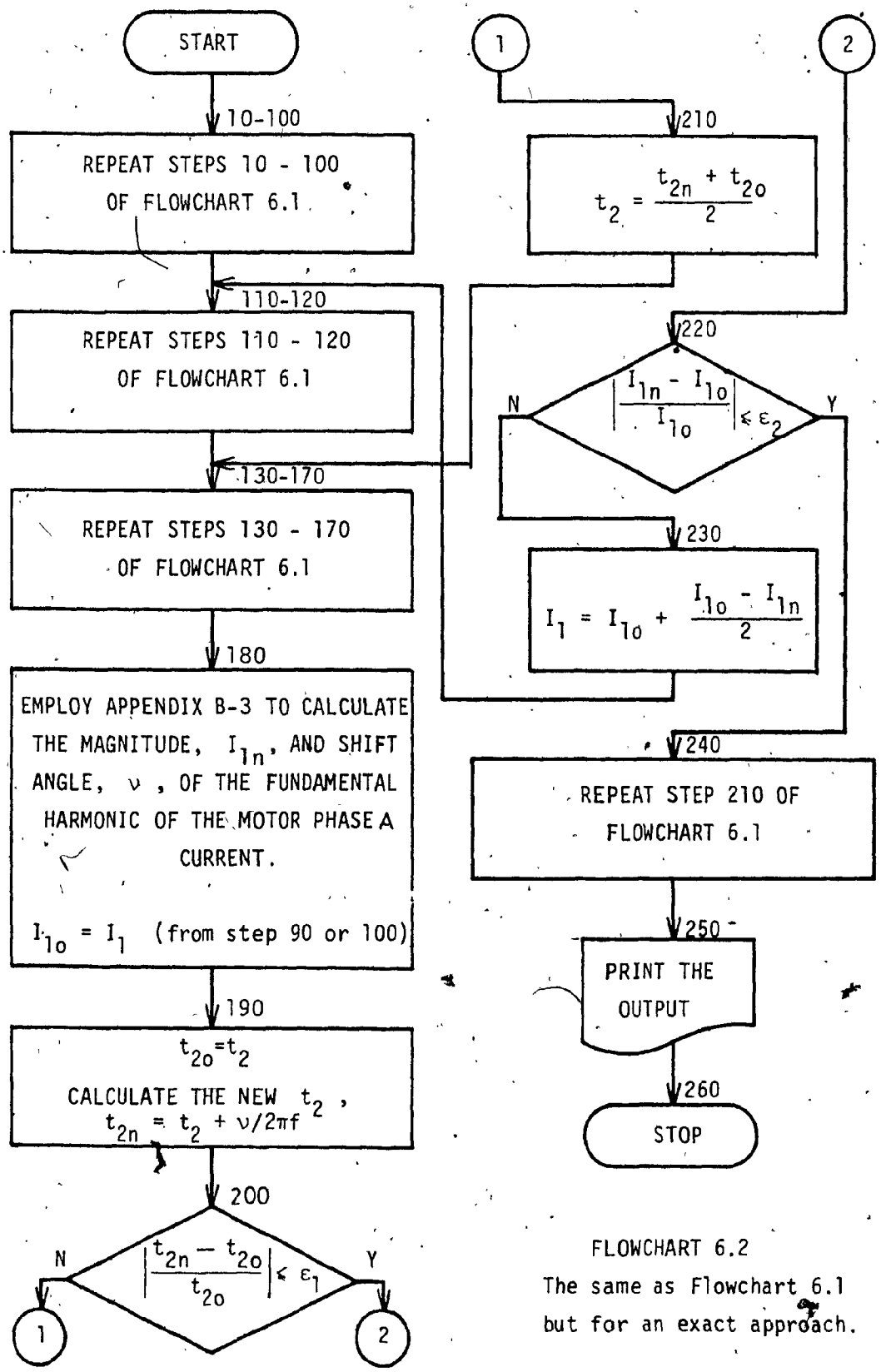

FLOWCHART 6.2
The same as Flowchart 6.1 but for an exact approach.

the details of the approximate approach. This flowchart avoids the calculation of the fundamental harmonic of the motor input current by using the Fourier analysis (Appendix B-3) for obtaining a new t_2 in each iteration. Instead, by assuming trapezoidal motor current waveforms, Eq. (3.6.1.27) is employed to find a new t_2 in each iteration. The execution time of the program defined by this flowchart is much shorter than the one proposed for the exact approach, flowchart (6.2).

For a more accurate solution, flowchart (6.2) can be applied. Most steps of flowcharts (6.1) and (6.2) are similar to each other. The main difference is the way in which t_2 is calculated for each iteration in them. Flowchart (6.2) will be used later for plotting waveforms and graphs describing the operation of the system for case (d).

6.8 WAVEFORMS AND RESULTS

The operation of an ASCI-induction motor drive with a clamping circuit and a constant dc link current was investigated in the previous sections. Flowchart 6.2 was provided for an exact solution of the system equations. This flowchart is employed for plotting two sets of graphs similar to graphs obtained for case (a). The first set shows the voltage and current waveforms for one specific operating point, point (B), in which the clamping circuit limits the peak value of the voltage spikes to the breakdown voltage of the string of zener diodes, V_Z. The specifications of point (B) is given in Appendix A-1. In the second set of graphs, the variations of variables in a clamped condition, case (d), are compared with those obtained in a non-clamped operation, case (a). This comparison reveals the effects of a clamping circuit on the performance of the drive. In order to distinguish the graphs plotted with a clamping circuit from those obtained in a non-clamped condition, two symbols are used with each figure in the second set of graphs. The notation CL identifies the operation with a clamping circuit, while NC signifies a non-clamped operation. Note that curves CL are plotted by using flowchart 6.2, while curves NC are the same as the graphs of figures 5.12 - 5.24, which were obtained by employing flowchart 3.2. Besides, in plotting all the graphs, the core-loss resistance, magnetizing and leakage inductances have been included as explained in section 5.2. In the following, each set of graphs is illustrated and discussed.

6.8.1 Voltage and current waveforms

Figures 6.18 - 6.24 display the voltage and current waveforms of the drive at operating point (B) (Appendix A-1). Figure 6.18 shows phase B voltage, fundamental harmonic and instantaneous currents in a clamped condition. The general forms of the waveforms in this figure are the same as in a no-clamping operation. The only difference is in the clamping of the voltage spikes by the zener diodes, which is clearly seen in fig. 6.18. The phase angle between i_{1B} and e_{1B}, ϕ_1, is also indicated in this figure. Recall that the voltage spikes are superimposed on the motor CEMF's so that the sinusoidal part of v_B shows the CEMF of phase B, e_{1B}. Figure 6.19 is similar to fig. 6.18 but with phase A fundamental harmonic and instantaneous currents. In the other graphs of the first set, wherever applicable, phase A current waveform is provided so that these graphs can be compared with experimental results. Figure 6.20 shows v_{AB} and i_A where the peak value that a voltage spike can reach is 1050 V as determined by the breakdown voltage of the zener diodes. Note that, while the duration of each voltage spike shows the interval of a transfer mode, the clamping period may be identified by the clamped part of each voltage spike.

Figure 6.21 exhibits the voltage across and the current through the zener diodes. The voltage waveform, v_z, shows six spikes in each inverter output frequency. Each voltage spike corresponds to a spike generated across two motor terminals during a transfer mode. The flat parts of these spikes illustrate the clamping periods. The other parts of v_z waveform merely show the motor rectified terminal

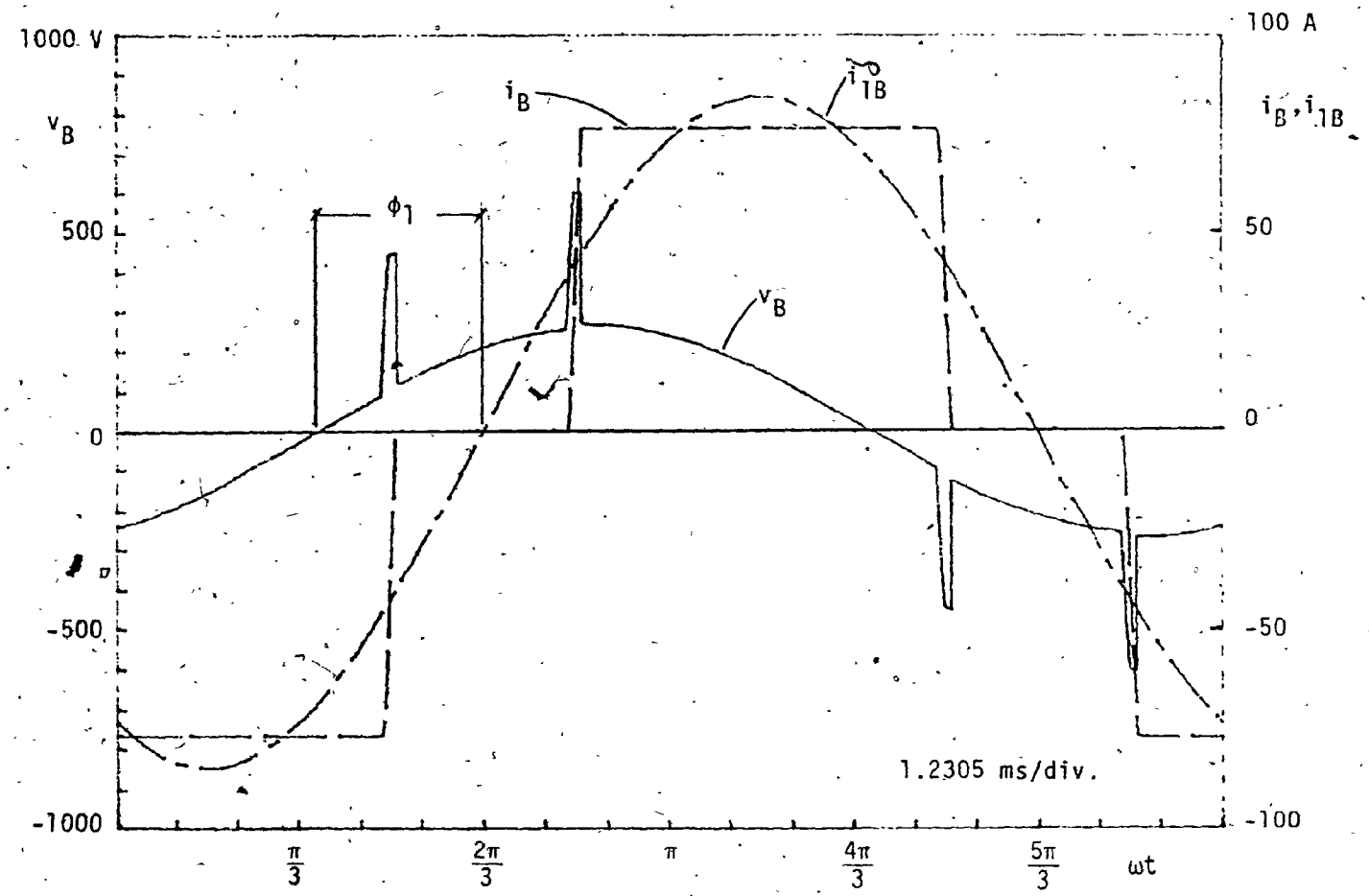

FIG. 6.18 The motor phase B voltage, instantaneous and fundamental harmonic current waveforms for a clamped operation at point (B).

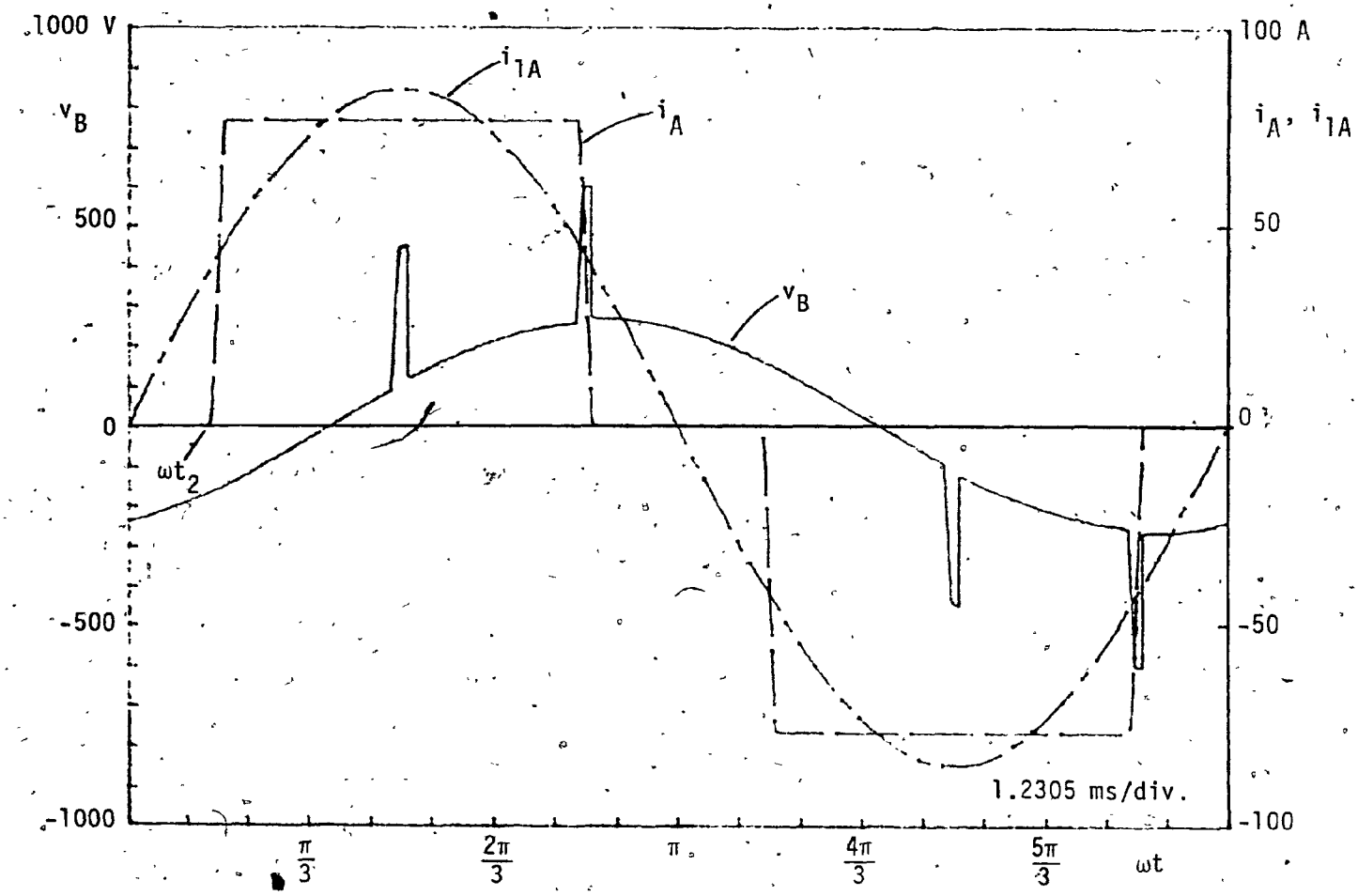

FIG. 6.19 The motor phase B voltage, the phase A instantaneous and fundamental harmonic current waveforms for a clamped operation at point (B).

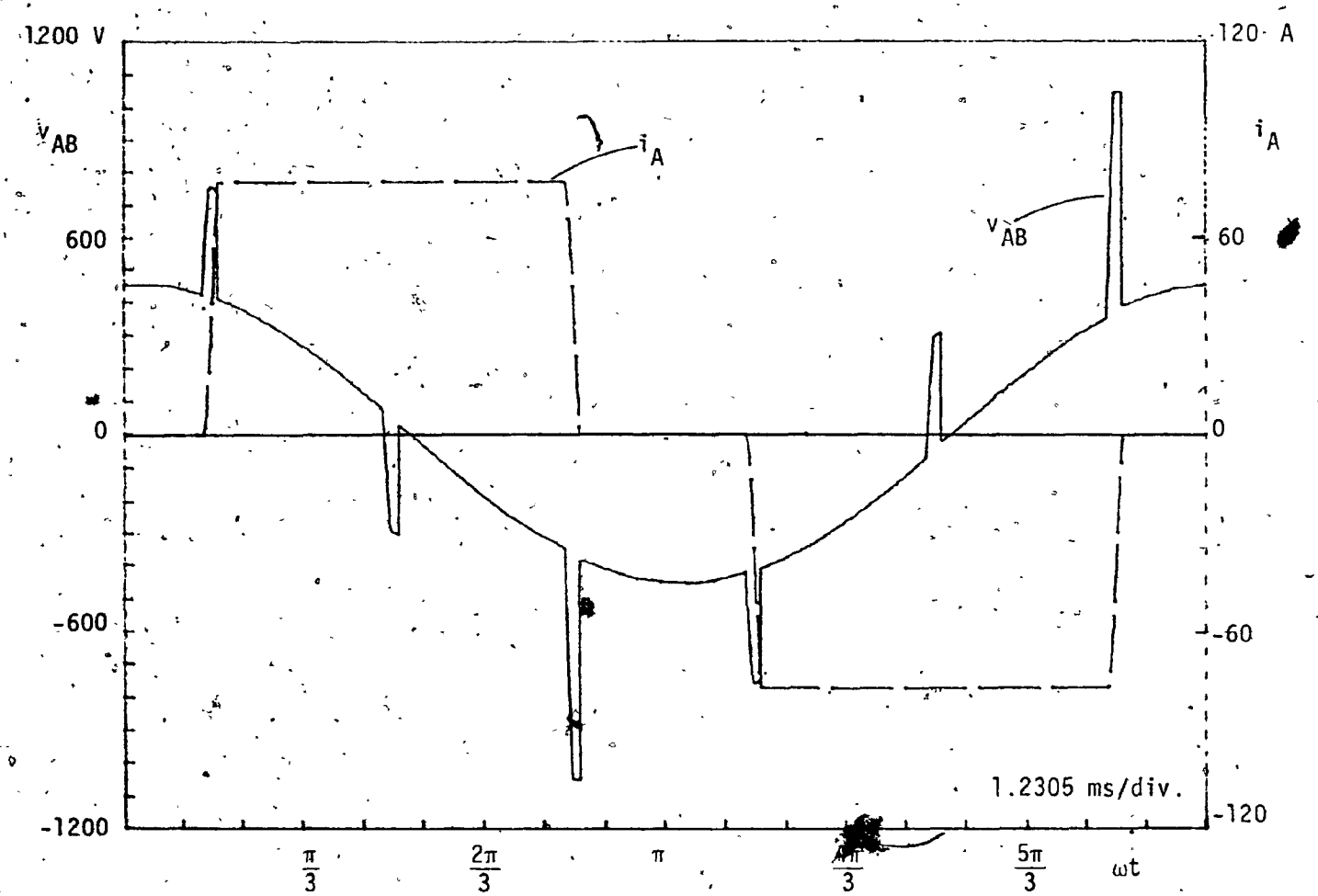

FIG. 6.20 The motor line AB voltage and phase A current waveforms for a clamped operation at point (B).

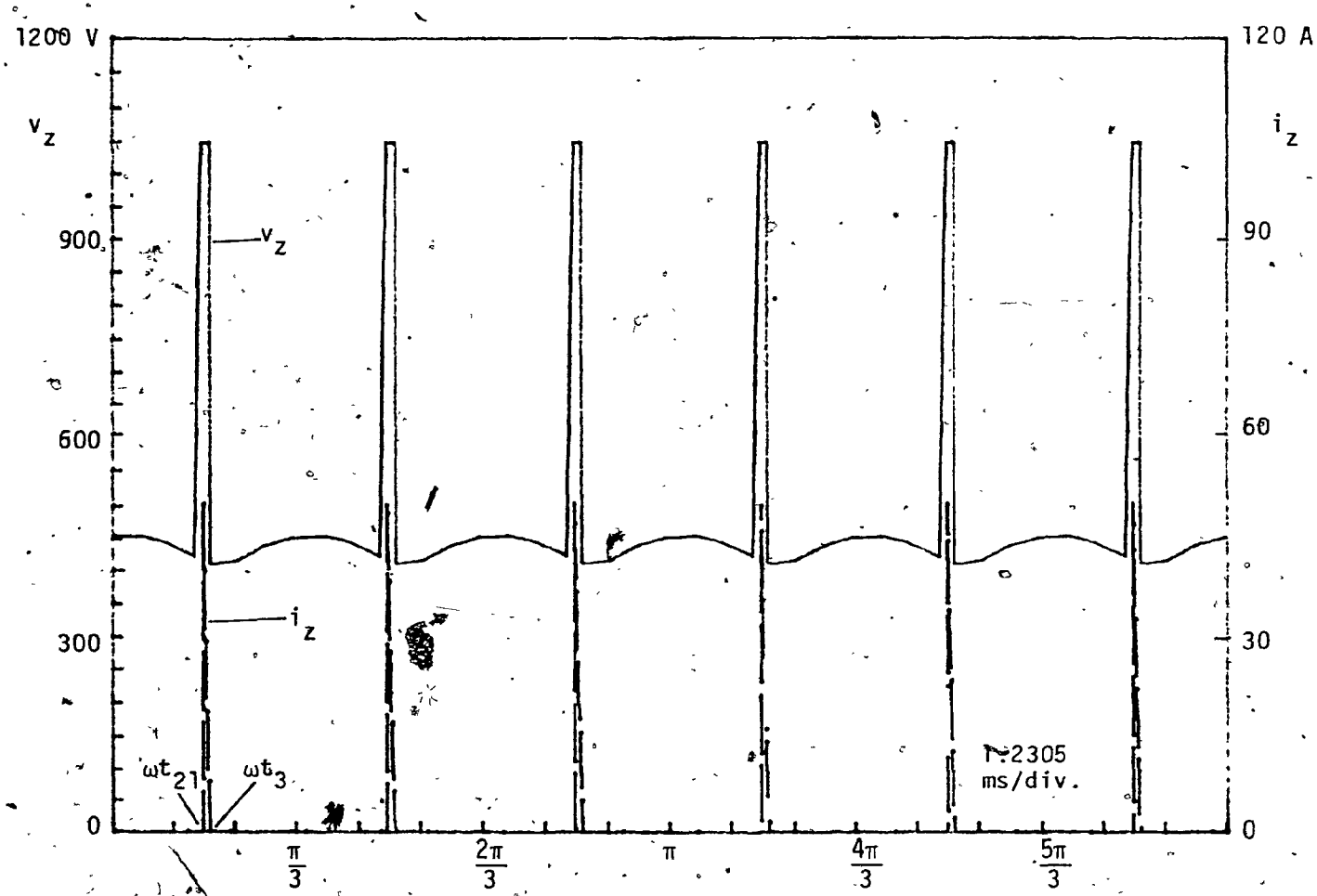

FIG. 6.21 The waveforms of the voltage across and the current through the string of zener diodes for a clamped operation at point (B).

voltages. The i_z waveform yields the current passed through the zener diodes in each clamping period. It is noticed that as soon as a voltage spike starts to be clipped off, the current in the clamping circuit jumps from zero to a maximum value which is then decreased gradually to zero. This current ceases flowing at the end of each clamping or transfer mode. The maximum value of the clamping circuit current is equal to the current in an out-going motor phase at the instant a clamping mode starts.

Figure 6.22 shows v_{C1} and i_{C1} at point (B). This figure demonstrates the change which occurs in the capacitor current waveform when the system goes under a clamping. It is noticed that at ωt_{21}, which is the beginning of a clamping mode, i_{C1} suddenly falls to zero while v_{C1} reaches its peak value, v_z. As it will be shown later, fig. 6.37, the RMS current of a commutating capacitor has a lesser value in a clamped condition than in a similar unclamped operation.

Figure 6.23 shows v_{D1} and i_{D1} in which the effect of voltage clamping is noticed in both waveforms. In v_{D1} the spikes are clipped off while in i_{D1} there is a sudden drop to zero at ωt_{81}. Note that v_{D1} is zero during $\omega(t_9-t_{81})$ without any current flowing through it. The diode minimum reverse voltage occurs at ωt_{14} while its maximum reverse voltage may appear at ωt_1 or at ωt_{18}, depending on the operating point.

The last figure in the first set shows v_I and I_d, fig. 6.24. Here again the clamped parts of the spikes show the clamping

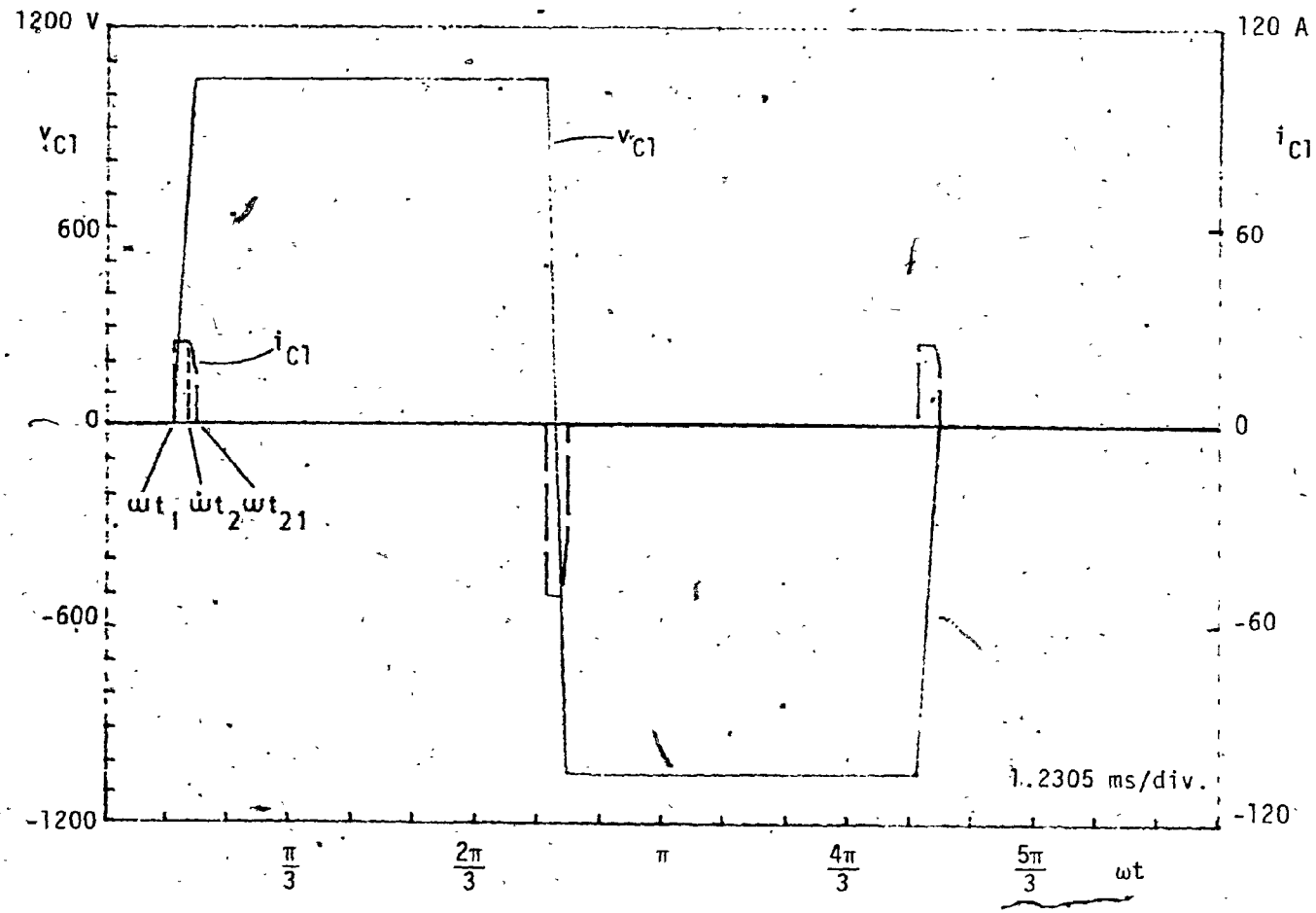

FIG. 6.22 The commutating capacitor C_1 voltage and current waveforms for a clamped operation at point (B).

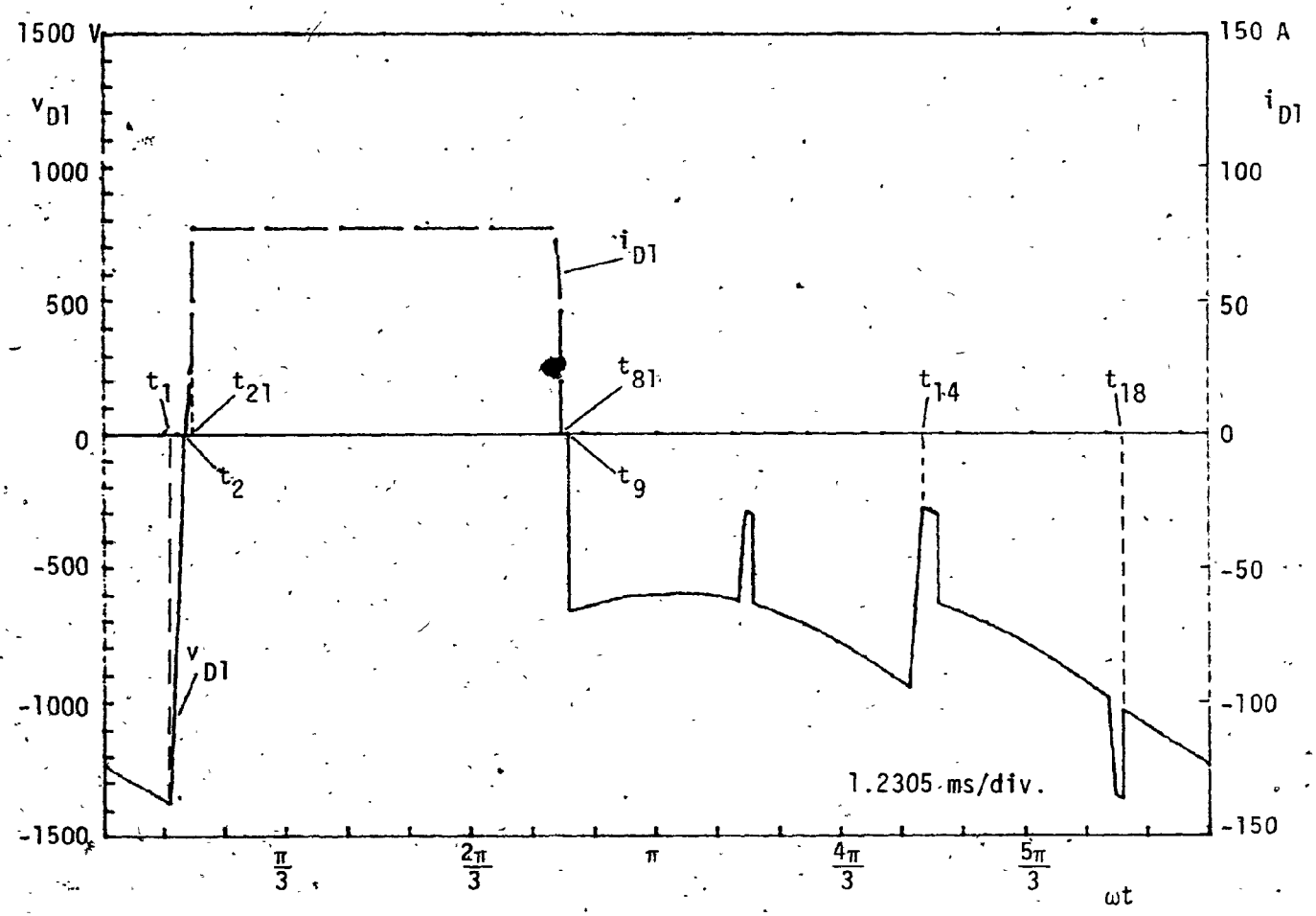

FIG. 6.23 The voltage and current waveforms of the diode D_1 for a clamped operation at point (B).

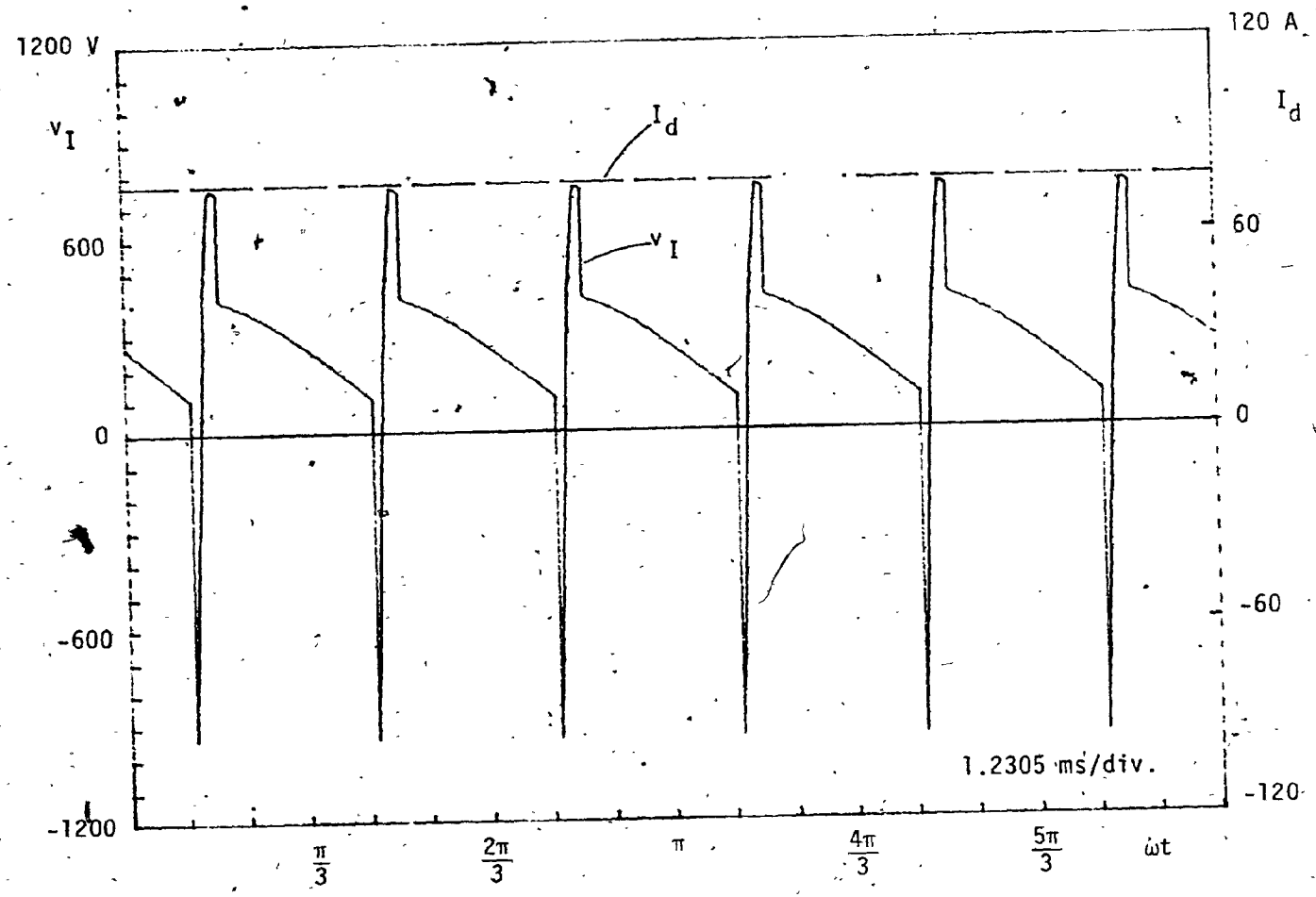

FIG. 6.24 The inverter input voltage and dc link current waveforms for a clamped operation at point (B).

periods.

6.8.2 Comparison between the variations of variables in case (d) and case (a).

In order to distinguish the effects of clamping on the system behaviour, the variations of each variable obtained in this case, curves CL , wherever applicalbe, are compared to their counterparts resulted in section (5.4), curves NC .

Figure 6.25 shows the duration of the clamping periods for different output torques. It is noticed from this figure that for T=0. PU torque, the clamping starts at f = 30 Hz and lasts up to f = 95 Hz . Also, the maximum clamping interval occurs at 60 Hz for this torque. For T=.5 PU, the clamping starts at f = 25 Hz and continues for the whole range of frequency (f_{max} = 125 Hz) . For T=1. PU and up, the clamping occurs at all frequencies. The maximum frequency for T=1., 1.5 and 2. PU torque is seen to be f = 110, 80 and 70 Hz, respectively. The reason can be extracted from figures 6.26 and 6.27. Figure 6.26 shows the power loss in the clamping circuit. It is noticed that for T=1., 1.5 and 2. PU, increasing the frequency results in higher dissipation in the zener diodes. This power, along with the power consumed by the motor should be supplied by the bridge rectifier. Figure 6.27 displays the comparison of the bridge average output voltages, V_I , with clamping, curves CL , and without clamping, curves NC . While for curves NC there is a limit for V_I for T=1. and 2. PU, curves CL keep increasing as the fre-

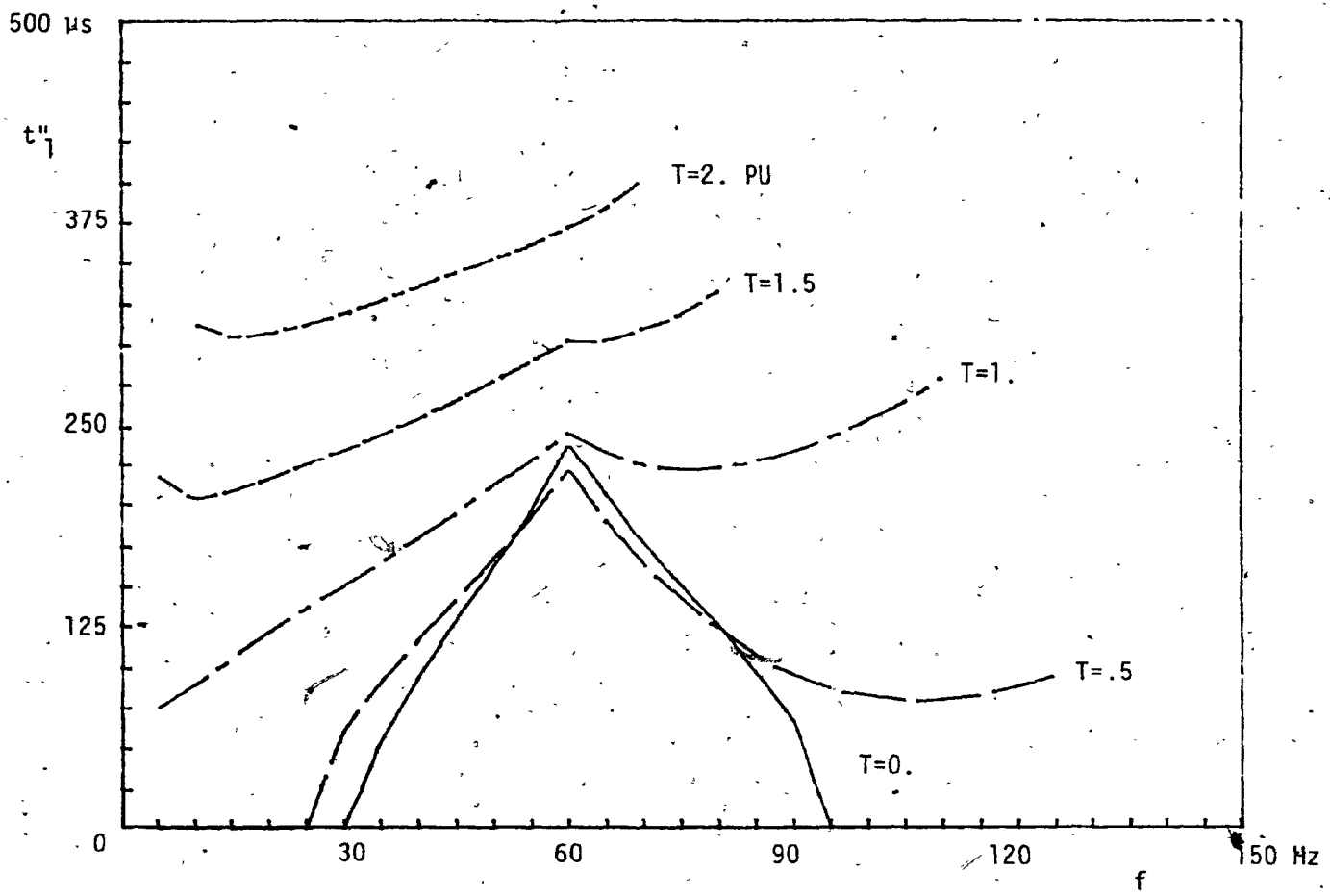

FIG. 6.25 Duration of a clamping mode (the second part of a transfer mode), t''_1, at different load conditions in case (d).

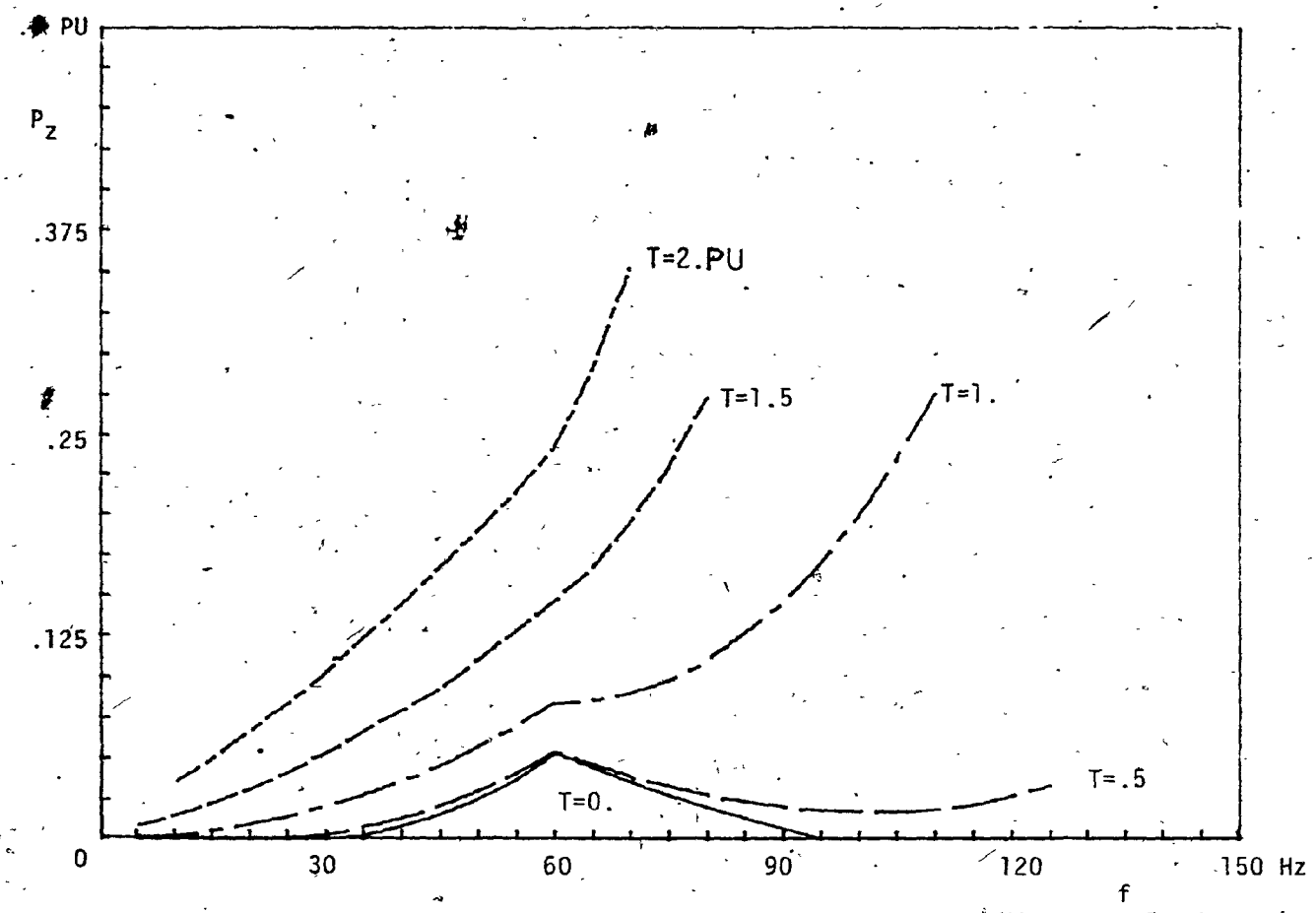

FIG. 6.26 Power loss in the zener clamping circuit, P_z, at different load conditions in case (d).

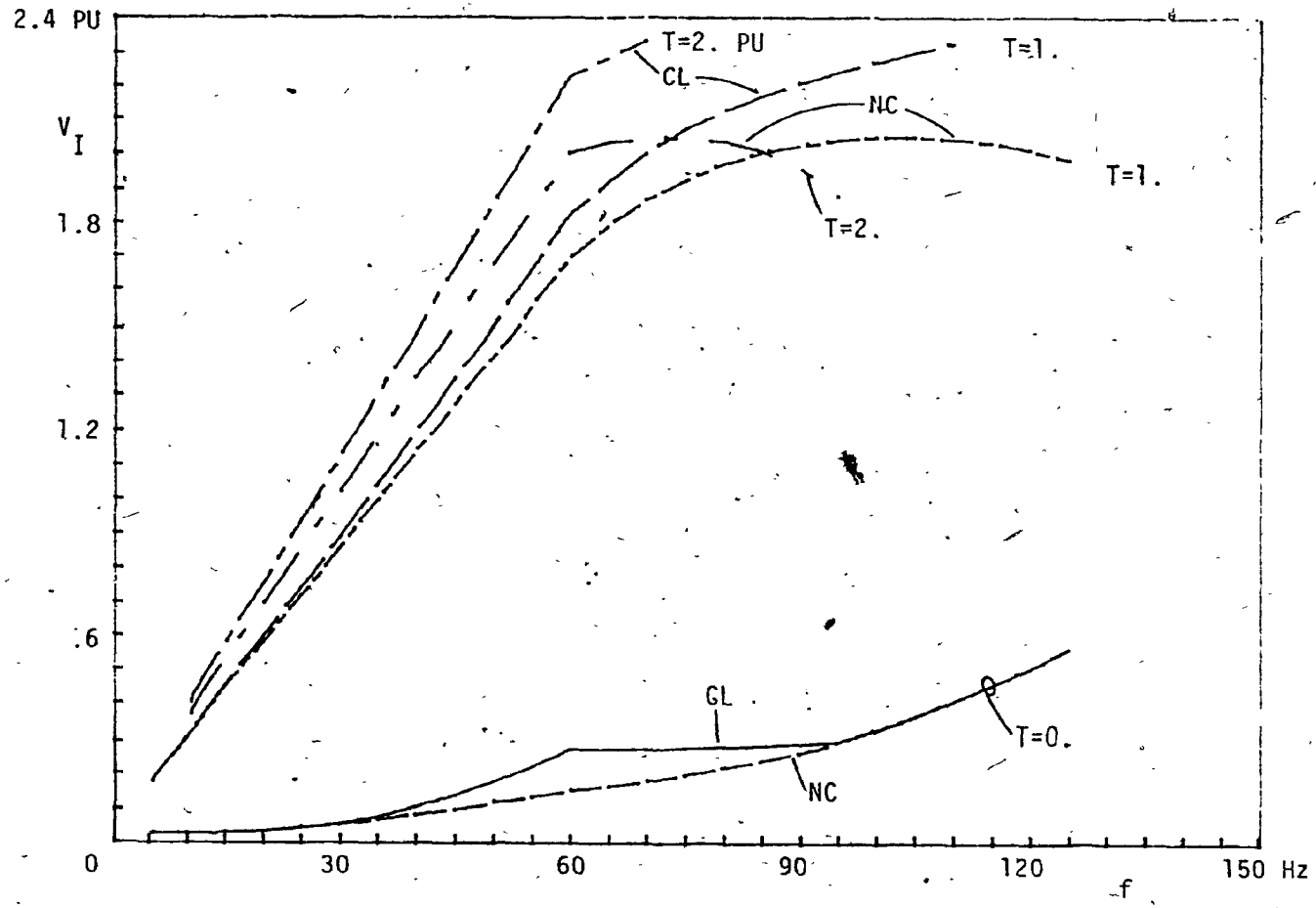

FIG. 6.27 Comparison of the inverter average input votlages, V_I, obtained in case (d), curves CL, with those calculated in case (a), curves NC, at different load conditions.

quency goes up. At some frequency for each torque there will be a situation at which the bridge firing angle reaches its minimum value, i.e. zero, for which V_I has its maximum possible value. For T=1. PU, this limit frequency is 110 Hz, while for T=2. PU it is 70 Hz. Going above these frequencies, if the corresponding torques are going to be kept as before, would not be possible. Increasing the frequencies beyond these limits causes a reduction in the output torques. Figures 6.28 and 6.29 show the maximum and RMS zener currents respectively. The zener diodes are designed according to their maximum power loss, fig. 6.26, and their maximum current, fig. 6.28, at the highest load and frequency.

The comparison between charging time and angles is reflected in figures 6.30 and 6.31, respectively. It is noticed that the effect of clamping is a decrease in these two quantities. For transfer times and angles, the clamping effect is in the opposite direction, figures 6.32 and 6.33. While curves NC in fig. 6.32 show an almost constant value at all torques for t_{tr}, curves CL show an increase in this variable which by increasing the torque this difference becomes even greater. The overall effect of clamping on commutation process is shown by figures 6.34 and 6.35, where curves CL indicate values almost the same as curves NC .

The commutating capacitor maximum voltage is displayed in figure 6.36, where a constant level, V_z, equal to the breakdown voltage of the zener diodes is maintained at all clamped operating points, curves CL . In a clamped condition, the capacitors are charged for

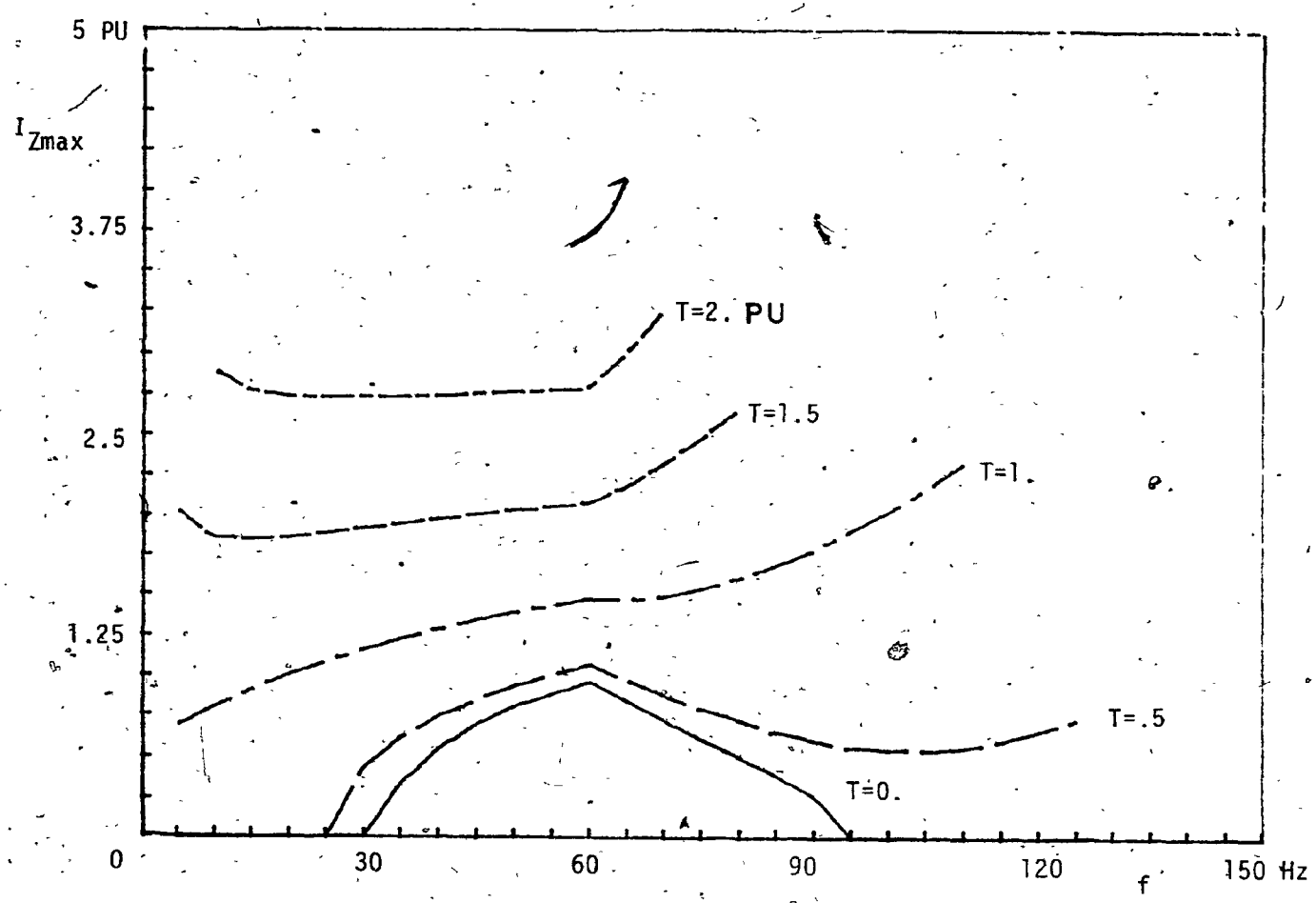

FIG. 6.28 Maximum current in the zener clamping circuit, I_{Zmax}, at different load conditions in case (d).

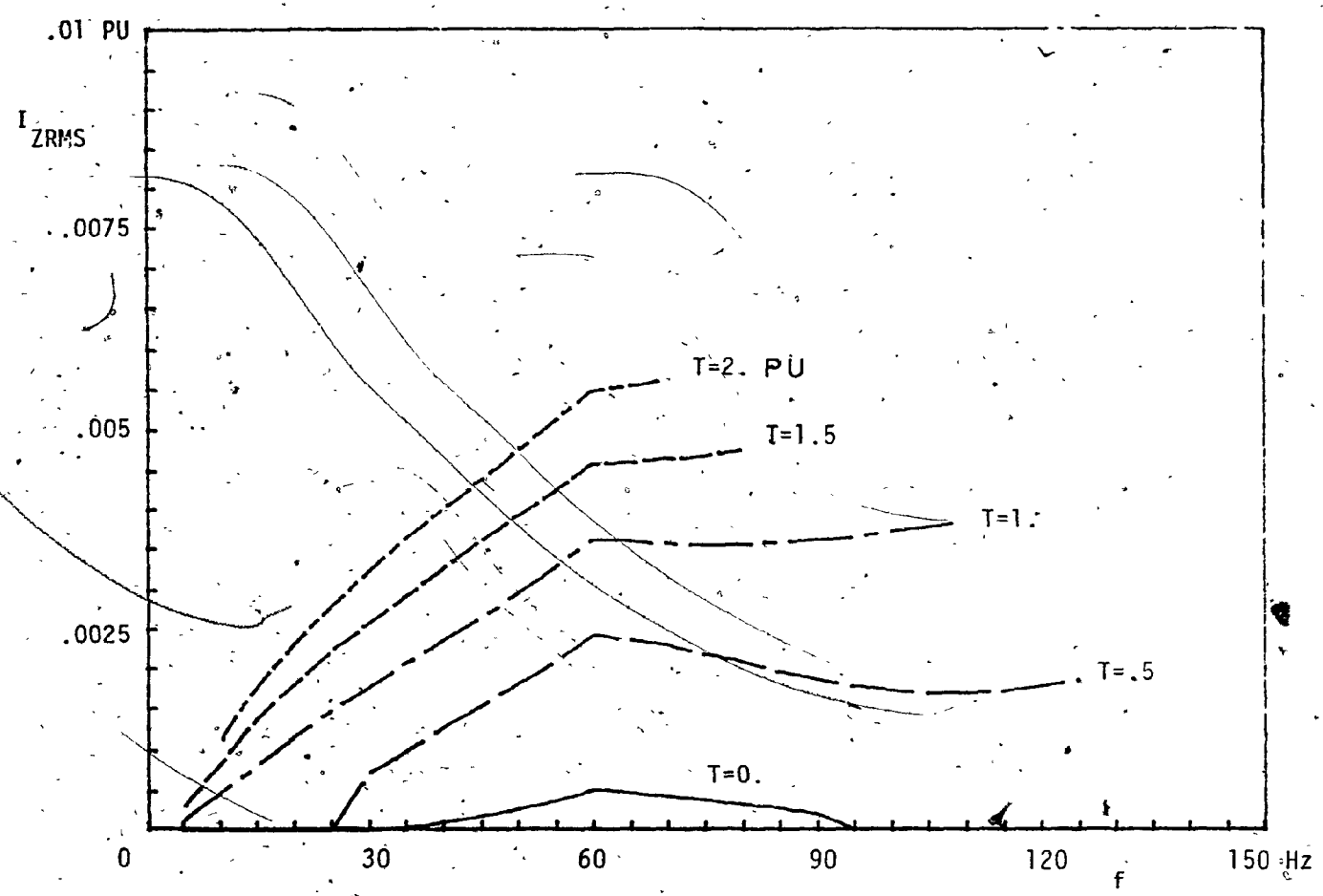

FIG. 6.29 RMS current of the zener clamping circuit, I_{ZRMS}, at different load conditions.

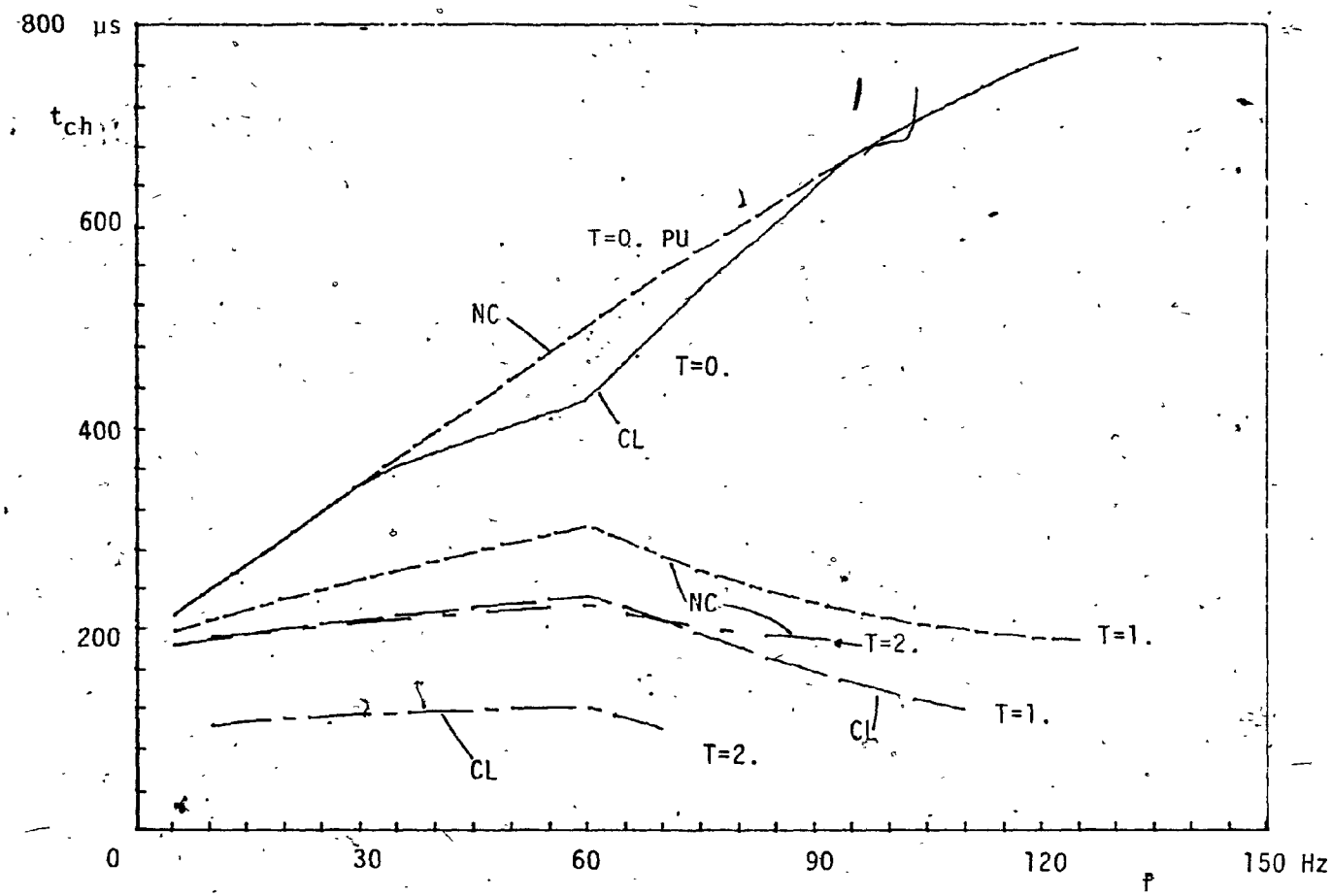

FIG. 6.30 Comparison of the charging mode intervals, t_{ch}, obtained in case (d), curves CL, with those calculated in case (a), curves NC, at different load conditions.

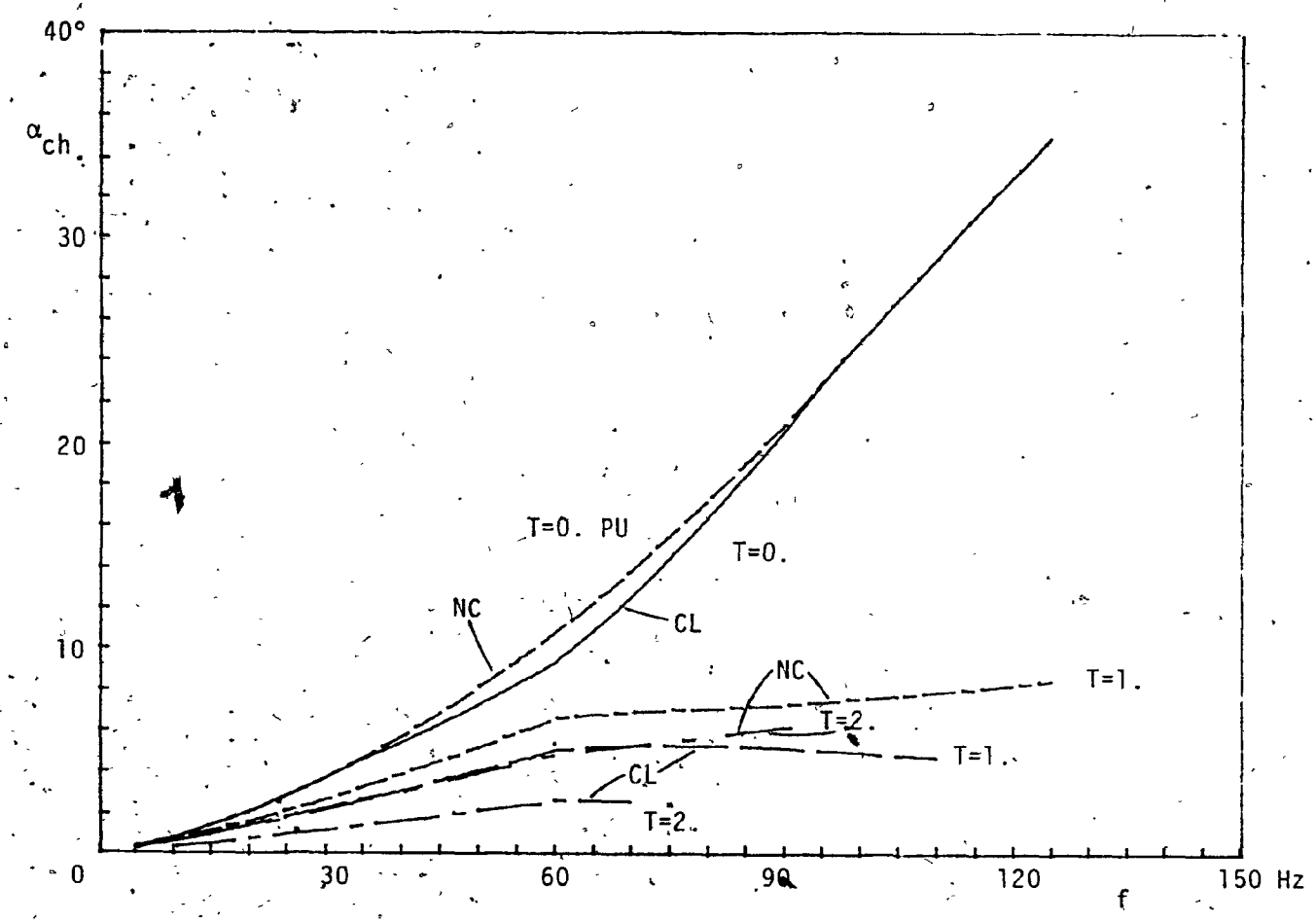

FIG. 6.31 Comparison of the charging mode angles, α_{ch}, obtained in case (d), curves CL, with those calculated in case (a), curves NC, at different load conditions.

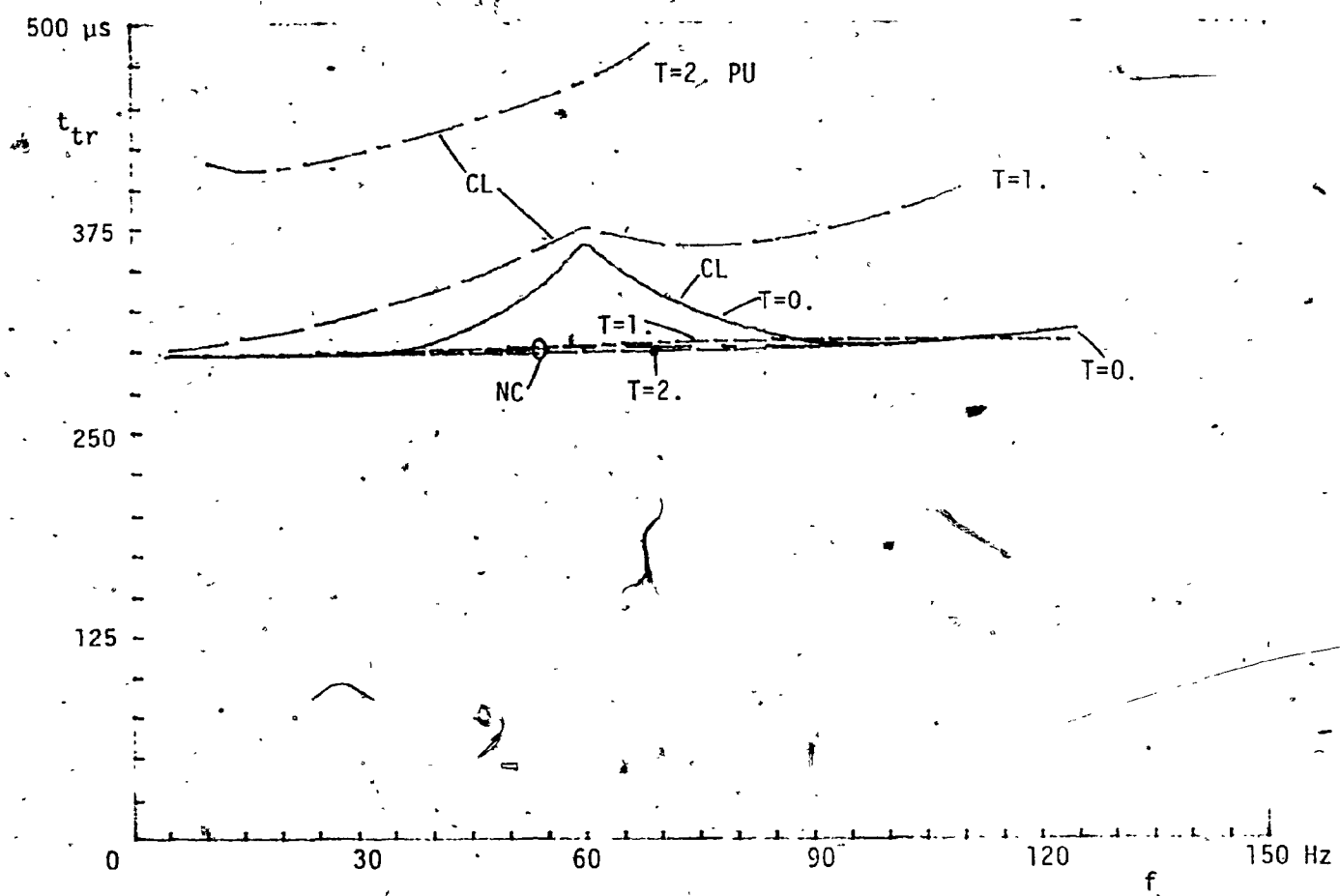

FIG. 6.32 Comparison of the transfer mode intervals, t_{tr}, obtained in case (d), curves CL, with those calculated in case (a), curves NC, at different load conditions.

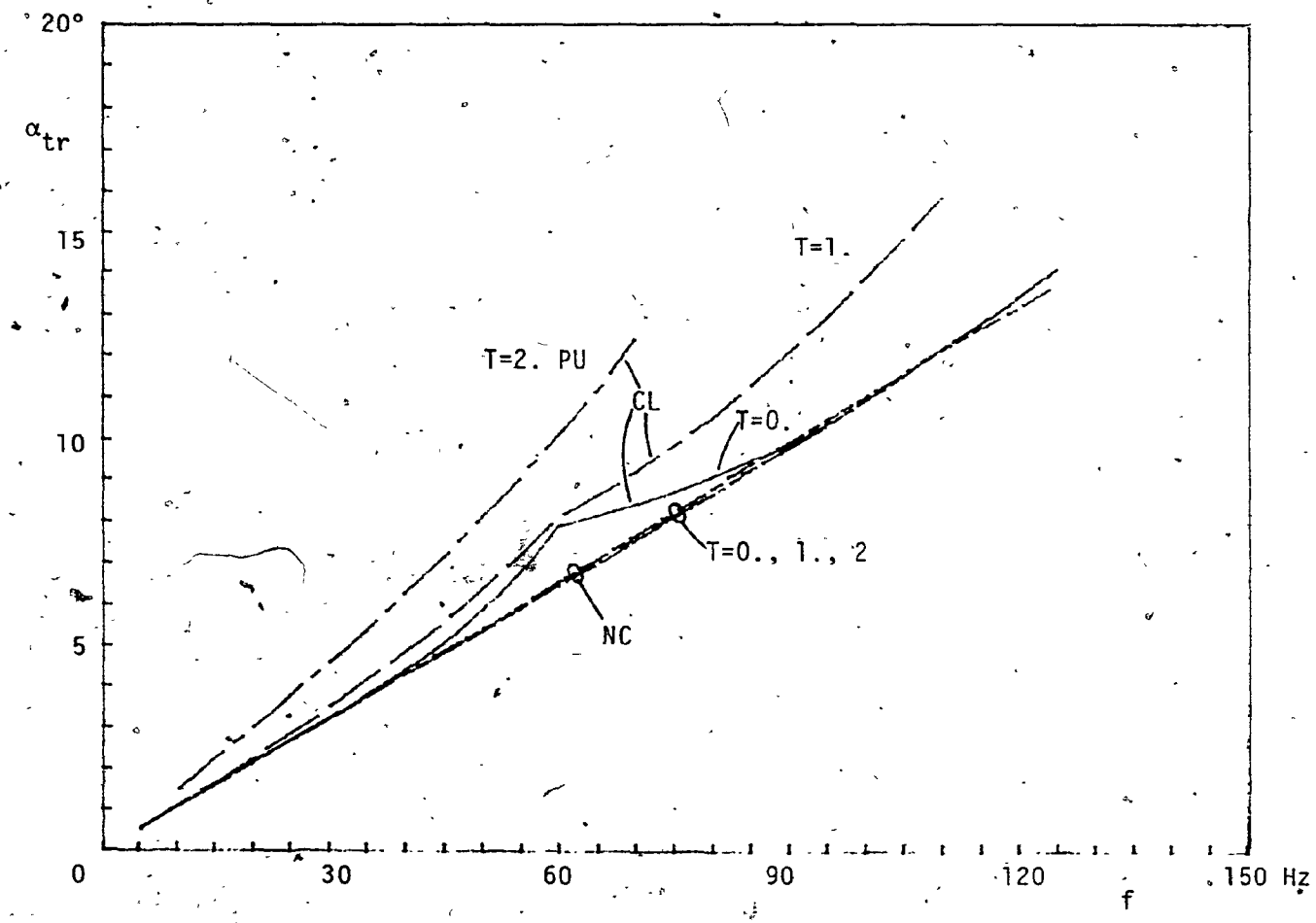

FIG. 6.33 Comparison of the transfer mode angles, α_{tr}, obtained in case (d), curves CL, with those calculated in case (a), curves NC, at different load conditions.

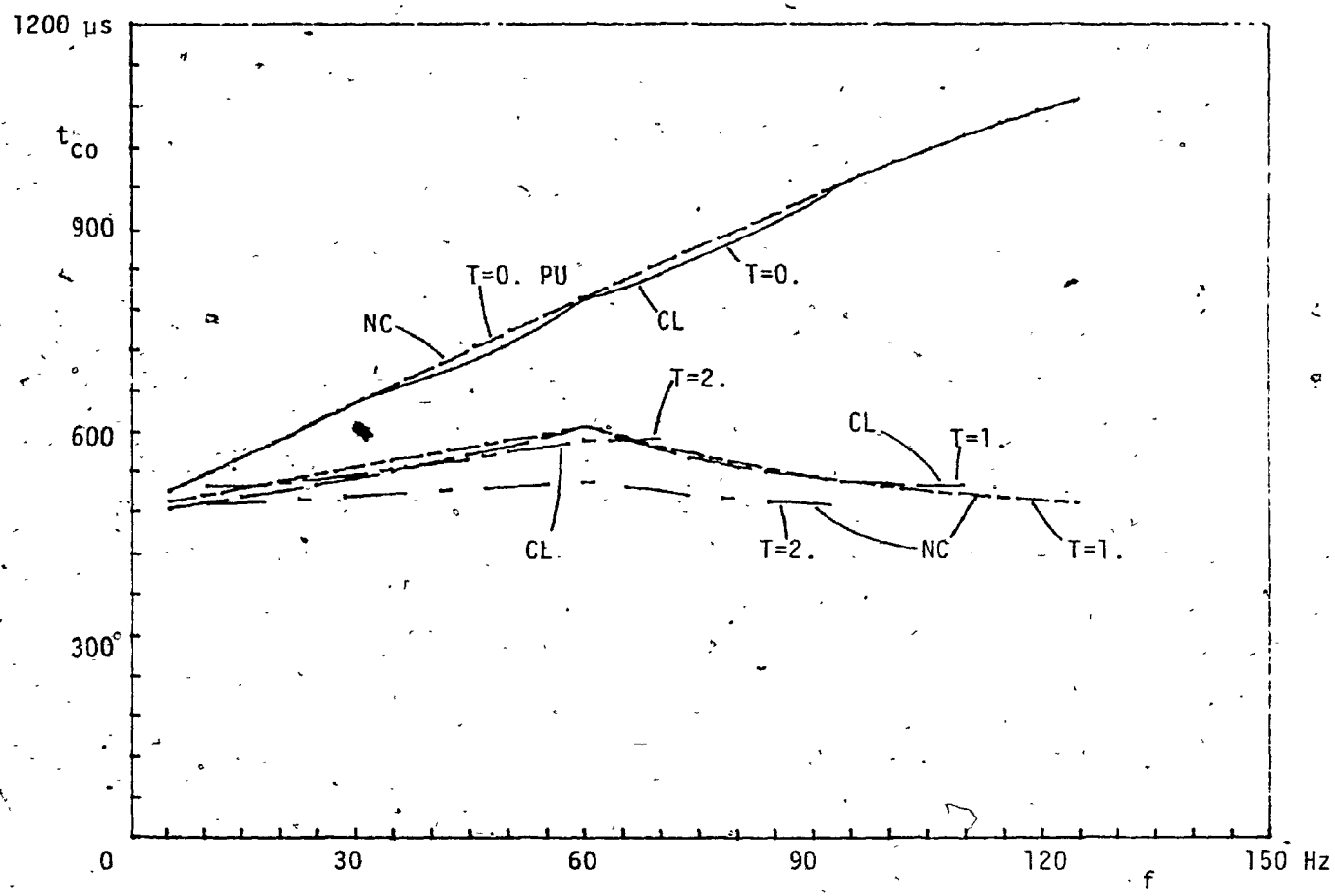

FIG. 6.34 Comparison of the commutation intervals, t_{co}, obtained in case (d), curves CL , with those calculated in case (a), curves NC , at different load conditions.

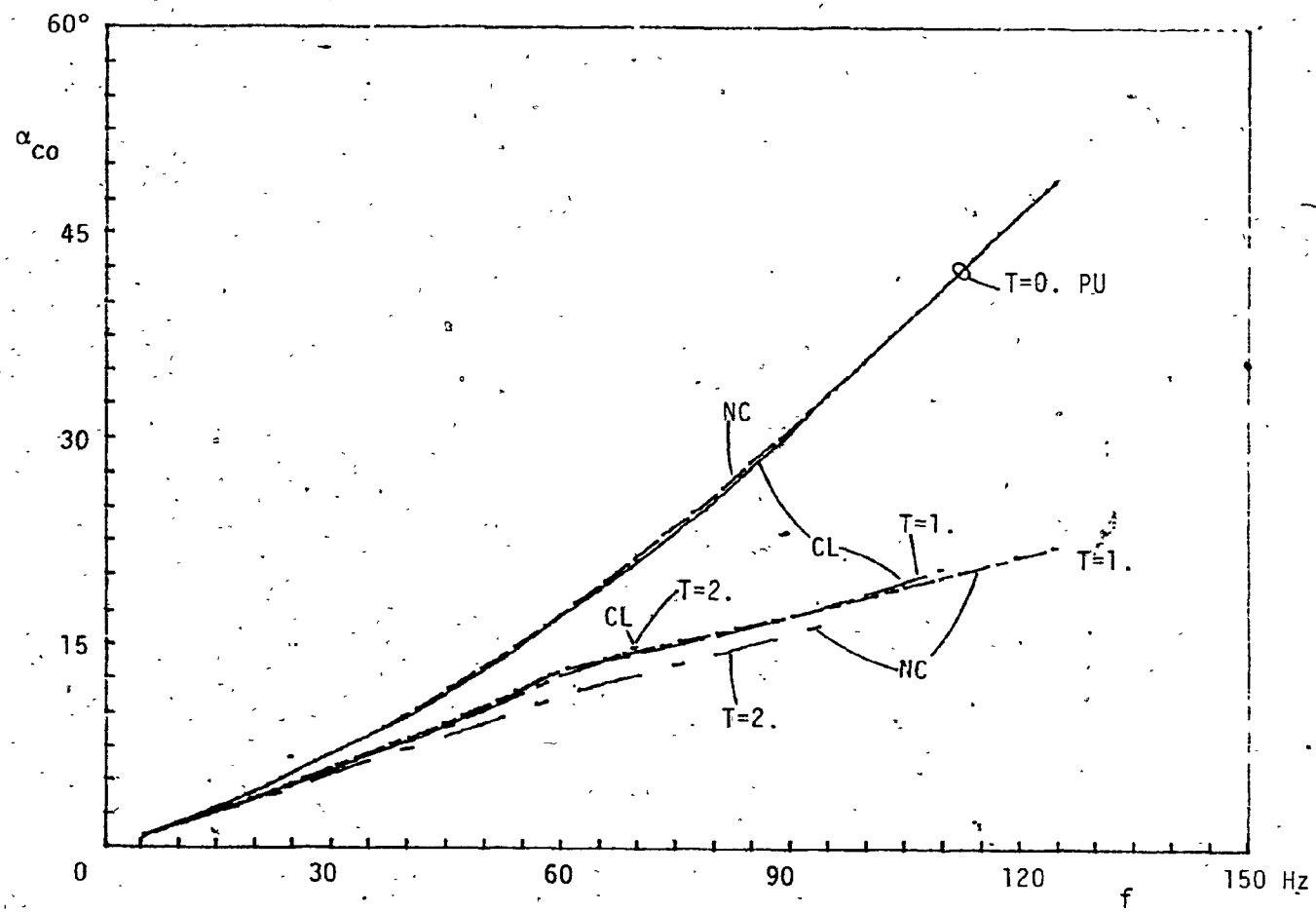

FIG. 6.35: Comparison of the commutation angles, α_{co}, obtained in case (d), curves CL, with those calculated in case (a), curves NC, at different load conditions.

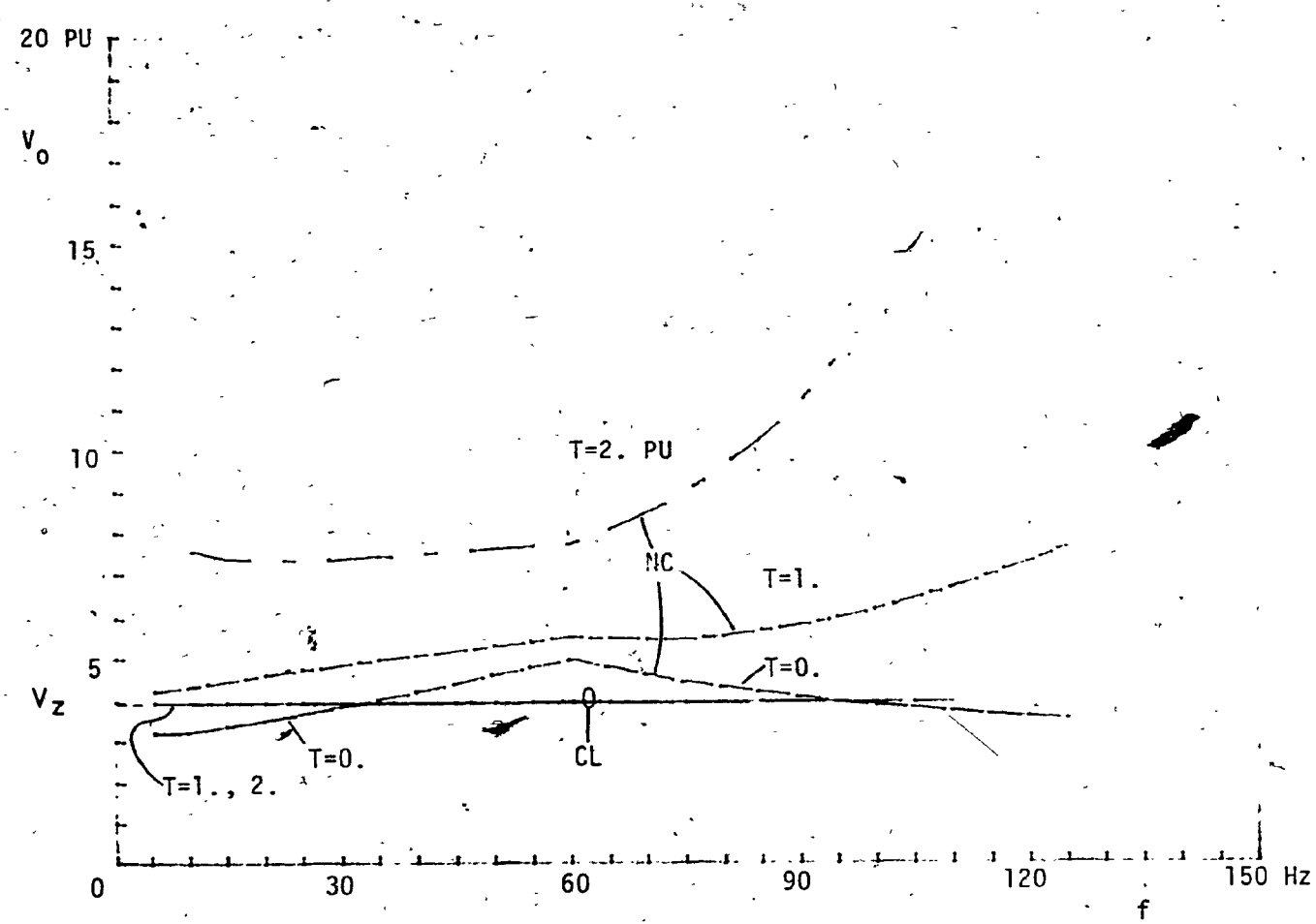

FIG. 6.36 Comparison of the capacitor maximum voltages, V_o, obtained in case (d), curves CL, with those calculated in case (a), curves NC, at different load conditions.

shorter intervals than in a non-clamped operation. The total charging period is obtained by adding t_{ch}, fig. 6.30, to the difference of t_{tr} and t''_1, e.g. $(t_{tr} - t''_1)$, as extracted from figures 6.32 and 6.25, respectively, while the same operating point is applied to all three figures. The result is implicitly demonstrated by figure 6.37 where the commutating RMS current is shown for two cases. As expected, at the same torque, curves CL show less RMS charging currents than curves NC.

Available thyristor turn-off time in a clamped condition is less than the time in an unclamped case, fig. 6.38. The reason is mainly due to shorter capacitor total charging periods which cause the capacitor maximum voltage to be limited to V_z.

Due to the clamping circuit losses, the system efficiency is decreased when there is a clamping of spikes, fig. 6.39. By including the thyristor and diode losses, this efficiency becomes even less so that it might not be reasonable to run the drive under some conditions for long periods.

At last, figures 6.40 and 6.41 show the results of comparison for the diode reverse minimum and maximum voltages. It is noticed from figure 6.40 that the clamping reduces the diode minimum reverse voltage, V_{DRmin}, so that the inverter becomes more susceptible to the transient forward biasing of the isolating diodes. The main reason is due to the limit which is imposed on the commutating capacitor maximum voltage, fig. 6.36, which also decreases the diode reverse maximum voltage, fig. 6.41.

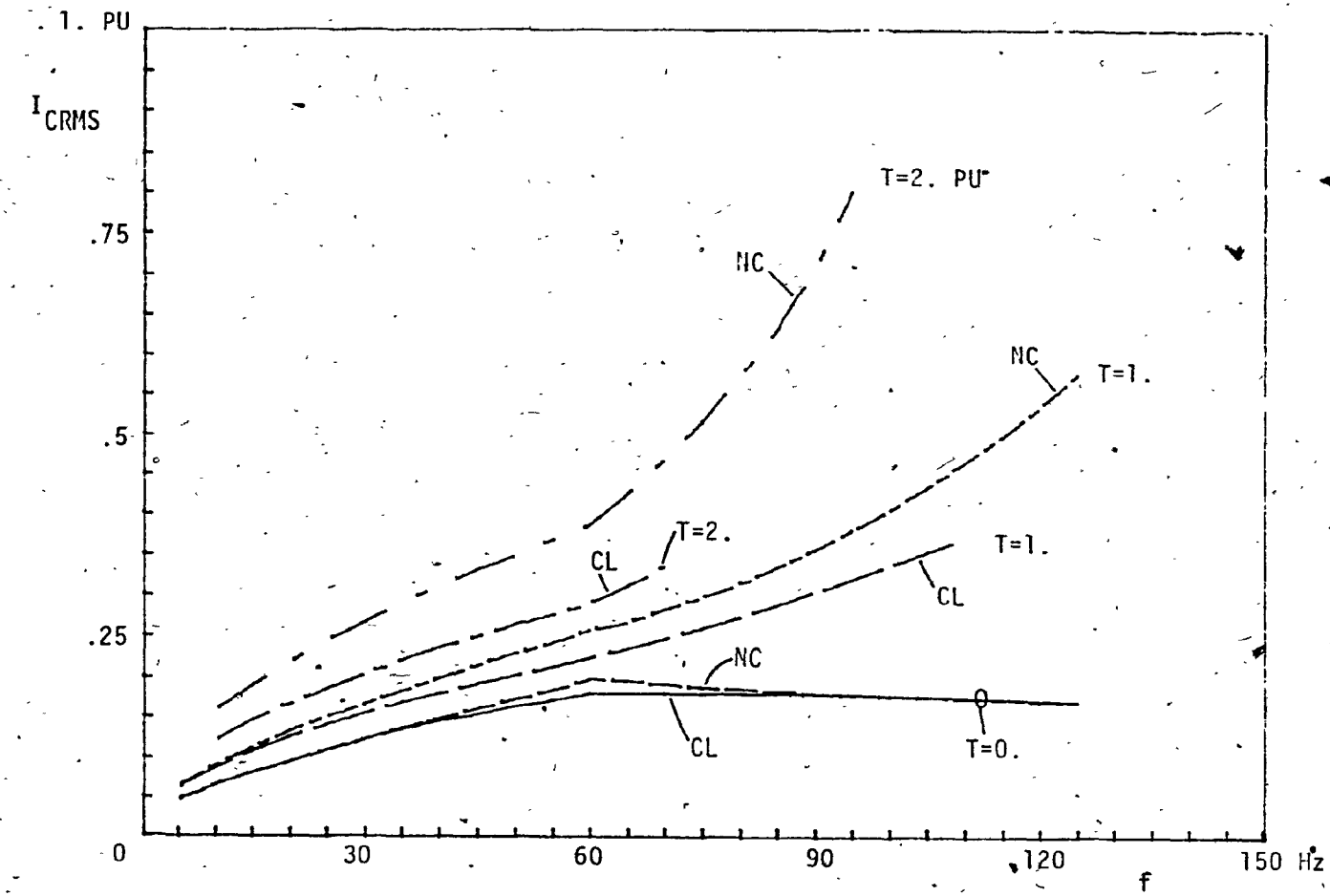

FIG. 6.37 Comparison of the commutating capacitor RMS currents, I_{CRMS}, obtained in case (d), curves CL, with those calculated in case (a), curves NC, at different load conditions.

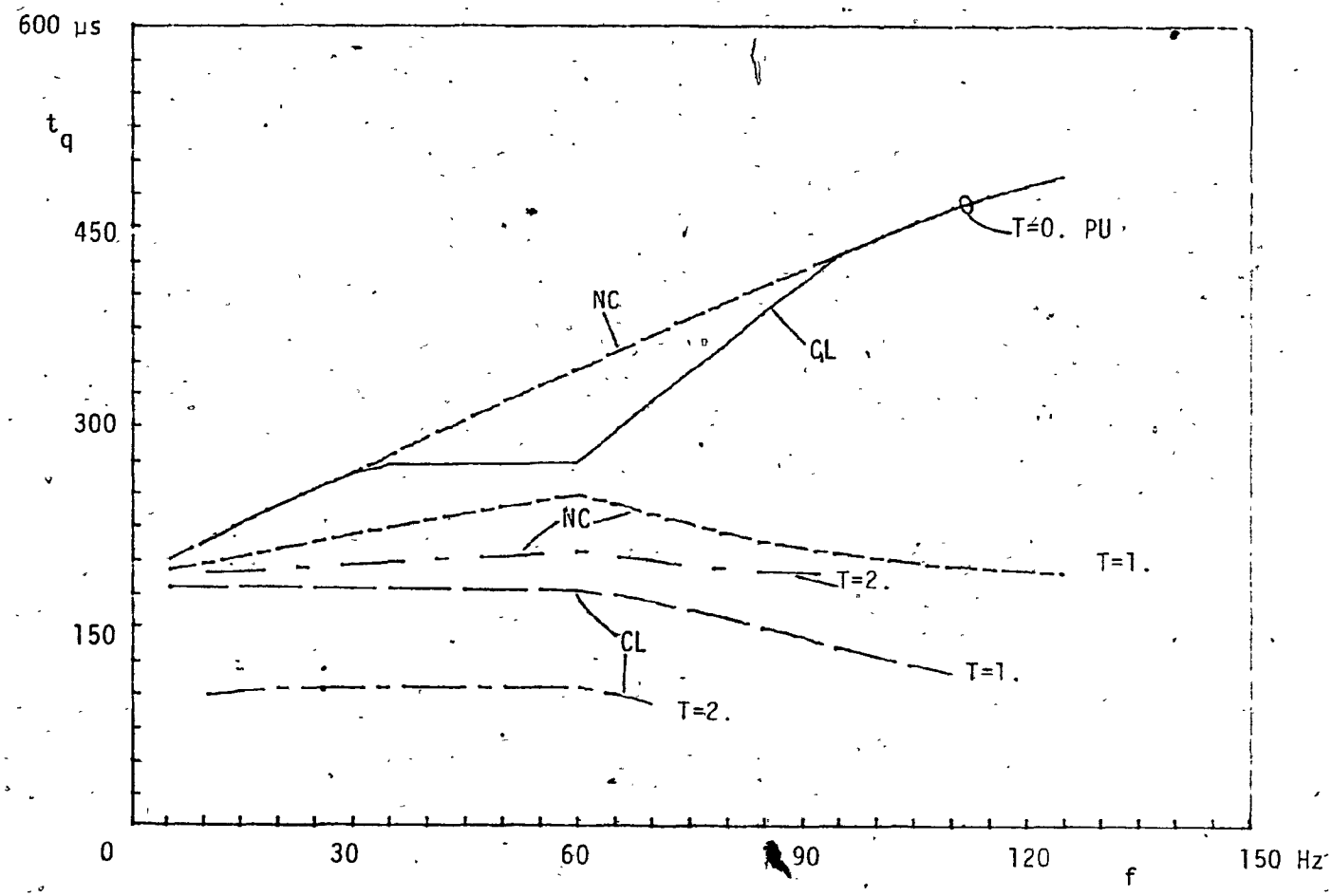

FIG. 6.38 Comparison of the available thyristor turn-off times, t_q, obtained in case (d), curves CL, with those calculated in case (a), curves NC, at different load conditions.

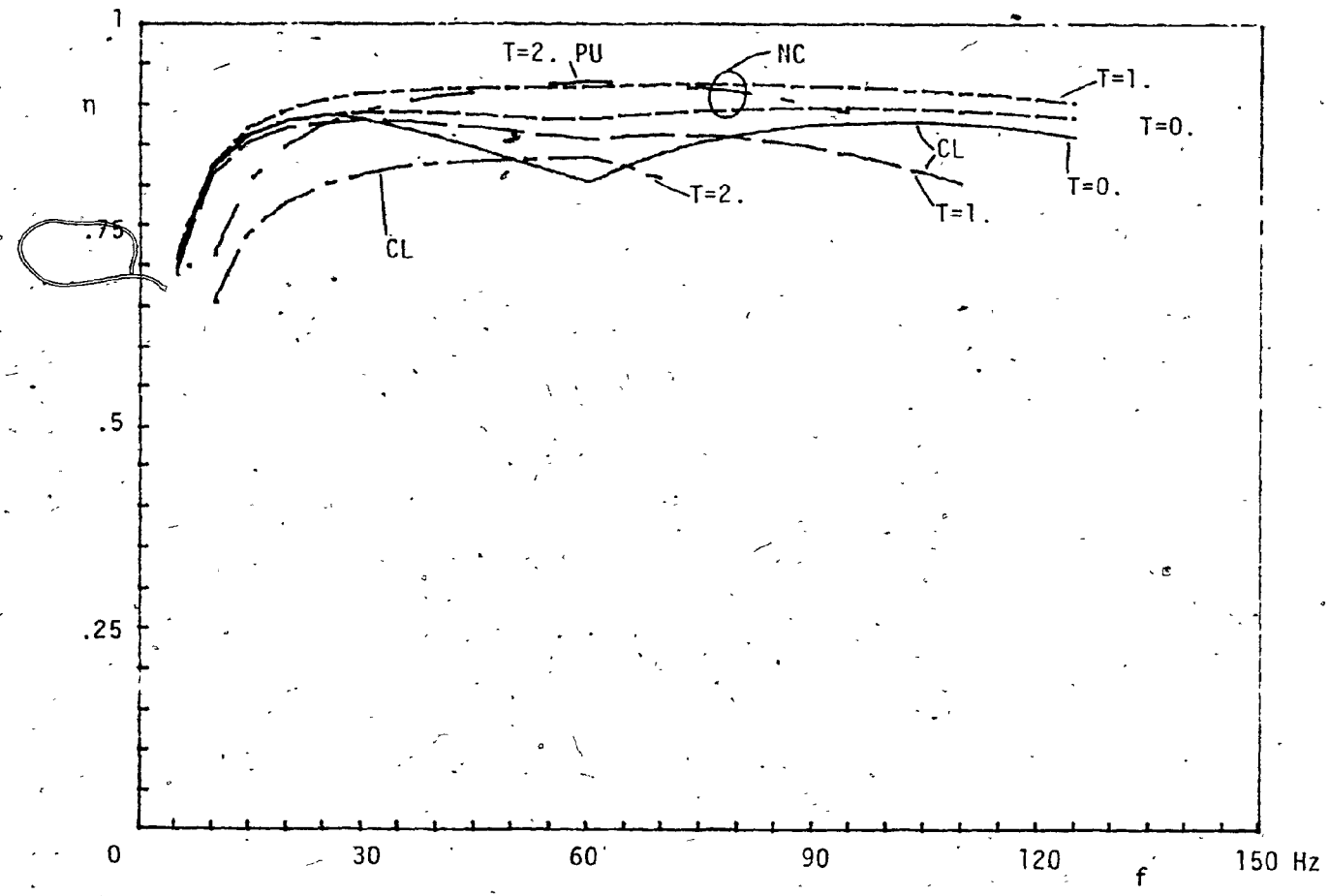

FIG. 6.39 Comparison of the system efficiencies (without considering thyrsitor and diode losses), η, obtained in case (d), curves CL, with those calculated in case (a), curves NC, at different load conditions.

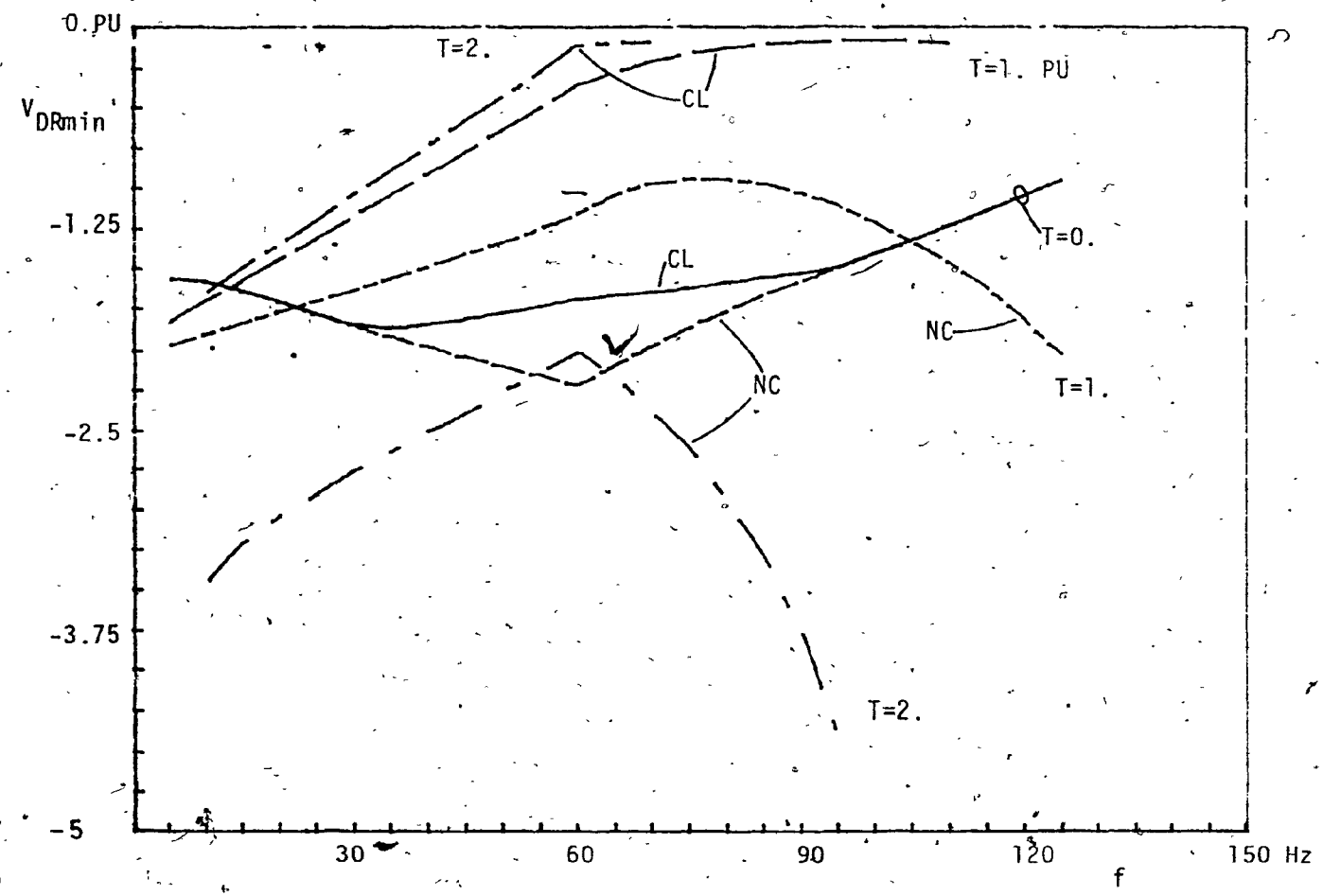

FIG. 6.40 Comparison of the diode minimum reverse voltages, V_{DRmin}, obtained in case (d), curves CL, with those calculated in case (a), curves NC, at different load conditions.

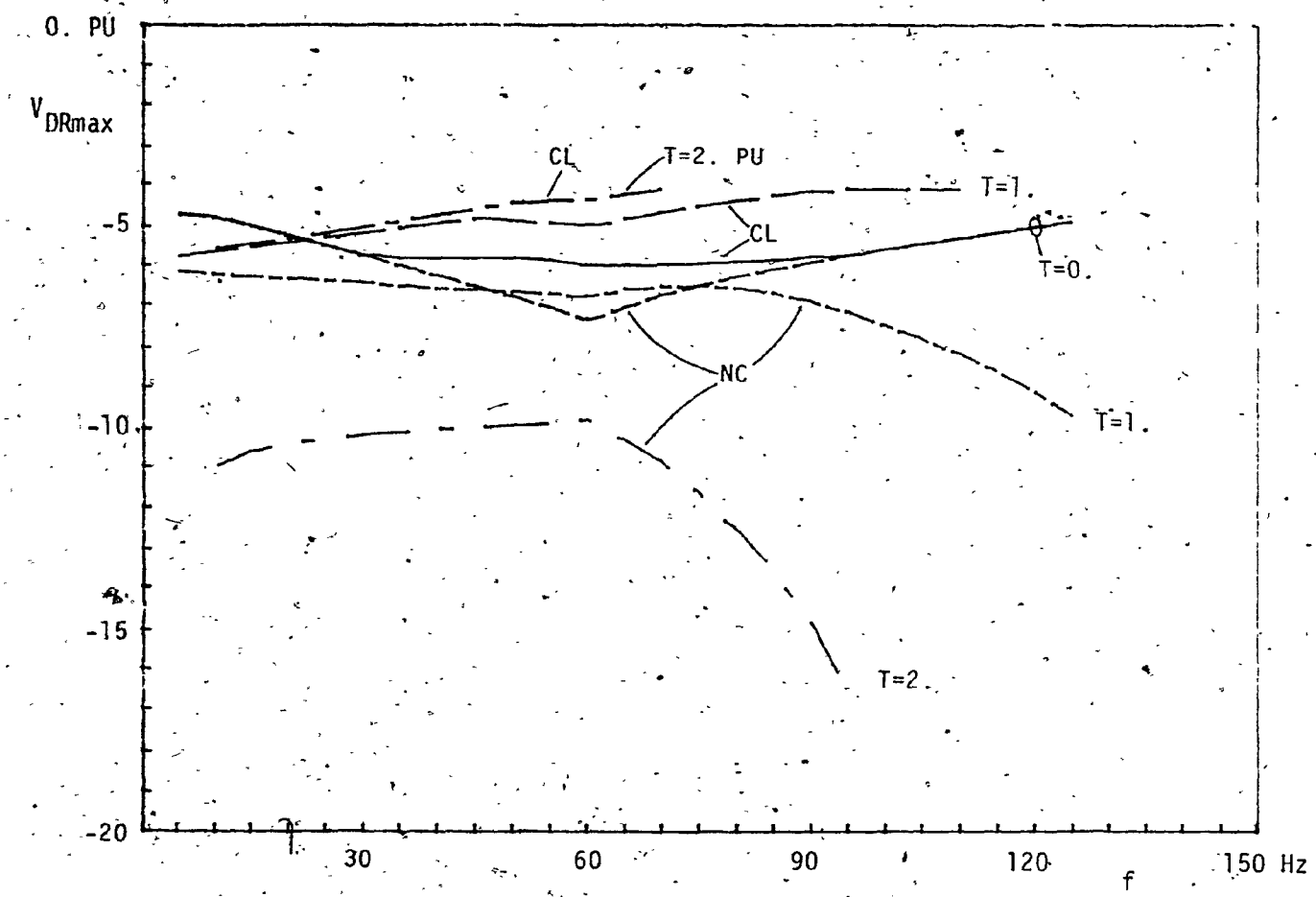

FIG. 6.41. Comparison of the diode maximum reverse voltages, V_{DRmax}, obtained in case (d), curves CL, with those calculated in case (a), curves NC, at different load conditions.

6.9 CONCLUSION

By employing a clamping circuit the peak value of voltage spikes generated across the terminals of an induction motor connected to an ASCI can be limited to a desired level. The steady-state operation of an ASCI-induction motor drive with a zener clamping circuit and a constant dc link current was analyzed in detail. The necessary expressions were obtained by studying four consecutive modes. One of these modes is the mode in which the second part of a transfer of a current from one phase to the other phase is completed through the zener diodes while the commutating capacitors stay out of the system. Two flowcharts, one approximate and one exact, were provided for calculating the system variables. Two sets of graphs were plotted by using the exact flowchart. The first set displayed the different current and voltage waveforms under one specific operating point. In the second set of graphs the variations of each variable obtained in a system with a clamping circuit were compared with those attained in a system without a clamping circuit. The salient result from the second set of graphs was that the use of a clamping circuit limits the maximum inverter output frequency. This limitation is the price which is paid for lower voltage ratings of the inverter components in such a system.

The case of a partial commutation overlap (with a clamping circuit) was also investigated. It was revealed that the same key equations (and the same flowcharts) used for determining the system variables in a no-overlap operation are still valid for a partial overlap operation. The only requirement is that no isolating diodes should get transiently forward biased.

CHAPTER VII

MATHEMATICAL MODELING OF THE ASCI-INDUCTION MOTOR DRIVE WITH A CONSTANT VOLTAGE ACROSS THE CONVERTER OUTPUT AND NO CLAMPING CIRCUIT CASE (g)

7.1 INTRODUCTION

In the previous chapters we studied the behaviour of the system assuming a smooth and constant dc link current. This implies a very large dc link inductance which is not realistic. In fact, this inductance is made as small as possible in the design of industrial current source-induction motor drives. The magnitude of the dc link inductance is usually ten times that of the sum of the stator and rotor leakage inductances per phase and is determined by the permissible ripple factor of the dc link current and also by the stability criteria [4 , 12].

It is obvious then that the assumption of a constant dc link current is inconsistent with the operation of a realistic ASCI. Since the average value of the voltage across the rectifier bridge output is constant for each operating point, the assumption of a constant dc link current can be replaced by the assumption of a constant rectifier output voltage. In this case the problem of an auto-sequentially commutated inverter fed by a constant current source changes into that of an ASCI fed by a constant voltage source.

Almost all of the expressions derived with the assumption of a constant voltage are different from those obtained in the analysis

of the system with a constant dc link current. The study of the system with the assumption of the constant voltage results in the following major points:

1) During each charging mode we have an RLC circuit which results in an oscillatory component in the dc link current. This oscillatory component is partially responsible for the 'bumps' which are easily distinguished in any waveforms of the dc link or motor input currents in an actual ASCI-induction motor drive.

2) Since the dc link current is not constant any longer the commutating capacitors are charged at a different rate which affects the charging time.

3) Due to ripples in the motor input currents, the motor terminal voltages are distorted not only during the transfer modes which are characterized by voltage spikes but almost during the whole period of the inverter output. In this sense the waveforms obtained in the analysis represent better the operation of the actual system.

4) The input power to the motor and as a result the inverter average input voltage can be calculated more accurately, since we consider the total motor input current rather than the fundamental harmonic only.

In the constant dc link current approach it was shown that the beginning of the transfer mode, t_2, was the main unknown (section (3.6.2)) which enabled us to calculate all of the other system unknowns. However, the constant voltage assumption results

in four main unknowns with all other variables being dependent on some or all of these four main unknowns. The main unknowns are

1) t_1 the instant at which the thyristor T_1 is triggered.

2) V_d the converter output dc voltage.

3) i_{d1} the dc link current at $t=t_1$.

4) V_o the maximum voltage of the commutating capacitors.

Obviously, an iterative procedure has to be used to find the main unknowns. The iterations will converge faster if we have a good initial guess for the four variables at the first iteration. This can be achieved if we use the results of a constant current study (flowchart 3.2) and apply them as initial guesses for the first iteration. The program organization is given in flowchart 7.1.

The assumption of a constant voltage across the bridge output has been already used in the stability studies [12], the analysis being based mainly on a square current waveform. However, the [illegible]ation process with a constant input voltage has not been examined and the system study presented in this chapter is believed to be original.

Owing to the tedious and long analysis which results from the constant voltage assumption, we will confine ourselves only to the case in which the commutation angle is less than 60°. Besides, it is assumed, as in the previous cases, that the diodes do not become

transiently forward biased. Also, all the assumptions made in section (2.6) except number 4 are still valid.

As in Case (a), we have three distinct modes during each 60° of the inverter output period and we begin our study by considering the charging mode.

7.2 MODE 1 OR CHARGING MODE

This mode begins at $t=t_1$ when the thyristor T_1 is fired and ends at $t=t_2$ when the diode D_1 starts conducting, figs. 7.2 and 7.3. The same notations used in the previous sections to describe the charging mode are also applied here. The mode sequence is indicated in Tables 1.1-1.3, so that fig. 7.1 shows the circuit of the system just before firing the thyristor T_1 at $t=t_1$. The voltage across the voltage source, V_d, shown in this figure represents the average rectified voltage of the 3-phase bridge or any other dc source feeding the inverter. It is assumed that the system operates in a steady state, so that V_d stays constant for all modes belonging to one period of the inverter output. V_d and t_1 are two of the main unknowns whose values should be determined. The dc link current is not constant and its instantaneous value is denoted by i_d. The average value of i_d, i.e., I_d, is obtained by using (2.5.3). R_f and L_f show, respectively, the resistance and the inductance of the dc link choke. The other notations are the same as before. Just before firing T_1, the conducting components are T_5, D_5, T_6, D_6 and the terminal A of the motor is open circuited, fig. 7.1.

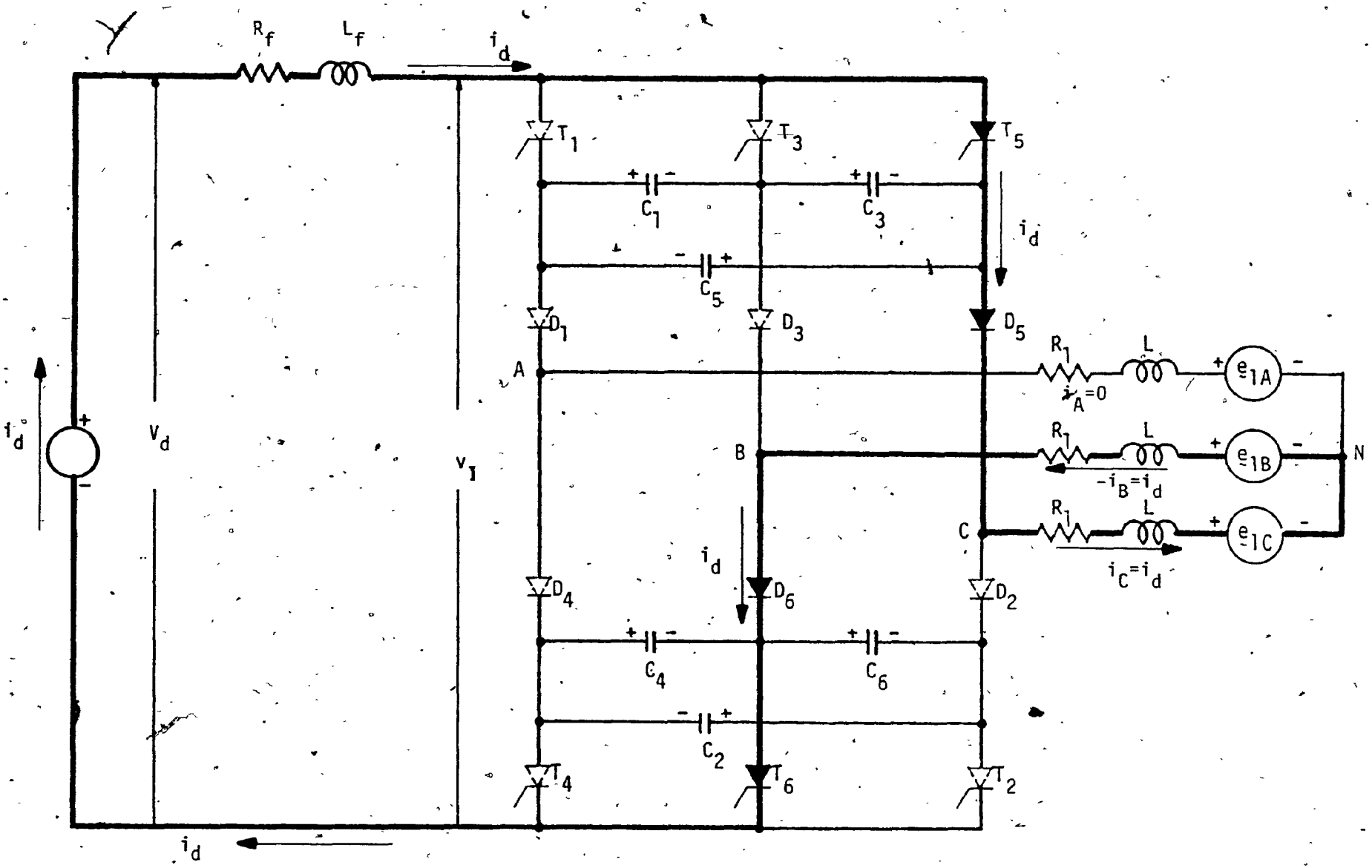

FIG. 7.1 ASCI-induction motor operation in mode 18 of case (g). The dc link input voltage is assumed to be constant. This mode ends at $t=t_1$ when the thyristor T_1 is fired.

At $t=t_1$ the thyristor T_1 is triggered, thus turning off T_5, fig. 7.2. As the commutation of T_5 is supposed to be instantaneous, the magnitude of the dc link current, i_d, just before and after firing T_1 remains essentially constant so that

$$i_d(t_1^-) = i_d(t_1^+) = i_d(t_1) = i_{d1} \tag{7.2.1}$$

The magnitude of the dc link current at $t=t_1$, i.e., i_{d1}, <u>is also one of the main unknowns</u> which must be found. After the gating of T_1 its current i_d splits into two capacitor currents, while the phase A remains open circuited as before. Therefore

$$\begin{aligned} i_{C1}(t) &= i_{C3}(t) = -\frac{1}{3}\, i_d(t) \\ -i_{C5}(t) &= \frac{2}{3}\, i_d(t) \\ i_A(t) &= 0\ , \quad i_B(t) = -i_C(t) = -i_d(t) \end{aligned} \tag{7.2.2}$$

The fundamental component of each motor line current and the CEMF for each phase are the same as given by (3.3.6-7), respectively. Then the instantaneous motor terminal and line-to-line voltages are

$$\begin{aligned} v_A(t) &= e_{1A}(t) = E_1 \sin(\omega t+\phi_1) \\ v_B(t) &= -(R_1+LP)i_d(t)+E_1 \sin(\omega t+\phi_1-\tfrac{2\pi}{3}) \\ v_C(t) &= (R_1+LP)i_d(t)+E_1 \sin(\omega t+\phi_1-\tfrac{4\pi}{3}) \end{aligned} \tag{7.2.3}$$

$$\begin{aligned} v_{AB}(t) &= (R_1+LP)i_d(t)+E_1\sqrt{3}\cos(\omega t+\phi_1-\pi/3) \\ v_{BC}(t) &= -2(R_1+LP)i_d(t)+E_1\sqrt{3}\cos(\omega t+\phi_1-\pi) \\ v_{CA}(t) &= (R_1+LP)i_d(t)-E_1\sqrt{3}\cos(\omega t+\phi_1-\tfrac{2\pi}{3}) \end{aligned} \tag{7.2.4}$$

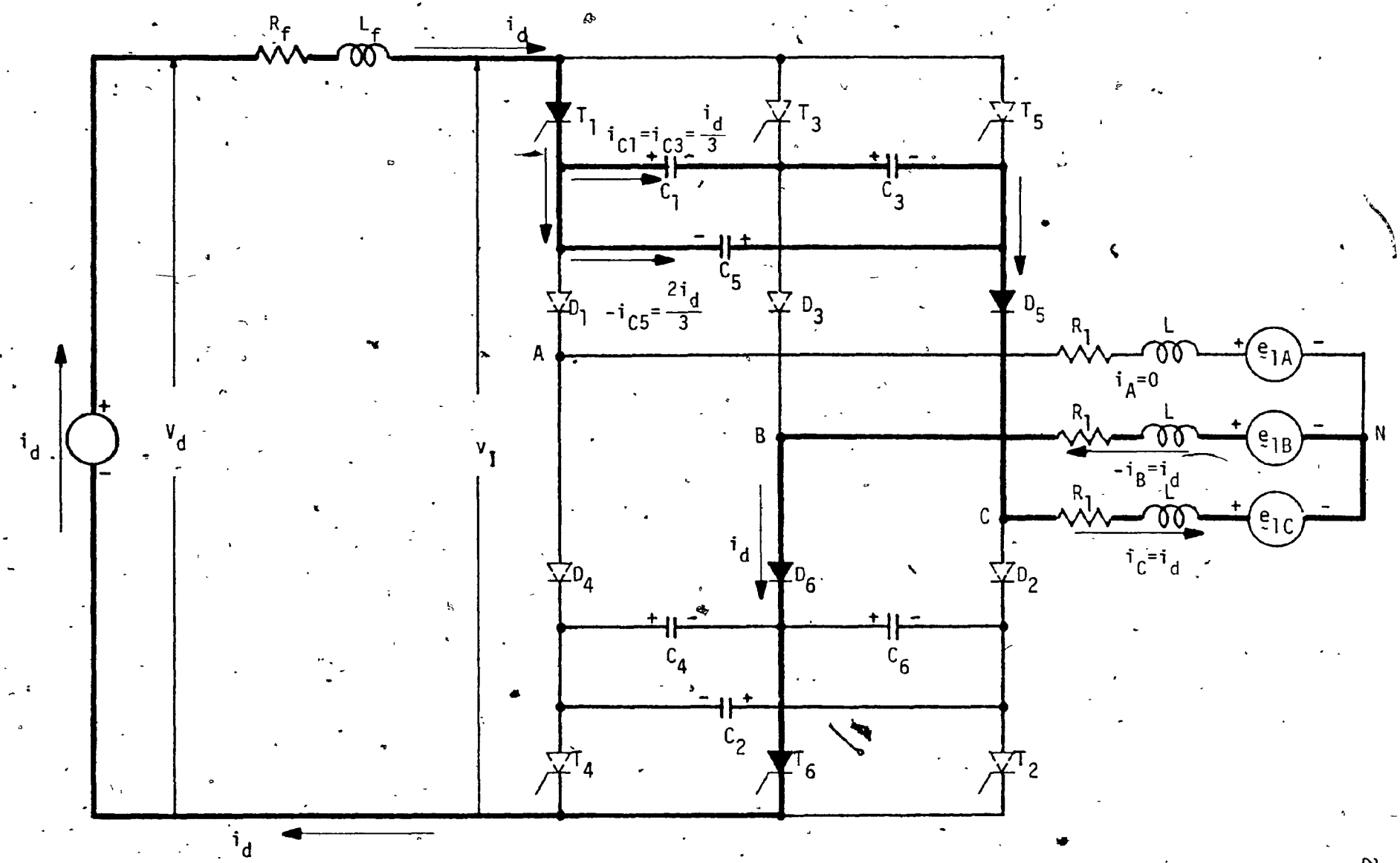

FIG. 7.2 ASCI-induction motor operation in mode 1 of case (g). The dc link input voltage is assumed to be constant. Firing T_1 at $t=t_1$ commutates T_5 and the upper group capacitors start to be charged. This mode ends at $t=t_2$ when D_1 commences to conduct.

where p stands for $\frac{d}{dt}$. According to Table 1.1 at $t=t_1$ the upper group capacitor voltages are

$$v_{C1}(t_1) = 0 \; ; \quad v_{C3}(t_1) = -V_o \; ; \quad v_{C5}(t_1) = +V_o \qquad (7.2.4a)$$

where the maximum capacitor voltage, V_o, is the other main unknown to be found. The instantaneous upper group capacitor voltages during the charging mode are

$$v_{C1}(t) = \frac{1}{C}\int_{t_1}^{t} i_{C1}(t)\, dt = \frac{1}{3C}\int_{t_1}^{t} i_d(t)\, dt$$

$$v_{C3}(t) = \frac{1}{3C}\int_{t_1}^{t} i_d(t)\, dt - V_o \qquad (7.2.5)$$

$$v_{C5}(t) = -\frac{2}{3C}\int_{t_1}^{t} i_d(t)\, dt + V_o$$

The lower group commutating capacitor voltages are constant during this mode and their values are expressed by (3.3.13).

The thyristor voltages during this mode are

$$v_{T1}(t) = 0 \; ; \quad v_{T3}(t) = v_{C1}(t) \; ; \quad v_{T5}(t) = -v_{C5}(t) \qquad (7.2.6)$$

$$v_{T2}(t) = +V_o \; ; \quad v_{T4}(t) = +V_o \; ; \quad v_{T6}(t) = 0 \qquad (7.2.7)$$

The diode currents and voltages during this mode are

$$i_{D1}(t) = i_{D3}(t) = i_{D2}(t) = i_{D4}(t) = 0$$

$$i_{D5}(t) = i_{D6}(t) = i_d(t) \qquad (7.2.8)$$

$$v_{D1}(t) = -v_{C5}(t) + v_{CA}(t)$$

$$v_{D3}(t) = v_{C3}(t) + v_{CB}(t) \qquad (7.2.9)$$

$$v_{D5}(t) = 0$$

$$v_{D2}(t) = v_{CB}(t) + v_{C6}(t) = v_{CB}(t)-V_o$$

$$v_{D4}(t) = v_{AB}(t) - v_{C4}(t) = v_{AB}(t)-V_o \qquad (7.2.10)$$

$$v_{D6}(t) = 0$$

and the inverter input voltage is

$$v_I(t) = -v_{C5}(t) + v_{CB}(t) \qquad (7.2.11)$$

To find the expression showing the variations of $i_d(t)$ during the charging mode we consider the loop consisting of V_d, L_f, R_f, T_1, C_5, D_5, motor phases C and B, D_6 and T_6. For this loop we can write

$$V_d = (R_f+L_f p)i_d(t) - v_{C5}(t) + v_{CB}(t) \qquad (7.2.12)$$

But $v_{BC}(t)$ and $v_{C5}(t)$ were given by (7.2.4) and (7.2.5) respectively, so that (7.2.12) becomes,

$$V_d = (R_f+2R_1)i_d(t)+(L_f+2L)pi_d(t) + \frac{2}{3C}\int_{t_1}^{t} i_d(t)\,dt-V_o$$

$$+ E_1\sqrt{3}\cos(\omega t+\phi_1) \qquad (7.2.13)$$

Introducing

$$R_{eq} = R_f+2R_1$$

$$L_{eq} = L_f+2L \qquad (7.2.14)$$

it then results

$$V_d = R_{eq} i_d(t) + L_{eq} p i_d(t) + \frac{2}{3C} \int_{t_1}^{t} i_d(t)\, dt - V_o$$

$$+ E_1 \sqrt{3} \cos(\omega t + \phi_1) \qquad (7.2.15)$$

Equation (7.2.15) is the main expression from which $i_d(t)$ should be obtained in mode 1. Differentiating (7.2.15) yields

$$R_{eq} \frac{di_d(t)}{dt} + L_{eq} \frac{d^2 i_d(t)}{dt^2} + \frac{2}{3C} i_d(t) - \omega E_1 \sqrt{3} \sin(\omega t + \phi_1) = 0 \qquad (7.2.16)$$

Introducing the new time scale, t_a, so that,

$$t_a = t - t_1 \qquad (7.2.17)$$

and considering the damping factor, α_1, expressed by

$$\frac{R_{eq}}{2L_{eq}} = \alpha_1 = \frac{\alpha}{2} \qquad (7.2.18)$$

Eq. (7.2.16) can be written in a new form

$$\frac{d^2 i_d(t_a)}{dt_a^2} + \alpha \frac{di_d(t_a)}{dt_a} + \frac{2}{3CL_{eq}} i_d(t_a) - \frac{\omega E_1 \sqrt{3}}{L_{eq}} \sin(\omega t_a + \phi_2) = 0 \qquad (7.2.19)$$

where $\phi_2 = \omega t_1 + \phi_1$ (7.2.20)

The Laplace transform of (7.2.19) yields

$$s^2 I_d(s) - s i_{d1} - i'_{d1} + \alpha [s I_d(s) - i_{d1}]$$

$$+ \frac{2}{3CL_{eq}} I_d(s)$$

$$-\frac{\omega E_1\sqrt{3}}{L_{eq}}\left[\frac{\omega\cos\phi_2}{s^2+\omega^2}+\frac{s\sin\phi_2}{s^2+\omega^2}\right]=0 \qquad (7.2.21)$$

In this expression $I_d(s)$ is the Laplace transform of $i_d(t_a)$; i_{d1} shows the dc link current, $i_d(t_a)$, at $t_a=0$ and i'_{d1} is the slope of $i_d(t_a)$ at $t_a=0^+$ which can be obtained from (7.2.15). To find i'_{d1} , just change t to t_a in (7.2.15)

$$V_d = R_{eq}i_d(t_a)+L_{eq}\frac{di_d(t_a)}{dt_a}+\frac{2}{3C}\int_0^{t_a} i_d(t_a)\,dt_a-V_o$$

$$+E_1\sqrt{3}\cos(\omega t_a+\phi_2) \qquad (7.2.22)$$

Then, at $t_a=0^+$ or at $t=t_1^+$ the above equation gives

$$V_d = R_{eq}i_{d1}+L_{eq}i'_{d1}-V_o+E_1\sqrt{3}\cos(\omega t_1+\phi_1)$$

from which

$$i'_{d1}=\frac{1}{L_{eq}}\left[V_d-R_{eq}i_{d1}+V_o-E_1\sqrt{3}\cos(\omega t_1+\phi_1)\right] \qquad (7.2.23)$$

It can be seen that, in addition to the motor and the dc link parameters, i'_{d1} is also a function of V_d, i_{d1}, V_o and t_1. Moreover, it will be noticed that in derivation of each new expression, the values of the required constants depend on some or all of these four variables (V_d, i_{d1}, V_o and t_1) so that knowing these four quantities results in the calculation of every other unknown. Later on, it will be noticed that each of these variables is calculated by using an implicit function so that the use of an iterative approach is unavoidable. At the beginning of each iteration, the main variables

are assigned some values. These values are called 'initial values' and are denoted as

t_{o1} = Initial value for t_1 at the start of each iteration
V_{od} = " " " V_d " " " " " "
i_{od1} = " " " i_{d1} " " " " " "
V_{oo} = " " " V_o " " " " " "

(7.2.24)

The method used in computing these values is given in flowchart 7.1. However, for the first iteration, the initial values are chosen as the results of the constant dc link current study (flowchart 3.2). Then, to calculate i'_{d1} at each iteration, the initial values of the main unknowns (t_{o1}, V_{od}, i_{od1} and V_{oo}) belonging to the same iteration should be inserted into (7.2.23). The same procedure applies to the calculation of all the other variables and constants.

Solving (7.2.21) for $I_d(s)$ results in

$$I_d(s) = \frac{\omega E_1\sqrt{3}}{L_{eq}} \cdot \frac{\omega \cos\phi_2 + s\sin\phi_2}{(s^2+\omega^2)(s^2+\alpha s+2/3CL_{eq})} + \frac{s i_{d1} + \alpha i_{d1} + i'_{d1}}{s^2+\alpha s+2/3CL_{eq}} \qquad (7.2.25)$$

The resonant frequency, ω_o, and the ringing frequency, ω_1, are defined by

$$\omega_o = 1/(\tfrac{3}{2}\,CL_{eq})^{1/2} = (2/3CL_{eq})^{1/2}$$
$$\omega_1 = (\omega_o^2-\alpha_1^2)^{1/2} \qquad (7.2.26)$$

where α_1 is given by (7.2.18). Recall that

$$s^2+\alpha s+\omega_o^2 = (s+\frac{\alpha}{2})^2+\omega_o^2-\frac{\alpha^2}{4} = (s+\alpha_1)^2+\omega_o^2-\alpha_1^2 \qquad (7.2.27)$$

Therefore, (7.2.25) can be written as:

$$I_d(s) = \frac{\omega E_1\sqrt{3}\sin\phi_2}{L_{eq}} \cdot \frac{s+\omega\cot\phi_2}{(s^2+\omega^2)[(s+\alpha_1)^2+\omega_1^2]}$$

$$+ i_{d1}\frac{s+2\alpha_1+i'_{d1}/i_{d1}}{[(s+\alpha_1)^2+\omega_1^2]} \qquad (7.2.28)$$

The inverse Laplace transform of $I_d(s)$ will yield j_d as a function of time, t_a.

$$i_d(t_a) = \frac{\omega E_1\sqrt{3}\sin\phi_2}{L_{eq}}[A_2e^{-\alpha_1 t_a}\sin(\omega_1 t_a+\alpha_2)$$

$$+ B_2\sin(\omega t_a+\beta_2)]+i_{d1}[A_3e^{-\alpha_1 t_a}\sin(\omega_1 t_a+\alpha_3)]$$

(7.2.29)

Recalling that, from (7.2.26), $\omega_1^2+\alpha_1^2 = \omega_o^2$, the constants in (7.2.29) are:

$$A_2 = \frac{1}{\omega_1}\left[\frac{(\omega\cot\phi_2-\alpha_1)^2+\omega_1^2}{(\omega_o^2-\omega^2)^2+4\alpha_1^2\omega^2}\right]^{1/2}$$

$$B_2 = \left[\frac{1+\cot^2\phi_2}{(\omega_o^2-\omega^2)^2+4\alpha_1^2\omega^2}\right]^{1/2}$$

$$\alpha_2 = \arctan\frac{\omega_1}{\omega\cot\phi_2-\alpha_1} - \arctan\frac{-2\alpha_1\omega_1}{\alpha_1^2-\omega_1^2+\omega^2} \qquad (7.2.30)$$

$$\beta_2 = \arctan \frac{1}{\cot\phi_2} + \arctan \frac{-2\alpha_1\omega}{\omega_0^2-\omega^2}$$

$$A_3 = \frac{1}{\omega_1} [(\alpha_1+i'_{d1}/i_{d1})^2+\omega_1^2]^{1/2}$$

$$\alpha_3 = \arctan \frac{\omega_1}{\alpha_1+i'_{d1}/i_{d1}} \qquad (7.2.31)$$

A more compact form of (7.2.29) can be obtained as follows

$$i_d(t_a) = e^{-\alpha_1 t_a}[K_1\sin(\omega_1 t_a+\alpha_2)+K_2\sin(\omega_1 t_a+\alpha_3)] + K_3\sin(\omega t_a+\beta_2) \qquad (7.2.32)$$

where

$$K_1 = \frac{1}{L_{eq}} (A_2\omega E_1\sqrt{3} \sin \phi_2)$$

$$K_2 = A_3 i_{d1} \qquad (7.2.33)$$

$$K_3 = \frac{1}{L_{eq}} (B_2\omega E_1\sqrt{3} \sin \phi_2)$$

or

$$i_d(t_a) = e^{-\alpha_1 t_a}(K_4\sin\omega_1 t_a+K_5\cos\omega_1 t_a)+K_3\sin(\omega t_a+\beta_2) \qquad (7.2.34)$$

in which

$$K_4 = K_1\cos\alpha_2 + K_2\cos\alpha_3 \qquad (7.2.35)$$

$$K_5 = K_1\sin\alpha_2 + K_2\sin\alpha_3$$

and, at last,

$$i_d(t_a) = K_6 e^{-\alpha_1 t_a}\sin(\omega_1 t_a+\alpha_6)+K_3\sin(\omega t_a+\beta_2) \qquad (7.2.36)$$

where $K_6 = (K_4^2+K_5^2)^{1/2}$, $\alpha_6 = \arctan \frac{K_5}{K_4}$ (7.2.37)

Equation (7.2.36) shows that during the charging mode the dc link current consists of two components:

a) A sinusoidal component with a frequency, ω, the same as that in the CEMF.

b) A damped sinusoidal component with a damping factor equal to α_1 and a frequency equal to ω_1.

In typical ASCI-induction motor drives $\omega_1 >> \omega$ so that the second term on the right-hand side of (7.2.36) is almost constant over this period and the variations of the dc link current during the charging mode, $i_d(t_a)$, is mainly determined by the other term in (7.2.36). Later on the oscilograms of the dc link current will prove this point.

The charging mode ends at $t=t_2$ or at $t_a=t_{a1}$, the instant at which the diode D_1 becomes forward biased, fig. 7.2. The duration of the charging mode, t_{ch}, is given by

$$t_{ch} = t_2-t_1 = t_{a1} \qquad (7.2.38)$$

To find t_{ch}, from (7.2.9) one can write

$$v_{D1}(t) = v_{CA}(t) - v_{C5}(t) \qquad (7.2.39)$$

where v_{CA} and v_{C5} were given by (7.2.4) and (7.2.5), respectively. Replacing t by t_a according to (7.2.17) in the above equations, (7.2.39) can be rewritten as

$$v_{D1}(t_a) = (R_1+LP)i_d(t_a) - E_1\sqrt{3}\cos(\omega t_a+\phi_2-\frac{2\pi}{3})$$
$$+\frac{2}{3C}\int_0^{t_a} i_d(t_a)\,dt_a - V_o. \qquad (7.2.40)$$

This expression gives the voltage across D_1 during mode 1. At the end of this mode, i.e. at $t=t_{a1}$, the diode D_1 becomes forward biased so that (7.2.40) becomes

$$(R_1+LP)i_d(t_{a1}) - E_1\sqrt{3}\cos(\omega t_{a1}+\phi_2-\frac{2\pi}{3})$$
$$+\frac{2}{3C}\int_0^{t_{a1}} i_d(t_a)\,dt_a - V_o = 0 \qquad (7.2.41)$$

where $\quad pi_d(t_{a1}) = \left.\frac{d_{id}}{dt_a}\right|_{t_a=t_{a1}}$

The duration of the charging mode, t_{a1}, is found by solving (7.2.41), in which the only unknown is t_{a1}. To find a simpler form for (7.2.41), $i_d(t_a)$ is replaced by (7.2.36). Then the integral term in (7.2.41) can be written as

$$\int_0^{t_{a1}} i_d(t_a)dt_a = \int_0^{t_{a1}} [K_6 e^{-\alpha_1 t_a}\sin(\omega_1 t_a+\alpha_6)$$
$$+ K_3\sin(\omega t_a+\beta_2)]dt_a \qquad (7.2.42)$$

The right hand side can be developed as

$$\int_0^{t_{a1}} e^{-\alpha_1 t_a}\sin(\omega_1 t_a+\alpha_6)\,dt_a = H_6 \qquad (7.2.43)$$

where

$$H_6 = H_1(H_2+H_3+H_4+H_5)$$

$$H_1 = 1/(\alpha_1^2+\omega_1^2)$$

$$H_2 = -\alpha_1 e^{-\alpha_1 t_{a1}} \sin(\omega_1 t_{a1}+\alpha_6)$$

$$H_3 = -\omega_1 e^{-\alpha_1 t_{a1}} \cos(\omega_1 t_{a1}+\alpha_6)$$

$$H_4 = \alpha_1 \sin \alpha_6$$

$$H_5 = \omega_1 \cos \alpha_6 \qquad (7.2.44)$$

and

$$\int_0^{t_{a1}} \sin(\omega t+\beta_2)\, dt_a = H_9 \qquad (7.2.45)$$

where

$$H_9 = \frac{1}{\omega}(H_7+H_8) \quad ; \quad H_7 = \cos \beta_2 \qquad (7.2.46)$$

$$H_8 = -\cos(\omega t_{a1}+\beta_2) \qquad (7.2.47)$$

Inserting (7.2.43 and 45) into (7.2.42) results in

$$\int_0^{t_{a1}} i_d(t_a)\, dt_a = K_6 H_6 + K_3 H_9 \qquad (7.2.48)$$

The other terms in (7.1.41) are

$$i_d(t_{a1}) = -K_6(H_2/\alpha_1) + K_3 H_{10} \qquad (7.2.49)$$

where

$$H_{10} = \sin(\omega t_{a1}+\beta_2) \qquad (7.2.50)$$

and

$$pi_d(t_{a1}) = K_6(H_2-H_3) - K_3 \omega H_8 \qquad (7.2.51)$$

where H_2, H_3 and H_8 were given in (7.2.44 and 47).

Putting (7.2.46, 47 and 49) into (7.2.40) yields

$$R_1[-K_6(H_2/\alpha_1) + K_3H_{10}]+L[K_6(H_2-H_3)-K_3\omega H_8]$$

$$-E_1\sqrt{3}\cos(\omega t_{a1}+\phi_2-\frac{2\pi}{3})+\frac{2}{3C}(K_6H_6+K_3H_9)-V_o = 0 \quad (7.2.52)$$

Now, by applying one of the numerical root-finding methods (e.g. bisection method) we can solve the above nonlinear equation to obtain t_{a1} which is the duration of the charging mode. In the next section we will study the system during mode 2 which starts at $t = t_2 = t_1+t_{a1}$ when D_1 becomes forward biased.

7.3 MODE 2 OR TRANSFER MODE

This mode lasts from $t=t_2$ to $t=t_3$. At $t=t_2$ mode 1 ends and D_1 starts conducting, fig. 7.3. For this mode a new time scale, t_1' is also chosen so that

$$t' = t-t_2 \quad (7.3.1)$$

where $$t_2 = t_1+t_{a1} \quad (7.3.2)$$

Since there is no voltage drop across D_1 during this mode it results in

$$v_{CS}(t') = v_{CA}(t') \quad (7.3.3)$$

in which $0<t'<t_3-t_2$. Specifically, at the beginning of the transfer mode, $t'=0$, from (7.3.3) we can conclude

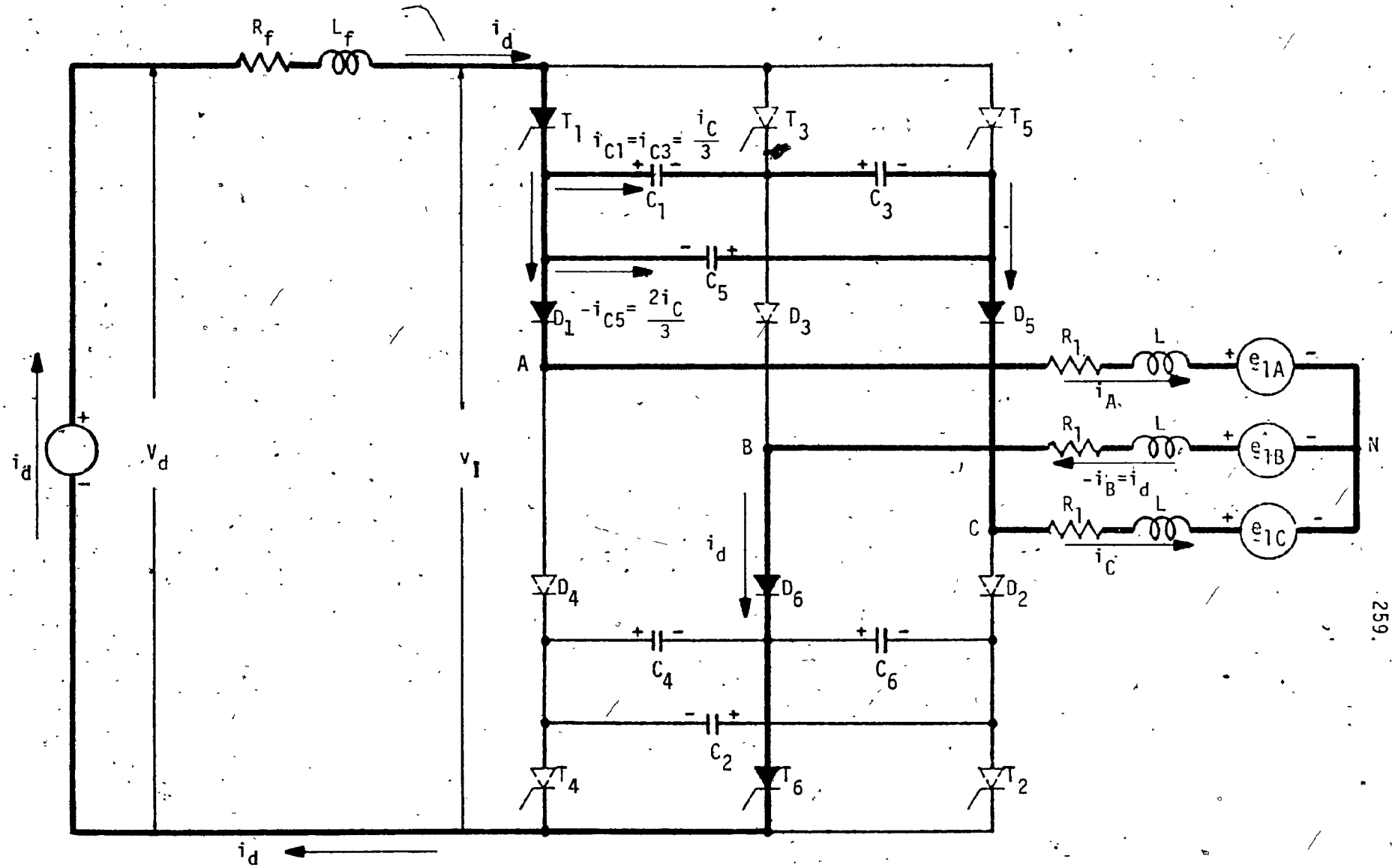

FIG. 7.3 ASCI-induction motor operation in mode 2 of case (g). The dc link input voltage is assumed to be constant. Conduction of D_1 at $t=t_2$ starts a transfer mode in the upper group where phase C current is being transferred to phase A. This mode ends at $t=t_3$ when D_5 is blocked because of current starvation.

$v_{C5}(0) = v_{CA}(0)$ when t' is the independent variable

$v_{C5}(t_{a1}) = v_{CA}(t_{a1})$ " t_a " " " "

$v_{C5}(t_2) = v_{CA}(t_2)$ " t " " " "

(7.3.4)

Owing to the conduction of D_1 and D_5 during this mode, the currents flow through all three motor phases, fig. 7.3. The relationship between these currents is:

$$i_A(t') + i_C(t') = -i_B(t')$$

and $$i_B(t') = -i_d(t') \qquad (7.3.5)$$

Equations (7.3.3 and 5) along with (7.3.20) are the three main equations from which all the expressions describing this mode are derived.

From fig. 7.3 the following expressions can be directly written. The upper group capacitor currents are:

$$i_{C1}(t') = i_{C3}(t') = \frac{1}{3} i_C(t')$$

$$-i_{C5}(t') = \frac{2}{3} i_C(t') \qquad (7.3.6)$$

and the diode currents are:

$$i_{D3}(t') = i_{D2}(t') = i_{D4}(t') = 0$$

$$i_{D1}(t') = i_A(t')$$

$$i_{D5}(t') = i_C(t')$$

$$i_{D6}(t') = i_d(t') \qquad (7.3.7)$$

The motor terminal and line-to-line voltages are

$$v_A(t') = (R_1+Lp)i_A(t') + E_1\sin(\omega t'+\phi_3)$$

$$v_B(t') = -(R_1+Lp)i_d(t') + E_1\sin(\omega t'+\phi_3-\frac{2\pi}{3})$$

$$v_C(t') = (R_1+Lp)i_C(t') + E_1\sin(\omega t'+\phi_3-\frac{4\pi}{3}) \qquad (7.3.8)$$

$$v_{AB}(t') = (R_1+Lp)i_A(t')+(R_1+Lp)i_d(t')+E_1\sqrt{3}\cos(\omega t'+\phi_3-\frac{\pi}{3})$$

$$v_{BC}(t') = -(R_1+Lp)i_d(t')-(R_1+Lp)i_C(t')+E_1\sqrt{3}\cos(\omega t'+\phi_3-\pi)$$

$$v_{CA}(t') = (R_1+Lp)i_C(t')-(R_1+Lp)i_A(t')-E_1\sqrt{3}\cos(\omega t'+\phi_3-\frac{2\pi}{3})$$

$$(7.3.9)$$

where $\phi_3 = \omega t_2+\phi_1$ (7.3.10)

and p stands for $\frac{d}{dt'}$.

The upper group capacitor voltages are

$$v_{C1}(t') = \frac{1}{3C}\int_0^{t'} i_C(t')\,dt'+v_{C1}(t_{a1})$$

$$v_{C3}(t') = \frac{1}{3C}\int_0^{t'} i_C(t')\,dt'+v_{C3}(t_{a1})$$

$$v_{C5}(t') = -\frac{2}{3C}\int_0^{t'} i_C(t')\,dt'+v_{C5}(t_{a1}) \qquad (7.3.11)$$

in which

$$v_{C1}(t_{a1}) = \frac{1}{3C}\int_0^{t_{a1}} i_d(t_a)\,dt_a$$

$$v_{C3}(t_{a1}) = \frac{1}{3C}\int_0^{t_{a1}} i_d(t_a)\,dt_a-V_o$$

$$v_{C5}(t_{a1}) = -\frac{2}{3C}\int_0^{t_{a1}} i_d(t_a)\,dt_a+V_o \qquad (7.3.12)$$

where the integral term was provided by (7.2.48).

Also, for the voltages across the thyristors and the diodes we have the following

$$v_{T1}(t') = 0 \; ; \; v_{T3}(t') = v_{C1}(t') \; ; \; v_{T5}(t') = -v_{C5}(t') \tag{7.3.13}$$

$$v_{T2}(t') = +V_o \; ; \; v_{T4}(t') = +V_o \; ; \; v_{T6}(t') = 0 \tag{7.3.14}$$

$$\begin{aligned} v_{D1}(t') &= v_{D5}(t') = v_{D6}(t') = 0 \\ v_{D3}(t') &= v_{C3}(t') + v_{CB}(t') \\ v_{D2}(t') &= v_{CB}(t') - V_o \\ v_{D4}(t') &= v_{AB}(t') - V_o \end{aligned} \tag{7.3.15}$$

At last, the inverter input voltage is

$$v_I(t') = v_{AB}(t')$$

As well, at the beginning of mode 2, i.e. at $t=t_2^+$ or at $t'=0^+$, the phase and the capacitor currents are

$$\begin{aligned} i_A(0^+) &= 0 \\ i_C(0^+) &= -i_B(0^+) = i_d(0^+) \end{aligned} \tag{7.3.16}$$

$$\begin{aligned} -i_{C5}(0^+) &= \frac{2}{3}\, i_C(0^+) = \frac{2}{3}\, i_d(0^+) \\ i_{C1}(0^+) &= i_{C3}(0^+) = \frac{1}{3}\, i_C(0^+) = \frac{1}{3}\, i_d(0^+) \end{aligned} \tag{7.3.17}$$

where all the variables are functions of t'.

In order to find the expressions defining the different currents during this mode we consider two loops in fig. 7.3:

1. The loop consisting of C_5, D_5, phase C, phase A and D_1.
2. The loop consisting of V_d, R_f, L_f, T_1, D_1, phase A, phase B, D_6 and T_6.

In the first loop (7.3.3) holds true. By substituting $v_{CA}(t')$ from (7.3.9), $v_{C5}(t')$ from (7.3.11) and $v_{C5}(t_{a1})$ from (7.3.12) into (7.3.3) we obtain

$$-\frac{2}{3C}\int_0^{t'} i_C(t')dt' - \frac{2}{3C}\int_0^{t_{a1}} i_d(t_a)dt_a + V_o = (R_1+Lp)[i_C(t')-i_A(t')]$$
$$- E_1\sqrt{3}\cos(\omega t'+\phi_3-\frac{2\pi}{3}) \qquad (7.3.18)$$

For the second loop, as V_d remains constant throughout the period we can write

$$V_d = (R_f+L_f p)i_d(t') + v_{AB}(t') \qquad (7.3.19)$$

Using $v_{AB}(t')$ from (7.3.9) and applying (7.3.5), Eq. (7.3.19) can be written in a new form:

$$V_d = (R_{eq}+L_{eq}p)i_A(t')+(R_a+L_a p)i_C(t')$$
$$+ E_1\sqrt{3}\cos(\omega t'+\phi_3-\frac{\pi}{3}) \qquad (7.3.20)$$

where R_{eq} and L_{eq} were given by (7.2.14) and

$$R_a = R_1+R_f$$
$$L_a = L+L_f \qquad (7.3.21)$$

The expressions given by (7.3.18) and (7.3.20) are the two nonlinear equations from which $i_A(t')$, $i_C(t')$ and as a result $i_d(t')$ should

be found. In order to solve the problem, first we find $i_A(t')$ from (7.3.20)

$$i_A(t') = \frac{1}{R_{eq}+L_{eq}p}\,[V_d-(R_a+L_a p)i_C(t')$$

$$- E_1\sqrt{3}\cos(\omega t'+\phi_3-\pi/3)] \qquad (7.3.22)$$

Differentiating (7.3.18) and remembering that the second and the third terms on the left hand side of that equation are constants we obtain

$$-\frac{2}{3C}\,i_C(t') = (R_1+LP)[pi_C(t')-pi_A(t')]$$

$$- E_1\sqrt{3}\,p\cos(\omega t'+\phi_3-\frac{2\pi}{3}) \qquad (7.3.23)$$

where $p = \frac{d}{dt'}$.

Now, substituting $i_A(t')$ from (7.3.22) into (7.3.23) and noticing that $(R_1+LP)pV_d = 0$, after some manipulations one obtains

$$p^3 i_C(t')+Q_1 p^2 i_C(t')+ Q_2 p i_C(t') + Q_3 i_C(t')$$

$$+ Q_4[R_{eq}\sin(\omega t'+\theta_2)-R_1\sin(\omega t'+\theta_1)]$$

$$+ \omega Q_4[L_{eq}\cos(\omega t'+\theta_2)-L\cos(\omega t'+\theta_1)] = 0 \qquad (7.3.24)$$

in which the constants are

$$\theta_1 = \omega t_2+\phi_1-\pi/3 = \phi_3-\pi/3$$

$$\theta_2 = \theta_1-\pi/3$$

$$Q_1 = (R_{eq}L+R_1L_{eq}+R_aL+R_1L_a)/(LL_{eq}+LL_a)$$

$$Q_2 = (R_1R_{eq}+2L_{eq}/3C+R_1R_a)/(LL_{eq}+LL_a)$$

$$Q_3 = (2R_{eq}/3C)/(LL_{eq}+LL_a)$$

$$Q_4 = (\omega E_1\sqrt{3})/(LL_{eq}+LL_a) \qquad (7.3.25)$$

Since (7.3.24) is of third order and it should yield only $i_C(t')$, the state variable technique is chosen for solving this differential equation. The state variables are

$$i_C(t') = x_1 \quad ; \quad pi_C(t') = x_2$$

$$p^2 i_C(t') = x_3$$

$$p^3 i_C(t') = \frac{dx_3}{dt'} \tag{7.3.26}$$

The state vector then is

$$[X] = \begin{bmatrix} x_1 \\ x_2 \\ x_3 \end{bmatrix} \tag{7.3.27}$$

From (7.3.24 and 26) the result is

$$\frac{d}{dt'}[X] = [A][X] + [B]r(t') \tag{7.3.28}$$

where

$$[A] = \begin{bmatrix} 0 & 1 & 0 \\ 0 & 0 & 1 \\ -Q_3 & -Q_2 & -Q_1 \end{bmatrix} \tag{7.3.29}$$

$$[B] = \begin{bmatrix} 0 \\ 0 \\ -Q_4 \end{bmatrix} \tag{7.3.30}$$

and

$$r(t') = [R_{eq}\sin(\omega t'+\theta_2) - R_1\sin(\omega t'+\theta_1)] + \omega[L_{eq}\cos(\omega t'+\theta_2) - L\cos(\omega t'+\theta_1)] \tag{7.3.31}$$

where $[X]$ is given by (7.3.27).

The Laplace transform of (7.3.28) yields

$$s[X(s)]-[X(0^+)] = [A][X(s)]-[B]R(s) \qquad (7.3.32)$$

In the above equation $[X(0^+)]$ is the initial state vector evaluated at $t'=0^+$. Solving for $[X(s)]$ in (7.3.32)

$$[X(s)] = \{s[I]-[A]\}^{-1}[X(0^+)]+\{s[I]-[A]\}^{-1}[B]R(s) \qquad (7.3.33)$$

where $[I]$ is the unity matrix and $\{s[I]-[A]\}^{-1}$ is the inverse of $\{s[I]-[A]\}$. The inverse Laplace transform of (7.3.33) is

$$[X(t')] = [\phi(t')][X(0^+)]+\int_0^{t'} [\phi(t'-\tau)][B]r(\tau)d\tau \qquad (7.3.34)$$

in which $[\phi(t')]$ is the state transition matrix of $[A]$

$$[\phi(t')] = L^{-1}[\{s[I]-[A]\}^{-1}] = e^{[A]t'} \quad t'\geq 0 \qquad (7.3.35)$$

Equation (7.3.34) is the state transition equation of the system during the transfer mode. The expanded form of (7.3.34) is

$$\begin{bmatrix} x_1(t') \\ x_2(t') \\ x_3(t') \end{bmatrix} = \begin{bmatrix} \phi_{11}(t') & \phi_{12}(t') & \phi_{13}(t') \\ \phi_{21}(t') & \phi_{22}(t') & \phi_{23}(t') \\ \phi_{31}(t') & \phi_{32}(t') & \phi_{33}(t') \end{bmatrix} \begin{bmatrix} x_1(0^+) \\ x_2(0^+) \\ x_3(0^+) \end{bmatrix}$$

$$+\int_0^{t'} \begin{bmatrix} \phi_{11}(t'-\tau) & \phi_{12}(t'-\tau) & \phi_{13}(t'-\tau) \\ \phi_{21}(t'-\tau) & \phi_{22}(t'-\tau) & \phi_{23}(t'-\tau) \\ \phi_{31}(t'-\tau) & \phi_{32}(t'-\tau) & \phi_{33}(t'-\tau) \end{bmatrix} \begin{bmatrix} 0 \\ 0 \\ -Q_4 \end{bmatrix} \times$$

$$\left\{[R_{eq}\sin(\omega\tau+\theta_2)-R_1\sin(\omega\tau+\theta_1)]+\omega[L_{eq}\cos(\omega\tau+\theta_2) -L\cos(\omega\tau+\theta_1)]\right\} d\tau \qquad (7.3.36)$$

From (7.3.26) we know that $x_1(t') = i_C(t')$ so that from (7.3.36) we obtain

$$i_C(t') = x_1(t') = \phi_{11}(t')x_1(0^+)+\phi_{12}(t')x_2(0^+)$$
$$+ \phi_{13}(t')x_3(0^+)+\int_0^{t'} -Q_4\phi_{13}(t'-\tau)\{[R_{eq}\sin(\omega\tau+\phi_2)$$
$$- R_1\sin(\omega\tau+\theta_1)]+\omega[L_{eq}\cos(\omega\tau+\theta_2)-L\cos(\omega\tau+\phi_1)]\}d\tau \tag{7.3.37}$$

To obtain a complete analytical form for $i_C(t')$ in the above expression we should know the elements of the state transition matrix, $[\phi(t')]$, plus the initial state vector, $[X(0^+)]$. First we will find $[\phi(t')]$ and later $[X(0^+)]$ will be obtained. Thus from (7.3.35) and (7.3.29):

$$\{s[I]-[A]\} = \begin{bmatrix} s & -1 & 0 \\ 0 & s & -1 \\ Q_3 & Q_2 & s+Q_1 \end{bmatrix} \tag{7.3.38}$$

The determinant of the above is

$$\det.|s(I)-[A]| = \Delta = s(s^2+sQ_1+Q_2) + Q_3 \tag{7.3.39}$$

The inverse of (7.3.38) yields

$$\{s[I]-[A]\}^{-1} = \frac{1}{\Delta}\,\text{adj}\,\{s[I]-[A]\} \tag{7.3.40}$$

where

$$\text{adj}\,\{s[I]-[A]\} = \begin{bmatrix} s^2+sQ_1+Q_2 & s+Q_1 & 1 \\ -Q_3 & s^2+sQ_1 & s \\ -sQ_3 & -sQ_2-Q_3 & s^2 \end{bmatrix} \tag{7.3.41}$$

From (7.3.40-41) and (7.3.35) one obtains

$$[\phi(t')] = L^{-1}\{\frac{1}{\Delta}\begin{bmatrix} s^2+sQ_1+Q_2 & s+Q_1 & 1 \\ -Q_3 & s^2+sQ_1 & s \\ -sQ_3 & -sQ_2-Q_3 & s^2 \end{bmatrix}\} \qquad (7.3.42)$$

When comparing (7.3.42) with (7.3.36) the result is

$$\phi_{11}(t') = L^{-1}\{\frac{s^2+sQ_1+Q_2}{s(s^2+sQ_1+Q_2)+Q_3}\}$$

$$\phi_{12}(t') = L^{-1}\{\frac{s+Q_1}{s(s^2+sQ_1+Q_2)+Q_3}\}$$

$$\phi_{13}(t') = L^{-1}\{\frac{1}{s(s^2+sQ_1+Q_2)+Q_3}\} \qquad (7.3.43)$$

In order to evaluate the functions in (7.3.43) we should find the denominator roots. If we call these roots D_{10}, D_{11} and D_{12} we have:

$$\Delta = s^3+s^2Q_1+sQ_2+Q_3 = (s-D_{12})(s-D_{10})(s-D_{11}) \qquad (7.3.44)$$

By introducing a new variable y, defined as:

$$s = y-Q_1/3$$

the characteristic equation becomes

$$\Delta = y^3 + ay+b \qquad (7.3.45)$$

where $a = \frac{1}{3}(3Q_2-Q_1^2)$; $b = \frac{1}{27}(2Q_1^3-9Q_1Q_2+27Q_3)$ (7.3.46)

In practical ASCI-motor drives we always have

$$\frac{b^2}{4} + \frac{a^3}{27} > 0 \qquad (7.3.47)$$

so that Δ in (7.3.45) has one real and two complex conjugate roots:

$$y_1 = A+B$$

$$y_2 = -\frac{A+B}{2} + j\sqrt{3}\,\frac{A-B}{2}$$

$$y_3 = -\frac{A+B}{2} - j\sqrt{3}\,\frac{A-B}{2} \qquad (7.3.48)$$

where A and B are two real numbers

$$A = \sqrt[3]{-\frac{b}{2} + \sqrt{\frac{b^2}{4} + \frac{a^3}{27}}}$$

$$B = \sqrt[3]{-\frac{b}{2} - \sqrt{\frac{b^2}{4} + \frac{a^3}{27}}} = -\sqrt[3]{\frac{b}{2} + \sqrt{\frac{b^2}{4} + \frac{a^3}{27}}} \qquad (7.3.49)$$

We can now find the roots of Δ in (7.3.44). From (7.3.45) and (7.3.48) these roots are

$$s_1 = D_{12} = y_1 - \frac{Q_1}{3}$$

$$s_2 = D_{10} = y_2 - \frac{Q_1}{3}$$

$$s_3 = D_{11} = y_3 - \frac{Q_1}{3} \qquad (7.3.50)$$

According to (7.3.48-49), s_1 is the real root and the other two are the complex conjugate ones. Equations (7.3.50) can be written in a new form

$$s_1 = D_{12} = A+B - \frac{Q_1}{3}$$

$$s_2 = D_{10} = m+jn$$

$$s_3 = D_{11} = m-jn \qquad (7.3.51)$$

where m and n are two real numbers

$$m = -\frac{A+B}{2} - \frac{Q_1}{3}$$

$$n = \sqrt{3}\,\frac{A-B}{2} \qquad (7.3.52)$$

Putting (7.3.51) into (7.3.44) gives a new form for the system determinant

$$\Delta = s^3+s^2Q_1+sQ_2+Q_3 = (s-D_{12})[(s-m)^2+n^2] \qquad (7.3.53)$$

Using the expression given by (7.3.53), the inverse Laplace transform of each function in (7.3.43) is found as follows

$$\phi_{11}(t') = L^{-1}\{\frac{s^2+sQ_1+Q_2}{s^3+s^2Q_1+sQ_2+Q_3}\} = L^{-1}\{\frac{s^2+sQ_1+Q_2}{[(s-m)^2+n^2](s-D_{12})}\}$$

$$\phi_{11}(t') = D_{13}e^{mt'}\sin(nt'+\delta_{13})+D_{14}e^{D_{12}t'} \qquad (7.3.54)$$

in which $D_{13} = \frac{1}{n}\left[\frac{(m^2-n^2+mQ_1+Q_2)^2+n^2(2m+Q_1)^2}{(m-D_{12})^2+n^2}\right]^{1/2}$ (7.3.55)

$$D_{14} = \frac{D_{12}^2+D_{12}Q_1+Q_2}{(m-D_{12})^2+n^2}$$

$$\delta_{13} = \arctan\frac{n(2m+Q_1)}{m^2-n^2+mQ_1+Q_2} - \arctan\frac{n}{m-D_{12}} \qquad (7.3.56)$$

$$\phi_{12}(t') = L^{-1}\{\frac{s+Q_1}{s^3+s^2Q_1+sQ_2+Q_3}\} = L^{-1}\{\frac{s+Q_1}{[(s-m)^2+n^2](s-D_{12})}\}$$

$$\phi_{12}(t') = D_{15}e^{mt'}\sin(nt'+\delta_{15})+D_{16}e^{D_{12}t'} \qquad (7.3.57)$$

where $D_{15} = \frac{1}{n}\left[\frac{(m+Q_1)^2+n^2}{(m-D_{12})^2+n^2}\right]^{1/2}$

$$D_{16} = \frac{D_{12}+Q_1}{(m-D_{12})^2+n^2}$$

$$\delta_{15} = \text{arc tan}\,\frac{n}{m+Q_1} + \text{arc tan}\,\frac{n}{m-D_{12}} \tag{7.3.58}$$

$$\phi_{13}(t') = L^{-1}\left\{\frac{1}{s^3+s^2Q_1+sQ_2+Q_3}\right\} = L^{-1}\left\{\frac{1}{[(s-m)^2+n^2](s-D_{12})}\right\}$$

$$\phi_{13}(t') = D_{17}e^{mt'}\sin(nt'+\delta_{17})+D_{18}e^{D_{12}t'} \tag{7.3.59}$$

in which $D_{17} = \frac{1}{n[(m-D_{12})^2+n^2]^{1/2}}$

$$D_{18} = \frac{1}{(m-D_{12})^2+n^2}$$

$$\delta_{17} = -\text{arc tan}\,\frac{n}{m-D_{12}} \tag{7.3.60}$$

The input function $r(\tau)$ in (7.3.34) is the same as $r(t')$ given by (7.3.31) in which t' has been replaced by τ. After some manipulations we obtain

$$r(\tau) = D_{19}\sin\omega\tau+D_{20}\cos\omega\tau \tag{7.3.61}$$

where $D_{19} = R_{eq}\cos\theta_2-R_1\cos\theta_1-\omega L_{eq}\sin\theta_2+\omega L\sin\theta_1$

$$D_{20} = R_{eq}\sin\theta_2-R_1\sin\theta_1+\omega L_{eq}\cos\theta_2-\omega L\cos\theta_1. \tag{7.3.62}$$

It must be remembered that θ_1 and θ_2 were given by (7.3.25).

Substituting $\phi_{13}(t')$ given by (7.3.59) in which t' is replaced by $(t'-\tau)$ and $r(\tau)$ from (7.3.61) into (7.3.37), the integral

term in this equation becomes

$$\int_0^{t'} \phi_{13}(t'-\tau)r(\tau)d\tau = \int_0^{t'} \{D_{17}e^{m(t'-\tau)}\sin[n(t'-\tau)+\delta_{17}]$$

$$+ D_{18}e^{D_{12}(t'-\tau)}\}[D_{19}\sin\omega\tau+D_{20}\cos\omega\tau]d\tau \qquad (7.3.63)$$

To obtain the analytical form of the above equation we should split $\sin[n(t'-\tau)+\delta_{17}]$ into two terms and do the integrations term by term. Owing to the long calculations, all the stages in solving (7.3.63) are not shown here. After a few steps we obtain

$$\int_0^{t'} \phi_{13}(t'-\tau)r(\tau)d\tau = D_{17}D_{19}\sin(nt'+\delta_{17})[-mD_{22}\sin D_{24}t'-$$

$$D_{22}D_{24}\cos D_{24}t'+D_{22}D_{24}e^{mt'}-D_{23}m\sin D_{25}t'-D_{23}D_{25}\cos D_{25}t'+$$

$$D_{23}D_{25}e^{mt'}]+D_{17}D_{20}\sin(nt'+\delta_{17})[-mD_{22}\cos D_{24}t'+D_{22}D_{24}\sin D_{24}t'+$$

$$D_{22}me^{mt'}-D_{23}m\cos D_{25}t'+D_{23}D_{25}\sin D_{25}t'+D_{23}me^{mt'}]-$$

$$D_{17}D_{19}\cos(nt'+\delta_{17})[-mD_{23}\cos D_{25}t'+D_{23}D_{25}\sin D_{25}t'+mD_{23}e^{mt'}+$$

$$D_{22}m\cos D_{24}t'-D_{22}D_{24}\sin D_{24}t'-mD_{22}e^{mt'}]-D_{17}D_{20}\cos(nt'+\delta_{17})\cdot$$

$$[-mD_{22}\sin D_{24}t'-D_{22}D_{24}\cos D_{24}t'+D_{22}D_{24}e^{mt'}+D_{23}m\sin D_{25}t'+$$

$$D_{23}D_{25}\cos D_{25}t'-D_{23}D_{24}e^{mt'}]+\left(\frac{D_{18}D_{19}\omega+D_{18}D_{20}D_{12}}{D_{12}^2+\omega^2}\right)e^{D_{12}t'}+$$

$$\frac{1}{D_{12}^2+\omega^2}[(-D_{18}D_{19}D_{12}+D_{18}D_{20}\omega)\sin\omega t'+(-D_{18}D_{19}\omega$$

$$-D_{18}D_{20}D_{12})\cos\omega t'] \qquad (7.3.64)$$

where the new constants are

$$D_{22} = \frac{1}{2[m^2+(\omega+n)^2]}$$

$$D_{23} = \frac{1}{2[m^2+(\omega-n)^2]}$$

$$D_{24} = \omega+n$$

$$D_{25} = \omega-n \qquad (7.3.65)$$

Again after some manipulations (7.3.64) becomes

$$\int_0^{t'} \phi_{13}(t'-\tau)r(\tau)d\tau = D_{17}\sin(nt'+\delta_{17})[D_{28}\sin D_{24}t'+D_{29}\cos D_{24}t'$$

$$+ D_{30}\sin D_{25}t'+D_{31}\cos D_{25}t'+D_{32}e^{mt'}]-D_{17}\cos(nt'+\delta_{17})\cdot$$

$$[D_{29}\sin D_{24}t'-D_{28}\cos D_{24}t'-D_{31}\sin D_{25}t'+D_{30}\cos D_{25}t'$$

$$+ D_{33}e^{mt'}]-D_{26}e^{D_{12}t'}+D_{27}\sin\omega t'+D_{26}\cos\omega t' \qquad (7.3.66)$$

where $D_{26} = \dfrac{-(D_{18}D_{19}\omega+D_{18}D_{20}D_{12})}{D_{12}^2+\omega^2}$

$$D_{27} = \frac{D_{18}D_{20}\omega-D_{18}D_{19}D_{12}}{D_{12}^2+\omega^2}$$

$$D_{28} = D_{20}D_{22}D_{24} - mD_{22}D_{19}$$

$$D_{29} = -(D_{22}D_{24}D_{19} + mD_{22}D_{20})$$

$$D_{30} = D_{20}D_{23}D_{25} - mD_{23}D_{19}$$

$$D_{31} = -(D_{19}D_{23}D_{25} + mD_{20}D_{23})$$

$$D_{32} = -(D_{29}+D_{31})$$

$$D_{33} = D_{28}-D_{30} \qquad (7.3.67)$$

Equation (7.3.66) can then be written as

$$\int_0^{t'} \phi_{13}(t'-\tau)r(\tau)d\tau = D_{17}\sin(nt'+\delta_{17})[D_{34}\sin(D_{24}t'+\delta_{34})$$
$$+ D_{35}\sin(D_{25}t'+\delta_{35})+D_{32}e^{mt'}]-D_{17}\cos(nt'+\delta_{17})\cdot$$
$$[D_{36}\sin(D_{24}t'+\delta_{36})+D_{37}\sin(D_{25}t'+\delta_{37})+D_{33}e^{mt'}]$$
$$- D_{26}e^{D_{12}t'}+D_{27}\sin\omega t'+D_{26}\cos\omega t' \qquad (7.3.68)$$

in which

$$D_{34} = (D_{28}^2+D_{29}^2)^{1/2} \quad ; \quad \delta_{34} = \text{arc tan}\,\frac{D_{29}}{D_{28}}$$

$$D_{35} = (D_{30}^2+D_{31}^2)^{1/2} \quad ; \quad \delta_{35} = \text{arc tan}\,\frac{D_{31}}{D_{30}}$$

$$D_{36} = (D_{28}^2+D_{29}^2)^{1/2} \quad ; \quad \delta_{36} = \text{arc tan}\,\frac{-D_{28}}{D_{29}}$$

$$D_{37} = (D_{30}^2+D_{31}^2)^{1/2} \quad ; \quad \delta_{37} = \text{arc tan}\,\frac{D_{30}}{-D_{31}} \qquad (7.3.69)$$

From the list of the constants in (7.3.69) one obtains

$$D_{34} = D_{36}$$
$$\delta_{36} = \delta_{34}\pm\pi/2$$
$$\delta_{37} = \delta_{35}+\pi/2 \qquad (7.3.70)$$

Using (7.3.70) in (7.3.68) we finally obtain

$$\int_0^{t'} \phi_{13}(t'-\tau)r(\tau)d\tau = D_{40}\cos(\omega t'+\delta_{40})+D_{42}\cos(\omega t'+\delta_{42})$$
$$+ D_{44}e^{mt'}\sin(nt'+\delta_{44})-D_{26}e^{D_{12}t'}+D_{39}\sin(\omega t'+\delta_{39}) \qquad (7.3.71)$$

where the new constants are

$$D_{38} = (D_{32}^2+D_{33}^2)^{1/2} \quad ; \quad \delta_{38} = \text{arc tan}\,\frac{-D_{33}}{D_{32}}$$

$$D_{39} = (D_{27}^2+D_{26}^2)^{1/2} \quad ; \quad \delta_{39} = \text{arc tan}\,\frac{D_{26}}{D_{27}}$$

$$D_{40} = D_{17}D_{34}$$

$$D_{41} = D_{24}-n = \omega+n-n = \omega \; ; \quad \delta_{40} = \delta_{34}-\delta_{17}$$

$$D_{42} = -D_{17}D_{35}$$

$$D_{43} = n+D_{25} = n+\omega-n = \omega \; ; \quad \delta_{42} = \delta_{17}+\delta_{35}$$

$$D_{44} = D_{17}D_{38} \quad ; \quad \delta_{44} = \delta_{17}+\delta_{38} \qquad (7.3.72)$$

Note that in the above list D_{24} and D_{25} have been replaced by their equivalent terms as given in (7.3.65). Inserting (7.3.54, 57, 59 and 71) into (7.3.37) yields

$$\begin{aligned} i_C(t') = x_1(t') = {} & [D_{13}e^{mt'}\sin(nt'+\delta_{13})+D_{14}e^{D_{12}t'}]x_1(0^+) \\ & + [D_{15}e^{mt'}\sin(nt'+\delta_{15})+D_{16}e^{D_{12}t'}]x_2(0^+) \\ & + [D_{17}e^{mt'}\sin(nt'+\delta_{17})+D_{18}e^{D_{12}t'}]x_3(0^+) \\ & -Q_4[D_{40}\cos(D_{41}t'+\delta_{40})+D_{42}\cos(D_{43}t'+\delta_{42})+D_{44}e^{mt'}\sin(nt'+\delta_{44}) \\ & - D_{26}e^{D_{12}t'}+D_{39}\sin(\omega t'+\delta_{39})] \qquad (7.3.73) \end{aligned}$$

Regrouping the variables we obtain

$$i_C(t') = x_1(t') = D_{46}e^{mt'}\sin nt' + D_{47}e^{mt'}\cos nt' + D_{48}e^{D_{12}t'}$$
$$+ D_{49}\cos(\omega t'+\delta_{40}) + D_{50}\cos(\omega t'+\delta_{42}) + D_{51}\sin(\omega t'+\delta_{39}) \tag{7.3.74}$$

where

$$D_{46} = D_{13}x_1(0^+)\cos\delta_{13} + D_{15}x_2(0^+)\cos\delta_{15} + D_{17}x_3(0^+)\cos\delta_{17} - Q_4D_{44}\cos\delta_{44}$$
$$D_{47} = D_{13}x_1(0^+)\sin\delta_{13} + D_{15}x_2(0^+)\sin\delta_{15} + D_{17}x_3(0^+)\sin\delta_{17} - Q_4D_{44}\sin\delta_{44}$$
$$D_{48} = D_{14}x_1(0^+) + D_{16}x_2(0^+) + D_{18}x_3(0^+) + Q_4D_{26}$$
$$D_{49} = -Q_4D_{40}$$
$$D_{50} = -Q_4D_{42}$$
$$D_{51} = -Q_4D_{39} \tag{7.3.75}$$

Equation (7.3.74) can also be written in the following form

$$i_C(t') = x_1(t') = D_{52}e^{mt'}\sin(nt'+\delta_{52}) + D_{48}e^{D_{12}t'} + D_{49}\cos(\omega t+\delta_{40})$$
$$+ D_{50}\cos(\omega t'+\delta_{42}) + D_{51}\sin(\omega t'+\delta_{39}) \tag{7.3.76}$$

in which $D_{52} = (D_{46}^2 + D_{47}^2)^{1/2}$

$$\delta_{52} = \arctan\frac{D_{47}}{D_{46}} \tag{7.3.77}$$

Equation (7.3.76) gives the variations of i_C during the transfer mode. Note that this equation has been derived on the assumption that Δ in (7.3.44) has one real and two complex conjugate roots. In (7.3.75) all the constants except $x_1(0^+)$, $x_2(0^+)$ and $x_3(0^+)$ have known values.

The initial vector $[x(0^+)]$ is found in the following way. According to (7.3.21) it can be written

$$x_1(0^+) = i_C(0^+)$$

$$x_2(0^+) = \left.\frac{di_C}{dt'}\right|_{t'=0^+}$$

$$x_3(0^+) = \left.\frac{d^2 i_C}{dt'^2}\right|_{t'=0^+} \qquad (7.3.78)$$

But because of the leakage inductance, the phase A current cannot have a step change, so that, according to fig. 7.2 and 7.3:

$$i_A(t_2^-) = i_A(t_2^+) = 0 \qquad (7.3.79)$$

But from (7.3.5), when t and t_a are the independent variables, the result is

$$i_C(t_2^+) = i_d(t_2^+) = i_d(t_{a1}) \qquad (7.3.80)$$

Also since the dc link current is continuous

$$i_d(t_2^-) = i_d(t_2^+) = i_d(t_{a1}) \qquad (7.3.81)$$

which yields

$$i_C(t_2^+) = i_C(t_2^-) = i_d(t_2^+) = i_d(t_2^-) = i_d(t_{a1}) \qquad (7.3.82)$$

or for the case when t' is the independent variable

$$i_C(0^+) = i_C(0^-) = i_d(0^+) = i_d(0^-) = i_d(t_{a1}) \qquad (7.3.83)$$

Comparing (7.3.83) with (7.3.78) one obtains

$$x_1(0^+) = i_C(0^+) = i_d(t_{a1}) \tag{7.3.84}$$

Now we should derive the other two terms in (7.3.78). From fig. 7.2 and (7.2.38) for $t=t_2^-$ we have

$$v_{D1}(t_2^-) = v_{CA}(t_2^-) - v_{C5}(t_2^-) = 0 \tag{7.3.85}$$

which yields

$$v_{CA}(t_2^-) = v_{C5}(t_2^-) \tag{7.3.86}$$

and from fig. 7.3 and (7.3.4)

$$v_{CA}(t_2^+) = v_{C5}(t_2^+) \tag{7.3.87}$$

From the fact that v_{C5} cannot have a step change, we conclude that

$$v_{C5}(t_2^-) = v_{C5}(t_2^+) = v_{CA}(t_2^-) = v_{CA}(t_2^+) \tag{7.3.88}$$

Combining (7.3.79) and (7.3.83) with (7.3.88) yields

$$\left.\frac{di_A}{dt}\right|_{t=t_2^+} = \left.\frac{di_A}{dt'}\right|_{t'=0^+} = 0 \tag{7.3.89}$$

Using (7.3.79), (7.3.84) and (7.3.89), equation (7.3.20) at $t'=0^+$ can be written as

$$V_d = R_a x_1(0^+) + L_a \left.\frac{di_C}{dt'}\right|_{t'=0^+} + E_1\sqrt{3}\cos(\phi_3 - \frac{\pi}{3})$$

or

$$x_2(0^+) = \left.\frac{di_C}{dt'}\right|_{t'=0^+} = \frac{1}{L_a}[V_d - R_a x_1(0^+) - E_1\sqrt{3}\cos\theta_1] \quad (7.3.90)$$

where θ_1 can be obtained from (7.2.10) and (7.2.25).

To obtain $x_3(0^+)$ we differentiate (7.3.18) and (7.3.20), respectively, taking into account that some of the terms are constants. Using (7.3.79, 83, 89 and 90) the results at $t'=0^+$ are

$$-\frac{2}{3C}\cancel{i_d(t_a)} = R_1 x_3(0^+) + L\left.\frac{d^2 i_C}{dt'^2}\right|_{t'=0^+} - L\left.\frac{d^2 i_A}{dt'^2}\right|_{t'=0^+}$$

$$+ \omega E_1\sqrt{3}\sin\theta_2 \quad (7.3.91)$$

$$L_{eq}\left.\frac{d^2 i_A}{dt'^2}\right|_{t'=0^+} + R_a x_2(0^+) + L_a\left.\frac{d^2 i_C}{dt'^2}\right|_{t'=0^+} - \omega E_1\sqrt{3}\sin\theta_1 = 0$$

$$(7.3.92)$$

where θ_1 and θ_2 were given in (7.3.25). From the above two equations

$$x_3(0^+) = \left.\frac{d^2 i_C}{dt'^2}\right|_{t'=0^+} = y_{14}$$

$$\frac{d^2 i_A}{dt'^2} = y_{14} + y_{13} \quad (7.3.93)$$

in which

$$y_{13} = \frac{1}{L}\left(\frac{2}{3C}x_1(0^+) + R_1 x_2(0^+) + \omega E_1\sqrt{3}\sin\theta_2\right)$$

$$y_{14} = \frac{1}{L_a + L_{eq}}\left(-L_{eq} y_{13} - R_a x_2(0^+) + \omega E_1\sqrt{3}\sin\theta_1\right) \quad (7.3.94)$$

Having the equation of phase C current, as given by (7.3.76), we can now find the phase A current during this mode.

From (7.3.10, 20 and 25) one can obtain

$$V_d = (R_{eq}+L_{eq}p)i_A(t')+(R_a+L_ap)i_C(t')+E_1\sqrt{3}\cos(\omega t'+\theta_1) \tag{7.3.95}$$

Substituting $i_C(t')$ and its first derivative from (7.3.76) into the above equation yields

$$\begin{aligned} V_d = {} & e^{mt'}[D_{53}\sin(nt'+\delta_{52})+D_{54}\cos(nt'+\delta_{52})+D_{55}e^{D_{12}t'} \\ & + D_{56}\sin(\omega t'+\delta_{40})+D_{57}\cos(\omega t'+\delta_{40})+D_{58}\sin(\omega t'+\delta_{42}) \\ & + D_{59}\cos(\omega t'+\delta_{42})+D_{60}\sin(\omega t'+\delta_{39})+D_{61}\cos(\omega t'+\delta_{39}) \\ & + R_{eq}i_A(t')+L_{eq}i_A'(t')+E_1\sqrt{3}\cos(\omega t'+\theta_1) \end{aligned} \tag{7.3.96}$$

where

$$\begin{aligned} D_{53} &= R_aD_{52}+mL_aD_{52} \\ D_{54} &= nL_aD_{52} \\ D_{55} &= R_aD_{48}+L_aD_{12}D_{48} \\ D_{56} &= -L_aD_{49}D_{41} \\ D_{57} &= R_aD_{49} \\ D_{58} &= -L_aD_{50}D_{43} \\ D_{59} &= R_aD_{50} \\ D_{60} &= R_aD_{51} \\ D_{61} &= \omega L_aD_{51} \end{aligned} \tag{7.3.97}$$

or

$$V_d = D_{62}e^{mt'}\sin(nt'+\beta_{62})+D_{55}e^{D_{12}t'}+D_{63}\sin(\omega t'+\beta_{63})$$

$$+ D_{64}\sin(\omega t'+\beta_{64})+D_{65}\sin(\omega t'+\beta_{65})+R_{eq}i_A(t')$$

$$+ L_{eq}i_A'(t')+E_1\sqrt{3}\cos(\omega t'+\theta_1) \qquad (7.3.98)$$

in which

$$D_{62} = (D_{53}^2+D_{54}^2)^{1/2} \quad ; \quad \delta_{62} = \text{arc tan}\,\frac{D_{54}}{D_{53}}$$

$$D_{63} = (D_{56}^2+D_{57}^2)^{1/2} \quad ; \quad \delta_{63} = \text{arc tan}\,\frac{D_{57}}{D_{56}}$$

$$D_{64} = (D_{58}^2+D_{59}^2)^{1/2} \quad ; \quad \delta_{64} = \text{arc tan}\,\frac{D_{59}}{D_{58}}$$

$$D_{65} = (D_{60}^2+D_{61}^2)^{1/2} \quad ; \quad \delta_{65} = \text{arc tan}\,\frac{D_{61}}{D_{60}}$$

$$\beta_{62} = \delta_{52}+\delta_{62}$$

$$\beta_{63} = \delta_{40}+\delta_{63}$$

$$\beta_{64} = \delta_{42}+\delta_{64}$$

$$\beta_{65} = \delta_{39}+\delta_{65} \qquad (7.3.99)$$

Equation (7.3.98) is a nonlinear first order differential equation from which $i_A(t')$ should be found. The Laplace transform of this equation gives

$$\frac{V_d}{s} = D_{62}\sin\beta_{62}\left[\frac{s+D_{66}}{(s-m)^2+n^2}\right] + \frac{D_{55}}{s-D_{12}} + D_{63}\frac{s\sin\beta_{63}+\omega\cos\beta_{63}}{s^2+\omega^2}$$

$$+ D_{64}\frac{s\sin\beta_{64}+\omega\cos\beta_{64}}{s^2+\omega^2} + D_{65}\frac{s\sin\beta_{65}+\omega\cos\beta_{65}}{s^2+\omega^2}$$

$$+ R_{eq} I_A(s) + L_{eq}[sI_A(s) - i_A(0^+)] + E_1\sqrt{3}\,\frac{s\cos\theta_1 - \omega\sin\theta_1}{s^2+\omega^2} \tag{7.3.100}$$

in which $D_{66} = -m+n \cot \beta_{62}$ (7.3.101)

According to (7.3.79), at the beginning of the transfer mode the phase A current is zero. Therefore $I_A(s)$ is obtained from (7.3.100) as

$$I_A(s) = \frac{V_d}{L_{eq}}\frac{1}{s(\alpha+s)} - \frac{D_{62}\sin\beta_{62}}{L_{eq}}\frac{s+D_{66}}{[(s-m)^2+n^2](s+\alpha)}$$

$$- \frac{D_{55}}{L_{eq}}\frac{1}{(s-D_{12})(s+\alpha)} - \frac{D_{67}}{L_{eq}}\frac{s+\omega D_{68}/D_{67}}{(s^2+\omega^2)(s+\alpha)}$$

$$- \frac{D_{69}}{L_{eq}}\frac{s+\omega D_{70}/D_{69}}{(s^2+\omega^2)(s+\alpha)} - \frac{D_{71}}{L_{eq}}\frac{s+\omega D_{72}/D_{71}}{(s^2+\omega^2)(s+\alpha)} \tag{7.3.102}$$

in which α is given by (7.2.18) and the other constants are

$$D_{67} = D_{63} \sin \beta_{63} \tag{7.3.103}$$

$$D_{68} = D_{63} \cos \beta_{63}$$

$$D_{69} = D_{64} \sin \beta_{64}$$

$$D_{70} = D_{64} \cos \beta_{64}$$

$$D_{71} = D_{65} \sin \beta_{65} + E_1\sqrt{3} \cos \theta_1$$

$$D_{72} = D_{65} \cos \beta_{65} - E_1\sqrt{3} \sin \theta_1 \tag{7.3.104}$$

or

$$I_A(s) = D_{73}\frac{1}{s(s+\alpha)} - \frac{D_{73a}}{L_{eq}}\frac{s+D_{66}}{[(s-m)^2+n^2](s+\alpha)}$$

$$- D_{74}\frac{1}{(s-D_{12})(s+\alpha)} - D_{75}\frac{s+\omega D_{76}}{(s^2+\omega^2)(s+\alpha)}$$

$$- D_{77}\frac{s+\omega D_{78}}{(s^2+\omega^2)(s+\alpha)} - D_{79}\frac{s+\omega D_{80}}{(s^2+\omega^2)(s+\alpha)} \qquad (7.3.105)$$

in which

$$D_{73} = \frac{V_d}{L_{eq}} \quad ; \quad D_{73a} = D_{62}\sin\beta_{62}$$

$$D_{74} = D_{55}/L_{eq} \quad ; \quad D_{75} = D_{67}/L_{eq}$$

$$D_{76} = D_{68}/D_{67} \quad ; \quad D_{77} = D_{69}/L_{eq}$$

$$D_{78} = D_{70}/D_{69} \quad ; \quad D_{79} = D_{71}/L_{eq}$$

$$D_{80} = D_{72}/D_{71} \qquad (7.3.106)$$

The inverse Laplace transform of (7.3.105) is found term by term or

$$L^{-1}\{\frac{1}{s(s+\alpha)}\} = D_{81}e^{-\alpha t'}+D_{82} = \frac{1}{\alpha}(1-e^{-\alpha t'}) \qquad (7.3.107)$$

where

$$D_{81} = \frac{1}{\alpha} \quad ; \quad D_{82} = \frac{1}{\alpha} \qquad (7.3.108)$$

$$L^{-1}\{\frac{s+D_{66}}{[(s-m)^2+n^2][s+\alpha]}\} = D_{83}e^{mt'}\sin(nt'+\delta_{88})+D_{84}e^{-\alpha t'} \qquad (7.3.109)$$

where

$$D_{83} = \frac{1}{n}\left[\frac{(m+D_{66})^2+n^2}{(m+\alpha)^2+n^2}\right]^{1/2}$$

$$D_{84} = \frac{D_{66}-\alpha}{(m+\alpha)^2+n^2}$$

$$\delta_{83} = \text{arc tan}\,\frac{n}{m+D_{66}} - \text{arc tan}\,\frac{n}{m+\alpha} \qquad (7.3.110)$$

$$L^{-1}\left\{\frac{1}{(s-D_{12})(s+\alpha)}\right\} = D_{85}e^{D_{12}t'}+D_{86}e^{-\alpha t'} = D_{85}(e^{D_{12}t'}-e^{-\alpha t'}) \qquad (7.3.111)$$

in which

$$D_{85} = \frac{1}{D_{12}+\alpha} \quad ; \quad D_{86} = \frac{1}{-\alpha-D_{12}} = -D_{85} \qquad (7.3.112)$$

$$L^{-1}\left\{\frac{s+\omega D_{76}}{(s^2+\omega^2)(s+\alpha)}\right\} = D_{87}\sin(\omega t'+\delta_{87})+D_{88}e^{-\alpha t'} \qquad (7.3.113)$$

where

$$D_{87} = \left[\frac{D_{76}^2+1}{\alpha^2+\omega^2}\right]^{1/2} \quad ; \quad D_{88} = \frac{\omega D_{76}-\alpha}{\alpha^2+\omega^2}$$

$$\delta_{87} = \text{arc tan}\,1/D_{76} - \text{arc tan}\,\omega/\alpha \qquad (7.3.114)$$

$$L^{-1}\left\{\frac{s+\omega D_{78}}{(s^2+\omega^2)(s+\alpha)}\right\} = D_{89}\sin(\omega t'+\delta_{89})+D_{90}e^{-\alpha t'} \qquad (7.3.115)$$

in which

$$D_{89} = \left[\frac{D_{78}^2+1}{\alpha^2+\omega^2}\right]^{1/2} \quad ; \quad D_{90} = \frac{\omega D_{78}-\alpha}{\alpha^2+\omega^2}$$

$$\delta_{89} = \text{arc tan}\,1/D_{78} - \text{arc tan}\,\omega/\alpha \qquad (7.3.116)$$

$$L^{-1}\left\{\frac{s+\omega D_{80}}{(s^2+\omega^2)(s+\alpha)}\right\} = D_{91}\ \sin(\omega t'+\delta_{91})+D_{92}e^{-\alpha t'} \qquad (7.3.117)$$

where

$$D_{91} = \left[\frac{D_{80}^2+1}{\alpha^2+\omega^2}\right]^{1/2} \quad ; \quad D_{92} = \frac{\omega D_{80}-\alpha}{\alpha^2+\omega^2}$$

$$\delta_{91} = \text{arc tan } 1/D_{80} - \text{arc tan } \omega/\alpha \qquad (7.3.118)$$

Using (7.3.107-118), the inverse Laplace transform of (7.3.105) provides us with the expression for the phase A current during mode 2

$$i_A(t') = D_{93}e^{-\alpha t'}+\frac{V_d}{R_{eq}}(1-e^{-\alpha t'})+D_{94}e^{mt'}\sin(nt'+\delta_{83})$$

$$+ D_{95}\sin(\omega t'+\delta_{87})+D_{96}\sin(\omega t'+\delta_{89})$$

$$+ D_{97}\sin(\omega t'+\delta_{91})+D_{98}e^{D_{12}t'} \qquad (7.3.119)$$

in which the new constants are

$$D_{93} = D_{74}D_{85} - \frac{D_{84}D_{73a}}{L_{eq}} - D_{75}D_{88}-D_{77}D_{90}-D_{79}D_{92}$$

$$D_{94} = -D_{83}D_{73a}/L_{eq} \quad ; \quad D_{95} = -D_{75}D_{87}$$

$$D_{96} = -D_{77}D_{89} \quad ; \quad D_{97} = -D_{79}D_{91}$$

$$D_{98} = -D_{74}D_{85} \quad ; \quad \frac{D_{73}}{\alpha} = \frac{V_d}{L_{eq}}\frac{L_{eq}}{R_{eq}} = \frac{V_d}{R_{eq}} \qquad (7.3.120)$$

It should be remembered that in (7.3.119), t' varies between zero and (t_3-t_2) ; also, this equation has been derived under the

condition that Δ_1 in (7.3.44) has one real and two complex conjugate roots.

The expression for the dc link current during the transfer mode, $i_d(t')$, can easily be obtained by adding (7.3.76) to (7.3.119)

$$i_d(t') = i_C(t')+i_A(t') = e^{mt'}(D_{99}\sin nt'+D_{100}\cos nt')$$
$$+ D_{101}\cos\omega t'+D_{102}\sin\omega t'+D_{103}\cos\omega t'+D_{104}\sin\omega t'$$
$$+ D_{105}\sin\omega t'+D_{106}\cos\omega t'+D_{107}e^{D_{12}t'}+D_{93}e^{-\alpha t'}$$
$$+ \frac{V_d}{R_{eq}}(1-e^{-\alpha t'}) \qquad (7.3.121)$$

in which

$$D_{99} = D_{52}\cos\delta_{52}+D_{94}\cos\delta_{83} \;;\; D_{100} = D_{52}\sin\delta_{52}+D_{94}\sin\delta_{83}$$
$$D_{101} = D_{49}\cos\delta_{40}+D_{95}\sin\delta_{87} \;;\; D_{102} = -D_{49}\sin\delta_{40}+D_{95}\cos\delta_{87}$$
$$D_{103} = D_{50}\cos\delta_{42}+D_{96}\sin\delta_{89} \;;\; D_{104} = -D_{50}\sin\delta_{42}+D_{96}\cos\delta_{89}$$
$$D_{105} = D_{51}\cos\delta_{39}+D_{97}\cos\delta_{91} \;;\; D_{106} = D_{51}\sin\delta_{39}+D_{97}\sin\delta_{91}$$
$$D_{107} = D_{48}+D_{98} \qquad (7.3.122)$$

or

$$i_d(t') = D_{108}e^{mt'}\sin(nt'+\delta_{108})+D_{109}\sin(\omega t'+\delta_{109})$$
$$+ D_{110}\sin(\omega t'+\delta_{110})+D_{111}\sin(\omega t'+\delta_{111})$$
$$+ D_{107}e^{D_{12}t'}+D_{93}e^{-\alpha t'}+\frac{V_d}{R_{eq}}(1-e^{-\alpha t'}) \qquad (7.3.123)$$

where

$$D_{108} = (D_{99}^2+D_{100}^2)^{1/2} \quad ; \quad \delta_{108} = \arctan D_{100}/D_{99}$$

$$D_{109} = (D_{101}^2+D_{102}^2)^{1/2} \quad ; \quad \delta_{109} = \arctan D_{101}/D_{102}$$

$$D_{110} = (D_{103}^2+D_{104}^2)^{1/2} \quad ; \quad \delta_{110} = \arctan D_{103}/D_{104}$$

$$D_{111} = (D_{105}^2+D_{106}^2)^{1/2} \quad ; \quad \delta_{111} = \arctan D_{106}/D_{105}$$

(7.3.124)

The transfer mode ends at $t=t_3$ or at $t'=t_1'=t_3-t_2$ when i_C becomes zero and D_5 is blocked. The duration of the transfer mode is equal to

$$t_{tr} = t_1' = t_3-t_2 \qquad (7.3.125)$$

To obtain t_1', we should solve the nonlinear equation of (7.3.76) so that

$$i_C(t_1') = D_{52}e^{mt_1'}\sin(nt_1'+\delta_{52})+D_{48}e^{D_{12}t_1'}+D_{49}\cos(\omega t_1'+\delta_{40})$$

$$+D_{50}\cos(\omega t_1'+\delta_{42})+D_{51}\sin(\omega t_1'+\delta_{39}) = 0 \qquad (7.3.126)$$

To find t_1' from the above equation, one of the numerical root-finding methods (such as bisection method) can be used. Note that the calculated value of t_1' depends on the motor parameters and the four initial values of V_d, i_{d1}, V_o and t_1.

7.3.1 Calculation of the Maximum Commutating Capacitor Voltage, V_o

As in the case with a constant dc link current, at the end of mode 2 the voltage across C_5 reaches $-V_o$ and remains constant during the next mode.

$$v_{C5}(t_1') = v_{C5}(t_3) = -V_o \qquad (7.3.1.1)$$

or

$$v_{C5}(t_1') = -\frac{2}{3C}\int_0^{t_1'} i_C(t')dt' + v_{C5}(t_2) = -V_o \qquad (7.3.1.2)$$

but from (7.2.12) we have

$$v_{C5}(t_2) = v_{C5}(t_{a1}) = -\frac{2}{3C}\int_0^{t_{a1}} i_d(t_a)dt_a + V_o \qquad (7.3.1.3)$$

in which the integral term was given by (7.2.46). Substituting (7.3.1.3) and (7.2.46) into (7.2.1.2) one gets

$$v_{C5}(t_1') = -\frac{2}{3C}\int_0^{t_1'} i_C(t')dt' - \frac{2}{3C}(K_6H_6+K_3H_9)+V_o = -V_o \qquad (7.3.1.4)$$

from which results

$$V_o = \frac{1}{3C}\left[K_6H_6+K_3H_9+\int_0^{t_1'} i_C(t')dt'\right] \qquad (7.3.1.5)$$

In the above expression only the integral term should be calculated. The expression for $i_C(t')$ was given by (7.3.75) and its integration yields

$$\int_0^{t_1'} i_C(t')dt' = U_1(U_2+U_3+U_4)+U_5+U_6+U_7+U_8 \qquad (7.3.1.6)$$

where $U_1 = D_{52}/(m^2+n^2)$; $U_2 = me^{mt_1'}\sin(nt_1'+\delta_{52})$

$U_3 = -ne^{mt_1'}\cos(nt_1'+\delta_{52})$; $U_4 = -m\sin\delta_{52}+n\cos\delta_{52}$

$U_5 = \frac{D_{48}}{D_{12}}(e^{D_{12}t_1'}-1)$; $U_6 = \frac{D_{49}}{\omega}[\sin(\omega t_1'+\delta_{40})-\sin\delta_{40}]$

$$U_7 = \frac{D_{50}}{\omega}\,[\sin(\omega t_1'+\delta_{42})-\sin\delta_{42}]$$

$$U_8 = \frac{D_{51}}{\omega}\,[\cos\delta_{39}-\cos(\omega t_1'+\delta_{39})] \qquad (7.3.1.7)$$

or

$$\int_0^{t_1'} i_C(t')dt' = U_9 \qquad (7.3.1.8)$$

where

$$U_9 = U_1(U_2+U_3+U_4)+U_5+U_6+U_7+U_8 \qquad (7.3.1.9)$$

Inserting (7.2.1.8) into (7.2.1.5) yields,

$$V_o = \frac{1}{3C}\,[K_6H_6+K_3H_9+U_9] \qquad (7.3.1.10)$$

The above equation is the implicit function from which V_o is calculated; the constants on the right hand side of this equation are obtained for each iteration knowing the initial values of the main variables (7.2.24). It is obvious that V_o calculated from (7.3.1.10) is not necessarily the same as V_{oe} which has been used as an initial value for the commutating capacitor maximum voltage. In addition, the value of V_o changes whenever one or more of the intial values (t_{o1}, V_{od}, i_{od1} and V_{oo}) are changed.

7.4 MODE 3 OR NORMAL MODE

This mode is defined from $t=t_3$, the instant at which D_5 becomes reverse biased to $t=t_4$ the moment at which T_2 is triggered. Since the current in phase C becomes zero at the end of mode 2, only in phase A and phase B currents flow during this mode, fig. 7.4. We can easily calculate the duration of this mode if we know the duration of

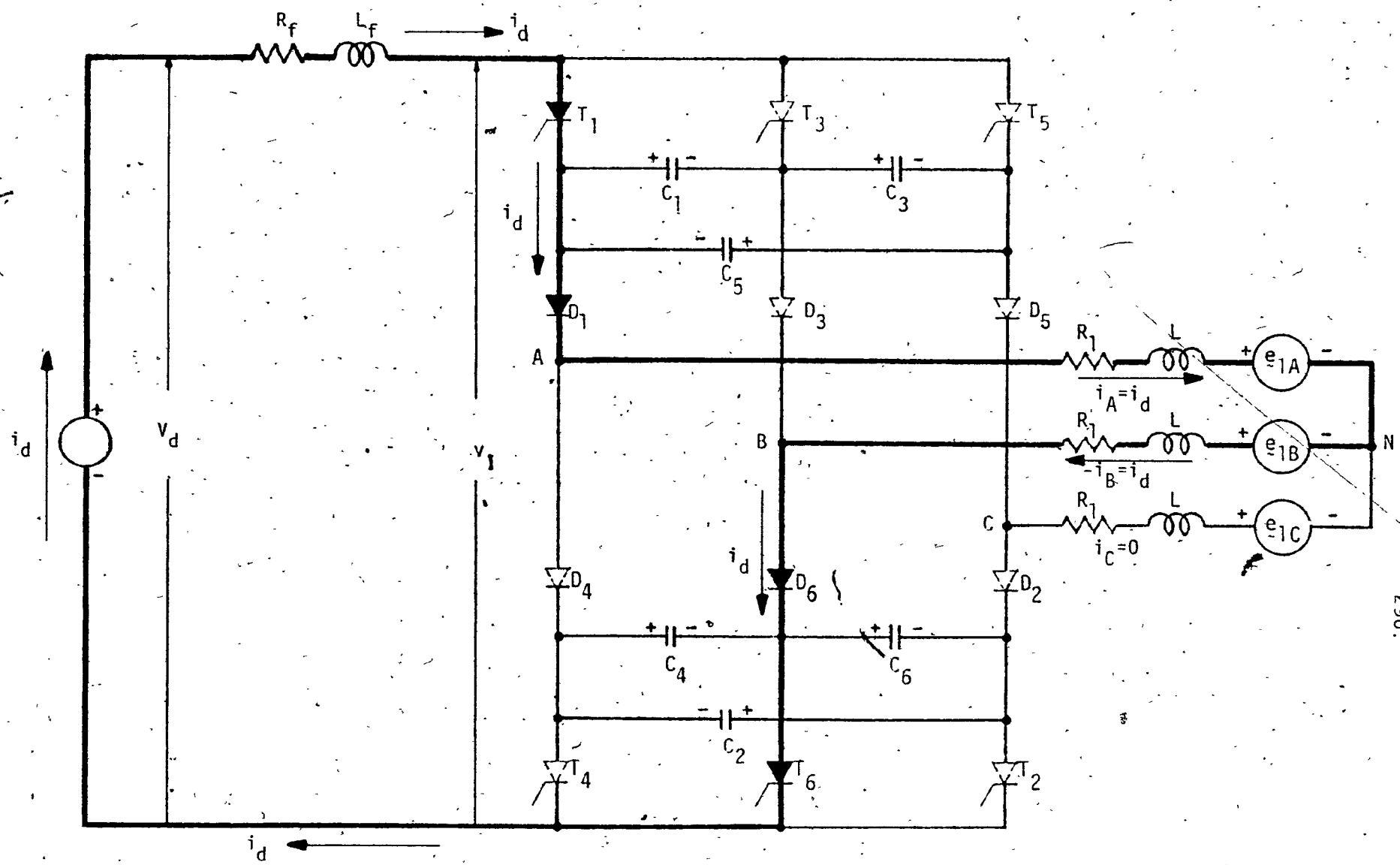

FIG. 7.4 ASCI-induction motor operation in mode 3 of case (g). The dc link input voltage is assumed to be constant. At $t=t_3$ the phase C current has been completely transferred to phase A so that a normal mode starts in the upper group. This mode ends at $t=t_4$ when T_2 is fired.

the commutation period which consists of the charging time and the transfer time:

$$t_{co} = t_{ch}+t_{tr} = t_{a1}+t_1' \qquad (7.4.1)$$

where t_{a1} and t_1' are obtained by solving (7.2.52) and (7.3.126), respectively. As the time interval between firing two consecutive thyristors is $\frac{\pi}{3\omega}$ sec., the normal time is

$$t_{no} = \frac{\pi}{3\omega} - (t_{ch}+t_{tr}) = \frac{\pi}{3\omega} - (t_{a1}+t_1') = \frac{\pi}{3\omega} - t_{co} \qquad (7.4.2)$$

Selecting a new time scale, t'', for this mode where

$$t'' = t-t_3 \qquad (7.4.3)$$

the result is

$$t_{no} = t_1'' = t_4-t_3 = \frac{\pi}{3\omega} - t_{co} \qquad (7.4.4)$$

In order to obtain the expression which defines this mode, consider the loop consisting of V_d, R_f, L_f, T_1, D_1, phase A, phase B, D_6 and T_6. Thus

$$V_d = R_{eq}i_d(t'')+L_{eq}pi_d(t'') + e_{1A}(t'')-e_{1B}(t'') \qquad (7.4.5)$$

where R_{eq} and L_{eq} were given by (7.2.14). Also, the phase currents during this mode are

$$i_A(t'') = -i_B(t'') = i_d(t'')$$
$$i_C(t'') = 0 \qquad (7.4.6)$$

while the capacitor currents are all zero. Therefore, all the capacitor and thyristor voltages remain constant during this mode, their

corresponding values being determined at the end of mode 2 , e.i., at $t=t_3$ or at $t'=t_1'$. For example, the upper group capacitor voltages are

$$v_{C1}(t'') = v_{C1}(t_3) = v_{C1}(t_1') = +V_o$$

$$v_{C3}(t'') = v_{C3}(t_3) = v_{C3}(t_1') = 0$$

$$v_{C5}(t'') = v_{C5}(t_3) = v_{C5}(t_1') = -V_o \qquad (7.4.7)$$

The fundamental component of each line current and the CEMF for each phase are the same as those given by (3.3.6-7). However, if these expressions are required to be functions of t'' then t should be replaced by t'' in the above equations. For example, for the CEMF's one can write

$$e_{1A}(t'') = E_1 \sin(\omega t''+\theta_3)$$

$$e_{1B}(t'') = E_1 \sin(\omega t''+\theta_3 - \frac{2\pi}{3})$$

$$e_{1C}(t'') = E_1 \sin(\omega t''+\theta_3 - \frac{4\pi}{3}) \qquad (7.4.8)$$

where $\theta_3 = \omega t_3 + \phi_1$ (7.4.9)

From (7.4-6, 8 and 9) and fig. 7.4 the motor terminal and line-to-line voltages are

$$v_A(t'') = (R_1+LP)i_d(t'') + E_1\sin(\omega t''+\theta_3)$$

$$v_B(t'') = -(R_1+LP)i_d(t'') + E_1\sin(\omega t''+\theta_3 - \frac{2\pi}{3})$$

$$v_C(t'') = E_1\sin(\omega t''+\theta_3 - \frac{4\pi}{3}) \qquad (7.4.10)$$

$$v_{AB}(t'') = 2(R_1+LP)i_d(t'') + E_1\sqrt{3}\cos(\omega t''+\theta_3-\pi/3)$$

$$v_{BC}(t'') = -(R_1+LP)i_d(t'') + E_1\sqrt{3}\cos(\omega t''+\theta_3-\pi)$$

$$v_{CA}(t'') = -(R_1+LP)i_d(t'') - E_1\sqrt{3}\cos(\omega t''+\theta_3-\frac{2\pi}{3}) \tag{7.4.11}$$

Also, the diode currents and voltages during this mode are

$$i_{D1}(t'') = i_{D6}(t'') = i_d(t'')$$

$$i_{D2}(t'') = i_{D3}(t'') = i_{D4}(t'') = i_{D5}(t'') = 0 \tag{7.4.12}$$

$$v_{D1}(t'') = v_{D6}(t'') = 0$$

$$v_{D3}(t'') = -v_{C1}(t'')+v_{AB}(t'') = -V_o+v_{AB}(t'')$$

$$v_{D5}(t'') = +v_{C5}(t'')+v_{AB}(t'') = -V_o+v_{AC}(t'')$$

$$v_{D2}(t'') = v_{CB}(t'')+v_{C6}(t'') = v_{CB}(t'')-V_o$$

$$v_{D4}(t'') = v_{AB}(t'')-v_{C4}(t'') = v_{AB}(t'')-V_o \tag{7.4.13}$$

and, at last, the inverter input voltage is

$$v_I(t'') = v_{AB}(t'') \tag{7.4.14}$$

The expression for the dc link current $i_d(t'')$, during this mode should be obtained next. From (7.4.5 and 8) we have

$$V_d = R_{eq}i_d(t'')+L_{eq}pi_d(t'') + E_1\sqrt{3}\cos(\omega t''+\theta_3-\frac{\pi}{3}) \tag{7.4.15}$$

The Laplace transform of the above equation yields

$$\frac{V_d}{s} = R_{eq}I_d(s)+L_{eq}[sI_d(s)-i_d(0^+)]+E_1\sqrt{3}\,\frac{s\cos\psi-\omega\sin\psi}{s^2+\omega^2} \tag{7.4.16}$$

where $i_d(0^+)$ is the dc link current at the beginning of this mode or at the end of mode 2

$$i_d(0^+) = i_d(t_1') \tag{7.4.17}$$

and

$$\psi = \theta_3 - \frac{\pi}{3} \tag{7.4.18}$$

From (7.4.16) we extract $I_d(s)$

$$I_d(s) = \frac{V_d}{L_{eq}} \frac{1}{s(s+\alpha)} + \frac{i_d(t_1')}{s+\alpha} - \frac{E_1\sqrt{3}}{L_{eq}} \cos\psi \frac{s-\omega\tan\psi}{(s^2+\omega^2)(s+\alpha)} \tag{7.4.19}$$

where $\alpha = R_{eq}/L_{eq}$. The inverse Laplace transform of each right hand side term gives

$$L^{-1}\{\frac{1}{s(s+\alpha)}\} = \frac{1}{\alpha}(1-e^{-\alpha t''}) \tag{7.4.20}$$

$$L^{-1}\{\frac{1}{s+\alpha}\} = e^{-\alpha t''} \tag{7.4.21}$$

$$L^{-1}\{\frac{s-\omega\tan\psi}{(s^2+\omega^2)(s+\alpha)}\} = D_{112}\sin(\omega t''+\delta_{112})+D_{113}e^{-\alpha t''} \tag{7.4.22}$$

in which

$$D_{112} = [\frac{1+\tan^2\psi}{\alpha^2+\omega^2}]^{1/2}$$

$$D_{113} = \frac{-\alpha-\omega\tan\psi}{\alpha^2+\omega^2}$$

$$\delta_{112} = \text{arc tan}\frac{1}{-\tan\psi} - \text{arc tan}\frac{\omega}{\alpha} \tag{7.4.23}$$

The inverse Laplace transform of (7.4.19) then becomes

$$i_d(t'') = D_{114}e^{-\alpha t''} + \frac{V_d}{R_{eq}} + D_{115}\sin(\omega t''+\delta_{112}) \qquad (7.4.23)$$

where

$$D_{114} = i_d(t_1') - \frac{V_d}{R_{eq}} - \frac{D_{113}E_1\cos\psi\sqrt{3}}{L_{eq}}$$

$$D_{115} = -E_1\ D_{112}\ \sqrt{3}\ \frac{\cos\psi}{L_{eq}} \qquad (7.4.24)$$

At the end of this mode, i.e. at $t''=t_1''$ or at $t=t_4$, the next thyristor, T_4, is fired and we have a new charging mode which is similar to mode 1 but with a $\frac{\pi}{3}$ rad delay angle. During one period of the inverter output frequency we have six charging, transfer and normal modes so that after each $\frac{\pi}{3}$ rad we should have the same conditions in the system regarding the values of the variables. Specifically, the dc link current, i_d, should have the same value at the beginning of mode 1 and at the end of mode 3

$$i_d(t_1) = i_d(t_4) = i_d(t_1'') = i_{d1} \qquad (7.4.25)$$

The above equation is one of the constraints which helps us find the values of the four main variables of the system. From (7.4.23 and 25) the result is then

$$D_{114}e^{-\alpha t_1''} + \frac{V_d}{R_{eq}} + D_{115}\sin(\omega t_1''+\delta_{112}) = i_{d1} \qquad (7.4.26)$$

where t_1'' is calculated from (7.4.3).

7.5 SOLUTION OF THE EQUATIONS

In the previous sections we described the system during the three distinct modes of operation. The four main variables which define the system behaviour during each mode are

1. The beginning of the charging mode, t_1 .
2. The rectifier average output voltage, V_d .
3. The dc link current at the beginning of a charging mode, i_{d1} .
4. The maximum voltage across the commutating capacitors, V_o .

These four variables are interrelated with the other system unknowns through nonlinear equations which were derived in the previous three sections.

In order to establish an algorithm for finding these unknowns we should first list all the unknowns as well as the variable equations.

The unknowns are:

$$V_d\ ,\ i_{d1}\ ,\ V_o\ ,\ t_1\ ,\ t_{ch}\ ,\ t_2\ ,\ t_{tr}\ ,$$
$$t_3\ ,\ t_{no}\ ,\ t_4\ ,\ t_{co}\ \text{ and }\ I_d \qquad (7.5.1)$$

The equations from which the above unknowns should be found

are as follows:

$$t_{ch} = t_{a1} = t_2 - t_1 \tag{7.2.37}$$

$$R_1[-K_6(H2/\alpha 1) + K_3H_{10}] + L[K_6(H_2-H_3) - K_3\omega H_8]$$
$$- E_1\sqrt{3}\cos(\omega t_{a1} + \phi_2 - \frac{2\pi}{3}) + \frac{2}{3C}(K_6H_6 + K_3H_9) - V_o = 0 \tag{7.2.50}$$

$$t_{tr} = t'_1 = t_3 - t_2 \tag{7.2.123}$$

$$D_{52}e^{mt'_1}\sin(nt'_1 + \delta_{52}) + D_{48}e^{D_{12}t'_1} + D_{49}\cos(\omega t'_1 + \delta_{40})$$
$$+ D_{50}\cos(\omega t'_1 + \delta_{42}) + D_{51}\sin(\omega t'_1 + \delta_{39}) = 0 \tag{7.3.124}$$

$$V_o = \frac{1}{3C}[K_6H_6 + K_3H_9 + U_9] \tag{7.3.1.10}$$

$$t_{co} = t_{ch} + t_{tr} = t_{a1} + t'_1 = t_3 - t_1 \tag{7.4.1}$$

$$t_{no} = t''_1 = \frac{\pi}{3\omega} - t_{co} \tag{7.4.2}$$

$$t_{no} = t''_1 = t_4 - t_3 \tag{7.4.3}$$

$$D_{114}e^{-\alpha t''_1} + \frac{V_d}{R_{eq}} + D_{115}\sin(\omega t''_1 + \delta_{112}) = i_{d1} \tag{7.4.25}$$

Comparing the number of the unknowns (which is 12) with

the number of the equations (which is 9), one finds that three more equations are needed in order to solve the problem. In the following, it will be shown how to obtain I_d, V_d and t_1 which then decreases the number of unknowns to 9, same as the number of equations.

7.5.1 Calculation of the dc link average current, I_d

The expressions of the dc link current during modes 1, 2 and 3 were given by (7.2.35),(7.3.121) and (7.4.22), respectively. The average dc link current will then be equal to

$$I_d = \frac{1}{(\pi/3\omega)} [I_{av1} t_{a1} + I_{av2} t'_1 + I_{av3} t''_1] \tag{7.5.1.1}$$

in which I_{av1}, I_{av2} and I_{av3} are the average values of the dc link current during the charging, transfer and normal modes with t_{a1}, t'_1 and t''_1 as the corresponding mode durations.

$$I_{av1} = \frac{1}{t_{a1}} \int_0^{t_{a1}} i_d(t_a) dt_a \tag{7.5.1.2}$$

$$I_{av2} = \frac{1}{t'_1} \int_0^{t'_1} i_d(t') dt' \tag{7.5.1.3}$$

$$I_{av3} = \frac{1}{t''_1} \int_0^{t''_1} i_d(t'') dt'' \tag{7.5.1.4}$$

The integral term in (7.5.1.2) was earlier calculated and was given by (7.2.46),

$$I_{av1} = \frac{1}{t_{a1}} (K_6 H_6 + K_3 H_9) \qquad (7.5.1.5)$$

The other integrals are:

$$\int_0^{t'_1} i_d(t')dt' = D_{108}D_{120}(D_{121}+D_{122}) + D_{109}D_{123}$$

$$+ D_{110}D_{124} + D_{111}D_{125} + D_{107}D_{126}$$

$$+ D_{93}D_{127} + \frac{V_d}{R_{eq}} D_{128} \qquad (7.5.1.6)$$

where:

$$D_{120} = \frac{1}{m^2+n^2}$$

$$D_{121} = e^{mt'_1} [m \sin(nt'_1 + \delta_{108}) - n \cos(nt'_1 + \delta_{108})]$$

$$D_{122} = -m \sin \delta_{108} + n \cos \delta_{108}$$

$$D_{123} = \frac{1}{\omega} [\cos \delta_{109} - \cos(\omega t'_1 + \delta_{109})]$$

$$D_{124} = \frac{1}{\omega} [\cos \delta_{110} - \cos(\omega t'_1 + \delta_{110})]$$

$$D_{125} = \frac{1}{\omega} [\cos \delta_{111} - \cos(\omega t'_1 + \delta_{111})]$$

$$D_{126} = \frac{1}{D_{12}} (e^{D_{12}t'_1} - 1)$$

$$D_{127} = \frac{1}{\alpha}\left(1 - e^{-\alpha t'_1}\right)$$

$$D_{128} = t'_1 + \frac{1}{\alpha}\left(e^{-\alpha t'_1} - 1\right) \qquad (7.5.1.7)$$

Then: $$I_{av2} = \frac{D_{129}}{t'_1} \qquad (7.5.1.8)$$

in which:

$$D_{129} = D_{108}D_{120}(D_{121} + D_{122}) + D_{109}D_{123} + D_{110}D_{124}$$

$$+ D_{111}D_{125} + D_{107}D_{126} + D_{93}D_{127} + \frac{V_d}{R_{eq}} D_{128} \qquad (7.5.1.9)$$

And

$$\int_0^{t''_1} i_d(t'')dt'' = D_{114}D_{130} + D_{131} + D_{115}D_{132} \qquad (7.5.1.10)$$

where:

$$D_{130} = \frac{1}{\alpha}\left(1 - e^{-\alpha t''_1}\right)$$

$$D_{131} = V_d t''_1 / R_{eq}$$

$$D_{132} = \frac{1}{\omega}\left[\cos\delta_{112} - \cos(t''_1 + \delta_{112})\right] \qquad (7.5.1.11)$$

Then: $$I_{av3} = \frac{D_{133}}{t''_1} \qquad (7.5.1.12)$$

in which: $D_{133} = D_{114}D_{130} + D_{131} + D_{115}D_{132}$ (7.5.1.13)

Replacing (7.5.1.5, 8, and 12) in (7.5.1.1) yields:

$$I_d = \frac{3\omega}{\pi}\,[K_6H_6 + K_3H_9 + D_{129} + D_{133}] \qquad (7.5.1.14)$$

7.5.2 Calculation of the motor input power and the rectifier average output voltage, V_d

In order to be able to calculate the rectifier average output voltage, V_d, it is indispensable to know the motor input power and the average dc link current. In this case, it follows:

$$V_d = P_{tm}/I_d + R_f \cdot I_d \qquad (7.5.2.1)$$

in which P_{tm} is the total motor input power, R_f being the dc link resistance and I_d is the average dc link current given by (7.5.1.14).

Since the induction motor equivalent circuit used in this thesis is the one shown by fig. 2.10, the calculation of the motor input power can be easily attained by knowing the motor parameters, operating point, CEMF and line current during each mode. The motor CEMF was obtained according to the steps explained in section (2.3) and the motor line current expressions were derived in previous sections. Since the motor line current during one cycle of the inverter output

consists of different parts, the calculation of the motor input power would be best done by employing some kind of numerical integration, e.g. Romberg's method. However, owing to the current waveform symmetry, the calculation of P_{tm} will be done only for half a cycle and the results will be doubled.

Figure 7.5 shows, for a general case, the motor phase A instantaneous current, i_A, its fundamental component, i_{1A}, and the corresponding CEMF, e_{1A}, during half a cycle. Note that, as before, the origin of time, $t=0$, is the positive crossover of the fundamental harmonic of the phase A current. Also, the different instants of time, the duration of each mode, the number of the equation expressing each part of i_A waveform and the other information have been given in fig. 7.5. It is seen that i_A consists of seven parts during half a cycle which lasts for $(\frac{2\pi}{3\omega} + t'_1)$ sec.

Due to the repetition of the dc link current, i_d, after each three consecutive modes, the magnitude of i_A at the beginning of each mode is equal to i_{d1}, i_{d2} or i_{d3}. Then the following relationships result,

$$i_d(t_4) = i_d(t_7) = i_d(t_1) = i_{d1}$$

$$i_d(t_5) = i_d(t_8) = i_d(t_2) = i_{d2}$$

$$i_d(t_3) = i_d(t_6) = i_d(t_9) = i_{d3} \qquad (7.5.2.2)$$

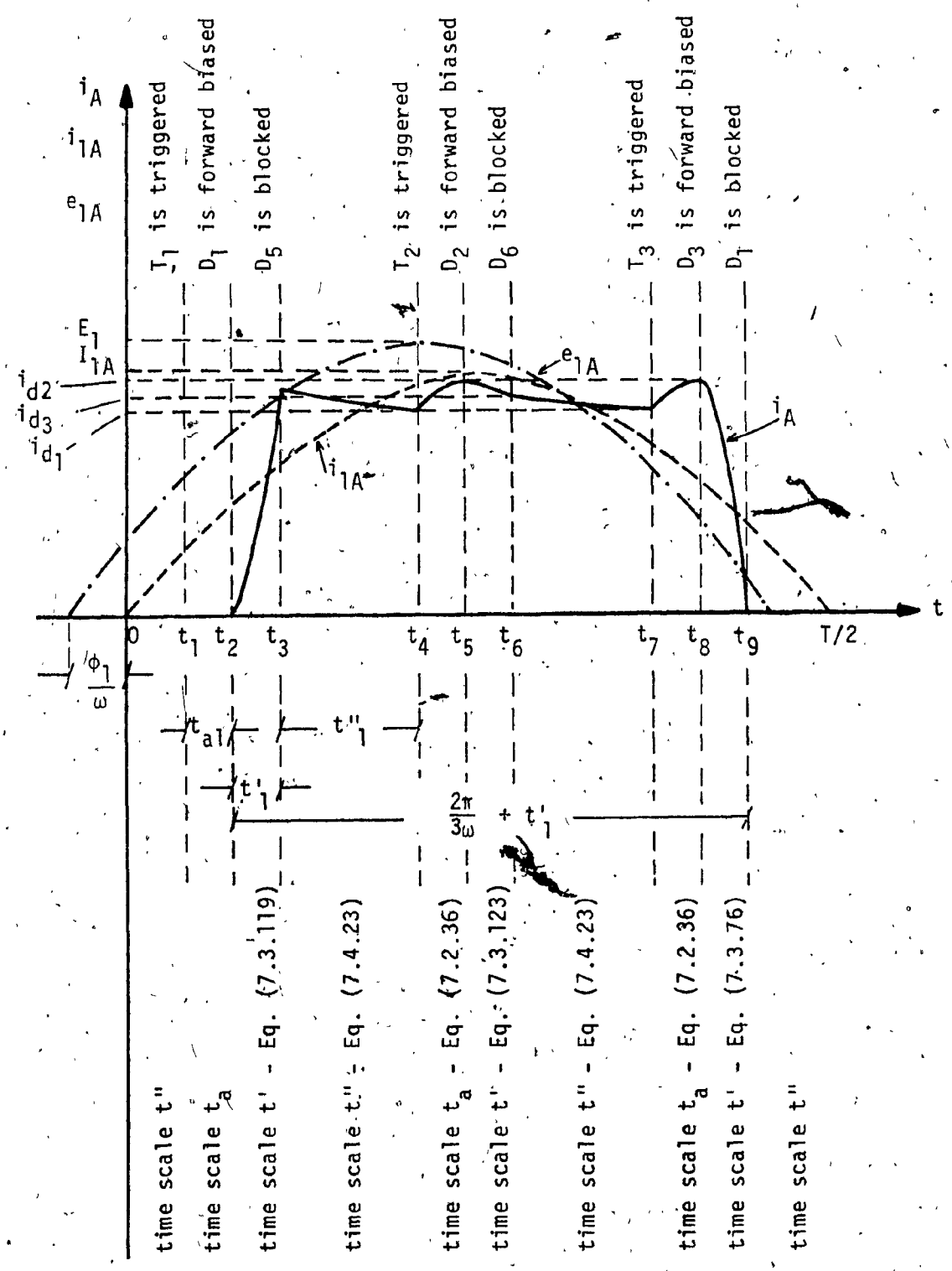

FIG. 7.5 Phase A CEMF, instantaneous and fundamental component of current during half a cycle in case (g). The time scale of each mode as well as the corresponding equation number of i_A have also been specified.

According to fig. 2.9c, the per phase motor input power is consumed in two parts. A small portion is dissipated as heat in the stator resistance, R_1, while the rest is absorbed by the CEMF, E_1. This last part is then responsible for generating the output torque as well as the heat loss in R_m and R_2. Since the input power is the same for each half cycle, the per phase total input power can be written as:

$$P_1 = \frac{2}{T}\left[\int_{t_2}^{t_9} R_1 i_A^2(t)dt + \int_{t_2}^{t_9} e_{1A}(t)i_A(t)dt\right] \qquad (7.5.2.3)$$

Since for each part of i_A waveform in fig. 7.5 a new time scale has been chosen, the above expression can be written in a new form:

$$\begin{aligned} P_1 = \frac{2}{T}\{R_1[&\int_0^{t'_1} i_A^2(t')dt' + \int_0^{t''_1} i_d^2(t'')dt'' + \int_0^{t_{a1}} i_d^2(t_a)dt_a \\ &+ \int_0^{t'_1} i_d^2(t')dt' + \int_0^{t''_1} i_d^2(t'')dt'' + \int_0^{t_{a1}} i_d^2(t_a)dt_a \\ &+ \int_0^{t'_1} i_C^2(t')dt'] + [\int_0^{t'_1} e_{11A}(t')i_A(t')dt' \\ &+ \int_0^{t''_1} e_{12A}(t'')i_d(t'')dt'' + \int_0^{t_{a1}} e_{13A}(t_a)i_d(t_a)dt_a \\ &+ \int_0^{t'_1} e_{14A}(t')i_d(t')dt' + \int_0^{t''_1} e_{15A}(t'')i_d(t'')dt'' \\ &+ \int_0^{t_{a1}} e_{16A}(t_a)i_d(t_a)dt_a + \int_0^{t'_1} e_{17A}(t')i_C(t')dt']\} \end{aligned} \qquad (7.5.2.4)$$

where

$$e_{11A}(t') = E_1 \sin(\omega t' + \omega t_2 + \phi_1)$$

$$e_{12A}(t'') = E_1 \sin(\omega t'' + \omega t_3 + \phi_1)$$

$$e_{13A}(t_a) = E_1 \sin(\omega t_a + \omega t_4 + \phi_1)$$

$$e_{14A}(t') = E_1 \sin(\omega t' + \omega t_5 + \phi_1)$$

$$e_{15A}(t'') = E_1 \sin(\omega t'' + \omega t_6 + \phi_1)$$

$$e_{16A}(t_a) = E_1 \sin(\omega t_a + \omega t_7 + \phi_1)$$

$$e_{17A}(t') = E_1 \sin(\omega t' + \omega t_8 + \phi_1)$$

$$t_2 = t_1 + t_{a1}$$

$$t_3 = t_2 + t'_1$$

$$t_4 = t_3 + t''_1$$

$$t_5 = t_4 + t_{a1}$$

$$t_6 = t_5 + t'_1$$

$$t_7 = t_6 + t''_1$$

$$t_8 = t_7 + t_{a1} \qquad (7.5.2.5)$$

The motor total input power then results to be,

$$P_{tm} = 3P_1 \quad w \qquad (7.5.2.6)$$

where P_1 is calculated numerically using (7.5.2.4). It should be remembered that for each set of V_d, i_{d1}, t_1 and V_o a definite value for I_d and P_{tm} are obtained. The final values of V_d, i_{d1}, t_1 and V_o as well as the other variables will be determined by the last iteration. The suggested algorithm will be given later, flow-chart (7.1).

7.5.3 Calculation of t_1 and the fundamental component of the motor line current

The last variable whose value is needed during each iteration is t_1. To obtain the value of t_1 for each iteration, it is necessary to calculate the fundamental harmonic of the motor phase A current and its corresponding shift angle with respect to the old origin of time. The details of the Fourier analysis required for the above calculation is given in Appendix C-1. If the shift angle thus

acquired is called ν , the new t_1 becomes:

$$t_{1n} = t_{1o} + \nu/\omega \qquad (7.5.3.1)$$

where t_{1o} is the value of t_1 used in the last iteration, and ω is the operating point frequency.

At this point there are the same number of equations as unknowns so that a flowchart can be provided. The next section gives the essential details of such a flowchart.

7.5.4 Flowchart for case (g)

A flowchart for an exact solution of the equations resolved in case (g) is suggested and explained in this section, flowchart 7.1. The dc link parameters, R_f and L_f , are the two new input data which should be added to the list of input data used in flowchart 3.2, step 10. In order to shorten the execution time of the computer program employing this flowchart, some of the output data of flowchart 3.2, which is run for the same operating point, are used as the initial values in the first iteration of flowchart 7.1. These are the values of V_I , t_1, V_o , t_{ch} and t_{tr} , step 30. Steps 40-100 are the same as steps 50-110 in flowchart 3.2 and are repeated in flowchart 7.1. The main structure of the flowchart is based on finding the values of the four main unknowns (V_o , V_d , t_1 and i_{d1}) from which the values of the other unknowns can be easily calculated. The four main unknowns constitute four simultaneous nonlinear implicit equations of the following general form:

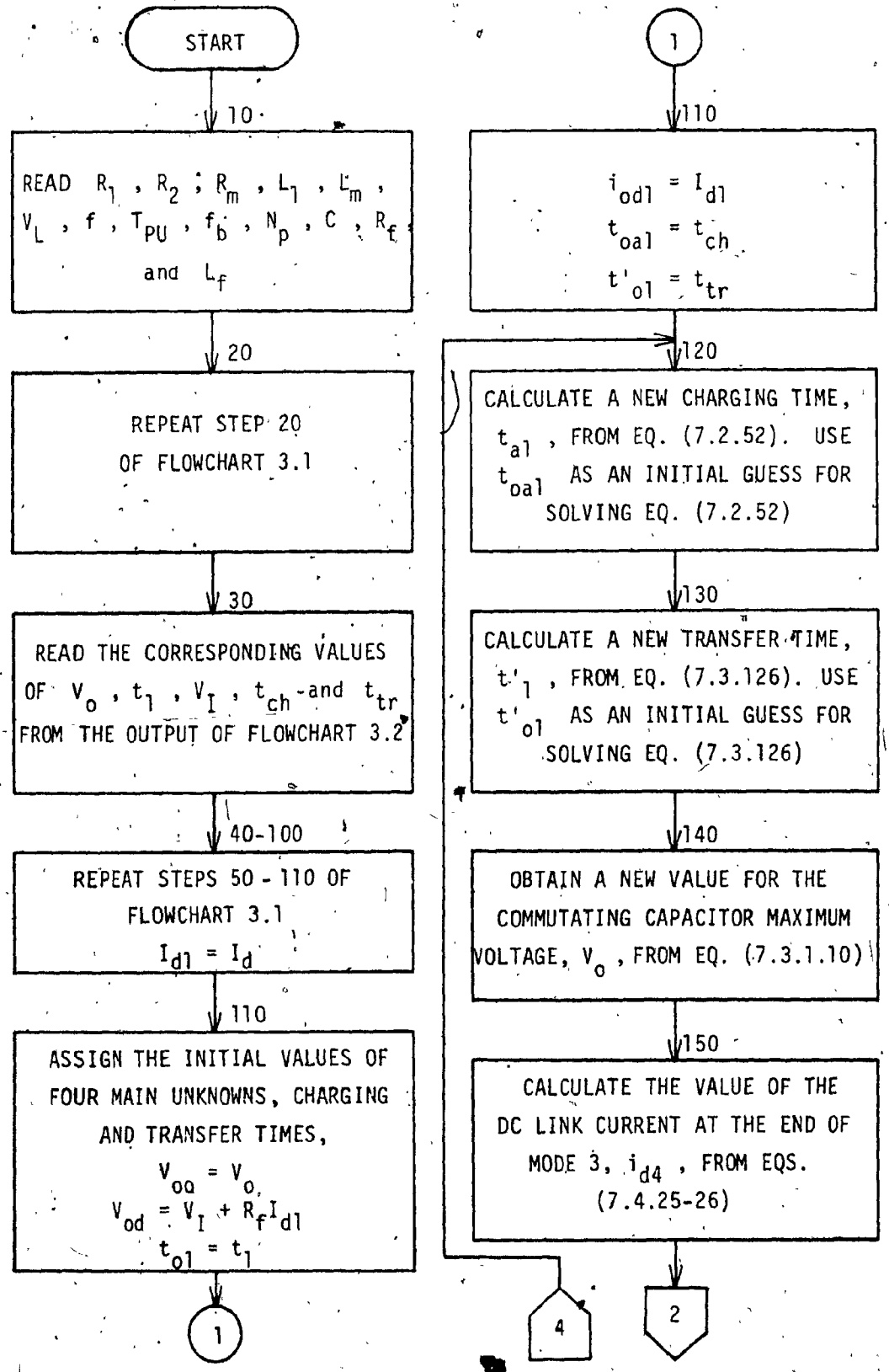
START
10
READ R_1, R_2, R_m, L_1, L_m, V_L, f, T_{PU}, f_b, N_p, C, R_f and L_f
20
REPEAT STEP 20 OF FLOWCHART 3.1
30
READ THE CORRESPONDING VALUES OF V_o, t_1, V_I, t_{ch} and t_{tr} FROM THE OUTPUT OF FLOWCHART 3.2
40-100
REPEAT STEPS 50 - 110 OF FLOWCHART 3.1
$I_{d1} = I_d$
110
ASSIGN THE INITIAL VALUES OF FOUR MAIN UNKNOWNS, CHARGING AND TRANSFER TIMES,
$V_{oa} = V_o$
$V_{od} = V_I + R_f I_{d1}$
$t_{o1} = t_1$
1
1
110
$i_{od1} = I_{d1}$
$t_{oa1} = t_{ch}$
$t'_{o1} = t_{tr}$
120
CALCULATE A NEW CHARGING TIME, t_{a1}, FROM EQ. (7.2.52). USE t_{oa1} AS AN INITIAL GUESS FOR SOLVING EQ. (7.2.52)
130
CALCULATE A NEW TRANSFER TIME, t'_1, FROM EQ. (7.3.126). USE t'_{o1} AS AN INITIAL GUESS FOR SOLVING EQ. (7.3.126)
140
OBTAIN A NEW VALUE FOR THE COMMUTATING CAPACITOR MAXIMUM VOLTAGE, V_o, FROM EQ. (7.3.1.10)
150
CALCULATE THE VALUE OF THE DC LINK CURRENT AT THE END OF MODE 3, i_{d4}, FROM EQS. (7.4.25-26)
4
2

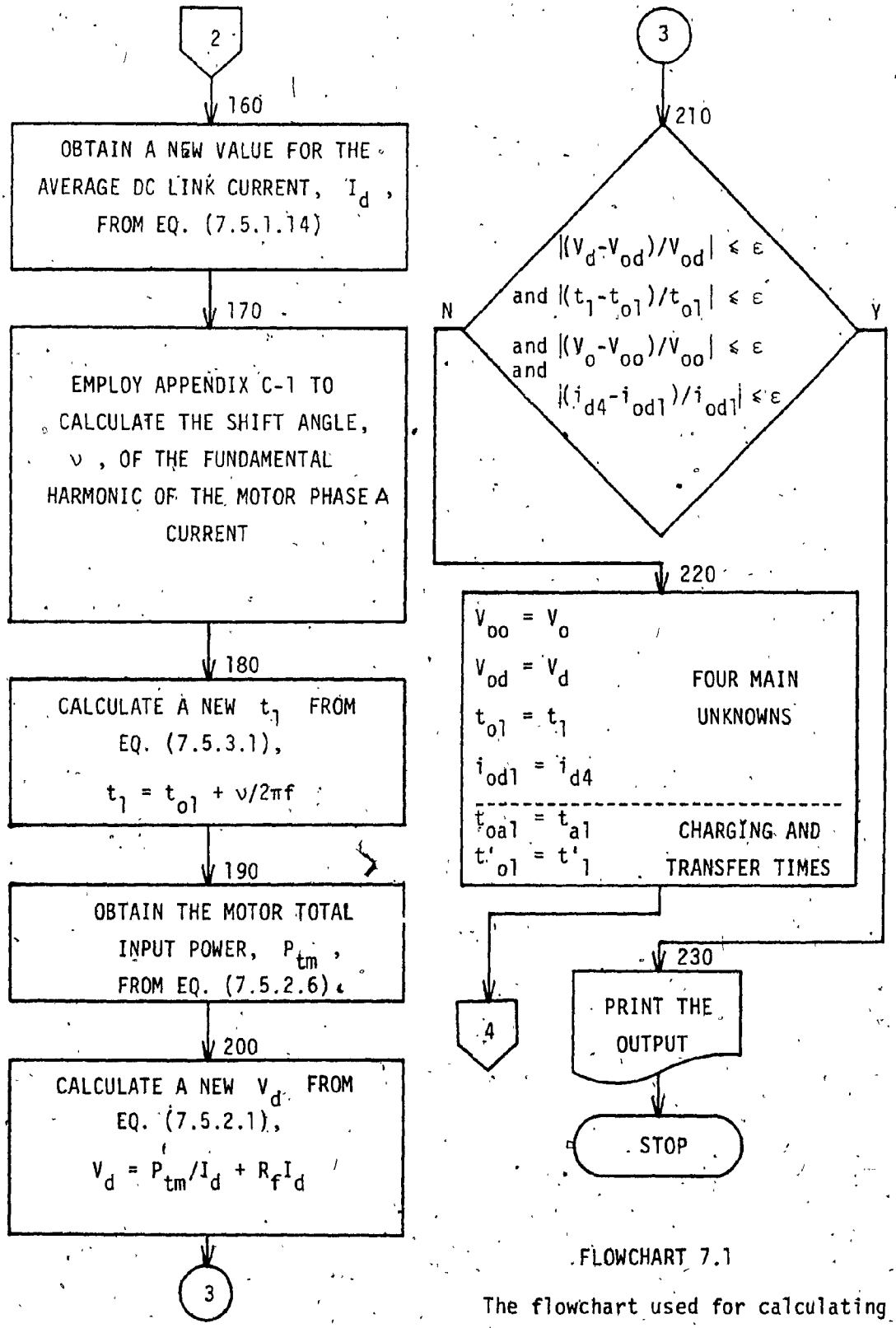

FLOWCHART 7.1

The flowchart used for calculating the variables of an ASCI-induction motor drive in case (g).

$$V_o = f_1(V_o , V_d , t_1 , i_{d1})$$

$$V_d = f_2(V_o , V_d , t_1 , i_{d1})$$

$$t_1 = f_3(V_o , V_d , t_1 , i_{d1})$$

$$i_{d1} = f_4(V_o , V_d , t_1 , i_{d1}) \qquad (7.5.4.1)$$

The easiest way to solve the above set of equations is by appointing some initial value to each unknown (step 110) and finding a new value for each of them (steps 140-200). The calculated new set of the unknowns are then used in the next iteration for generating another set for the unknowns (step 220). This procedure is repeated for a number of times so that the values of the main variables obtained in two consecutive iterations, with some allowable error, become the same (step 210). Aside from the mathematical conditions necessary for convergence of such iterations, the initial values used in the first iteration have an important role for establishing the convergence criteria. As long as these initial values are as near as possible to the expected results of system of equations in (7.5.4.1), the possibility of divergence is very low. Since the output of flowchart 3.2, which by itself is an exact solution of the system with a constant dc link current, is used in the first iteration (step 30), flowchart 7.1 yields the desired results without any difficulty. Chapter VIII in which the theoretical waveforms are compared with those obtained practically, discloses this point. Note that the charging and transfer times, t_{ch} ,

t_{tr} , are not among the main unknowns. The values of these two variables are found from their corresponding expressions [Eqs.(7.2.52), (7.3.126)] in each iteration (steps 120-130). Since these two equations are nonlinear, their solution takes less time if approximate values near to the exact results are known for t_{ch} and t_{tr} .. For this reason, their corresponding values are read from the output data of flowchart 3.2 in the first iteration (step 30). In addition, in each iteration, the calculated values of these two variables obtained in the last iteration are employed as starting values for solving each of the corresponding nonlinear equations (step 220).

7.6 WAVEFORMS AND RESULTS

The operation of an ASCI-induction motor, assuming a constant voltage at the sending terminals of the dc link, was done in the previous sections. This study was performed for a case without a commutation overlap in the inverter. Flowchart 7.1 was provided for the calculation of the system unknowns under the above conditions. This flowchart is now employed for generating two sets of graphs similar to the graphs in cases (a) and (d). Since the peak values of the voltage spikes are not limited by the clamping circuit, the same operating point, point (A), is used for obtaining the voltage and current waveforms in the first set of graphs. In the second set of graphs, the same control strategy is employed for determining the motor terminal voltage. In addition, the magnetizing and leakage inductances, as well as the core-loss resistance, are regarded in the same way as discussed in section (5.2). In order to compare the results of case (a) with

those of case (g) each waveform or curve is plotted first by employing flowchart 7.1 and then by using flowchart 3.2. The graphs obtained through flowchart 3.2 are essentially the same as those given in figures 5.1 - 5.24. Each waveform or curve is specified by letters CV or CI. CV notation stands for the constant dc link input voltage assumption, while CI denotes the constant dc link current assumption. In other words, CV indicates that flowchart 7.1 has been used for obtaining the result while CI implies the application of flowchart 3.2. From this point on, CV and CI will be used with the meanings explained above. The variation of each variable in the second set of graphs has been plotted for three constant torques only; thus preventing the crowding of too many curves on the same figure. In the following, the plotted graphs will be shown, and wherever necessary, explanations will be given.

7.6.1 Voltage and current waveforms

Figures 7.6 - 7.11 show the voltage and current waveforms for operating point (A) (Appendix A-1) at different points of the system obtained by the CV and CI assumptions. These figures reveal two major differences between the simulated graphs attained in case (a) and those of case (g). Firstly, the dc link current is no longer smooth, fig. 7.11, but has ripples similar to the actual waveforms. Secondly, the commutating capacitor maximum voltage, V_0, has a higher level in case (g) than in case (a), fig. 7.9. The ripples in the dc link current are also seen in the motor input current, fig. 7.6. It is clear from this figure that each "bump" is generated during a commutation period.

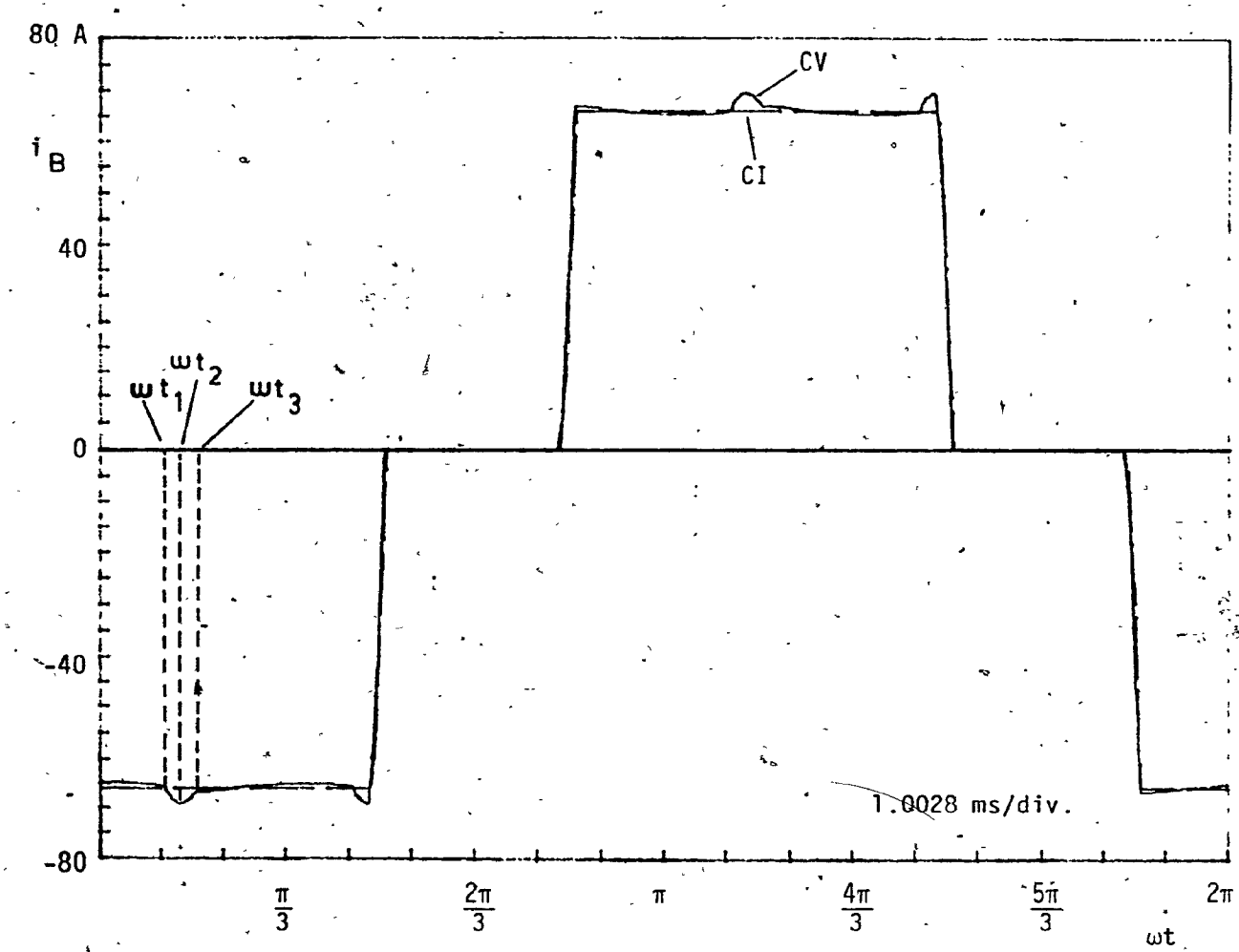

FIG. 7.6 Comparison of the motor phase B curent waveform obtained in case (g), curve CV , with the one resulted in case (a), curve CI , at operating point (A).

It was mentioned in section (7.2) that the expression giving the variations of the dc link current during a charging mode, Eq. (7.2.36), can be considered to consist of a constant term and a damped sinusoidal one. This conclusion is verified by the curve CV shown in figure 7.6 where the first half of a ripple occurs during a charging mode ($t_1 < t < t_2$). The same reasoning can be applied to the second half of each ripple in the dc link current waveform, which appears during a transfer mode ($t_2 < t < t_3$).

The dc link current ripples also affect the motor terminal voltages. Figure 7.7 exhibits the waveforms of the phase B voltage, fundamental component and instantaneous currents. The ripples identified by 1-4 on waveform CV of v_B are caused by the ripples in the phase B current, during commutation intervals, and are only recognized when the CV approach is chosen for simulation. The other difference between waveforms CV and CI of v_B, which is not clear on figure 7.7, corresponds to the peak value of each voltage spike. The spikes on waveform CV have a higher level than those on waveform CI, which are mainly due to the value of V_o, fig. 7.9. Figure 7.7 also shows the shift angle, ϕ_1, between the sinusoidal part of v_B and i_{1B}.

The same discussion given above for v_B also hold for v_{AB}, fig. 7.8. In this figures, six ripples are distinguished on the v_{AB} waveform which are shown by 1-6. Note that all ripples 1-6 are produced by the variation of the dc link current during six consecutive charging modes. That part of the ripples caused by the dc link current variation during the transfer modes are added to the main voltage spikes and can-

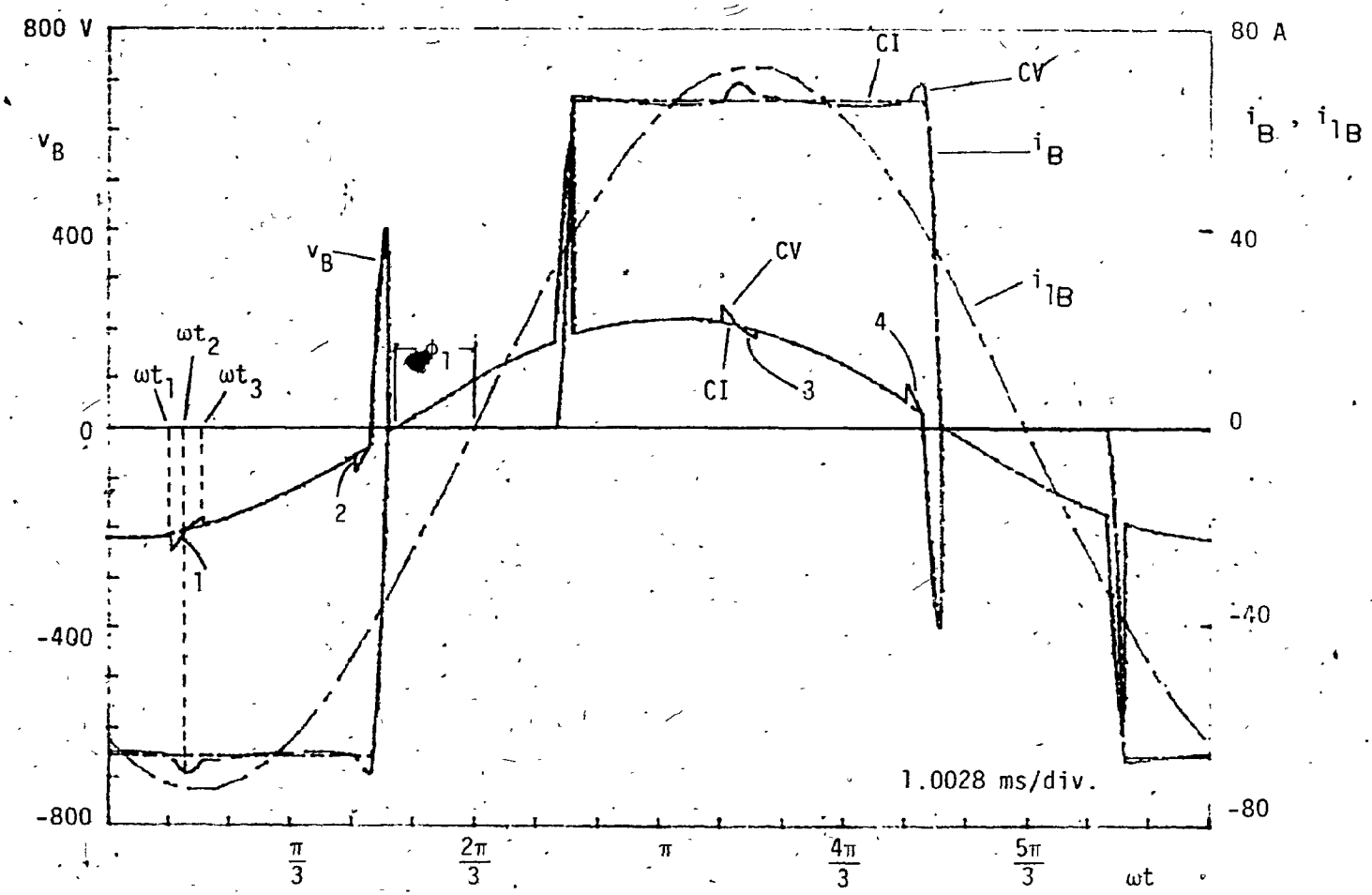

FIG. 7.7 Comparison of the motor phase B voltage waveform, the phase B instantaneous and fundamental harmonic current waveforms obtained in case (g), curves CV ; with those resulted in case (a), curves CI , at operating point (A).

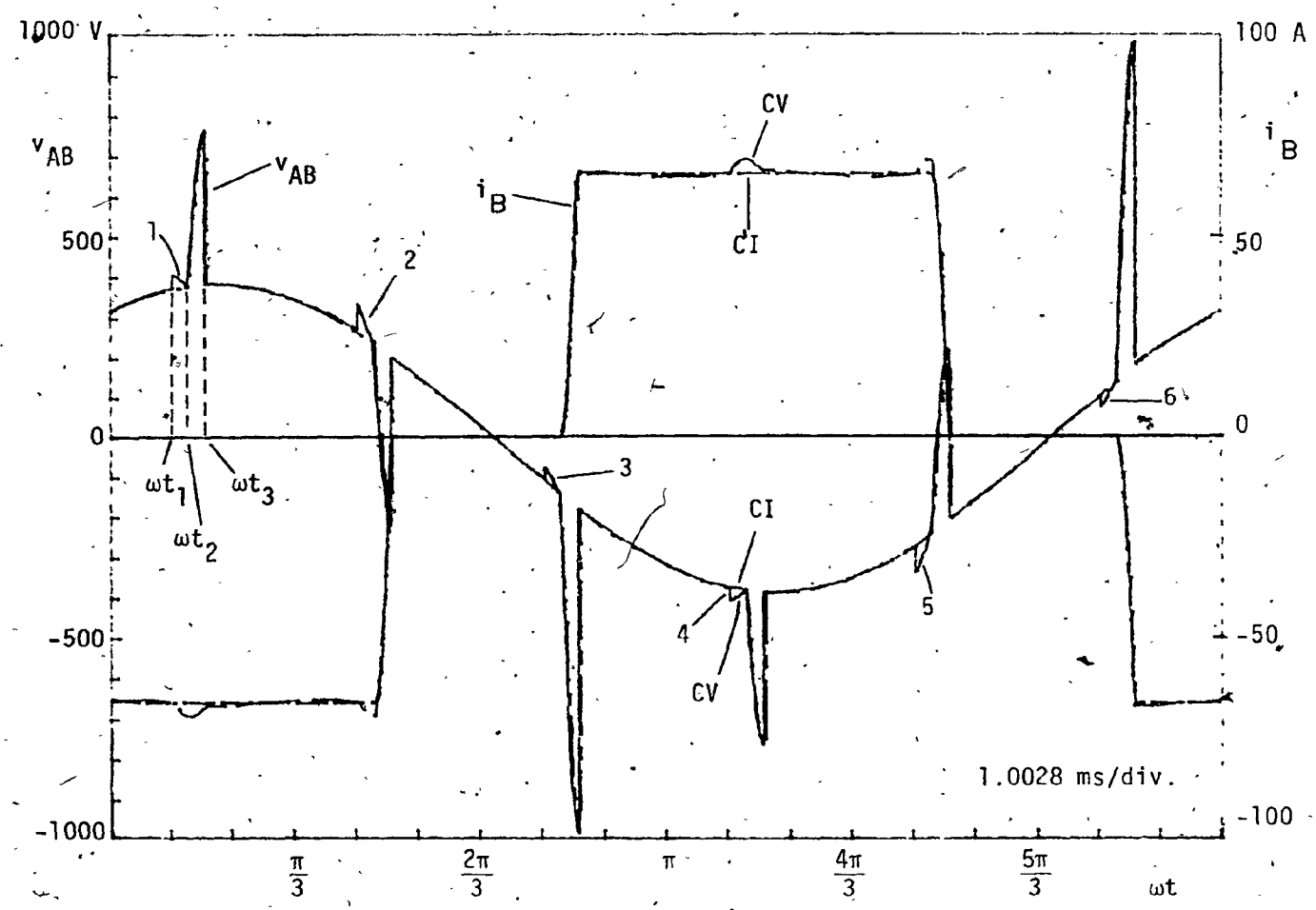

FIG. 7.8 Comparison of the motor line AB voltage and phase B current waveforms obtained in case (g), curves CV , with those resulted in case (a), curves CI , at operating point (A).

not be distinguished on this figure.

The difference in the maximum values of the commutating capacitor voltage, V_o, obtained by the CV and CI approaches, are clearly seen on figure 7.9. It is noticed that using the derivations of case (g) follows a higher level for V_o than employing the method discussed for case (a). Note that the higher value of V_o is closer to the value resulted in an actual system. Figure 7.9 also displays the capacitor current waveforms. The waveforms CV and CI for the current are similar to each other except at the top of each pulse. It is noticed that the first half of each ripple, as explained in figure 7.6, is superimposed on the top of each pulse of capacitor current shown by CI. Although this difference is negligible, it again demonstrates a better analogy to the actual case.

The diode D_3 voltage and phase B current waveforms are presented in figure 7.10. The difference in V_o (fig. 7.9) is clearly reflected in V_{D3} waveform. Besides, two voltage ripples, (1) and (2), with the same explanations given for figure 7.8, are viewed in figure 7.10.

And at last, figure 7.11 gives the inverter input voltage and the dc link current waveforms. The waveforms of the inverter input voltage obtained through the two methods are essentially the same, except at the positive and negative peak values, which are hardly clear in this figure. The dc link current waveforms in this figure, give a better view of the difference existing between the resulted dc link variations through the two methods. Six ripples are seen on curve CV

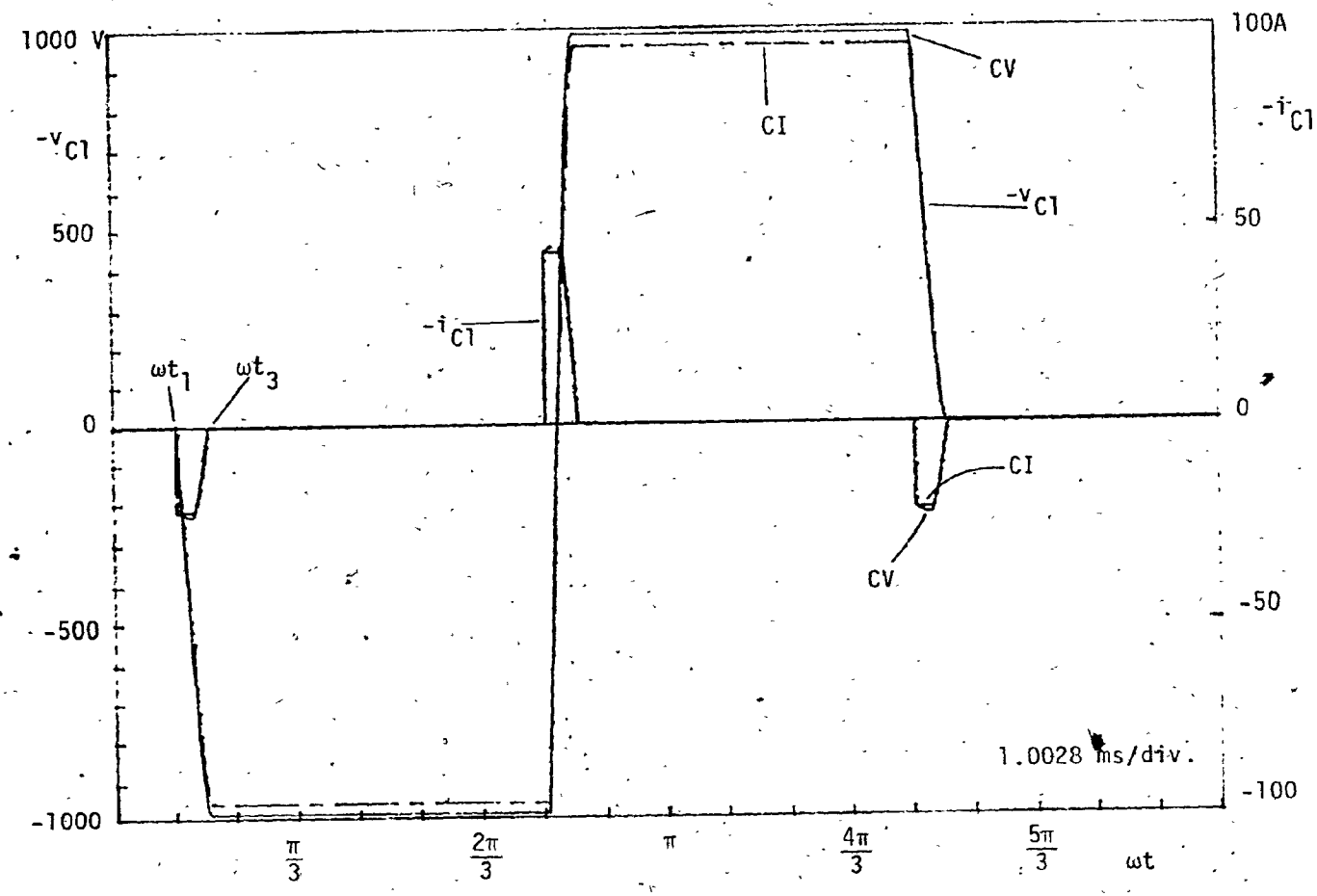

FIG. 7.9 Comparison of the commutating capacitor voltage and current waveforms obtained in case (g), curves CV , with those resulted in case (a), curves CI , at operating point (A).

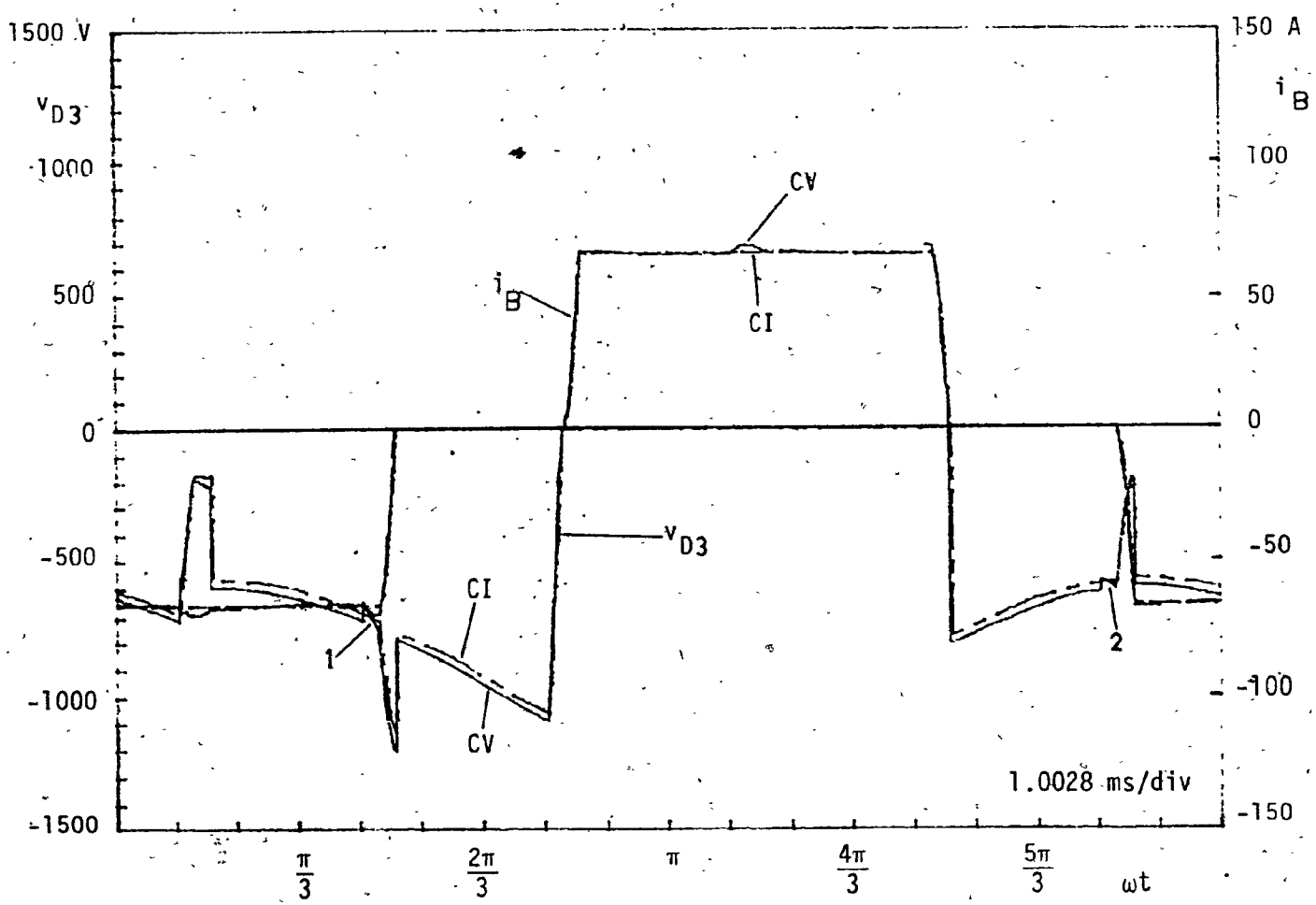

FIG. 7.10 Comparison of the diode D3 voltage and motor phase B current waveforms obtained in case (g), curves CV , with those resulted in case (a), curves CI , at operating point (A).

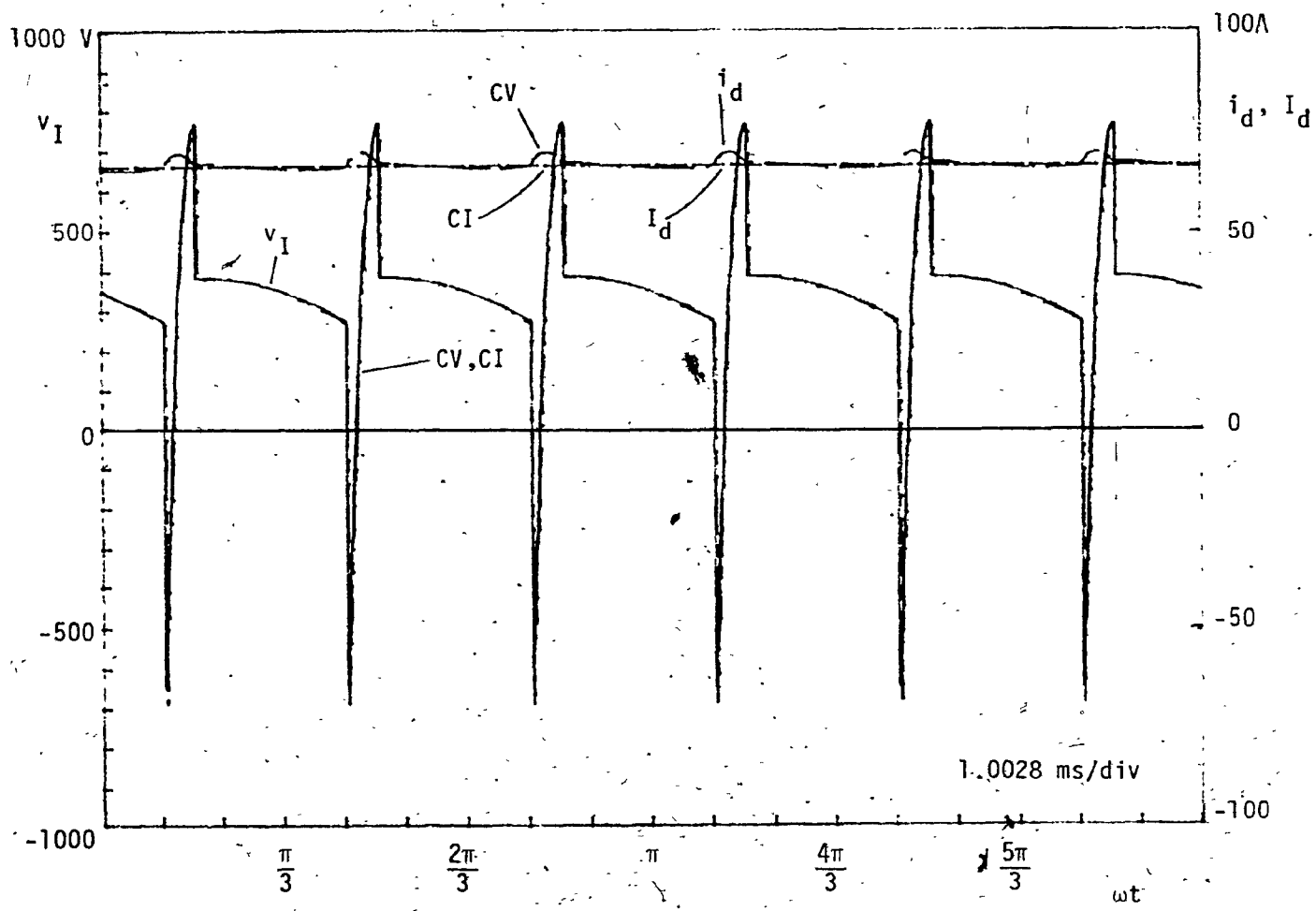

FIG. 7.11 Comparison of the inverter input voltage, the instantaneous and average dc link current waveforms obtained in case (g), curves CV , with those resulted in case (a); curves CI , for operating point (A).

which yield the number of the commutation intervals during one inverter output cycle. It can be stated that the dc link current has a frequency six times that of the inverter output frequency. The curve CI basically shows the average value of the curve CV.

The voltage waveform across the thyristor T_1 was not provided in this set of graphs. The reason is that this waveform is essentially the same as figure 5.4, but with a higher maximum voltage. The value of this maximum voltage is determined from the waveform CV of the capacitor C_1 voltage, fig. 7.5.

7.6.2 Variations of the variables

The second set of graphs exhibit the comparison between the variations of different variables of the system obtained in case (g), curves CV, with those already plotted in case (a), curves CI. These graphs are generated for three different torque levels, T = 0., 1. and 2. PU, figures 7.12 - 7.21. The discussions given in section 5.4 apply to these figures also and are not repeated here. It is seen from figures 7.12 - 7.21 that the variations of each variable in case (g), under different load conditions, are essentially the same as those determined in case (a). The major differences worth mentioning are:

(1) At no-load-high frequency operating conditions, the CV assumption results in smaller commutation angles than the CI assumption does, fig. 7.17. This means that the use of the CI assumption provides a safe margin for avoiding the commutation overlap.

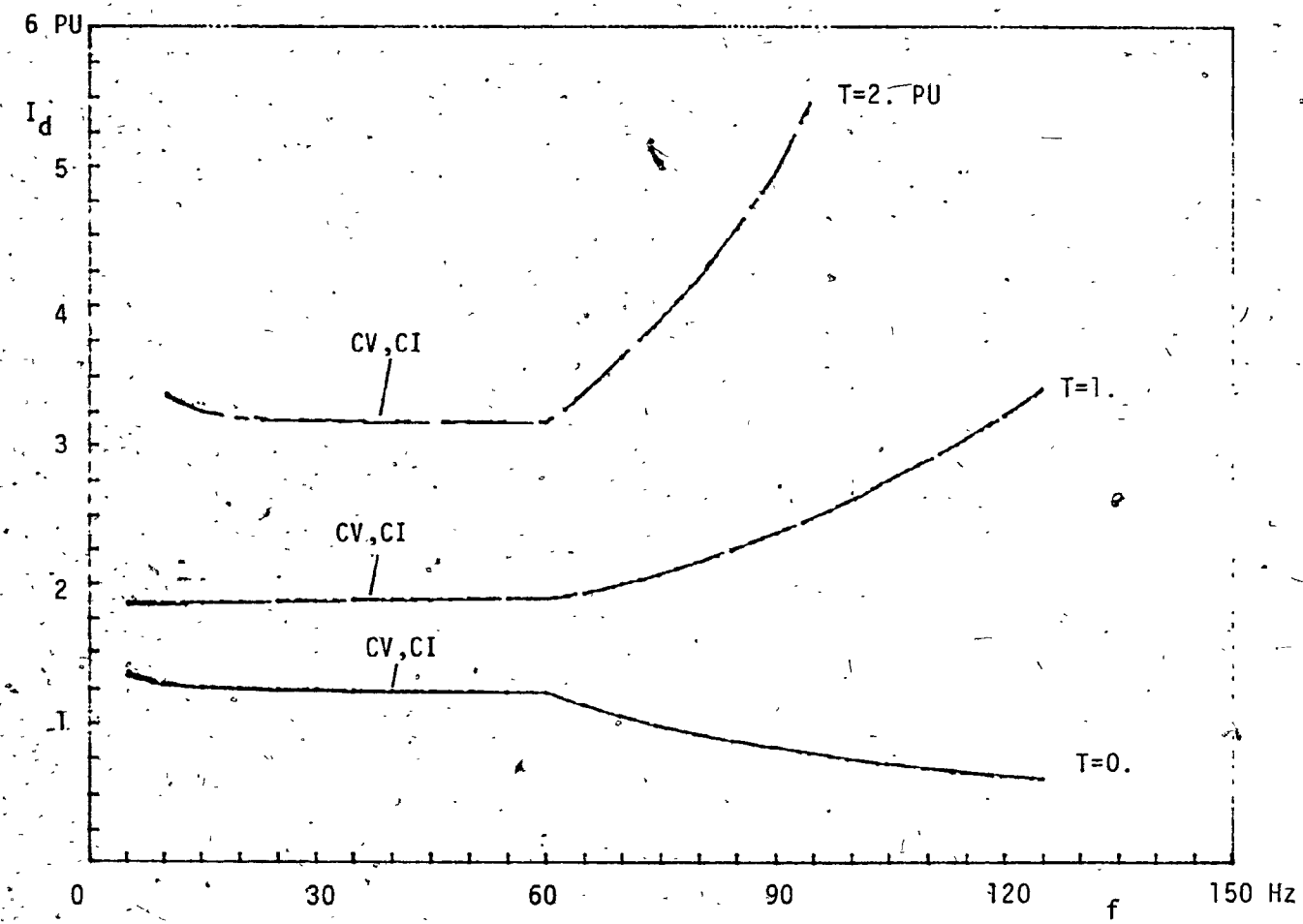

FIG. 7.12 Comparison of the average values of the dc link current, I_d, obtained in case (g), curves CV, with those calculated in case (a), curves CI at constant torque-variable frequency operating conditions.

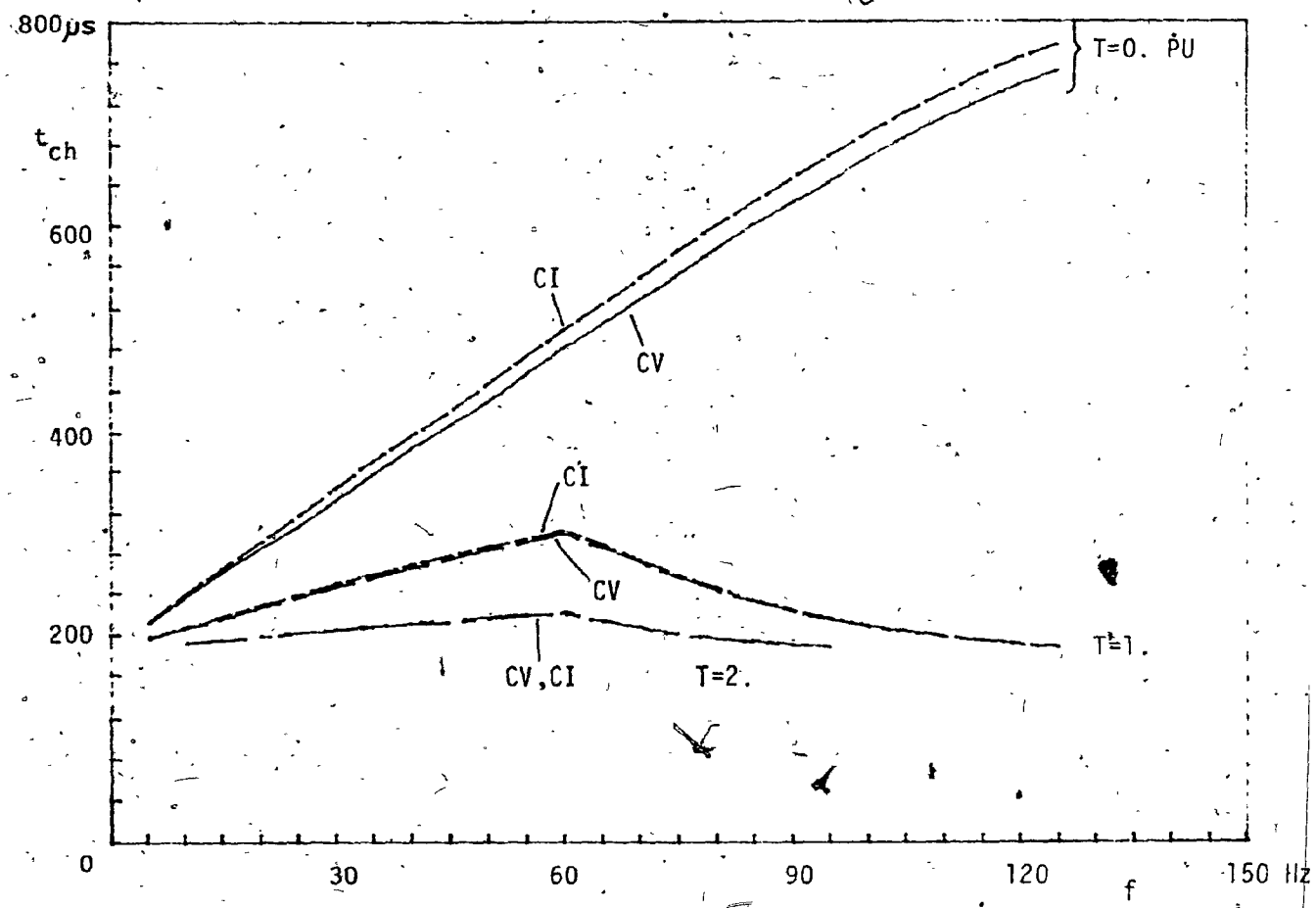

FIG. 7.13 Comparison of the charging mode intervals, t_{ch}, obtained in case (g), curves CV, with those calculated in case (a), curves CI, at constant torque-variable frequency operating conditions.

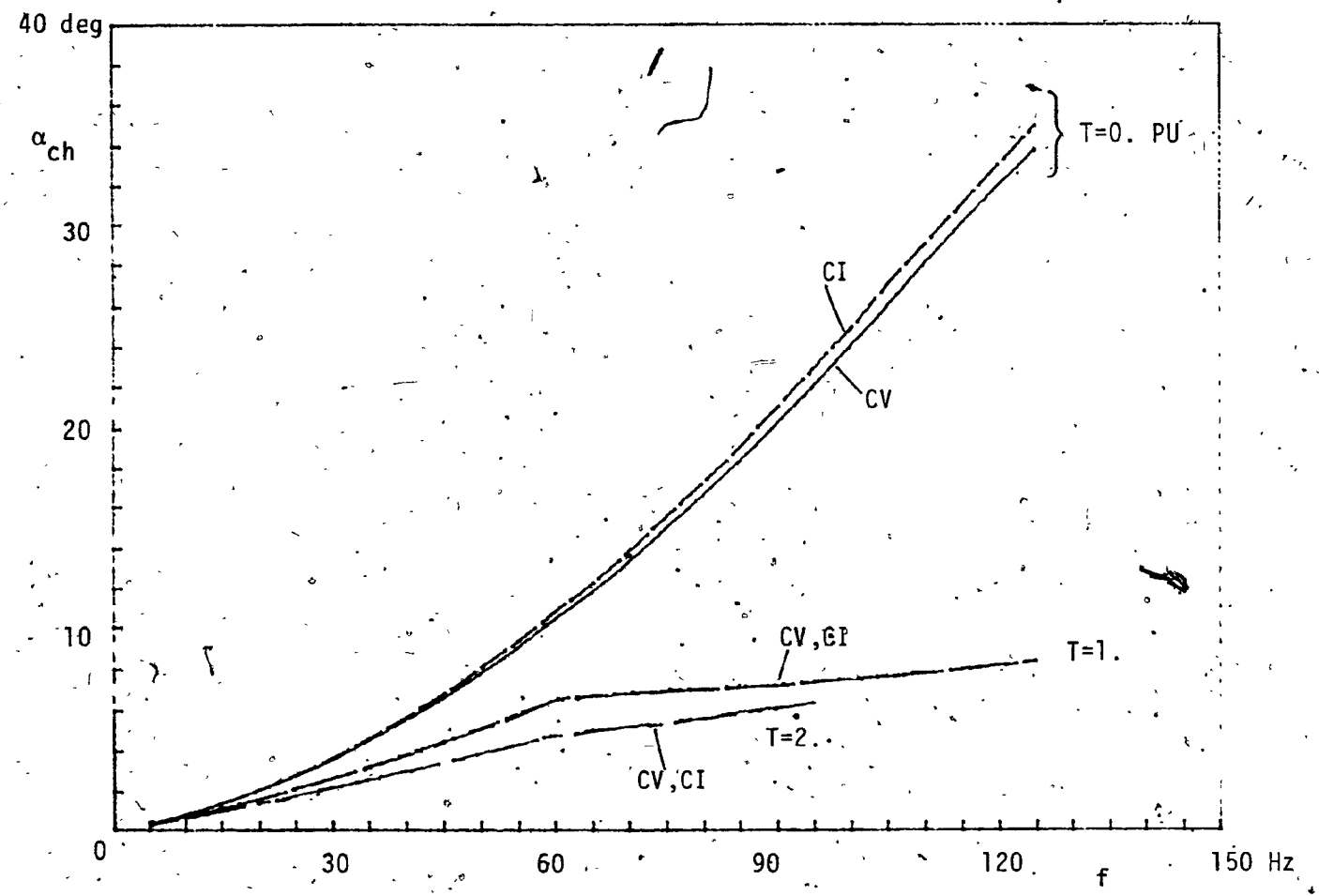

FIG. 7.14 Comparison of the charging mode angles, α_{ch}, obtained in case (g), curves CV, with those calculated in case (a), curves CI, at constant torque-variable frequency operating points.

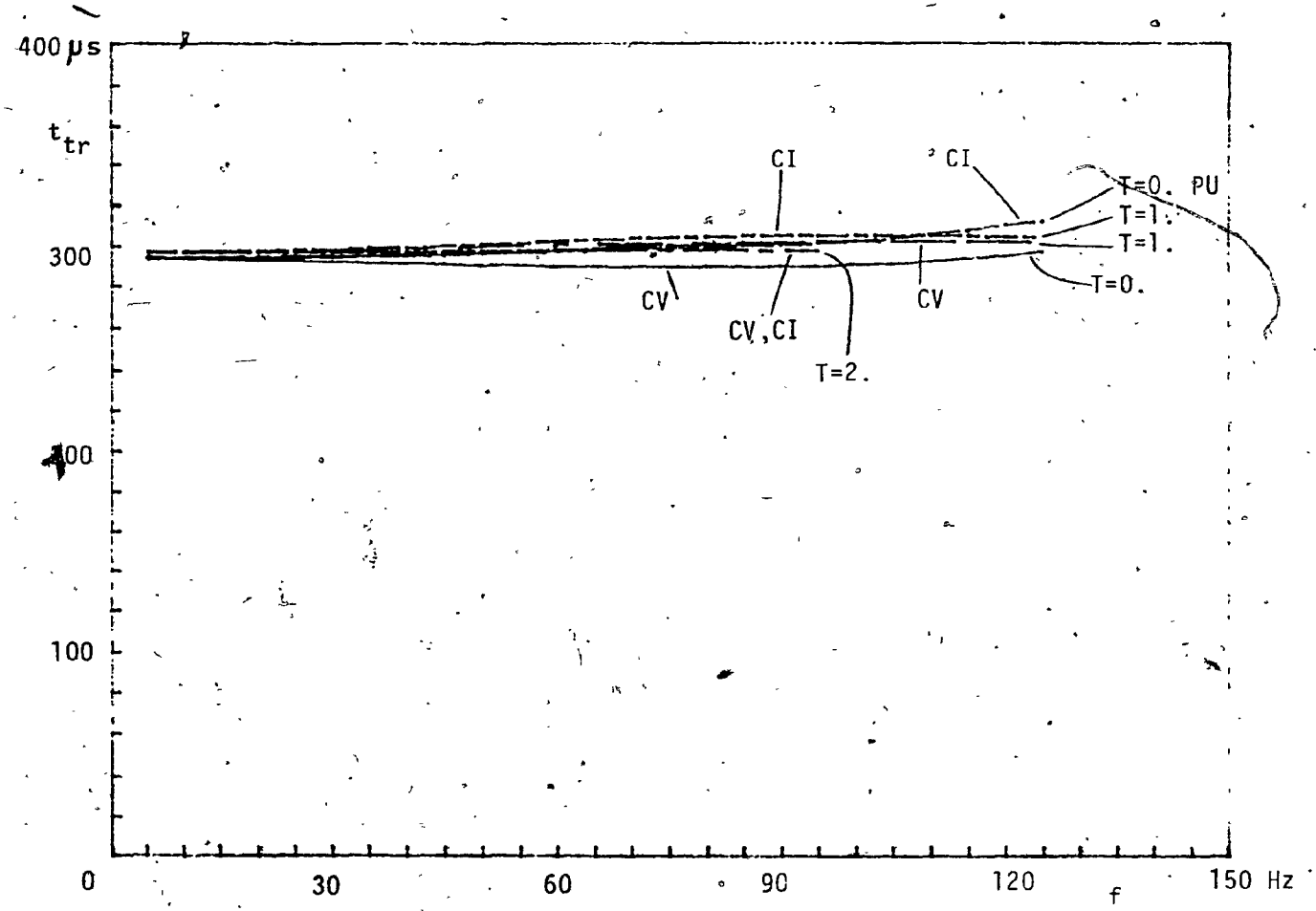

FIG. 7.15 Comparison of the transfer mode intervals, t_{tr}, obtained in case (g), curves CV, with those obtained in case (a), curves CI, at constant torque-variable frequency operating points.

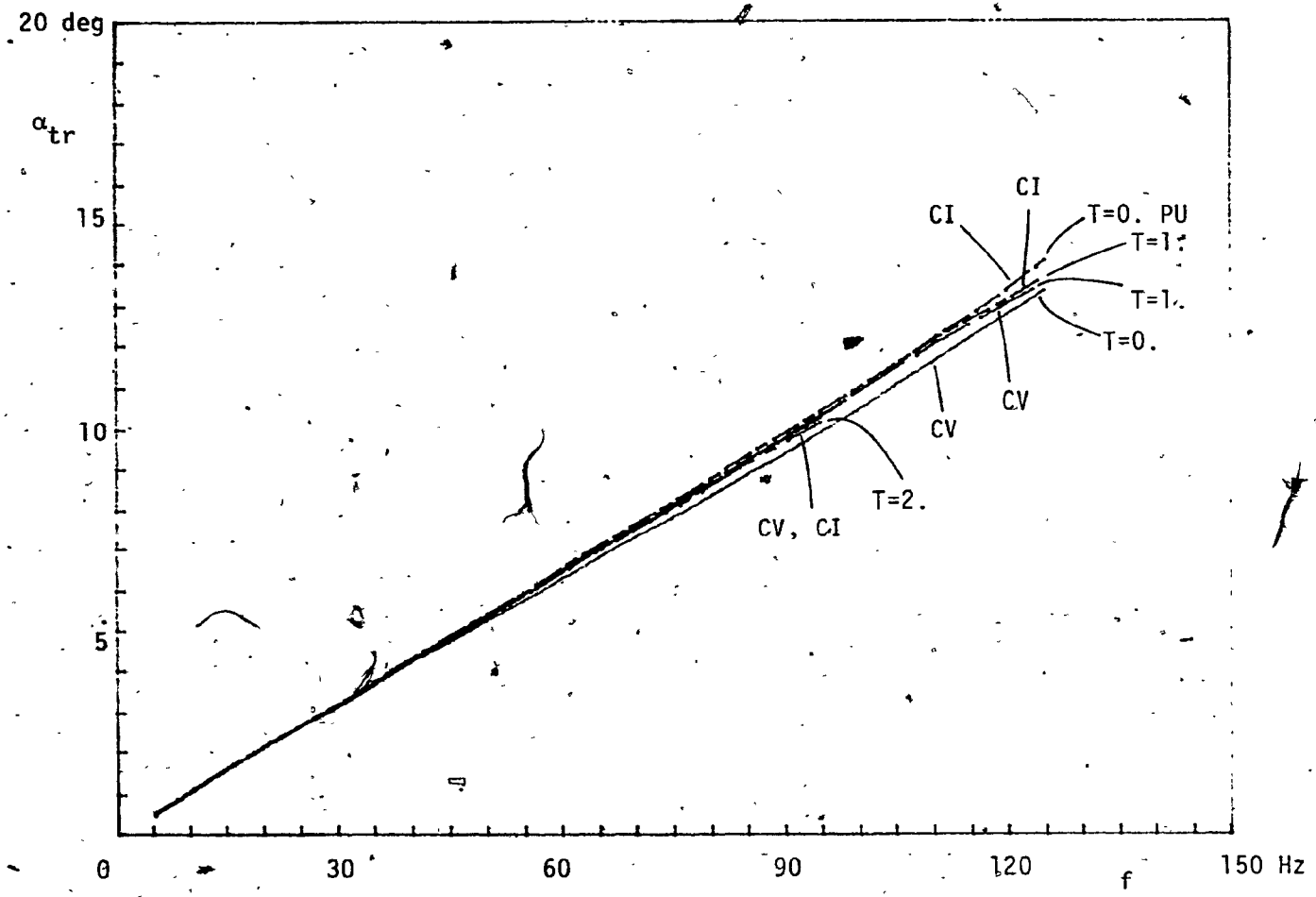

FIG. 7.16 Comparison of the transfer mode angles, α_{tr}, obtained in case (g), curves CV, with those obtained in case (a), curves CI, at constant torque-variable frequency operating points.

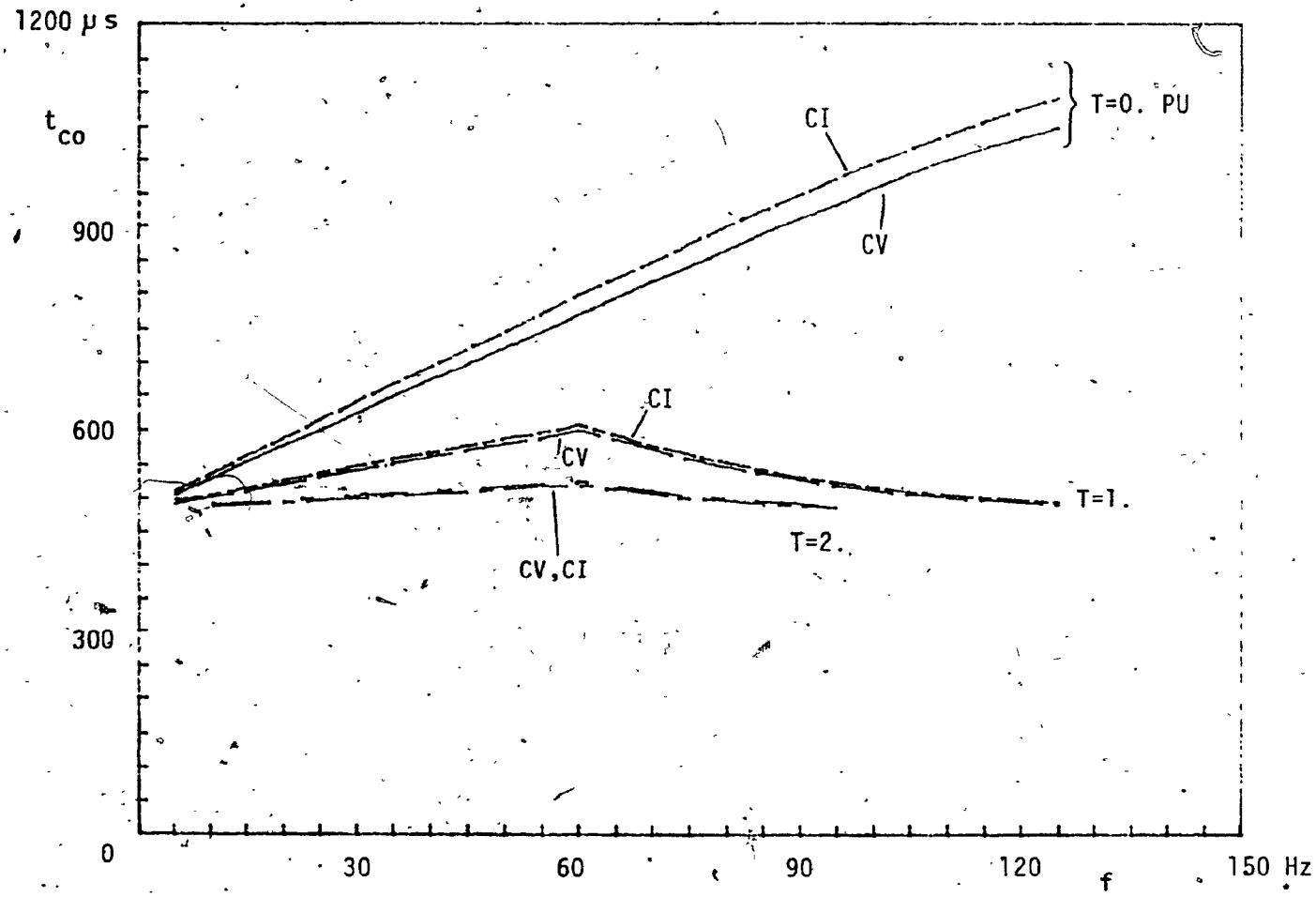

FIG. 7.17 Comparison of the commutation intervals, t_{co}, obtained in case (g), curves CV, with those obtained in case (a), curves CI, at constant torque-variable frequency operating conditions.

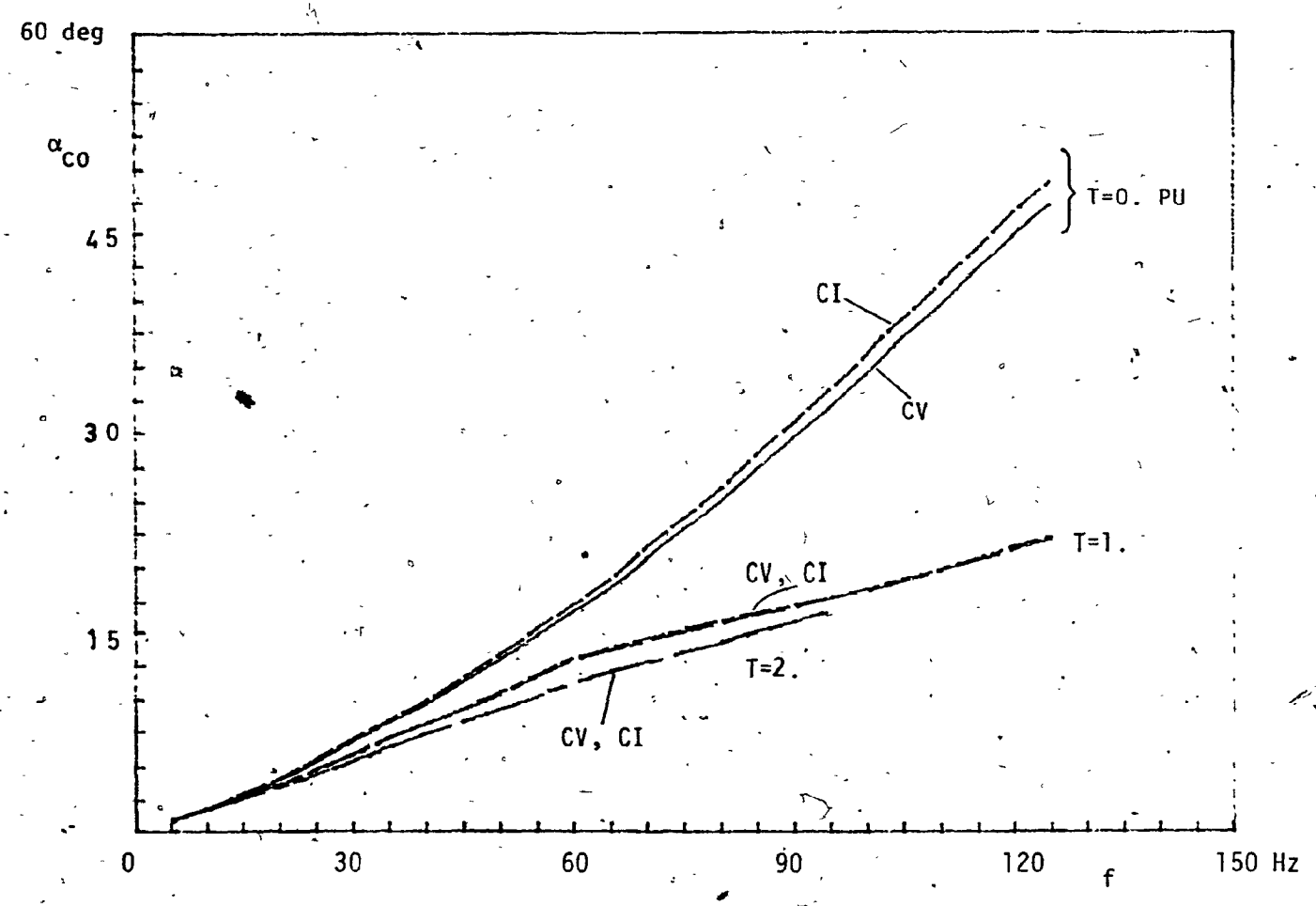

FIG. 7.18 Comparison of the commutation angles, α_{co}, obtained in case (g), curves CV, with those obtained in case (a), curves CI, at constant torque-variable frequency operating conditions.

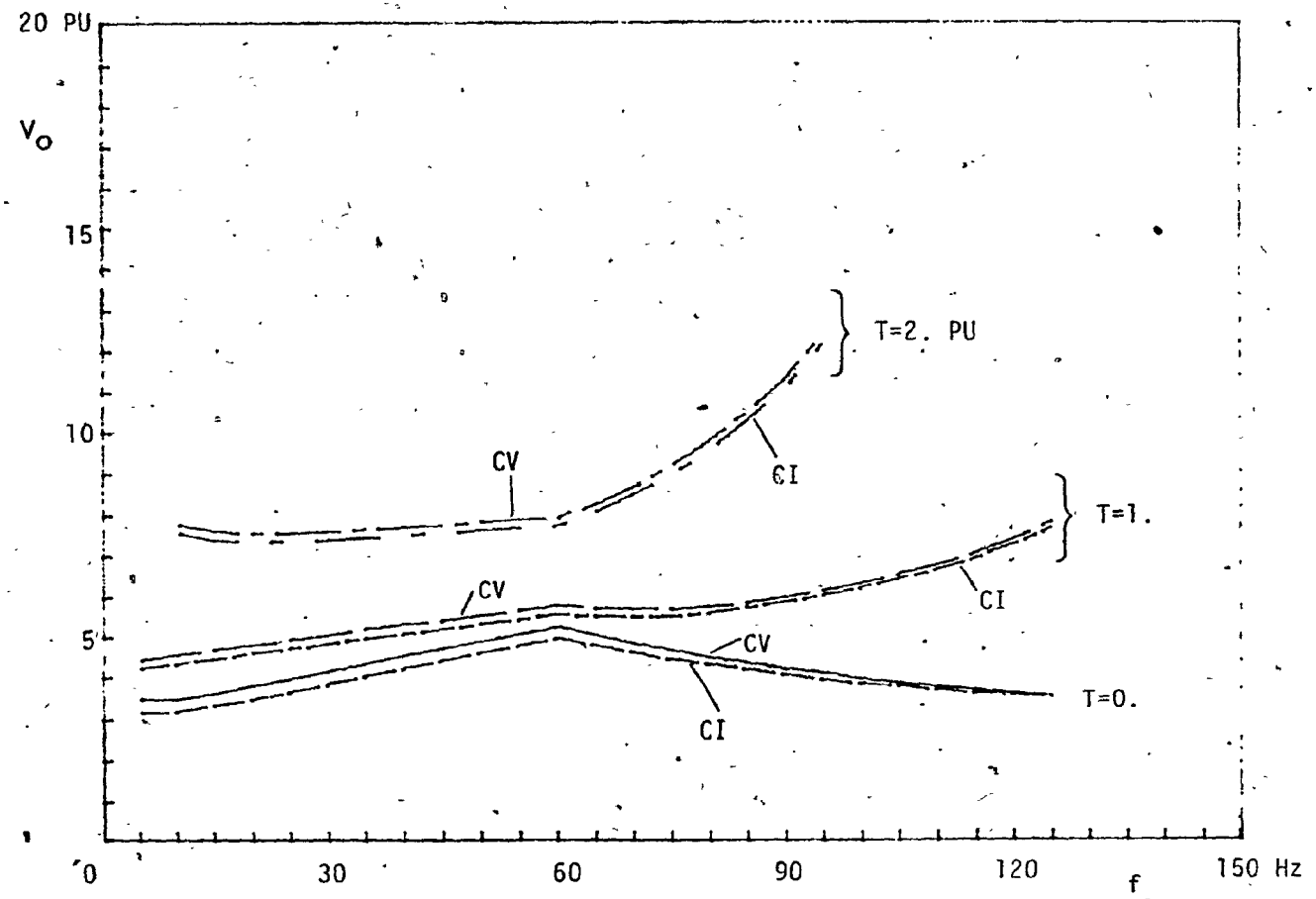

FIG. 7.19 Comparison of the capacitor maximum voltages, V_o, obtained in case (g), curves CV, with those obtained in case (a); curves CI, at constant torque-variable frequency operating conditions.

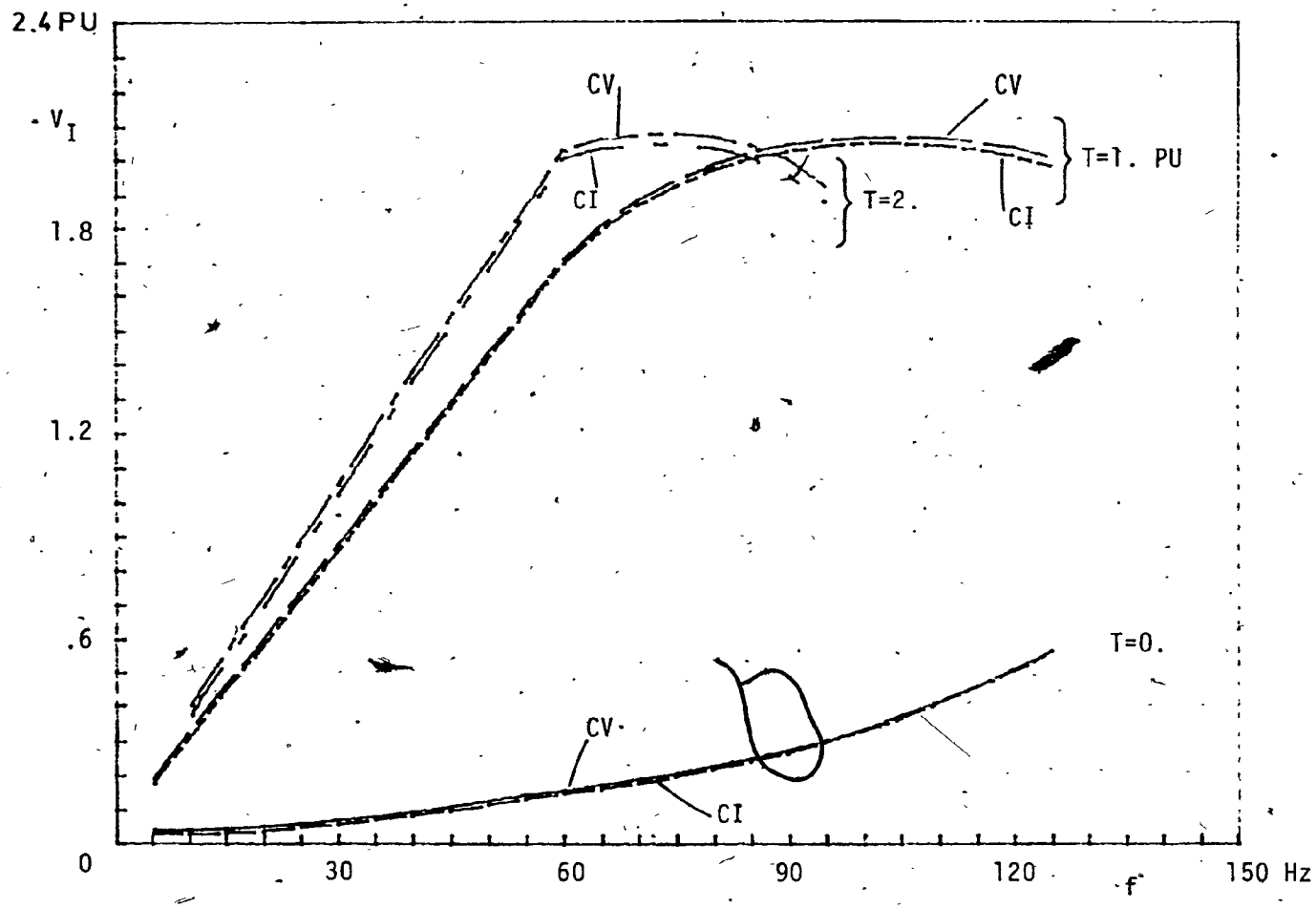

FIG. 7.20 Comparison of the inverter input average voltages, V_I, obtained in case (g), curves CV, with those calculated in case (a), curves CI, at constant torque-variable frequency operating conditions.

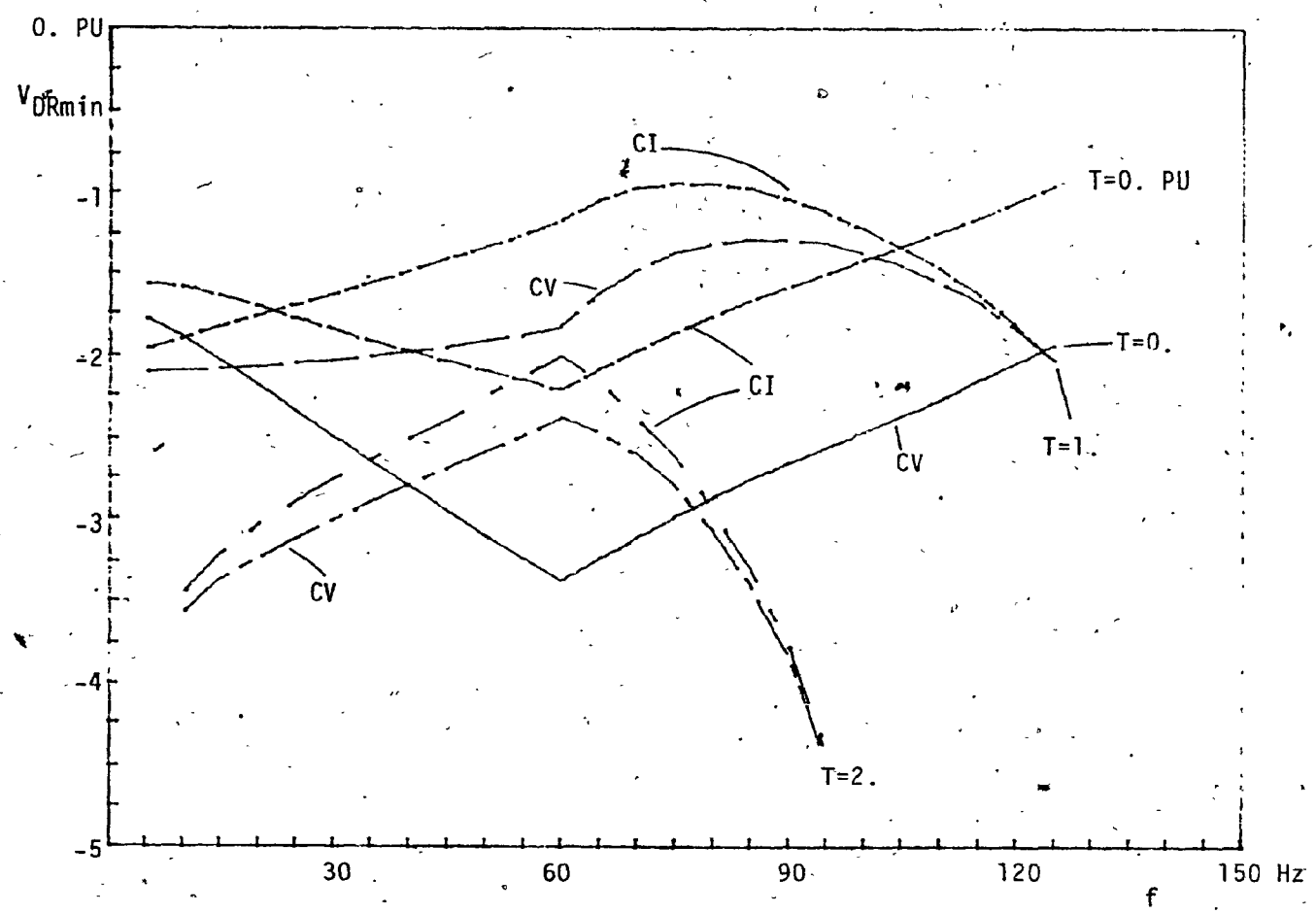

FIG. 7.21 Comparison of the diode minimum reverse voltages, V_{DRmin}, obtained in case (g), curves CV, with those calculated in case (a), curves CI, at constant torque-variable frequency operating conditions.

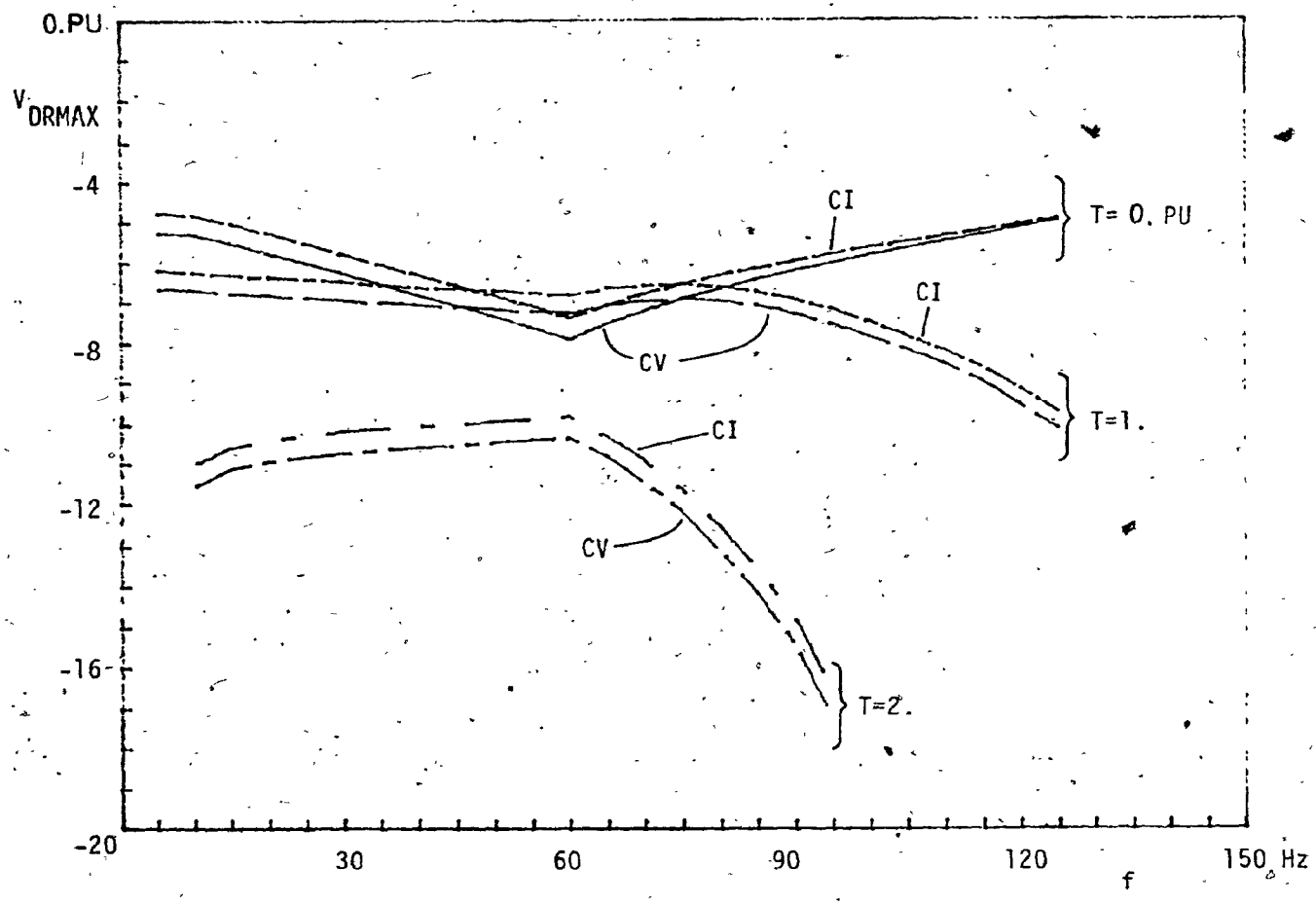

FIG. 7.22 Comparison of the diode maximum reverse voltages, V_{DRmax}, obtained in case (g), curves CV, with those calculated in case (a), curves CI, at constant torque-variable frequency operating conditions.

(2). A higher value for the commutating capacitor maximum voltage, V_o , is obtained in case (g) than the value determined in case (a), fig. 7.18. This difference was already noticed in figure 7.9 and figure 7.18 verifies it. This difference in V_o is again reflected in the diode maximum and minimum reverse voltages, figs. 7.20 - 7.21.

Aside from the above two major differences, there is almost no other dissimilarity between the results obtained by the CV assumption and those obtained by the CI assumption.

7.7 CONCLUSION

By abolishing the constant dc link current assumption and using instead the constant dc link input voltage assumption, an exact analysis of an ASCI-induction motor drive was accomplished. In this way, the parameters of the dc link were included in the system and their effects were studied. Due to the tedious and long derivations involved in this stage of the study, only the no-overlap operation was examined. The system operation, then, resulted in three distinct modes similar to those in case (a). The difficulty with this approach was that the values of four main variables should be known in order to proceed further. These unknowns were:

(1) The value of the dc link current at the time of firing a thyristor,

(2) The value of the commutating capacitor maximum

voltage,

(3) The instant at which a thyristor is triggered in regard to the origin of time, and

(4) The value of the dc link sending end terminal voltage.

The origin of time was selected according to assumption 14 in section (2.6) and the thyristor T_1 was chosen as the thyristor which is fired first. The derivations in each mode were then done in terms of the four main unknowns. At the end, (n-3) equations were obtained where n is the number of the unknowns. The missing three equations were provided by considering the following facts:

(1) Due to the way in which the origin of time has been selected, the fundamental harmonic of phase A current should pass the origin of time with a positive slope.

(2) The value of the dc link current at the end of the third mode should be the same as its value at the beginning of the first mode.

(3) The total motor input power can be calculated numerically and by obtaining the average value of the dc link current, the dc voltage of the source feeding the system can be computed.

Based on these three facts, a flowchart was proposed which gave the value of each unknown through a number of iterations. The results of employing the suggested flowchart were shown by two sets of graphs. In these graphs, the results of the constant current assumption were also shown for the sake of comparison. It was revealed that, although the constant voltage assumption provides a dc link current with ripples and a higher commutating capacitor maximum voltage when compared with the constant dc link current assumption, these differences are negligible and the exact method used in case (a) yields results compatible with those obtained in this chapter.

CHAPTER VIII

COMPARISON BETWEEN SIMULATED AND EXPERIMENTAL RESULTS

8.1 INTRODUCTION

The operation of an ASCI-induction motor drive was studied in basically two different ways in the previous chapters. In one method, the derivations of system equations were based on the assumption of a constant dc link current, while in the other approach, a constant dc link input voltage was the main assumption. Two main cases were studied with the constant dc link current assumption. First, case (a), which studied the system without a clamping circuit. Second, case (d), in which a Zener clamping circuit limited the peak values of the voltage spikes. With the constant voltage assumption, only the case without a clamping circuit was studied, case (g). Two sets of graphs were obtained in each of the above cases [(a), (d), (g)]. In this chapter, the voltage and current waveforms obtained experimentally are compared with those plotted theoretically. The comparison is done for two operating points, one point for the case without a clamped voltage and the other for the case with a clamped voltage.

8.2 EXPERIMENTAL RESULTS FOR A NO-CLAMPING OPERATION

The operating point for a no-clamping operation is point (A) as specified in Appendix A-1. The comparison is done between the experimental results obtained for point (A) and the simulated waveforms

of figures 7.6 - 7.11 and a few more graphs as shown in this section. These figures show, at the same time, the results obtained in case (a) and case (g). Thus the differences between the actual waveforms and those plotted by the constant dc link current or the constant dc link input voltage assumption can be easily distinguished and discussed.

Figures 8.1 - 8.8 display the actual waveforms obtained at operating point (A). The figure with which each of the experimental waveforms should be compared is also specified under each oscillogram. Note that all the oscillograms start at $t = t_1$, the instant at which the thyristor T_1 is fired. When comparing with the simulated results this difference in time origin should be considered. In the simulated figures the origin of time is chosen as defined by assumption 14 in section (2.6).

For a better comparison between the experimental and simulated results, a few expanded simulated waveforms have been included in this section, figures 8.5, 8.8 and 8.11. The comparison reveals a very good correspondence between the simulated and experimental waveforms. For example, the ripple in the middle of the motor phase B current pulse (curve CV) in figure 7.6 is quite similar to its counterpart in figure 8.1. Besides, in the same figure, ripple 3 on the V_B waveform, which is generated by the ripple of the i_B waveform is considerably similar to its mate on the V_B waveform of figure 8.1. There are also very good agreements between the different mode intervals (charging, transfer, commutation) obtained through simulations and experiments. For the other variables, this coincidence also exists. Note that the simulated waveforms obtained by the constant dc link

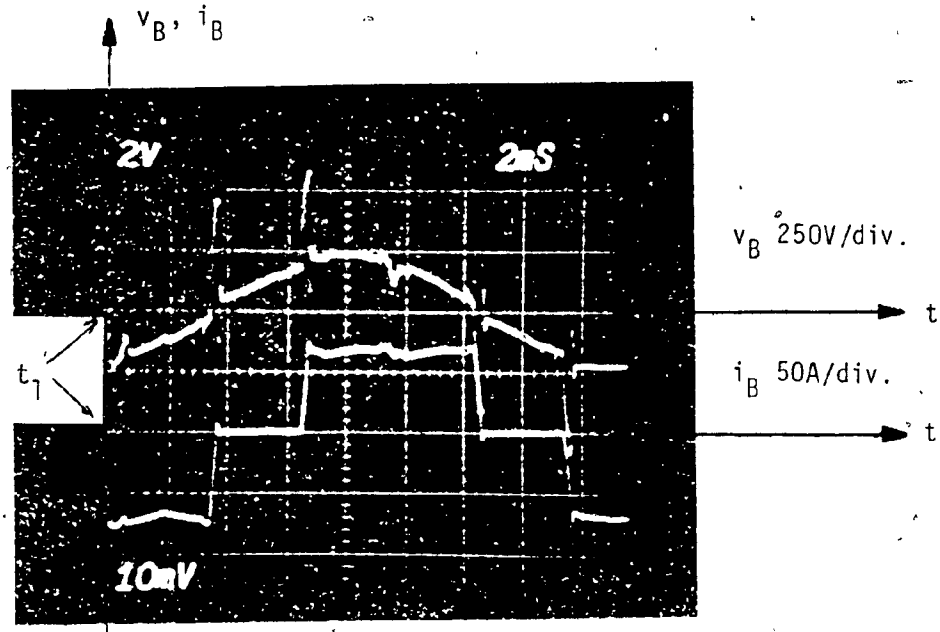

FIG. 8.1 Waveforms of motor phase B voltage and current at operating point (A). Compare this figure with Figure 7.7.

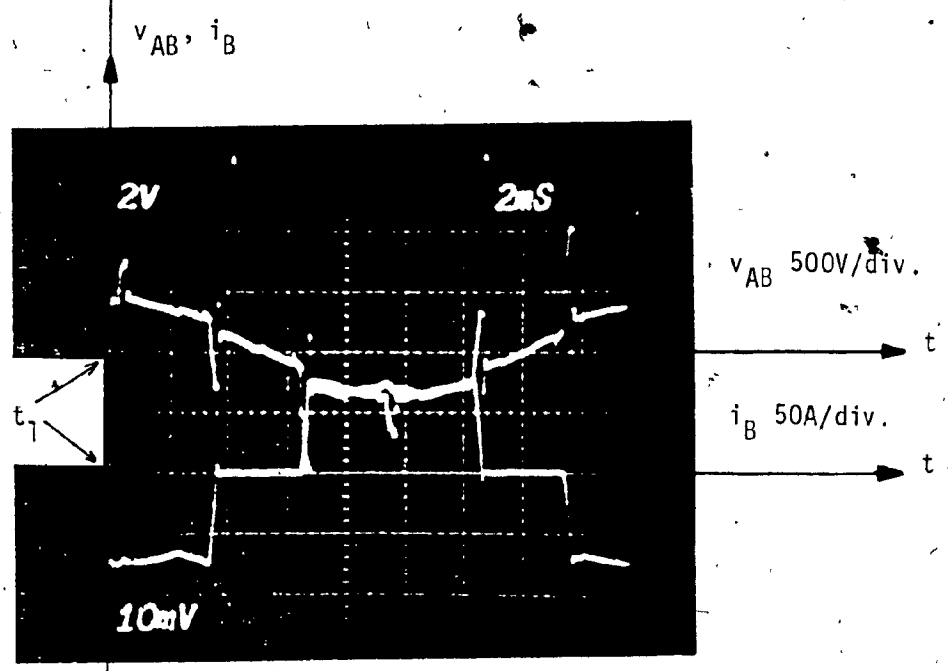

FIG. 8.2 Waveforms of motor voltage across terminals A-B and phase B current at operating point (A). Compare this figure with Figure 7.8.

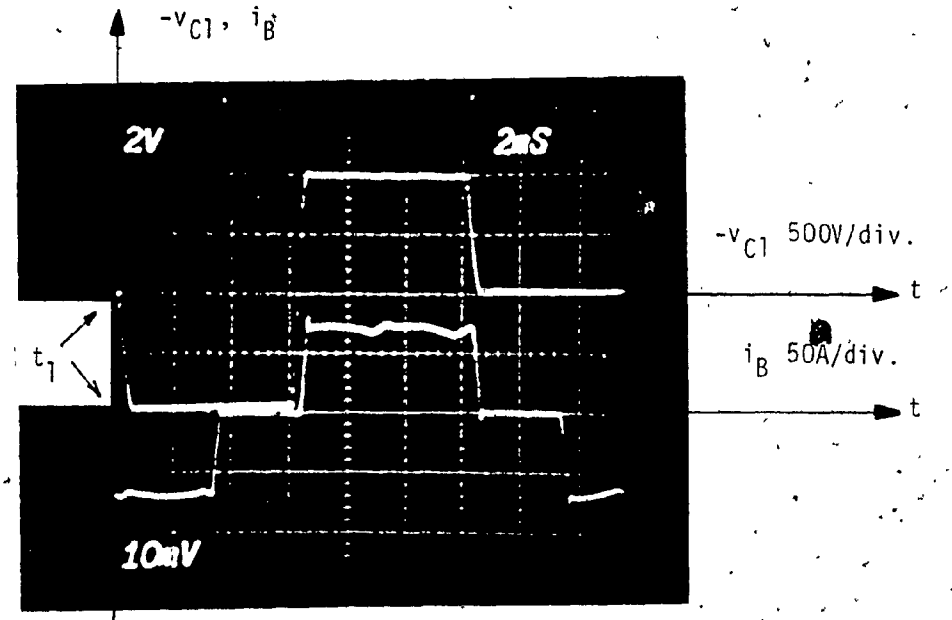

FIG. 8.3 Waveforms of inverter capacitor C_1 voltage and motor phase B current at operating point (A). Compare this figure with Figures 7.6 and 7.9.

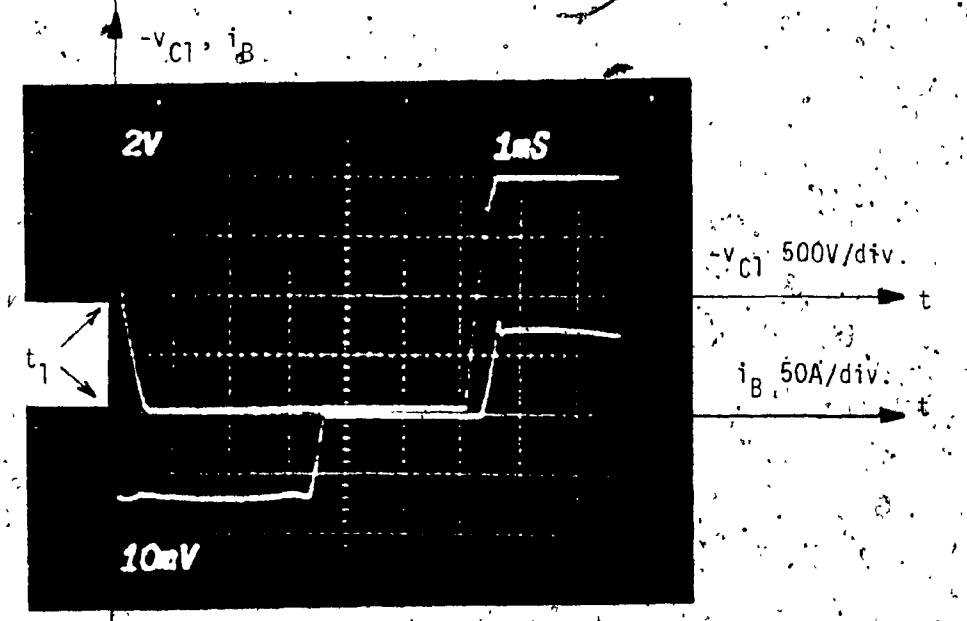

FIG. 8.4 As above, but with an expanded time scale. Compare this figure with Figure 8.5.

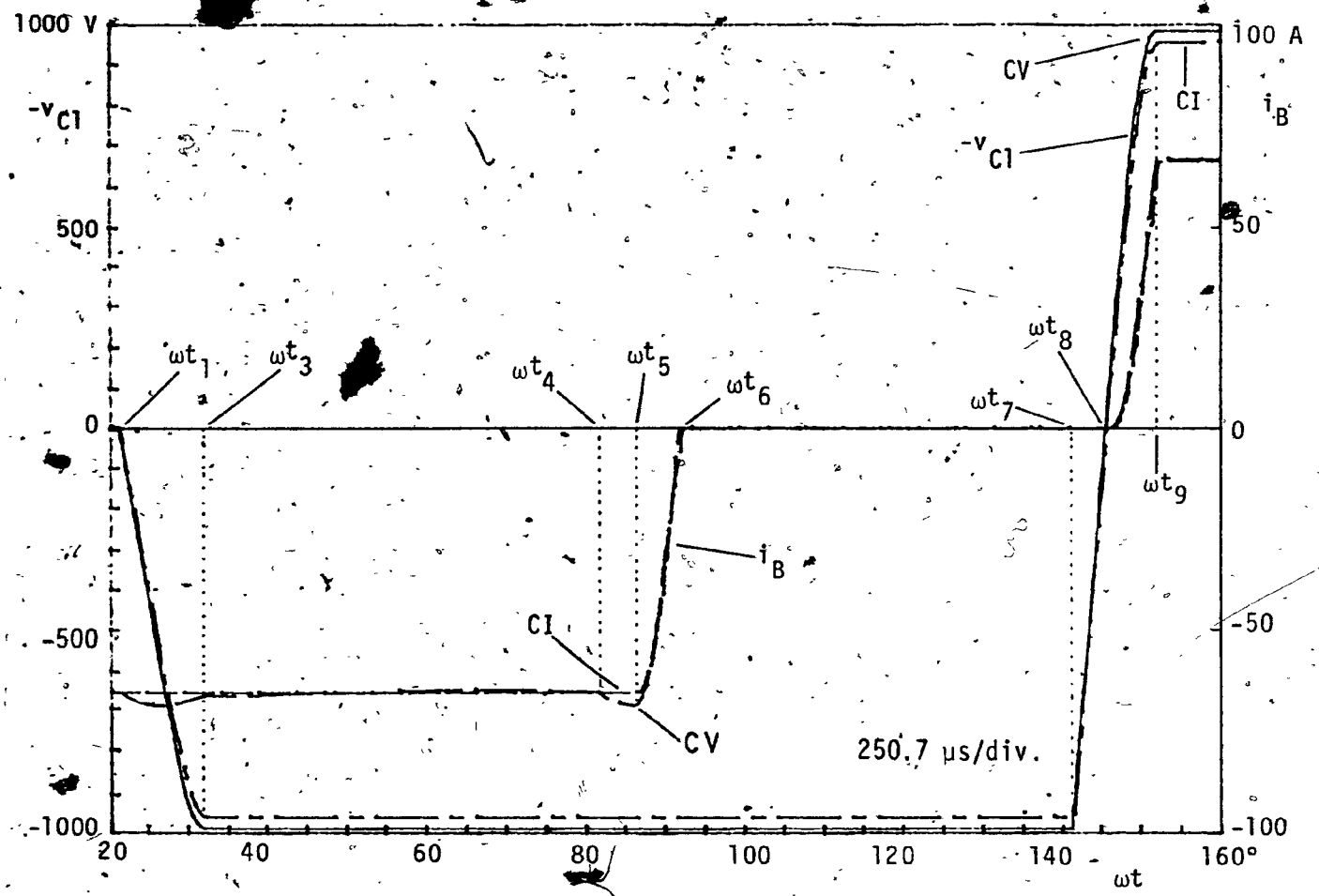

FIG. 8.5 Expanded waveforms of $-v_{C1}$ and i_B at operating point (A) obtained in case (g), curves CV, and in case (a), curves CI.

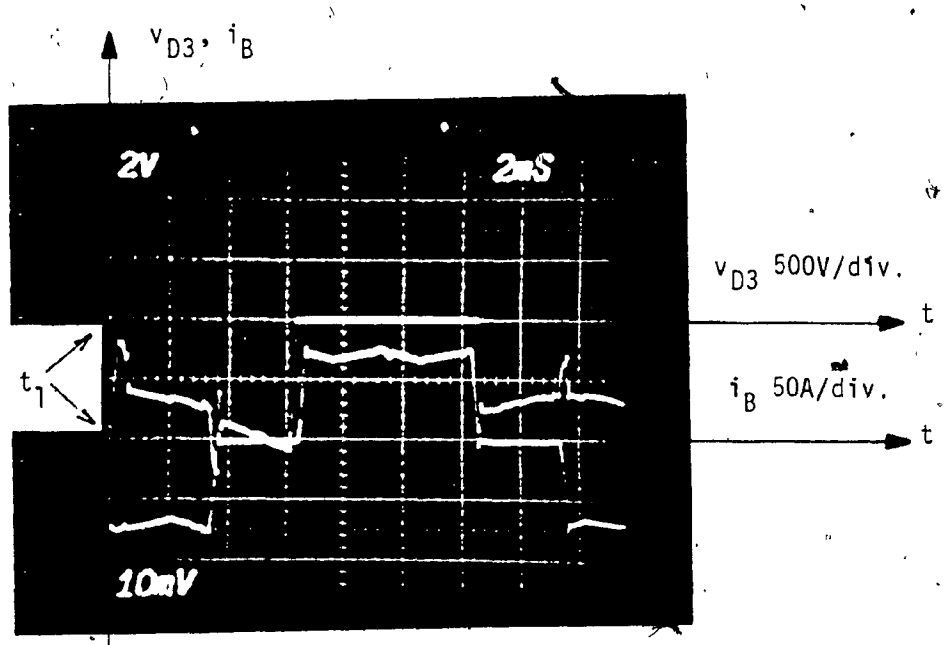

FIG. 8.6 Waveforms of inverter diode D_3 voltage and motor phase B current at operating point (A). Compare this figure with Figure 7.10.

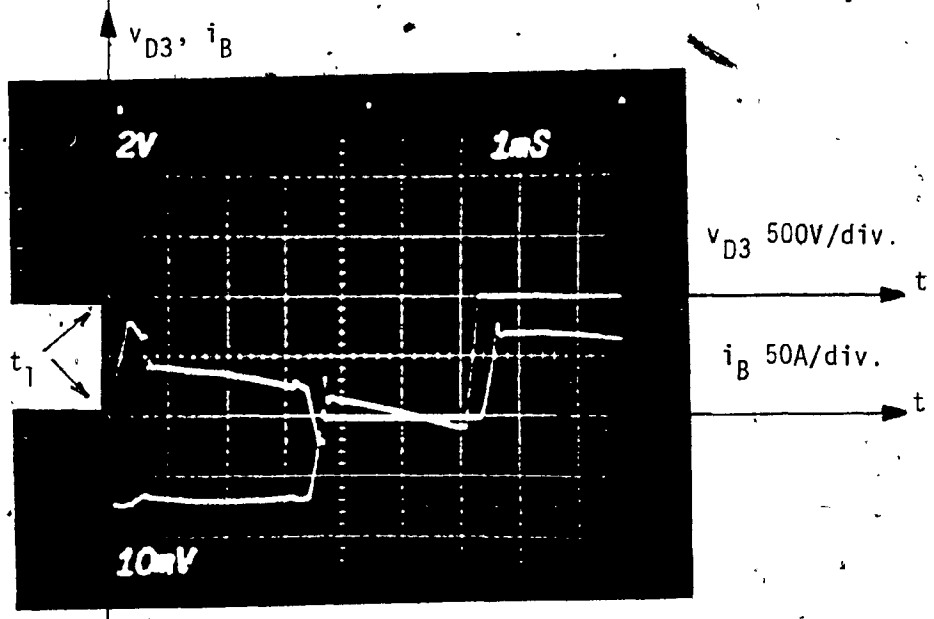

FIG. 8.7 Same as above, but with an expanded time scale. Compare this figure with Figure 8.8.

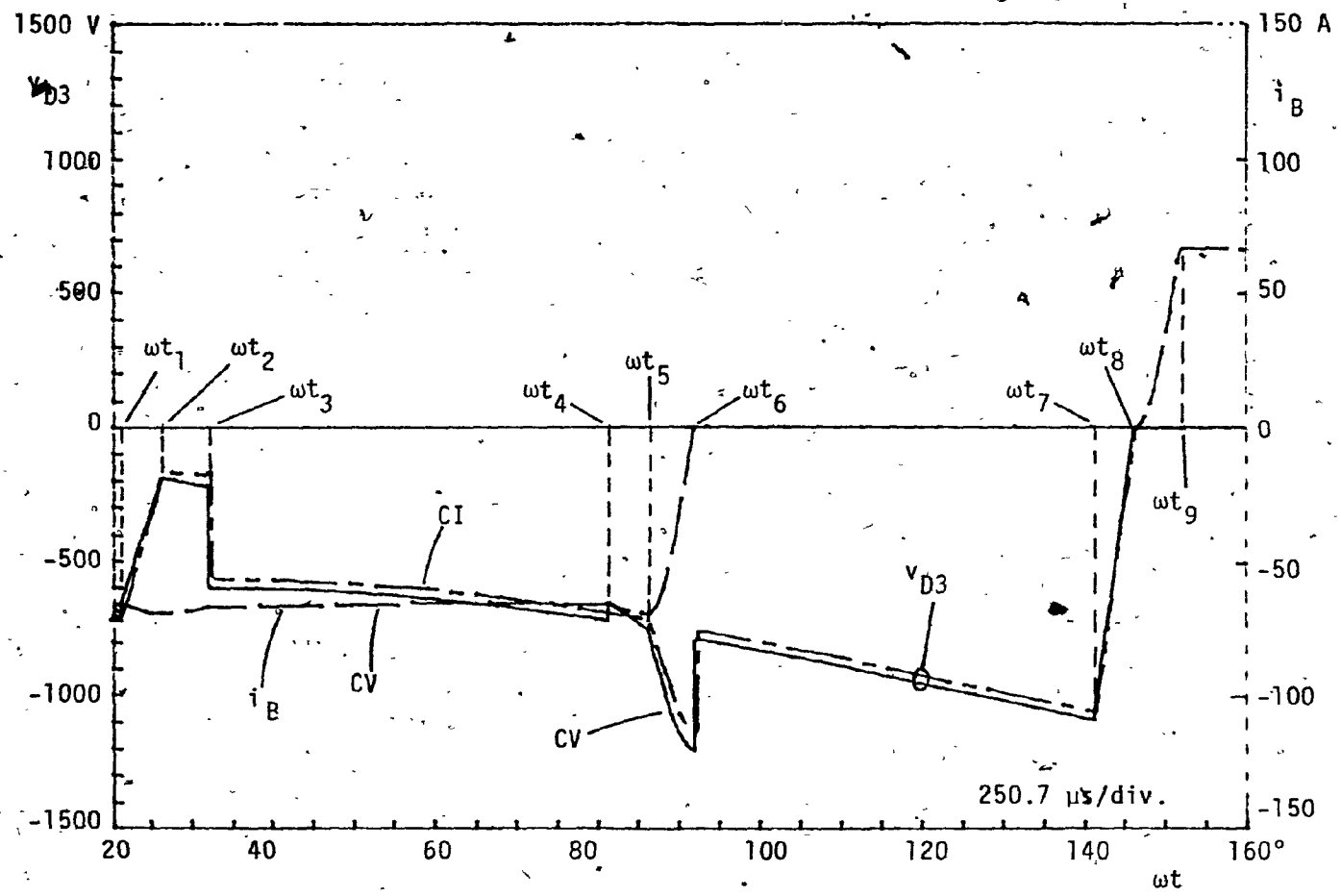

FIG. 8.8 Expanded waveforms of v_{D3} and i_B at operating point (A) obtained in case (g), curves CV, and in case (a), curves CI.

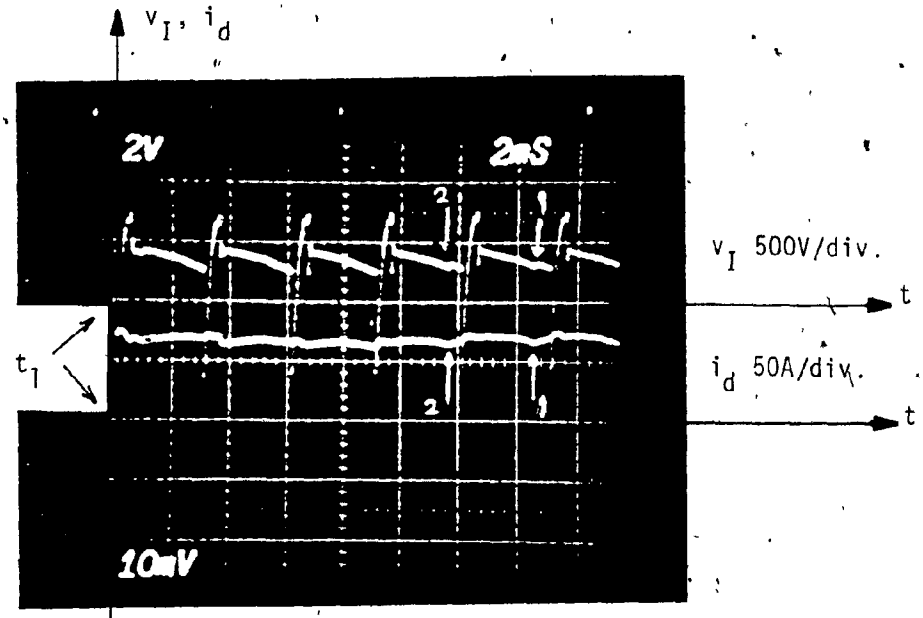

FIG. 8.9 Waveforms of inverter input voltage and dc link current at operating point (A). Compare this figure with Figure 7.11.

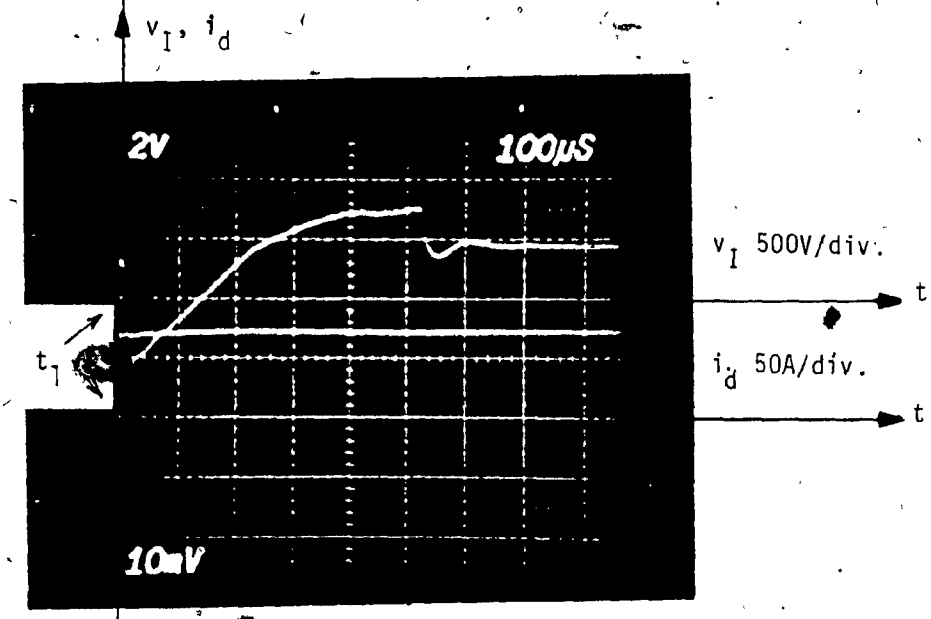

FIG. 8.10 Same as above, but with an expanded time scale. Compare this figure with Figure 8.11.

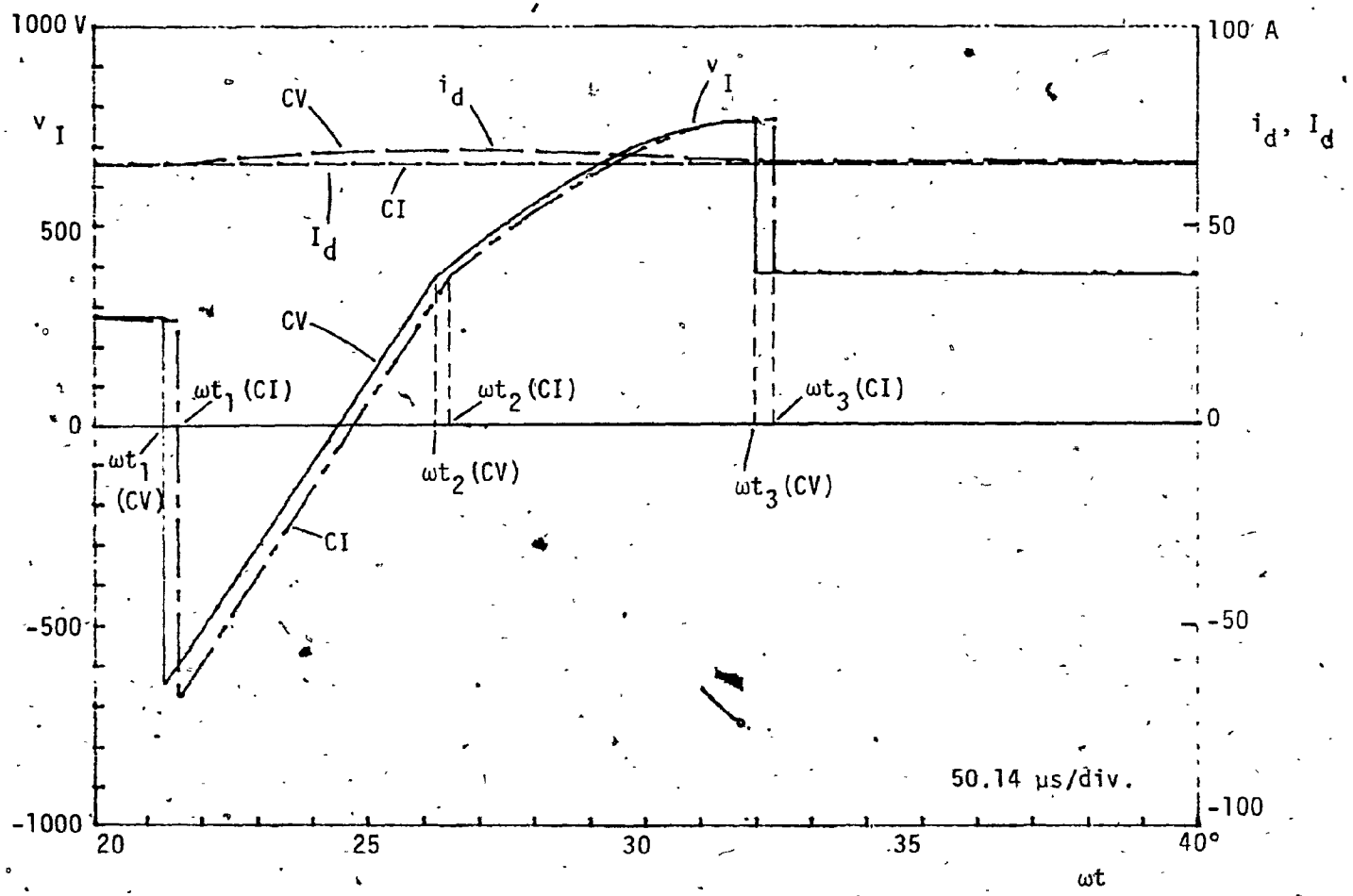

FIG. 8.11 Same as Fig. 7.11, but with an expanded time scale.

input voltage assumption (curves CV) are more in harmony with the experimental waveforms than those plotted through a constant dc link current assumption.

Obviously, one point cannot be predicted on the simulated waveforms and that is the effect of the variation of the dc link input voltage on the plotted waveforms. In the actual drive of this study, the inverter was fed by a six pulse controlled rectifier bridge connected to a 60 Hz line. The output of such a bridge has a frequency of 360 Hz, which is well known, so that the time between firing two consecutive SCR's in the bridge is equal to 2.77 ms. The effect of firing each of the bridge thyristors on the inverter waveforms can be best noticed in figure 8.9. In this figure, two points have been indicated on the inverter input voltage waveform (points 1 and 2). These two points show two consecutive firing instants of the bridge thyristors. Each thyristor turn-on in the bridge generates similar break points on the different voltage waveforms of the inverter-induction motor (in addition to V_I waveform in figure 8.9, these break points are seen clearly on the voltage waveforms of figures 8.1, 8.2 and 8.6). The effect of firing each bridge SCR on the dc link and on the motor input current waveforms is a fall or minimum point. Two of these points have also been shown in figure 8.9. Due to the difference between the inverter output frequency at point (A) (55.4 Hz) and that of the bridge (60 Hz), the minimum points on the current waveforms and the break points on the voltage waveforms are not stationary on these waveforms but they keep moving either to the left or to the right

side of each oscillogram (each break point lags the previous one by 2.77 ms). For the case that the inverter output frequency is less than the bridge input frequency, which is the case of the experiments, the motion of the break or minimum points is to the left. For the case of the inverter output frequency being more than the bridge input frequency, these points are pushed to the right. The movement to the left can be easily verified from figures 8.1, 8.2, 8.3, 8.6 and 8.9.

8.3 EXPERIMENTAL RESULTS FOR A CLAMPED OPERATION

For the system under a clamped voltage operation point (B) with specifications given in Appendix A-1 was used for generating the voltage and current waveforms in section (6.8), figs. 6.18 - 6.24. In this section, the experimental oscillograms are shown and compared with those obtained by simulation. As in the previous section, a few expanded simulated waveforms are also included in this section, figs. 8.14, 8.17, 8.20, 8.23 and 8.26.

Although figures 6.18 - 6.24, 8.14, 8.17, 8.20, 8.23 and 8.26 have been plotted with a constant dc link current assumption, they show a very good agreement with those obtained experimentally. The discussion presented in the previous section regarding the effect of the firing of the bridge SCR's on the inverter and motor voltage and current waveforms can also be visualized in the experimental oscillograms of this section. Besides the bridge firing effect, comparison between the simulated and experimental graphs show another point which

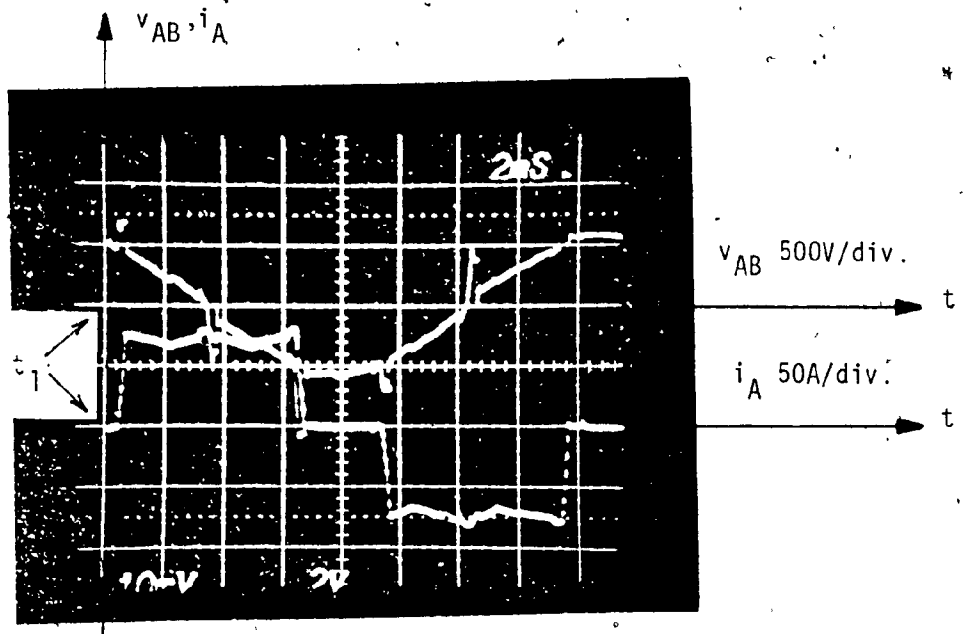

FIG. 8.12 Waveforms of motor voltage across terminals A-B and phase A current at operating point (B). Compare this figure with Figure 6.20.

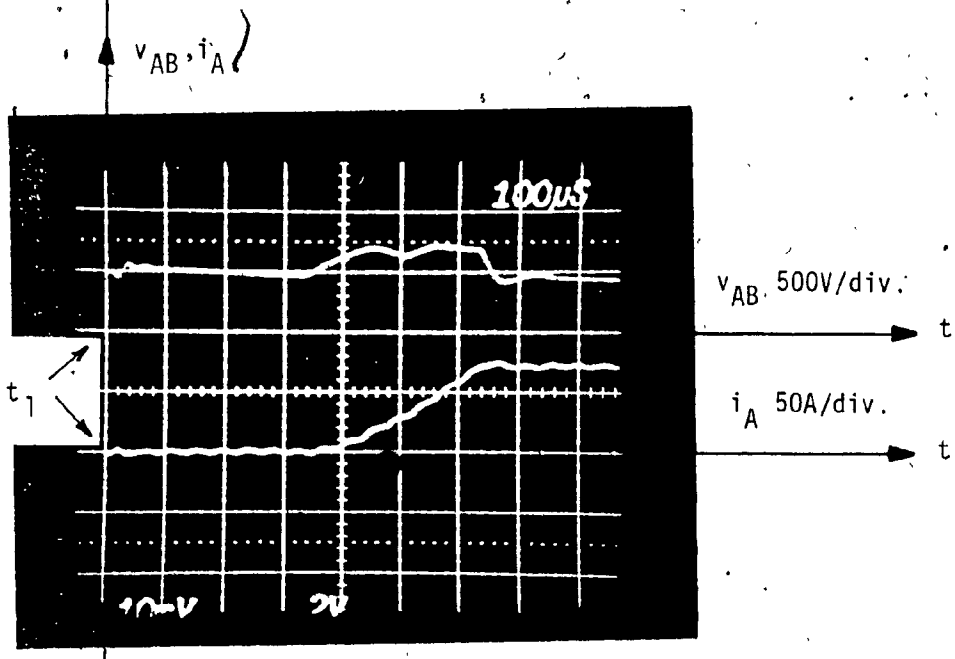

FIG. 8.13 Same as above, but with an expanded time scale. Compare this figure with Figure 8.14.

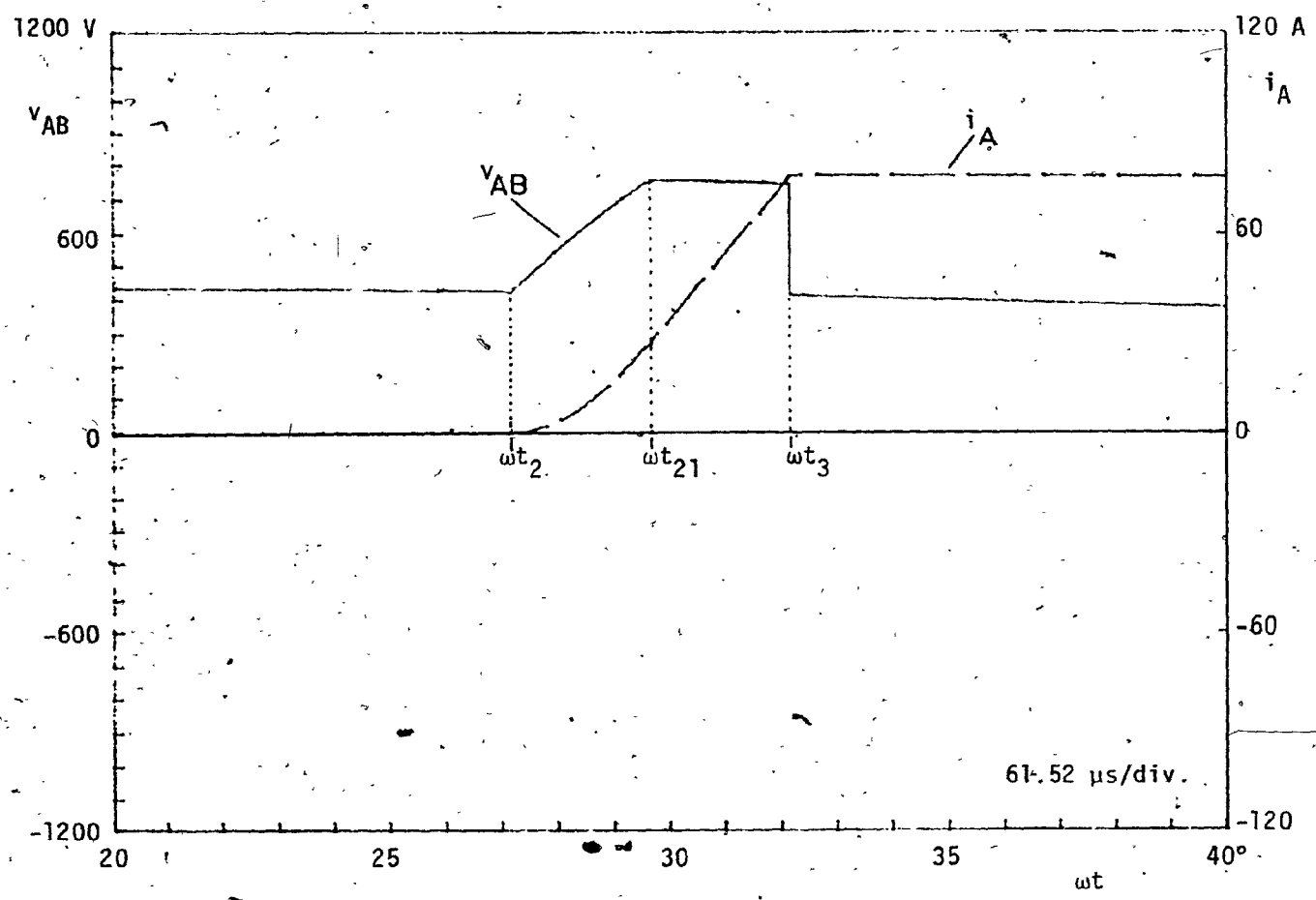

FIG. 8.14 Same as Fig. 6.20, but with an expanded time scale.

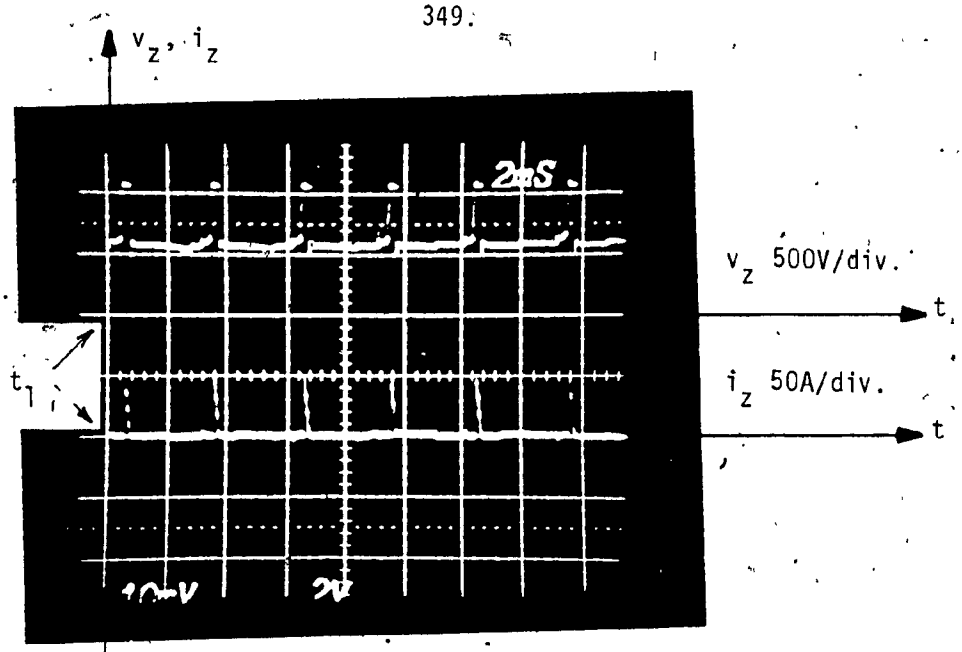

FIG. 8.15 Waveforms of voltage across the string of zener diodes and current through them at operating point (B). Compare this figure with Figure 6.21.

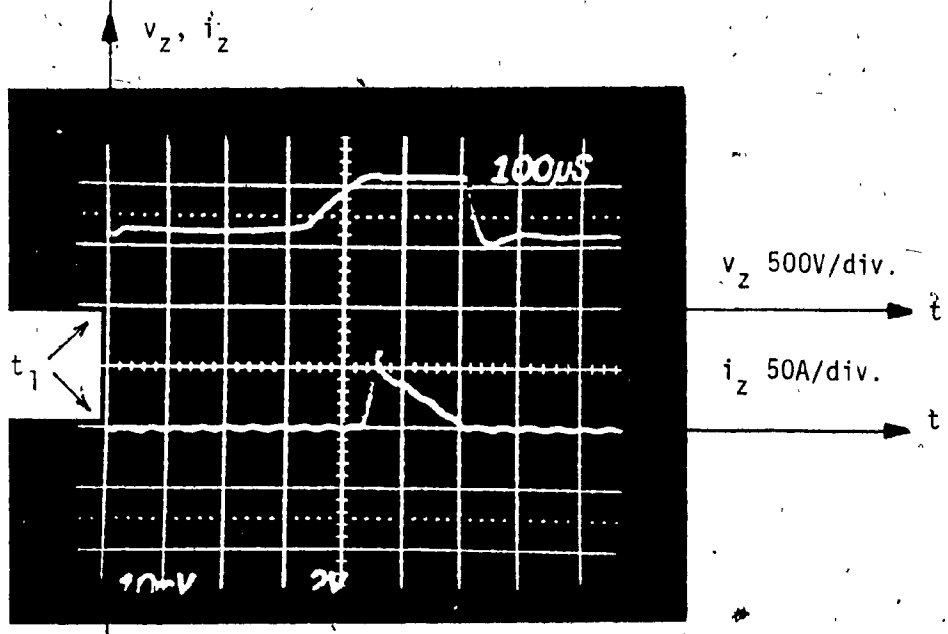

FIG. 8.16 Same as above, but with an expanded time scale. Compare this figure with Figure 8.17.

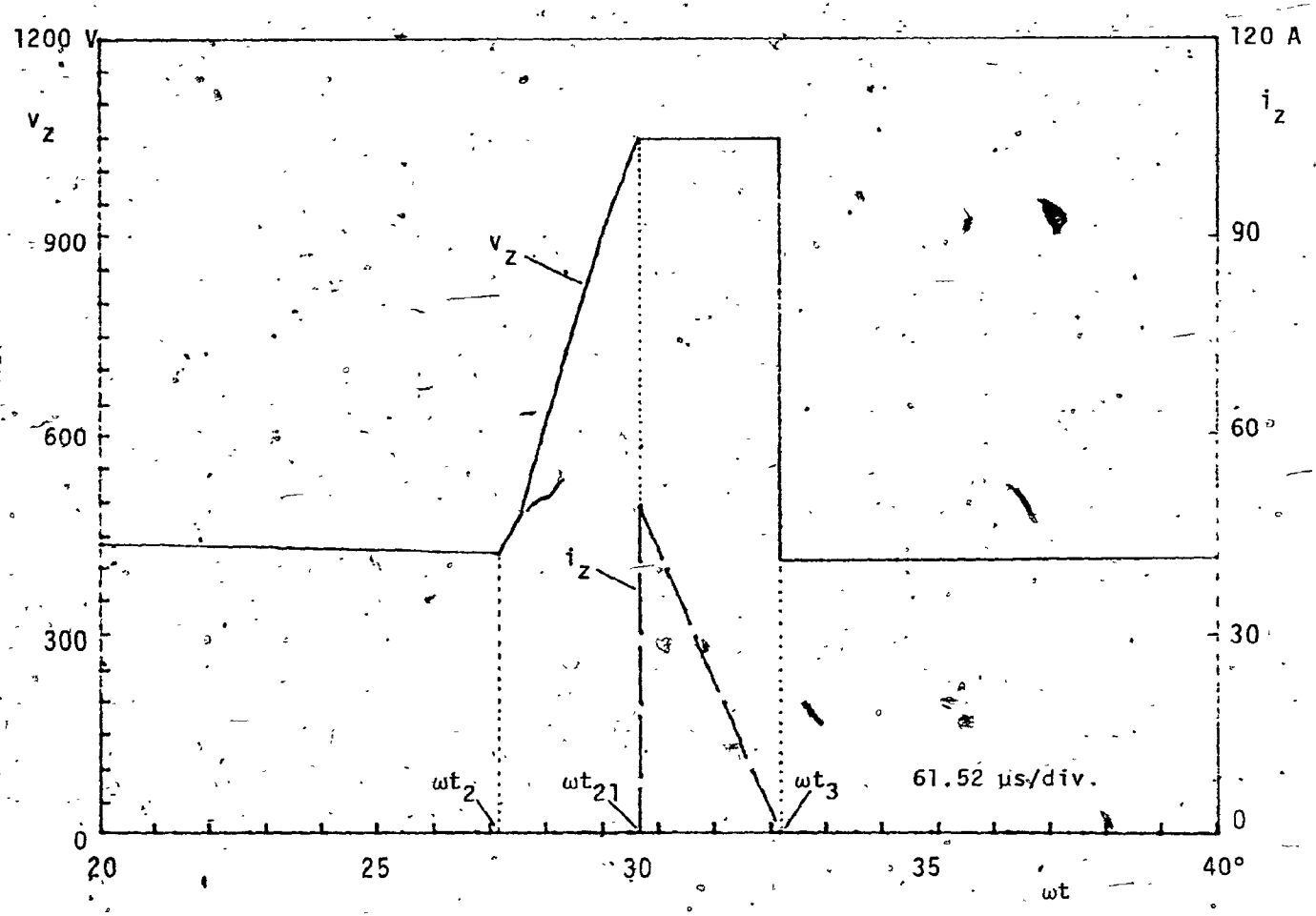

Fig. 8.17 Same as Fig. 6.21, but with an expanded time scale.

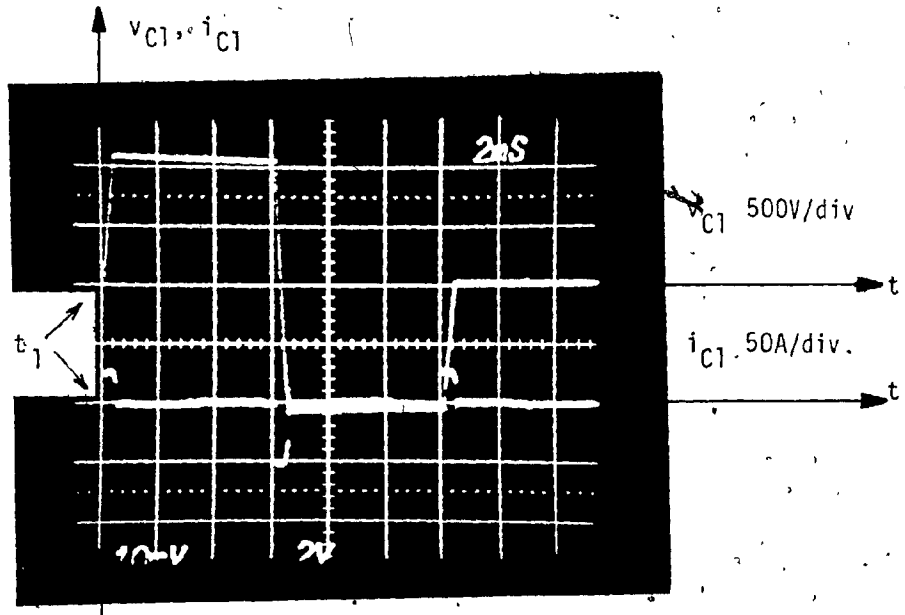

FIG. 8.18 Waveforms of inverter capacitor C_1 voltage and current at operating point (B). Compare this figure with Figure 6.22.

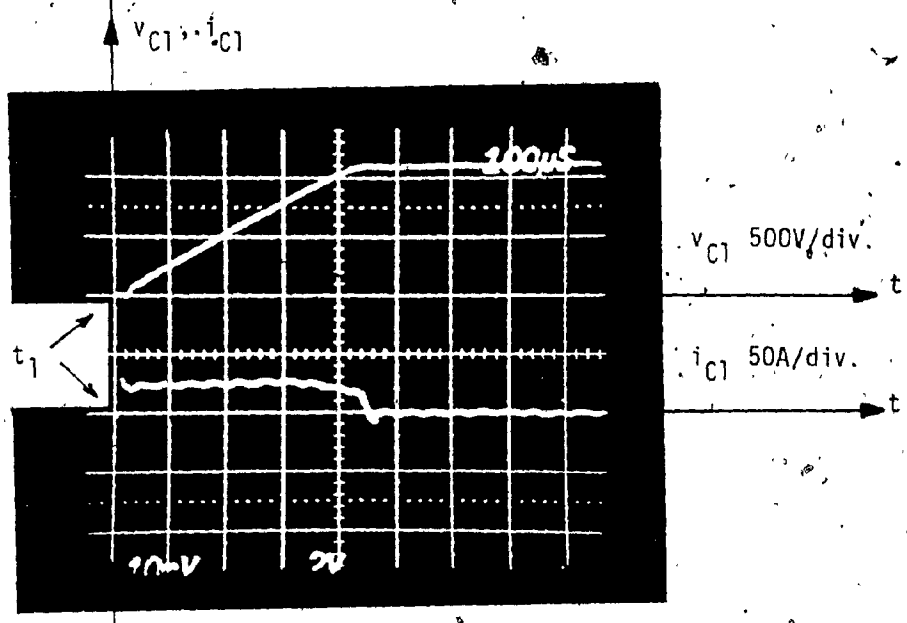

FIG. 8.19 Same as above, but with an expanded time scale. Compare this figure with Figure 8.20.

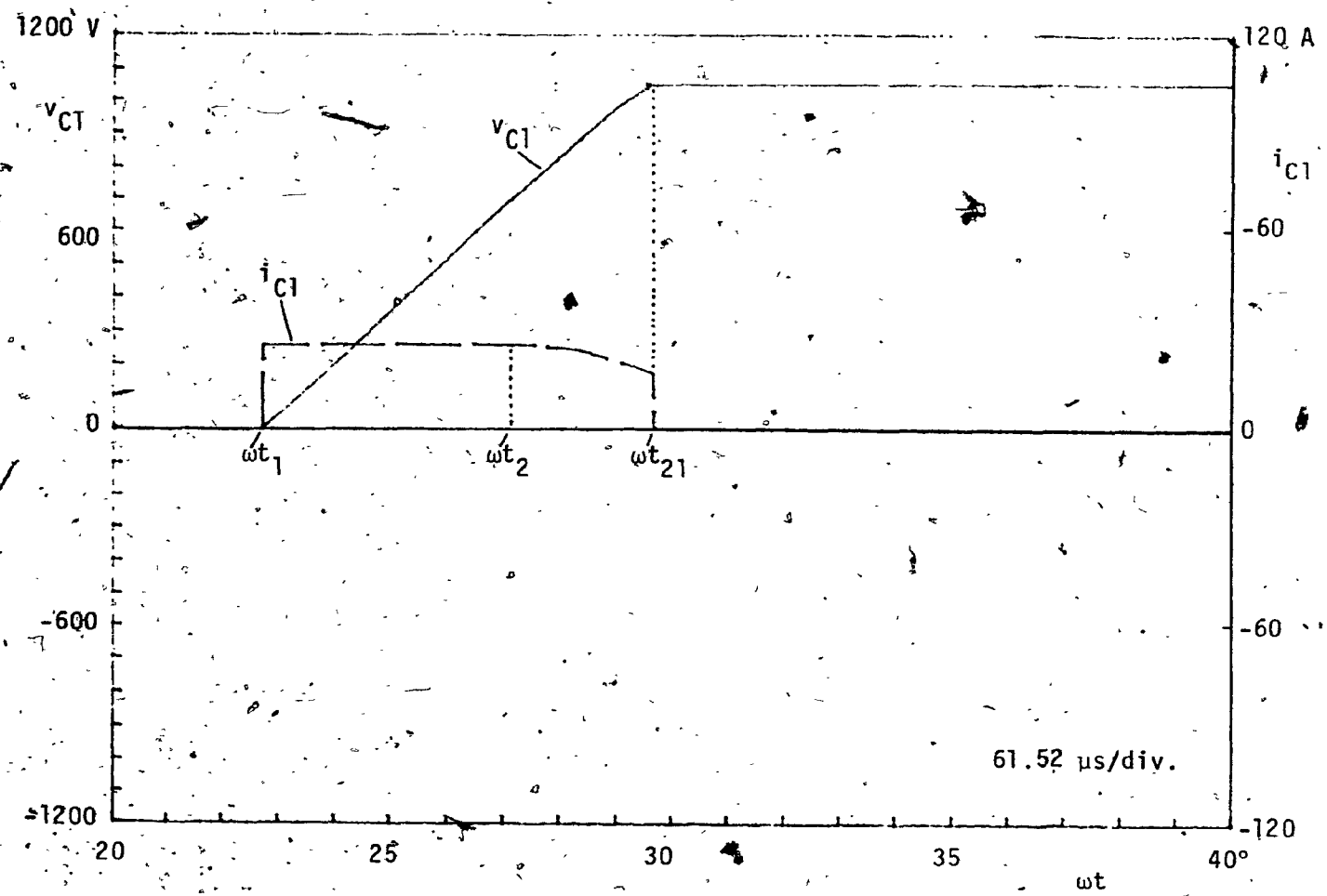

Fig. 8.20 Same as Fig. 6.22, but with an expanded time scale.

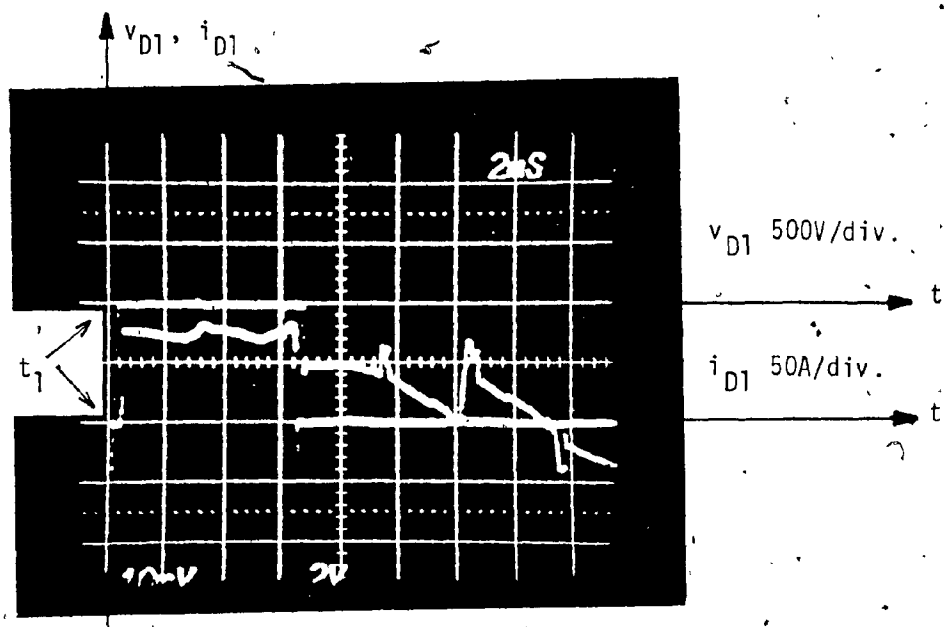

FIG. 8.21 Waveforms of inverter diode D_1 voltage and current at operating point (B). Compare this figure with Figure 6.23.

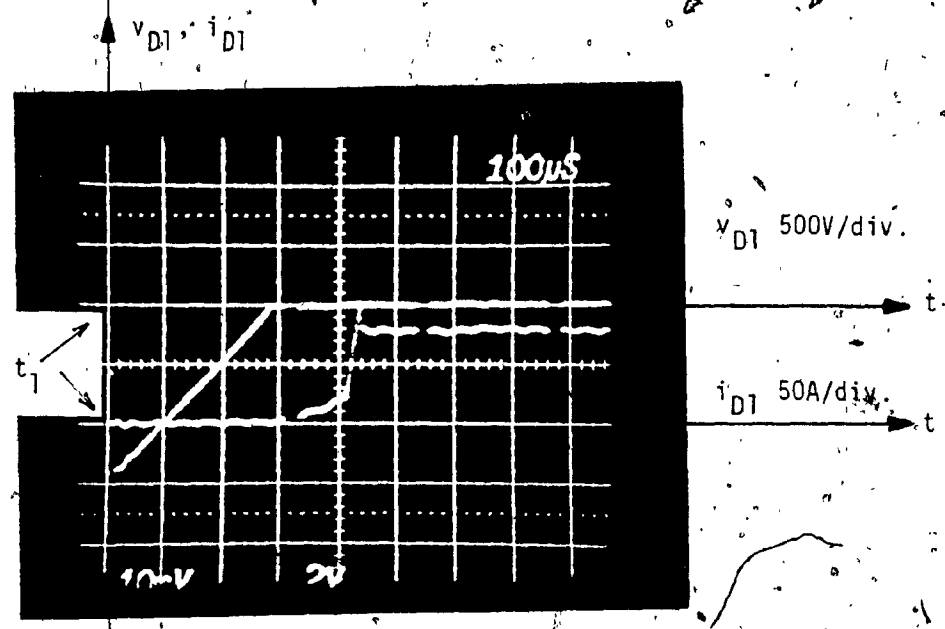

FIG. 8.22 Same as above, but with an expanded time scale. Compare this figure with Figure 8.23.

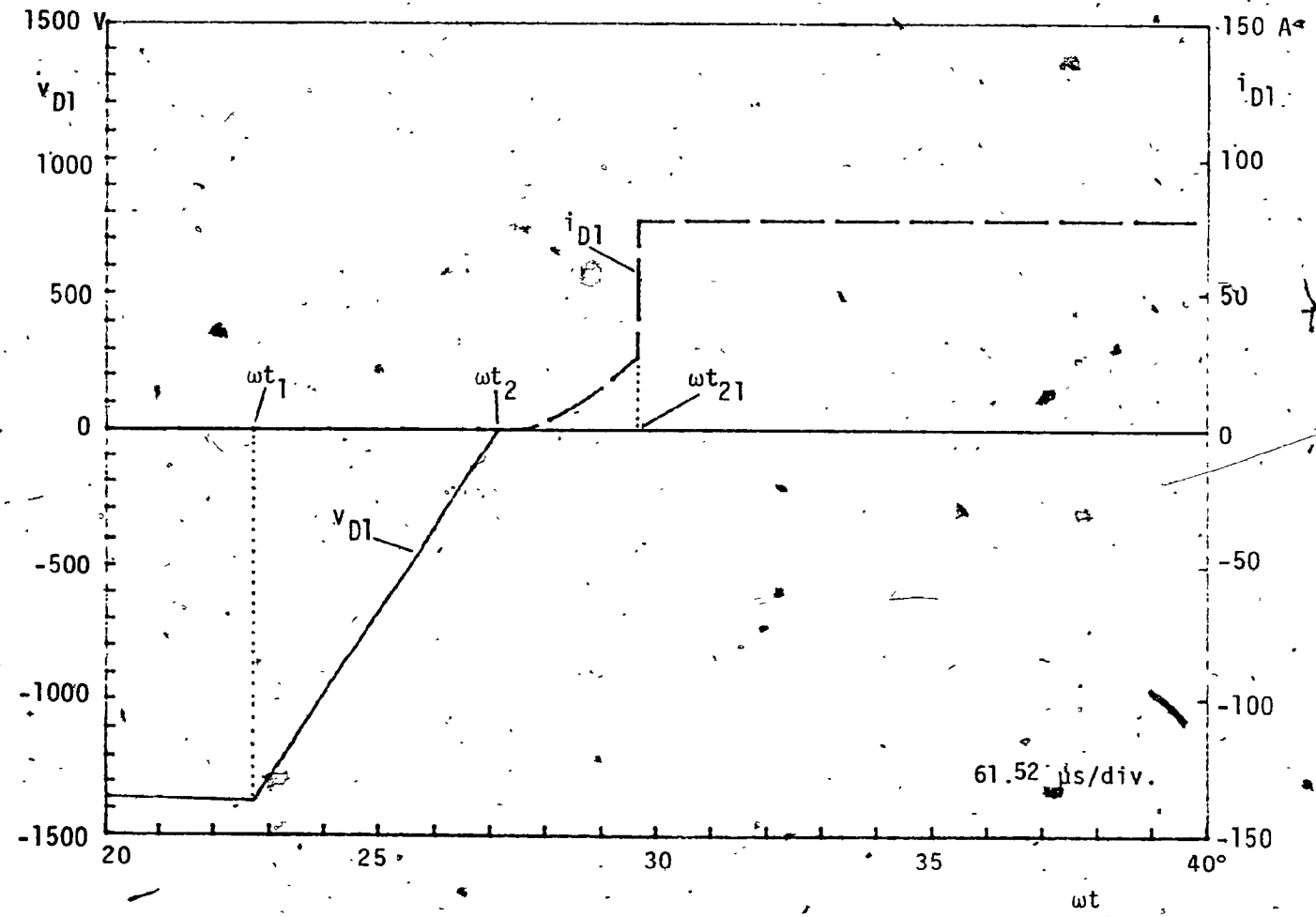

Fig. 8.23 Same as Fig. 6.23, but with an expanded time scale.

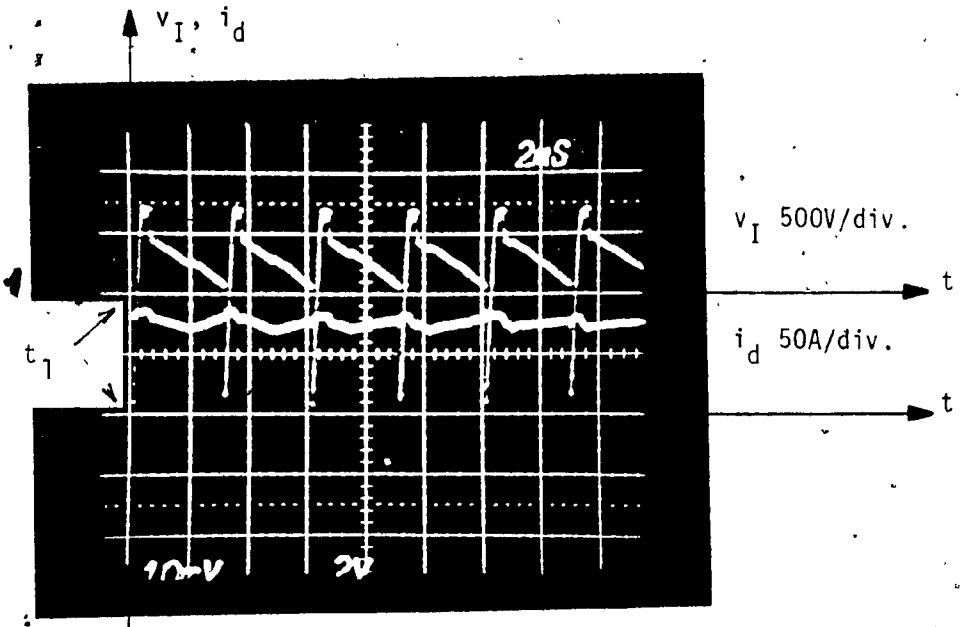

FIG. 8.24 Waveforms of inverter input voltage and dc link current at operating point (B). Compare this figure with Figure 6.24.

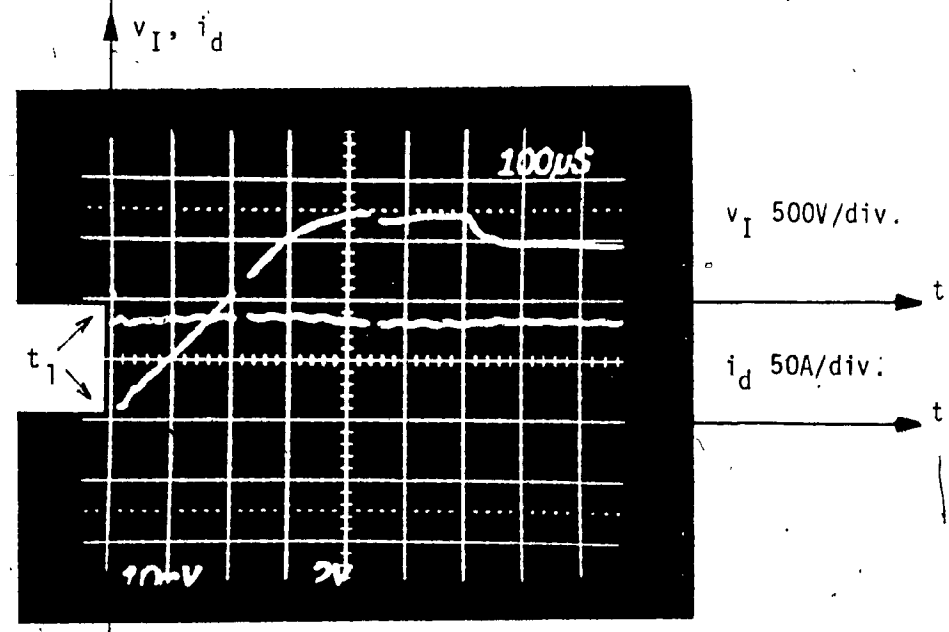

FIG. 8.25 Same as above, but with an expanded time scale. Compare this figure with Figure 8.26

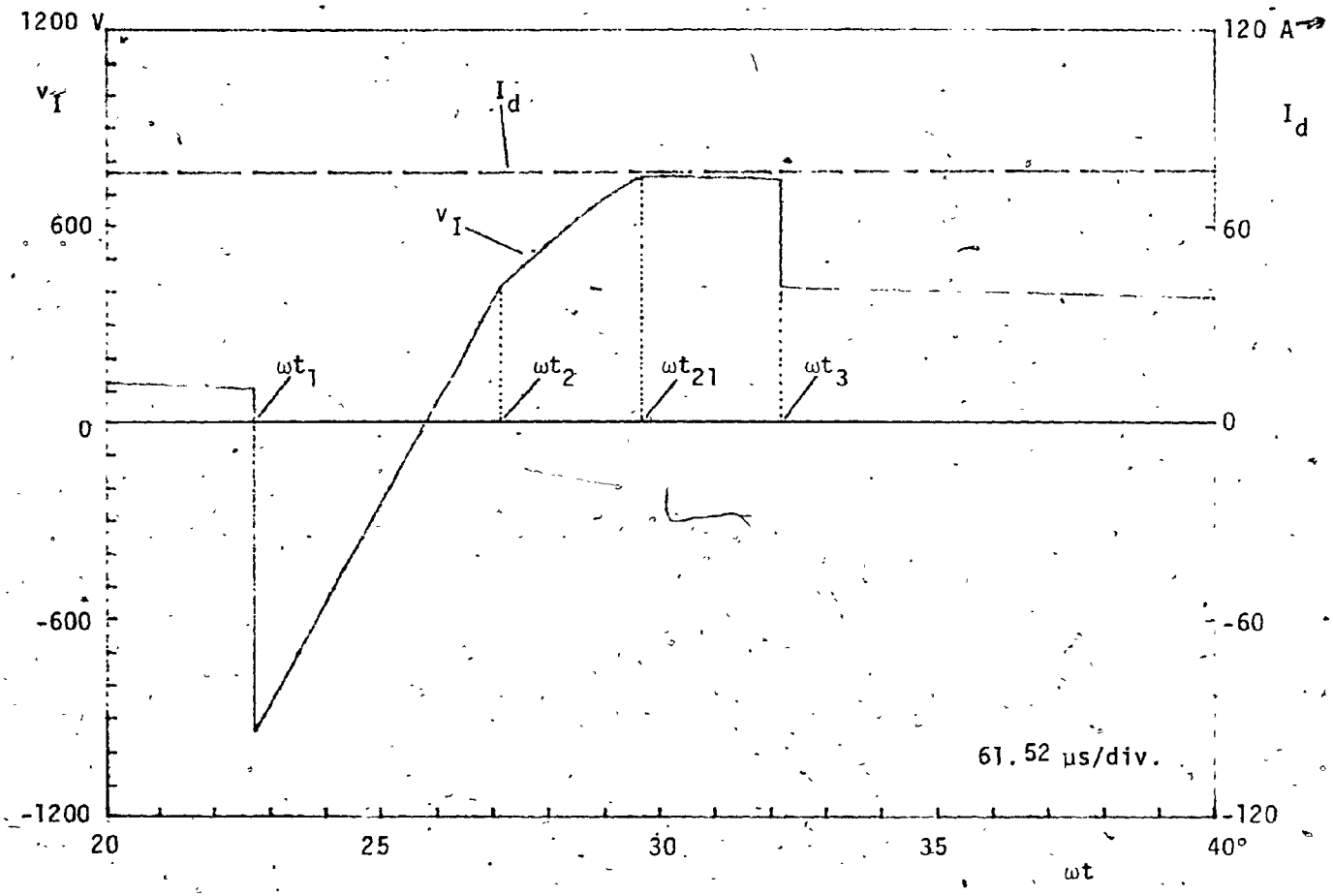

Fig. 8.26 Same as Fig. 6.24, but with an expanded time scale.

cannot be predicted by the plotted graphs. The fact that switching components (thyristors and diodes) are not ideal but have finite turn-on and -off times can be attested by studying some of the experimental results. As an example, comparing figure 8.16 with figure 8.17, it is noticed that the difference in the rise time of the zener diodes current in these two figures is due to the actual turn-on time of these diodes. Figure 8.17 shows a sudden rise in the zener current from zero to the maximum value while in figure 8.16 such a rise takes about 20 μs.

8.4 CONCLUSION

In this chapter, the simulated waveforms were compared with those obtained from a real system. The comparison was performed for two operating points; one in which the voltage spikes are not clipped off by the clamping circuit and the other in which the clamping circuit enters into the system. For the first operating point, the simulated waveforms obtained through a constant dc link input voltage (curves CV) showed a very good analogy to the actual waveforms and for the second operating point there was still a good correspondence between the theoretical and experimental results.

The important conclusion from the comparisons is that the assumption of a constant dc link current, as long as an exact method is followed for obtaining the unknowns (flowchart 3.2 and 6.2), yields results which can be confidently used for design of the system. In this respect, including the magnetizing and leakage inductance saturations contributes to the accuracy of the results.

CHAPTER IX

CONCLUSION

The design of an auto-sequentially commutated inverter (ASCI) can be done quickly and accurately if a computer program is generated for this purpose. In addition, such a program contributes to the fast determination of the effects which the different, dc link, inverter and motor parameters impose on the performance of the system. To achieve this goal, a detailed study of an ASCI-induction motor drive operating under steady-state conditions was accomplished in different stages. All the steps of the study were based on a series equivalent circuit of an induction motor suitable for connection to the output of an ASCI. The use of such a series equivalent circuit provides a simple expression for the motor terminal voltage, in which the effects of all current harmonics are included. The series equivalent circuit developed in this thesis also takes into account the effect of the core-loss resistance neglected in the other studies. The magnitude of the fundamental harmonic of the motor input current is required for calculating the motor CEMF in the series equivalent circuit. This is fulfilled by applying the motor operating point characteristics to the induction motor exact equivalent circuit. The fundamental harmonic of the motor input current is also used for estimation of the average value of the dc link current. The accuracy of this estimation depends on the duration of a transfer mode compared with the period of the inverter output current. In this respect,

the less a transfer mode period, the more accurate the dc link current.

Although the study was done for several cases, it can be divided into two principal parts:

1. The dc link current is assumed to be constant, which is the same as supposing a very large dc link reactance, and

2. The dc link input voltage is considered to be constant at each operating point, so that the dc link parameters are included in the system.

Under the first assumption, the operation of the system was studied with and without a clamping circuit. In both these conditions, the partial commutation overlap was also explained and discussed. With the second assumption, only the case with no commutation overlap and no clamping circuit was considered.

The operation of the system with a constant dc link current and without a clamping circuit while there is no commutation overlap was called case (a). This case, in which the commutation angle is less than 60°, resulted in 18 distinct modes in each inverter output cycle. The necessary expressions describing the system were obtained by studying three consecutive modes. The number of equations were found to be one less than the number of the unknowns. The missing equation was obtained by two methods: approximate and exact. In the approximate approach, the waveform of the motor input current was assumed to consist

of trapezoidal pulses. This simplification provided a simple expression for the beginning of a transfer mode (t_2) in terms of the transfer mode duration. In the exact method, the beginning of a transfer mode was found through iterations. Thus in both methods, the number of equations became the same as the number of the unknowns.

For the operation of the system under a constant dc link current and without a clamping circuit while the commutation angle exceeds 60° but remains less than 120°, two cases were considered. In case (b), the charging angle is less than 60°, while in case (c), this angle is more than 60°. Under the condition that no diodes become transiently forward biased, it was concluded that the same flowchart used for calculating the unknowns in case (a) can be employed in cases (b) and (c).

Two sets of graphs were plotted for case (a). The first set showed the different voltage and current waveforms at one specific operating point, while the second one gave the variations of each variable under constant torque-variable frequency conditions. The values of the magnetizing and leakage inducatances were determined from the corresponding curves. Also, an appropriate core-loss resistance was chosen for each motor input frequency. The important conclusion from the diode voltage waveform was that it showed the instant at which the diode might become forward biased. The second set of graphs revealed that two operating points are critical in the design of the system; one at a no-load and at the maximum frequency, and the other at the maximum load and frequency.

The voltage ratings of the inverter components depend on the peak value of the voltage spikes. In some applications, the high values of the voltage spikes might not be desirable from economical or technical points of view. A zener clamping circuit which has a simple circuit and a quite straight-forward operation was considered for limiting the peak values of the spikes. The system operation under a constant dc link current and with a zener clamping circuit was studied in three cases, (d), (e) and (f). In all three cases, the number of modes were increased from 18 to 24 so that four consecutive modes were required to be studied in order to establish the necessary expressions. Case (d) dealt with a no-overlap operation while cases (e) and (f) dealt with partial commutation overlap performance. A complete study was done for case (d), which resulted in the essential expressions for calculating the unknowns. As in case (a), one equation was missing. Two methods, approximate and exact, were set up for obtaining the missing equation and for calculating the unknowns. The same procedures as in case (a) were followed for computing the unknowns in the approximate and exact methods. The exact approach was then employed for plotting two sets of graphs, as in case (a). From the first set, which showed different voltage and current waveforms, it was resolved that the general forms of the waveforms remain the same as in a no-clamping operation. The only difference is that the voltage spikes are limited to some level determined by the breakdown voltage of the zener diodes. In the second set, each curve was plotted with its counterpart from case (a). In this way, the effect of clamping on the performance of the system could be determined. One

significant conclusion from this set of graphs was the fact that the maximum operating frequency has a lower value, under similar conditions, than the case without a clamping circuit. The reason is the high power loss in the zener diodes. It was shown that under high frequencies and with torques higher than the rated torque, the bridge feeding the inverter cannot provide the required voltage across its output terminals. In addition, in practical applications where each switching component has some power loss, the efficiency of the system with a clamping circuit becomes very low at high frequencies. Hence, the operation of the drive under these conditions and for long periods is not recommended.

In case (e) and case (f), the partial commutation overlap was studied while the system goes under clamping. It became clear that, as long as the diodes do not become transiently forward biased, the same flowchart used in case (d) can be employed for calculating the values of the unknowns in these two cases.

The assumption of a constant dc link input voltage was applied to a no-overlap, no-clamping operation. The derived expressions were based on four main variables of the system. These variables were:

1. The value of the constant voltage across the dc link input terminals,

2. The maximum voltage of the commutating capacitors,

3. The instant the thyristor T_1 is fired, and

4. The magnitude of the dc link current when T_1 is triggered.

The equations were obtained through solving differential equations and the procedure was almost very long compared with the constant dc link approach. The number of obtained equations were three less than the number of variables, so that the computations of the shift angle of the fundamental harmonic of the motor phase A current and of the motor total input power were necessary in each iteration. These two computations led to the calculation of the first and third main variables specified above. The fact that the dc link current should have the same magnitude at the beginning of each mode and at 60° later, provided a procedure for obtaining the fourth main unknown. Four simultaneous nonlinear implicit equations were solved iteratively. The results were achieved when the four main unknowns obtained, with allowable error, the same values in two consecutive iterations. This procedure was then applied to plotting two sets of graphs as in the other cases. In all the figures, the graphs of case (a) were also added so that the comparison between the two approaches could be done easily. This comparison showed that the commutating capacitors obtain a higher maximum voltage by this method than through a constant dc link assumption. Generally speaking, both methods yielded almost the same results.

The comparison between the simulated and experimental results were conducted for two operating points. At the first operating point, the peak value of the voltage spike was less than the zener diodes breakdown voltage , while at the second operating point, the clamping circuit clipped off the excess voltage. For the first operating point, the comparison showed that the simulated results obtained through the constant voltage assumption are nearer to the actual waveforms and the dc link current ripples resemble the ripples on the actual current waveforms. The same conclusion was also deduced for the ripples produced by the current ripples on the voltage waveforms. The firing instants of the thyristors in the bridge circuit were clear on the actual oscillograms while, due to the constant voltage assumption across the bridge output, the simulated results did not show the points. In a real system, these firing instants move on the voltage and current waveforms, either to the left or to the right. If the inverter output frequency is less than the bridge input frequency, the direction of the motion is to the left. Otherwise, it would be to the right. For the second operating point, there was also a good correlation between the simulated and experimental results, although the constant dc link current was employed for obtaining the simulated results.

As a whole, in this thesis, the following contributions were made to the analysis and design of an ASCI-induction motor drive under steady state conditions:

1. The development of the series equivalent circuit of an induction motor in which the core-loss resistance was included;

2. The effects of the commutation circuit as well as the variations of the motor CEMF during each commutation period were considered in all steps of the study. Also, the stator resistance was not neglected;

3. The exact evaluation of each variable under different load conditions was done first by assuming a constant dc link current. This analysis is valid for all frequencies, including the partial commutation overlap operation as long as the diodes do not become transiently forward biased and the system does not enter into a full commutation overlap;

4. In another step, the exact evaluation of each variable and the partial commutation overlap analysis were accomplished for the system under a constant dc link current and with a zener clamping circuit. The effect of the clamping circuit on the performance of the system was also investigated;

5. In the last step, the dc link parameters were included in the system by assuming a constant voltage across the dc link input terminals. An exact algorithm was used for determining each variable. The effect of a constant voltage assumption on the performance of the system was also covered in this step.

REFERENCES

1. K.P. Phillips, "Current Source Converter for AC Motor Drives," Conf. Rec. IEEE - IGA 6th Annual Meeting, October 18-21, 1971, pp. 385-392.

2. R.B. Maag, "Characteristics and Application of Current Source/Slip Regulated AC Induction Motor Drives," Conf. Rec. IEEE - IGA 6th Annual Meeting, October 18-21, 1971, pp. 411-416.

3. W. Farrer and J.D. Miskin, "Quasi-Sine-Wave Fully Regenerative Inverter," Proc. IEE, Vol. 120, No. 9, Sept. 1973, pp. 969-976.

4. M.B. Brennen, "A Comparative Analysis of Two Commutation Circuits for Adjustable Current Input Inverters Feeding Induction Motors," Conf. Rec. PESC, 1973, pp. 201-212.

5. T.A. Lipo and E.P. Cornell, "State Variable Steady-State Analysis of a Controlled Current Induction Motor Drive," Conf. Rec. IEEE-IAS 9th Annual Meeting, October 7-10, 1974, Part II, pp. 851-859.

6. I. Yasuoka and Y. Tsunehiro, "Estimation of Commutating Capacitance of Current-Impressed Inverter Used for an Induction Motor Drive," Elec. Eng. in Japan, Vol. 94, No. 4, 1974, pp. 48-55.

7. R.H. Nelson and R.A. Radomski, "Design Methods for Current Source Inverter/Induction Motor Drive Systems," IEEE Trans., Vol. IECI-22, No. 2., May 1974, pp. 141-145.

8. G.R. Slemon and S.B. Dewan, "Induction Motor Drive with Current Source Inverter," Conf. Rec. IEEE - IAS 9th Annual Meeting, October 7-10, 1974, Part I, pp. 411-417.

9. M.K. Parasuram and B. Ramaswami, "Analysis and Design of a Current-Fed Inverter," Preprints, 2nd IFAC Symposium on Control in Power Electronics and Electrical Drives, Dusseldorf, April 1977, Pergamon Press, Oxford, pp. 235-245.

10. A.H. Mittag, "Electric Valve Converting Apparatus", U.S. Patent 1,946,292 (to G.E.), Feb. 6, 1934.

11. E.E. Ward, "Inverter Suitable for Operation over a Range of Frequency," Proc. IEE, Vol. 111, No. 8, August 1964, pp. 1423-1434.

12. N. Samaki and N. Sato, "Steady-State and Stability Analysis of Induction Motor Drives by Current Source Inverter," IEEE Trans., Vol. IA-13, No. 3, May/June 1977, pp. 244-253.

13. E.P. Cornell and T.A. Lipo, "Modeling and Design of Controlled Current Induction Motor Drive Systems," Conf. Rec. IEEE - IAS

10th Annual Meeting, Sept. 28 - Oct. 2, 1975, pp. 612-620.

14. K. Moll and D. Schroder, "Applicable Frequency Range of Current Source Converters," Preprints, 2nd IFAC Symposium on Control in Power Electronics and Electrical Drives, Dusseldorf, April 1977, Pergamon Press, Oxford, pp. 231-234.

15. W. Lienau, "Commutation Modes of a Current-Source Inverter," Preprints, 2nd IFAC Symposium on Control in Power Electronics and Electrical Drives, Dusseldorf, April 1977, Pergamon Press, Oxford, pp. 219-229.

16. J. Lazar, "The operational Modes of a Current Source Inverter Induction Motor Drive System," Preprints, 2nd IFAC Symposium on Control in Power Electronics and Electrical Drives, Dusseldorf, April 1977, Pergamon Press, Oxford, pp. 443-451.

17. Ph. Lataire, "Analysis and simulation of the working of a Current Fed Induction Motor Drive using Symmetrical Components of Instantaneous Potentials and Currents," Conf. Rec. IEEE - IAS 13th Annual Meeting, Oct. 1-5, 1978, pp.

18. V. Subrahmanyam, D. Subbarayudu and M.V.C. Rao, "On the Utility of Signal Flow Graphs in the Analysis of Current Controlled Induction Motor," Preprints, 2nd IFAC Symposium on Control in Power Electronics and Electrical Drives, Dusseldorf, April 1977, Pergamon Press, Oxford, pp. 443-451.

19. L. Abraham, "Transient Characteristics and Limits of a Squirrel-Cage Motor Fed from a Frequency Converter with D.C. Current Link," Preprints, 2nd IFAC Symposium on Control in Power Electronics and Electrical Drives, Dusseldorf, April 1977, Pergamon Press, Oxford, pp. 475-481.

20. M.L. MacDonald and P.C. Sen, "Control Loop Study of Induction Motor Drives Using DQ Model," Conf. Rec. IEEE - IAS 13th Annual Meeting, Oct. 1-5, 1978, pp. 897-903.

21. F. Harashima and M. Hyashi, "Dynamic Performance of Current Source Inverter Fed Induction Motors," Conf. Rec. IEEE - IAS 13th Annual Meeting, Oct. 1-5, 1978, pp. 904-909.

22. M.P. Kazmierkowski, et.al., "Induction Motor Drive Systems Controlled by Frequency Converter with Current Source Inverter," Conf. Rec. IEEE - IAS, 13th Annual Meeting, Oct. 1-5, 1978, pp. 1067-1072.

23. S.B. Dewan and K. Gallant, "Analysis of a Single Phase Current Source Inverter," Conf. Rec. IEEE - IAS 9th Annual Meeting, Oct. 7-10, 1974, Part II, pp. 1025-1039.

24. W. McMurray, "The Performance of a Single-Phase Current-Fed Inverter with Counter EMF-Inductive Load," Conf. Rec. IEEE - IAS Power Semiconductor Conference, March 1977, pp. 482-496.

25. A. Joshi, "A.C. traction Drives Using Current Source Inverter," Ph.D. Thesis, Dept. of Electrical Engineering, University of Toronto, 1978.

26. M. Abbas and D.W. Novotny, "Stator Referred Equivalent Circuits for Inverter Driven Electric Machines," Conf. Rec. IEEE - IAS 13th Annual Meeting, Oct. 1-5, 1978, pp. 828-835.

APPENDIX A-1

THE INDUCTION MOTOR RELEVANT DATA

(A). SPECIFICATIONS OF THE RATED OPERATING POINT

Power	=	50.00 HP
Voltage	=	460.00 Volts
Frequency	=	60.00 Hz
Stator Leakage Inductance	=	.436 mH (unsaturated)
Referred Rotor Leakage Inductance	=	.748 mH (unsaturated)
Referred Magnetizing Inductance	=	15.280 mH (saturated)
Stator Resistance	=	.06560 Ω
Referred Rotor Resistance	=	.03832 Ω
Number of Poles	=	4
Slip	=	.00835
Torque	=	197.88 Nm
Power Factor	=	.72
Current	=	71 A

(B) MAGNETIZING AND TOTAL LEAKAGE INDUCTANCE CURVES

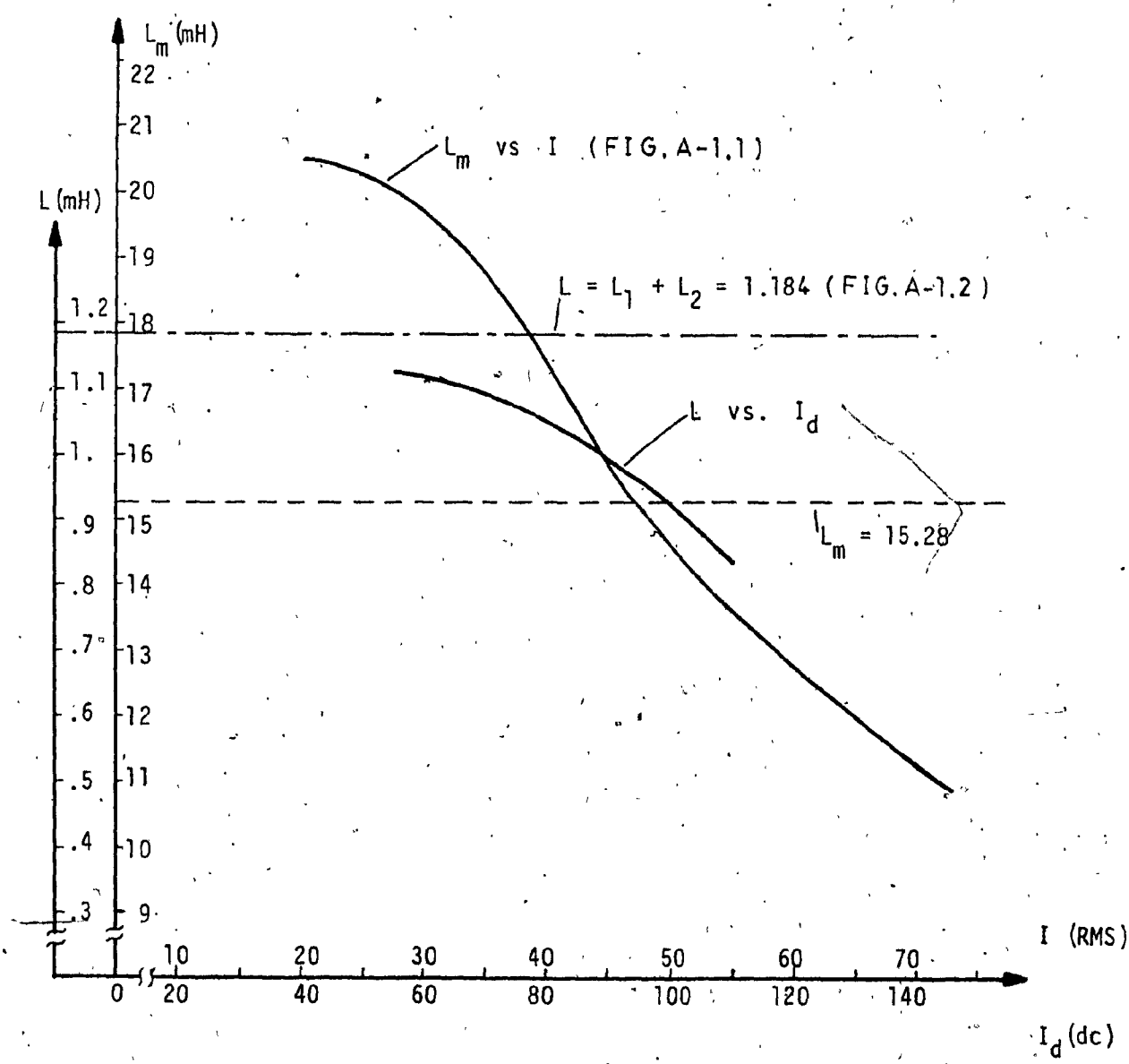

FIG. A-1.1 Measured values of the magnetizing inductance. I is the motor input RMS current at no-load conditions.

FIG. A-1.2 Measured values of the motor total leakage inductance ($L = L_1 + L_2$) as a function of the dc link current.

(C) CORE-LOSS RESISTANCE CURVE

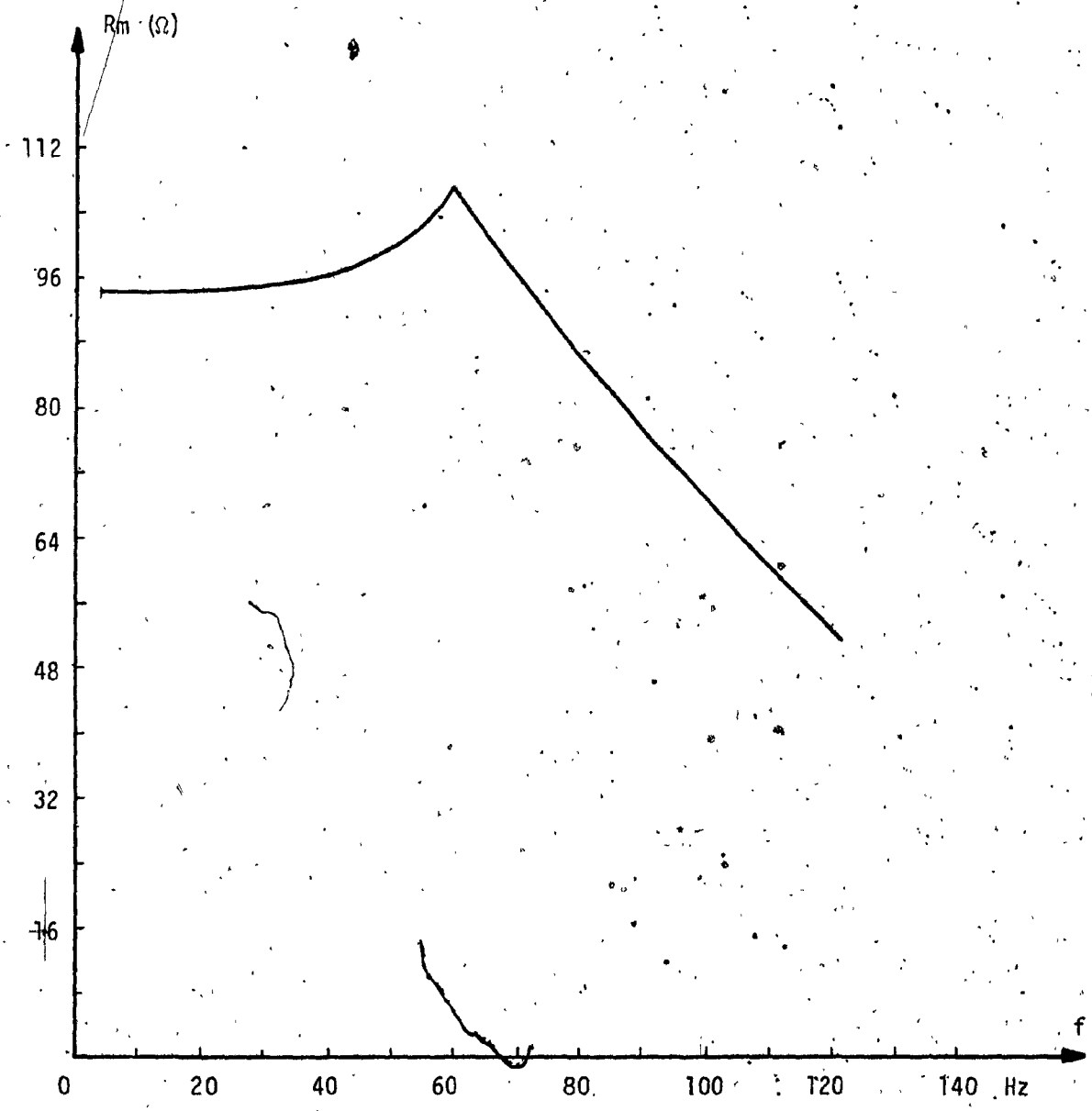

FIG. A-1.3 Approximate core-loss resistance of the 50 HP induction motor according to the manufacturer's data. The motor operates at a constant torque from 0 to 60 Hz and with a constant horsepower from 60 to 120 Hz. An ideal sine wave is assumed at all frequencies.

(D) SPECIFICATIONS OF OPERATING POINT (A)

f	= 55.40 Hz	V_{ph}	= 166.68 V (RMS)
I	= 51.42 A (RMS)	I_d	= 66.00 A (dc)
slip	= .01033	T	= 118.51 Nm
V_d	= 358.00 V (dc)	L_m	= 20.100 mH
L	= 1.100 mH	R_m	= 101.6 Ω

(E) SPECIFICATIONS OF OPERATING POINT (B)

f	= 45.15 Hz	V_{ph}	= 200.49 V (RMS)
I	= 60.01 A (RMS)	I_d	= 76.96 A (dc)
slip	= .00610	T	= 125.09 Nm
V_d	= 269.00 V (dc)	L_m	= 13.752 (mH)
L	= 1.047 mH	R_m	= 96.7 Ω

(F) BASE QUANTITIES

Base power = Motor rated output power = 37,300 W = P_b

Base voltage = Motor rated voltage/$\sqrt{3}$ = 265.58 V = V_b

Base current = $\frac{P_b}{V_b}$ = 46.82 A = I_b

Base impedance = $\frac{V_b}{I_b}$ = 5.6737 Ω = Z_b

Base torque = Motor rated torque = 197.88 Nm = T_b

APPENDIX A-2

THE INDUCTION MOTOR PERFORMANCE AT A CONSTANT OUTPUT TORQUE AND WITH VARIABLE FREQUENCIES

The notation used in Tables A-2.1 and A-2.2 are as follows:

F1	Frequency of the fundamental harmonic of MMF, (f_1)
F5	Frequency of the 5th harmonic of MMF, ($5f_1$)
F7	Frequency of the 7th harmonic of MMF, ($7f_1$)
PIKE1	Peak value of the fundamental harmonic of CEMF, (E_1)
PIKI1f	Motor peak fundamental component of the input current (I_{1S})
PHI1D	Phase angle between PIKE1 and PIKI1F, (ϕ_1), in deg.
PHITD	Phase angle between VPIK and PIKI1F in deg.
PFC=COS(PHITD)	Motor power factor
RMSI1F	Motor RMS fundamental component of the input current, ($I_{1S}/\sqrt{2}$)
SL1	Motor slip due to the fundamental harmonic of MMF, (S_1)
SL5	Motor slip due to the 5th harmonic of MMF, (S_5)
SL7	Motor slip due to the 7th harmonic of MMF, (S_7)
TOR.NM	Motor output torque, (T), in Nm
TMAXPU	Motor pull-over torque in PU
VPIK	Motor peak fundamental harmonic of terminal voltage, (V_{1S})
ZEQ1	Air-gap impedance due to the fundamental harmonic of MMF, (Zeq_1), according to Fig. 2.8
ZEQ5	Air-gap impedance due to the 5th harmonic of MMF, (Zeq_5), according to Fig. 2.8

ZEQ7	Air-gap impedance due to the 7th harmonic of MMF, (Zeq_7), according to Fig. 2.8
ZH1	Stator and rotor leakage reactances due to the fundamental harmonic of MMF, (X_1+X_2), according to Fig. 2.8
ZH5	Stator and rotor leakage reactances due to the 5th harmonic of MMF, $5(X_1+X_2)$, according to Fig. 2.8
ZH7	Stator and rotor leakage reactances due to the 7th harmonic of MMF, $7(X_1+X_2)$, according to Fig. 2.8

MOTOR PERFORMANCE AT TORQUE= .70 PU BASE KVA= 37.300 KW BASE VOLTAGE=

BASE CURRENT= 46.82 A BASE IMPEDANCE= 5.67 OHM BASE TORQUE= 197.88 N.M.

FI	SL1	RMSI1F	PIKI1F	PIKE1	PHITO	PFC	PH
5.00	.060030	57.09	80.73	28.93	47.82	.6714	5
10.00	.030230	57.05	80.67	57.65	51.05	.6287	5
15.00	.020240	57.03	80.66	86.29	52.14	.6137	5
20.00	.015240	57.06	80.70	114.92	52.65	.6066	5
25.00	.012190	57.03	80.65	143.54	53.02	.6015	5
30.00	.010170	57.04	80.66	172.16	53.23	.5986	5
35.00	.008730	57.06	80.70	200.77	53.36	.5968	5
40.00	.007640	57.06	80.70	229.38	53.48	.5951	5
45.00	.006800	57.09	80.73	257.99	53.54	.5943	5
50.00	.006120	57.09	80.74	286.60	53.61	.5933	5
55.00	.005570	57.12	80.78	315.21	53.63	.5929	5
60.00	.005100	57.10	80.75	343.83	53.71	.5919	5
65.00	.005540	56.49	79.89	343.36	49.74	.6463	4
70.00	.005990	56.62	80.07	342.84	46.07	.6937	4
75.00	.006440	57.29	81.03	342.24	42.82	.7335	[illegible]
80.00	.006890	58.40	82.59	341.57	39.98	.7662	[illegible]
85.00	.007360	59.95	84.79	340.79	37.51	.7932	[illegible]
90.00	.007830	61.77	87.35	339.90	35.45	.8146	[illegible]
95.00	.008320	63.90	90.37	338.88	33.73	.8317	[illegible]
100.00	.008820	66.24	93.67	337.71	32.35	.8448	[illegible]
105.00	.009330	68.74	97.21	336.38	31.29	.8545	[illegible]
110.00	.009850	71.43	101.02	334.86	30.51	.8615	[illegible]
115.00	.010420	74.33	105.12	333.10	29.98	.8662	[illegible]
120.00	.011020	77.48	109.57	331.05	29.70	.8687	[illegible]
125.00	.011620	80.59	113.97	328.78	29.64	.8691	[illegible]

TABLE A-2.1 The induction motor data for T=.7 PU torque and with F=5-125 Hz obtained from

37.300 KW BASE VOLTAGE= 265.58 V

BASE TORQUE= 197.88 N.M.

	PHITD	PFC	PHI1D	TOR.NM	VPIK	TMAXPU
	47.82	.6714	51.61	138.43	34.65	2.0543
	51.05	.6287	51.39	138.40	65.64	3.1548
	52.14	.6137	51.25	138.42	96.64	3.8510
	52.65	.6066	51.12	138.62	127.63	4.3059
	53.02	.6015	51.11	138.40	158.63	4.6203
	53.23	.5986	51.05	138.40	189.62	4.8486
	53.36	.5968	50.99	138.50	220.61	5.0213
	53.48	.5951	50.97	138.44	251.61	5.1551
	53.54	.5943	50.92	138.55	282.60	5.2642
	53.61	.5933	50.90	138.50	313.60	5.3527
	53.63	.5929	50.85	138.61	344.59	5.4265
	53.71	.5919	50.86	138.42	375.59	5.4890
	49.74	.6463	46.23	138.42	375.59	4.7297
	46.07	.6937	41.87	138.55	375.59	4.1175
	42.82	.7335	37.87	138.54	375.59	3.5168
	39.98	.7662	34.24	138.41	375.59	3.2022
	37.51	.7932	30.92	138.51	375.59	2.8549
	35.45	.8146	27.96	138.45	375.59	2.5611
	33.73	.8317	25.28	138.53	375.59	2.3104
	32.35	.8448	22.88	138.55	375.59	2.0948
	31.29	.8545	20.74	138.48	375.59	1.9080
	30.51	.8615	18.82	138.43	375.59	1.7452
	29.98	.8662	17.07	138.46	375.59	1.5023
	29.70	.8687	15.46	138.61	375.59	1.4752
	29.64	.8691	14.05	138.38	375.59	1.3645

nd with F=5-125 Hz obtained from Figure 2.9a

MOTOR PERFORMANCE AT TORQUE= .70 PU BASE KVA= 37.300 KW BASE VOLTAGE=

BASE CURRENT= 46.82 A BASE IMPEDANCE= 5.67 OHM BASE TORQUE= 197.88 N.M.

F1	ZH1	ZEQ1	F5	SL5	ZEQ5	ZH5
5.00000	.03720	.35835	25.00000	1.18799	.02977	.18598
10.00000	.07439	.71460	50.00000	1.19395	.03115	.37196
15.00000	.11159	1.06988	75.00000	1.19595	.03349	.55795
20.00000	.14879	1.42400	100.00000	1.19695	.03656	.74393
25.00000	.18598	1.77972	125.00000	1.19756	.04017	.92991
30.00000	.22318	2.13423	150.00000	1.19797	.04419	1.11589
35.00000	.26038	2.48794	175.00000	1.19825	.04851	1.30188
40.00000	.29757	2.84254	200.00000	1.19847	.05307	1.48786
45.00000	.33477	3.19550	225.00000	1.19864	.05781	1.67384
50.00000	.37196	3.54977	250.00000	1.19878	.06268	1.85982
55.00000	.40916	3.90212	275.00000	1.19889	.06766	2.04581
60.00000	.44636	4.25782	300.00000	1.19898	.07272	2.23179
65.00000	.48355	4.29796	325.00000	1.19889	.07785	2.41777
70.00000	.52075	4.28166	350.00000	1.19880	.08305	2.60375
75.00000	.55795	4.22383	375.00000	1.19871	.08828	2.78973
80.00000	.59514	4.13577	400.00000	1.19862	.09356	2.97572
85.00000	.63234	4.01940	425.00000	1.19853	.09887	3.16170
90.00000	.66954	3.89117	450.00000	1.19843	.10421	3.34768
95.00000	.70673	3.75005	475.00000	1.19834	.10957	3.53366
100.00000	.74393	3.60517	500.00000	1.19824	.11496	3.71965
105.00000	.78113	3.46025	525.00000	1.19813	.12036	3.90563
110.00000	.81832	3.31488	550.00000	1.19803	.12578	4.09161
115.00000	.85552	3.16867	575.00000	1.19792	.13122	4.27759
120.00000	.89271	3.02141	600.00000	1.19780	.13667	4.46357
125.00000	.92991	2.88472	625.00000	1.19768	.14213	4.64956

TABLE A-2.2 Comparison of different impedances in Fig. 2.8 for

1 of

37.300 KW BASE VOLTAGE= 265.58 V

BASE TORQUE= 197.88 N.M.

	ZEQ5	ZH5	F7	SL7	ZEQ7	ZH7
8799	.02977	.18598	35.00000	.86572	.04088	.26038
9395	.03115	.37196	70.00000	.86146	.04325	.52075
9595	.03349	.55795	105.00000	.86003	.04671	.78113
9695	.03656	.74393	140.00000	.85932	.05111	1.04150
9756	.04017	.92991	175.00000	.85888	.05625	1.30188
9797	.04419	1.11589	210.00000	.85860	.06196	1.56225
9825	.04851	1.30188	245.00000	.85839	.06808	1.82263
9847	.05307	1.48786	280.00000	.85823	.07452	2.08300
9864	.05781	1.67384	315.00000	.85811	.08121	2.34338
9878	.06268	1.85982	350.00000	.85802	.08808	2.60375
9889	.06766	2.04581	385.00000	.85794	.09511	2.86413
9898	.07272	2.23179	420.00000	.85787	.10225	3.12450
9889	.07785	2.41777	455.00000	.85793	.10949	3.38488
9880	.08305	2.60375	490.00000	.85800	.11681	3.64525
9871	.08828	2.78973	525.00000	.85806	.12420	3.90563
9862	.09356	2.97572	560.00000	.85813	.13164	4.15600
9853	.09887	3.16170	595.00000	.85819	.13914	4.42538
9843	.10421	3.34768	630.00000	.85826	.14667	4.68675
9834	.10957	3.53366	665.00000	.85833	.15424	4.94713
9824	.11496	3.71965	700.00000	.85840	.16184	5.20750
9813	.12036	3.90563	735.00000	.85848	.16947	5.46788
9803	.12578	4.09161	770.00000	.85855	.17713	5.72825
9792	.13122	4.27759	805.00000	.85863	.18481	5.98863
9780	.13667	4.46357	840.00000	.85872	.19252	6.24900
9768	.14213	4.64956	875.00000	.85880	.20024	6.50938

fferent impedances in Fig. 2.8 for the 1st, 5th and 7th harmonics.

APPENDIX A-3

CALCULATION OF THE MOTOR SLIP KNOWING FREQUENCY, VOLTAGE AND TORQUE

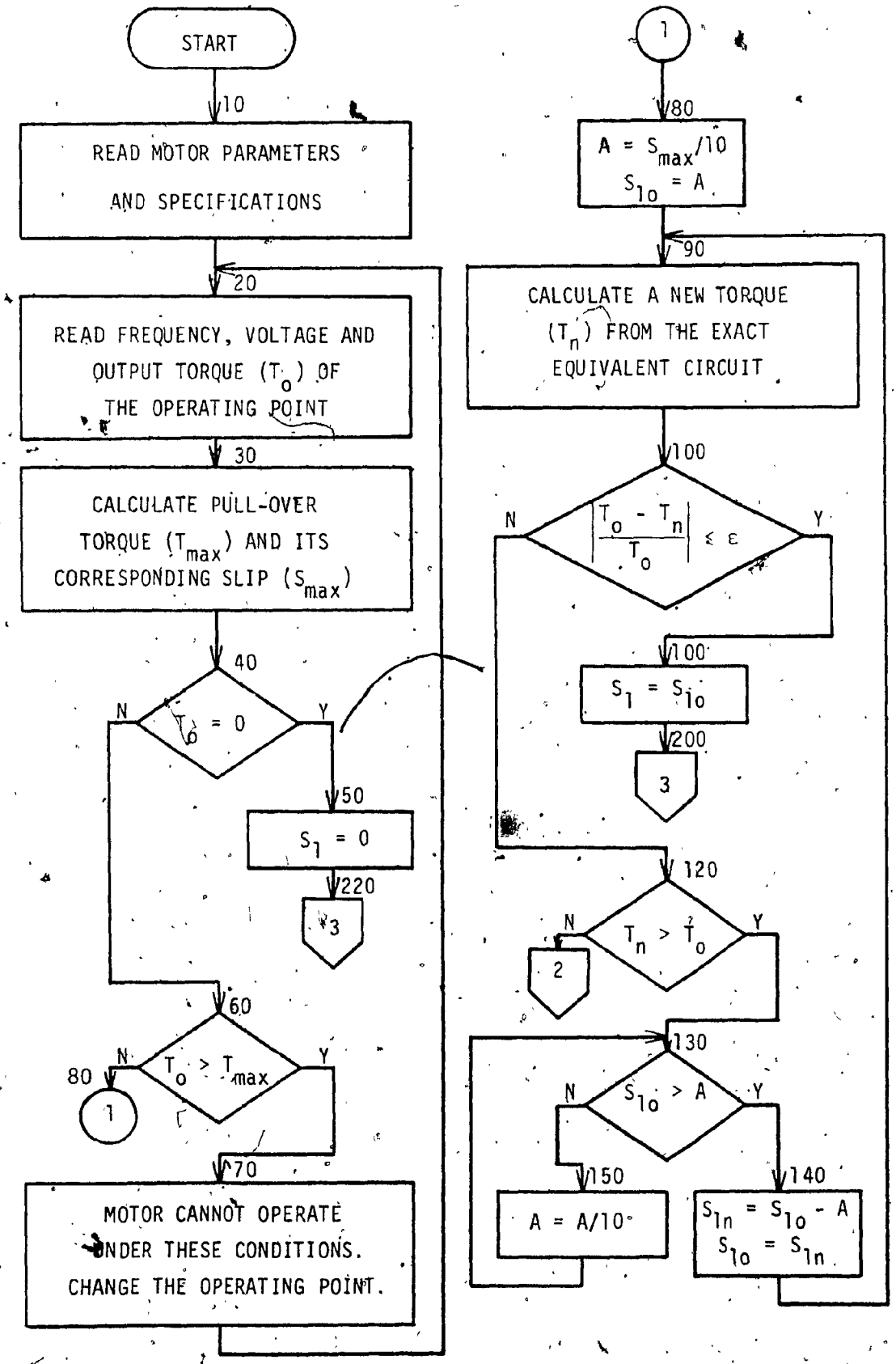

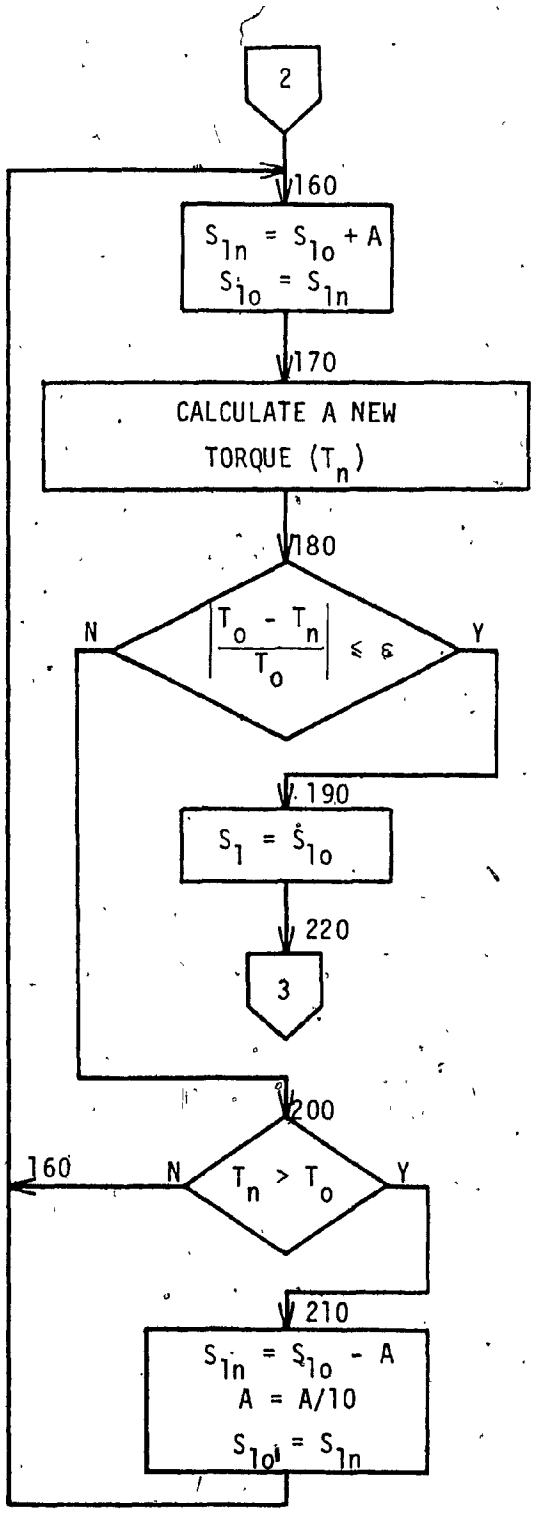

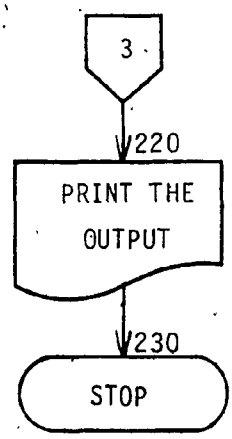

FLOWCHART A-3

This flowchart is employed in finding the slip of an operating point when its frequency, voltage and output torque are known. Subscript o shows the calculated value in a previous iteration while n implies the newly calculated variable. ε denotes the relative error.

APPENDIX B-1

The Fourier series of a trapezoidal waveform as shown below is equal to:

$$i_A = \frac{8I_d}{\omega t_1' \Pi} \sum_{n=1}^{\infty} \frac{1}{n^2} \cos \frac{n\Pi}{6} \sin \frac{n\omega t_1'}{2} \sin n\omega t$$

$$n = 1, 5, 7, 11, \ldots$$

The fundamental harmonic of i_A is:

$$i_{1A} = \frac{8I_d}{\omega t_1' \Pi} \cos \frac{\Pi}{6} \sin \frac{\omega t_1'}{2} \sin \omega t$$

or

$$i_{1A} = \frac{4I_d \sqrt{3}}{\omega t_1' \Pi} \sin \frac{\omega t_1'}{2} \sin \omega t$$

in which t_1' is a constant and equal to a transfer mode duration.

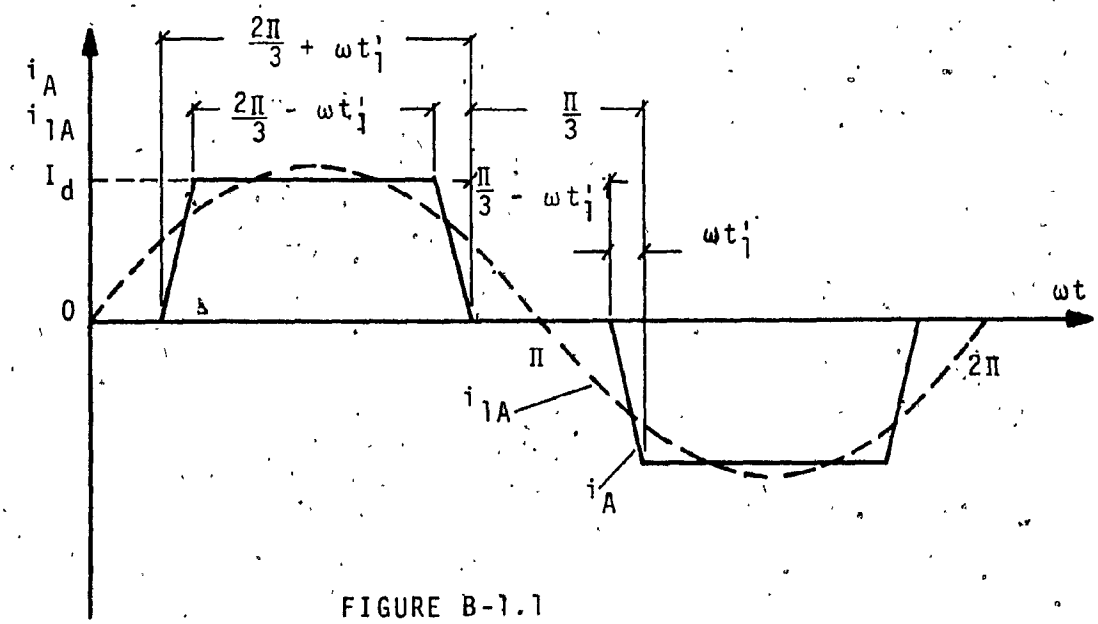

FIGURE B-1.1

APPENDIX B-2

CALCULATION OF THE FUNDAMENTAL COMPONENT OF THE MOTOR INPUT CURRENT WITH A CONSTANT DC LINK CURRENT AND NO CLAMPING CIRCUIT (Case (a), (b) or (c))

Figure B-2.1 shows the waveforms of the instantaneous and the fundamental component of the phase A current for a general operating point in case (a), (b) or (c). It is seen that i_A waveform is composed of eight parts which are shown by i_{A1}-i_{A8} in fig. B-2.1. It is also seen that except i_{A2}, i_{A4}, i_{A6} and i_{A8} the other parts have constant values in this figure. The expression of i_{A2} is the same as (3.4.29) which yields i_A during the transfer mode while t_2 is the origin of time,

$$i_{A2}(t') = i_A(t') \qquad (3.4.29)$$

The expressions giving the variations of i_{A4}, i_{A6} and i_{A8} can also be obtained easily if the origin of time is selected at t_8, t_{11} and t_{17} respectively,

$$i_{A4}(t') = i_C(t') \qquad 0 < t' < t_9 - t_3 \qquad (3.4.32)$$

$$i_{A6}(t') = -i_A(t') \qquad 0 < t' < t_{12} - t_{11} \qquad (3.4.29)$$

$$i_{A8}(t') = -i_C(t') \qquad 0 < t' < t_{18} - t_{17} \qquad (3.4.32)$$

Before going further, it is better to find shorter forms for $i_A(t')$ and $i_C(t')$ in the above expressions. Using (3.4.28) and expanding (3.4.29) one obtains

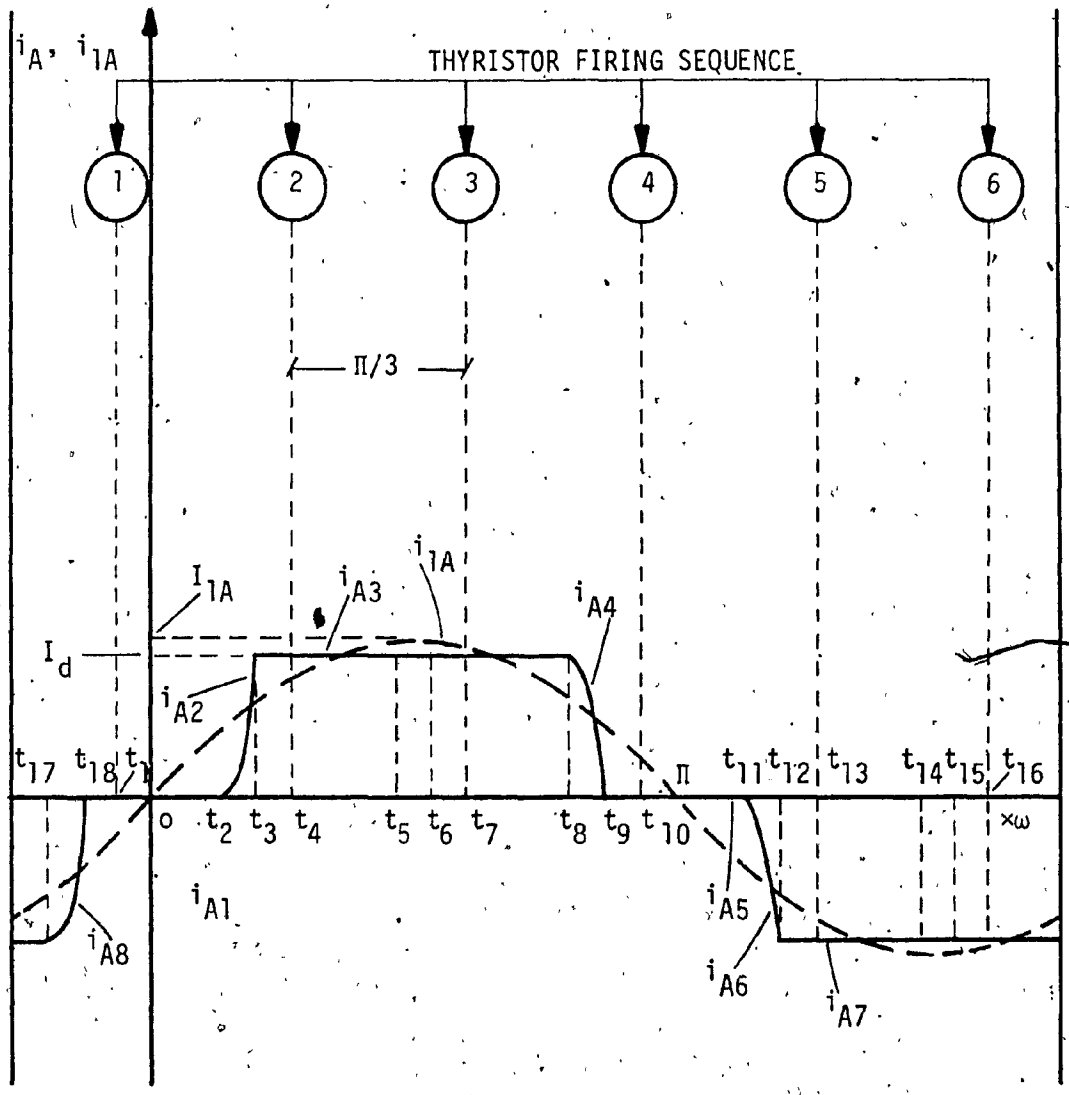

FIG. B-2.1 Motor phase A instantaneous and fundamental component of current for the drive with a constant dc link current and without a clamping circuit. i_{A1} - i_{A8} show the different parts of i_A during one cycle. For more details refer to FIG. 3.11

$$i_A(t) = \left(\frac{V_1}{2L\omega_1} + I_d \frac{\omega_o}{\omega_1} \cos\beta - \frac{V_1}{2L} A_2 \cos\gamma\right) e^{-\alpha t'} \sin\omega_1 t'$$

$$+ \left(I_d \frac{\omega_o}{\omega_1} \sin\beta - \frac{V_1}{2L} A_2 \sin\gamma\right) e^{-\alpha t'} \cos\omega_1 t'$$

$$- \frac{V_1}{2L} B_2 \sin(\omega t' + \delta) + I_d \qquad \text{(B-2.1)}$$

The new constants are

$$C_{10} = \frac{V_1}{2L\omega_1} + I_d \frac{\omega_o}{\omega_1} \cos\beta - \frac{V_1}{2L} A_2 \cos\gamma$$

$$C_{11} = I_d \frac{\omega_o}{\omega_1} \sin\beta - \frac{V_1}{2L} A_2 \sin\gamma$$

$$C_{12} = - \frac{V_1}{2L} B_2 \qquad \text{(B-2.2)}$$

Inserting (B-2.2) into (B-2.1) provides

$$i_A(t') = C_{10} e^{-\alpha t'} \sin\omega_1 t' + C_{11} e^{-\alpha t'} \cos\omega_1 t'$$

$$+ C_{12} \sin(\omega t' + \delta) + I_d \qquad \text{(B-2.3)}$$

or $\quad i_A(t') = C_{13} e^{-\alpha t'} \sin(\omega_1 t' + \gamma_{10}) + C_{12} \sin(\omega t' + \delta) + I_d$

where $\quad C_{13} = (C_{10}^2 + C_{11}^2)^{\frac{1}{2}}$

$$\gamma_{10} = \text{arc tan} \frac{C_{11}}{C_{10}} \qquad \text{(B-2.4)}$$

Also for $i_C(t')$ we can write

$$i_C(t') = I_d - i_A(t')$$

or $$i_C(t') = -C_{13}e^{-\alpha t'}\sin(\omega_1 t'+\gamma_{10})-C_{12}\sin(\omega t'+\delta) \qquad \text{(B-2.5)}$$

To calculate the Fourier coefficients, t' should be changed into t in (B-2.4) and (B-2.5). From section (3.4) we know that

$$t'' = t-t_2 \qquad (3.4.15)$$

Putting (3.4.15) back into (B-2.4) yields

$$i_{A2}(t) = C_{13}e^{-\alpha t}e^{\alpha t_2}\sin(\omega_1 t-\omega_1 t_2+\gamma_{10})$$
$$+ C_{12}\sin(\omega t-\omega t_2+\delta)+I_d$$

or $$i_{A2}(t) = C_{13a}e^{-\alpha t}\sin(\omega_1 t+\gamma_{11})+C_{12}\sin(\omega t+\delta_1)+I_d \qquad \text{(B-2.6)}$$

where $C_{13a} = C_{13}e^{\alpha t_2}$

$$\gamma_{11} = \gamma_{10}-\omega_1 t_2$$

$$\delta_1 = \delta-\omega t_2 \qquad \text{(B-2.7)}$$

Also, i_{A4} starts at $t=t_8$ so that we can write

$$t' = t-t_8 \qquad \text{(B-2.8)}$$

Replacing t' in (B-2.5) by (B-2.8) gives

$$i_{A4}(t) = -C_{13}e^{-\alpha t}e^{\alpha t_8}\sin(\omega_1 t-\omega_1 t_8+\gamma_{10})$$
$$-C_{12}\sin(\omega t-\omega t_8+\delta)$$

or $$i_{A4}(t) = C_{13b}e^{-\alpha t}\sin(\omega_1 t+\gamma_{12})-C_{12}\sin(\omega t+\delta_2) \qquad \text{(B-2.9)}$$

where $C_{13b} = -C_{13}e^{\alpha t_8}$

$$\gamma_{12} = \gamma_{10} - \omega_1 t_8$$

$$\delta_2 = \delta - \omega t_8 \qquad \text{(B-2.10)}$$

For calculating the Fourier coefficients there is no need to obtain $i_{A6}(t)$ and $i_{A8}(t)$ since from fig. B-2.1 we can write

$$i_A(t) = -i_A(t+T/2) \qquad \text{(B-2.11)}$$

Then the Fourier coefficients for the fundamental component are

$$a_1 = \frac{2}{\pi}\int_0^{\pi} i_A(x)\cos x\, dx$$

$$b_1 = \frac{2}{\pi}\int_0^{\pi} i_A(x)\sin x\, dx$$

where $x = \omega t$ or $t = \frac{x}{\omega}$ (B-2.12)

and the fundamental component of i_A is

$$i_{1A}(t) = a_1 \cos x + b_1 \sin x = I_{1A}\sin(x+\gamma_{13})$$

where $I_{1A} = (a_1^2+b_1^2)^{\frac{1}{2}}$

$$\gamma_{13} = \arctan\frac{a_1}{b_1} \qquad \text{(B-2.13)}$$

here I_{1A} is the amplitude of the fundamental component of i_A and γ_{13} is its corresponding phase angle. Note that due to the way the origin of time has been chosen (assumption 14 in section 2.6), in ideal case the value of γ_{13} should be zero.

The different parts of i_A during half a cycle which are needed for calculating a_1 and b_1 in (B-2.12) are then expressed by the following relationships

$$
\begin{aligned}
i_{A1}(t) &= 0 && 0 < t < t_2 \\
i_{A2}(t) &= \text{Eq. (B-2.6)} && t_2 < t < t_3 \\
i_{A3}(t) &= I_d && t_3 < t < t_8 \\
i_{A4}(t) &= \text{Eq. (B-2.9)} && t_8 < t < t_9 \\
i_{A5}(t) &= 0 && t_9 < t < \frac{\pi}{\omega}
\end{aligned}
\qquad \text{(B-2.14)}
$$

The Fourier coefficients in (B-2.12) can now be written as

$$
\begin{aligned}
a_1 &= a_{11} + a_{12} + a_{13} + a_{14} + a_{15} \\
b_1 &= b_{11} + b_{12} + b_{13} + b_{14} + b_{15}
\end{aligned}
\qquad \text{(B-2.15)}
$$

Each term in (B-2.15) can be calculated by the following expressions in which

$$
\begin{aligned}
x_2 &= \omega t_2 \\
x_3 &= \omega t_3 = \omega(t_2 + t_1') \\
x_8 &= \omega t_8 = \omega(t_2 + \frac{2\pi}{3\omega}) \\
x_9 &= \omega t_9 = \omega(t_8 + t_1')
\end{aligned}
\qquad \text{(B-2.16)}
$$

where t_1' is the duration of the transfer mode and is obtained from (3.4.35).

$$a_{11} = \frac{2}{\pi}\int_{0}^{x_2} i_{A1}(x)\cos x\, dx = 0 \qquad \text{(B-2.17)}$$

$$a_{12} = \frac{2}{\pi}\int_{x_2}^{x_3} i_{A2}(x)\cos x\, dx$$

or

$$a_{12} = \frac{2}{\pi}\left(C_{13a}y_{21} + C_{12}y_{22} + I_d y_{23}\right) \qquad \text{(B-2.18)}$$

where

$$y_{21} = \int_{x_2}^{x_3} e^{-\frac{\alpha^*}{\omega}x}\sin\left(\frac{\omega_1}{\omega}x + \gamma_{11}\right)\cos x\, dx$$

$$y_{22} = \int_{x_2}^{x_3} \sin(x+\delta_1)\cos x\, dx$$

$$y_{23} = \int_{x_2}^{x_3} \cos x\, dx \qquad \text{(B-2.19)}$$

$$a_{13} = \frac{2}{\pi} I_d \int_{x_3}^{x_8} \cos x\, dx = \frac{2}{\pi} I_d y_{31} \qquad \text{(B-2.20)}$$

where

$$y_{31} = \int_{x_3}^{x_8} \cos x\, dx \qquad \text{(B-2.21)}$$

$$a_{14} = \frac{2}{\pi}\int_{x_8}^{x_9} i_{A4}(x)\cos x\, dx$$

or

$$a_{14} = \frac{2}{\pi}\left(C_{13b}y_{41} - C_{12}y_{42}\right) \tag{B-2.22}$$

in which

$$y_{41} = \int_{x_8}^{x_9} e^{-\frac{\alpha}{\omega}x} \sin\left(\frac{\omega_1}{\omega}x + \gamma_{12}\right) \cos x \, dx$$

$$y_{42} = \int_{x_8}^{x_9} \sin(x + \delta_2) \cos x \, dx \tag{B-2.23}$$

$$a_{15} = \frac{2}{\pi}\int_{x_9}^{\pi} i_{A5}(x) \cos x \, dx = 0 \tag{B-2.24}$$

$$b_{11} = \frac{2}{\pi}\int_{0}^{x_2} i_{A1}(x) \sin x \, dx = 0 \tag{B-2.25}$$

$$b_{12} = \frac{2}{\pi}\int_{x_2}^{x_3} i_{A2}(x) \sin x \, dx$$

or

$$b_{12} = \frac{2}{\pi}\left(C_{13a}u_{21} + C_{12}u_{22} + I_d u_{23}\right) \tag{B-2.26}$$

where

$$u_{21} = \int_{x_2}^{x_3} e^{-\frac{\alpha}{\omega}x} \sin\left(\frac{\omega_1}{\omega}x + \gamma_{11}\right) \sin x \, dx$$

$$u_{22} = \int_{x_2}^{x_3} \sin(x + \delta_1) \sin x \, dx$$

$$u_{23} = \int_{x_2}^{x_3} \sin x \, dx \tag{B-2.27}$$

$$b_{13} = \frac{2}{\pi}\int_{x_3}^{x_8} i_{A3}(x)\ \sin x\ dx = \frac{2}{\pi} I_d u_{31} \qquad \text{(B-2.28)}$$

in which

$$u_{31} = \int_{x_3}^{x_8} \sin x\ dx \qquad \text{(B-2.29)}$$

$$b_{14} = \frac{2}{\pi}\int_{x_8}^{x_9} i_{A4}(x)\ \sin x\ dx$$

or

$$b_{14} = \frac{2}{\pi}\left(C_{13b}u_{41} - C_{12}u_{42}\right) \qquad \text{(B-2.30)}$$

where $$u_{41} = \int_{x_8}^{x_9} e^{-\frac{\alpha}{\omega}x} \sin\left(\frac{\omega_1}{\omega}x + \gamma_{12}\right) \sin x\ dx$$

$$u_{42} = \int_{x_8}^{x_9} \sin(x+\delta_2)\ \sin x\ dx \qquad \text{(B-2.31)}$$

and

$$b_{15} = \frac{2}{\pi}\int_{x_9}^{\pi} i_{A5}(x)\ \sin x\ dx = 0 \qquad \text{(B-2.32)}$$

The general forms of the integrals in the above expressions are as follows:

$$G_1 = \int_{x_i}^{x_j} e^{ax}\ \sin(bx+c)\ \cos x\ dx$$

$$= \frac{1}{2}\int_{x_i}^{x_j} e^{ax}\ \sin[(b+1)x+c]dx + \frac{1}{2}\int_{x_i}^{x_j} e^{ax}\sin[(b-1)x+c]dx$$

$$G_1 = \frac{1}{2[a^2+(b+1)^2]}\{e^{ax}[a\sin((b+1)x+c)-(b+1)\cos((b+1)x+c)]\}_{x_i}^{x_j}$$

$$+ \frac{1}{2[a^2+(b-1)^2]}\{e^{ax}[a\sin((b-1)x+c)-(b-1)\cos((b-1)x+c)]\}_{x_i}^{x_j}$$

Defining two new constants

$$h_1 = b+1$$

$$h_2 = b-1$$

At last we can write

$$G_1 = \frac{1}{2(a^2+h_1^2)}\{e^{ax_j}[a\sin(h_1x_j+c)-h_1\cos(h_1x_j+c)]$$

$$- e^{ax_i}[a\sin(h_1x_i+c)-h_1\cos(h_1x_i+c)]\}$$

$$+ \frac{1}{2(a^2+h_2^2)}\{e^{ax_j}[a\sin(h_2x_j+c)-h_2\cos(h_2x_j+c)]$$

$$- e^{ax_i}[a\sin(h_2x_i+c)-h_2\cos(h_2x_i+c)]\} \qquad \text{(B-2.33)}$$

$$G_2 = \int_{x_i}^{x_j}\sin(x+c)\cos x\,dx = \frac{1}{2}\int_{x_i}^{x_j}\sin(2x+c)\,dx + \frac{1}{2}\int_{x_i}^{x_j}\text{sinc}\,dx$$

or

$$G_2 = \frac{1}{4}[\cos(2x_i+c)-\cos(2x_j+c)]+(x_j-x_i)\,\frac{\text{sinc}}{2} \qquad \text{(B-2.34)}$$

$$G_3 = \int_{x_i}^{x_j}\cos x\,dx = \sin x_j - \sin x_i \qquad \text{(B-2.35)}$$

$$G_4 = \int_{x_i}^{x_j} e^{ax} \sin(bx+c) \quad \sin x \, dx$$

$$= \frac{1}{2}\int_{x_i}^{x_j} e^{ax} \cos[(b-1)x+c]dx - \frac{1}{2}\int_{x_i}^{x_j} e^{ax} \cos[(b+1)x+c]\,dx$$

As before

$$h_1 = b+1$$

$$h_2 = b-1$$

which yields

$$G_4 = \frac{1}{2(a^2+h_2^2)} \{e^{ax_j}[a\cos(h_2x_j+c)+h_2\sin(h_2x_j+c)]$$

$$- e^{ax_i}[a\cos(h_2x_i+c)+h_2 \sin(h_2 x_i+c)]\}$$

$$- \frac{1}{2(a^2+h_1^2)} \{e^{ax_j}[a\cos(h_1 x_j+c)+h_1 \sin(h_1 x_j+c)]$$

$$- e^{ax_i}[a\cos(h_1 x_i+c)+h_1 \sin(h_1 x_i+c)]\} \qquad \text{(B-2.36)}$$

$$G_5 = \int_{x_i}^{x_j} \sin(x+c)\sin x \, dx$$

or

$$G_5 = (x_j-x_i) \frac{\cos c}{2} - \frac{1}{4} [\sin(2x_j+c)-\sin(2x_i+c)] \qquad \text{(B-2.37)}$$

$$G_6 = \int_{x_i}^{x_j} \sin x \, dx = \cos x_i - \cos x_j \qquad \text{(B-2.38)}$$

APPENDIX B-3

CALCULATION OF THE FUNDAMENTAL COMPONENT OF THE MOTOR INPUT CURRENT WITH A CONSTANT DC LINK CURRENT AND A CLAMPING CIRCUIT (Case (d), (e) or (f)).

Figure B-3.1 shows the waveforms of the instantaneous and the fundamental component of the phase A current when a zener diode clamping circuit which limits the voltage spikes in an ASCI-induction motor drive is under conduction. The procedure for finding the fundamental harmonic of i_A is the same as in Appendix B-2. In this case a complete cycle of i_A consists of twelve parts, fig. B-3.1. The constant parts of i_A in fig. B-3.1 are i_{A1}, i_{A4}, i_{A7} and i_{A10}. Thus the Fourier coefficients for the fundamental component of i_A, i.e., i_{1A}, should be obtained considering the other parts of i_A in fig. B-3.1. Again, the calculations are done for half a cycle of i_A (Eq. (B-2.11)).

The expressions giving $i_{A2}(t)$ and $i_{A5}(t)$ are the same as (B-2.6) and (B-2.9) in Appendix B-2. The expressions of $i_{A3}(t)$ and $i_{A6}(t)$ are obtained from (6.4.16) and (6.4.17), respectively, when t'' is replaced by t in the following way.

From fig. B-3.1 it is seen that i_{A3} changes from $t=t_{21}$ to $t=t_3$ so that t'' in (6.4.16) is equal to:

$$t'' = t - t_{21} \qquad \text{(B-3.1)}$$

By putting t'' according to (B-3.1) into (6.4.16) and doing some

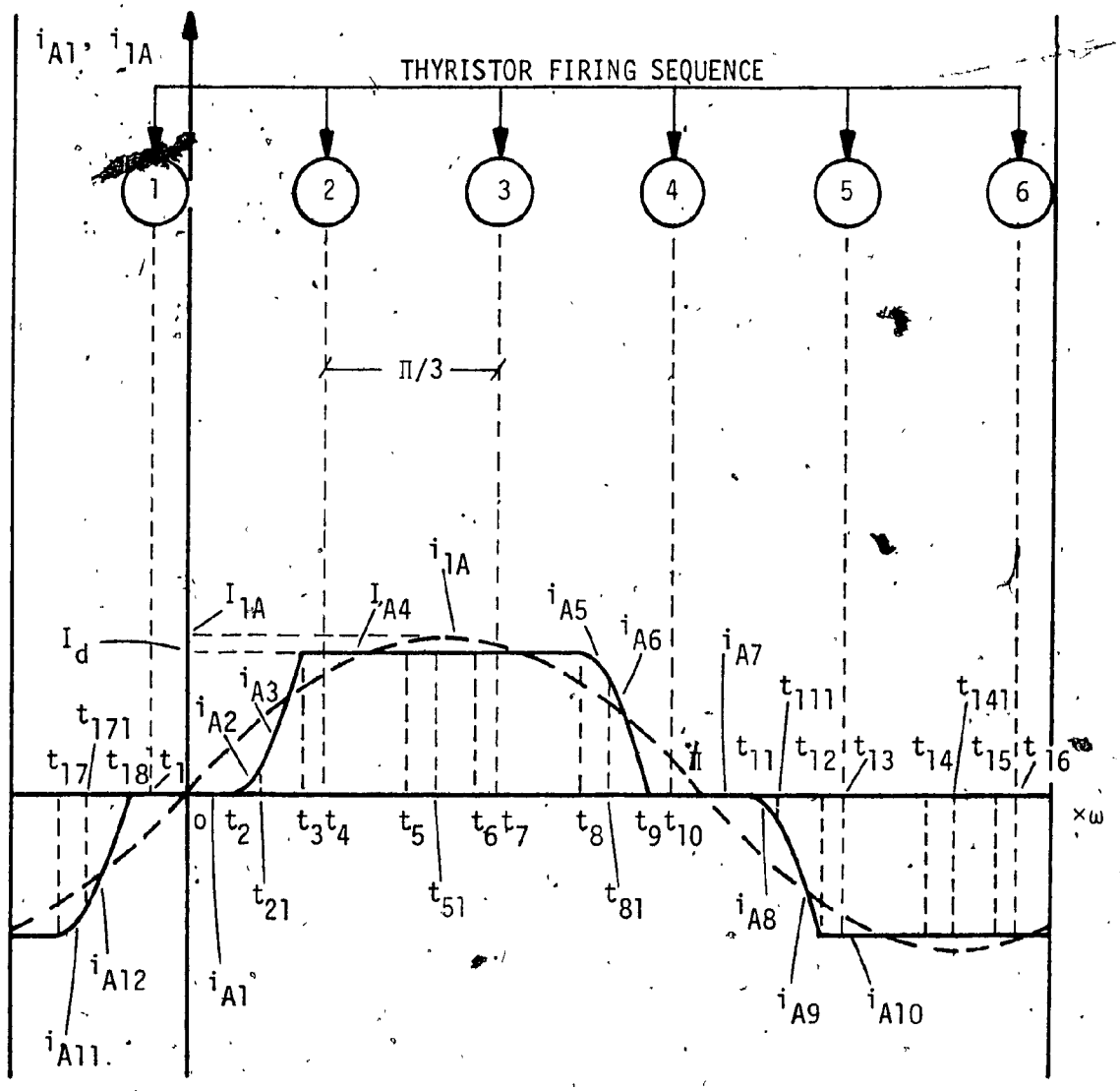

FIG. B-3.1 Motor phase A instantaneous and fundamental component of current for the drive with a constant dc link current and with a zener clamping circuit. i_{A1} - i_{A12} show the different parts of i_A during one cycle. For more details refer to FIG. 6.7.

simplifications one obtains

$$i_{A3}(t) = C_{20}+C_{25}e^{-\alpha_1 t}+C_{26}\sin(\omega t+\beta_5)-C_{27}\sin(\omega t+\beta_6) \quad \text{(B-3.2)}$$

in which $C_{25} = C_{21}e^{\alpha_1 t_{21}}$

$$C_{26} = C_{22}\, C_{23}$$

$$C_{27} = C_{22}\, C_{24}$$

$$\beta_5 = \beta_4-\omega t_{21}$$

$$\beta_6 = \beta_3-\omega t_{21} \quad \text{(B-3.3)}$$

In the same way for i_{A6} we have,

$$t'' = t-t_{81} \quad \text{(B-3.4)}$$

which by inserting it into (6.4.17) and doing some simplifications we obtain

$$i_{A6}(t) = C_{28}-C_{29}e^{-\alpha_1 t}-C_{26}\sin(\omega t+\beta_7)+C_{27}\sin(\omega t+\beta_8) \quad \text{(B-3.5)}$$

where $C_{28} = I_d-C_{20}$

$$C_{29} = C_{21}e^{\alpha_1 t_{81}}$$

$$\beta_7 = \beta_4-\omega t_{81}$$

$$\beta_8 = \beta_3-\omega t_{81} \quad \text{(B-3.6)}$$

Now we can calculate the Fourier coefficients for the fundamental component of i_A ,

$$a_1 = \frac{2}{\pi}\int_0^{\pi} i_A(x)\cos x\, dx$$

$$b_1 = \frac{2}{\pi}\int_0^{\pi} i_A(x)\sin x\, dx$$

where $x = \omega t$ or $t = \frac{x}{\omega}$ (B-3.7)

Also the fundamental component of i_A results to be

$$i_{1A}(x) = a_1 \cos x + b_1 \sin x = I_{1A}\sin(x+\phi)$$

where $I_{1A} = (a_1^2+b_1^2)^{\frac{1}{2}}$

$$\phi = \arctan\frac{a_1}{b_1} \qquad \text{(B-3.8)}$$

As explained in Appendix B-2, in ideal case the value of ϕ should be zero.

We can now arrange the different parts of i_A which are needed for calculating a_1 and b_1 in (B-3.7) in the following way

$i_{A1}(t) = 0$	$0 < t < t_2$
$i_{A2}(t) =$ Eq. (B-2.6)	$t_2 < t < t_{21}$
$i_{A3}(t) =$ Eq. (B-3.2)	$t_{21} < t < t_3$
$i_{A4}(t) = I_d$	$t_3 < t < t_8$
$i_{A5}(t) =$ Eq. (B-2.9)	$t_8 < t < t_{81}$
$i_{A6}(t) =$ Eq. (B-3.5)	$t_{81} < t < t_9$
$i_{A7}(t) = 0$	$t_9 < t < \frac{\pi}{\omega}$ (B-3.9)

$$a_1 = a_{11}+a_{12}+a_{13}+a_{14}+a_{15}+a_{16}+a_{17}$$

$$b_1 = b_{11}+b_{12}+b_{13}+b_{14}+b_{15}+b_{16}+b_{17} \qquad \text{(B-3.10)}$$

Each term in (B-3.10) can be obtained by the following expressions in which

$$x_2 = \omega t_2$$

$$x_{21} = \omega t_{21} = \omega(t_2+t_1')$$

$$x_3 = \omega t_3 = \omega(t_{21}+t_1'')$$

$$x_8 = \omega t_8 = \omega(t_2+\frac{2\pi}{3\omega})$$

$$x_{81} = \omega t_{81} = \omega(t_8+t_1')$$

$$x_9 = \omega t_9 = \omega(t_{81}+t_1'') \qquad \text{(B-3.11)}$$

where t_1' and t_1'' are the durations of the first and second part of the transfer mode and are obtained from (6.3.3) and (6.4.19), respectively.

$$a_{11} = \frac{2}{\pi}\int_0^{x_2} i_{A1}(x)\cos x\,dx = 0 \qquad \text{(B-3.12)}$$

$$a_{12} = \frac{2}{\pi}\int_{x_2}^{x_{21}} i_{A2}(x)\cos x\,dx = \text{Eq. (B-2.18)} \qquad \text{(B-3.13)}$$

but with x_3 replaced by x_{21}.

$$a_{13} = \frac{2}{\pi}\int_{x_{21}}^{x_3} i_{A3}(x)\cos x\,dx$$

or $$a_{13} = \frac{2}{\pi}(C_{20}y_{31}+C_{25}y_{32}+C_{26}y_{33}-C_{27}y_{34}) \qquad \text{(B-3.14)}$$

where $$y_{31} = \int_{x_{21}}^{x_3} \cos x \, dx$$

$$y_{32} = \int_{x_{21}}^{x_3} e^{-\frac{\alpha_1}{\omega}x} \cos x \, dx$$

$$y_{33} = \int_{x_{21}}^{x_3} \sin(x+\beta_5)\cos x \, dx$$

$$y_{34} = \int_{x_{21}}^{x_3} \sin(x+\beta_6)\cos x \, dx \qquad \text{(B-3.15)}$$

a_{14} = Eq. (B-2.20)

a_{15} = Eq. (B-2.22) but with x_9 replaced by x_{81}.

$$a_{16} = \frac{2}{\pi}\int_{x_{81}}^{x_9} i_{A6}(x)\cos x \, dx$$

or $$a_{16} = \frac{2}{\pi}(C_{28}y_{61}-C_{29}y_{62}-C_{26}y_{63}+C_{27}y_{64}) \qquad \text{(B-3.16)}$$

where $$y_{61} = \int_{x_{81}}^{x_9} \cos x \, dx$$

$$y_{62} = \int_{x_{81}}^{x_9} e^{-\frac{\alpha_1}{\omega}x} \cos x \, dx$$

$$y_{63} = \int_{x_{81}}^{x_9} \sin(x+\beta_7)\cos x \, dx$$

$$y_{64} = \int_{x_{81}}^{x_9} \sin(x+\beta_8)\cos x \, dx \qquad \text{(B-3.17)}$$

$$a_{17} = \frac{2}{\pi}\int_{x_9}^{\frac{\pi}{\omega}} i_{A7}(x)\cos x \, dx = 0$$

$$b_{11} = \frac{2}{\pi}\int_{0}^{x_2} i_{A1}(x)\sin x \, dx = 0 \qquad \text{(B-3.18)}$$

$$b_{12} = \frac{2}{\pi}\int_{x_2}^{x_{21}} i_{A2}(x)\sin x \, dx = \text{Eq. (B-2.26)}$$

but with x_3 replaced by x_{21}.

$$b_{13} = \frac{2}{\pi}\int_{x_{21}}^{x_3} i_{A3}(x)\sin x \, dx$$

or $$b_{13} = \frac{2}{\pi}\left(C_{20}u_{31}+C_{25}u_{32}+C_{26}u_{33}-C_{27}u_{34}\right) \qquad \text{(B-3.19)}$$

where $$u_{31} = \int_{x_{21}}^{x_3} \sin x \, dx$$

$$u_{32} = \int_{x_{21}}^{x_3} e^{-\frac{\alpha_1}{\omega}x} \sin x \, dx$$

$$u_{33} = \int_{x_{21}}^{x_3} \sin(x+\beta_5)\sin x \, dx$$

$$u_{34} = \int_{x_{21}}^{x_3} \sin(x+\beta_6)\sin x \, dx \qquad \text{(B-3.20)}$$

b_{14} = Eq. (B-2.28)

b_{15} = Eq. (B-2.30) but with x_9 replaced by x_{81}.

$$b_{16} = \frac{2}{\pi}\left(C_{28}u_{61} - C_{29}u_{62} - C_{26}u_{63} + C_{27}u_{64}\right) \qquad \text{(B-3.21)}$$

where $$u_{61} = \int_{x_{81}}^{x_9} \sin x \, dx$$

$$u_{62} = \int_{x_{81}}^{x_9} e^{-\frac{\alpha_1}{\omega}x} \sin x \, dx$$

$$u_{63} = \int_{x_{81}}^{x_9} \sin(x+\beta_7)\sin x \, dx$$

$$u_{64} = \int_{x_{81}}^{x_9} \sin(x+\beta_8)\sin x \, dx \qquad \text{(B-3.22)}$$

The general forms of all the integrals except two of them are given by (B-2.33-38) in Appendix B-2. The remaining two integrals have the following forms

$$G_7 = \int_{x_i}^{x_j} e^{ax} \cos x \, dx$$

or

$$G_7 = \frac{1}{a^2+1} \left[e^{ax_j}(a \cos x_j + \sin x_j) - e^{ax_i}(a \cos x_i + \sin x_i) \right] \tag{B-3.23}$$

$$G_8 = \int_{x_i}^{x_j} e^{ax} \sin x \, dx$$

or

$$G_8 = \frac{1}{a^2+1} \left[e^{ax_j}(a \sin x_j - \cos x_j) - e^{ax_i}(a \sin x_i - \cos x_i) \right] \tag{B-3.24}$$

APPENDIX C-1

CALCULATION OF THE FUNDAMENTAL COMPONENT OF THE MOTOR INPUT CURRENT FOR THE CONSTANT VOLTAGE MODEL AND WITH NO CLAMPING CIRCUIT (Case (g))

Figure C-1.1 shows the waveforms of the instantaneous and the fundamental component of the phase A current during half a cycle in Case (g). As mentioned in Appendix B-2 (Eq. (B-2.11)), the Fourier coefficients for the fundamental harmonic of i_A are calculated only for half a cycle. In this case, from figure C-1.1 it is seen that i_A consists of nine parts during each half a cycle. These parts are shown by i_{A1} - i_{A9}. Only i_{A1} and i_{A9} have constant values which are equal to zero. The equation numbers and the time bases for the other parts of i_A have been specified in the same figure.

To obtain the Fourier coefficients, the time scale in each of the equations giving i_{A2} - i_{A8} in figure C-1.1 should be changed to t. In the following, the equation number, the relationship between the old and the new time scale and the new form of each part of i_A in terms of t are specified.

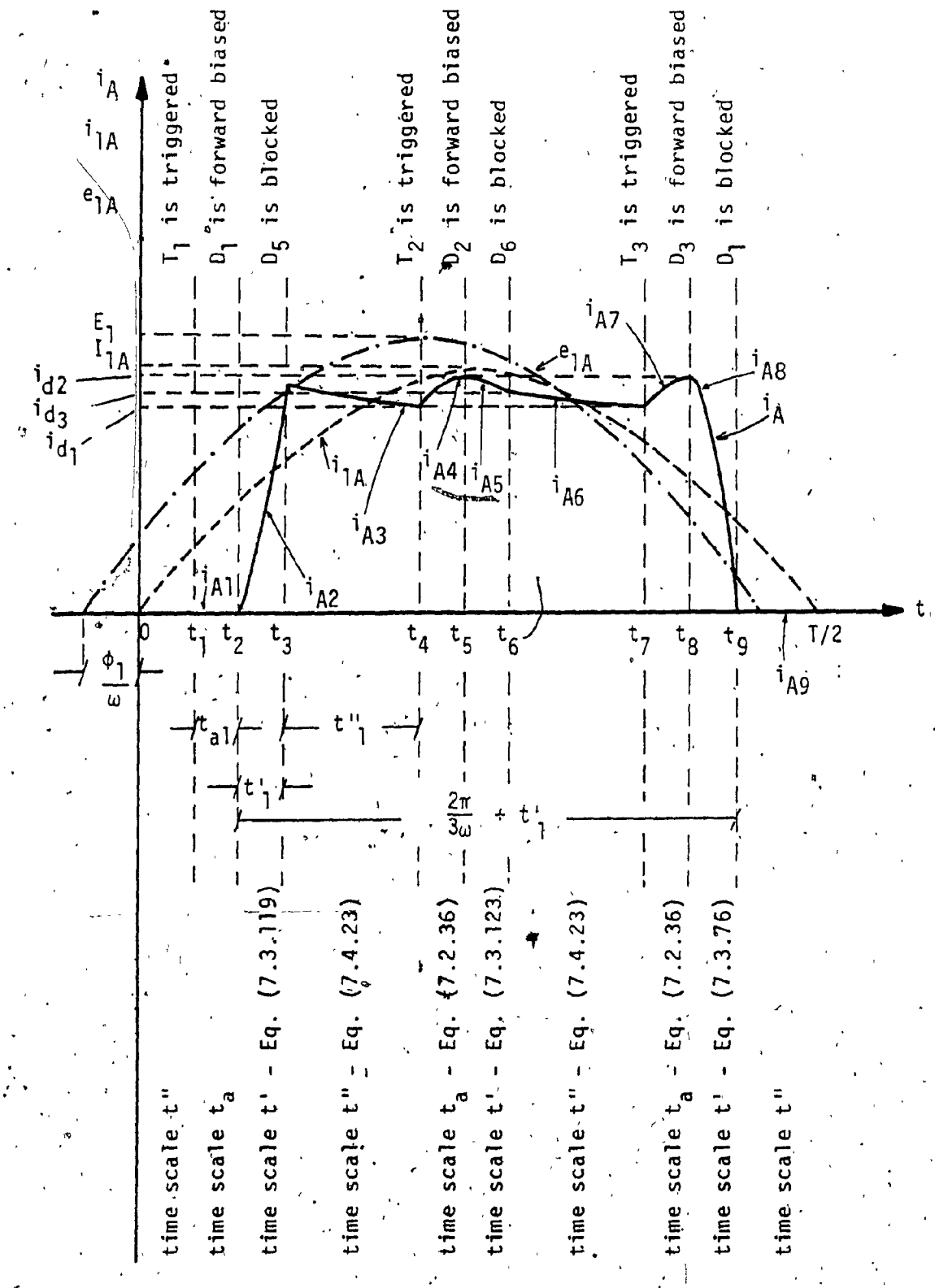

FIG. C-1.1 Motor phase A CEMF, instantaneous and fundamental component of current for the drive with a constant dc link input voltage and without a clamping circuit. i_{A1}-i_{A9} show the different parts of i_A during half a cycle.

1) $i_{A2}(t') = \text{Eq. } (7.3.119)$

$$t' = t - t_2 \text{ with } t_2 < t < t_3 \qquad \text{(C-1.1)}$$

$$i_{A2}(t) = DC_{10}\, e^{-\alpha t} + DC_{11} + DC_{12}\, e^{mt} \sin(nt + \beta_{10}) + DC_{13}\, e^{D_{12}t} + DA_{11} \sin(\omega t + \beta_{11}) \qquad \text{(C-1.2)}$$

where

$$DC_{10} = (D_{93} - \frac{V_d}{R_{eq}})\, e^{\alpha t_2} \; ; \; DC_{11} = \frac{V_d}{R_{eq}}$$

$$DC_{12} = D_{94}\, e^{-mt_2} \; ; \; \beta_{10} = -nt_2 + \delta_{83}$$

$$DC_{13} = D_{98}\, e^{-D_{12}t_2} \; ; \; B_{11} = -\omega t_2 + \lambda_3 \qquad \text{(C-1.3)}$$

2) $i_{A_3}(t'') = \text{Eq.}(7.4.23)$

$$t'' = t - t_3 \text{ with } t_3 < t < t_4 \qquad \text{(C-1.4)}$$

$$i_{A_3}(t) = DC_{14}\, e^{-\alpha t} + DC_{11} + D_{115} \sin(\omega t + \beta_{12}) \qquad \text{(C-1.5)}$$

in which

$$DC_{14} = D_{114}\, e^{\alpha t_3}\ ; DC_{11} = \frac{V_d}{R_{eq}}$$

$$\beta_{12} = \omega t_3 + \delta_{112} \qquad \text{(C-1.6)}$$

3) $i_{A4}(t_a)$ = Eq. (7.2.36)

$$t_a = t - t_4 \text{ with } t_4 < t < t_5 \qquad \text{(C-1.7)}$$

$$i_{A4}(t) = DC_{15}\, e^{-\alpha_1 t} \sin(\omega_1 t + \beta_{13})$$

$$+ K_3 \sin(\omega t + \beta_{14}) \qquad \text{(C-1.8)}$$

where

$$DC_{15} = K_6\, e^{-\alpha_1 t_4}\ ;\ \beta_{13} = -\omega_1 t_4 + \alpha_6$$

$$\beta_{14} = -\omega t_4 + \beta_2 \qquad \text{(C-1.9)}$$

4) $i_{A5}(t')$ = Eq. (7.3.123)

$$t' = t - t_5 \text{ with } t_5 < t < t_6 \qquad \text{(C-1.10)}$$

$$i_{A5}(t) = DC_{16}\, e^{mt} \sin(nt+\beta_{15})$$

$$+ DB_{12} \sin(\omega t+\beta_{16}) + DC_{17}\, e^{D_{12}t}$$

$$+ DC_{18}\, e^{-\alpha t} + DC_{11} \qquad \text{(C-1.11)}$$

in which

$$\left(\begin{array}{l} DC_{16} = D_{108}\, e^{-mt_5} \;;\; \beta_{15} = -nt_5 + \delta_{108} \\ \beta_{16} = -\omega t_5 + \gamma_{12} \;;\; DC_{17} = D_{107}\, e^{-D_{12}t_5} \end{array} \right)$$

$$DC_{18} = \left(D_{93} - \frac{V_d}{R_{eq}}\right) e^{\alpha t_5} \qquad \text{(C-1.12)}$$

5) $i_{A6}(t'') = \text{Eq. (7.4.23)}$

$$t'' = t - t_6 \text{ with } t_6 < t < t_7 \qquad \text{(C-1.13)}$$

$$i_{A6}(t) = DC_{19}\, e^{-\alpha t} + DC_{11} + DC_{115} \sin(\omega t+\beta_{17}) \qquad \text{(C-1.14)}$$

where

$$DC_{19} = D_{114}\, e^{\alpha t_6} \;;\; DC_{11} = \frac{V_d}{R_{eq}}$$

$$\beta_{17} = -\omega t_6 + \delta_{112} \qquad \text{(C-1.15)}$$

6) $i_{A7}(t_a)$ = Eq. (7.2.36)

$$t_a = t - t_7 \text{ with } t_7 < t < t_8 \qquad \text{(C-1.16)}$$

$$i_{A7}(t) = DC_{20}\, e^{-\alpha_1 t} \sin(\omega_1 t + \beta_{18})$$

$$+ K_3 \sin(\omega t + \beta_{19}) \qquad \text{(C-1.17)}$$

where

$$DC_{20} = K_6\, e^{\alpha_1 t_7} \; ; \; \beta_{18} = -\omega_1 t_7 + \alpha_6$$

$$\beta_{19} = -\omega t_7 + \beta_2 \qquad \text{(C-1.18)}$$

7) $i_{A8}(t')$ = Eq. (7.3.76)

$$t' = t - t_8 \text{ with } t_8 < t < t_9 \qquad \text{(C-1.19)}$$

$$i_{A8}(t) = DC_{21} e^{D_{12} t} + DC_{22}\, e^{mt} \sin(nt + \beta_{20})$$

$$+ DA_3 \sin(\omega t + \beta_{21}) \qquad \text{(C-1.20)}$$

in which

$$DC_{21} = D_{48}\, e^{-D_{12} t_8} \; ; \; DC_{22} = D_{52}\, e^{-m t_8}$$

$$\beta_{20} = -n t_8 + \delta_{52} \; ; \; \beta_{21} = -\omega t_8 + \lambda_1 \qquad \text{(C-1.21)}$$

The Fourier coefficients for the fundamental component of i_A can now be calculated:

$$a_1 = \frac{2}{\Pi} \int_0^{\Pi} i_A(x) \cos x \, d x$$

$$b_1 = \frac{2}{\Pi} \int_0^{\Pi} i_A(x) \sin x \, d x \qquad \text{(C-1.22)}$$

where

$$x = \omega t \text{ or } t = \frac{x}{\omega}$$

Also for the fundamental component of i_A it can be written:

$$i_{1A}(x) = a_1 \cos x + b_1 \sin x = I_{1A} \sin(x+\phi)$$

in which

$$I_{1A} = (a_1^2 + b_1^2)^{1/2}$$

$$\phi = \text{arc tan} \frac{a_1}{b_1} \qquad \text{(C-1.23)}$$

As explained in Appendix B-2, in ideal case the value of ϕ should be equal to zero.

To calculate a_1 and b_1 in (C-1.22), the different parts of i_A during half a cycle can be summarized in the following way:

$$
\begin{aligned}
i_{A1}(t) &= 0 && 0 < t < t_2 \\
i_{A2}(t) &= \text{Eq. (C-1.2)} && t_2 < t < t_3 \\
i_{A3}(t) &= \text{Eq. (C-1.5)} && t_3 < t < t_4 \\
i_{A4}(t) &= \text{Eq. (C-1.8)} && t_4 < t < t_5 \\
i_{A5}(t) &= \text{Eq. (C-1.11)} && t_5 < t < t_6 \\
i_{A6}(t) &= \text{Eq. (C-1.14)} && t_6 < t < t_7 \\
i_{A7}(t) &= \text{Eq. (C-1.17)} && t_7 < t < t_8 \\
i_{A8}(t) &= \text{Eq. (C-1.20)} && t_8 < t < t_9 \\
i_{A9}(t) &= 0 && t_9 < t < \frac{\Pi}{\omega}
\end{aligned}
\qquad \text{(C-1.24)}
$$

It then results,

$$a_1 = a_{11} + a_{12} + a_{13} + a_{14} + a_{15} + a_{16} + a_{17} + a_{18} + a_{19}$$

$$b_1 = b_{11} + b_{12} + b_{13} + b_{14} + b_{15} + b_{16} + b_{17} + b_{18} + b_{19}$$

(C-1.25)

Each term in (C-1.25) is calculated according to the following realtionships in which t has been changed into x where $x = \omega t$.

$$a_{11} = \frac{2}{\Pi} \int_0^{x_2} i_{A1}(x) \cos x \, d x = 0 \qquad \text{(C-1.26)}$$

$$a_{12} = \frac{2}{\Pi} \int_{x_2}^{x_3} i_{A2}(x) \cos x \, d x = \frac{2}{\Pi} (DC_{10} \, XI_{11}$$

$$+ DC_{11} \, XI_{21} + DC_{12} \, XI_{31} + DC_{13} \, XI_{12}$$

$$+ DA_{11} \, XI_{51}) \qquad \text{(C-1.27)}$$

where

$$XI_{11} = \int_{x_2}^{x_3} e^{-\frac{\alpha}{\omega} x} \cos x \, d x$$

$$XI_{21} = \int_{x_2}^{x_3} \cos x \, d x$$

$$XI_{31} = \int_{x_2}^{x_3} e^{\frac{m}{\omega} x} \sin(\frac{n}{\omega} x+\beta_{10}) \cos x \, d x$$

$$XI_{12} = \int_{x_2}^{x_3} e^{\frac{D_{12}}{\omega} x} \cos x \, d x$$

$$XI_{51} = \int_{x_2}^{x_3} \sin(x+\beta_{11}) \cos x \, d x \qquad \text{(C-1.28)}$$

$$a_{13} = \frac{2}{\Pi} \int_{x_3}^{x_4} i_{A3}(x) \cos x \, d x = \frac{2}{\Pi}(DC_{14} \, XI_{13}$$

$$+ DC_{11} \, XI_{22} + D_{115} \, XI_{52}) \qquad \text{(C-1.29)}$$

in which

$$XI_{13} = \int_{x_3}^{x_4} e^{-\frac{\alpha}{\omega} x} \cos x \, d x$$

$$XI_{22} = \int_{x_3}^{x_4} \cos x \, d x$$

$$XI_{52} = \int_{x_3}^{x_4} \sin(x+\beta_{12}) \cos s \, d x \qquad \text{(C-1.30)}$$

$$a_{14} = \frac{2}{\Pi} \int_{x_4}^{x_5} i_{A4}(x) \cos x \, d x = \frac{2}{\Pi} (DC_{15} \, XI_{32}$$

$$+ K_3 \, XI_{53}) \qquad \text{(C-1.31)}$$

where

$$XI_{32} = \int_{x_4}^{x_5} e^{-\frac{\alpha 1}{\omega} x} \sin\left(\frac{\omega 1}{\omega} x+\beta_{13}\right) \cos x \, d x$$

$$XI_{53} = \int_{x_4}^{x_5} \sin (x+\beta_{14}) \cos x \, d x \qquad \text{(C-1.32)}$$

$$a_{15} = \frac{2}{\Pi} \int_{x_5}^{x_6} i_{A_5} (x) \cos x \, d x = \frac{2}{\Pi} (DC_{16} \, XI_{33}$$

$$+ DB_{12} \, XI_{54} + DC_{17} \, XI_{14} + DC_{18} \, XI_{15} + DC_{11} \, XI_{23})$$

(C-1.33)

in which

$$XI_{33} = \int_{x_5}^{x_6} e^{\frac{m}{\omega} x} \sin \left(\frac{n}{\omega} x+\beta_{15}\right) \cos x \, d x$$

$$XI_{54} = \int_{x_5}^{x_6} \sin (x+\beta_{16}) \cos x \, d x$$

$$XI_{14} = \int_{x_5}^{x_6} e^{\frac{D_{12}}{\omega} x} \cos x \, d x$$

$$XI_{15} = \int_{x_5}^{x_6} e^{-\frac{\alpha}{\omega} x} \cos x \, d x$$

$$XI_{23} = \int_{x_5}^{x_6} \cos x \, d x \qquad \text{(C-1.34)}$$

$$a_{16} = \frac{2}{\Pi}\int_{x_6}^{x_7} i_{A6}(x) \cos x \, d x = \frac{2}{\Pi} (DC_{19} \; XI_{131}$$

$$+ DC_{11} \; XI_{221} + D_{115} \; XI_{521}) \qquad \text{(C-1.35)}$$

where

$$XI_{131} = \int_{x_6}^{x_7} e^{-\frac{\alpha}{\omega} x} \cos x \, d x$$

$$XI_{221} = \int_{x_6}^{x_7} \cos x \, d x$$

$$XI_{521} = \int_{x_6}^{x_7} \sin(x+\beta_{17}) \cos x \, d x \qquad \text{(C-1.36)}$$

$$a_{17} = \frac{2}{\Pi} \int_{x_7}^{x_8} i_{A7}(x) \cos x \, d x = \frac{2}{\Pi} (DC_{20} \; XI_{321}$$

$$+ K_3 \; XI_{531}) \qquad \text{(C-1.37)}$$

in which

$$XI_{321} = \int_{x_7}^{x_8} e^{-\frac{\alpha_1}{\omega} x} \sin\left(\frac{\omega_1}{\omega} x+\beta_{18}\right) \cos x \, d x$$

$$XI_{531} = \int_{x_7}^{x_8} \sin(x+\beta_{19}) \cos x \, d x \qquad \text{(C-1.38)}$$

$$a_{18} = \frac{2}{\Pi} \int_{x_8}^{x_9} i_{A8}(x) \cos x \, d x = \frac{2}{\Pi} (DC_{21} \; XI_{16}$$

$$DC_{22} \; XI_{34} + DA_3 \; XI_{55}) \qquad \text{(C-1.39)}$$

where

$$XI_{16} = \int_{x_8}^{x_9} e^{\frac{D_{12}}{\omega} x} \cos x \, d x$$

$$XI_{34} = \int_{x_8}^{x_9} e^{\frac{m}{\omega} x} \sin(\tfrac{n}{\omega} x + \beta_{20}) \cos x \, d x$$

$$XI_{55} = \int_{x_8}^{x_9} \sin(x + \beta_{21}) \cos x \, d x \qquad \text{(C-1.40)}$$

$$a_{19} = \frac{2}{\Pi} \int_{x_9}^{\Pi} i_{A9}(x) \cos x \, d x = 0 \qquad \text{(C-1.41)}$$

$$b_{11} = \frac{2}{\Pi} \int_{0}^{x_2} i_{A1}(x) \sin x \, d x = 0 \qquad \text{(C-1.42)}$$

$$b_{12} = \frac{2}{\Pi} \int_{x_2}^{x_3} i_{A2}(x) \sin x \, d x = \frac{2}{\Pi} (DC_{10} \; XI_{61}$$

$$+ DC_{11} \; XI_{71} + DC_{12} \; XI_{81} + DC_{13} \; XI_{62} + DA_{11} \; XI_{91})$$

$$\text{(C-1.43)}$$

where

$$XI_{61} = \int_{x_2}^{x_3} e^{-\frac{\alpha}{\omega} x} \sin x \, d x \; ; \; XI_{71} = \int_{x_2}^{x_3} \sin x \, d x$$

$$XI_{81} = \int_{x_2}^{x_3} e^{\frac{m}{\omega} x} \sin(\frac{n}{\omega} x+\beta_{10}) \sin x \, d x$$

$$XI_{62} = \int_{x_2}^{x_3} e^{\frac{D_{12}}{\omega}} \sin x \, d x$$

$$XI_{91} = \int_{x_2}^{x_3} \sin(x+\beta_{11}) \sin x \, d x \qquad \text{(C-1.44)}$$

$$b_{13} = \frac{2}{\Pi} \int_{x_3}^{x_4} i_{A3}(x) \sin x \, d x = \frac{2}{\Pi} (DC_{14} \, XI_{63}$$

$$+ DC_{11} \, XI_{72} + D_{115} \, XI_{92}) \qquad \text{(C-1.45)}$$

where

$$XI_{63} = \int_{x_3}^{x_4} e^{\frac{\alpha}{\omega} x} \sin x \, d x$$

$$XI_{72} = \int_{x_3}^{x_4} \sin x \, d x$$

$$XI_{92} = \int_{x_3}^{x_4} \sin(x+\beta_{12}) \sin x \, d x \qquad \text{(C-1.46)}$$

$$b_{14} = \frac{2}{\Pi} \int_{x_4}^{x_5} i_{A4}(x) \sin x \, d x = \frac{2}{\Pi} (DC_{15} \, XI_{82}$$

$$+ K_3 \, XI_{93}) \qquad \text{(C-1.47)}$$

in which

$$XI_{82} = \int_{x_4}^{x_5} e^{-\frac{\alpha_1}{\omega} x} \sin \left(\frac{\omega_1}{\omega} x + \beta_{13}\right) \sin x \, d x$$

$$XI_{93} = \int_{x_4}^{x_5} \sin (x + \beta_{14}) \sin x \, d x \qquad \text{(C-1.48)}$$

$$b_{15} = \frac{2}{\Pi} \int_{x_5}^{x_6} i_{A5}(x) \sin x \, d x = \frac{2}{\Pi} (DC_{16} \, XI_{83}$$

$$+ DB_{12} \, XI_{94} + DC_{17} \, XI_{64} + DC_{18} \, XI_{65} + DC_{11} \, XI_{73})$$

$$\text{(C-1.49)}$$

where

$$XI_{83} = \int_{x_5}^{x_6} e^{\frac{m}{\omega} x} \sin \left(\frac{n}{\omega} x + \beta_{15}\right) \sin x \, d x$$

$$XI_{94} = \int_{x_5}^{x_6} \sin (x + \beta_{16}) \sin x \, d x$$

$$XI_{64} = \int_{x5}^{x_6} e^{\frac{D_{12}}{\omega} x} \sin x \, d x$$

$$XI_{65} = \int_{x_5}^{x_6} e^{-\frac{\alpha}{\omega} x} \sin x \, d x$$

$$XI_{73} = \int_{x_5}^{x_6} \sin x \, d x \qquad \text{(C-1.50)}$$

$$b_{16} = \frac{2}{\Pi} \int_{x_6}^{x_7} i_{A6}(x) \sin x . d x = \frac{2}{\Pi} (DC_{19} \, XI_{631}$$

$$+ DC_{11} \, XI_{721} + D_{115} \, XI_{921}) \qquad \text{(C-1.51)}$$

in which

$$XI_{631} = \int_{x_6}^{x_7} e^{-\frac{\alpha}{\omega} x} \sin x \, d x$$

$$XI_{721} = \int_{x_6}^{x_7} \sin x \, d x$$

$$XI_{921} = \int_{x_6}^{x_7} \sin (x+\beta_{17}) \sin x \, d x \qquad \text{(C-1.52)}$$

$$b_{17} = \frac{2}{\Pi} \int_{x_7}^{x_8} i_{A7}(x) \sin x \, d x = \frac{2}{\Pi} (DC_{20} \, XI_{821}$$

$$+ K_3 \, XI_{931}) \qquad \text{(C-1.53)}$$

where

$$XI_{821} = \int_{x_7}^{x_8} e^{-\frac{\alpha_1}{\omega} x} \sin (\frac{\omega_1}{\omega} x + \beta_{18}) \sin x \, d x$$

$$XI_{931} = \int_{x_7}^{x_8} \sin(x+\beta_{19}) \sin x \, d x \quad \text{(C-1.54)}$$

$$b_{18} = \frac{2}{\Pi} \int_{x_8}^{x_9} i_{A8}(x) \sin x \, d x = \frac{2}{\Pi} (DC_{21} \, XI_{66}$$

$$+ DC_{22} \, XI_{84} + DA_3 \, XI_{95}) \quad \text{(C-1.55)}$$

where

$$XI_{66} = \int_{x_8}^{x_9} e^{\frac{D_{12}}{\omega} x} \sin x \, d x$$

$$XI_{84} = \int_{x_8}^{x_9} e^{\frac{m}{\omega} x} \sin\left(\frac{n}{\omega} x + \beta_{20}\right) \sin x \, d x$$

$$XI_{95} = \int_{x_8}^{x_9} \sin(x+\beta_{21}) \sin x \, d x \quad \text{(C-1.56)}$$

$$b_{19} = \frac{2}{\Pi} \int_{x_9}^{\Pi} i_{A9}(x) \sin x \, d x = 0 \quad \text{(C-1.57)}$$

The types of integrals involved in the preceding computations are the same as integrals G_1 - G_6 given by (B-2.33) - (B-2.38) and integrals G_7 - G_8 shown by (B-3.23) - (B-3.24) in Appendices B2 and B3, respectively.